Topics of LIGO Physics: Quantum Noise in Advanced Interferometers and Template Banks for Compact-Binary Inspirals

Thesis by

Yanbei Chen

In Partial Fulfillment of the Requirements

for the Degree of

Doctor of Philosophy

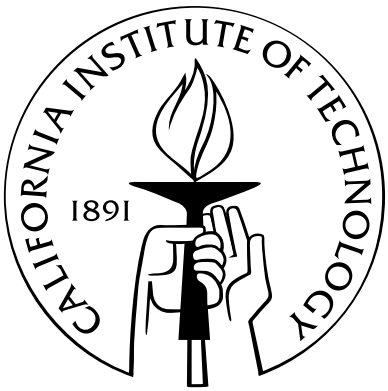

California Institute of Technology

Pasadena, California

2003

(Defended May 8, 2003)

Acknowledgements

First of all, I would like to thank Kip Thorne, for being a great teacher and advisor, for constant support and encouragements on my study and research, and for painstakingly teaching me how to write scientific papers. I am deeply thankful to Alessandra Buonanno, for fruitful collaborations on numerous projects, which have contributed to a great portion of what I learned over the past few years, as well as 6 chapters of this thesis. I am very thankful to Michele Vallisneri for exciting collaborations on the binary-inspiral projects, also for sharing with me the LaTeX files of his thesis, which greatly accelerated the preparation of this thesis. I am very thankful to Patricia Purdue for sharing the original idea of speed meter and for collaborating with me on the analysis of the Purdue-Chen speed meters. I am also very thankful to Ron Drever, from whom I learned about Sagnac interferometers as gravitational-wave detectors.

I am very thankful to Nergis Mavalvala for collaboration on the analysis of heterodyne readout scheme. I wish to thank Nergis and Biplab Bhawal, Erika D'Ambrosio, Riccardo de Salvo, Adreas Freise, Peter Fritschel, Martin Hewitson, Yuri Levin, Yuk Tung Liu, Jim Mason, Guido Mueller, Richard O'Shaughnessy, Malik Rakhmanov, Shanti Rao, David Shoemaker, Ken Strain, Alan Weinstein, Phil Willems and Benno Willke for teaching and discussing with me the experimental (optical, mechanical, thermal and quantum) physics in current and future gravitational-wave interferometers. I especially thank Stan Whitcomb for numerious stimulating discussions about advanced interferometer configurations, and for teaching me a lot of experimental physics. I am also thankful to Hideo Mabuchi for discussions on quantum measurement theory and quantum optics. I am very thankful to Karsten Danzmann, Roman Schnabel, Jan Harms, Simon Chelkowski, Alexander Franzen, Henning Vahlbruch at AEI-Hannover for discussions and in particular for collaboration on the study the variational input-squeezing scheme for signal recycled interferometers (this work is not included in this thesis). I wish to thank Vladimir Braginsky and Farid Khalili for enlightening discussions on gravitational-wave detectors as quantum measurement devices, where their insights are so valuable.

I wish to thank Kashif Alvi, Theocharis Apostolatos, Stas Babak, Leor Barack, Luc Blanchet, Sukanta Bose, Patrick Brady, Duncan Brown, David Chernoff, Teviet Creighton, Curt Cutler, Sanjeev Dhurandhar, Jeff Edlund, Achamveedu Gopakumar, Philippe Grandclément, Ik Siong Heng, Bala Iyer, Vicky Kalogera, Erik Katsavounidis, Larry Kidder, Shane Larson, Soumya Mohanty,

Soma Mukherjee, Ben Owen, Yi Pan, B.S. Sathyaprakash, Peter Shawhan, Massimo Tinto, Alberto Vecchio, and Linqing Wen for discussions on Post-Newtonian waveforms and/or data analysis issues.

Special thanks go to Albrecht Rüdiger, for all the warm encouragements I received from him and for his painstaking proofreadings and comments on my manuscripts.

Although this thesis in the end contains only theory, I wish to thank colleagues at the Australian National University, where for the first time I did some research in experimental physics: David McClelland, Malcom Gray, Glenn de Vine, Conor Mow-Lowry, Ben Sheard, Bram Slagmolen, John Sandeman and Ping Koy Lam. A great deal of thanks go to Glenn, who had been so patient with me all along in the experiment. I am also deeply thankful to Stan and Laurie Whitcomb, who had been so kind in arranging everything for my wife and me.

In addition to the above, I would like to thank Mihai Bondarescu, Lior Burko, Hua Fang, Jonathan Gair, Mike Hartl, Scott Hughes, Frans Pretorius, Lee Lindblom, and Mark Scheel for useful discussions and all others who attend Kip and Lee's group meeting, where a lot more of the interesting discussions are made. I am also very grateful to Chris Mach, who has been solving so many computer problems for me.

I would like to thank Shirley Hampton, Jennifer Formichelli, Donna Driscoll and Helen Ticehurst for helping me with administrative matters.

I am greatly indebted to my family, for providing a tradition of academic excellence, and for encouraging and inspiring me all through my education. I thank my wife, Ying, for taking care of everything, and for putting up with the amount of time and effort I have been devoting to my study and research.

Research presented in this thesis is supported by NSF grants PHY-9900776, PHY-0099568, also by the David and Barbara Groce Fund at the San Diego Foundation. I wish to thank Dr. and Mrs. David and Barbara Groce for their generous donation to Kip, from which I obtained precious travel funds.

Abstract

This thesis deals with the planning for advanced interferometric gravitational-wave detectors (of second generation and beyond), as well as the detection of inspiral waves using initial interferometers (LIGO-I).

In the design of advanced interferometric gravitational-wave detectors, the interferometer's quantum-noise performance will likely be one of the central issues — due to the so-called Standard Quantum Limit, which prevents the more conventional interferometer designs from improving beyond second-generation sensitivity. This issue is studied in the first part (Chapters 2 – 7) of this thesis, by presenting a sequence of papers written by the author and collaborators for journal publications:

- In Chapters 2 – 4 (in collaboration with Alessandra Buonanno), the signal recycling optical configuration proposed for LIGO-II is studied in the two-photon quantum-optics formalism. Contrary to previous beliefs, we show in Chapter 2 that this configuration can already beat the Standard Quantum Limit by a moderate amount (factor ~ 2 in power) in a relatively broad frequency band ($\Delta f \sim f$) — due to optomechanical resonances induced by the detuned signal recycling configuration, through the *optical spring* effect, which is discussed in detail in Chapter 3. The optomechanical resonance is shown to be always unstable, and hence must be suppressed by an appropriate control system. An idealized linear control scheme is analyzed in the Heisenberg picture, and shown to leave the interferometer's noise spectrum unchanged. In Chapter 4, we derive a scaling law in the interferometer parameters that can help the design and optimization of signal recycled interferometers. The physics of these interferometers, as expressed in scaling-invariant forms, can thus also be much more easily understood.

- In Chapter 5 (in collaboration with Alessandra Buonanno and Nergis Mavalvala), the quantum noise in heterodyne readout schemes for advanced configurations is studied. In these readout schemes, more than one output quadrature can be measured, but at the price of additional noise. It is shown in the chapter that the additional heterodyne noise can largely overcome the advantage brought by the ability of measuring multiple output quadratures. In particular, for interferometers without detuning, the heterodyne readout schemes, even by measuring multiple output quadratures, cannot yield a better performance than an ordinay homodyne detection.

- In Chapter 6 (in collaboration with Patricia Purdue), a "Speed-Meter interferometer" with Michelson topology, invented by the author based on the previous works of BGKT (Braginsky, Khalili, Gorodetsky and Thorne) and Patricia Purdue, is analyzed as a candidate design for third-generation interferometers (LIGO-III or EURO). This Purdue-Chen speed meter, as the (in fact mathematically equivalent) BGKT speed meters, can beat the Standard Quantum Limit by a uniform factor in a broad frequency band using ordinary homodyne detection — given enough optical power, with an SQL-beating factor (in power) roughly proportional to the optical power. For example, it can beat the SQL by a factor of 10 in power for $f \lesssim 150\,\mathrm{Hz}$, as a circulating power of 820 kW and input squeezing factor of $e^{2R} = 10$ are used. However, the Purdue-Chen speed meter, requiring one additional kilometer-scale cavity to be added to the dark port of a conventional Michelson interferometer, has a topology that can be far more easily implemented than the BGKT speed meters. [It requires one less such kilometer-scale cavity than the QND position meter proposed by KLMTV (Kimble, Levin, Matsko, Thorne and Vyatchanin), the only plausible proposal for LIGO-III before this thesis.] The speed meter is also shown to be characteristically much less susceptible to optical losses than QND schemes based on conventional interferometers (position meters). It is also shown that additional, KLMTV-like optical filters can greatly enhance the high-frequency performance of speed meters.

- In Chapter 7, the quantum noise of Sagnac interferometers is analyzed, with the simple motivation that, as Sagnac interferometers only measure the time-dependent part of relative mirror motion, they must be automatically speed meters — without the need of any additional kilometer-scale cavities. A broadband QND performance similar to that of the Michelson speed meters is easily confirmed. This, combined with certain technical advantages of the Sagnac optical topology, in particular the compatibility with all-reflective optical systems, makes Sagnac interferometers a strong candidate for third generation interferometers.

The second part (Chapters 8 and 9) of this thesis contains two papers, written by Alessandra Buonanno, Michele Vallisneri and the author, for journal publications, that study the detection in initial interferometers of late-stage–inspiral waves from binary black holes or neutron-star–black-hole binaries, which are among the most promising sources. Two issues arise in the late-stage inspirals that can complicate the construction of templates required by the optimal matched filtering technique which is going to be used for detecting such signals:

- If the black hole carries a significant spin that is misaligned with the orientation of the binary orbit, the orbital plane will precess under general relativistic spin-orbit and spin-spin effects, and modulate the gravitational waveform significantly. Templates for non-spinning binaries are incapable of catching these waves, while (naively) 15 parameters are required to describe

fully the waveform — yet constructing and searching over a 15-parameter template family does not seem to be practical.

- In later stages of the inspiral, Post-Newtonian (PN) techniques used to calculate the motion and waveforms break down, deteriorating the accuracy of the resulting theoretical templates, thereby lowering detection efficiency.

In Chapter 8, we study the PN breakdown in non-spinning binaries, by reviewing various available PN models (with different prescriptions, carried up to different orders), and comparing their waveform predictions. Our study suggests that different PN models, although give rather different predictions on the waveforms of a specific binary (due to loss of accuracy at the late stages of inspirals), yield waveforms that span similar function spaces. In light of this, we propose the use of *Detection Template Families (DTFs)* — phenomenological templates that are capable of mimicking to a high extent all the predictions of different PN models and hence plausible to catch the true waveform, yet do not provide straightforward parameter estimation of the detected binary. Two classes of such DTFs are proposed, one in the frequency domain, which takes the form of the PN-expanded Stationary-Phase-Approximated template, but with the Taylor-expansion coefficients left free, rather than having them predicted by PN expansion; the other in the time domain, which uses directly the Padè or Effective-One-Body (two particular PN prescriptions) waveforms, but letting the mass ratio (ratio of reduced mass to total mass) go higher than its physical upper bound, 0.25.

In Chapter 9, we study precessing binaries, with only one version of adiabatic Post-Newtonian model, as provided by Kidder. After studying the precession dynamics following the work of ACST (Apostolatos, Cutler, Sussman and Thorne), we construct a DTF, based on a modification of the *Apostolatos' ansatz*, that can mimic the modulated waveforms reasonably well, while keeping a small number of parameters that need be searched over in a one-by-one manner (intrinsic parameters) — by converting most of the parameters into *extrinsic* parameters, which can be searched over automatically. In that chapter, we also propose a prescription of searching over the entire physical parameter space of neutron-star–black-hole binaries (in circular orbits, with neutron-star spin ignored), by means of converting as many parameters into extrinsic parameters as possible, leaving only 4 (intrinsic) parameters to be searched over one by one. This prescription is currently being investigated by Yi Pan, Alessandra Buonanno, Michele Vallisneir and the author.

Contents

Acknowledgements **iii**

Abstract **v**

1 Introduction **1**

1.1 Analysis and design of advanced gravitational-wave interferometers: beating the Standard Quantum Limit 1

1.1.1 The Standard Quantum Limit and Quantum Nondemolition 3

1.1.2 Signal recycled interferometers in LIGO-II 7

1.1.3 Gravitational-wave interferometers with heterodyne readout scheme 11

1.1.4 Speed-meter interferometers with Michelson topology 13

1.1.5 Sagnac interferometers as speed meters 16

1.2 Detecting compact binary objects with first-generation interferometric gravitational-wave detectors 21

1.2.1 Post-Newtonain waveforms of late-stage inspirals with vanishing spins 22

1.2.2 Detection Template Families for nonspinning binaries 27

1.2.3 Challenge and importance of detecting spinning compact binaries 29

1.2.4 Features of precession dynamics and the Apostolatos Ansatz 31

1.2.5 The Modified Apostolatos Ansatz and DTF for spinning binaries 32

1.3 Bibliography 37

2 Quantum noise in second generation, signal-recycled laser interferometric gravitational-wave detectors **43**

2.1 Introduction 43

2.2 Signal-recycling interferometer: input–output relations 46

2.2.1 Naive extension of KLMTV's results to SR interferometers 46

2.2.2 Discussion of the naive result 53

2.3 Features of noise spectral density in SR interferometers 54

2.3.1 Evaluation of the noise spectral density: going below the standard quantum limit . . . 54
2.3.2 Effective shot noise and radiation-pressure noise . . . 58
2.3.3 Two special cases: extreme signal-recycling and resonant-sideband-extraction configurations . . . 61
2.3.3.1 Extreme signal-recycling (ESR) configuration: $\phi = 0$ . . . 62
2.3.3.2 Extreme resonant-sideband-extraction (ERSE) configuration: $\phi = \pi/2$ 62
2.4 Structure of resonances and instabilities . . . 64
2.4.1 Resonances of the closed system: $\rho = 1$ . . . 64
2.4.2 Semiclassical interpretation of resonances for small $\mathcal{K}$: pure optical resonances 67
2.4.3 Quantum mechanical discussion of the general case: two resonances and $\rho \neq 1$ 69
2.5 Inclusion of losses in signal-recycling interferometers . . . 70
2.6 Conclusions . . . 73
2.7 Appendix. Remark on commutation relations among quadrature fields in Caves-Schumaker two-photon formalism . . . 77
2.8 Bibliography . . . 81

3 Signal recycled laser-interferometer gravitational-wave detectors as optical springs 85
3.1 Introduction . . . 85
3.2 Quantum-measurement systems . . . 89
3.2.1 General conditions defining a measurement system . . . 89
3.2.2 Equations of motion of a linear quantum-measurement system: the force-susceptibility formalism . . . 92
3.2.3 Conditions defining a linear measurement system in terms of susceptibilities . 96
3.2.4 Effective description of measurement systems . . . 98
3.3 Dynamics of signal recycled interferometers: equations of motion . . . 101
3.3.1 Identifying the dynamical variables and their interactions . . . 102
3.3.2 Free evolutions of test mass and optical field . . . 104
3.3.3 Coupled evolution of test mass and optical field: ponderomotive rigidity . . . 108
3.4 Dynamics of signal recycled interferometers: resonances and instabilities . . . 111
3.4.1 Physical origins of the two pairs of resonances . . . 112
3.4.2 Quantitative investigation of the resonances . . . 113
3.4.3 Characterization of mechanical instabilities . . . 116
3.5 Control systems for signal recycled interferometers . . . 118
3.5.1 Generic feedback control systems: changing the dynamics without affecting the noise . . . 118

3.5.2 An example of a servo system: effective damping of the test-mass 121
3.6 Conclusions 123
3.7 Appendix. Basic properties of linear systems 125
3.8 Bibliography 131

4 Scaling law in signal recycled laser-interferometer gravitational-wave detectors 135
4.1 Introduction 135
4.2 Derivation of scaling law 138
4.2.1 Equivalent three-mirror–cavity description of signal-recycled interferometer . 138
4.2.2 The scaling law in generic form 141
4.2.3 The scaling law in terms of interferometer parameters 142
4.3 Input–output relation and noise spectral density in terms of characteristic parameters 145
4.3.1 Input–output relation 145
4.3.2 Noise spectral density 147
4.4 Optomechanical dynamics in terms of characteristic parameters 148
4.4.1 Radiation-pressure force 148
4.4.2 Equivalence between noise correlations and change of dynamics 150
4.4.3 Equivalence to a single detuned cavity and frequency-dependent rigidity . . . 153
4.4.4 Optical spring equivalent to mechanical spring but at zero temperature . . . 157
4.5 Input–output relation at all orders in transmissivity of internal test-mass mirrors . . 159
4.5.1 Free optical resonant frequencies 160
4.5.2 Input–output relation and noise spectral density 160
4.6 Conclusions 165
4.7 Appendix. Useful relations in the quadrature formalism 169
4.8 Appendix. The Stokes relations 173
4.9 Appendix. Input–output relations at second order in transmissivity of internal test masses 175
4.10 Bibliography 177

5 Quantum noise in laser-interferometer gravitational-wave detectors with a heterodyne readout scheme 179
5.1 Introduction 179
5.2 The radio-frequency modulation-demodulation scheme in advanced LIGO 182
5.2.1 Overview of Advanced LIGO optical configuration 182
5.2.2 Modulation and demodulation processes 183
5.2.3 Demodulated output of LIGO interferometers 185
5.2.4 Features of the RF modulation-demodulation scheme 188

5.3 Noise spectral density and the effect of the additional noise . . . 189
5.3.1 Total noise spectral density . . . 189
5.3.2 Conventional interferometers . . . 190
5.3.3 Signal-recycled interferometers . . . 193
5.4 More general discussion of heterodyne schemes: minimal additional noise and quantum limit . . . 195
5.4.1 Quantum Limit for the additional heterodyne noise . . . 195
5.4.2 Impact of the Quantum Limit on conventional interferometers . . . 200
5.5 Conclusions . . . 202
5.6 Bibliography . . . 203

6 Practical speed meter designs for QND gravitational-wave interferometers 207
6.1 Introduction . . . 208
6.2 Mathematical description of the interferometer . . . 215
6.3 Speed meter in the lossless limit . . . 217
6.3.1 Mathematical analysis . . . 217
6.3.2 Optimization . . . 220
6.3.3 Discussion of three-cavity speed-meter design . . . 225
6.4 Squeezed vacuum and FD homodyne dectection . . . 226
6.4.1 Injection of squeezed vacuum into dark port . . . 226
6.4.2 Frequency-dependent homodyne detection . . . 228
6.5 Optical losses . . . 230
6.5.1 Internal losses . . . 231
6.5.2 Internal and external losses in compact form . . . 233
6.5.3 Performance of lossy speed meters and comparisons with other configurations 235
6.6 Conclusions . . . 239
6.7 Appendix. FP cavities as optical filters . . . 241
6.8 Appendix. Semi-analytical treatment of the loss terms . . . 243
6.8.1 Arms, Extraction mirror, and Sloshing cavity (AES) . . . 243
6.8.2 Port-closing mirror . . . 244
6.8.3 The RSE cavity . . . 245
6.8.4 Detection and filter cavities . . . 248
6.9 Appendix. Effects due to mode-mismatching: a simple analysis . . . 251
6.10 Appendix. Transmissivity mismatch between the internal mirror and the RSE mirror 255
6.11 Bibliography . . . 257

7 Sagnac interferometer as a speed-meter-type, quantum-nondemolition gravitational-wave detector 259

7.1 Introduction . . . 259

7.2 The Sagnac as a speed meter, and its input-output relations . . . 262

7.2.1 The Sagnac optical configuration . . . 262

7.2.2 The Sagnac's speed-meter behavior . . . 263

7.2.3 Input-output relations without a signal-recycling mirror . . . 264

7.2.4 Influence of signal recycling on the input-output relations . . . 266

7.2.5 Frequency dependence of coupling constants $\mathcal{K}$, and Sagnac interferometers as speed meters . . . 268

7.3 Noise spectral density . . . 268

7.4 Discussion of technical issues . . . 270

7.5 Conclusions . . . 270

7.6 Appendix. Input-output relations for the arms . . . 277

7.6.1 Optical delay line (DL) . . . 277

7.6.2 Ring-shaped Fabry-Perot cavity (FP) . . . 279

7.7 Bibliography . . . 283

8 Detection template families for gravitational waves from the final stages of binary–black-hole inspirals: Nonspinning case 285

8.1 Introduction . . . 285

8.2 The theory of matched-filtering signal detection . . . 291

8.2.1 The statistical theory of signal detection . . . 291

8.2.2 Template families and extrinsic parameters . . . 292

8.2.3 Imperfect detection and discrete families of templates . . . 295

8.2.4 Approximations for detector noise spectrum and gravitational-wave signal . . . 297

8.3 Adiabatic models . . . 301

8.3.1 Adiabatic PN expanded models . . . 301

8.3.2 Adiabatic PN resummed methods: Padé approximants . . . 307

8.4 Nonadiabatic models . . . 313

8.4.1 Nonadiabatic PN expanded methods: Hamiltonian formalism . . . 313

8.4.2 Nonadiabatic PN expanded methods: Lagrangian formalism . . . 321

8.4.3 Nonadiabatic PN resummed methods: the Effective-One-Body (EOB) approach 323

8.4.4 Features of the late dynamical evolution in nonadiabatic models . . . 330

8.5 Signal-to-noise ratio for the two-body models . . . 334

8.6 Performance of Fourier-domain detection templates, and construction of a Fourier-domain detection-template bank . . . 340
8.6.1 Internal match and metric . . . 343
8.6.2 Construction of the effective template bank: parameter range . . . 345
8.6.3 Construction of the effective templates bank: parameter density . . . 349
8.6.4 Parameter estimation with the detection template family . . . 353
8.6.5 Extension of the two-dimensional Fourier-domain detection template . . . 354
8.6.6 Extension of the Fourier-domain detection template family to more than two phasing parameters . . . 356
8.7 Performance of the time-domain detection templates and construction of the detection bank in time domain . . . 363
8.8 Summary . . . 373
8.9 Bibliography . . . 376

9 Detecting gravitational waves from precessing binaries of spinning compact objects: Adiabatic limit 381
9.1 Introduction . . . 381
9.2 Definition of the target model . . . 384
9.2.1 Equations for an adiabatic sequence of precessing spherical orbits . . . 385
9.2.2 Endpoint of evolution . . . 387
9.2.3 Gravitational waveforms . . . 387
9.2.4 Binary and detector parameters . . . 391
9.3 Analysis of precessional dynamics . . . 393
9.3.1 The ACST analysis . . . 394
9.3.2 Conservation laws and GW ending frequencies . . . 395
9.3.3 Energy radiated during inspiral and (estimated) total angular-momentum emitted after inspiral . . . 397
9.3.4 Spin-orbit and spin-spin effects on the accumulated orbital phase . . . 399
9.3.5 Simple and transitional precession of total angular momentum . . . 401
9.3.6 Apostolatos' power law for orbital precession . . . 403
9.4 Definition of modulated DTFs for precessing binaries . . . 407
9.4.1 A new convention for GW generation in spinning binaries . . . 407
9.4.2 Definition of a new DTF for precessing binaries . . . 411
9.4.3 Definition of the standard SPA template families . . . 413
9.5 GW data analysis with the DTF . . . 415
9.5.1 Maximization of the overlap over template parameters . . . 415

9.5.2 False-alarm statistics of the DTFs 417
9.6 Evaluation of DTF performance 421
9.6.1 Effect of directional parameters on FF and SA 421
9.6.2 A Monte Carlo procedure to evaluate DTF performance 423
9.6.3 Performance indices for the standard SPA templates and for the modulated DTFs 425
9.6.4 Modulated DTFs for NS–BH binaries 433
9.7 Summary 439
9.8 Appendix. Validity of the adiabatic sequence of spherical orbits 441
9.9 Appendix. Proof that the precessing convention yields $\omega = \dot{\Phi}_S$ 445
9.10 Bibliography 447

List of Figures

1.1 Schematic views of the optical topologies of LIGO-I and LIGO-II 2

1.2 Quantum noise spectra of conventional and signal recycled interferometers 8

1.3 Optical topology of the Purdue-Chen speed meter 14

1.4 Quantum noise spectra of the Purdue-Chen speed meters and comparison with conventional and the KLMTV interferometers (position meters) 15

1.5 Optical topologies of typical Sagnac interferometers 17

1.6 Quantum noise spectra of Sagnac interferometers and comparison with Michelson (Purdue-Chen) speed meters 19

1.7 Relative visible volumes of non-spinning, equal-mass binaries with various total masses as observed by LIGO-I interferometers 24

1.8 The source (binary) frame and the detector frame 30

1.9 Definitions of the orbital and spin orientation angles 30

1.10 Dependence of neutron-star–black-hole average fitting factors on spin-orbit misalignment, for non-spinning template families and the modulated BCV template family . . 36

2.1 Schematic view of a LIGO-II signal-recycling interferometer 47

2.2 Quantum noise spectra of a signal-recycling interferometer, in the first and second output quadrautres, compared with the Standard Quantum Limit and the semiclassical result 56

2.3 Quantum noise spectra of signal-recycling interferometer, in several different output quadratures 57

2.4 Quantum noise spectra of the Extreme Signal Recycling (ESR) and Extreme Resonant Sideband Extraction (ERSE) configurations. 63

2.5 Dependence of the signal-recycled quantum noise spectra on the signal-recycling detuning phase 66

2.6 Quantum noise spectra of signal-recycling interferometers with low power and varying detuning phase. 68

2.7 Sketch of a signal-recycling interferometer with optical losses. 74

2.8 Quantum noise spectra of a lossy signal-recycing interferometer, in the first and second output quadratures, compared with the ideal ones. 74

3.1 Schematic view of signal- and power-recycled interferometer 86
3.2 Schematic diagram of a measurement device 89
3.3 Schematic diagram of a linear measurement system 93
3.4 Identification of the dynamical variables Z and F in signal-recycled interferometers . 101
3.5 Amplitude and phase of the response function R_{FF}, as functions of frequnecy 112
3.6 The optical spring 113
3.7 Shift of the optical and mechanical resonances due to increased optical power 115
3.8 Dependence of the optomechanical instability on the detuning phase 118
3.9 A control scheme for signal-recycling interferometers 119
3.10 Quenching of the instability by the effective damping introduced by the control system 122

4.1 Optical topology of a signal recycled interferometer — signal recycling cavity regarded as one single effective mirror for the signal sideband 138
4.2 Signal recycled interferometer reduced to a three-mirror cavity 140
4.3 Plot of signal recycling parameters ρ and $\phi - \pi/2$ versus bandwidth ϵ, for typical values of λ 142
4.4 Plot of signal recycling parameters ρ and $\phi - \pi/2$ versus T, for typical sets of optical resonances 144
4.5 Plot of $\sqrt{S_{h,2}}$ (continuous lines) and $\sqrt{S_{h,2}^{\min}}$ versus frequency 154
4.6 Plot of $\sqrt{S_h}$ versus frequency for the triple-zero configuration and a typical three-single-zero configuration 156
4.7 Plot of $R \equiv S_x(f)/(2\hbar\,|\Im[\chi(f)]|)$ versus frequency 157
4.8 Fractional error in λ and ϵ due to the first-order-T approximation 159
4.9 Comparison between first-order T-expanded noise spectra and the exact ones 162
4.10 Camparison between the first-order λ-ϵ-$\iota_c^{1/3}$-expanded noise spectra and the exact ones 164
4.11 Camparison between the first-order λ-ϵ-$\iota_c^{1/3}$-expanded, second-order λ-ϵ-$\iota_c^{1/3}$-expanded, and the exact noise spectra 166
4.12 Stokes' relations of two-port linear systems 173

5.1 Schematic plot of a signal and power recycled LIGO interferometer 182
5.2 Schematic plot of the ouput frequency spectrum, with signal sidebands and Schnupp modulation sidebands 184
5.3 Quantum noise spectra of conventional interferometers with heterodyne readout schemes 191

5.4 Quantum noise spectra of a signal recycled interferometer with balanced heterodyne readout schemes . . . 194
5.5 Quantum noise spectrum of a signal recycled interferometer with a totally unbalanced heterodyne readout scheme and variable-quadrature optimization . . . 196

6.1 Comparison of typical noise curves (with losses) for several interferometer configurations 209
6.2 Simple version of three-cavity design for speed-meter interferometer . . . 211
6.3 Practical three-cavity speed-meter design . . . 213
6.4 Squeezed-variational three-cavity speed-meter design . . . 214
6.5 Typical curves for the coupling constant $\kappa(\omega)$ in terms of the sloshing frequency Ω . . . 219
6.6 Typical curves for the coupling constant $\kappa(\omega)$ in terms of the optimal frequency $\omega_{\rm opt}$. 221
6.7 Squared amount by which the speed meter beats the SQL . . . 222
6.8 Noise curves corresponding to the ξ^2 curves in preceding plot . . . 222
6.9 Noise curves for varying optimal frequencies . . . 224
6.10 Comparison of typical noise curves for frequency-dependent and fixed-angle homodyne detection . . . 230
6.11 Moduli-squared of the loss factors . . . 236
6.12 Noise curves showing the effects of losses . . . 237
6.13 Comparison of noise curves of a conventional interferometer and a speed meter . . . 238
6.14 Comparison of the speed meter's κ^* with the position meter's $\mathcal{K}_*$ . . . 239
6.15 Comparison of noise curves for a squeezed-variational position meter and speed meter 240
6.16 Schematic diagram for RSE loss . . . 246

7.1 Schematic plot of a Sagnac interferometer with optical delay lines in the arms. . . . 272
7.2 Schematic plot of a Sagnac interferometer with ring cavities in the arms. . . . 272
7.3 Plot of the coupling constant versus frequency for non-signal-recycled Sagnac interferometers . . . 273
7.4 Plot of the coupling constant versus frequency for signal recycled Sagnac interferometers 274
7.5 Quantum noise spectra of non-signal-recycled Sagnac interferometers . . . 275
7.6 Quantum noise spectra of signal recycled Sagnac interferometers . . . 276

8.1 Noise spectra of LIGO-I and VIRGO . . . 298
8.2 Normalized flux function $\mathcal{F}_{T_N}/\mathcal{F}_{\rm Newt}$ versus v, at different PN orders for equal-mass binaries . . . 302
8.3 Taylor-expanded energy function $\mathcal{E}_{T_N}$ versus v, and percentage difference between neighboring PN orders . . . 303

8.4 Frequency-domain amplitude versus frequency, for T-approximated waveforms, at different PN orders . . . 306
8.5 Normalized flux function $\mathcal{F}_{P_N}/\mathcal{F}_{\rm Newt}$ versus v, at different PN orders . . . 308
8.6 Padè-expanded energy function $\mathcal{E}_{P_N}$ versus v, and percentage difference between neighboring PN orders . . . 309
8.7 Frequency-domain amplitude versus frequency, for P-approximated waveforms, at different PN orders . . . 310
8.8 Percentage difference between Taylor- and Padè- expanded energy and flux functions, at different PN orders . . . 311
8.9 Inspiraling orbits for HT$(1, 1.5)$ and HT$(3, 3.5)$ models . . . 318
8.10 Frequency-domain amplitude versus frequency, for HT- and HP- approximated waveforms, at different PN orders . . . 319
8.11 Frequency-domain amplitude versus frequency, for L-approximated waveforms, at different PN orders . . . 322
8.12 Effect of the arbitrary EOB parameter $\tilde{z}_1$ on the binding energy and ISCO frequency 327
8.13 Binding energy as functions of v, for equal-mass BBHs, as predicted by various PN models . . . 328
8.14 Frequency-domain amplitude versus frequency, for EP-approximated waveforms, at different PN orders . . . 331
8.15 Ending points of H models at 3 PN order for low values of η . . . 332
8.16 Signal-to-noise ratio at 100 Mpc versus total mass M, for selected PN models . . . 334
8.17 Effect of the plunge on the signal-to-noise ratio . . . 335
8.18 Iso-match contours in the $(\Delta\psi_0, \Delta\psi_{3/2})$ plane, and the $\Delta f_{\rm cut}$ required to obtain required matches . . . 344
8.19 Projection of the ET$(2, 2.5)$ waveforms onto the frequency-domain effective template space . . . 346
8.20 Projection of the PN waveforms onto the $(\psi_0,\psi_{3/2})$ plane . . . 348
8.21 Projection of the E models with nonzero $\tilde{z}_1$ into the $(\psi_0, \psi_{3/2})$ plane . . . 351
8.22 Projections of HT and HP models at 2PN and L models into the $(\psi_0, \psi_{3/2})$ plane . . 352
8.23 Projection of the models P$(2, 2.5)$, ET$(2, 2.5)$, ET$(3, 3.5, 0)$, and SPA(1.5) onto the three-parameter Fourier-domain detection template . . . 356
8.24 (X, Z) section of Fig. 8.23 . . . 357
8.25 Comparison of projection results into the three- and two-dimensional Fourier-domain detection template families . . . 359
8.26 Projection of 2PN waveforms onto the P$(2, 2.5)$ effective template space . . . 365
8.27 Projection of 3PN waveforms onto the P$(2, 2.5)$ effective template space . . . 365

8.28 Projection of 2PN waveforms onto the EP(3, 3.5) effective template space 367
8.29 Projection of 3PN waveforms onto the EP(3, 3.5) effective template space 367
8.30 Determinant of the mismatch metric for the P(2, 2.5) model and for the EP(3, 3.5, 0) model 368

9.1 Source and radiation frames in the FC convention 388
9.2 Detector and radiation frames in the FC convention 389
9.3 Specification of the initial Newtonian orbital angular momentum in the source frame . 391
9.4 Specification of the initial directions of the spins with respect to the FC orthonormal basis $\{\mathbf{e}_1, \mathbf{e}_2, \mathbf{e}_3\}$ 392
9.5 Ending frequencies of a binary black hole $(15 + 15)\,M_\odot$ and a neutron-star–black-hole binary $(10 + 1.4)\,M_\odot$, depending on initial spin-orbit misalignment 396
9.6 Ending frequencies of a binary black hole $(20 + 5)\,M_\odot$, depending on initial spin-orbit misalignment 397
9.7 Orbital energy and total angular momentum at the ending point of evolution 397
9.8 Example of transitional precession 402
9.9 Example of simple precession 403
9.10 Dependence of signal amplitude on the initial $\hat{\mathbf{J}}_N \cdot \hat{\mathbf{N}}$ 425
9.11 Distributions of fitting factors against the 2PN target model of the DTFs and SPA template families 426
9.12 Projections of the 2PN target signals onto the $(\psi_0\,\psi_{3/2})_2$ DTF 430
9.13 Projection of the 2PN target signals onto the $(\psi_0\,\psi_{3/2}\,\mathcal{B})_6$ DTF 430
9.14 Dependence of average fitting factors on initial spin-orbit misalignment 433
9.15 Projection of the $(10 + 1.4)M_\odot$ NS–BH target signals onto the $(\psi_0\,\psi_{3/2}\,\mathcal{B})_6$ DTF . . . 437
9.16 Projection of the $(10 + 1.4)M_\odot$ NS–BH target signals onto the $(\psi_0\,\psi_{3/2}\,\mathcal{B})_6$ DTF, continued 437

List of Tables

1.1 Estimated inspiral event rates for LIGO-I and LIGO-II 22

1.2 Parameters required to describe the waveform of a precessing binary in circular orbits 29

1.3 Average fitting factors of nonspinning templates and modulated BCV templates for spinning binary black holes and neutron-star–black-hole binaries 35

2.1 Summary of LIGO-II parameters [20]. 48

5.1 Basic quantities of Advanced LIGO interferometers 187

5.2 Quantities derived from those listed in Tab. 5.1 189

6.1 Three-arm speed-meter interferometer parameters and their fiducial values 224

6.2 Loss factors due to shot noise and radiation pressure for each type of cavity in the interferometer 234

6.3 Fiducial values for the fractional losses 235

7.1 Expressions for $\Psi_{\rm arm}$, $\mathcal{K}_{\rm arm}$, $\Psi_{\rm sagnac}$ and $\mathcal{K}_{\rm sagnac}$ for DL and FP Sagnac interferometers 264

8.1 Post-Newtonian models of two-body dynamics defined in this chapter 299

8.2 Locations of the MECO/ISCO, as predicted by various PN models 304

8.3 Test for the Cauchy convergence of the T-approximants 305

8.4 Test for the Cauchy convergence of the P-approximants 310

8.5 Test for the Cauchy convergence of the HT- and HP- approximants 317

8.6 Fitting factors for the projection of L waveforms onto T, P, EP and HP models at 2PN and 3PN orders 323

8.7 Mutual fitting factors between L and T models at $(2,0)$ and $(2,1)$ orders 323

8.8 Test for the Cauchy convergence of the EP-approximants 330

8.9 Fitting factors between several PN models, at 2PN and 3PN orders 336

8.10 Fitting factors between several PN models, at 2PN and 3PN orders, continued from Table 8.9 337

8.11 Fitting factors between T and ET models, at 2PN and 3PN orders, and for different choices of the arbitrary flux parameter $\hat{\theta}$ . . . 338
8.12 Fitting factors for the projection of EP$(3, 3.5, 0)$ templates onto themselves, for various choices of the parameters z_1 and z_2 . . . 339
8.13 End-to-end matches and ending frequencies along the BH mass lines of Fig. 8.20 . . . 347
8.14 Estimation of chirp masses from the effective template space . . . 353
8.15 Fitting factors for the projection of the target models (in the rows) onto the $(\psi_0, \psi_{3/2}, \alpha, f_{\rm cut})$ Fourier-domain detection template family . . . 362
8.16 Fitting factors for the projection of the target models (in the rows) onto the P$(2, 2.5)$ detection template family . . . 370
8.17 Fitting factors for the projection of the target models (in the rows) onto the EP$(3, 3.5, 0)$ detection template family . . . 372

9.1 Classification of binary, GW-propagation, and detector parameters. . . . 392
9.2 Modulational effects in the accumulated orbital phase . . . 399
9.3 Deviation of the total angular momentum from its initial direction . . . 401
9.4 Approximation of precession phases using power laws . . . 405
9.5 Comparison between ACST, FC and precessing conventions, based on their building elements . . . 410
9.6 Specification of the DTFs examined in this chapter. . . . 413
9.7 Detection thresholds for various linear-combination DTFs . . . 419
9.8 Average fitting factors against 2PN and 3.5PN target models, of the DTFs and SPA template families, for binary black holes . . . 427
9.9 Average fitting factors against 2PN and 3.5PN target models, of the DTFs and SPA template families, for neutron-star–black-hole binary . . . 427
9.10 Fitting factors against selected PN models of *nonspinning* binaries (see Chapter 8), for the SPAc and $(\psi_0\, \psi_{3/2}\, \alpha)_4$ template families . . . 429

Chapter 1

Introduction

After decades of planning and development, an international array of earth-based, broadband (10 Hz — 10 kHz), laser-interferometer gravitational-wave detectors, consisting of LIGO [1], VIRGO [2], GEO600 [3] and TAMA300 [4], has begun operation. In particular, the network's leading detector, LIGO, has finished its second Science Run (S2), and is expected to reach full design sensitivity by 2004. The detection of gravitational waves by these detectors, and their subsequent observations with ever improving sensitivity, will provide a new way for mankind to observe the universe. We are in an exciting stage of obtaining real science data from first-generation gravitational-wave interferometers, and planning for future upgrades of these detectors. This thesis is centered around these two issues. In this introductory chapter, I will summarize these two aspects separately. (See Secs. 1.1 and 1.2.)

1.1 Analysis and design of advanced gravitational-wave interferometers: beating the Standard Quantum Limit

Laser interferometer gravitational-wave detectors use laser interferometry to measure tiny forces exerted by the gravitational waves on mirror-endowed test masses, which hang nearly freely (with pendulum frequencies ~ 1 Hz) from seismic isolation stacks (see Fig. 1 for the optical topology of LIGO-I interferometers). The first-generation LIGO interferometers are expected to reach a noise level in the gravitational-wave channel as low as $\sqrt{S_h} \sim 3 \cdot 10^{-23}\,\mathrm{Hz}^{-1/2}$ (square root of power spectral density in the dimensionless strain h) in a broad frequency band centered around 160 Hz, with sensitivity limited by shot noise (at high frequencies, $f > 240$ Hz), suspension thermal noise (at intermediate frequencies, 40 Hz $< f <$ 240 Hz) and seismic noise (at low frequencies, $f <$ 40 Hz).

Although it is plausible that gravitational waves be detected by first-generation interferometers, a significant upgrade must be made before a rich program in observational gravitational-wave physics can be carried out [5]. The first upgrade for LIGO (called LIGO-II, or *Advanced LIGO* [6]) is planned for completion in 2008, with a design sensitivity ($\sqrt{S_h}$) 15 times better than the initial detectors. [See Fig. 1.1 for the proposed topology of LIGO-II interferometers, and Table 1.1 for

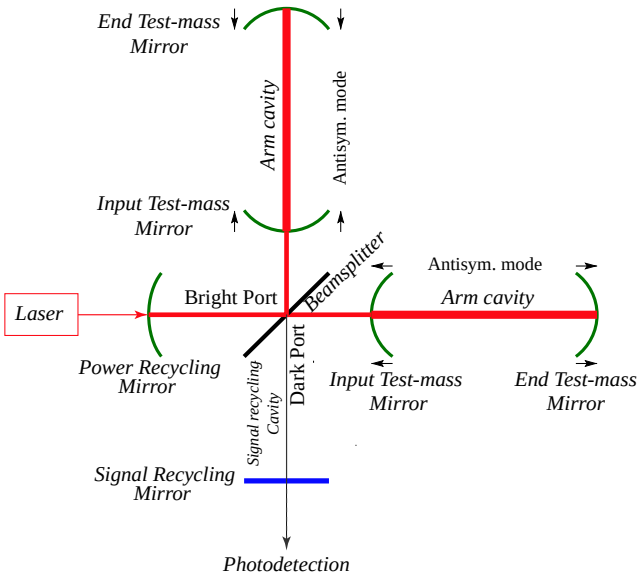

Figure 1.1: Schematic views of LIGO-I (without the signal recycling mirror) and the proposed LIGO-II (with signal recycling mirror added) interferometers. Gravitational waves exert tiny forces on the end test-mass mirrors (ETMs), whose antisymmetric motion is then measured by Michelson interferometry. Fabry-Perot cavities [formed by the input test-mass mirrors (ITMs) and the ETMs] in the Michelson arms can enhance the interferometer's sensitivity by increasing the circulating power inside the arms and the storage time of signal light. A power recycling mirror at the bright port can further increase the input power. (For LIGO-II) A signal recycling mirror at the dark port can reshape the noise spectrum and optimize for specific astrophysical sources.

current astrophysical estimates of event rates of compact binary inspirals (which are regarded as the most promising sources) for LIGO-I and LIGO-II.] A third generation of gravitational-wave interferometers, expected to be operative in the early 2010s, has already begun being widely discussed in the gravitational-wave community. These include LIGO-III, the second upgrade of the LIGO interferometers, and EURO, a European counterpart.

In second-generation interferometers and beyond, the quantum noises — noises due to the quantum fluctuations of optical fields and the quantum mechanical behavior of the test masses — will be of major importance. In fact, quantum noise performance will likely be one of the central issues for interferometer design, because of a so-called Standard Quantum Limit, which prevents the more conventional interferometer designs from improving beyond second-generation sensitivity. The first part of this thesis (Chapters 2–7) deals with the quantum noise of advanced interferometer configurations, with two aims: (i) analyzing the quantum noise spectrum of existing advanced interferometer configurations (such as the signal recycling interferometers in LIGO-II, Chapters 2–5), and (ii) identifying (or inventing) LIGO-III–era configurations that have superior quantum-noise performances (Chapters 6 and 7). While reaching for the second aim, some considerations of experimental possibilities within the next decade are also presented.

Chapters 2–7 are a sequence of papers written by the author and collaborators (Buonanno for Chapters 2–4, Buonanno and Mavalvala for Chapter 5, and Purdue for Chapter 6) for journal publications. As such, they embody the step-by-step developement of the author's understanding of the subject. We begin our introduction with a discussion of the concept of Standard Quantum Limit and its implications for gravitational-wave interferometers.

1.1.1 The Standard Quantum Limit and Quantum Nondemolition

The Standard Quantum Limit was first discovered by Braginsky in the 1960s [7, 8]. It arises in continuous measurements of the position x of a free mass m, whose Heisenberg operator $\hat{x}(t)$ at different times does not commute:

$$[\hat{x}(t), \hat{x}(t')] = i\hbar(t - t')/m\,. \tag{1.1}$$

This commutator is easily derived from the free-evolution equation

$$\hat{x}(t) = \hat{x} + \frac{\hat{p}}{m}(t - t') \tag{1.2}$$

and the commutator

$$[\hat{x}, \hat{p}] = i\hbar\,. \tag{1.3}$$

A simple way to explain the Standard Quantum Limit is to compare a gravitational-wave detector to a device that measures the positions of a free test mass successively, at times separated by τ. At a certain time t, an initial measurement of x reduces the quantum state of the test mass into one with position and momentum widths Δx and Δp, with Δx the precision of the measurement, and Δp the momentum uncertainty due to the measurement's back-action. Quantum mechanics imposes a lower limit to the back action, via the Heisenberg Uncertainty Principle, such that immediately after the initial measurement,

$$\Delta x(t)\Delta p(t) \geq \hbar^2/4\,. \tag{1.4}$$

This back-action–induced momentum perturbation will enter the subsequent future evolution of position, via free evolution between the measurements, and will thereby contribute to the future measurement noise. Assuming *statistical independence* between x and p, one has, just before the next measurement,

$$\Delta x(t+\tau) = \sqrt{\Delta x(t)^2 + \frac{\tau^2 \Delta p(t)^2}{m^2}} > \Delta x_{\rm SQL} = \sqrt{\frac{\hbar\tau}{m}}\,. \tag{1.5}$$

Here $\Delta x_{\rm SQL}$ is the Standard Quantum Limit. By contrast, devices that measure an observable whose Heisenberg operators at different times commute,

$$[\hat{O}(t), \hat{O}(t')] = 0\,, \tag{1.6}$$

are not subject to the Standard Quantum Limit, since back-action–induced perturbations on the conjugate observable will not enter the measured observable's evolution at later times. Such an observable, which can be measured continuously and precisely without having its accuracy disturbed by quantum back action, is called (by Braginsky [7, 8]) a Quantum Nondemolition (QND) observable. The device that measures it is called a QND device.

A real gravitational-wave interferometer is a composite quantum mechanical system made up of test masss and optical fields. The actual quantum measurement is performed on a particular quadrature of the outgoing optical field, via homodyne or heterodyne detection. [1] The Heisenberg operator of the measured quadrature field commutes with itself at different times. [2] The quantum mechanical description of gravitational-wave interferometers was established by Caves [11], who pointed out that the quantum noise of these devices can be attributed to the vacuum optical fields that enter the interferometer from the detection port (usually the dark port in the case of Michelson and Sagnac interferometers). This was further elucidated by Braginsky, Gorodetsky, Khalili, Matsko,

[1] This is called an "extracavity" readout scheme, and is used by all current gravitational-wave interferometers and all interferometer designs studied in this thesis. Complementary to it are "intracavity" readout schemes, for example Braginsky and Khalili's "optical-bar" detectors [9].

[2] This is true when $\Omega_{\rm GW} \ll \omega_0$ (laser frequency), see Caves and Schumaker [10] and Sec. 2.7 of this thesis.

Thorne and Vyatchanin [12], who showed that in the linearized description of gravitational-wave interferometers, the Heisenberg operator $\hat{x}(t)$ of the test-mass position appears in the output signal only at the resonant frequencies of the entire interferometer, and therefore can be readily filtered out without affecting the overall, broadband performance of the interferometer. As a result, the output quantum noise is due solely to the input quantum fluctuations that have entered the system from the detection port.

The contents of the output fluctuation fields can usually be formally classified as the shot noise (Δx in the above naive model), and the radiation-pressure noise (Δp in the above naive model) — as can be identified by looking at the way they scale with the optical power [see, e.g., KLMTV [15], or Sec. 3.2 of this thesis]. Schematically, one has

$$\hat{o}(t) = \int^{t} dt' K(t-t') \left[x_{\rm GW}(t') + \hat{x}^{(0)}(t') + \hat{\mathcal{Z}}(t') + \int^{t'} dt'' \int^{t''} dt''' \frac{\hat{\mathcal{F}}(t''')}{\mu} \right] . \tag{1.7}$$

Here K is the time-domain transfer function of the interferometer; $x_{\rm GW}(t)$ is the gravitational–wave-induced motion of the test-mass coordinate (difference of two interferometer arm lengths) that the interferometer measures; $\hat{x}^{(0)}(t)$ is the free-evolution operator of that test-mass coordinate, which has support only at zero frequency; [3] μ is the reduced mass of that test-mass coordinate (equal to $m/4$ for the LIGO configuration, where m is the real mirror mass); while $\hat{\mathcal{Z}}(t) \propto I^{-1/2}$ and $\hat{\mathcal{F}}(t) \propto I^{1/2}$ (I being the optical power) are the optical field operators that correspond to the shot noise and fluctuating radiation-pressure force, respectively, and which originate from the optical fields that enter the interferometer from the detection port. As is shown, e.g., in Sec. 3.2.4, operators $\hat{\mathcal{Z}}(t)$ and $\hat{\mathcal{F}}(t)$ have the following commutation relations,

$$\left[\hat{\mathcal{Z}}(t), \hat{\mathcal{Z}}(t')\right] = \left[\hat{\mathcal{F}}(t), \hat{\mathcal{F}}(t')\right] = 0, \quad \left[\hat{\mathcal{Z}}(t), \hat{\mathcal{F}}(t')\right] = -i\hbar\delta(t-t') \,, \tag{1.8}$$

which, together with Eqs. (1.1) and (1.7), imply the vanishing self commutator of the output:

$$[\hat{o}(t), \hat{o}(t')] = 0 \,. \tag{1.9}$$

The commutators (1.8) place the following constraint on the (single-sided) spectral densities (see, e.g., Chapter 6 of Ref. [8])

$$S_{\mathcal{Z}}(\Omega) S_{\mathcal{F}}(\Omega) - S_{\mathcal{Z}\mathcal{F}}(\Omega) S_{\mathcal{F}\mathcal{Z}}(\Omega) \geq \hbar^2 \,, \tag{1.10}$$

while the output (1.7) leads to the following noise spectral density (assuming that the influence of

[3] Or rather at the pendulum frequency, which is in any case very low ($\sim 1\,$Hz).

$\hat{x}^{(0)}$ is filtered out),

$$S_x(\Omega) = S_{\mathcal{Z}}(\Omega) + 2R_{xx}(\Omega)\Re\left[S_{\mathcal{Z}\mathcal{F}}(\Omega)\right] + R_{xx}^2(\Omega)S_{\mathcal{F}}(\Omega)\,. \tag{1.11}$$

Here $R_{xx}(\Omega) = -1/(\mu\Omega^2)$ is the mechanical susceptibility of the measured test-mass coordinate, and Ω is angular frequency. When $\mathcal{Z}$ (shot noise) and $\mathcal{F}$ (radiation-pressure noise) are uncorrelated, Eqs. (1.10) and (1.11) imply

$$S_x \geq 2|R_{xx}|\sqrt{S_{\mathcal{Z}}S_{\mathcal{F}}} \geq \frac{2\hbar}{\mu\Omega^2} \equiv S_x^{\rm SQL}\,. \tag{1.12}$$

The quantity $S_x^{\rm SQL}$ is the Standard Quantum Limit (SQL) for position measurement, discovered by Braginsky [7, 8]. Because a gravitational wave with dimensionless strain $h(t)$ produces the position signal $x^{\rm GW}(t) = Lh(t)$, where L is the arm length [cf. Eq. (1.7)], the corresponding Standard Quantum Limit for h is (for LIGO topology, where $\mu = m/4$)

$$S_h^{\rm SQL} = \frac{2\hbar}{\mu\Omega^2L^2} = \frac{8\hbar}{m\Omega^2L^2}\,. \tag{1.13}$$

With $L = 4\,\mathrm{km}$, $m = 40\,\mathrm{kg}$, we have $\sqrt{S_h^{\rm SQL}} = 2\cdot10^{-24}(100\,\mathrm{Hz}/f)\,\mathrm{Hz}^{-1/2}$. For a gravitational-wave interferometer with LIGO-I topology (Fig. 1.1) and input-output optics (vacuum-field input at the dark port, and ordinary homodyne detection of the output phase quadrature), $\mathcal{Z}$ and $\mathcal{F}$ are truly uncorrelated, so this is a true limit on the sensitivity. To beat this limit one must change the interferometer topology or input-output optics. LIGO-II interferometers were first designed to work on the Standard Quantum Limit, without beating it, thus gaining a factor of ~ 15 in sensitivity with respect to LIGO-I (cf. the first paragraph of Sec. 1.1).

It is not hard to devise interferometer topologies and readout schemes for which $\mathcal{Z}$ and $\mathcal{F}$ are correlated, thereby allowing the SQL to be beaten. For one reason, as Caves has pointed out, $\mathcal{Z}$ and $\mathcal{F}$ both arise from fluctuation fields that leak into the interferometers from the detection port [11], it is then (in principle) possible to correlate them by means of additional input-output optics, for example by injecting squeezed vacuum into the dark port, as proposed by Caves [11] and Unruh [13], or by detecting frequency-dependent quadratures in the output, as proposed by Vyatchanin, Matsko and Zubova [14]. Interferometers that beat the Standard Quantum Limit by means of input-output manipulations are examples of "QND interferometers."

Based on these pioneering works of Caves, Unruh and Vyatchanin, Matsko and Zubova, KLMTV (Kimble, Levin, Matsko, Thorne and Vyatchanin) studied using input-output optics to convert conventional interferometers with LIGO-I topology into QND interferometers [15]. In particular, they proposed using detuned Fabry-Perot cavities as optical filters to achieve the desired frequency dependence in the $\mathcal{Z}$-$\mathcal{F}$ correlations. They also studied the influence of optical losses on the performance

of the resulting QND interferometers, and found that to keep the loss-induced noise at an acceptable level requires the optical filters to be kilometers in length [for plausible level of mirror quality within the next decade]. Even so, optical losses still affect significantly the performance of the KLMTV interferometers (QND position meters) at low frequencies, decreasing their observation bandwidth. Nevertheless, the KLMTV schemes were plausible for implementation in the time scale of LIGO-III, and were the only plausible broadband QND configurations for LIGO-III before the work presented in this thesis.

1.1.2 Signal recycled interferometers in LIGO-II

Research described in this thesis begins with a quantum mechanical study of the *signal recycled* optical configuration proposed for LIGO-II [6]. Signal recycling was invented by Meers [16], (based on earlier ideas of Drever [17], which we will mention briefly in Sec. 1.1.5, but with drastic simplification). Meers proposed adding another mirror, the *Signal Recycling Mirror*, at the dark port of a conventional Michelson interferometer, thereby feeding part of the output signal light back into the arms [See Fig. 1.1]. The signal recycling mirror forms a composite cavity with the input test-mass mirror (ITM) of the Michelson arms, the *signal recycling cavity*. The finesse of this signal recycling cavity can be used to control the storage time of signal sidebands inside the interferometer, while the detuning of the signal recycling cavity can alter the resonant frequences. As a whole, signal recycling can modify the optical resonant structure of the entire interferometer, providing a tool for reshaping the noise spectrum and optimizing for specific astrophysical sources. For example, the interferometer can be narrow-banded around a certain frequency with amplified sensitivity to search for sources within that specific band. Actually, the phrase "Signal Recycling" only refers to configurations where the signal recycling mirror *increases* the storage time of signal sidebands inside the interferometer. An opposite regime, proposed by Mizuno et al. [18], where the signal recycling mirror *decreases* the storage time (from arm-cavity storage time), is called *Resonant Sideband Extraction* (RSE). The RSE technique allows the use of high-finesse (and hence low bandwidth) arm cavities without limiting the observation bandwidth. The reference design of LIGO-II resides in the RSE regime.

In Chapter 2, Buonanno and I calculated the quantum noise spectrum of signal recycled interferometers in LIGO-II, simply by incorporating the signal recycling mirror into the analysis of KLMTV for the LIGO-I topology [see Fig. 1.1]. Contrary to the previously popular belief [6], we found that the noise spectrum of detuned signal recycling interferometers is capable of beating the Standard Quantum Limit, though only by a moderate amount (factor of ~ 2 in power), in a relatively broad frequency band ($\Delta f \sim f$) [see Fig. 1.2]. Technically, this beating of the Standard Quantum Limit can be attributed to the correlation between the shot and radiation-pressure noises built up by the signal recycling mirror, as we show in Chapter 2, where the output of signal recycling interferometers

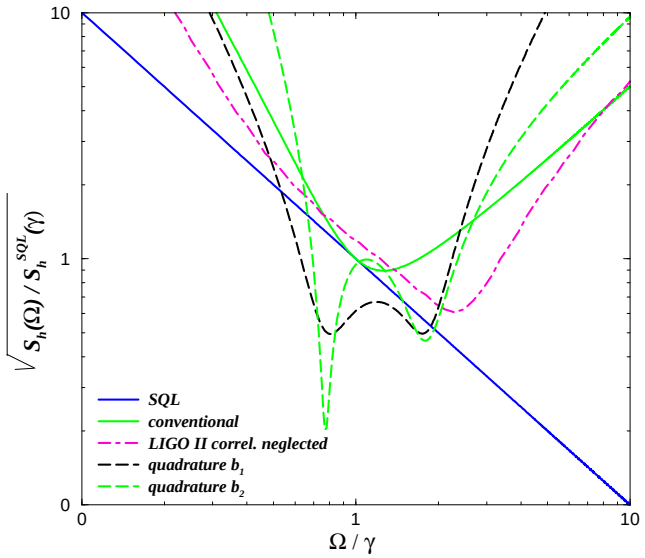

Figure 1.2: Quantum noise spectra of the conventional interferometer (light solid curve), the signal recycling interferometer with semiclassical treatment (dash-dot curve) and two-photon quantum-optics treatment [dark dash curve for the first output (amplitude) quadrature, light dash curve for the second output (phase) quadrature, See Sec. 2.3]. The SQL is shown as dark solid line. Here γ stands for the arm-cavity half linewidth, which equals to $2\pi \times 100\,\mathrm{Hz}$ in our example. $S_h^{\mathrm{SQL}}(\gamma)$ is the Standard Quantum Limit at γ.

is put *effectively* into the [apparently free-mass] form of Eq. (1.7), with $\mathcal{Z}$ and $\mathcal{F}$ correlated.

A closer look at the noise spectrum leads to a deeper understanding of signal recycling interferometers. The signal recycling noise spectrum found in Chapter 2 usually has two minima (see Fig. 1.2), one corresponding (roughly) to the optical resonance produced by signal recycling, and a second resonance at a lower frequency. As pointed out in Chapter 2 and further clarified in Chapter 3, the lower resonance is due to the optomechanical coupling provided by detuned signal recycling: any motion of the mirrors phase modulates the carrier light, the phase-modulation sidebands enter the detuned signal recycling cavity, where they are converted partially into amplitude modulations which combine with the carrier to provide a pressure that acts back onto the mirrors — producing a time-delayed position-dependent radiation-pressure force. Schematically,

$$\text{mirror motion} \overset{\sqrt{I}}{\Longrightarrow} \text{PM sideband} \overset{\phi}{\Longrightarrow} \text{AM sideband} \overset{\sqrt{I}}{\Longrightarrow} \text{motion-dependent force} \tag{1.14}$$

[Here I stands for the optical power, ϕ stands for the signal recycling detuning.] The position dependence of this classical radiation-pressure force can be thought of as an *optical spring*. (The same optomechanical coupling was previously recognized by Braginsky, Gorodetsky and Khalili in a different context and used to design their "optical-bar" gravitational-wave detector [9].) The optical spring can shift the mechanical resonance of the system from 0 (free mass) up into the detection band, enhancing the sensitivity of the interferometer.

With the dynamics of the system modified, the free-mass Standard Quantum Limit no longer applies to detuned signal recycled interferometers. The Standard Quantum Limit for a resonator with two resonant frequencies is more relevant to this situation [although we know it still might not be a limiting sensitivity due to possible correlations]. That Standard Quantum Limit does have two dips around the two resonances, due to amplified responses of the system near resonance. An interesting question one might ask is: which is more responsible for the SQL-beating of detuned signal recycled interferometers, classical dynamics or quantum correlations? This *can* be a misleading question to ask, since the two are in fact different ways of representing the same system. On the one hand, as we have already seen in detuned signal recycled interferometers, if we start from classical optomechanics and develop the formal classification of shot and radiation-pressure noises as in Eq. (1.7), then correlations arise naturally. On the other hand, if we start from a measurement with shot-noise–radiation-pressure-noise correlations (as shown by Syrtsev and Khalili [19], discussed further by Khalili [20], and briefly re-discussed in Chapter 4 in the context of signal recycling interferometers), the correlations can be removed by *effectively* modifying the dynamics. Nevertheless, a useful way to look at the particular case of signal recycled interferometers is to see how much the output light from the interferometer deviates from a classical state, given a vacuum input state. As we show in Chapter 2, the output light is in a squeezed state but only with a mild squeezing factor; while the classical transfer function (from gravitational-wave strain h to output field) clearly exhibits the same resonant structure as the noise spectrum. In this sense, the classical dynamics seems to be more important than the quantum correlation. This fact can also be inferred from Fig. 2.3, where we see that the quantum noise has the same resonant structure (and beat the free-mass SQL) in *all* output quadratures; this could not be true if squeezing were behind it, since the characteristic of squeezed states is that noise suppression in one quadrature is obtained at the price of noise amplification in the orthogonal quadrature.

Returning to practical issues, in Chapter 3 we found that the optomechanical resonance produced by the optical spring is always unstable, and its instability must be suppressed by a suitable control system. One example of such a control system is given, which filters the dark-port output and feeds back a force, proportional to the filtered output, onto the test masses. A Heisenberg-picture analysis of this idealized linear control system in Chapter 3 predicts that no additional noise need be added. However, a more correct analysis, for realistic electro-optical feedback systems, needs to be carried out, and the author is now embarking on such an analysis in the Schrödinger picture.

Chapters 2 and 3 use the KLMTV notation and viewpoint — a viewpoint originally intended for conventional interferometers without signal recycling. Results are obtained to the leading order of T, the power transmissivity of the input test-mass mirror (ITM). This is easy for a first calculation, but turns out to be cumbersome for further analysis of the result, and for appreciating the underlying physics. In Chapter 4, we carry out a more elegant study of signal recycled interferometers, from

a viewpoint which can in some sense be regarded as a conceptual extension of Mizuno's study on Resonant Sideband Extraction — an extension into interferometers with high optical power and nontrivial optomechanical dynamics. Following the suggestion of Mizuno [18], we focus explicitly on the antisymmetric modes of the optical fields and mirror motions (modes with opposite signs but equal amplitudes in the two arms).

Because the signal recycling cavity proposed for LIGO-II is so short, $l \sim 10\,\text{meters}$, it satisfies $\mathcal{F}\Omega l/c \ll 1$, with $\mathcal{F}$ its finesse. This permits us to effectively replace the cavity by a single mirror, thereby reducing the parameter space by one dimension, from $\{T$, ρ (signal recycling mirror reflectivity), ϕ (signal recycling detuning phase)$\}$ to the reflectivity and position of the effective mirror, and to $\{\lambda, \epsilon\}$, where $\omega_0 + \lambda - i\epsilon$ is the complex optical resonant frequency of the antisymmetric optical fields. The interferometer is thereby mapped to a single detuned cavity with one movable mirror. [The radiation-pressure effects on the ITM can be moved to the end test-mass mirror (ETM) by changing the reduced mass of the system.] In addition, only the circulating power inside the arm cavities, I_c, or rather the combination

$$\iota_c \equiv \frac{8\omega_0 I_c}{mLc}\,, \tag{1.15}$$

(where ω_0 is the carrier frequency and $m = 4\mu$ the mirror mass, μ the reduced mass of the antisymmetric mode of mirror motion) together with the Standard Quantum Limit [Eq. (1.13)] is further required to describe the dynamics of the interferometer and the noise spectrum. Practically, this reduction of parameter space yields a "scaling law." For example, as experimentalists would like to alter T so as to adjust the input power on the beamsplitter, this reduction gives a way of returning to the same quantum noise spectrum at the chosen T by adjusting the signal recycling parameters, such that ϵ and λ return to the same value, and maintaining the same circulating power in the arms. More generally, this scaling law can also help designing detuned signal recycling experiments with drastically different mass, length scales and optical powers. Theoretically, the expressions in Chapter 4 are much simpler than their counterparts in Chapters 2 and 3. In particular, the optical spring constant of Chapters 2 and 3 is written as

$$\frac{K(\Omega)}{\mu} = -\frac{\iota_c \lambda}{(\Omega - \lambda + i\epsilon)(\Omega + \lambda + i\epsilon)}\,, \tag{1.16}$$

and the resonances of the interferometer are given by the roots of the following characteristic equation:

$$\Omega^2\left[(\Omega + i\epsilon)^2 - \lambda^2\right] + \lambda\iota_c = 0 \tag{1.17}$$

Moreover, with the simplification made possible by this reduction, in Chapter 4, we carry out a calculation in which the propagations of the optical fields are kept to all orders, instead of only keeping the leading order in T, as was done by KLMTV.

Finally, it is worth pointing out that, although LIGO-II is the focus of this thesis, a first-generation interferometer, GEO 600, already uses the signal recycling topology, although instead of Fabry-Perot arm cavities it has a folded-arm Michelson topology. The final commissioning of GEO 600 is currently under way, and will likely be completed in several months. In the light of the work described in Chapters 2 and 3, Jan Harms et al. have carried out a parallel study of the GEO interferometer, in a fashion similar to Chapter 2, with similar results [21]. [A connection between the schemes with and without arm cavities can also be established using the results in Chapter 4, via the equivalence between a signal recycled interferometer with arm cavities and a single detuned cavity.] Interestingly, although the first-generation GEO 600 interferometer has a substantially lower optical power (10 kW) than planned for LIGO-II (800 kW), due to its smaller mirror mass and shorter arm length, the optical-spring–induced resonant frequency of GEO 600 can already be within the interferometer's detection band (it can be as large as 50 Hz). Although the resulting enhancement in sensitivity may well be masked by thermal and technical noises, the optical spring effect might still be observed through the GEO 600 transfer function during its calibration stage.

1.1.3 Gravitational-wave interferometers with heterodyne readout scheme

Since gravitational-wave interferometers we consider all operate on a dark fringe (in order to suppress laser noise), the intensity of the light exiting the detection port in principle is quadratic in the gravitational-wave amplitude, and therefore insensitive to it, to first order. The standard way to circumvent this is to interfere the signal field with a relatively strong local-oscillator (LO) field, so that the intensity of the total optical field, detected at the beat frequency, varies linearly with the gravitational-wave amplitude. The various choices of the LO-field parameters and resulting methods of measuring the gravitational-wave–induced signal at the dark port are referred to as *readout schemes.*

In Chapters 2–3, the quantum noise spectrum of LIGO-II is evaluated assuming a homodyne readout scheme, in which the LO field oscillates at exactly the same frequency as the carrier: a specific (frequency-independent) quadrature of the output optical field will be detected, depending on the phase of the LO field. Alternatively, a heterodyne detection scheme, in which the LO field has a frequency different from the carrier laser, can be used, as in LIGO-I. The heterodyne LO fields can be obtained by phase modulating the carrier laser (at radio frequency) before it enters the interferometerm and building a (Schnupp) asymmetry [22] between the Michelson arms (by integer number of carrier wavelengths) so as to allow these phase-modulation sidebands to enter the dark port. The heterodyne detection scheme usually allows the detection of multiple output quadratures, but at the same time it introduces additional noise due to the frequency mixing that happens during the photodetection stage, as was realized by Gea-Banacloche and Leuchs [23] and by Schnupp [22]. Studies of the additional heterodyne noise and its supression were carried out by Niebauer et al. [24],

and by Meers and Strain [25], for situations where the phase quadrature alone is measured. However, for the signal recycled interferometers of LIGO-II, and for more advanced gravitational-wave interferometers, where measuring multiple quadratures can be very helpful, the impact of the additional heterodyne noise that comes together with the variable-quadrature measurement had not been studied until this thesis. [4] This task was taken on by Buonanno, Mavalvala and me. In Chapter 5, we carry out a study of heterodyne readout schemes for advanced configurations, taking into account both the variable-quadrature optimization and the additional heterodyne noise.

In the first part of Chapter 5, we calculate the quantum noise of signal recycled interferometers with sine-wave modulation/demodulation heterodyne schemes [this work will serve as a basis (among other technical considerations) for the LIGO Scientific Collaboration's choice and optimization of the LIGO-II readout scheme.] It is found that the enhancement in sensitivity due to the variable-quadrature optimization can be largely counteracted by the additional heterodyne noise.

In the second part of Chapter 5, we take a more general point of view and consider arbitrary modulation and demodulation waveforms. It is crucial to underline that any heterodyne scheme implemented by the modulation/demodulation process is *frequency independent* in nature, in the sense that the way each output quadrature is measured by a certain demodulation waveform is independent of frequency. Simply put, all output quadratures are available for measurement at all frequencies, and this makes a noise-free variable-quadrature optimization clearly incompatible with the Heisenberg Uncertainty Principle, since different output quadratures do not commute with each other. [5] Accordingly, a theoretical constraint on the additional heterodyne noise, in the form of a *frequency independent quantum limit*, can be derived: For each modulation/demodulation scheme, there exists a frequency independent noise ellipse (the same as the one that describes the noise spectrum of different quadratures in a squeezed state [10]), which bounds from below the additional heterodyne noise for different quadratures.

This quantum limit does not constrain the sensitivity achievable on any single quadrature, since the noise ellipse can become extremely elongated. This is consistent with the findings of Schnupp [22] and Meers and Strain [25]. However, as soon as *some* sensitivity is demanded for more than one quadrature, the additional heterodyne noise becomes obligatory. The frequency independence of the quantum limit constrains seriously any attempt to use the variable-quadrature optimization to convert non-QND interferomters into QND interferometers. As we show in Sec. 5.4.2, for interferometers with no detuning, [e.g., conventional interferometers, or the speed-meter interferometers described in Chapters 6 and 7], the quantum limited heterodyne detection with variable-quadrature optimization gives a noise spectrum equivalent to that obtained by an ordinary homodyne detection

[4] A proposal of using heterodyne detection to obtain variable-quadrature optimization in advanced gravitational interferometers was recently made by Somiya [26], without taking full consideration of the additional heterodyne noise.

[5] Note that this is fundamentally different from the variational-output scheme [14, 15], which only measures one quadrature at a given frequency, by means of a frequency-dependent rotation of output quadratures.

on the same interferometer, but with less (or equal) optical power. As a consequence, interferometers that do not exhibit QND performances with ordinary homodyne detections will not become QND after using the heterodyne scheme.

1.1.4 Speed-meter interferometers with Michelson topology

As was mentioned in Sec. 1.1.1, measuring a QND observable explicitly can make a gravitational-wave interferometer immune to the Standard Quantum Limit. For a free test mass, the momentum is such an observable, by virtue of having commuting Heisenberg operators at different times. Motivated by this fact, Braginsky and Khalili proposed measuring the speed of a free test mass, which is closely related to its momentum [27]. Two gedanken designs were studied in Ref. [27], with the second one deemed easier to realize in gravitational-wave detectors. [6] This second gedanken design requires two weakly coupled resonators with equal eigenfrequency. Resonator 1 is pumped on resonance, while resonator 2 is left empty. Any change of the position of one end of resonator 1 causes a length change that phase modulates the carrier field, generating signal sidebands; no signals are generated inside resonator 2, since it is empty. As a property of weakly coupled resonators, the signal sidebands generated in resonator 1 "slosh" [move back and forth] between these two resonators, *flipping sign* each time they return into resonator 1, thereby canceling any sensitivity to time-independent position. For motions with frequencies below the *sloshing frequency*, speed is recorded in the sideband fields extracted from resonator 1; at higher frequencies the output signal is a combination of speed and higher time derivatives of position.

Braginsky, Gorodetsky, Khalili and Thorne (BGKT) analyzed a microwave version of this original "speed-meter design," and proposed an optical version modeled straightforwardly from the microwave system, with *four* kilometer-scale cavities. Purdue [29] analyzed the proposal of BGKT in detail, showing that a broadband QND performance can indeed be achieved with ordinary homodyne detection. The QND performance of the speed meter is shown to be characterized by a spectrum that beats the Standard Quantum Limit by a relatively constant factor below the "sloshing frequency." A plausible amount of circulating power (megawatt scale, similar to the requirement of the QND position meter proposed by KLMTV [15]) is required for the speed meter to beat the SQL by a significant amount. However, as Purdue found, an exorbitant amount of pumping power (nearly gigawatt scale) is needed to achieve the required circulating power. In addition, a large amount of light (nearly megawatt level) comes out of the interferometer together with the signal light, complicating the photodetection process.

Based on the work of Purdue, I invented a mathematically equivalent configuration that can fit more easily into the facility of LIGO, and can solve the problem of high pumping power and high

[6] The first gedanken design described in Ref. [27] was then regarded as harder to realize — but that is no longer true, see Sec. 1.1.5.

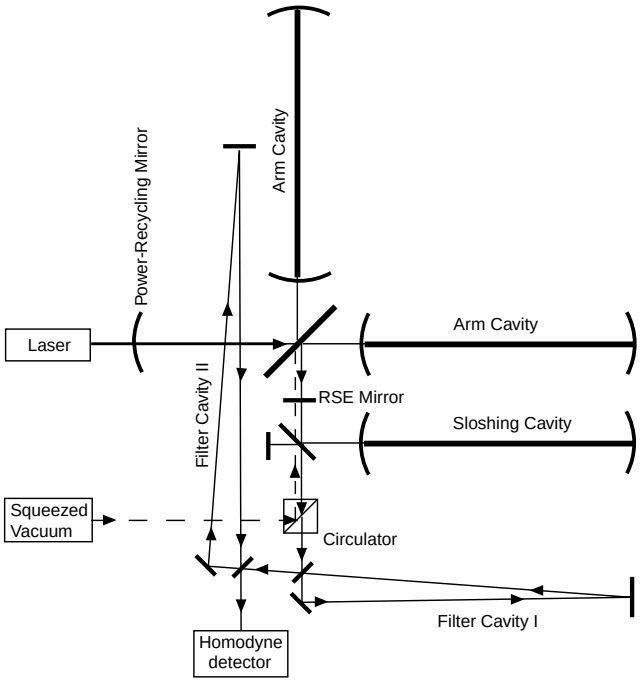

Figure 1.3: Optical topology of the Purdue-Chen speed meter. A kilometer-scale sloshing cavity is added at the dark port of a Michelson interferometer, folded back to share the vacuum tube with one of the arms. The folding mirror is left somewhat transmissive to allow the extraction of signal. Cavities can be used in the arms to enhance the circulating power, but an RSE mirror must added to compensate the effect of the arm-cavity on the signal sidebands. Input squeezing and variational readout can be implemented using the proposal of KLMTV, with a circulator and two kilometer-scale optical filter cavities.

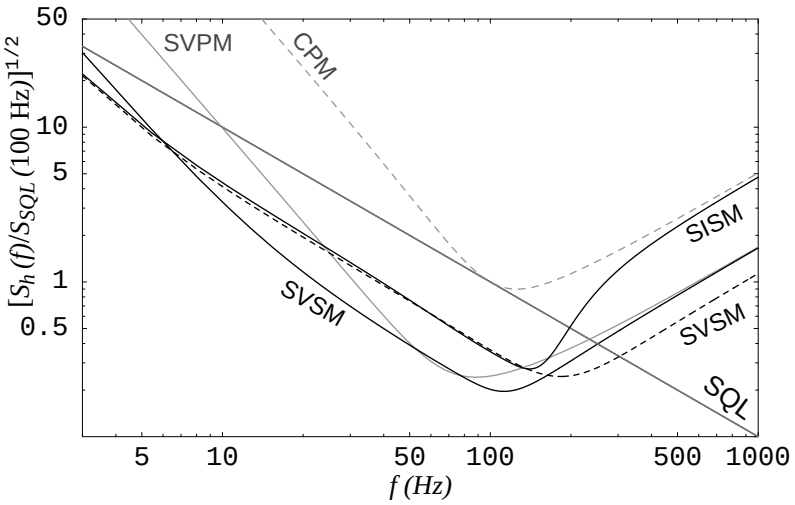

Figure 1.4: Quantum noise spectra of Purdue-Chen speed meters [one squeezed-input speed meter (SISM) and two squeezed variational speed meters (SVSM) with different parameters] and comparison with conventional interferometer (conventional position meter, CPM) and KLMTV interferometer (squeezed variational position meter, SVPM). The circulating power of all configurations is 820 kW, with input squeeze factor $e^{2R} = 10$ (CPM does not have squeezing). Optical-loss level thought to be practical in the next decade is used.

static output power. (See Fig. 1.3 for its optical topology.) This design is analyzed by Purdue and me in Chapter 5. In this Purdue-Chen speed meter, resonator 1 is the antisymmetric mode of a Michelson interferometer. The symmetric mode can be pumped in the usual way from the bright port, which then couples the antisymmetric motions of the mirrors to the antisymmetric optical mode in a manner of a conventional interferometer such as LIGO-I. Power recycling techniques can also be used to enhance the circulating power, as in LIGO-I. An additional cavity with equal length is placed in the dark port, forming resonator 2, which is empty. The (highly reflective) common input mirror of the two optical resonators is called the *sloshing mirror*. In practice, the sloshing cavity will have to be folded back into one of the interferometer arms; the folding mirror can be made partially transmissive, forming an output coupler which allows signal sidebands to be extracted from resonator 1. [In our analysis, one of the two ports opened by the output coupler was closed for ease of treatment.] In principle, there would be no static output light, since the detection is made at a dark port. Arm cavities can also be used to further enhance the circulating power and decrease the power going through the beamsplitter; their effect on the signal sideband can be removed by putting an RSE mirror at the dark port, making an impedance-matched cavity with the arm-cavity input mirror.

The QND performance of this Purdue-Chen speed meter can be further enhanced by the use of input squeezing and variational output techniques on the speed meter. As we show in Sec. 6.4.1, input squeezing with frequency-independent squeeze angle can increase the *effective* optical power

by the squeeze factor (as in Caves' original proposal for conventional interferometers [11]; see also KLMTV [15]), thereby enhancing the sensitivity by the same factor (in power) for frequencies below the sloshing frequency. We also show that, using two detuned FP cavities as optical filters in the output can enhance high-frequency performance greatly. As a by-product of our research, in Sec. 6.7, we work out the most general frequency-dependent rotation angle in quadrature fields achievable by detuned (high finesse) FP cavities, and give a prescription for solving for the corresponding filter parameters needed — an issue left untackled by KLMTV [15].

Finally, Purdue and I study the influence of optical losses in speed-meter interferometers. The mirror quality thought achievable by the next decade (10 ppm loss per bounce) dictates that the sloshing cavity, as well as the (optional) output filters have lengths of kilometers, in order to achieve a sensitivity a factor 5 (in amplitude) below the Standard Quantum Limit. This reduces the practicality of adding these cavities. On the other hand, these speed meters were able to achieve a broadband QND performance with one such additional cavity (one less than the KLMTV interferometers); and were found to be significantly less susceptible to losses than the KLMTV interferometers, due to the shape of their transfer functions. The full noise spectra of speed meter designs, with optical losses included are summarized and compared with KLMTV interferometers (QND position meters) in Sec. 6.5.3. (See Fig. 1.4).

1.1.5 Sagnac interferometers as speed meters

The Sagnac interferometer was invented by Sagnac in 1913 for rotation sensing [30]. In this interferometer, the input light beam is split in two, the two beams then travel along opposite directions of the same loop path, and are then brought together to interfere with each other. For a rigid loop path, the phase difference gained by the two light beams is proportional to the area circumscribed by the loop, times the angular frequency of the loop path with respect to an inertial frame.

Sagnac interferometers can also be used to detect gravitational waves. Historically, the Sagnac topology was used by Drever in Ref. [17] to explain a way of resonantly amplifying the signal light. This idea was later modified (rather drastically) by Meers into the currently widely used technique of signal recycling [16]. Later on, the Sagnac was considered more seriously [31, 32, 33] as an alternative to the Michelson due to several technical advantages, including (i) a simpler control scheme, (ii) greater tolerance to reflectivity imbalance, and (iii) easier implementation with an all-reflective optical system, in which one can achieve tolerance to higher optical power, and use test-mass materials with lower thermal noises (e.g., silicon, which is nontransparent) [33, 34]. However, technical disadvantages also exist, for example, lower tolerance to beamsplitter ratio errors and mirror tilt errors [35]. It was also found that the control scheme will no longer be simple when arm cavities or recycling techniques are implemented into the Sagnac interferometer [36]. Moreover, in the low–laser-power regime, an analysis of the shot-noise limited spectrum did not reveal new features

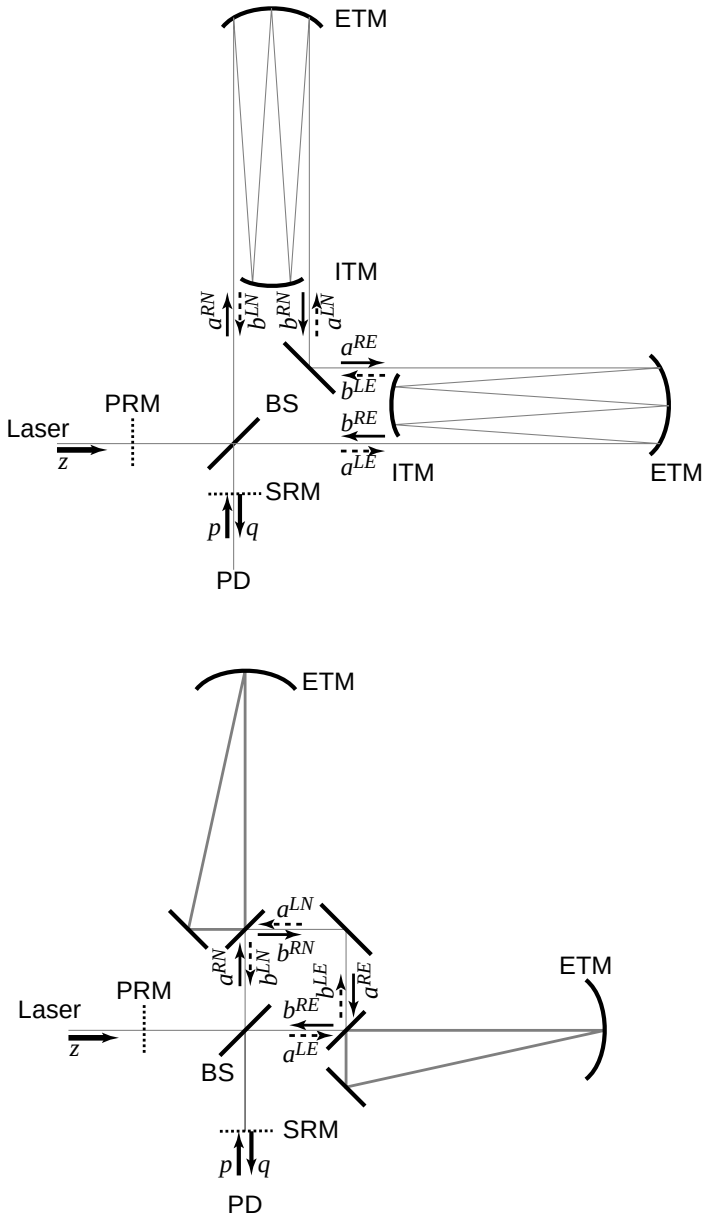

Figure 1.5: Signal recycled Sagnac interferometers with optical delay lines (upper panel) or ring-shaped Fabry-Perot cavities (lower panel) in the arms.

in the Sagnac noise curve that cannot be mimicked by signal recycled Michelson topologies [37]. As a consequence, despite the attractiveness of all-reflective optics, little effort has been made to shift away from the much more mature Michelson topology and build Sagnac interferometers in major third-generation interferometers.

As has long been known, Sagnac interferometers only sense the *time-dependent* part of test-mass motion. Surprisingly, until the work described in Chapter 7 of this thesis, nobody seems to have seriously realized that this implies that Sagnac interferometers are speed meters automatically — *without the need of any additional kilometer-scale cavities*. This fact follows naturally as we explain how a Sagnac gravitational-wave interferometer works.

In a Sagnac interferometer (see Fig. 1.5), the input light beam is split in two by the beamsplitter; the two beams can be denoted R ("right propagation") and L ("left propagation"). The R beam is sent into the North (N) arm first, and then fed into the East (E) arm; while the L beam enters the two arms in the opposite order, E first and N second. When the two beams recombine at the beamsplitter, the phase gained by each of them separately can be written as

$$\delta\phi_{\rm R} \sim {\rm x}_{\rm N}(t) + x_{\rm E}(t+\tau_{\rm arm})\,, \tag{1.18}$$

$$\delta\phi_{\rm L} \sim {\rm x}_{\rm E}(t) + x_{\rm N}(t+\tau_{\rm arm})\,, \tag{1.19}$$

where $\tau_{\rm arm}$ is the (average) time each photon stays in the arm, $x_{\rm N}(t)$ and $x_{\rm E}(t)$ are the (tiny) differences of the North and East arm lengths to their reference values (which resonates with the carrier laser). The output signal will then be proportional to

$$\delta\phi_{\rm R} - \delta\phi_{\rm L} \sim [x_{\rm N}(t) - x_{\rm N}(t+\tau_{\rm arm})] - [x_{\rm E}(t) - x_{\rm E}(t+\tau_{\rm arm})]\ , \tag{1.20}$$

which is sensitive to the *change* of arm-length difference during the light's travel. As we infer from Eq. (1.20), for motions with frequencies much lower than $1/\tau_{\rm arm}$, a speed measurement is obtained; and at higher frequencies the signal contains a combination of speed and higher time derivatives of position.

Nobody before has taken seriously this speed-meter-like response function of the Sagnac interferometer and asked for its quantum-mechanical implications [QND performance]. In Chapter 7, it takes only a trivial calculation to confirm the "quantum speed meter" performance of ideal Sagnac interferometers, i.e., a performance similar to that of the Michelson speed meter in Chapter 6, namely, a uniform beating of the Standard Quantum Limit in a broad frequency band, with ordinary homodyne detection. [See Sec. 7.3, for performances of ideal Sagnac interferometers; example noise spectra are also shown in Fig. 1.6.] In particular, signal recycled Sagnac interferometers with ring cavities (lower panel of Fig. 1.5) in the arms can be shown to have the same input-output relation as

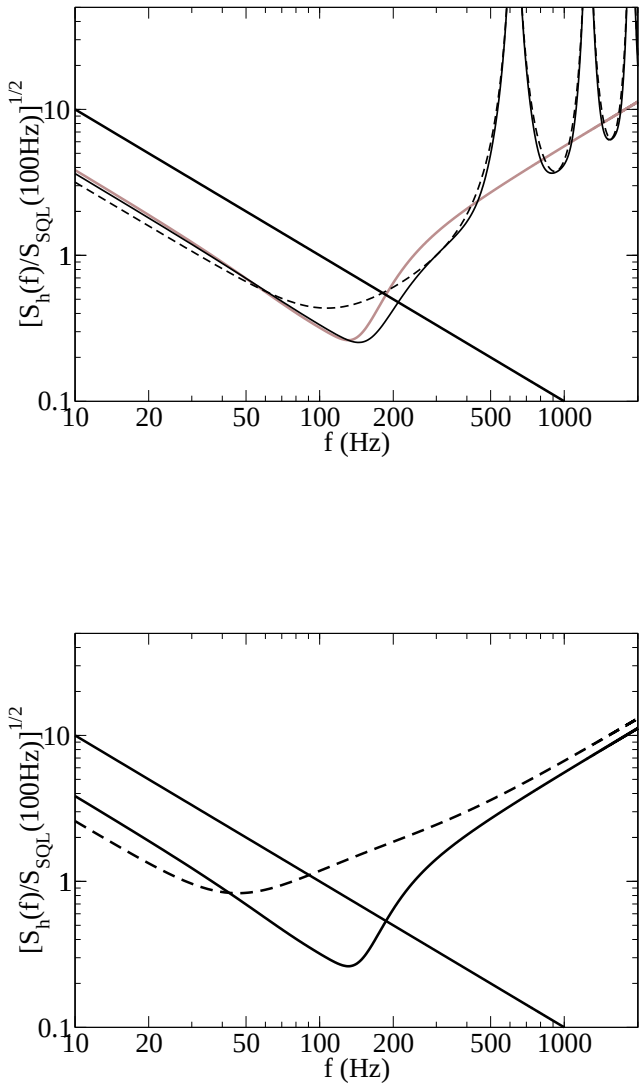

Figure 1.6: Quantum noise of ideal Sagnac interferometers with optical delay lines (DL for short, upper panel) or ring-shaped Fabry-Perot cavities (FP for short, lower panel) in the arms. In both configurations, a total circulating power of 820 kW and input (power) squeeze factor of $e^{2R} = 10$ is assumed; solid curves stand for signal recycled Sagnac interferometers, dashed curves stand for Sagnac interferometers without signal recycling, solid straight lines stand for the Standard Quantum Limit, and gray curves stand for a fiducial Michelson speed meter for comparison. For the DL scheme, the light bounces for $\mathcal{B} = 60$ times in each arm, and the signal recycling amplitude reflectivity is $\rho = 0.12$; in the FP scheme, the power transmissivity of the input test-mass mirror is $T = 0.0564$, and the signal recycling amplitude reflectivity is $\rho = 0.268$. In this case, the Michelson Speed Meter curve coincides with the signal recycled Sagnac curve.

the Michelson speed meters (lower panel of Fig. 1.6). In this way, Sagnac interferometers might well be the easiest-to-build QND interferometers. This, combined with the promise of all-reflective optics, can make the Sagnac interferometer a strong candidate for third-generation gravitational-wave interferometers. [Technical issues, including the influence of optical losses, will have to be analyzed thoroughly, although it is plausible that, like other speed meters, the Sagnac interferometer is also less susceptible to optical losses than QND position meters.]

Interestingly, a careful comparison between Sagnac interferometers and the first gedanken experiment of Braginsky and Khalili in Ref. [27] will reveal an enlightening resemblence between the two schemes. In fact, the Sagnac interferometer can in some sense be regarded as its practical implementation in optics. Khalili, in an independent but subsequent work [28], also realized this link, and deduced the quantum speed meter performance of Sagnac interferometers.

1.2 Detecting compact binary objects with first-generation interferometric gravitational-wave detectors

The inspirals of binary compact objects, formed by neutron stars (NS) or black holes (BH), are among the most promising sources for earth-based gravitational-wave detectors. (A brief summary of inspiral event rates detectable by LIGO-I and LIGO-II, compiled by Cutler and Thorne [5], is given in Table 1.1. A full survey of the detection of black-hole binary coalescence has been made by Flanagan and Hughes [38].) The binary orbits are generally assumed to have circularized under radiation reaction by the time the gravitational-wave frequency reaches the detection band (above 40 Hz for initial interferometers, 10 Hz for second-generation interferometers) [39]. [7] In early stages of (the circular) inspiral, the motion is well described by Post-Newtonian (PN) calculations [45], as characterized by an adiabatic sequence of shrinking circular orbits (with increasing orbital frequency); the gravitational waveform is well approximated by the quadrupole formula, which in this case gives a *chirp* signal, namely, a quasi-periodic signal with slowly increasing amplitude and frequency. The early-stage inspiral waves can be extracted from the noisy output of gravitational-wave interferometers most efficiently by means of matched filtering, which correlates the output of the interferometer with theoretical templates [46]. However, as radiation reaction shrinks the binary orbit and accelerates the orbital motion, more general relativistic effects will begin to influence the binary evolution and thence the theoretical template and complicate the data analysis process:

- For spinning binaries, spin-orbit and spin-spin couplings will cause the orientation of the binary orbit [47, 48], and thus its relative orientation with respect to the detector, to change in a time scale longer than the orbital period but shorter than the radiation reaction time scale, yielding a complicated modulated waveform [49, 50, 51, 54]. A large number of parameters (naively 15 of them) are required to describe the waveform completely, making the search over the template bank extremely high in computational cost.

- As the evolution goes on further, the accuracy of the Post-Newtonian expansion will deteriorate and fail to give theoretical predictions accurate enough for the purpose of matched-filtering data analysis [55, 56].

Eventually, the adiabatic sequence of inspiraling orbits will break down due to dynamical instabilities, at the Innermost Stable Circular Orbit (ICSO) [also called the Last Stable Orbit (LSO)], and the binary's orbits will plunge toward each other and merge into a single very perturbed black hole or neutron star. A correct understanding of the non-linear physics and the gravitational waveforms of the late-stage inspiral and merger phases require numerical relativity, which as yet is too immature

[7] Recent work by Miller and Hamilton [40] has suggested additional sources in globular clusters that might increase the event rate dramatically, but some of which might involve eccentric orbits in the LIGO detection band [41]. Eccentric orbits are not considered in this thesis.

	NS/NS	NS/BH	BH/BH in field	BH/BH in clusters
Event rate in our galaxy (yr^{-1})	10^{-6}–$5\cdot10^{-4}$	$\lesssim 10^{-7}$–10^{-4}	$\lesssim 10^{-7}$–10^{-5}	$\sim 10^{-6}$–10^{-5}
visible range of LIGO-I	20 Mpc	43 Mpc	100 Mpc	100 Mpc
Event rate of LIGO-I (yr^{-1})	$3\cdot10^{-4}$–0.3	$\lesssim 4\cdot10^{-4}$–0.6	$\lesssim 4\cdot10^{-3}$–0.6	$\sim$ 0.04–0.6
visible range of LIGO-II	300 Mpc	650 Mpc	$z = 0.4$	$z = 0.4$
Event rate of LIGO-II (yr^{-1})	1–800	$\lesssim$ 1–1500	$\lesssim$ 30–4000	$\sim$ 300–4000

Table 1.1: Event-rate estimates of binary inspirals for the LIGO-I and LIGO-II (*Wideband* configuration [6]) 3-detector networks, as compiled by Cutler and Thorne [5], based on the works of Belczynski et al. [42], and Kalogera et al. [43]. The range of the LIGO detector networks are obtained assuming an optimal matched filtering detection, with false-alarm probability of 10^{-3} during one year's observation [5]. The event rates of NS-NS binaries *in our galaxy* (or "per Milky-Way-Equivalent galaxy" in the universe) are obtained from both observational surveys of binary pulsars (with the help of an appropriate *scaling* [44]) and theoretical *population synthesis* approaches, while the event rates of NS-BH and BH-BH binaries *in our galaxy* are currently available only from population synthesis, due to the absence of observational data. The event rate *of LIGO interferometers* are obtained from the galaxy rate and the visible range of these interferometers by assuming uniform distribution of sources in the universe.

to provide reliable waveform predictions. As the perturbations of the final black hole become mild enough through gravitational radiation, the (oscillatory) motion of the black hole and the associated gravitational waveforms can again be calculated theoretically, using black-hole perturbation theory. This is known as the ringdown phase (see Flanagan and Hughes [38] for detailed discussions of detection techniques for the three stages).

The two issues mentioned above are likely to be very important for the detection of inspiral waves in LIGO-I, yet previous template families might not be able to cope with them. In Chapters 8 and 9 of this thesis, Buonanno, Vallisneri and I study these two issues seriously, with the goal of providing new template families that will deal with them effectively and enhance the inspiral event rate. In the following I discuss them briefly (in reversed order).

1.2.1 Post-Newtonain waveforms of late-stage inspirals with vanishing spins

Let us first recognize the importance of late-stage inspirals, using the example of non-spinning compact binaries. In the leading Post-Newtonian approximation, the chirp signal has a frequency-domain magnitude of

$$|\tilde{h}(f)| \propto \frac{\mathcal{M}^{5/6}}{d} f^{-7/6}\Theta(f_{\mathrm{ISCO}} - f)\,, \quad \mathcal{M} = M\eta^{3/5}\,, \tag{1.21}$$

where $\mathcal{M}$ is the *chirp mass* (with $M = m_1 + m_2$ the total mass and $\eta = m_1 m_2/M^2$ the mass ratio, i.e., ratio of reduced mass to total mass), and d is the distance from the source to the detector. A cutoff is made at the ISCO frequency, which can be estimated roughly from the Schwarzchild ISCO frequency, with the mass of the Schwarzchild black hole equal to the total mass (an estimate that is

correct only for $\eta \to 0$):

$$f_{\rm ISCO} = 4400\,{\rm Hz}\left(\frac{M_\odot}{M}\right) . \tag{1.22}$$

Note that the higher the total mass M, the lower the ISCO frequency, as the waveform only depends on the ratio t/M in the time domain, or fM in the frequency domain. The signal-to-noise ratio (SNR) given by optimal matched filtering is

$${\rm SNR} = \sqrt{2\int_{-\infty}^{+\infty} df\,\frac{|\tilde{h}(f)|^2}{S_h(f)}} \propto \frac{\mathcal{M}^{5/6}}{d}\sqrt{\int_0^{\frac{4400\,{\rm Hz}}{M/M_\odot}} df\,\frac{f^{-7/3}}{S_h(f)}} = \frac{M^{5/6}\eta^{1/2}}{d}\sqrt{\int_0^{\frac{4400\,{\rm Hz}}{M/M_\odot}} df\,\frac{f^{-7/3}}{S_h(f)}} . \tag{1.23}$$

Here $S_h(f)$ is the (sigle-sided) noise spectral density in h. [See notation in, e.g., Eq. (1.13).] From Eq. (1.23), we can see that, for binaries at a fixed distance (oriented in the same way with respect to the detector) [38, 5]:

- The higher the mass ratio η, the higher the SNR.
- In the low-mass regime, where $f_{\rm ISCO}$ lies above the detection band (higher than $\sim 240\,{\rm Hz}$ for LIGO-I, which corresponds to total mass lower than $\sim 20\,M_\odot$), higher SNRs are obtained by increasing the total mass M, with ${\rm SNR} \propto M^{5/6}$.
- For binaries with high enough masses such that $f_{\rm ISCO}$ lies within the detection band, increasing further the total mass will eventually result in lower SNRs.

These features of the SNR can be represented more quantitatively in terms of the volume of the universe that is visible with a fixed SNR (thus a fixed false-alarm probability) as a function of the binary's masses:

$$V \propto d^3 \propto \mathcal{M}^{5/2}\left[\int_0^{\frac{4400\,{\rm Hz}}{M/M_\odot}} df\,\frac{f^{-7/3}}{S_n(f)}\right]^{3/2} = M^{5/2}\eta^{3/2}\left[\int_0^{\frac{4400\,{\rm Hz}}{M/M_\odot}} df\,\frac{f^{-7/3}}{S_n(f)}\right]^{3/2} . \tag{1.24}$$

This relative visible volume is plotted (for equal-mass binaries) in Fig. 1.7. As we can see from the graph, the visible volume is dramatically larger for heavier binaries, peaking at a total mass of $\approx 35\,M_\odot$ (with a visible range of ≈ 200 times the value for neutron-star binaries), for which the Schwarzchild ISCO frequency is 126 Hz, which lies right in the middle of the LIGO-I detection band. It should be noted that different Post-Newtonian expansions will give different predictions for the cutoff frequency, and hence different V-M curves (see Figs. 8.16 and 8.17), which give different turning points in total masses. Nevertheless, it is clear that binary black holes whose inspirals end within the detection band are favored by the detector, which means total masses ~ 20 – $60\,M_\odot$ for LIGO-I detectors. Current astrophysical theories suggest that in binaries only black holes with masses smaller than $\sim 15 M_\odot$ can form directly from the collapse of stellar objects, but a recent study by Miller and Hamilton has suggested that higher-mass black holes can form from four-body

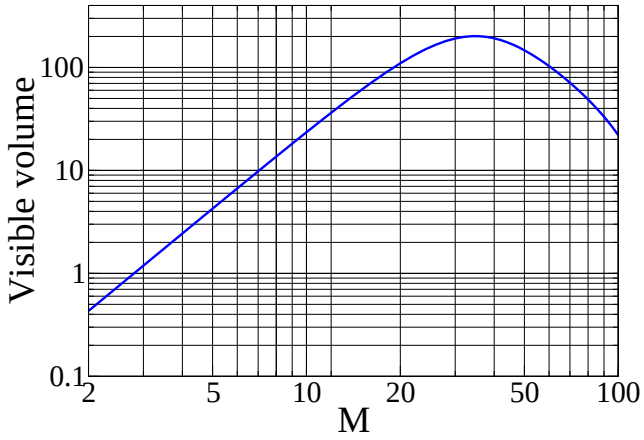

Figure 1.7: Relative visible volumes of LIGO-I interferometers for non-spinning, comparable-mass binaries with various total masses as observed by LIGO-I interferometers. These visible volumes are based on the leading-order waveform and the Schwarzchild-ISCO cutoff in the frequency-domain amplitude of the signal, with noise spectral density that of the LIGO-I design. The relative visible volume is set to unity for neutron-star binaries (with neutron-star masses set to $1.4\,M_\odot$ each). The visible volume peaks at $M \approx 35\,M_\odot$, with a maximum of ≈ 200.

interactions in globular clusters [40].

Having appreciated the importance of these "heavy" binary black holes, in Chapter 8, Buonanno, Vallisneri and I study effects associated with the failure of Post-Newtonian calculations for nonspinning "heavy" binary black holes. We study black holes with masses in the range of 5–20 $M_\odot$.

There exist three main approaches to Post-Newtonian expansions:

- *The Direct Approach*, where the equation of motion is obtained in the harmonic gauge, by expanding in powers of the orbital velocity divided by the speed of light, v/c [$1\,\mathrm{PN} = (v/c)^2$]:

$$\begin{aligned}\mathbf{a} \;=\; & \mathbf{a}_\mathrm{N} + \mathbf{a}_{1\,\mathrm{PN}} + \mathbf{a}_{2\,\mathrm{PN}} + \mathbf{a}_{3\,\mathrm{PN}} + \ldots \\ & + \mathbf{a}_{2.5\,\mathrm{PN}} + \mathbf{a}_{3.5\,\mathrm{PN}} + \ldots\,. \end{aligned} \tag{1.25}$$

  Integer PN orders (N, 1PN, 2PN, etc.) give dynamics with conserved orbital energy and angular momentum ("conservative dynamics") [57, 60], while the half-odd-number orders (starting from 2.5 PN) give the radiation reaction [58, 59], which drives the secular evolution of the orbit. Unfortunately, the PN-expanded acceleration has only been derived up to 3.5 PN order (with an undetermined regularization parameter in 3 PN), so the waveforms obtained from this approach can only be accurate up to 1 PN (since radiation reaction starts at 2.5 PN). A

Lagrangian can be derived from the conservative acceleration terms, so this approach is also called the *Lagrangian* approach in Chapter 8.

- *The Adiabatic Approach*, where energy and angular momentum fluxes in generic orbits have been calculated up to 3.5 orders beyond the quadrupole (2.5 PN) order [i.e., 6 orders after the leading Newtonian order, which corresponds to $(v/c)^{12}$!] but with undetermined regularization parameters in 3 PN [61, 62, 63]. The energy and angular momentum fluxes can then be used to construct a sequence of adiabatic orbits accurate up to 3.5 PN, by using the balance equation,

$$\dot{\mathcal{E}}(v) = -\mathcal{F}(v)\,, \tag{1.26}$$

  where $\mathcal{E}(v)$ is the orbital energy corresponding to the Keplerian orbital velocity $v \equiv (\pi M f)^{1/3}$ (with f *twice* the orbital frequency and $G = c = 1$), and $\mathcal{F}(v)$ is the corresponding energy flux.

- *The Hamiltonian approach*, where a Hamiltonian for the conservative dynamics has been derived up to 3 PN order, starting from the 3+1 decomposition formalism [64]. This Hamiltonian has also been shown to be equivalent to the one derived from the Lagrangian in the *Direct Approach* derived in harmonic gauge [65] (the undetermined 3 PN regularization parameter in the Direct-Approach conservative dynamics can be determined in the Hamiltonian Approach by means of dimensional regularization). Radiation reaction can be added to the Hamiltonian equations of motion as a generalized force which gives the correct energy and angular-momentum losses. The Hamiltonian approach can probe certain non-adiabatic effects, but cannot give the complete picture, since the radiation reaction is added assuming certain adiabaticity.

[See Secs. 8.4.2, 8.3.1 and 8.4.1 for more details on the three approaches respectively.] For binary black holes with total mass 10–40 $M_\odot$, the detection band of $f = 40$–240 Hz corresponds to Keplerian orbital speeds $v/c = 0.18$–0.53. At such high speeds, the Taylor-expanded flux $\mathcal{F}(v)$ (for example) at adjacent PN orders can differ a lot, as we see in Fig. 8.2, and does not seem to have converged at the currently available PN orders (up to 3.5 PN). [8] As for the Taylor-expanded Hamiltonian models (up to 3 PN), they usually cannot give the ISCO structure of dynamics (except at 1 PN, where the given ISCO frequency is obviously too small, see Table 8.2). With these signs of PN failure identified at the late-stage inspiral, *resummation* techniques have correspondingly been developed to improve the convergence of the PN expansions, in the absence of further inputs from higher PN orders. In Chapter 8, we discuss the following two prescriptions:

- *Padé approximants* [67, 68], where a Padé expansion is used to enhance the convergence of the Taylor-expanded forms given directly by the Post-Newtonian expansion, and the Padé

[8] In fact, for such high speeds, the PN expansion might not converge at all, since it could be an asymptotic expansion in nature [66].

expansion takes account of the expectation that the flux function $\mathcal{F}(v)$ should have a pole at the *light ring*. The Padé-expanded flux out to the orders that have been computed has been shown to converge much better than the Taylor-expanded versions, see Fig. 8.5.

- *Effective One-Body (EOB) Approach* [69, 70, 71, 72], where the two-body Hamiltonian dynamics is matched to that of a single test particle in a *deformed* Schwarzchild metric — with the deformation of the metric Post-Newtonian expanded in v/c. This approach recovers, in the resummed Hamiltonian, the late-stage dynamical features such as the ISCO and the light ring. Dynamics beyond the ISCO can be probed to a better extent by this approach than by the Taylor-expanded Hamiltonian approach.

[See Secs. 8.3.2 and 8.4.4 for further details on these resummation techniques.]

Data analysis oriented comparisons between different PN waveforms are based on the *overlap* (defined in Sec. 8.2.1) between the target signal and the template waveform. This overlap is equal to the fraction of optimal SNR achievable by an imperfect template, and therefore never exceeds unity. [The loss in visible volume with a fixed SNR, and hence event rate, is then $(\text{overlap})^3$, see arguments around Eq. (1.24).] A systematic comparison of PN waveforms in the Adiabatic approaches (Taylor and Padé) and the Effective One-body (EOB) approach (as the fiducial "exact" waveform) has been made by Damour, Iyer and Sathyaprakash (DIS) [67, 68, 55, 56], with a detailed numerical study carried up to 2.5 PN order. They formulated two types of tests:

- Comparison of physical predictions of the PN models (approach, prescription and order), in terms of the overlap between waveforms of *the same binary* as predicted by different PN models. This can be regarded as an internal convergence test of PN expansions, since if the PN expansion converges, all models should give similar results. In particular, if the two waveforms are generated from the same prescription (i.e., Taylor, or Padé, or EOB), but at different orders, this test is similar to a Cauchy convergence test of that approach.

- Setting waveforms from one PN model as the fiducial target signal (for which DIS use only EOB waveforms), and test whether using waveforms generated by another model (the template model) can successfully mimic the target, regardless of whether the optimal (M, η) used (in the template model) is the same as the target one. At the end, if the overlap is high, then the template family is regarded as *effectual*. If the resulting optimal (M, η) is close to the original one, then the template family is regarded as *faithful*.

In Chapter 8, we first (among other things) confirm the results of DIS, but with more models added, and without taking the EOB as the fiducial exact signal. We first test the Cauchy convergence, which was shown to be rather poor for Adiabatic Taylor (unless we skip the 2.5 PN order, see Table 8.3), and Taylor-expanded Hamiltonian models (Table 8.5) and better but not perfect for Adiabatic Padé

(Table 8.4) and EOB (see Table 8.8) models. Then, we go on to take the overlaps between 11 different typical models to test the effectualness and faithfulness of them against each other (see Table 8.11). Neither the effectualness nor the faithfulness is satisfactory, especially when Taylor-expanded Hamiltonians and 2.5 PN Taylor fluxes are involved. Nevertheless, overlaps obtained here are much higher than those obtained in the Cauchy tests. As a consequence, it is reasonable to *conjecture* that *the function space spanned by different PN waveforms are approximately the same, although the same waveform in the function space might correspond to different* (M, η)*'s in different PN models.*

1.2.2 Detection Template Families for nonspinning binaries

As a test of this conjecture, in Chapter 8 we use the 2.5 PN adiabatic Padé and 3.5 PN EOB waveforms, *allowing* η *to exceed its physical maximum,* 0.25*, and to take values up to* 1, and test the effectualness of each of them against all the other waveform families. For our choice of the target mass range, $5\,M_\odot < m_1,\, m_2 < 20\,M_\odot$, high overlaps are obtained, $\gtrsim 0.95$ with Padé and $\gtrsim 0.97$ with EOB, respectively, for reasonably well-behaved models, with some exceptions (see Tables 8.16 and 8.17). [The overlap achievable by a (continuous) template family for a target model is usually called the *fitting factor*, or FF, see, e.g., Ref. [52].] This means, the non-physical Padé and EOB waveforms could already be effectual template families for "heavy" binary black holes: since they can also mimic most PN predictions, it is plausible that they can mimic the real signal, with similar effectualness, or fitting factor, if the true signal lies "among" currently available different PN predictions. However, parameter estimation will not be straightforward from these "non-physical" templates: apparently because they involve η that exceeds the physical range, but more fundamentally because of the inherent disagreements between different PN models. We call such template families *Detection Template Families* (DTF), or *effective templates*. We shall focus on them (and shall ignore parameter estimation) throughout most of Chapters 8 and 9.

In addition to the time-domain, non-physical Padé and EOB DTFs, we also construct, in Chapter 8, a more versatile frequency-domain DTF, which is simpler in form [see Eqs. (8.107)–(8.109)],

$$h_{\rm eff}(f) = \mathcal{A}_{\rm eff}(f)\, e^{i\psi_{\rm eff}(f)}\,, \tag{1.27}$$

with

$$\mathcal{A}_{\rm eff}(f) = f^{-7/6}\left(1-\alpha\, f^{2/3}\right)\Theta(f_{\rm cut}-f)\,, \tag{1.28}$$

$$\psi_{\rm eff}(f) = 2\pi f t_0 + \phi_0 + f^{-5/3}\left(\psi_0 + \psi_{1/2}\, f^{1/3} + \psi_1\, f^{2/3} + \psi_{3/2}\, f + \psi_2\, f^{4/3} + \cdots\right). \tag{1.29}$$

Here $h_{\rm eff}$ has essentially the form of the Stationary-Phase-Approximated (SPA) Post-Newtonian

inspiral signal (see e.g., Ref. [73]), but with parameters α, $f_{\rm cut}$, t_0, ϕ and ψ_n left completely free:

- The cutoff frequency $f_{\rm cut}$ is introduced to incorporate the diverse ending frequencies predicted by different PN prescriptions (see Table 8.15). The term $\alpha f^{2/3}$ is the next-to-leading order PN correction to the frequency-domain amplitude, which can also mimic the edge effects caused by the end of the signal within the detection band.

- The ψ_n parameters, $n = 0, 1/2, 1, 3/2 \ldots$, can be obtained from PN expansion as functions of (M, η), but are left free here in the DTF to allow the exploration of the function space near the PN predictions. As it turns out, for binary black holes with $5\,M_\odot < m_1, m_2 < 20\,M_\odot$, since there are only 50-800 gravitational-wave cycles in the inspiral phase in the LIGO-I band, including ψ_0 and $\psi_{3/2}$ only (with other ψ_n's set to zero) is already sufficient to give high overlaps. [A DTF including ψ_0, ψ_1 and $\psi_{3/2}$ (which includes 1.5 PN SPA templates as a subset) is also considered in Sec. 8.6.6, to show why the ψ_0 and $\psi_{3/2}$ turned out to be sufficient.]

The ranges of parameters $(\psi_0, \psi_{3/2})$ required by the template family are determined empirically by "projecting" the various PN waveforms into the DTF, i.e., searching for the optimal DT that best matches each of the PN waveforms. [9] The effectualness of the DTF can be studied at the same time. In Sec. 8.6, the frequency-domain DTF is tested more thoroughly than the time-domain DTFs, against 26 different PN models, with numerical results of projection and effectualness shown in Table 8.5. The projection of these waveforms into the $(\psi_0, \psi_{3/2})$ space is shown in Figs. 8.20, together with required ranges of cutoff frequencies. A fitting factor of $\gtrsim 0.96$ is obtained for well-behaved models, with very few exceptions. In practical searches through a continuous template *family* performed in gravitational-wave detection, a discrete template *bank* will be needed. [10] The discretization will make the minimal overlaps achievable by the template *bank* (called the minimal match, or MM) be lower than the fitting factor of the continuous template *family*. A systematic way of laying down discrete templates on an optimal lattice in the parameter space, while guaranteeing the minimal match is the *metric* formalism [75, 76]. The metrics for the frequency- and time-domain DTFs are calculated in Secs. 8.6 and 8.7, respectively.

It is worth mentioning that this frequency-domain DTF shares some of the philosophy that underlies the application of the Fast Chirp Transformation (FCT) technique of Jenet and Prince to inspiral search [74]. The FCT deals with templates with phasings of the (polynomial-like) form of (1.29) by providing a schematic way of searching over the coefficients ψ_n.

Currently, the frequency-domain BCV template family, in the form of a template bank, is being implemented (with the help from the authors) for use in the LIGO S2 data analysis, and it will

[9] In fact, if the target is well approximated by the DTF, the optimization procedure, in terms of the local geometry of the function space around the optimal template and the target signal, is quite similar to a linear projection, as explained by, e.g., Chronopolous and Apostolatos [73].

[10] Although in some cases, analytical methods can be used to avoid the discretization in some parameter degrees of freedom, like the initial orbital phase, see, e.g., Ref. [67].

Binary			GW propagation	Detector orientation
M, η, S_1, S_2	θ_{S_1}, θ_{S_2}, $\phi_{S_1}-\phi_{S_2}$	$\theta_{\mathrm{L_N}}$, $\phi_{\mathrm{L_N}}$, $\phi_{S_1}+\phi_{S_2}$	Θ, φ	θ, ϕ, ψ
Basic	Local	Directional		

Table 1.2: Parameters (15 total) required to specify a precessing waveform [of binaries in circular orbits]: M [total mass], η [mass ratio], $(S_1, \theta_{S_1}, \phi_{S_1})$ [magnitude and initial orientation of first spin], $(S_2, \theta_{S_2}, \phi_{S_2})$ [magnitude and initial orientation of second spin], $(\theta_{L_\mathrm{N}}, \phi_{L_\mathrm{N}})$ [initial orientation of Newtonian angular momentum], (Θ, φ) [direction of wave propagation (from binary to detector)], and (θ, ϕ, ψ) [orientation of the detector], evaluated at a fiducial gravitational-wave frequency [twice the orbital frequency], e.g., at 30 Hz. See also Figs. 1.8 and 1.9 for detailed definitions of the angles. The time at which the inspiral passes the fiducial frequency and the corresponding orbital phase are not included in the parameter count. Among these 15 parameters, only 7 [the basic and local parameters] are needed to determine the dynamics of the binary.

become routine for future LIGO data analysis.

1.2.3 Challenge and importance of detecting spinning compact binaries

In the absence of radiation reaction, orbits with constant angular speed and radius, i.e., *spherical orbits*, still exist approximately, up to 1.5 PN for spinning binaries. However, the orientation of the "orbital plane" will not be constant, but will instead precess in space, due to spin-orbit and spin-spin couplings, *if* the spins are misaligned with the orbital angular momentum. The precession timescale is much longer than the orbital period, so it is still meaningful to talk about an adiabatic sequence of *precessing* circular orbits. As radiation reaction is added, the orbits will be both precessing and shrinking. If the magnitudes of the spins of (at least one of) the objects are not small compared to M^2 (with $G = c = 1$) and if the spins are misaligned significantly with the orbital angular momentum, the precession timescale will be much shorter than the radiation-reaction time scale, causing the orbit to precess for at least several cycles as its radius shrinks by a noticeable amount, thereby modulating the waveform significantly. Although Post-Newtonian prescriptions for calculating the evolution of *precessing binaries* exist, e.g., as given by Kidder [54], and should be reasonably accurate for neutron-star–black-hole binaries and low-mass binary black holes ($\lesssim 10\,M_\odot$ each), the number of parameters needed to characterize these binaries is uncomfortably high: 15 in total, see Table 1.2. This daunting number of parameters explains in part why up till now only a very limited data-analysis effort has been made to detect spinning binaries in first-generation gravitational-wave interferometers.

Although the spins of neutron stars are expected to be small (measured in M^2), and will perhaps not cause significant orbital precession, very little is known about the (magnitudes and orientations of the) spins of black holes in binaries. It is somewhat likely that the black holes will be rapidly spinning, due to accretion. It is also likely that, in neutron-star–black-hole binaries, the black hole spin can be significantly misaligned with the orbital angular momentum [77]; but not much is know about spin-orbit misalignments in binary black holes. Despite the lack of further concrete astrophysical information, it is clear that compact binaries with rapidly spinning black holes and

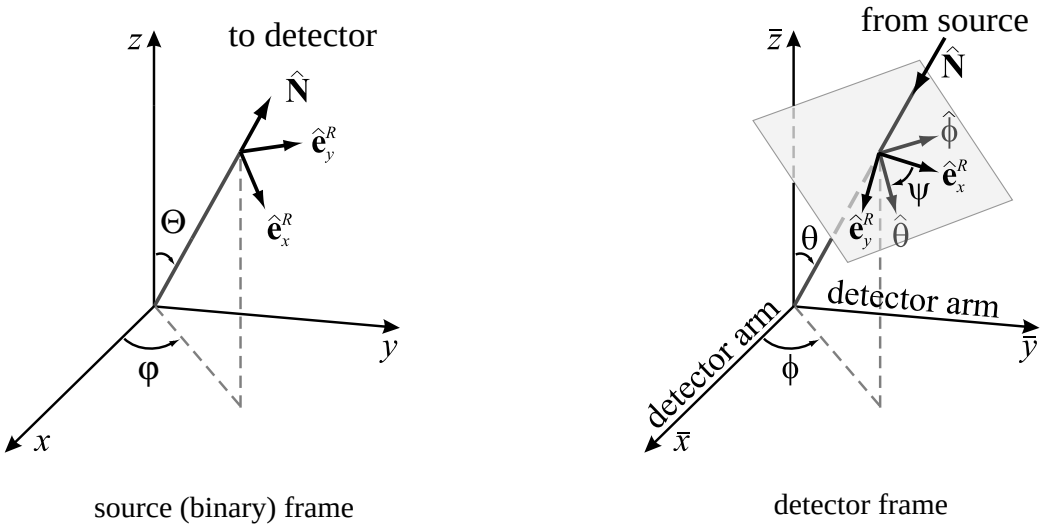

Figure 1.8: The source (binary) frame (left panel) and the detector frame (right panel).

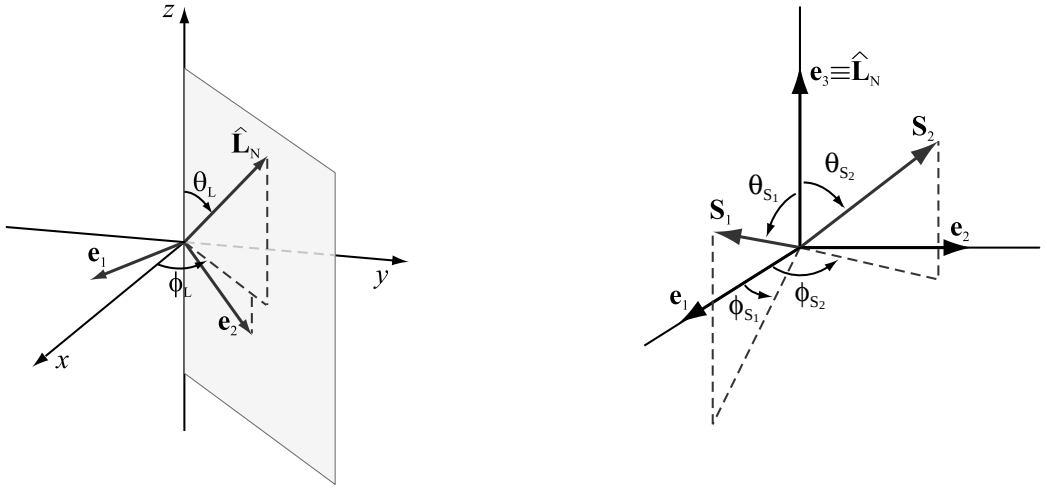

Figure 1.9: Definitions of the angles that describe the orientation of $\widehat{\mathbf{L}}_{\rm N}$ in the source frame [$(\theta_{L_{\rm N}}, \phi_{L_{\rm N}})$, left panel] and those that define the orientations of $\mathbf{S}_{1,2}$ with respect to $\widehat{\mathbf{L}}_{\rm N}$ [$(\theta_{S_1}, \phi_{S_1})$ and $(\theta_{S_2}, \phi_{S_2})$, right panel].

significant spin-orbit misalignment must be taken into account in the data analysis in order to detect inspiral waves efficiently with gravitational-wave interferometers. This issue is investigated in Chapter 9 by Buonanno, Vallisneri and me.

1.2.4 Features of precession dynamics and the Apostolatos Ansatz

The pioneering work of Apostolatos, Cutler, Sussman and Thorne (ACST) gave an intuitive physical picture of the evolution and waveforms of precessing binaries. In order to simplify their analysis, ACST included only the leading orders of the non-spinning part of the conservative dynamics and radiation reaction, and restricted themselves mostly to the special case when only one body is spinning, or the case when the two bodies have equal masses, and with spin-spin coupling ignored (we shall refer to these as the ACST special cases). (Apostolatos analyzed later the equal-mass case including spin-spin coupling [53].) ACST found that, for the vast majority of binary configurations, the total angular momentum **J** remains roughly constant in space, while the orbital angular momentum **L** (which is also the normal vector to the orbital plane) and total spin **S** both precess around it — with the angle between **L** and **S** constant. They called this *simple precession*. ACST also derived analytical formulas for the evolution of simple precessions (in the ACST special cases), and showed that, in simple precessions, the accumulated precession phase of **L** around **J** follows a power law in orbital frequency. Contrasting with simple precession is *transitional precession*, where **L** and **S** become almost anti-aligned and similar in magnitude, resulting in a nearly vanishing **J**, which then does not remain constant but tumbles in space. [11] The orbital orientation **L** also evolves irregularly in transitional precessions. Fortunately, transitional precessions only happen in a very small fraction of the parameter space, due to the stringent requirement on the near-cancellation between **L** and **S**. ACST studied qualitatively the modulated waveforms from precessing binaries in simple and transitional precessions, observing significant modulations in the waveforms induced by precessions.

Subsequently, Apostolatos studied quantitatively the impact of these modulations on data analysis [51]. It was shown that the precession-induced modulations, especially those of neutron-star–black-hole binaries with significant spin-orbit misalignment, were serious enough that nonspinning templates might miss these signals altogether. In order to cope with this, while keeping the size of the template family manageably small, Apostolatos invented two ansatz schemes [51, 52]. In these two schemes, phenomenological terms are added into the phasing of frequency-domain templates to simulate the precession-induced modulations, but leaving the amplitude unchanged, motivated by the argument that getting the template phasing correct is usually more crucial in achieving high fitting factors:

$$\Psi \to \Psi_{\rm PN}(M,\eta) + \Psi^{\rm I,\,II}_{\rm Apostolatos}\,, \tag{1.30}$$

[11] This can only happen briefly, for a few tumbles, since radiation reaction will drive **L** smaller and make **J** non-vanishing again, thus the name transitional precession.

with

$$\Psi^{\rm I}_{\rm Apostolatos} = A f^{-p}\,, \tag{1.31}$$

$$\Psi^{\rm II}_{\rm Apostolatos} = \mathcal{C}\cos\left(\mathcal{B} f^{-p} + \delta\right)\,. \tag{1.32}$$

Here, $p = -1$ or $-2/3$, depends on whether $\mathbf{L}$ is much larger than $\mathbf{S}$ or much smaller (but found to have similar effects in fitting factor). Ansatz I was devised to incorporate the monotonic contribution to the phasing made by the spin-orbit and spin-spin couplings, while Ansatz II was devised to mimic the oscillatory phase modulations caused by precession. As tested by Apostolatos in Ref. [51], Ansatz I can improve fitting factors on binary black holes with relatively high mass $(10+10)\,M_\odot$, but fails to work for neutron-star–black-hole binaries, e.g., the case of $(10+1.4)\,M_\odot$. As for Ansatz II, adding three more parameters, $(\mathcal{C}, \mathcal{B}, \delta)$, poses a great computational cost for the search — a five-dimensional parameter space might not be practical to search over in a one-by-one way. Apostolatos suggested a two-step hierarchy: searching over the mass parameters (M, η) in $\psi_{\rm PN}$ first, then fix the obtained (M, η) and search over ($\mathcal{C}$, $\mathcal{B}$, δ). Recently, Grandclément, Kalogera and Vecchio tested Ansatz II of Apostolatos (with the two-step hierarchy) on several neutron-star–black-hole and binary black hole (with low mass, not exceeding $10\,M_\odot$ each) systems (with approximated analytical target waveforms) and found that the performance was not satisfactory. [12]

1.2.5 The Modified Apostolatos Ansatz and DTF for spinning binaries

In Chapter 9, Buonanno, Vallisneri and I study the adiabatic dynamics of precessing binaries, mostly "heavy" BBH cases (with $5\,M_\odot < m_1, m_2 < 20\,M_\odot$), but also including one NS-BH case $[(10+1.4)\,M_\odot]$, including up to 2 PN orbital motion and radiation reaction, without restricting to the ACST special cases. We do not study the PN failure in this case, but instead use only the 2 PN adiabatic model, as given by Kidder in a comprehensive paper, Ref. [54], in which he derived the equations of motion (direct and adiabatic, in the sense of Sec. 1.2.1) for precessing binaries and expressions for the waveforms, and studied the dynamics and waveforms qualitatively. As we show in Sec. 9.3, the dynamics of these precessing binaries is qualitatively the same as found by ACST in lower-PN-order computations of the ACST special cases. In particular:

- The accumulated orbital phase $\Psi(t)$, obtained by integrating the instantaneous angular frequency,

$$\Psi(t) = \int^t \omega(t')dt'\,, \tag{1.33}$$

[12] One should be cautioned against saying that ansatz II is bad, since the low fitting factor might be due to the imperfectness of the two-step hierarchy. Nevertheless, since the two-step hierarchy could be the only obvious way of lowering computational cost, it is plausible to say that ansatz II, in its original form, is *not yet* practical for use in data analysis.

although affected by PN contributions that involve spins (which ACST *did not* take into account), deviates largely monotonically from the non-spinning phasing, and can be fit well with a polynomial in orbital frequency.

- The total angular momentum $\mathbf{J}$ still remain roughly constant in orientation for most of the configurations, while the precession phase of $\mathbf{L}$ around $\mathbf{J}$ is still roughly described by a power law in orbital frequency, except for the very rare cases of transitional precessions.

These were the starting points of the ansatz II of Apostolatos. However, we have developed a *modification* to this ansatz that allows the construction of DTFs that improve both the computational efficiency and the fitting factor:

We start by looking at the response of a gravitational-wave detector, which (at leading PN order) can be put into the following form

$$h(t) \propto \underbrace{\ddot{\mathcal{I}}^{ij}(t)}_{Q_{ij}} \underbrace{[\mathbf{T}_+(\Theta,\varphi)F_+(\theta,\phi,\psi) + \mathbf{T}_\times(\Theta,\varphi)F_\times(\theta,\phi,\psi)]_{ij}}_{P_{ij}}, \tag{1.34}$$

in which $\mathcal{I}^{ij}(t)$ is the instantaneous quadrupole moment of the binary, $\mathbf{T}_{+,\times}$ are the polarization tensors of waves propagating in the (Θ,φ) direction and $F_{+\,\times}$ are the antenna patterns of the detector, which depend on the detector orientation [see Fig. 1.8]. Moreover, in the leading PN order, we have [see Sec. 9.4]

$$Q_{ij}(t) \equiv \ddot{\mathcal{I}}_{ij}(t) \propto \omega^2(t)\,[\mathbf{e}_+(t)\cos 2\Psi(t) + \mathbf{e}_\times(t)\sin 2\Psi(t)]_{ij}\ , \tag{1.35}$$

where $\Psi(t)$ is the accumulated orbital phase [which does not oscillate], and

$$\mathbf{e}_+(t) \equiv \mathbf{e}_1(t)\otimes\mathbf{e}_1(t) - \mathbf{e}_2(t)\otimes\mathbf{e}_2(t)\,, \quad \mathbf{e}_\times(t) \equiv \mathbf{e}_1(t)\otimes\mathbf{e}_2(t) + \mathbf{e}_2(t)\otimes\mathbf{e}_1(t)\,, \tag{1.36}$$

with $\mathbf{e}_{1,2}(t)$ a time-dependent orthonormal basis of the precessing orbital plane that follows the precession in a non-rotational way (see Sec. 9.4.1, Appendix 9.9, in particular Eqs. (9.71) and (9.72), for the specific meaning of this). Since $\mathbf{e}_{1,2}(t)$ follow the orbital precession, it is plausible to modify the Apostolatos ansatz into

$$[\mathbf{e}_K]_{ij}\,(t) \sim \alpha_{K\,ij} + \beta_{K\,ij}\cos(\mathcal{B}f_t^{-p} + \delta_{K,\,ij})\,, \quad (p = 1, 2/3)\,, \qquad K = +, \times\,, \tag{1.37}$$

where f_t is twice the orbital frequency at time t. By inserting Eqs. (1.35)–(1.37) into Eq. (1.34) and Fourier transforming in the Stationary-Phase Approximation, we obtain

$$\begin{aligned}\tilde{h}(f) &\propto \left[\mathcal{C}_1 + i\,\mathcal{C}_2 + (\mathcal{C}_3 + i\,\mathcal{C}_4)\cos(\mathcal{B}f^{-p}) + (\mathcal{C}_5 + i\,\mathcal{C}_6)\sin(\mathcal{B}f^{-p})\right]\left[f^{-7/6}\exp(i\Psi_{\rm NM})\right] \\ &\equiv \sum_{j=1}^{6}\mathcal{C}_j\mathcal{A}_j(f)\exp(i\Psi_{\rm NM}) \equiv \mathcal{A}(f)\exp(i\Psi_{\rm NM})\,, \qquad (1.38)\end{aligned}$$

where the $\mathcal{C}_j$'s are real constants. Here $\Psi_{\rm NM}$ stands for a *non-modulated* phasing, with the form of Eq. (1.29). Again, we propose to use only two free parameters *in* $\Psi_{\rm NM}$: ψ_0 and $\psi_{3/2}$. It should be noted that, although the modulations are all added formally in the amplitude $\mathcal{A}(f)$, the fact that $\mathcal{A}_j$ can be complex means that the modulations act both on amplitude and phase. We call this template family the *modulated BCV* template family.

The amplitude-modulation form of the modulated BCV template (1.38) is very advantageous for search purposes. At each set of $(\psi_0, \psi_{3/2}, \mathcal{B})$, the linear coefficients $\mathcal{C}_{1,\ldots,6}$ parametrize a six-dimensional linear template subspace, in which the optimization of template-signal correlations over the entire linear subspace can be obtained by taking the correlations between the signal and a set of basis vectors [independent templates], and then combining, by taking the square root of the sum of the squares of each individual correlation. As a consequence, the one-by-one search only need be done in a three-dimensional parameter space, $(\psi_0, \psi_{3/2}, \mathcal{B})$. In the terminology of gravitational-wave data analysis, $\mathcal{C}_{1,\ldots,6}$, which do not need to be searched over one-by-one, are called *extrinsic parameters*, while the parameters $(\psi_0, \psi_{3/2}, \mathcal{B})$, which need to be searched over one-by-one, are *intrinsic parameters*. By employing a lot of extrinsic parameters, the modulated BCV template family is computationally very efficient. A well-known example of this extrinsic-parameter technique in gravitational-wave data analysis is the optimization for the initial orbital phase of inspiral templates (see e.g., Ref. [67]), where the linear template space is two-dimensional. A four-dimensional version has also been proposed for the combined search over the initial phase and the detector orientation, in both spinning binaries [78] and for Pulsars [79]. The Jenet-Prince Fast Chirp Transformation (FCP) is another (rather different) way of converting intrinsic parameters (ψ_n) into extrinsic parameters.

In Sec. 9.6, we test the performance of our modulated BCV template family in terms of fitting factors. In Table 1.3 (excerpted from Tables 9.8 and 9.9), the averaged fitting factors, assuming a uniform spatial distribution of the orientations of the initial spins and angular momenta, weighted by the cube of signal strength (measured by the optimal SNR at a fixed distance), is given (in the line labeled BCV2) for maximally spinning binary black holes with masses $(15+15)\,M_\odot$, $(10+10)\,M_\odot$, $(20+10)\,M_\odot$, $(20+5)\,M_\odot$ and $(7+5)\,M_\odot$, and a neutron-star–black-hole binary with masses $(10+1.4)\,M_\odot$ with maximally spinning black hole and nonspinning neutron star. For comparison,

	$(7+5)M_\odot$	$(10+10)M_\odot$	$(15+15)M_\odot$	$(20+5)M_\odot$	$(20+10)M_\odot$	$(10+1.4)M_\odot$
SPAc	0.937	0.956	0.955	0.910	0.946	0.813
BCV1	0.962	0.970	0.973	0.921	0.963	0.832
BCV2	0.983	0.990	0.989	0.979	0.988	0.945

Table 1.3: Average fitting factors of nonspinning templates (SPAc, the standard Stationary-Phase-Approximated nonspinning template with free higher cutoff frequency, and BCV1, the frequency-domain DTF proposed in Chapter 8) and modulated BCV templates (BCV2) for spinning binary black holes and neutron-star–black-hole binaries. Black holes are assumed to be maximally spinning, while neutron-star spins are neglected. A uniform distribution of initial spin and orbital orientations is assumed.

Table 1.3 also shows fitting factors of the Stationary-Phase-Approximated nonspinning templates [Eq. (1.34), with $\alpha = 0$, free cutoff frequency, and ψ_n values provided by PN calculations; denoted by SPAc] and of the frequency-domain DTF (for nonspinning binaries) proposed in Chapter 8 [defined by Eq. (1.34) and the text that follows, denoted by BCV1]. In the binary black hole case, the average fitting factor obtained by nonspinning templates were already higher than 0.9 (usually higher than 0.95). This is consistent with the findings of Apostolatos using his first ansatz [52]. The use of modulated BCV templates is shown to increase the average fitting factor, up to ~ 0.98. The average fitting factor obtained by nonspinning templates for the NS-BH binary is much lower, around 0.8, which means a nearly 50% loss in event rate, if in reality the angular momenta are distributed uniformly. The modulated BCV templates (BCV2) increase the average fitting factor up to $\sim$ 0.95. We have explained fitting factors for NS-BH binaries further, by looking at the average fitting factors for different initial misalignment between the black-hole spin and orbital angular momentum (averaged over the relative orientations between the binary as a whole and the detector), see Fig. 1.10. As expected, the nonspinning templates can catch the waveform well only for nearly aligned and anti-aligned configurations. The modulated BCV templates have a similar bias toward aligned and anti-aligned binaries, but much less, by improving significantly the fitting factor for misaligned binaries.

Unfortunately, the improvements in fitting factors do not come for free. Because (when one takes account of all the $\mathcal{C}_j$'s) there are many more modulated BCV templates than nonspinning templates, the noise would cause many more false-alarm events, if the same detection threshold on SNR were imposed. This must be compensated by raising the threshold, which, unfortunately, will decrease the visible range and therefore counteract the increase in overlap achieved by including the more diverse templates. A rigorous study of the false alarm rate of a template family usually requires a Monte Carlo simulation, which is very computationally intensive. In Chapter 9, we only give a very rough overestimate of the false-alarm probability. This overestimate yields a requirement of 8.5% in overlap increase in order to justify the use of a six-dimensional linear template space. This is only met in the NS-BH case. However, we should not simply rule out the modulated BCV template

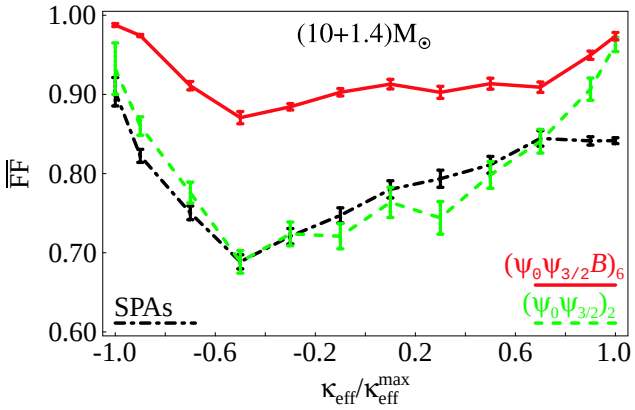

Figure 1.10: The dependence of the neutron-star–black-hole average fitting factor on the spin-orbit misalignment, $\kappa \equiv \hat{\mathbf{L}}_{\rm N} \cdot \hat{\mathbf{S}}$ (which is conserved throughout the evolution). Here SPAs stands for the standard, Stationary-Phase Approximated templates for nonspinning binaries, $(\psi_0\psi_{3/2})_2$ stands for the frequency-domain DTF proposed in Chapter 8 for nonspinning binaries (BCV1 templates), and $(\psi_0\psi_{3/2}B)_6$ stands for the modulated BCV templates.

family, since:

- A Monte Carlo simulation has to be done to determine whether this pessimistic estimate is accurate enough.
- Even if that is done, a realistic astrophysical distribution of the orientations of the spins and orbital angular momenta has to be known to answer the ultimate question of whether the modulated BCV templates can increase the event rate. Such knowledge is not likely in the near future.
- Even though the event rate might not be higher, having a less biased template bank might be beneficial.

An interesting conceptual problem will also arise in the study of the modulated BCV template family, if a Monte Carlo study confirms the high false-alarm probability: did the high false alarm originate from a "non-physical" reason, due to the inclusion of signals in the template bank that cannot be generated by a precessing binary, or from a "physical" reason, due to the diversity of precessing waveforms. This problem can be studied by including only the true, physical signals in the template bank, which has been regarded as impractical. However, it is not impractical for NS-BH binaries. Let us begin by asking how many parameters are absolutely required to be *searched over, one by one,* (i.e., how many intrinsic parameters are there) in the signal (1.34), for a generic binary:

- It is plausible that the parameters (Θ, φ) and (θ, ϕ, ψ) can be converted into extrinsic parameters, since the waveform depends on them only through the linear coefficients P_{ij}.

- In order to compute Q_{ij}, it might seem that all 10 binary parameters (Table 1.2) are needed. However, the overall orientation of the binary is not absolutely needed, in the following sense: we can choose an arbitrary frame, say, one in which $\mathbf{L}$ is along the z axis and $\mathbf{S}_1$ is in the x-z plane at $f = 30\,\mathrm{Hz}$, and compute Q_{ij} — this is already enough, since the arbitrariness in the orientation of this frame will be automatically accounted for by the (Θ, φ) and (θ, ϕ, ψ) parameters. In the end, 7 is the number of relevant parameters, which we call "basic" and "local parameters" in Table 1.2.

Although 7 is still too large for the dimensionality of the intrinsic parameter space, 3 of them are absent when the spin of one of the two bodies is unimportant, e.g., in NS-BH binaries. A four-dimensional intrinsic-parameter space is needed in this case, which is not extremely big. An exploration of this parameter space (now physical) will not only help clarify conceptually the origin of the high false alarm probability, but for the first time provide a practical way of searching over the physical templates of precessing binaries, which so far has been regarded as non-practical. Investigation of this approach is currently being made by Pan, Buonanno, Vallisneri and me.

1.3 Bibliography

[1] A. Abramovici et al., Science **256**, 325 (1992).

[2] B. Caron et al., Class. Quantum Grav. **14**, 1461 (1997).

[3] H. Lück et al., Class. Quantum Grav. **14**, 1471 (1997); B. Willke et al., Class. Quantum Grav. **19**, 1377 (2002).

[4] M. Ando et al., Phys. Rev. Lett. **86**, 3950 (2001).

[5] C. Cutler and K. S. Thorne, *An overview of gravitational-wave sources*, `gr-qc/0204090`.

[6] E. Gustafson, D. Shoemaker, K. A. Strain and R. Weiss, "LSC white paper on detector research and development," LIGO Document Number T990080-00-D.

[7] V. B. Braginsky, Sov. Phys. JETP **26** 831 (1968); V. B. Braginsky and Yu. I. Vorontsov, Sov. Phys. Uspekhi **17** 644 (1975); V. B. Braginsky, Yu. I. Vorontsov and F. Ya. Kahili, Sov. Phys. JETP **46** 705 (1977).

[8] V. B. Braginsky and F. Ya. Khalili, *Quantum measurement*, (Cambridge University Press, Cambridge, 1992).

[9] V. B. Braginsky, M. L. Gorodetsky and F. Ya. Khalili, Phys. Lett. A **232** 340 (1997); V. B. Braginsky, F. Ya. Khalili, Phys. Lett. A **257** 241 (1999).

[10] C. M. Caves and B. L. Schumaker, Phys. Rev. **A 31** 3068 (1985); B. L. Schumaker and C. M. Caves, Phys. Rev. **A 31** 3093 (1985).

[11] C. M. Caves, Phys. Rev. **D 23** 1693 (1981).

[12] V. B. Braginsky, M. L. Gorodetsky, F. Ya. Khalili, A. B. Matsko, K. S. Thorne and S. P. Vyatchanin, *Noise in gravitational-wave detectors is not influenced by test-mass quantization*, submitted to Phys. Rev. D, `gr-qc/0109003`.

[13] W. G. Unruh, in *Quantum Optics, Experimental Gravitation, and Measurement Theory*, eds. P. Meystre and M. O. Scully (Plenum, 1982), p. 647;

[14] S. P. Vyatchanin and A. B. Matsko, JETP **77** (1993) 218; S. P. Vyatchanin and E. A. Zubova, Phys. Lett. A **203** (1995) 269; S. P. Vyatchanin and A. B. Matsko, JETP **82** (1996) 1007; S. P. Vyatchanin and A. B. Matsko, JETP **83** (1996) 690; S.P. Vyatchanin, Phys. Lett. A **239** (1998) 201.

[15] H. J. Kimble, Yu. Levin, A. B. Matsko, K. S. Thorne and S. P. Vyatchanin, Phys. Rev. D **65**, 022002 (2002).

[16] B. J. Meers, Phys. Rev. D **38** 2317 (1988).

[17] R. Drever, in *Gravitational Radiation*, ed. N. Deruelle and T. Piran (North-Holland, Amsterdam, 1983), pp. 321-338.

[18] J. Mizuno, *Comparison of optical configurations for laser interferometric gravitatioanl-wave detectors*, PhD thesis, Max Planck Institute für Quantenoptik, Garching, Germany (1995); J. Mizuno, K. A. Strain, P. G. Nelson, J. M. Chen, R. Schilling, A. Rüdiger, W. Winkler and K. Danzmann, Phys. Lett. A **175** (1993) 273.

[19] A. V. Syrtsev and F. Ya. Khalili, JETP **79**, 3 (1994).

[20] F. Ya. Khalili, Phys. Lett. A **288**, 251 (2001).

[21] J. Harms, *Quantum Noise in the Laser-Interferometer Gravitational-wave Detector GEO 600*, diploma thesis, Universität Hannover, Hannover Germany (2002).

[22] L. Schnupp, unpublished talk at the *European Collaboration Meeting on Interferometric Detection of Gravitational Waves*, 1988, Sorrento, Italy.

[23] J. Gea-Banacloche and G. Leuchs, J. Mod. Opt **34**, 793 (1987).

[24] T. Niebauer, R. Schilling, K. Danzmann, A. Rüdiger and W. Winkler, Phys. Rev. A **43**, 5022 (1991).

[25] B. J. Meers and K. Strain, Phys. Rev. A **44**, 4693 (1991).

[26] K. Somiya, *New Photodetection Method Using Unbalanced Sidebands for Squeezed Quantum Noise in Gravitational Wave Interferometer,* gr-qc/0208029.

[27] V. B. Braginsky and F. Ya. Khalili, Phys. Lett. A **147**, 251 (1990).

[28] F. Ya. Khalili, *Quantum Speedmeter and Laser Interferometric Gravitational-Wave Antennae*, gr-qc/0211088.

[29] P. Purdue, Phys. Rev. D **66**, 022001 (2002);

[30] G. Sagnac, C. R. Acad. Sci. **95**, 1410 (1913).

[31] R. Weiss, in an unpublished NSF proposal, 1987.

[32] The TAMA team, *Gravitational-wave Astronomy,* Report for the Japanese government, Kyoto University, pp 286–287 (1992);

[33] K.-X. Sun, M. M. Fejer, E. Gustafson and R. L. Byer, Phys. Rev. Lett, **76**, 3053 (1996);

[34] K.-X. Sun and R. L. Byer, Gen. Rel. and Grav., **23**, 567 (1998); S. Traeger, P. Beyersdorf, L. Goddard, E.K. Gustafson, M. M. Fejer and R. L. Byer, Opt. Lett. **25**, 722 (2000); P. Beyersdorf, *The Polarization Sagnac interferometer for gravitational-wave detection,* Ph.D. Thesis, Stanford University, Feb. 2001.

[35] D. A. Shaddock, M.B. Gray and D.E. McClelland, Appl. Opt. **37**, 7995 (1998).

[36] B. Petrovichev, M. Gray and D. McClelland, Gen. Rel. and Grav., **30**, 1055 (1998).

[37] J. Mizuno, A. Rüdiger, R. Schilling, W. Winkler and K. Danzmann, Opt. Comm. **138**, 383 (1997).

[38] É. É. Flanagan and S. A. Hughes, Phys. Rev. D **57**, 4535 (1998); *ibid.*, 4566 (1998).

[39] C. W. Lincoln and C. M. Will, Phys. Rev. D **42** 1123 (1990).

[40] M. C. Miller and D.P. Hamilton, Astrophys. J. **576**, 894 (2002).

[41] L. Wen, "On the eccentricity distribution of coalescing black hole binaries driven by the Kozai mechanism in globular clusters," astro-ph/0211492, submitted to Astrohys. J.

[42] K. Belczynski, V. Kalogera, and T. Builk, Astrophys. J., in print (2002), astro-ph/0111452.

[43] V. Kalogera, R. Narayan, D.N. Spergel and J.H. Taylor, Astrophys. J. **556**, 340 (2001).

[44] E. S. Phinney, Astrophys. J., **380**, L17 (1991).

[45] T. Damour, *300 Years of Gravitation*, S. W. Hawking and W. Israel, eds. (Cambridge University Press, Cambridge, England, 1987); L. Blanchet, *Living Reviews in Relativity*, 2002-3 (2002), `http://www.livingreviews.org/Articles/Volume5/2002-3blanchet`.

[46] See, e.g., L.A. Wainstein and L.D. Zubakov, *Extraction of signals from noise* (Prentice-Hall, Englewood Cliffs, NJ, 1962).

[47] J. B. Hartle and K. S. Thorne, Phys. Rev. D **31**, 1815 (1984)

[48] B. M. Barker and R. F. O'Connell, Phys. Rev. D **12**,329 (1975)

[49] L. S. Finn and D. F. Chernoff, Phys. Rev. D **47**, 2198 (1993).

[50] T.A. Apostolatos, C. Cutler, G.J. Sussman and K.S. Thorne, Phys. Rev. D **49**, 6274 (1994).

[51] T. A. Apostolatos, Phys. Rev. D **52**, 605 (1995).

[52] T. A. Apostolatos, Phys. Rev. D **54**, 2421 (1996).

[53] T. A. Apostolatos, Phys. Rev. D **54**, 2438 (1996).

[54] L. E. Kidder, Phys. Rev. D **52** (1995) 821.

[55] T. Damour, B. R. Iyer and B. S. Sathyaprakash, Phys. Rev. D **63**, 044023 (2001).

[56] T. Damour, B. R. Iyer and B. S. Sathyaprakash, Phys. Rev. D **66**, 027502 (2002).

[57] T. Damour and N. Deruelle, Phys. Lett. A **87**, 81 (1981); T. Damour, C. R. Séances Acad. Sci. Ser. 2 **294**, 1355 (1982).

[58] B. R. Iyer and C. Will, Phys. Rev. Lett. **70**, 113 (1993); *Phys. Rev. D* **52**, 6882 (1995)

[59] A. Gopakumar, B. R. Iyer and S. Iyer, Phys. Rev. D **55**, 6030 (1997).

[60] L. Blanchet and B. Iyer, Class. and Quantum Grav. **20**, 755 (2003)

[61] L. Blanchet, T. Damour, B. R. Iyer, C. M. Will and A. G. Wiseman, Phys. Rev. Lett. **74**, 3515 (1995); L. Blanchet, T. Damour and B. R. Iyer, Phys. Rev. D **51**, 536 (1995); C. M. Will and A. G. Wiseman, Phys. Rev. D **54**, 4813 (1996).

[62] T. Damour, P. Jaranowski and G. Schäfer, Phys. Lett. B **513**, 147 (2001).

[63] L. Blanchet and G. Faye, Phys. Lett. A **271**, 58 (2000); J. Math. Phys **42**, 4391 (2001); Phys. Rev. D **63**, 062005 (2000); V. C. de Andrade, L. Blanchet and G. Faye, Class. Quant. Grav. **18**, 753 (2001).

[64] P. Jaranowski and G. Schäfer, Phys. Rev. D **57**, 7274 (1998); ibid. **60**, 124003 (1999).

[65] T. Damour, P. Jaranowski and G. Schäfer, Phys. Rev. D **63** 044021 (2001).

[66] L. Blanchet, Private communication.

[67] T. Damour, B. R. Iyer and B. S. Sathyaprakash, Phys. Rev. D **57**, 885 (1998).

[68] T. Damour, B. R. Iyer and B. S. Sathyaprakash, Phys. Rev. D **62**, 084036 (2000).

[69] A. Buonanno and T. Damour, Phys. Rev. D **59**, 084006 (1999).

[70] A. Buonanno and T. Damour, Phys. Rev. D **62**, 064015 (2000).

[71] T. Damour, P. Jaranowski and G. Schäfer, Phys. Rev. D **62**, 084011 (2000).

[72] T. Damour, Phys. Rev. D, **64** 124013 (2001).

[73] A. E. Chronopoulos and T. A. Apostolatos, Phys. Rev. D **64**, 042003 (2001).

[74] F. A. Jenet and T. Prince, Phys. Rev. D **62**, 122001 (2000).

[75] R. Balasubramanian, B. S. Sathyaprakash and S. V. Dhurandhar, Phys. Rev. D **53**, 3033 (1996).

[76] B. J. Owen and B. Sathyaprakash, Phys. Rev. D **60**, 022002 (1999).

[77] V. Kalogera, Astrophys. J., **541** 319 (2000).

[78] J. Creighton, private communication.

[79] P. Jaranowski, A. Królak and B. F. Schutz, Phys. Rev. D **58**, 063001 (1998).

Chapter 2

Quantum noise in second generation, signal-recycled laser interferometric gravitational-wave detectors

It has long been thought that the sensitivity of laser interferometric gravitational-wave detectors is limited by the free-mass standard quantum limit, unless radical redesigns of the interferometers or modifications of their input/output optics are introduced. Within a fully quantum-mechanical approach we show that in a second-generation interferometer composed of arm cavities and a signal recycling cavity, e.g., the LIGO-II configuration, (i) quantum shot noise and quantum radiation-pressure-fluctuation noise are dynamically correlated, (ii) the noise curve exhibits two resonant dips, (iii) the Standard Quantum Limit can be beaten by a factor of 2, over a frequency range $\Delta f/f \sim 1$, but at the price of increasing noise at lower frequencies.

Originally published as A. Buonanno and Y. Chen, Phys. Rev. D **64** 042006 (2001).

2.1 Introduction

Several laser interferometric gravitational-wave (GW) detectors [1] (interferometers for short), sensitive to the high-frequency band $10 - 10^3$ Hz, will become operative within about one year. In the first generation of these interferometers the Laser Interferometer Gravitational Wave Observatory (LIGO), TAMA and Virgo configurations [1] are characterized by kilometer-scale arm cavities with four mirror-endowed test masses, suspended from seismic-isolation stacks. Laser interferometry is used to monitor the relative change in the positions of the mirrors induced by the gravitational waves. The Heisenberg uncertainty principle, applied to the test masses of GW interferometers states that, if the relative positions are measured with high precision, then the test-mass momenta

[1] GEO's optical configuration differs from that of LIGO/TAMA/Virgo — it does not have Fabry-Perot cavities in its two Michelson arms, and the analysis made in this chapter does not directly apply to it. However, we note that GEO, already in its first implementation, does use the 'signal recycling' optical configuration with which this chapter deals.

will be perturbed. As time passes, the momentum perturbations will produce position uncertainties, which might mask the tiny displacements produced by gravitational waves. If the momentum perturbations and measurement errors are not correlated, a detailed analysis of the above process gives rise to the standard quantum limit (SQL) for interferometers: a limiting (single-sided) noise spectral density $S_h^{\rm SQL} = 8\hbar/(m\Omega^2 L^2)$ for the dimensionless gravitational-wave signal $h(t) = \Delta L/L$ [2]. Here m is the mass of each identical test mass, L is the length of the interferometer's arms, ΔL is the time evolving difference in the arm lengths, Ω is the GW angular frequency, and $\hbar$ is Planck's constant.

The concept of SQL's for high-precision measurements was first formulated by Braginsky [3]. He also demonstrated that it is possible to circumvent SQL's by changing the designs of the instruments, so they measure quantities which are not affected by the uncertainty principle by virtue of commuting with themselves at different times [3, 4] – as for example in speed-meter interferometers [5], which measure test-mass momenta instead of positions. Interferometers that circumvent the SQL are called quantum-nondemolition (QND) interferometers. Since the early 1970s, it has been thought that to beat the SQL for GW interferometers the redesign must be major. Examples are (i) speed-meter designs [5] with their radically modified optical topology, (ii) the proposal to inject squeezed vacuum into an interferometer's dark port [6], and (iii) the proposal to introduce two kilometer-scale filter cavities into the interferometer's output port [7] so as to implement frequency-dependent homodyne detection [8]. Both (ii) and (iii) intend to take advantage of the non-classical correlations of the optical fields. These radical redesigns require high laser power circulating in the arm cavities ($\gtrsim 1$ MW) and/or are strongly susceptible to optical losses which tend to destroy quantum correlations. In order to tackle these two important issues, Braginsky, Khalili and colleagues have recently proposed the GW "optical bar" scheme [9], where the test mass is effectively an oscillator, whose restoring force is provided by in-cavity optical fields. For "optical bar" detectors the free-mass SQL is no more relevant and one can beat the SQL using classical techniques of position monitoring. Moreover, this scheme has two major advantages: It requires much lower laser power circulating in the cavities [9], and is less susceptible to optical losses.

Research has also been carried out using successive independent monitors of free-mass positions. Yuen, Caves and Ozawa discussed and disputed about the applicability and the beating of the SQL within such models [10]. Specifically, Yuen and Ozawa conceived ways to beat the SQL by taking advantage of the so-called contractive states [10]. However, the class of interaction Hamiltonians given by Ozawa are not likely to be applicable to GW interferometers (for further details see Chapter 3).

Recently, we showed in Ref. [11] that it is possible to circumvent the SQL for LIGO-II-type signal-recycling (SR) interferometers [12, 13]. With their currently planned design, LIGO-II interferometers

can beat the SQL by modest amounts, roughly a factor two over a bandwidth $\Delta f \sim f$. [2] It is quite interesting to notice that the beating of the SQL in SR interferometers has a similar origin as in "optical bar" GW detectors mentioned above [9].

Braginsky and colleagues [15], building on earlier work of Braginsky and Khalili [4], have shown that for LIGO-type GW interferometers, the test-mass initial quantum state only affects frequencies $\lesssim 1\,\mathrm{Hz}$, the dependence on the initial quantum state can be removed filtering the output data at low frequency. Therefore, the SQL in GW interferometers is enforced only by the light's quantum noise, *not directly* by the test mass. As we discussed in [11], and we shall explicitly show below, we can decompose the optical noise of a SR interferometer into shot noise and radiation-pressure noise, using the fact that they transform differently under rescaling of the mirror mass m and the light power I_o. As long as there are no correlations between the light's shot noise and its radiation-pressure-fluctuation noise, the light firmly enforces the SQL. This is the case for conventional interferometers, i.e., for interferometers that have no SR mirror at the output dark port and a simple homodyne detection is performed (the type of interferometer used in LIGO-I/TAMA/Virgo). However, the SR mirror [12, 13] (which is being planned for LIGO-II [3] as a tool to reshape the noise curve, and thereby improve the sensitivity to specific GW sources [16]) produces *dynamical* shot-noise/back-action-noise correlations, and *these correlations break the light's ability to enforce the SQL*. These dynamical correlations come naturally from the nontrivial coupling between the test mass and the signal-recycled optical fields, which makes the dynamical properties of the entire optical-mechanical system rather different from the naive picture of a free mass buffeted by Poissonian radiation pressure. As a result, the SQL for a free test mass has no relevance for a SR interferometer. Its only remaining role is as a reminder of the regime where back-action noise is comparable to the shot noise. The remainder of this chapter is devoted to explaining these claims in great detail. To facilitate the reading we have put our discussion of the dynamical system formed by the optical fields and the mirrors into a Chapter 3.

The outline of this chapter is as follows. In Sec. 2.2 we derive the input–output relations for the whole optical system composed of arm cavities and a SR cavity, pointing out the existence of dynamical instabilities, and briefly commenting on the possibility and consequences of introducing a control system to suppress them. In Sec. 2.3 we evaluate the spectral density of the quantum noise. More specifically, in Sec. 2.3.1 we discuss the general case, showing that LIGO-II can beat the SQL when dynamical correlations between shot noise and radiation-pressure noise are produced by the SR mirror. In Sec. 2.3.2, making links to previous investigations, we decompose our expres-

[2] *If* all sources of thermal noise can also be pushed below the SQL. The thermal noise is a tough problem and for current LIGO-II designs with 30 kg sapphire mirrors, estimates place its dominant, thermoelastic component slightly above the SQL [14].

[3] The LIGO-II configuration will also use a power-recycling cavity to increase the light power at the beamsplitter. The presence of this extra cavity will not affect the quantum noise in the dark-port output. For this reason we do not take it into account.

sion for the optical noise into shot noise and radiation-pressure noise and express the dynamical correlations between the two noises in terms of physical parameters characterizing the SR interferometer; in Sec. 2.3.3 we specialize to two cases, the extreme signal-recycling (ESR) and extreme resonant-sideband-extraction (ERSE) configurations, where dynamical correlations are absent and a semiclassical approach can be applied [12, 13]. In Sec. 2.4 we investigate the structure of resonances of the optical-mechanical system and discuss their link to the minima present in the noise curves. Finally, Sec. 2.5 deals with the effects of optical losses, while Sec. 2.6 summarizes our main conclusions. The Appendix (Sec. 2.7) discusses the validity of the two-photon formalism in our context.

2.2 Signal-recycling interferometer: input–output relations

In Fig. 2.1 we sketch the SR configuration of LIGO-II interferometers. The optical topology inside the dashed box is that of conventional interferometers such as LIGO-I/TAMA/Virgo, which are Michelson interferometers with Fabry-Perot (FP) arm cavities. The principal noise input and the signal and noise output for the conventional topology are c_i and d_i in Fig. 2.1. In a recent paper, KLMTV [7] have derived the input–output $(c_i - d_i)$ relations for a conventional interferometer at the output dark port, immediately after the beam splitter, within a full quantum mechanical approach. In this section we shall derive the input–output $(a_i - b_i)$ relations for the whole optical system at the output port, i.e., immediately after the SR mirror, and shall evaluate the corresponding noise spectral density.

As we shall see, a naive application of the Fourier-based formalism developed in [7] gives ill-defined input–output relations, due to the presence of optical-mechanical instabilities. These instabilities have an origin similar to the dynamical instability of a detuned FP cavity induced by the radiation-pressure force acting on the mirrors, which has long been investigated in the literature [17, 18, 19]. To suppress the growing modes and make the KLMTV's formalism valid for SR interferometers, an appropriate control system should be introduced. The analysis of the resulting interferometer plus controller requires a detailed description of the dynamics of the whole system and for this we have found Braginsky and Khalili's theory of linear quantum measurement [4] very powerful and intuitive. We analyzed the details of the dynamics in Chapter 3, showing in particular that the results derived in this section by Fourier techniques, notably the noise spectral density curves, are correct and rigorously justified.

2.2.1 Naive extension of KLMTV's results to SR interferometers

As in Ref. [7] we shall describe the interferometer's light by the electric field evaluated on the optic axis (center of light beam) and at specific, fixed locations along the optic axis. Correspondingly, the electric fields that we write down will be functions of time only: all dependence on spatial position

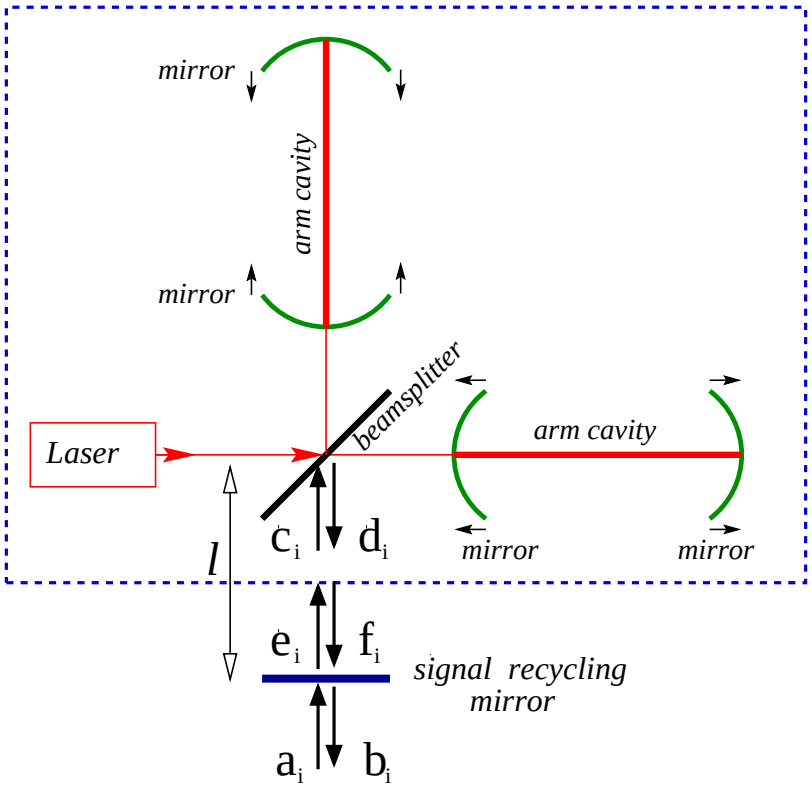

Figure 2.1: Schematic view of a LIGO-II signal-recycling interferometer. The interior of the dashed box refers to the conventional interferometer; c_i and d_i are the input and output fields at the beam splitter's dark port; a_i and b_i are the vacuum input and signal output of the whole optical system. The laser light enters the bright port of the beam splitter. The arrows close to arm cavities' extremities indicate gravitational-wave-induced mirror displacements.

will be suppressed from our formulae.

The input field at the bright port of the beam splitter, which is assumed to be infinitesimally thin, is a carrier field, described by a coherent state with power I_o and angular frequency ω_o. We assume [7] that the arm-cavity end mirrors oscillate around an equilibrium position that is on resonance with the carrier light. This means that there is no zeroth-order arm-cavity detuning (see the paper of Pai et al. [19] for a critical discussion of this assumption). Our most used interferometer parameters are given in Table 2.1 together with the values anticipated for LIGO-II.

We denote by $f_{\rm GW} = \Omega/2\pi$ the GW frequency, which lies in the range $10 - 1000$ Hz. Then the interaction of a gravitational wave with the optical system produces side-band frequencies $\omega_o \pm \Omega$ in the electromagnetic field at the output dark port. For this reason, similarly to KLMTV [7], we find it convenient to describe the quantum optics inside the interferometer using the two-photon formalism developed by Caves and Schumaker [21, 22]. In this formalism, instead of using the usual annihilation and creation operators for photons at frequency ω, we expand the field operators in terms of quadrature operators which can simultaneously annihilate a photon at frequency $\omega = \omega_o + \Omega$ while creating a photon at frequency $\omega = \omega_o - \Omega$ (or vice versa).

Quantity	*Symbol & value for* LIGO-II
Laser angular frequency	$\omega_o = 1.8 \times 10^{15}\,\mathrm{sec}^{-1}$
Arm-cavity length	$L = 4$ km
Arm-cavity input mirror transmissivity	$T = 0.033$ (power)
Arm-cavity half bandwidth	$\gamma = Tc/4L = 2\pi \times 100\,\mathrm{sec}^{-1}$
End-mirror mass	$m = 30$ kg
SQL for GW detection	$h^2_{\rm SQL} \equiv S_h^{\rm SQL} = 4 \times 10^{-48}/\mathrm{Hz}$
Light power at beam splitter	I_o
Light power to reach SQL	$I_{\rm SQL} = 1.0 \times 10^4$ W
GW angular frequency	Ω
SR cavity length	$l \approx 10$ m
SR mirror transmissivity	τ (amplitude)
SR cavity detuning	ϕ
Arm-cavity power loss	$\epsilon = 0.01$
SR power loss	$\lambda_{\rm SR} = 0.02$
Photodetector loss	$\lambda_{\rm PD} = 0.1$

Table 2.1: Summary of LIGO-II parameters [20].

More specifically, the quantized electromagnetic field in the Heisenberg picture evaluated at some fixed point on the optic axis, and restricted to the component propagating in one of the two directions along the axis is

$$\hat{E}(t) = \sqrt{\frac{2\pi\hbar}{\mathcal{A}\,c}} \int_0^{+\infty} \sqrt{\omega}\, \left[\hat{a}_\omega\, e^{-i\omega t} + \hat{a}^\dagger_\omega\, e^{+i\omega t}\right]\, \frac{d\omega}{2\pi}\,. \tag{2.1}$$

Here $\mathcal{A}$ is the effective cross sectional area of the laser beam and c is the speed of light. The annihilation and creation operators $\hat{a}_\omega$, $\hat{a}^\dagger_\omega$ in Eq. (2.1), which in the Heisenberg picture are fixed in time, satisfy the usual commutation relations

$$[\hat{a}_\omega, \hat{a}_{\omega'}] = 0\,, \qquad [\hat{a}^\dagger_\omega, \hat{a}^\dagger_{\omega'}] = 0\,, \qquad [\hat{a}_\omega, \hat{a}^\dagger_{\omega'}] = 2\pi\,\delta(\omega - \omega')\,. \tag{2.2}$$

Henceforth, to ease the notation we shall omit the hats on quantum operators. Defining the new operators (see Sec. IV of Ref. [21] [4])

$$a_+ \equiv a_{\omega_o+\Omega}\sqrt{\frac{\omega_o+\Omega}{\omega_o}}\,, \qquad a_- \equiv a_{\omega_o-\Omega}\sqrt{\frac{\omega_o-\Omega}{\omega_o}}\,, \tag{2.3}$$

and using the commutation relations (2.2), we find

$$[a_+, a^\dagger_{+'}] = 2\pi\,\delta(\Omega-\Omega')\,\left(1+\frac{\Omega}{\omega_o}\right)\,, \qquad [a_-, a^\dagger_{-'}] = 2\pi\,\delta(\Omega-\Omega')\,\left(1-\frac{\Omega}{\omega_o}\right)\,, \tag{2.4}$$

$$[a_+, a_{+'}] = 0 = [a_-, a_{-'}]\,, \qquad [a^\dagger_+, a^\dagger_{+'}] = 0 = [a^\dagger_-, a^\dagger_{-'}]\,, \qquad [a_+, a_{-'}] = 0 = [a_+, a^\dagger_{-'}]\,, \tag{2.5}$$

[4] Our notations are not exactly the same as those of Caves and Schumaker [21, 22], the correspondence is the following (ours → Caves-Schumaker): $\omega_0 \to \Omega$, $\Omega \to \epsilon$, $a_{\omega_0\pm\Omega} \to a_\pm$, $a_\pm \to \lambda_\pm a_\pm$, $a_{1,2} \to \alpha_{1,2}$. We refer to Sec. IV B of [21] for further details.

where $a_{\pm'}$ stands for $a_\pm(\Omega')$. Because the carrier frequency is $\omega_o \simeq 10^{15}\,\mathrm{s}^{-1}$ and we are interested in frequencies $\Omega/2\pi$ in the range $10 - -10^3$ Hz, we shall disregard in Eq. (2.5) the term proportional to Ω/ω_o. [In the Appendix (Sec. 2.7) we shall give a more complete justification of this by evaluating the effect the term proportional to Ω/ω_o would have on the final noise spectral density.] We can then rewrite the electric field, Eq. (2.1), as

$$E(t) = \sqrt{\frac{2\pi\hbar\,\omega_o}{\mathcal{A}\,c}}\,e^{-i\omega_o\,t}\int_0^{+\infty}(a_+(\Omega)\,e^{-i\Omega t} + a_-(\Omega)\,e^{i\Omega t})\,\frac{d\Omega}{2\pi} + \text{h.c.}\,, \tag{2.6}$$

where "h.c." means Hermitian conjugate. Following the Caves-Schumaker two-photon formalism [21, 22], we introduce the amplitudes of the two-photon modes as

$$a_1 = \frac{a_+ + a_-^\dagger}{\sqrt{2}}\,, \qquad a_2 = \frac{a_+ - a_-^\dagger}{\sqrt{2}i}\,; \tag{2.7}$$

a_1 and a_2 are called quadrature fields and they satisfy the commutation relations

$$\begin{aligned}
&[a_1, a_{2'}^\dagger] = -[a_2, a_{1'}^\dagger] = 2\pi i\delta(\Omega - \Omega')\,,\\
&[a_1, a_{1'}^\dagger] = 0 = [a_1, a_{1'}]\,, \qquad [a_2, a_{2'}^\dagger] = 0 = [a_2, a_{2'}]\,.
\end{aligned} \tag{2.8}$$

Expressing the electric field (2.6) in terms of the quadratures we finally get

$$E(a_i;t) = \cos(\omega_o\,t)\,E_1(a_1;t) + \sin(\omega_o\,t)\,E_2(a_2;t)\,, \tag{2.9}$$

with

$$E_j(a_j;t) = \sqrt{\frac{4\pi\hbar\,\omega_o}{\mathcal{A}\,c}}\int_0^{+\infty}(a_j\,e^{-i\Omega t} + a_j^\dagger\,e^{i\Omega t})\,\frac{d\Omega}{2\pi} \qquad j = 1, 2\,. \tag{2.10}$$

Note [as is discussed at length by BGKMTV [15] and was previewed by KLMTV (footnote 1 of Ref. [7])], that, $E_1(t)$ and $E_2(t)$ commute with themselves at any two times t and t', i.e., $[E_j(t), E_j(t')] = 0$, while $[E_1(t), E_2(t')] \sim i\delta(t - t')$. Hence, the quadrature fields $E_j(t)$ with $j = 1, 2$ are quantum-nondemolition quantities which can be measured with indefinite accuracy over time, i.e., measurements made at different times can be stored as independent bits of data in a classical storage medium without being affected by mutually-induced noise, while it is not possible to do this for $E_1(t)$ and $E_2(t)$ simultaneously. As BGKMTV [15] emphasized (following earlier work by Braginsky and Khalili [4]), this means that we can regard $E_1(t)$ and $E_2(t)$ separately as classical variables – though in each other's presence they behave nonclassically.

For GW interferometers the full input electric field at the dark port is $E(c_i;t)$ where c_1 and c_2 are the two input quadratures, while the output field at the dark port is $E(d_i;t)$, with d_1 and d_2 the two output quadratures (see Fig. 2.1). Assuming that the classical laser-light input field at the beam

splitter's bright port is contained only in the first quadrature, [5] and evaluating the back-action force acting on the arm-cavity mirrors disregarding the motion of the mirrors during the light round-trip time (quasi-static approximation), [6] KLMTV [7] derived the following input–output relations at side-band (GW) angular frequency Ω

$$d_1 = c_1\, e^{2i\beta}\,, \qquad d_2 = (c_2 - \mathcal{K} c_1)\, e^{2i\beta} + \sqrt{2\mathcal{K}}\, \frac{h}{h_{\rm SQL}}\, e^{i\beta}\,, \tag{2.11}$$

where $2\beta = 2\arctan \Omega/\gamma$ is the net phase gained by the sideband frequency Ω while in the arm-cavity, $\gamma = Tc/4L$ is the half bandwidth of the arm-cavity (T is the power transmissivity of the arm-cavity input mirrors and L is the length of the arm cavity), h is the Fourier transform of the gravitational-wave field, and $h_{\rm SQL}$ is the SQL for GW detection, explicitly given by

$$h_{\rm SQL}(\Omega) \equiv \sqrt{S_h^{\rm SQL}} = \sqrt{\frac{8\hbar}{m\Omega^2 L^2}}\,, \tag{2.12}$$

where m is the mass of each arm-cavity mirror. The quantity $\mathcal{K}$ in Eq. (2.11) is the effective coupling constant, which relates the motion of the test mass to the output signal,

$$\mathcal{K} = \frac{2(I_o/I_{\rm SQL})\gamma^4}{\Omega^2(\gamma^2+\Omega^2)}\,. \tag{2.13}$$

Finally, I_o is the input light power, and $I_{\rm SQL}$ is the light power needed by a conventional interferometer to reach the SQL at a side band frequency $\Omega = \gamma$, that is

$$I_{\rm SQL} = \frac{m\, L^2\, \gamma^4}{4\omega_o}\,. \tag{2.14}$$

(See in Table 2.1 the values of the interferometer parameters tentatively planned for LIGO-II [20].) We shall now derive the *new* input–output $(a_i - b_i)$ relations including the SR cavity. We indicate by l the length of the SR cavity and we introduce two dimensionless variables: $\phi \equiv [\omega_o l/c]_{\rm mod\, 2\pi}$, [7] the phase gained by the carrier frequency ω_o while traveling one way in the SR cavity, and $\Phi \equiv [\Omega l/c]_{\rm mod\, 2\pi}$ the additional phase gained by the sideband with GW frequency Ω (see Fig. 2.1). Note that we are assuming that the distances from the beam splitter to the two arm-cavity input mirrors are identical, equal to an integer multiple of the carrier light's wavelength, and are negligible compared to l.

Propagating the output electric field $E(d_i; t)$ up to the SR mirror, and introducing the operators

[5] For the KLMTV optical configuration and for ours, only a negligible fraction of the quantum noise entering the bright port emerges from the dark port.

[6] The description of a SR interferometer beyond the quasi-static approximation [19, 18] introduces nontrivial corrections to the back-action force, proportional to the power transmissivity T of the input arm-cavity mirrors. Since $T \simeq 0.033$ (see Table 2.1) we expect a small modification of our results, but an explicit calculation is strongly required to quantify these effects.

[7] Note that $\omega_o l/c = 2\pi m + \phi$, with m a large integer. Indeed, typically $\omega_o \simeq 10^{15}\,{\rm s}^{-1}$, $l \simeq 10\,{\rm m}$, hence $\omega_o l/c \gg 1$.

e_i and f_i which describe the fields that are immediately inside the SR mirror (see Fig. 1), we get the condition

$$E(f_i;t) = E\left(d_i; t - \frac{l}{c}\right) , \tag{2.15}$$

which, together with Eq. (2.9), provides the following equations

$$f_1 = (d_1 \cos\phi - d_2 \sin\phi)\, e^{i\Phi} , \qquad f_2 = (d_1 \sin\phi + d_2 \cos\phi)\, e^{i\Phi} . \tag{2.16}$$

Proceeding in an analogous way for the input electric field $E(c_i;t)$, we derive

$$e_1 = (c_1 \cos\phi + c_2 \sin\phi)\, e^{-i\Phi} , \qquad e_2 = (-c_1 \sin\phi + c_2 \cos\phi) e^{-i\Phi} . \tag{2.17}$$

Note that each of Eqs. (2.16), (2.17) correspond to a rotation of the quadratures d_1, d_2 (or c_1, c_2) plus the addition of an overall phase. Finally, denoting by a_i and b_i the input and output fields of the whole system at the output port (see Fig. 2.1) we conclude that the following relations should be satisfied at the SR mirror:

$$e_1 = \tau\, a_1 + \rho\, f_1 , \qquad e_2 = \tau\, a_2 + \rho\, f_2 , \tag{2.18}$$

$$b_1 = \tau\, f_1 - \rho\, a_1 , \qquad b_2 = \tau\, f_2 - \rho\, a_2 , \tag{2.19}$$

where $\pm\rho$ and τ are the amplitude reflectivity and transmissivity of the SR mirror, respectively. We use the convention that ρ and τ are real and positive, with the reflection coefficient being $+\rho$ for light coming from inside the cavity and $-\rho$ for light coming from outside. In this section we limit ourselves to a lossless SR mirror; therefore the following relation holds: $\tau^2 + \rho^2 = 1$.

Before giving the solution of the above equations, let us notice that the equations we derived so far for the quantum EM fields in the Heisenberg picture are exactly the same as those of classical EM fields. To deduced them it is sufficient to replace the quadrature operators by the Fourier components of the classical EM fields. The input-output relation we shall give below is also the same as in the classical case. In the latter we should assume that a fluctuating field enters the input port of the entire interferometer. More specifically, assuming a vacuum state in the input port, we can model the two input quadrature fields as two independent white noises. Then using the classical equations, we can derive the output fields which have the correct noise spectral densities.

Solving the system of Eqs. (2.11), (2.16)–(2.19) gives the final input–output relation:

$$\begin{pmatrix} b_1 \\ b_2 \end{pmatrix} = \frac{1}{M} \left[e^{2i(\beta+\Phi)} \begin{pmatrix} C_{11} & C_{12} \\ C_{21} & C_{22} \end{pmatrix} \begin{pmatrix} a_1 \\ a_2 \end{pmatrix} + \sqrt{2\mathcal{K}}\tau e^{i(\beta+\Phi)} \begin{pmatrix} D_1 \\ D_2 \end{pmatrix} \frac{h}{h_{\mathrm{SQL}}} \right] , \tag{2.20}$$

where, to ease the notation, we have defined

$$M = 1 + \rho^2\, e^{4i(\beta+\Phi)} - 2\rho\, e^{2i(\beta+\Phi)} \left(\cos 2\phi + \frac{\mathcal{K}}{2}\, \sin 2\phi\right) , \tag{2.21}$$

$$C_{11} = C_{22} = (1+\rho^2) \left(\cos 2\phi + \frac{\mathcal{K}}{2}\, \sin 2\phi\right) - 2\rho\, \cos\left(2(\beta+\Phi)\right) , \tag{2.22}$$

$$C_{12} = -\tau^2 \left(\sin 2\phi + \mathcal{K}\, \sin^2\phi\right) , \qquad C_{21} = \tau^2 \left(\sin 2\phi - \mathcal{K}\, \cos^2\phi\right) , \tag{2.23}$$

$$D_1 = -(1 + \rho\, e^{2i(\beta+\Phi)})\, \sin\phi , \qquad D_2 = -(-1 + \rho\, e^{2i(\beta+\Phi)})\, \cos\phi . \tag{2.24}$$

A straightforward calculation using $C_{ij} \in \Re$ and $C_{11}\, C_{22} - C_{12}\, C_{21} = |M|^2$, confirms that the quadratures $b_i, b_i^\dagger$ satisfy the commutation relations (2.8), as they should since like a_i and $a_i^\dagger$ they represent free fields. Let us also observe that both the quadratures b_1 and b_2 in Eq. (2.20) contain the gravitational-wave signal h and that it is not possible to put the signal into just one of the quadratures through a transformation that preserves the commutation relations of b_1 and b_2. Indeed, the most general transformation that preserves the commutation relations is of the form

$$\begin{pmatrix} \widetilde{b}_1 \\ \widetilde{b}_2 \end{pmatrix} = e^{i\,\alpha} \begin{pmatrix} L_{11} & L_{12} \\ L_{21} & L_{22} \end{pmatrix} \begin{pmatrix} b_1 \\ b_2 \end{pmatrix} , \qquad L_{ij} \in \Re , \quad \det L_{ij} = 1 , \tag{2.25}$$

where α is an arbitrary phase. Because the D_i are complex [see Eq. (2.24)], it is impossible to null the h contribution either in $\widetilde{b}_1$ or $\widetilde{b}_2$.

Henceforth, we limit our analysis to $\Phi = 0$, which corresponds to a SR cavity much shorter than the arm-cavities, e.g., $l \simeq 10\,\mathrm{m}$. We assume for simplicity that there is no radio-frequency (MHz) modulation/demodulation of the carrier and the signal [20]; instead, some frequency-independent quadrature

$$\begin{aligned} b_\zeta \quad &= b_1\, \sin\zeta + b_2\, \cos\zeta \\ &= \frac{1}{M}\, \Big[e^{2i\beta}(C_{11}\, \sin\zeta + C_{21}\, \cos\zeta)\, a_1 + e^{2i\beta}(C_{12}\, \sin\zeta + C_{22}\, \cos\zeta)\, a_2 \\ &\quad + \sqrt{2\mathcal{K}}\, \tau\, e^{i\beta}\, (D_1\, \sin\zeta + D_2\, \cos\zeta)\, \frac{h}{h_{\mathrm{SQL}}}\Big] , \end{aligned} \tag{2.26}$$

is measured via homodyne detection [8]. [8] Before going on to evaluate the noise spectral density in the measured quadrature b_ζ, let us first comment on the results obtained in this section.

[8] It is still unclear what detection scheme (direct homodyne detection or RF modulation/demodulation) will be used in LIGO-II. The decision will require a quantum-mechanical analysis of the additional noise introduced by the modulation/demodulation process, which will be given in Chapter 5.

2.2.2 Discussion of the naive result

There is a major delicacy in the input–output relation given by Eq. (2.18). By naively transforming it from the frequency domain back into the time domain, we deduce that the output quadratures depend on the gravitational-wave field and the input optical fields both in the past *and in the future*. Mathematically this is due to the fact that the coefficient $1/M$, in front of h and a_i $(i = 1, 2)$ in Eq. (2.20), contains poles both in the lower *and in the upper* complex plane. This situation is a very common one in physics and engineering (it occurs for example in the theory of linear electronic networks [24] and the theory of plasma waves [25]), and the cure for it is well known: in order to construct an output field that only depends on the past, we have to alter the integration contour in the inverse-Fourier transform, going above (with our convention of Fourier transform) all the poles in the complex plane. This procedure, which can be justified rigorously using Laplace transforms [26], makes the output signal infinitely sensitive to driving forces in the infinitely distant past. The reason is simple and well known in other contexts: our optical mechanical system possesses instabilities, which can be deduced from the homogeneous solution $b_i^{\rm hom}$ of Eqs. (2.11), (2.15) and (2.19), which has eigenfrequencies given by $M = 0$. Because the zeros of the equation $M = 0$ are generically complex and may have positive imaginary parts (see also Chapter 3), we end up with homogeneous solutions that grow exponentially. [9]

To quench the instabilities of a SR interferometer we have to introduce a proper control system. In Chapter 3 we have given an example of such a control system, which we briefly illustrate here. Let us suppose that the observed output is b_ζ and we feed back a linear transformation of it to control the dynamics of the end mirrors. This operation corresponds to making the following substitution in Eq. (2.26):

$$h \to h + \mathcal{C}\, b_\zeta, \tag{2.27}$$

where $\mathcal{C}$ is some *retarded* kernel. Solving again for b_ζ, we get

$$\begin{aligned} b_\zeta^{\mathcal{C}} \quad &= \frac{1}{M_{\mathcal{C}}} \Big[e^{2i\beta}(C_{11}\,\sin\zeta + C_{21}\,\cos\zeta)\,a_1 + e^{2i\beta}(C_{12}\,\sin\zeta + C_{22}\,\cos\zeta)\,a_2 \\ &\quad + \sqrt{2\mathcal{K}}\,\tau\, e^{i\beta}\,(D_1\,\sin\zeta + D_2\,\cos\zeta)\,\frac{h}{h_{\rm SQL}} \Big]\,, \end{aligned} \tag{2.28}$$

simply replacing the M in (2.26) by $M_{\mathcal{C}}$, which depends on $\mathcal{C}$. Note that, by contrast with the *uncontrolled* output Eq. (2.20), the output field $b_\zeta^{\mathcal{C}}$ is no longer a free electric field, i.e., a quadrature field defined in half open space, satisfying the radiative boundary condition. This is due to the fact that part of it has been fed back into the arm cavities. Nevertheless, in the time domain, $b_\zeta^{\mathcal{C}}$ commutes with itself at different times. In Chapter 3 we have shown that there exists a well-defined $\mathcal{C}$ that

[9] Quadrature operators with *complex* frequency can be defined by analytical continuations of quadrature operators with *real* frequency considered as analytical functions of Ω.

makes Eq. (2.28) well defined in the time domain, getting rid of the instabilities. As a consequence, $M_{\mathcal{C}}$ has zeros only in the lower-half complex plane and we can neglect the homogeneous solution $M_{\mathcal{C}}\, b_\zeta^{\mathcal{C}\,\mathrm{hom}} = 0$ because it decays exponentially in time.

Finally, let us remember the important fact that the introduction of this kind of control system only changes the normalization of the output field. As a consequence, the noise spectral density is *not* affected. However, an extra noise will be present due to the electronic device that provides the control force on the end mirrors. K. Strain estimated that it can be kept smaller than about 10% of the quantum noise [27].

2.3 Features of noise spectral density in SR interferometers

In light of the discussion at the end of the last section, we shall use Eq. (2.28) as the starting point of our derivation of the noise spectral density of a (stabilized) SR interferometer.

2.3.1 Evaluation of the noise spectral density: going below the standard quantum limit

The noise spectral density is calculated as follows [7]. Equation (2.28) tells us that the interferometer noise, expressed as an equivalent gravitational-wave Fourier component, is

$$h_n \equiv \frac{h_{\mathrm{SQL}}}{\sqrt{2\mathcal{K}}}\,\Delta b_\zeta\,, \tag{2.29}$$

where

$$\Delta b_\zeta = \frac{(C_{11}\,\sin\zeta + C_{21}\,\cos\zeta)\,a_1 + (C_{12}\,\sin\zeta + C_{22}\,\cos\zeta)\,a_2}{\tau\,(D_1\,\sin\zeta + D_2\,\cos\zeta)}\,. \tag{2.30}$$

Then the (single-sided) spectral density $S_h^\zeta(f)$, with $f = \Omega/2\pi$, associated with the noise h_n can be computed by the formula (Eq. (22) of Ref. [7])

$$\frac{1}{2}\,2\pi\,\delta(\Omega-\Omega')\,S_h^\zeta(f) = \langle \mathrm{in}|h_n(\Omega)\,h_n^\dagger(\Omega')|\mathrm{in}\rangle_{\mathrm{sym}} \equiv \frac{1}{2}\langle \mathrm{in}|h_n(\Omega)\,h_n^\dagger(\Omega') + h_n^\dagger(\Omega')\,h_n(\Omega)|\mathrm{in}\rangle\,. \tag{2.31}$$

Here we put the superscript ζ on S_h^ζ to remind ourselves that this is the noise when the output is monitored at carrier phase ζ by homodyne detection. Assuming that the input of the whole SR interferometer is in its vacuum state, as is planned for LIGO-II, i.e., $|\mathrm{in}\rangle = |0_a\rangle$, and using

$$\langle 0_a|a_i\,a_{j'}^\dagger|0_a\rangle_{\mathrm{sym}} = \frac{1}{2}\,2\pi\,\delta(\Omega-\Omega')\,\delta_{ij}\,, \tag{2.32}$$

(Eq. (25) of Ref. [7]) we find that Eq. (2.31) can be recast in the simple form (note that $C_{ij} \in \Re$):

$$S_h^\zeta = \frac{h_{\rm SQL}^2}{2\mathcal{K}} \, \frac{\left(C_{11}\,\sin\zeta + C_{21}\,\cos\zeta\right)^2 + \left(C_{12}\,\sin\zeta + C_{22}\,\cos\zeta\right)^2}{\tau^2\,\left|D_1\,\sin\zeta + D_2\,\cos\zeta\right|^2} \,. \tag{2.33}$$

For comparison, let us recall some properties of the noise spectral density for conventional interferometers (for a complete discussion see Ref. [7]). To recover this case we have to take the limit $\phi \to 0$ and $\rho \to 0$ in the above equations or simply use Eq. (2.11) (in a conventional interferometer there are no instabilities). In particular, for a conventional interferometer, Eqs. (2.26) and (2.29) take the much simpler form [10]

$$b_\zeta^{\rm conv} = \cos\zeta\,\{[a_2 + (\tan\zeta - \mathcal{K})\,a_1]\;e^{2i\beta}\}\,, \qquad h_n^{\rm conv} = \frac{h_{\rm SQL}}{\sqrt{\mathcal{K}}}\,e^{i\beta}\;[a_2 + (\tan\zeta - \mathcal{K})\,a_1]\;, \tag{2.34}$$

and the noise spectral density reads

$$S_h^{\zeta,{\rm conv}} = \frac{h_{\rm SQL}^2}{2\mathcal{K}}\;\left[1 + (\tan\zeta - \mathcal{K})^2\right]\;. \tag{2.35}$$

As has been much discussed by Matsko, Vyatchanin and Zubova [8] and by KLMTV [7], and as we shall see in more detail in Sec. 2.3.2, taking as the output b_ζ, instead of the quadrature b_2 in which all the signal h is encoded, builds up correlations between shot noise and radiation-pressure noise. We refer to correlations of this kind, which are introduced by the special read-out scheme, as *static* correlations by contrast with those produced by the SR mirror, which we call *dynamical* since they are built up dynamically, as we shall discuss in Sec. 2.4. The static correlations allow the noise curves for a conventional interferometer to go below the SQL when $I_o = I_{\rm SQL}$, as was originally observed by Matsko, Vyatchanin and Zubova [8]. However, if ζ is frequency independent as it must be when one uses conventional homodyne detection, then the SQL is beaten, $S_h^{\zeta,{\rm conv}} \leq h_{\rm SQL}^2$, only over a rather narrow frequency band and only by a very modest amount. On the other hand, as Matsko, Vyatchanin and Zubova [8] showed, and one can see from Eq. (2.35), if we could make the homodyne detection angle ζ frequency dependent, then choosing [7] $\zeta(\Omega) \equiv \arctan\mathcal{K}(\Omega)$, would remove completely (in the absence of optical losses) the second term in the square parenthesis of Eq. (2.35), which is the radiation-pressure noise, leaving only the shot noise in the interferometer output, i.e., $S_h^{\zeta,{\rm conv}} = h_{\rm SQL}^2/2\mathcal{K}$. In order to implement frequency dependent homodyne detection, KLMTV [7] have recently propose to place two 4km-long filter cavities at the interferometer dark port and follow them by conventional homodyne detection. This experimentally challenging proposal would allow the interferometer to beat the SQL at frequency $f = 100$ Hz by a factor $\sqrt{S_h^{\rm conv}}/\sqrt{S_h^{\rm SQL}} \sim 0.24$, over a band of $\Delta f \sim f$, at light power $I_o = I_{\rm SQL}$, and by $\sqrt{S_h^{\rm conv}}/\sqrt{S_h^{\rm SQL}} \sim 0.18$ if $I_o \simeq 3.2 I_{\rm SQL}$. In conclusion, already in conventional interferometers it

[10] Note that our definition of ζ differs from the one used in [7].

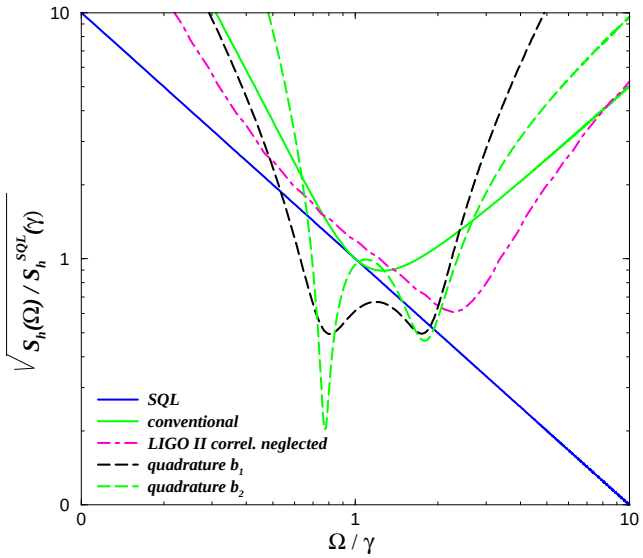

Figure 2.2: Log-log plot of $\sqrt{S_h(\Omega)}/\sqrt{S_h^{\rm SQL}(\gamma)}$ versus Ω/γ for (i) the quadratures $b_1^{\mathcal{C}}$ ($\zeta = \pi/2$) and $b_2^{\mathcal{C}}$ ($\zeta = 0$) with $\rho = 0.9$, $\phi = \pi/2 - 0.47$ and $I_o = I_{\rm SQL}$, (ii) the SQL, (iii) a conventional interferometer with $I_o = I_{\rm SQL}$, and (iv) the noise curve of LIGO-II [20] one would obtain if shot-noise / radiation-pressure correlations were (naively) neglected. For LIGO-II, $\gamma = 2\pi \times 100\,{\rm Hz}$ (top axis) and $\sqrt{S_h^{\rm SQL}(\gamma)} = 2 \times 10^{-24}\,{\rm Hz}^{-1/2}$. These curves do not include seismic and thermal noises; for LIGO-II the latter is expected to be slightly above the SQL [14].

is possible to beat the SQL provided that we measure b_ζ and build up proper *static* correlations between shot noise and radiation-pressure noise.

Let us now go back to SR interferometers. They have the interesting property of building up *dynamically* the correlations between shot noise and radiation-pressure noise, thanks to the SR mirror. Indeed, even if we restrict ourselves to the noise curves associated with the two quadratures $b_1^{\mathcal{C}}$ and $b_2^{\mathcal{C}}$, i.e., we do not measure $b_\zeta^{\mathcal{C}}$, the SR interferometer can still go below the SQL. Moreover, if the SR interferometer works at the SQL power, i.e., $I_o = I_{\rm SQL}$, as is tentatively planned for LIGO-II, then the noise curves [Eq. (2.33)] can exhibit one or two resonant dips whose depths increase and widths decrease as the SR-mirror's reflectivity is raised. (We postpone the discussion of this interesting feature to Sec. 2.4.) These resonances allow us to reshape the noise curves and beat the SQL by much larger amounts than in a conventional interferometer with static correlations introduced by frequency-independent homodyne detection.

More specifically, the noise spectral density, Eq. (2.33), depends on the physical parameters which characterize the SR interferometer (see Table 2.1): the light power I_o, the SR detuning ϕ, the reflectivity of the SR mirror ρ and the homodyne phase ζ. To give an example of LIGO-II noise curves, in Fig. 2.2 we plot the $\sqrt{S_h(\Omega)}$ for the two quadratures $b_1^{\mathcal{C}}$ ($\zeta = \pi/2$) and $b_2^{\mathcal{C}}$ ($\zeta = 0$), for: $\rho = 0.9$, $\phi = \pi/2 - 0.47$ and $I_o = I_{\rm SQL}$. Also shown for comparison are the SQL line, the noise

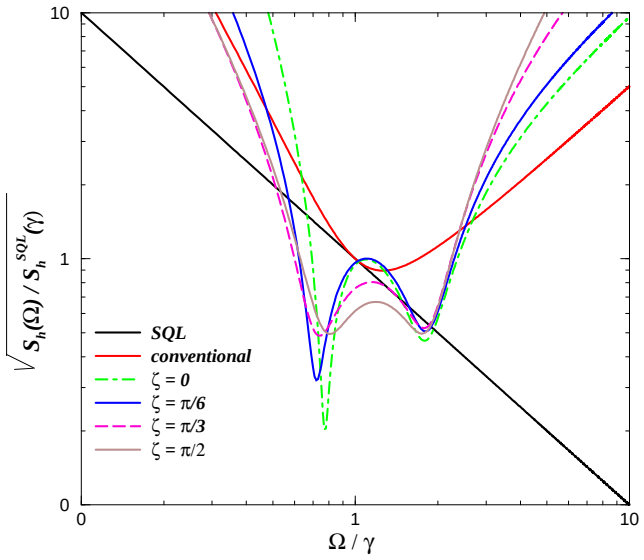

Figure 2.3: Log-log plot of $\sqrt{S_h(\Omega)/S_h^{\rm SQL}(\gamma)}$ versus Ω/γ for the following choices of the frequency independent homodyne phase: $\zeta = 0$, $\zeta = \pi/6$, $\zeta = \pi/3$ and $\zeta = \pi/2$, with $\rho = 0.9$, $\phi = \pi/2 - 0.47$ and $I_o = I_{\rm SQL}$. The plot also shows the noise curve for a conventional interferometer and the SQL line. For LIGO-II, $\gamma = 2\pi \times 100\,{\rm Hz}$ (top axis) and $\sqrt{S_h^{\rm SQL}(\gamma)} = 2 \times 10^{-24}\,{\rm Hz}^{-1/2}$.

curve one would obtain if one ignored the correlations between the shot noise and radiation-pressure noise[20], [11] and for a conventional interferometer with $I_o = I_{\rm SQL}$ and $\zeta = 0$, explicitly given by [7]

$$S_h^{\zeta=0,{\rm conv}} = \frac{S_h^{\rm SQL}}{2}\left(\mathcal{K} + \frac{1}{\mathcal{K}}\right). \tag{2.36}$$

The sensitivity curves for the two quadratures go substantially below the SQL and show two interesting resonant valleys. In Fig. 2.3 we plot the noise curves $\sqrt{S_h(\Omega)}$ for different values of the frequency independent homodyne angle ζ, choosing the same parameters used in Fig. 2.2, i.e., $\rho = 0.9$, $\phi = \pi/2 - 0.47$ and $I_o = I_{\rm SQL}$. Note that the location of the resonant dips does not depend much on the angle ζ. This property is confirmed analytically in Sec. 2.4 in the case of a highly-reflecting SR mirror, by an analysis that elucidate the underlying physics.

Before ending this section, let us give an idea of the performances achievable in a SR interferometer *if its thermal noise can be made negligible* [14]. We have estimated the signal-to-noise ratio for inspiraling binaries, which are among the most promising sources for the detection of GW with earth-based interferometers. The square of the signal-to-noise ratio for a binary system made of

[11] Before the research reported in this chapter, the LIGO community computed the noise curves for SR interferometers by (i) evaluating the shot noise $S_h^{\rm shot}$, (ii) then (*naively* assuming no correlations between shot noise and radiation-pressure noise) using the uncertainty principle $S_h^{\rm shot}\, S_h^{\rm RP} \geq \left(S_h^{\rm SQL}\right)^2/4$, with the equality sign to evaluate the radiation-pressure noise $S_h^{\rm RP}$, (iii) then adding the two. This procedure gave the noise curve labeled "correlations neglected" in Fig. 2.2; see Fig. 2 of Ref. [20].

black holes and/or neutron stars is given by

$$\left(\frac{S}{N}\right)^2 = 4\int_0^{+\infty} \frac{|h(f)|^2}{S_h(f)}\, df\,. \tag{2.37}$$

Using the Newtonian quadrupole approximation, for which the waveform's Fourier transform is $|h(f)|^2 \propto f^{-7/3}$, and introducing in the above integral a lower cutoff due to seismic noise at $\Omega_s = 0.1\gamma$ ($f_s \simeq 10$ Hz), we get for the parameters used in Fig. 2.2:

$$\frac{(S/N)_1}{(S/N)_{\rm conv}} \simeq 1.83\,, \qquad \frac{(S/N)_2}{(S/N)_{\rm conv}} \simeq 1.98\,, \tag{2.38}$$

where $(S/N)_1$, $(S/N)_2$ and $(S/N)_{\rm conv}$ use for the noise spectral density either that of the first quadrature $b_1^{\mathcal{C}}$ or the second quadrature $b_2^{\mathcal{C}}$ or the conventional interferometer, respectively. A more thorough analysis of signal-to-noise ratio for inspiraling binaries inevitably requires the specification of the readout scheme. We assume a homodyne readout scheme here, while the heterodyne scheme will be discussed in Chapter 4.

2.3.2 Effective shot noise and radiation-pressure noise

In this section we shall discuss the crucial role played by shot-noise / radiation-pressure correlations that are present in LIGO-II's quadrature outputs (2.20) and noise spectral densities (2.33), in beating the SQL. Our analysis is based on the general formulation of linear quantum measurement theory developed by Braginsky and Khalili [4] and assumes also the results obtained in [15], and Chapter 3.

To identify the radiation pressure and the shot noise contributions in the total optical noise, we use the fact that they transform differently under rescaling of the mirror mass. Indeed, it is straightforward to show that in the total optical noise there exist only two kinds of terms. There are terms that are invariant under rescaling of the mass and terms that are proportional to $1/m$. Hence, quite generally we can rewrite the output $\mathcal{O}$ of the whole optical system as [4] and Chapter 3

$$\mathcal{O}(\Omega) = \mathcal{Z}(\Omega) + \mathcal{R}_{xx}(\Omega)\,\mathcal{F}(\Omega) + L\,h(\Omega)\,, \tag{2.39}$$

where by output we mean one of the two quadratures $b_1^{\mathcal{C}}$, $b_2^{\mathcal{C}}$ or a combination of them, e.g., $b_\zeta^{\mathcal{C}}$ (modulo a normalization factor) and where $\mathcal{R}_{xx}$ is the susceptibility of the antisymmetric mode of motion of the four mirrors [4], given by

$$\mathcal{R}_{xx}(\Omega) = -\frac{4}{m\,\Omega^2}\,. \tag{2.40}$$

The observables $\mathcal{Z}$ and $\mathcal{F}$ in Eq. (2.39) do not depend on the mirror masses m, and satisfy the

commutation relations (Eq. (2.19) in Chapter 3)

$$[\mathcal{F}(\Omega),\mathcal{F}^\dagger(\Omega')]=0=[\mathcal{Z}(\Omega),\mathcal{Z}^\dagger(\Omega')]\,,\qquad [\mathcal{Z}(\Omega),\mathcal{F}^\dagger(\Omega')]=-2\pi i\hbar\delta(\Omega-\Omega')\,. \tag{2.41}$$

We shall refer to $\mathcal{Z}$ and $\mathcal{F}$ as the *effective* shot noise and *effective* radiation-pressure force, respectively, because we will show in Chapter 3 that for a SR interferometer the *real* back-action force acting on the test masses is not proportional to the effective radiation-pressure noise, but instead is a combination of the two effective observables $\mathcal{Z}$ and $\mathcal{F}$. When the shot noise and radiation-pressure noise are correlated, the real back-action force does not commute with itself at different times, [12] which makes the analysis in terms of real quantities more complicated than in terms of the effective ones. We prefer to discuss our results in terms of real quantities separately (Chapter 3), in a more formal context which uses the description of a GW interferometer as a linear quantum-measurement device [4].

The noise spectral density, written in terms of the effective operators $\mathcal{Z}$ and $\mathcal{F}$, reads [4]

$$S_h=\frac{1}{L^2}\left\{S_{\mathcal{Z}\mathcal{Z}}+2\mathcal{R}_{xx}\,\Re\left[S_{\mathcal{F}\mathcal{Z}}\right]+\mathcal{R}_{xx}^2\,S_{\mathcal{F}\mathcal{F}}\right\}\,, \tag{2.42}$$

where the (one-sided) cross spectral density of two operators is expressible, by analogy with Eq. (2.31), as

$$\frac{1}{2}\,S_{\mathcal{A}\mathcal{B}}(\Omega)2\pi\,\delta\left(\Omega-\Omega'\right)=\frac{1}{2}\left\langle\mathcal{A}(\Omega)\mathcal{B}^\dagger(\Omega')+\mathcal{B}^\dagger(\Omega')\mathcal{A}(\Omega)\right\rangle. \tag{2.43}$$

In Eq. (2.42) the terms containing $S_{\mathcal{Z}\mathcal{Z}}$, $S_{\mathcal{F}\mathcal{F}}$ and $\Re\left[S_{\mathcal{F}\mathcal{Z}}\right]$ should be identified as effective shot noise, back-action noise and a term proportional to the effective correlation between the two noises, respectively [4]. Relying on the commutators (2.41) between the effective field operators one can derive (see Ref. [4] and Chapter 3) the following uncertainty relation for the (one-sided) spectral densities and cross correlations of $\mathcal{Z}$ and $\mathcal{F}$:

$$S_{\mathcal{Z}\mathcal{Z}}\,S_{\mathcal{F}\mathcal{F}}-S_{\mathcal{Z}\mathcal{F}}\,S_{\mathcal{F}\mathcal{Z}}\geq\hbar^2\,. \tag{2.44}$$

Equation (2.44) does not, in general, impose a lower bound on the noise spectral density Eq. (2.42). However, in a very important type of measurement it does, namely, for interferometers with uncorrelated shot noise and back-action noise, e.g., LIGO-I/TAMA/Virgo. In this case $S_{\mathcal{Z}\mathcal{F}}=0=S_{\mathcal{F}\mathcal{Z}}$ [7] and inserting the vanishing correlations into Eqs. (2.43), (2.44), one easily finds that the noise

[12] We will show in Chapter 3 that as a consequence of this identification the antisymmetric mode of motion of the four mirrors acquires an optical-mechanical rigidity and a SR interferometer responds to GW signal like an optical spring. This phenomenon was already observed in optical bar detectors by Braginsky's group [9].

spectral density has a lower bound which is given by the standard quantum limit, i.e.,

$$S_h(\Omega) \geq S_h^{\rm SQL}(\Omega) \equiv \frac{2\,|R_{xx}(\Omega)|\,\hbar}{L^2} = \frac{8\hbar}{m\Omega^2\,L^2} = h_{\rm SQL}^2(\Omega)\,. \tag{2.45}$$

From this it follows that to beat the SQL one must create correlations between shot noise and back-action noise.

Before investigating those correlations in a SR inteferometer, we shall first show how such correlations can be built up statically in a conventional (LIGO-I/TAMA/Virgo) interferometer by implementing frequency-independent homodyne detection at some angle ζ [8, 7]. By identifying in the interferometer output (2.34) the terms independent of m as effective shot noise and those inversely proportional to m as effective back-action noise, we get the effective field operators $\mathcal{Z}_\zeta^{\rm conv}$ and $\mathcal{F}_\zeta^{\rm conv}$:

$$\mathcal{Z}_\zeta^{\rm conv}(\Omega) = \frac{e^{i\beta}\,L\,h_{\rm SQL}}{\sqrt{2\mathcal{K}}}\,\left(a_2 + a_1\,\tan\zeta\right)\,, \qquad \mathcal{F}_\zeta^{\rm conv}(\Omega) = \frac{\hbar\,e^{i\beta}\,\sqrt{2\mathcal{K}}}{L\,h_{\rm SQL}}\,a_1\,. \tag{2.46}$$

[We remind the readers that $h_{\rm SQL} \propto 1/\sqrt{m}$ and that $\mathcal{K} \propto 1/m$.] Evaluating the spectral densities of those operators using Eqs. (2.43) and (2.32), we obtain the following expressions for the spectral densities and their static correlations:

$$S_{\mathcal{Z}_\zeta\mathcal{Z}_\zeta}^{\rm conv}(\Omega) = \frac{L^2\,h_{\rm SQL}^2}{2\mathcal{K}}\,(1+\tan^2\zeta)\,, \qquad S_{\mathcal{F}_\zeta\mathcal{F}_\zeta}^{\rm conv}(\Omega) = \frac{2\mathcal{K}\,\hbar^2}{L^2\,h_{\rm SQL}^2}\,, \qquad S_{\mathcal{Z}_\zeta\mathcal{F}_\zeta}^{\rm conv}(\Omega) = \hbar\,\tan\zeta = S_{\mathcal{F}_\zeta\mathcal{Z}_\zeta}^{\rm conv}(\Omega)\,. \tag{2.47}$$

By inserting these in Eq. (2.42) and optimizing the coupling constant $\mathcal{K}$, we see that the SQL can be beaten for any $0 < \zeta < \pi/2$, i.e., whenever there are nonvanishing correlations. See Refs. [7, 8] for further details.

Let us now derive the correlations between shot noise and back action noise in SR interferometers. Because in this case the correlations are built up dynamically by the SR mirror and are present in all quadratures, as an example, we limit ourselves to the two quadratures $b_1^{\mathcal{C}}$ and $b_2^{\mathcal{C}}$. Identifying in Eqs. (2.29), (2.30) the effective shot and back-action noise terms due to their m dependences, we obtain the effective field operators $\mathcal{Z}_1$, $\mathcal{Z}_2$, $\mathcal{F}_1$ and $\mathcal{F}_2$

$$\begin{aligned}
\mathcal{Z}_1(\Omega) &= -\frac{e^{i\beta}\,L\,h_{\rm SQL}}{\sqrt{2\mathcal{K}}}\,\frac{\left[a_1\,(-2\rho\,\cos 2\beta + (1+\rho^2)\,\cos 2\phi) + a_2\,(-1+\rho^2)\,\sin 2\phi\right]\,\csc\phi}{\tau\,(1+e^{2i\beta}\,\rho)}\,,\\
\mathcal{Z}_2(\Omega) &= -\frac{e^{i\beta}\,L\,h_{\rm SQL}}{\sqrt{2\mathcal{K}}}\,\frac{\left[a_1\,(1-\rho^2)\,\sin 2\phi + a_2\,(-2\rho\,\cos 2\beta + (1+\rho^2)\,\cos 2\phi)\right]\,\sec\phi}{\tau\,(-1+e^{2i\beta}\,\rho)}\,,
\end{aligned} \tag{2.48}$$

and

$$\mathcal{F}_1(\Omega) = \frac{\hbar\, e^{i\beta}\,\sqrt{2\mathcal{K}}}{L\, h_{\rm SQL}}\,\frac{\left[a_1\,(1+\rho^2)\,\cos\phi + a_2\,(-1+\rho^2)\,\sin\phi\right]}{\tau\,(1+e^{2i\beta}\,\rho)}\,,$$
$$\mathcal{F}_2(\Omega) = \frac{\hbar\, e^{i\beta}\,\sqrt{2\mathcal{K}}}{L\, h_{\rm SQL}}\,\frac{\left[a_1\,(-1+\rho^2)\,\cos\phi + a_2\,(1+\rho^2)\,\sin\phi\right]}{\tau\,(-1+e^{2i\beta}\,\rho)}\,. \tag{2.49}$$

Evaluating the spectral densities of the above operators through Eqs. (2.43) and (2.32) we obtain the following expressions:

$$S_{\mathcal{F}_1\mathcal{F}_1}(\Omega) = \frac{\hbar^2\,2\mathcal{K}}{L^2\,h_{\rm SQL}^2}\,\frac{1+\rho^4+2\rho^2\cos\phi}{(1-\rho^2)\,(1+\rho^2+2\rho\,\cos 2\beta)}\,,$$
$$S_{\mathcal{F}_2\mathcal{F}_2}(\Omega) = \frac{\hbar^2\,2\mathcal{K}}{L^2\,h_{\rm SQL}^2}\,\frac{1+\rho^4-2\rho^2\cos\phi}{(1-\rho^2)\,(1+\rho^2-2\rho\,\cos 2\beta)}\,, \tag{2.50}$$

and

$$S_{\mathcal{Z}_1\mathcal{Z}_1}(\Omega) = \frac{L^2\,h_{\rm SQL}^2}{2\mathcal{K}}\,\frac{\left[4(-1+\rho^2)^2\,\cos^2\phi + (-2\rho\,\cos 2\beta + (1+\rho^2)\,\cos 2\phi)^2\,\csc^2\phi\right]}{(1-\rho^2)\,(1+\rho^2+2\rho\,\cos 2\beta)}\,,$$
$$S_{\mathcal{Z}_2\mathcal{Z}_2}(\Omega) = \frac{L^2\,h_{\rm SQL}^2}{2\mathcal{K}}\,\frac{\left[4(-1+\rho^2)^2\,\sin^2\phi + (-2\rho\,\cos 2\beta + (1+\rho^2)\,\cos 2\phi)^2\,\sec^2\phi\right]}{(1-\rho^2)\,(1+\rho^2-2\rho\,\cos 2\beta)}\,. \tag{2.51}$$

Finally, for the correlations between the shot noise and back-action noise we get

$$S_{\mathcal{F}_1\mathcal{Z}_1}(\Omega) = S_{\mathcal{Z}_1\mathcal{F}_1}(\Omega) = -\frac{\hbar\,\left[(-1+\rho^2)^2 - 2\rho\,(1+\rho^2)\,\cos 2\beta + 4\rho^2\,\cos 2\phi\right]\,\cot\phi}{(1-\rho^2)\,(1+\rho^2+2\rho\,\cos 2\beta)}\,,$$
$$S_{\mathcal{F}_2\mathcal{Z}_2}(\Omega) = S_{\mathcal{Z}_2\mathcal{F}_2}(\Omega) = \frac{\hbar\,\left[(-1+\rho^2)^2 + 2\rho\,(1+\rho^2)\,\cos 2\beta - 4\rho^2\,\cos 2\phi\right]\,\tan\phi}{(1-\rho^2)\,(1+\rho^2-2\rho\,\cos 2\beta)}\,. \tag{2.52}$$

These correlations depend on the sideband angular frequency Ω and are generically different from zero. However, when $\phi = 0$ and $\phi = \pi/2$ the correlations are zero. We shall analyze these two extreme configurations in the following section.

2.3.3 Two special cases: extreme signal-recycling and resonant-sideband-extraction configurations

In this section we discuss two extreme cases that are well known and have been much investigated in the literature using a semiclassical analysis [12, 13]. In these two cases the dynamical correlations between shot noise and radiation-pressure noise are zero. This has two implications: (i) the semiclassical analysis and predictions [12, 13] are correct (when straightforwardly complemented by radiation pressure noise), and (ii) the noise curves are always above the SQL. Of course, static correlations can always be introduced by measuring the quadrature b_ζ. In these two extreme cases there are no instabilities and the input–output relation of the SR interferometer can be obtained

from the conventional noise by just rescaling the parameter $\mathcal{K}$ [Eq. (2.13)].

2.3.3.1 Extreme signal-recycling (ESR) configuration: $\phi = 0$

For $\phi = 0$, the gravitational-wave signal appears only in the second quadrature b_2 but not in the first quadrature b_1 (see Eq. (2.26) with $\zeta = 0$ and $\pi/2$, respectively). Defining

$$\widetilde{\mathcal{K}} \equiv \frac{\mathcal{K}\,\tau^2}{1+\rho^2-2\rho\,\cos 2\beta}\,, \tag{2.53}$$

it is straightforward to deduce that the spectral density of the noise takes the simple form

$$S_h^{\rm ESR} = \frac{S_h^{\rm SQL}}{2}\,\left(\frac{1}{\widetilde{\mathcal{K}}}+\widetilde{\mathcal{K}}\right)\,. \tag{2.54}$$

In the left panel of Fig. 2.4 we plot $\sqrt{S_h^{\rm ESR}(\Omega)/S_h^{\rm SQL}(\gamma)}$ versus Ω/γ for different choices of the reflectivity ρ. As we vary the reflectivity of the SR mirror the minimum of the various curves is shifted along the SQL line, and the shape of the noise curve change a bit because both $\mathcal{K}$ and β in Eqs. (2.53), (2.54) depend on frequency. Moreover, for $\Omega/\gamma \gg 1$ and $\Omega/\gamma \ll 1$ the curves are well above the conventional interferometer noise. This effect becomes worse and worse as $\rho \to 1$ and is described by the formulas

$$\frac{S_h^{\rm ESR}(\Omega)}{S_h^{\rm SQL}(\gamma)} \to \frac{1}{4}\frac{\Omega^2}{\gamma^2}\,\left(\frac{1+\rho}{1-\rho}\right)\,\frac{I_{\rm SQL}}{I_o}\,, \qquad \frac{\Omega}{\gamma}\gg 1\,; \qquad \frac{S_h^{\rm ESR}(\Omega)}{S_h^{\rm SQL}(\gamma)} \to \frac{\gamma^4}{\Omega^4}\,\left(\frac{1+\rho}{1-\rho}\right)\,\frac{I_o}{I_{\rm SQL}}\,, \qquad \frac{\Omega}{\gamma}\ll 1\,. \tag{2.55}$$

The signal-to-noise ratio for inspiraling binaries is given in this case (for $\rho = 0.9$, $I_o = I_{\rm SQL}$) by

$$\frac{(S/N)_{\rm ESR}}{(S/N)_{\rm conv}} \simeq 0.73\,. \tag{2.56}$$

Hence, this LIGO-II configuration ($\phi = 0$) is not appealing. The noise curves could be better than the ones for a conventional interferometer in the range $\sim 20-60$ Hz, depending on the value of ρ, but they get worse everywhere else, and overall, for any ρ the signal-to-noise ratio for inspiraling binaries is lower than in the case of a conventional interferometer.

2.3.3.2 Extreme resonant-sideband-extraction (ERSE) configuration: $\phi = \pi/2$

For $\phi = \pi/2$, using Eq. (2.26) with $\zeta = \pi/2$, we find that only the first quadrature b_1 contains the gravitational-wave signal. Introducing

$$\overline{\mathcal{K}} \equiv \frac{\mathcal{K}\,\tau^2}{1+\rho^2+2\rho\,\cos 2\beta}\,, \tag{2.57}$$

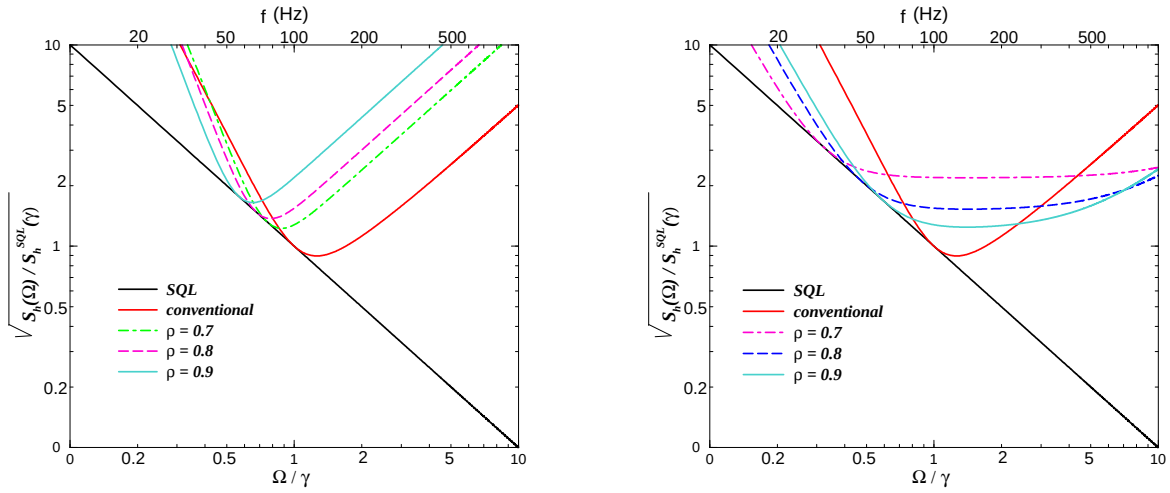

Figure 2.4: Log-log plot of $\sqrt{S_h^{\rm ESR}(\Omega)/S_h^{\rm SQL}(\gamma)}$ versus Ω/γ for the extreme signal-recycling configuration (left panel) $\phi = 0$ with $\rho = 0.7$, $\rho = 0.8$, $\rho = 0.9$ and $I_o = I_{\rm SQL}$ and for the extreme resonant-sideband-extraction configuration (right panel) $\phi = \pi/2$ with $\rho = 0.7$, $\rho = 0.8$ and $\rho = 0.9$, with $I_o = I_{\rm SQL}$. Also plotted for comparison are the noise curve for a conventional interferometer and the SQL line. For further detail on these well-known configurations, see Refs. [12, 13].

(which depends on frequency through both $\mathcal{K}$ and β), we easily deduce that the noise spectral density reads

$$S_h^{\rm ERSE} = \frac{S_h^{\rm SQL}}{2}\left(\frac{1}{\overline{\mathcal{K}}} + \overline{\mathcal{K}}\right). \tag{2.58}$$

The right panel of Fig. 2.4 shows $\sqrt{S_h^{\rm ERSE}(\Omega)/S_h^{\rm SQL}(\gamma)}$ as a function of Ω/γ for different values of the reflectivity ρ. As for the ESR configuration discussed above, when we vary the reflectivity of the SR mirror the minimum of the various curves moves along the SQL line. But by contrast with the ESR configuration, for $\Omega/\gamma \gg 1$ and $\Omega/\gamma \ll 1$ the curves are significantly below the conventional-interferometer noise. This effect becomes better and better as $\rho \to 1$ and is described by the asymptotic limits

$$\frac{S_h^{\rm ERSE}(\Omega)}{S_h^{\rm SQL}(\gamma)} \to \frac{1}{4}\frac{\Omega^2}{\gamma^2}\left(\frac{1-\rho}{1+\rho}\right)\frac{I_{\rm SQL}}{I_o}, \qquad \frac{\Omega}{\gamma} \gg 1; \qquad \frac{S_h^{\rm ERSE}(\Omega)}{S_h^{\rm SQL}(\gamma)} \to \frac{\gamma^4}{\Omega^4}\left(\frac{1-\rho}{1+\rho}\right)\frac{I_o}{I_{\rm SQL}}, \qquad \frac{\Omega}{\gamma} \ll 1. \tag{2.59}$$

In conclusion, in the ERSE configuration ($\phi = \pi/2$), the situation is in some sense the reverse of the ESR scheme ($\phi = 0$). In the former the bandwidths are much larger than in either the ESR of the conventional interferometer. However, the more broadband curves are obtained at the cost of losing sensitivity in the frequency range $\sim 70 - 250$ Hz and this explains why the maximum signal-to-noise

ratio for inspiraling binaries,

$$\frac{(S/N)_{\rm ERSE}}{(S/N)_{\rm conv}} \simeq 1.096 \qquad \text{for} \quad \rho = 0.48 \quad \text{and} \quad I_o = I_{\rm SQL}\,. \tag{2.60}$$

is not very different from that of a conventional interferometer. Finally, let us observe that our two extreme cases are linked mathematically by taking $\rho \to -\rho$ ($\overline{\mathcal{K}} \to \widetilde{\mathcal{K}}$) and exchanging the two quadratures. For much further analysis and detail of the ERSE and ESR configurations, see Refs. [12, 13].

2.4 Structure of resonances and instabilities

We now turn our attention from the well-known extreme configurations, for which previous analysis gave correct predictions, to the more general case $0 < \phi < \pi/2$. As Figs. 2.2 and 2.3 show, the noise curves for a SR interferometer with frequency independent homodyne detection generically exhibit resonant features that vary as I_o, ρ, ϕ and ζ are changed. These resonances are closely related to the optical-mechanical resonances of the dynamical system formed by the optical field and the mirrors. A thorough study of this system must investigate explicitly the motion of the mirrors, instead of including it implicitly in the formulae as we did in this chapter. It can be most clearly worked out using the formalism of linear quantum measurements [4], which we will extend to SR interferometers in Chapter 3. In this section, we limit our investigation to the resonant structures in the amplitudes of the optical fields, and for simplicity we work in the limit of a totally reflecting SR mirror, i.e., $\rho = 1$. This limit provides simple analytical expressions for the resonant frequencies as functions of the SR detuning phase ϕ and the light power I_o. We shall comment on the general case $\rho \neq 1$, which we will discuss at length in Chapter 3, only at the end of this section.

2.4.1 Resonances of the closed system: $\rho = 1$

We shall investigate the free oscillation modes of the whole interferometer when the GW signal is absent [$h(\Omega) = 0$] and there is no output field ($\rho = 1$), so the system is closed. We consider the regime of classical electrodynamics, i.e., we work with the two classical quadrature fields E_1 and E_2, satisfying the same equations of motion as the quantum-field operators c_1 and c_2 (see Fig. 2.1). We shall evaluate the stationary modes, notably the eigenmodes and eigenvalues of the whole optico-mechanical system made of the end mirrors and the signal recycled optical field. We achieve this by propagating the in-going fields E_1 and E_2 (entering the beam splitter's dark port) into the conventional interferometer, along a complete round trip, and then through the SR cavity back to the starting point. The round-trip propagation leads to the following homogeneous equation

for the eigenmodes:

$$\left[\begin{pmatrix}\cos 2\phi & -\sin 2\phi\\ \sin 2\phi & \cos 2\phi\end{pmatrix} e^{2i\beta}\begin{pmatrix}1 & 0\\ -\mathcal{K} & 1\end{pmatrix} - \mathrm{I}\right]\begin{pmatrix}E_1\\ E_2\end{pmatrix} = 0\,, \tag{2.61}$$

which can be simplified into the more interesting form:

$$T\begin{pmatrix}e^{2i(\alpha+\beta)}-1 & \\ 0 & e^{2i(-\alpha+\beta)}-1\end{pmatrix}T^{-1}\begin{pmatrix}E_1\\ E_2\end{pmatrix} = 0\,, \qquad 2\alpha \equiv \arccos\left(\cos 2\phi + \frac{\mathcal{K}}{2}\sin 2\phi\right)\,, \tag{2.62}$$

where T is a matrix whose precise form is unimportant. Note that the definition of the function arccos ensures that $\Re(2\alpha)$ ranges from 0 to π. The free oscillation condition is then given by

$$\cos 2\beta_{\mathrm{res.}} = \cos 2\alpha = \cos 2\phi + \frac{\mathcal{K}}{2}\sin 2\phi\,. \tag{2.63}$$

Solving Eq. (2.63) explicitly in terms of the frequency Ω, we obtain the rather simple analytical equation for the position of the resonances:

$$\frac{\Omega^2_{\mathrm{res.}}}{\gamma^2} = \frac{1}{2}\left[\tan^2\phi \pm \sqrt{\tan^4\phi - \frac{4I_o}{I_{\mathrm{SQL}}}\,\tan\phi}\right]\,. \tag{2.64}$$

This equation is characterized by three regimes ($0 < \phi < \pi$):

- $\phi > \pi/2$: one real and one imaginary resonant frequency;
- $\arctan[(4I_o/I_{\mathrm{SQL}})^{1/3}] < \phi < \pi/2$: two real resonant frequencies;
- $0 < \phi < \arctan[(4I_o/I_{\mathrm{SQL}})^{1/3}]$: two complex conjugate resonant frequencies.

Equation (2.64) is very similar to the resonance equation that Braginsky, Gorodetsky and Khalili have derived for their proposal "Optical bar gravitational wave detectors" (see Appendix D of Ref. [9]).

For very low light power, $I_o \ll I_{\mathrm{SQL}}$, the second term under the square root on the RHS of Eq. (2.64) goes to 0 and the four roots tend to $\Omega = 0$ (double root) and $\Omega = \pm\gamma\tan\phi$. We interpret this limit as follows (see Chapter 3 for further details): When the coupling between the motion of the mirror and the optical field is zero ($I_o \to 0$), the resonant frequencies of the entire system are given by the resonances of the test mass, i.e., the free-oscillation modes of a test mass ($\Omega = 0$), plus the resonances of the optical field, i.e., the electromagnetic modes of the entire cavity with fixed mirrors, given by $\Omega = \pm\gamma\tan\phi$ [12]. When the light power is increased toward I_{SQL}, the coupling between the free test mass and the optical field drives the four resonant frequencies away from their decoupled values. By analyzing the four coupled resonant frequencies, we can easily identify the

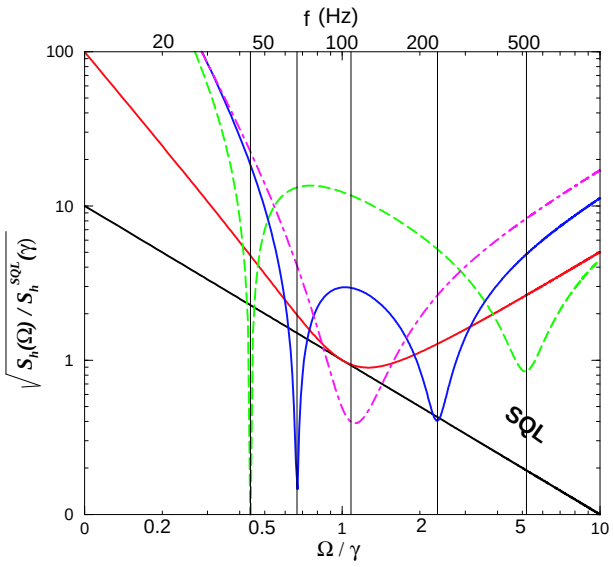

Figure 2.5: Log-log plot of $\sqrt{S_h(\Omega)/S_h^{\rm SQL}(\gamma)}$ versus Ω/γ for $I_o = I_{\rm SQL}$, $\rho = 0.95$ and $\zeta = 0$ (i.e., the second quadrature $b_2^{\mathcal{C}}$ is measured). The detuning phase ϕ takes the values (going from right to left): $\pi/2 - 0.19$, $\pi/2 - 0.39$ and $\pi/2 - 0.59$. The vertical grid lines have been drawn by using Eq. (2.64) and taking the real part of $\Omega_{\rm res.}$. These lines agree well with the positions of the resonant dips.

ones with the $-$ $(+)$ sign in Eq. (2.64) as remnants of the resonant frequencies of the free test mass (optical field). (For a more thorough discussion of these results see Chapter 3, where we explicitly examine the mirror motion.)

Let us observe that Eq. (2.63) can also be obtained as follows. By expanding the noise spectral density (2.33) for $\tau \to 0$, we get:

$$\frac{S_h(\Omega)}{h_{\rm SQL}^2(\Omega)} = \frac{\left(-2\,\cos 2\,\beta + 2\,\cos 2\,\phi + \mathcal{K}\,\sin 2\,\phi\right)^2}{8\,\mathcal{K}\,\left[\cos^2\beta\,(\sin^2\zeta - \cos^2\phi) + \cos^2\phi\,\cos^2\zeta\right]}\,\frac{1}{\tau^2} + \mathcal{O}(\tau^0)\,. \tag{2.65}$$

The leading term of the expansion goes to zero when $2\cos 2\phi - 2\cos 2\beta_{\rm res.} + \mathcal{K}\sin 2\phi = 0$, which is exactly the resonant condition (2.63) for the closed system derived above. This means that for (open) SR interferometers with highly reflecting SR mirrors, the dips in the noise curves agree with the resonances of the closed system.

In practice, the real part of the resonant frequencies (2.64) for the closed system turns out to be a good approximation to the positions of the valleys in the noise spectral density of an (open) SR interferometer with high SR-mirror reflectivity. To illustrate this fact, in Fig. 2.5 we plot the noise curves $\sqrt{S_h(\Omega)}$ for the second quadrature $b_2^{\mathcal{C}}$ with $I_o = I_{\rm SQL}$, $\rho = 0.95$ and varying ϕ. The vertical lines have been drawn by solving Eq. (2.64) numerically for Ω and taking its real part, i.e., the real part of the resonant frequencies of the closed systems. There is indeed very good agreement. This

suggests that the gain in sensitivity comes from a resonant amplification effect; see the discussion at the end of the Sec. 2.4.3.

If the imaginary part of the resonant frequency is positive (negative) then, with our convention for the Fourier transform, the solution is unstable (stable). The best noise sensitivity curves have detuning phase ϕ in the range $\arctan[(4I_o/I_{\rm SQL})^{1/3}] \lesssim \phi \lesssim \pi/2$, which for $\rho = 1$ correspond to two real resonant frequencies, and no instability. However, as soon as we allow the transmissivity of the SR mirror τ to be different from zero (as it must be in a real interferometer), we always find that one of the two resonant frequencies has a positive imaginary part (see Chapter 3). A more detailed analysis of the dynamics of the system has shown that this is a rather weak instability which typically develops on a time scale of $\lesssim 0.1\gamma$ and can be cured by introducing an appropriate control system (as discussed in Chapter 3).

2.4.2 Semiclassical interpretation of resonances for small $\mathcal{K}$: pure optical resonances

In this section we shall focus on the optical-field resonances and shall relate our results to previous semiclassical analyses of SR interferometers [12, 13].

The test-mass motion affects the optical fields through the term $\mathcal{K} = 2\,(I_o/I_{\rm SQL})\,\gamma^4/\left(\Omega^2(\Omega^2+\gamma^2)\right)$, where the factor $I_o/I_{\rm SQL}$ can be considered a measure of the strength of the coupling. The quantity $\mathcal{K}$ governs both the resonant condition and the relative magnitude of shot noise and radiation-pressure noise. In particular, when $\mathcal{K}$ is very small, Eq. (2.63) simplifies to $\cos 2\phi - \cos 2\beta_{\rm res.} = 0$, which can be solved easily, giving:

$$2(\pm\beta_{\rm res.} + \phi) = 2\pi\, n\,, \qquad \text{i.e.} \quad \Omega_{\rm res.} = \pm\gamma \tan\phi\,, \tag{2.66}$$

with n an integer. Equation (2.66) can be explained with a simple optics argument: The quantity $\pm 2\beta$ is the phase gained by the upper and lower GW sidebands while in an arm cavity, while ϕ is the phase gained when traveling one way down the SR cavity. Thus $2(\pm\beta+\phi)$ is just the round-trip phase, and Eq. (2.66) is the resonant condition for the entire (closed) interferometer. Hence, the presence of $\mathcal{K}$ in the resonant condition (2.63) provides the deviation from a pure optical resonance. Moreover, $\mathcal{K}$ is also an indicator of the different scalings of I_o and m in the final expressions for the noises, and therefore it governs the relative magnitude of the shot noise and radiation-pressure noise – the smaller the $\mathcal{K}$, the more important the shot noise compared to radiation pressure noise. When $\mathcal{K}$ is small, a semi-classical argument helps to explain the features of our noise curves. If we are close to the resonance, then feeding back the signal at that frequency increases the peak sensitivity while decreasing the bandwidth. Different schemes of such narrow-banding have been proposed, e.g., see Drever [28]. The scheme discussed here, in which the signal at the dark port is fed back into the

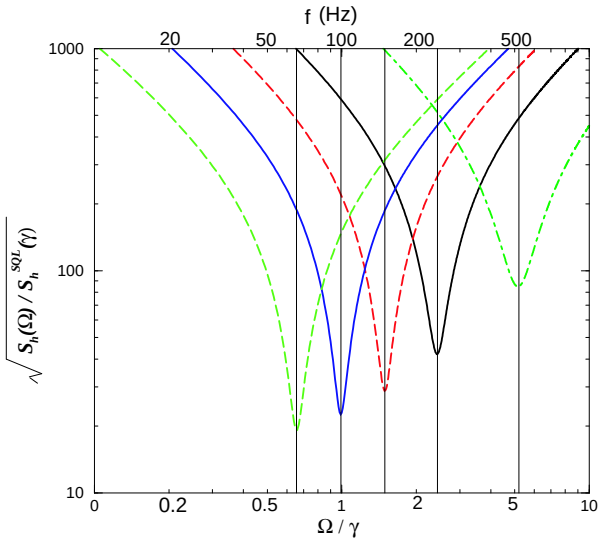

Figure 2.6: Log-log plot of $\sqrt{S_h(\Omega)/S_h^{\rm SQL}(\gamma)}$ versus Ω/γ for $\zeta = 0$ (i.e., $b_2^{\mathcal{C}}$ is measured) and for extremely low light power and high reflectivity: $I_o = 10^{-4} I_{\rm SQL}$ and $\rho = 0.95$. ϕ takes the values (going from right to left): $\pi/2 - 0.19$, $\pi/2 - 0.39$, $\pi/2 - 0.59$, $\pi/2 - 0.79$ and $\pi/2 - 0.99$. A series of resonances appear whose positions agree with the vertical grid lines drawn according to $\Omega_{\rm res.}/\gamma = |\tan\phi|$ [Eq. (2.66)].

arm cavities, is called signal recycling (in the narrower sense), and was invented by Meers [12]. If, on the other hand, we are far enough from the resonances, sideband signals are not encouraged to go back into the interferometer; in particular, at $|\beta_{\text{anti-res.}}| \simeq |\beta_{\text{res.}} \pm \pi/2|$, there is antiresonance, and the signal is encouraged to go out. This is what is generally called resonant sideband-extraction and was invented by Mizuno [13], see Sec. 2.3.3. The range in between, $\beta_{\text{res.}} < \beta < \beta_{\text{anti-res.}}$, is called 'detuned' signal recycling and has recently been demonstrated experimentally on the 30 m laser interferometer at Garching, Germany by Freise et al. [29] and at Caltech on a table-top experiment by Mason [30].

As an example of resonance (not anti-resonance), we plot in Fig. 2.6 the spectral density $S_h(\Omega)$ when the second quadrature $b_2^{\mathcal{C}}$ is measured, for very low light power $I_o = 10^{-4}\, I_{\rm SQL}$ and high reflectivity $\rho = 0.95$, and for various values of the detuning phase ϕ. The vertical grid lines in Fig. 2.6 are drawn according to Eq. (2.66) and indeed, there is excellent agreement.

It is interesting to note that although for LIGO-II $I_o = I_{\rm SQL}$, there is still a frequency band where $\mathcal{K}$ is relatively small. This is due to the fact that $\mathcal{K}$ drops very fast as Ω increases. In that frequency band the semiclassical formalism gives a correct result for the optical resonances [27]. However, since the semiclassical approach does not take into account the motion of the arm-cavity end mirrors, it can only describe one resonance (and not two) in the entire spectrum.

2.4.3 Quantum mechanical discussion of the general case: two resonances and $\rho \neq 1$

The correspondence between the optical-mechanical resonances and the minima of the noise curves suggests that the gain in sensitivity comes from a resonant amplification of the input signal, i.e., of the gravitational force acting on the mirrors, as already observed for optical bar GW detectors by Braginsky's group [9]. Let us discuss this point more deeply.

The quantum part of the input–output relation (2.20) (with $|\Phi| \ll 1$ as we have assumed throughout this chapter) reads

$$b_i^{\rm quant} = \frac{e^{2i\beta}\, C_{ij}}{M}\, a_j\,, \qquad i,j = 1,2\,. \tag{2.67}$$

We find it convenient to renormalize the quantum transfer matrix:

$$\mathcal{M}_{ij} \equiv \frac{C_{ij}}{|M|}\,, \qquad i,j = 1,2 \tag{2.68}$$

so $\det \mathcal{M}_{ij} = 1$. Note that this $\mathcal{M}_{ij}$ is normalized with respect to unit quantum noise. Because the C_{ij} are real, the matrix $\mathcal{M}$ depends on three real parameters and we can always decompose it into two rotations $R(\theta)$, $R(\varphi)$ and a squeeze $S(r)$ (see for details Ref. [22]), e.g., $\mathcal{M} = R(\theta)\, R(\varphi)\, S(r)\, R(-\varphi)$, with

$$R(\theta) = \begin{pmatrix} \cos\theta & -\sin\theta \\ \sin\theta & \cos\theta \end{pmatrix}\,, \qquad S(r) = \begin{pmatrix} e^{r} & 0 \\ 0 & e^{-r} \end{pmatrix}\,, \tag{2.69}$$

where the factor e^r describes the stretching ($r > 0$) or squeezing ($r < 0$) of the quantum fluctuations in the quadrature b_i [see Eqs. (2.67), (2.68)]. Note that classical optical fields always have a zero squeeze factor.

To express the squeeze parameter r in terms of the physical parameters describing the SR interferometer, we simply take the trace of the matrix $\mathcal{M}\,\mathcal{M}^\dagger$, obtaining

$$e^{2r} + e^{-2r} = 2 + \frac{\tau^4\, \mathcal{K}^2}{|M|^2}\,. \tag{2.70}$$

Hence, in a SR interferometer the squeezing (generally called ponderomotive squeezing) is induced by the back-action force acting on the mirror through the effective coupling $\mathcal{K}$. In particular, for small $\mathcal{K}$, we have $e^{2r} + e^{-2r} \approx 2$ and the squeeze factor r goes to 0, which means the output field is classical. For our discussion below the specific expressions of θ and φ in terms of the physical parameters are unimportant.

From the previous discussions and the results derived in Chapter 3 we have learned that the zeros of $M(\Omega)$ are the resonant frequencies of the optical-mechanical system and the valleys of the

noise spectral densities are their real parts. It is straightforward to show that for Ω equal to the real part of the resonances $|M| \propto \tau^2$. Hence, on resonance, for typical values of the physical quantities I_o, ρ and ϕ, the RHS of Eq. (2.70) goes to a constant when $\tau \to 0$. This means that the squeeze factor r does not grow much around the resonances. On the other hand, the absolute value of the output signal strength [the term involving h in Eq. (2.20)], is given by

$$\frac{\sqrt{2\mathcal{K}}\,\tau\,|D_i|}{h_{\rm SQL}\,|M|}\,h\,, \qquad i=1,2\,, \tag{2.71}$$

and because on resonance $1/|M| \sim 1/\tau^2$, when $\tau \to 0$ the classical signal is resonantly amplified and the amplification becomes stronger and stronger as $\tau \to 0$ (closed system).

This means that, by contrast with QND techniques based on static correlations between shot noise and radiation-pressure noise [7, 8], in SR interferometers the ponderomotive squeezing *does not* seem to be the major factor that enables the interferometer to beat the SQL. Indeed, whereas the amplitude of the classical output signal is amplified near the resonances, the nonclassical behavior of the output light is not resonantly amplified. Therefore, the beating of the SQL in SR interferometers comes from a resonant amplification of the input signal: the whole system acts like an optical spring,[13] as we have described more thoroughly in Chapter 3, and it was also derived for optical bar GW detectors by Braginsky's group [9].

2.5 Inclusion of losses in signal-recycling interferometers

In this section we shall compute how optical losses affect the noise in a SR inteferometer using the lossy input–output relations for a conventional interferometer [7] and doing a similar treatment of losses in the SR cavity. We shall continue to use our extension of the KLMTV's formalism as developed in Sec. 2.2.

KLMTV [7] described the noise that enters the arm cavities of a conventional interferometer at the loss points on the mirrors in terms of a noise operator, whose state is the vacuum, with quadratures n_1 and n_2. The resulting lossy input–output relations read [7]

$$d_1 = c_1\,e^{2i\beta}\left(1-\frac{\mathcal{E}}{2}\right)+\sqrt{\mathcal{E}}\,e^{i\beta}\,n_1\,, \tag{2.72}$$

$$\begin{aligned} d_2 = {} & c_2\,e^{2i\beta}\left(1-\frac{\mathcal{E}}{2}\right)+\sqrt{\mathcal{E}}\,e^{i\beta}\,n_2+\sqrt{2\mathcal{K}}\,\frac{h}{h_{\rm SQL}}\,e^{i\beta}\,\left[1-\frac{\epsilon}{4}\,(3+e^{2i\beta})\right] \\ & -\mathcal{K}\,e^{2i\beta}\left\{c_1\,\left[1-\frac{\epsilon}{2}\,(3+e^{2i\beta})\right]+\sqrt{\frac{\epsilon}{2}}\,n_1\right\}\,, \end{aligned} \tag{2.73}$$

where $\epsilon = 2\mathcal{L}/T$ and $\mathcal{L}$ is the loss coefficient per round trip in the arm-cavity. For LIGO-II T and

[13] In this sense we could refer to a signal recycled interferometer as a SPRING detector, which could also stand for Signal Power Recycling Interferometer Gravitational-wave detector!

$\mathcal{L}$ are expected to be $T = 0.033$ and $\mathcal{L} \sim 200 \times 10^{-6}$, so $\epsilon \sim 0.01$. The quantity $\mathcal{E}$ which appears in Eqs. (2.72) and (2.73) is frequency dependent and is given by

$$\mathcal{E} = \frac{2\epsilon}{1 + (\Omega/\gamma)^2} \,. \tag{2.74}$$

In the present analysis, as in Ref. [7], we do not take into account losses coming from the beam splitter. We expect their effect to be small compared to the losses introduced by the SR cavity and the photodetection process. Fig. 2.7 sketches the way we have incorporated losses. We describe the loss inside the SR cavity by the fraction of photons lost at each bounce of the interior field off the SR mirror, $\lambda_{\rm SR}$, and we introduce associated noise quantum operators p_i $(i = 1, 2)$ into the inward-propagating field operator at the SR mirror (see left panel of Fig. 2.7). Equations (2.18) then become

$$e_1 = \sqrt{1 - \lambda_{\rm SR}}\,(\tau\, a_1 + \rho\, f_1) + \sqrt{\lambda_{\rm SR}}\, p_1 \,, \qquad e_2 = \sqrt{1 - \lambda_{\rm SR}}\,(\tau\, a_2 + \rho\, f_2) + \sqrt{\lambda_{\rm SR}}\, p_2 \,, \tag{2.75}$$

and the noise operators p_i satisfy the commutation relations (2.8). We also assume that the state of p_i is the vacuum. We include the losses of the photodetection process in an effective way, by modifying the output field operators and introducing another noise field q_i with $i = 1, 2$ (see right panel of Fig. 2.7):

$$b_1^{\rm L} = \sqrt{1 - \lambda_{\rm PD}}\,(\tau\, f_1 - \rho\, a_1) + \sqrt{\lambda_{\rm PD}}\, q_1 \,, \qquad b_2^{\rm L} = \sqrt{1 - \lambda_{\rm PD}}\,(\tau\, f_2 - \rho\, a_2) + \sqrt{\lambda_{\rm PD}}\, q_2 \,. \tag{2.76}$$

Here, $\lambda_{\rm PD}$ is the photodetector loss. The noise quadrature fields q_i describe additional shot noise due to photodetection and are assumed to satisfy Eq. (2.8) and to be in the vacuum state. Following the procedure described in Sec. 2.2, we derive from Eqs. (2.72), (2.73), (2.75) and (2.76) the following input–output relations for the lossy SR interferometer (for simplicity we set $\Phi = 0$):

$$\begin{aligned}
\begin{pmatrix} b_1^{\rm L} \\ b_2^{\rm L} \end{pmatrix} \;=\; & \frac{1}{M^{\rm L}} \left[e^{2i\beta} \begin{pmatrix} C_{11}^{\rm L} & C_{12}^{\rm L} \\ C_{21}^{\rm L} & C_{22}^{\rm L} \end{pmatrix} \begin{pmatrix} a_1 \\ a_2 \end{pmatrix} + \sqrt{2\mathcal{K}}\,\tau\, e^{i\beta} \begin{pmatrix} D_1^{\rm L} \\ D_2^{\rm L} \end{pmatrix} \frac{h}{h_{\rm SQL}} + e^{2i\beta} \begin{pmatrix} P_{11} & P_{12} \\ P_{21} & P_{22} \end{pmatrix} \begin{pmatrix} p_1 \\ p_2 \end{pmatrix} \right. \\
& \left. + e^{2i\beta} \begin{pmatrix} Q_{11} & Q_{12} \\ Q_{21} & Q_{22} \end{pmatrix} \begin{pmatrix} q_1 \\ q_2 \end{pmatrix} + e^{2i\beta} \begin{pmatrix} N_{11} & N_{12} \\ N_{21} & N_{22} \end{pmatrix} \begin{pmatrix} n_1 \\ n_2 \end{pmatrix} \right] ,
\end{aligned} \tag{2.77}$$

where, to ease the notation, we have defined

$$\begin{aligned}
M^{\rm L} \;=\; & 1 + \rho^2\, e^{4i\beta} - 2\rho \left(\cos 2\phi + \frac{\mathcal{K}}{2} \sin 2\phi \right) e^{2i\beta} + \lambda_{\rm SR}\, \rho \left(-\rho\, e^{2i\beta} + \cos 2\phi + \frac{\mathcal{K}}{2} \sin 2\phi \right) e^{2i\beta} \\
& + \epsilon\, \rho \left[2\cos^2\beta\, (-\rho\, e^{2i\beta} + \cos 2\phi) + \frac{\mathcal{K}}{2} \left(3 + e^{2i\beta}\right) \sin 2\phi \right] e^{2i\beta} \,.
\end{aligned} \tag{2.78}$$

Note that $M^{\rm L}$, like M in Eq. (2.21), has zeros in the lower- and upper-half complex Ω plane. Hence, the lossy SR interferometer, like the lossless one, also suffers from instabilities. Nevertheless, we have shown in Chapter 3 that an appropriate control system can cure them, as in the lossless case. In the following equations we give the various quantities which appear in Eq. (2.77) accurate to linear order in ϵ and $\lambda_{\rm SR}$ but to all orders in $\lambda_{\rm PD}$. (We expect $\lambda_{\rm SR}\sim 0.02$ and $\lambda_{\rm PD}\sim 0.1$ [27].) The various quantities read

$$\begin{aligned}
C_{11}^{\rm L} &= C_{22}^{\rm L} = \sqrt{1-\lambda_{\rm PD}}\,\left\{(1+\rho^2)\,\left(\cos 2\phi + \frac{\mathcal{K}}{2}\,\sin 2\phi\right) - 2\rho\,\cos 2\beta\right.\\
&\quad -\frac{1}{4}\epsilon\,\left[-2(1+e^{2i\beta})^2\,\rho + 4(1+\rho^2)\cos^2\beta\,\cos 2\phi + (3+e^{2i\beta})\,\mathcal{K}\,(1+\rho^2)\,\sin 2\phi\right]\\
&\quad \left.+\,\lambda_{\rm SR}\,\left[e^{2i\beta}\rho - \frac{1}{2}\,(1+\rho^2)\,\left(\cos 2\phi + \frac{\mathcal{K}}{2}\,\sin 2\phi\right)\right]\right\}\,,\\
C_{12}^{\rm L} &= \sqrt{1-\lambda_{\rm PD}}\,\tau^2\,\left\{-(\sin 2\phi + \mathcal{K}\,\sin^2\phi) + \frac{1}{2}\epsilon\,\sin\phi\,\left[(3+e^{2i\beta})\,\mathcal{K}\,\sin\phi + 4\cos^2\beta\,\cos\phi\right]\right.\\
&\quad \left.+\frac{1}{2}\lambda_{\rm SR}\,(\sin 2\phi + \mathcal{K}\,\sin^2\phi)\right\}\,,\\
C_{21}^{\rm L} &= \sqrt{1-\lambda_{\rm PD}}\,\tau^2\,\left\{(\sin 2\phi - \mathcal{K}\,\cos^2\phi) + \frac{1}{2}\epsilon\,\cos\phi\,\left[(3+e^{2i\beta})\,\mathcal{K}\,\cos\phi - 4\cos^2\beta\,\sin\phi\right]\right.\\
&\quad \left.+\frac{1}{2}\lambda_{\rm SR}\,(-\sin 2\phi + \mathcal{K}\,\cos^2\phi)\right\}\,;
\end{aligned} \tag{2.79}$$

$$\begin{aligned}
D_1^{\rm L} &= \sqrt{1-\lambda_{\rm PD}}\,\left\{-(1+\rho\,e^{2i\beta})\,\sin\phi + \frac{1}{4}\epsilon\,\left[3+\rho+2\rho\,e^{4i\beta}\right.\right.\\
&\quad \left.\left.+e^{2i\beta}\,(1+5\rho)\right]\,\sin\phi + \frac{1}{2}\lambda_{\rm SR}\,e^{2i\beta}\,\rho\sin\phi\right\}\,,\\
D_2^{\rm L} &= \sqrt{1-\lambda_{\rm PD}}\,\left\{-(-1+\rho\,e^{2i\beta})\,\cos\phi + \frac{1}{4}\epsilon\,\left[-3+\rho+2\rho\,e^{4i\beta}\right.\right.\\
&\quad \left.\left.+e^{2i\beta}\,(-1+5\rho)\right]\,\cos\phi + \frac{1}{2}\lambda_{\rm SR}\,e^{2i\beta}\,\rho\cos\phi\right\}\,;
\end{aligned} \tag{2.80}$$

$$\begin{aligned}
P_{11} &= P_{22} = \frac{1}{2}\sqrt{1-\lambda_{\rm PD}}\,\sqrt{\lambda_{\rm SR}}\,\tau\,(-2\rho\,e^{2i\beta} + 2\cos 2\phi + \mathcal{K}\,\sin 2\phi)\,,\\
P_{12} &= -\sqrt{1-\lambda_{\rm PD}}\,\sqrt{\lambda_{\rm SR}}\,\tau\,\sin\phi\,(2\cos\phi + \mathcal{K}\,\sin\phi)\,,\\
P_{21} &= \sqrt{1-\lambda_{\rm PD}}\,\sqrt{\lambda_{\rm SR}}\,\tau\,\cos\phi\,(2\sin\phi - \mathcal{K}\,\cos\phi)\,;
\end{aligned} \tag{2.81}$$

$$\begin{aligned}
Q_{11} &= Q_{22} = \sqrt{\lambda_{\rm PD}}\,\left\{e^{-2i\beta} + \rho^2\,e^{2i\beta} - \rho\,(2\cos 2\phi + \mathcal{K}\,\sin 2\phi) + \frac{1}{2}\epsilon\,\rho\,\left[e^{-2i\beta}\,\cos 2\phi\right.\right.\\
&\quad \left.+e^{2i\beta}\,(-2\rho - 2\rho\,\cos 2\beta + \cos 2\phi + \mathcal{K}\,\sin 2\phi) + 2\cos 2\phi + 3\mathcal{K}\,\sin 2\phi\right]\\
&\quad \left.-\frac{1}{2}\lambda_{\rm SR}\,\rho\,\left[2\rho\,e^{2i\beta} - 2\cos 2\phi - \mathcal{K}\,\sin 2\phi\right]\right\}\,,\\
Q_{12} &= 0 = Q_{21}\,;
\end{aligned} \tag{2.82}$$

$$
\begin{aligned}
N_{11} &= \sqrt{1-\lambda_{\rm PD}}\,\sqrt{\frac{\epsilon}{2}}\,\tau\,\left\{\mathcal{K}\,(1+\rho\,e^{2i\beta})\,\sin\phi+2\cos\beta\,\left[e^{-i\beta}\cos\phi-\rho e^{i\beta}(\cos\phi+\mathcal{K}\,\sin\phi)\right]\right\}\,,\\
N_{22} &= -\sqrt{1-\lambda_{\rm PD}}\,\sqrt{2\epsilon}\,\tau\,(-e^{-i\beta}+\rho\,e^{i\beta})\,\cos\beta\,\cos\phi\,,\\
N_{12} &= -\sqrt{1-\lambda_{\rm PD}}\,\sqrt{2\epsilon}\,\tau\,(e^{-i\beta}+\rho\,e^{i\beta})\,\cos\beta\,\sin\phi\,,\\
N_{21} &= \sqrt{1-\lambda_{\rm PD}}\,\sqrt{\frac{\epsilon}{2}}\,\tau\,\left\{-\mathcal{K}\,(1+\rho)\,\cos\phi+2\cos\beta\,\left(e^{-i\beta}+\rho\,e^{i\beta}\right)\,\cos\beta\,\sin\phi\right\}\,.
\end{aligned}
\tag{2.83}
$$

Similarly to Sec. 2.3.1, we follow KLMTV's method [7] to derive the noise spectral density of a lossy SR interferometer [see Eq. (2.33)]:

$$
\begin{aligned}
S_h^\zeta = \frac{h_{\rm SQL}^2}{2\mathcal{K}\,\tau^2\,\left|D_1^L\,\sin\zeta+D_2^L\,\cos\zeta\right|^2} \qquad & \Big[\left|C_{11}^L\,\sin\zeta+C_{21}^L\,\cos\zeta\right|^2+\left|C_{12}^L\,\sin\zeta+C_{22}^L\,\cos\zeta\right|^2+\\
& |P_{11}\,\sin\zeta+P_{21}\,\cos\zeta|^2+|P_{12}\,\sin\zeta+P_{22}\,\cos\zeta|^2+\\
& |Q_{11}\,\sin\zeta+Q_{21}\,\cos\zeta|^2+|Q_{12}\,\sin\zeta+Q_{22}\,\cos\zeta|^2+\\
& |N_{11}\,\sin\zeta+N_{21}\,\cos\zeta|^2+|N_{12}\,\sin\zeta+N_{22}\,\cos\zeta|^2\Big]\,.
\end{aligned}
\tag{2.84}
$$

Exploring numerically this equation, we find that for the loss levels expected in LIGO-II ($\epsilon\sim 0.01, \lambda_{\rm PD}\sim 0.1, \lambda_{\rm SR}\sim 0.02$ [20]), the optical losses have only a modest influence on the noise curves of a lossless SR interferometer. For example, in Fig. 2.8 we compare the lossless noise spectral densities with the lossy ones for the two quadratures b_1 and b_2. The main effect of the loss is to smooth out the deep resonant valleys. More specifically, for (i) the physical parameters used in Fig. 2.2, (ii) a net fractional photon loss of 1% in the arm cavities ($\epsilon = 0.01$) and 2% in each round trip in the SR cavity ($\lambda_{\rm SR} = 0.02$), and (iii) a photodetector efficiency of 90% ($\lambda_{\rm PD} = 0.1$), we find that the losses produce a fractional loss in signal-to-noise ratio for inspiraling binaries [see Eqs. (2.36), (2.37)] of 8% and 21%, for the first and second quadratures, respectively.

The reason why we get a modest effect from optical losses as compared to schemes using squeezing or FD homodyne detections[14] rests on the fact that our gain in sensitivity mostly comes from resonant amplification, which is much less susceptible to losses than quantum correlations. This general consideration has long been understood by Braginsky, Khalili and colleagues and underlies their motivation for the GW "optical bar" detectors [9].

2.6 Conclusions

In this chapter we have extended the quantum formalism recently developed [7] for conventional interferometers (LIGO-I/TAMA/Virgo), to SR interferometer such as LIGO-II. The introduction

[14] Note that in KLMTV [7] they assumed a loss factor for end-mirrors which is 10% of our value, and they also did not take into account losses coming from the photodetection.

Figure 2.7: Sketchy view of the lossy signal-recycling interferometer. Optical losses in the signal-recycling cavity (on the left) are described by the noise quadratures p_i, while losses due to the photodetection process (on the right) are included through the noise quadratures q_i.

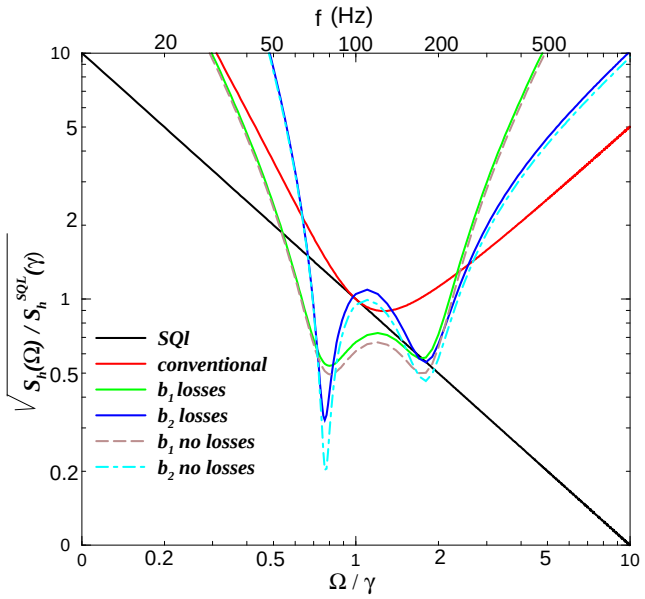

Figure 2.8: Log-log plot of $\sqrt{S_h(\Omega)/S_h^{\rm SQL}(\gamma)}$ versus Ω/γ for the two quadratures b_1 ($\zeta = \pi/2$) and b_2 ($\zeta = 0$), including and not including losses, with $\rho = 0.9$, $\phi = \pi/2 - 0.47$, $I_o = I_{\rm SQL}$, $\epsilon = 0.01$, $\lambda_{\rm SR} = 0.02$ and $\lambda_{\rm PD} = 0.1$. The noise curve for a conventional interferometer and the SQL are shown as well.

of the SR cavity has been planned as an important tool to reshape the noise curves, making the interferometer work either in broadband or in narrowband configurations. This flexibility is expected to improve the observation of specific GW sources [16]. Quite remarkably, our quantum mechanical analysis has revealed other significant features of the SR cavity.

First, the SR mirror produces dynamical correlations between quantum shot noise and radiation-pressure-fluctuation noise which break the light's ability to enforce the SQL of a free mass, allowing the noise curves to go below the SQL by modest amounts: roughly a factor two over a bandwidth $\Delta f \sim f$. Before our work, researchers were unaware of the shot-noise / radiation-pressure correlations and thus omitted them in their semiclassical analysis of the straw-man design of LIGO-II [20]. The goal of beating the SQL in LIGO-II can be achieved only *if* all sources of thermal noise can also be pushed below the SQL and indeed much R&D will go into trying to push them downward. It turns out that even with current estimates of the LIGO-II thermal noise [14], which are a little above the SQL, the net noise (thermal plus optical) is significantly affected by the shot-noise/ radiation-pressure correlations. Indeed, the correlations lift the noise at low frequencies $10\,\mathrm{Hz} \lesssim \Omega/2\pi \lesssim 50$ Hz, as compared to the semiclassical estimations, even though in this frequency range the optical noise may already be very much larger than the SQL. This is due to the inaccuracy of the semiclassical method in estimating the effect of the radiation-pressure force, which is important in this region. In the middle frequency range, i.e., near 100 Hz, the SQL-beating effect cannot lower the total noise much because of the thermal contribution. The effect of the correlations in the implementation of LIGO-II will be clarified and sharpened once the readout scheme has be specified.

Second, we have learned that the *dynamical* correlations arise naturally from the nontrivial coupling between the antisymmetric mode of motion of the four arm-cavity mirrors and the signal recycled optical fields. This dynamical coupling invalidates the naive picture, according to which the arm cavity mirrors are subject only to random quantum-vacuum fluctuations. The SR interferometer responds to a GW signal as an optical spring (see Chapter 3), and this oscillatory response gives the possibility for resonant amplification of the GW signal. The optical-mechanical system is characterized by two resonances and one of them is always unstable, so a control system must be introduced to stabilize it (see Chapter 3). In the limit of a highly reflecting SR mirror we have worked out analytically a very simple equation which locates the positions of the resonant frequencies. Whereas the amplitude of the classical output signal is amplified near the resonances, the quantum noise is not particularly affected by them. All this suggests that the beating of the SQL in SR interferometers comes primarily from the resonant amplification of the input GW signal, as also occurs in "optical bar" GW detectors [9].

The inclusion of losses does not greatly affect the SR interferometer. This is due to the fact that the improvement in the noise curves rests primarily on a resonant amplification and only modestly on ponderomotive squeezing. It is worthwhile to point out that the SR interferometers bear strong

similarity to the "optical bar" detectors proposed by Braginsky, Khalili and colleagues [9]. Both of them can be viewed as oscillators with two different eigenfrequencies. However, because in SR interferometers the light plays the double role of providing the restoring force and being a probe to monitor the mirror displacements, we are forced to introduce in SR interferometers much higher laser power, to circulate in the arm cavities ($\sim 1\,\mathrm{MWatt}$), than in the "optical bar" scheme. Nevertheless, like the "optical bar" scheme, the SR interferometer is still less susceptible to optical losses than many other schemes designed to beat the SQL.

It is now important to identify the best SR configuration, i.e., the choice of the physical parameters (light power I_o, SR detuning ϕ, reflectivity of SR mirror ρ, quadrature phase ζ, and the read-out scheme: homodyne or modulation/demodulation) that optimizes the signal-to-noise ratio for inspiraling binaries, for low-mass X-ray binaries, and for other astrophysical GW sources. We shall discuss this issue elsewhere.

Finally, our analysis has shown that dynamical correlations, i.e., correlations that are intrinsic to the dynamics of the test mass-optical field system (i.e., they are not due to specific read-out schemes, as in the case of homodyne detection on a conventional interferometer), are present when the carrier frequency ω_o is detuned from resonance ($\phi \neq 0$) or antiresonance ($\phi \neq \pi/2$) in the SR cavity. This suggests a speculation that it could be worthwhile to investigate a LIGO-II configuration (see Table 2.1) without a signal recycling mirror, in which the correlations are produced by detuning the arm cavities. However, this case will require a very careful analysis of the radiation-pressure force acting on the arm-cavity mirrors [19, 18].

2.7 Appendix. Remark on commutation relations among quadrature fields in Caves-Schumaker two-photon formalism

As originally pointed out by Braginsky's group [4] and discussed by BGKMTV [15], the output variables of the GW interferometer should commute with themselves at different times, to guarantee that no other quantum noise is necessarily introduced into the measurement result once further manipulations are performed on the output. Indicating generically by $\mathcal{O}(t)$ the output quantity, the following conditions should be satisfied,

$$[\mathcal{O}(t), \mathcal{O}(t')] = 0 \qquad \forall\, t, t' \,, \qquad \Leftrightarrow \qquad [\mathcal{O}(\Omega), \mathcal{O}^\dagger(\Omega')] = 0 \qquad \forall\, \Omega, \Omega' \,. \tag{2.85}$$

If we assume that the system's output is one quadrature of the quantized electromagnetic field (EM) [see Eq. (2.10)], with the GW signal encoded at side-band frequency Ω around the carrier frequency ω_o, then the presence of terms proportional to Ω/ω_o in Eq. (2.5) prevents the output quadratures from commuting with themselves at different times. However, Braginsky et al. [15] anticipated that, in the case of LIGO-I/TAMA/Virgo, the quadrature fields at the dark port should anyway satisfy very accurately the Fourier-domain condition given by Eq. (2.85), because the side-band frequency Ω ($1\,\mathrm{Hz} \leq \Omega/2\pi \leq 10^3\,\mathrm{Hz}$) is much smaller than the carrier frequency ω_o ($\omega_o \sim 10^{15}\,\mathrm{s}^{-1}$). In this Appendix we investigate this approximation in much more detail, estimating the amount of extra noise which will be present in the final noise spectral density as a result of condition (2.85) being violated. Henceforth, for simplicity we restrict our analysis to conventional interferometers.

If the readout scheme is implemented by photodetection, then only a small frequency band around ω_o contains the final output signal. Hence, it is physically justified to introduce a cutoff Λ in the frequency domain which automatically discards all the Fourier components of the EM field outside the range $[\omega_o - \Lambda,\, \omega_o + \Lambda]$ with $0 \leq \Lambda \leq \omega_o$. As a consequence, Eq. (2.6) for the EM field can be rewritten as [see also Eqs. (4.22) of Ref. [21]]

$$\begin{aligned} E^\Lambda(t) &\equiv \int_{\omega_o-\Lambda}^{\omega_o+\Lambda} \sqrt{\frac{2\pi\hbar\omega}{\mathcal{A}c}}\, a_\omega\, e^{-i\omega t}\, \frac{d\omega}{2\pi} \,+\, \text{h.c.} \\ &= \sqrt{\frac{2\pi\hbar\omega_o}{\mathcal{A}c}}\, e^{-i\omega_o t} \int_0^\Lambda \frac{d\Omega}{2\pi} \left(a_+\, e^{-i\Omega t} + a_-\, e^{+i\Omega t}\right) \,+\, \text{h.c.} \\ &= \sqrt{\frac{4\pi\hbar\omega_o}{\mathcal{A}c}} \left[\cos(\omega_o t)\, \mathcal{O}_1^\Lambda(t) + \sin(\omega_o t)\, \mathcal{O}_2^\Lambda(t)\right] \,, \end{aligned} \tag{2.86}$$

where $a_+(\Omega)$ and $a_-(\Omega)$, with $\Omega < \Lambda$, are defined by Eq. (2.3) and the *rescaled* quadrature fields

$\mathcal{O}_i^\Lambda(t)$ are

$$\mathcal{O}_i^\Lambda(t) \equiv \int_0^\Lambda \frac{d\Omega}{2\pi}\left[a_i\, e^{-i\Omega t} + a_i^\dagger\, e^{i\Omega t}\right] \qquad i = 1,\, 2\,, \tag{2.87}$$

with the quadrature operators given by Eq. (2.7). Evaluating the commutation relations among the quadrature operators we find [see also Eqs. (4.31) of Ref. [21]]:

$$[a_1, a_{1'}] = [a_2, a_{2'}] = 0\,, \tag{2.88}$$

$$\left[a_1, a_{1'}^\dagger\right] = \left[a_2, a_{2'}^\dagger\right] = 2\pi\delta(\Omega - \Omega')\left(\frac{\Omega}{\omega_o}\right)\,, \tag{2.89}$$

$$\left[a_1, a_{2'}^\dagger\right] = -\left[a_2, a_{1'}^\dagger\right] = 2\pi i\delta(\Omega - \Omega')\,. \tag{2.90}$$

Note that Eq. (2.89) differs from the one appearing in Eq. (2.8), where we approximated a_i and $a_{i'}^\dagger$ as commuting. The non-vanishing commutation relations in Eq. (2.89) explicitly yield a non-vanishing two-time commutator for $\mathcal{O}_i^\Lambda$. In particular, a straightforward calculation gives ($i = 1, 2$)

$$C_{\mathcal{O}_i^\Lambda \mathcal{O}_i^\Lambda}(t, t') \equiv \left[\mathcal{O}_i^\Lambda(t), \mathcal{O}_i^\Lambda(t')\right] = i\frac{\Lambda^2}{\omega_o}\left[\frac{\Lambda\tau\cos(\Lambda\tau) - \sin(\Lambda\tau)}{\pi\left(\Lambda\tau\right)^2}\right]\,, \qquad \tau = t - t'\,. \tag{2.91}$$

Therefore $\mathcal{O}_i^\Lambda(t)$ cannot be the final output and there must be some unavoidable additional quantum noise due to the fact that $\mathcal{O}_i^\Lambda(t)$ has a non-vanishing two-time commutator. In LIGO-I/TAMA/Virgo this additional noise is introduced in the output during the final process of photodetection. A more detailed study would involve a very technical analysis of the photodetection's dynamics, but fortunately, as we shall see in the following, a simple estimation of the order of magnitude of this additional quantum noise suggests that it is very small and we can realistically neglect it.

We find it convenient to estimate the additional quantum noise by calculating the noise induced by the photodetector approximated as a linear measurement device coupled to the quadrature fields. [15] Having fixed the cutoff frequency Λ and working in the Fourier domain, we can write the final output as

$$\mathcal{O}_i^{out}(\Omega) = \mathcal{O}_i^\Lambda(\Omega) + Z_i^{\rm PD}(\Omega) + R_{\mathcal{O}_i^\Lambda \mathcal{O}_i^\Lambda}(\Omega)\, F_i^{\rm PD}(\Omega)\,, \tag{2.92}$$

where

$$R_{\mathcal{O}_i^\Lambda \mathcal{O}_i^\Lambda}(\Omega) \equiv \frac{i}{\hbar}\int_0^{+\infty} d\tau\, e^{i\Omega\tau}\, C_{\mathcal{O}_i^\Lambda \mathcal{O}_i^\Lambda}(t, t-\tau) = \frac{1}{2\pi\hbar\omega_o}\left(2\Lambda + i\pi\Omega + \Omega\ln\frac{\Lambda - \Omega}{\Lambda + \Omega}\right)\,. \tag{2.93}$$

The last two terms in Eq. (2.92) are the shot noise and the back-action noise of the photodetector (PD) and describe the efficiency and the strength of perturbation of the PD on the quadrature field, respectively. Let us assume that there is no correlation between $Z_i^{\rm PD}$ and $F_i^{\rm PD}$. Hence, $Z_i^{\rm PD}$ and

[15] Here we are assuming that as a consequence of the homodyne detection, the EM field impinging on the photodetector is composed of carrier light plus quantum fluctuations, and thus the light intensity measured by the photodetector is linear in the annihilation and creation operators.

$F_i^{\rm PD}$ satisfy the uncorrelated version (2.44) of the uncertainty relation, that is

$$S_{Z_i^{\rm PD}Z_i^{\rm PD}}S_{F_i^{\rm PD}F_i^{\rm PD}} \geq \hbar^2\,. \tag{2.94}$$

We are interested in evaluating the overall quantum noise. We first write the output in the form Signal + Noise as

$$\mathcal{O}_i^{\rm out}(\Omega) = \mathcal{P}_i h(\Omega) + \left[\mathcal{Q}_i^{\Lambda}(\Omega) + Z_i^{\rm PD}(\Omega) + R_{\mathcal{O}_i^{\Lambda}\mathcal{O}_i^{\Lambda}}(\Omega)F_i^{\rm PD}(\Omega)\right]\,, \tag{2.95}$$

where $\mathcal{P}_i h$ is the part of $\mathcal{O}_i^{\Lambda}(\Omega)$ that contains the signal, while $\mathcal{Q}_i^{\Lambda}(\Omega)$ contains the quantum fluctuations. Using Eq. (2.95), the overall noise spectral density is ($i = 1, 2$)

$$S_i(\Omega) = \frac{1}{|\mathcal{P}_i|^2}\left\{S_{\mathcal{Q}_i^{\Lambda}\mathcal{Q}_i^{\Lambda}}(\Omega) + S_{Z_i^{\rm PD}Z_i^{\rm PD}}(\Omega) + \left|R_{\mathcal{O}_i^{\Lambda}\mathcal{O}_i^{\Lambda}}(\Omega)\right|^2 S_{F_i^{\rm PD}F_i^{\rm PD}}(\Omega)\right\}\,. \tag{2.96}$$

The first term in Eq. (2.96) describes the quantum noise of an interferometer when the non-vanishing commutators of the quadrature fields have been ignored and ideal photodetection is applied. The second term in Eq. (2.96) describes the additional shot noise introduced by the photodetection process. Finally, the third term comes from the back-action force acting on the measured quadrature ($i = 1$ or 2) because it does not commute with itself at different times. Let us notice that, given Eq. (2.94), the second and third noise contributions appearing on the RHS of Eq. (2.96) are complementary. Indeed, the larger the shot noise, the weaker the minimum force the photodetector must apply to the quadrature fields and the smaller the back-action noise. More specifically, there is a lowest achievable value for the PD part in Eq. (2.96) given by

$$\begin{aligned} & \frac{1}{|\mathcal{P}_i|^2}\left[S_{Z_i^{\rm PD}Z_i^{\rm PD}}(\Omega) + \left|R_{\mathcal{O}_i^{\Lambda}\mathcal{O}_i^{\Lambda}}(\Omega)\right|^2 S_{F_i^{\rm PD}F_i^{\rm PD}}(\Omega)\right] \\ \geq\ & \frac{2|R_{\mathcal{O}_i^{\Lambda}\mathcal{O}_i^{\Lambda}}(\Omega)|\hbar}{|\mathcal{P}_i|^2}\,, \\ =\ & \frac{2}{|\mathcal{P}_i|^2}\left|\frac{\Lambda}{\pi\omega_o}\left(1 + \frac{\Omega}{2\Lambda}\ln\frac{\Lambda-\Omega}{\Lambda+\Omega}\right) + i\frac{\Omega}{\omega_o}\right|\,. \end{aligned} \tag{2.97}$$

Using Eq. (2.36) we derive $1/|\mathcal{S}_i|^2 = h_{\rm SQL}^2/2\mathcal{K}$ and $S_{\mathcal{Q}_i^{\Lambda}\mathcal{Q}_i^{\Lambda}} = (\mathcal{K}^2+1) > 1$. Recalling that $10\,{\rm Hz} \leq \Omega/2\pi \leq 10^3\,{\rm Hz}$ and $\omega_o \sim 10^{15}\,{\rm sec}^{-1}$, fixing Λ to a value larger than the typical Ω, e.g., $\Lambda/2\pi \sim 10\,{\rm MHz}$, and adjusting the PD such that $S_{Z_i^{\rm PD}Z_i^{\rm PD}}$ and $S_{F_i^{\rm PD}F_i^{\rm PD}}$ satisfy the minimal uncertainty relation [the equality sign in Eq. (2.94)], we find that the minimal achievable PD noise is $\sim 10^{-7}$ times the conventional shot noise. Therefore, we can totally ignore the quantum noise introduced by the fact that the quadrature fields do not commute with themselves at different times in Eq. (2.89). Note the importance of the cutoff Λ. If we had taken $\Lambda \sim \omega_o$, the limit on the PD noise would have been of the same order of magnitude as the shot noise for a conventional interferometer and it would

not have been realistic to neglect the quantum noise introduced by the non-vanishing commutation relations of the quadrature fields.

So far we evaluated the minimum quantum noise that the photodetector, coupled linearly to the quadrature field, can introduce. Let us now try to give a realistic value of it. To estimate $S_{Z_i^{\rm PD} Z_i^{\rm PD}}$, we can just recall that in the case of a lossy photodetector we have (see the discussion of lossy interferometers in Sec. 2.5)

$$Z_i^{\rm PD} \sim \sqrt{\lambda_{\rm PD}}\, p_i \,, \tag{2.98}$$

where p_i with $i = 1, 2$ are quadrature operators in the vacuum state. We expect $\lambda_{\rm PD} \sim 0.1 - 0.2$, hence $S_{Z_i^{\rm PD} Z_i^{\rm PD}} > 10^{-2} \times S^{\rm conv}_{\rm shot\,noise}$, which is five orders of magnitude larger than the lowest achievable limit discussed above with $\Lambda/2\pi \sim 10\,{\rm MHz}$. Therefore, if one can justify fixing the cutoff $\Lambda/2\pi$ at 10 MHz, and if the uncertainty relation (2.94) is satisfied with the equality sign, then one can conclude that the inefficiency will dominate over the minimum possible back-action noise by five orders of magnitude. Hence, we are justified in disregarding the non-vanishing two-time commutators of the quadrature fields in Eq. (2.89).

2.8 Bibliography

[1] A. Abramovici et al., Science **256** (1992) 325; C. Bradaschia et al., Nucl. Instrum. Meth. **A 289** (1990) 518; K. Danzmann et al., in *First Edoardo Amaldi Conference on Gravitational Wave Experiments*, Frascati 1994 (World Scientific, Singapore, 1995); K. Tsubono, in *First Edoardo Amaldi Conference on Gravitational Wave Experiments*, Frascati 1994 (World Scientific, Singapore, 1995).

[2] See, e.g., Secs. 9.5.2 and 9.5.3 of K. S. Thorne, in *Three Hundred Years of Gravitation*, eds. S. W. Hawking and W. Israel, (Cambridge University Press, Cambridge, 1987), and references therein.

[3] V. B. Braginsky, Sov. Phys. JETP **26** (1968) 831; V. B. Braginsky and Yu. I. Vorontsov, Sov. Phys. Uspekhi **17** (1975) 644; V. B. Braginsky, Yu. I. Vorontsov and F. Ya. Kahili, Sov. Phys. JETP **46** (1977) 705.

[4] V. B. Braginsky and F. Ya. Khalili, *Quantum Measurement*, ed. K. S. Thorne (Cambridge University Press, Cambridge, 1992).

[5] See, e.g., Appendix B of V. B. Braginsky, M. L. Gorodetsky, F. Ya. Khalili and K. S. Thorne, Phys. Rev. **D61** (2000) 044002 [gr-qc/9906108]; P. Purdue, in preparation.

[6] C. M. Caves, Phys. Rev. **D 23** (1981) 1693; W. G. Unruh, in *Quantum Optics, Experimental Gravitation, and Measurement Theory*, eds. P. Meystre and M. O. Scully (Plenum, 1982), p. 647; M. T. Jaekel and S. Reynaud, Europhys. Lett. **13** (1990) 301.

[7] H. J. Kimble, Yu. Levin, A. B. Matsko, K. S. Thorne and S. P. Vyatchanin, *Conversion of conventional gravitational-wave interferometers into QND interferometers by modifying input and/or output optics*, submitted to Phys. Rev. **D** [gr-qc/0008026]. It is referred to as KLMTV in this chapter.

[8] S. P. Vyatchanin and A. B. Matsko, JETP **77** (1993) 218; S. P. Vyatchanin and E. A. Zubova, Phys. Lett. **A 203** (1995) 269; S. P. Vyatchanin and A. B. Matsko, JETP **82** (1996) 1007; ibid. JETP **83** (1996) 690; S. P. Vyatchanin, Phys. Lett. **A 239** (1998) 201.

[9] V. B. Braginsky, M. L. Gorodetsky and F.Ya. Khalili, Phys. Lett. **A 232** (1997) 340; V. B. Braginsky and F. Ya. Khalili, Phys. Lett. **A 257** (1999) 241.

[10] H. P. Yuen, Phys. Rev. Lett. **51** (1983) 719; C. M. Caves, Phys. Rev. Lett. **54** (1985) 2465; M. Ozawa, Phys. Rev. Lett. **60** (1988) 385; Phys. Rev. **A 41** (1990) 1735; J. Maddox, Nature **331** (1988) 559.

[11] A. Buonanno and Y. Chen, *Optical noise correlations and beating the standard quantum limit in advanced gravitational-wave detectors*, GRP/00/549, accepted for publication in Class. Quantum Grav., [gr-qc/0010011].

[12] B. J. Meers, Phys. Rev. **D 38** (1988) 2317; J. Y. Vinet, B. Meers, C. N. Man and A. Brillet, Phys. Rev. **D 38** (1988) 433.

[13] J. Mizuno, *Comparison of optical configurations for laser interferometric gravitatioanl-wave detectors*, PhD thesis, Max-Planck-Institut für Quantenoptik, Garching, Germany (1995); J. Mizuno, K. A. Strain, P. G. Nelson, J. M. Chen, R. Schilling, A. Rüdiger, W. Winkler and K. Danzmann, Phys. Lett. **A 175** (1993) 273.

[14] V. B. Braginsky, M. L. Gorodetsky and S. P. Vyatchanin, Phys. Lett. **A 264** (1999) 1; Y. T. Liu and K. S. Thorne, Phys. Rev. **D 62** (2000) 122002; V. B. Braginsky, E. D'Ambrosio, R. O'Shaughnessy, S.E. Strigen, K. S. Thorne and S.P. Vyatchanin, in preparation.

[15] V. B. Braginsky, M.L. Gorodetsky, F.Ya. Khalili, A.B. Matsko, K. S. Thorne and S. P. Vyatchanin, *Noise in gravitational-wave detectors is not influenced by test-mass quantization*, in preparation. It is referred to as BGKMTV in this chapter.

[16] See, e.g., A. Abramovici et al. in Ref. [1]; K. S. Thorne, in *Proceedings of the Snowmass 95 Summer Study on Particle and Nuclear Astrophysics and Cosmology*, eds. E. W. Kolb and R. Peccei (World Scientific, Singapore, 1995), p. 398 [gr-qc/9506085]; K. S. Thorne, *The scientific case for advanced LIGO interferometers*, LIGO Document Number P-000024-00-D.

[17] A. Dorsel, J. D. McCullen, P. Meystre, E. Vignes and H. Walther, Phys. Rev. Lett. **51** (1983) 1550; N. Deruelle and P. Tourrenc, in *Gravitation, Geometry and Relativistic Physics* (Springer, Berlin, 1984); P. Meystre, E. M. Wright, J. D. McCullen and E. Vignes, J. Opt. Soc. Am. **2** (1985) 1830; J. M. Aguirregabria and L. Bel, Phys. Rev. **D 36** (1987) 3768; L. Bel, J. L. Boulanger and N. Deruelle, Phys. Rev. **A 7** (1988) 37.

[18] G. Heinzel, *Advanced optical techniques for laser interferometric gravitational-wave detectors*, PhD thesis, Max-Planck-Institut für Quantenoptik, Garching, Germany (1999); M. Rachmanov, *Dynamics of laser interferometric gravitational wave detectors*, PhD thesis, California Institute of Technology, Pasadena, CA, (2000).

[19] A. Pai, S. V. Dhurandhar, P. Hello and J-Y. Vinet, Euro. Phys. J. **D 8** (2000) 333.

[20] E. Gustafson, D. Shoemaker, K. Strain and R. Weiss, *LSC White paper on Detector Research and Development*, LIGO Document Number T990080-00-D (Caltech/MIT, 11 September 1999). See also www.ligo.caltech.edu/ligo2/.

[21] C. M. Caves and B. L. Schumaker, Phys. Rev. **A 31** (1985) 3068.

[22] B. L. Schumaker and C. M. Caves, Phys. Rev. **A 31** (1985) 3093.

[23] A. Buonanno, Y. Chen and N. Mavalvala, research in progress.

[24] See, e.g., R. C. Dorf, *Modern Control Systems*, (Addison-Wesley, Reading Massachusetts, 1990), Chap. 7 and 8.

[25] See, e.g., S. Ichimaru, *Basic Principles of Plasma Physics*, (Benjamin, Reading Massachusetts 1973).

[26] See, e.g., J. Mathews and R. L. Walker, *Mathematical Methods of Physics*, (Addison-Wesley, Reading Massachusetts, 1970).

[27] K. Strain, private communication.

[28] R. Drever, in *Gravitational Radiation*, ed. N. Deruelle and T. Piran (North-Holland, Amsterdam, 1983), pp. 321-338.

[29] A. Freise, G. Heinzel, K. A. Strain, J. Mizuno, K. D. Skeldon, H. Lück, B. Wilke, R. Schilling, A. Rüdiger, W. Wingler and K. Danzmann, Phys. Lett. **A277** (2000) 135 [gr-qc/0006026].

[30] J. Mason, *Signa l Extraction and Optical Design for an Advanced Gravitational Wave Interferometer*, PhD thesis, California Institute of Technology, Pasadena, CA (2001). [LIGO document P010010-00-R, www.ligo.caltech.edu/docs/P/P010010-00.pdf]

Chapter 3

Signal recycled laser-interferometer gravitational-wave detectors as optical springs

Using the force-susceptibility formalism of linear quantum measurements, we study the dynamics of signal recycled interferometers, such as LIGO-II. We show that, although the antisymmetric mode of motion of the four arm-cavity mirrors is originally described by a free mass, when the signal-recycling mirror is added to the interferometer, the radiation-pressure force not only disturbs the motion of that "free mass" randomly due to quantum fluctuations, but also and more fundamentally, makes it respond to forces as though it were connected to a spring with a specific optical-mechanical rigidity. This oscillatory response gives rise to a much richer dynamics than previously known for SR interferometers, which enhances the possibilities for reshaping the noise curves and, if thermal noise can be pushed low enough, enables the standard quantum limit to be beaten. We also show the possibility of using servo systems to suppress the instability associated with the optical-mechanical interaction without compromising the sensitivity of the interferometer.

Originally published as A. Buonanno and Y. Chen, Phys. Rev. D **65** 042001 (2002).

3.1 Introduction

Next year a network of broadband ground-based laser interferometers, aimed to detect gravitational waves (GWs) in the frequency band $10 - 10^4$ Hz, will begin operations. This network is composed of the Laser Interferometer Gravitational-wave Observatory (LIGO), VIRGO (whose operation will begin in 2004), GEO 600, and TAMA 300 [1]. Given the anticipated noise spectra and the current estimates of gravitational waves from various astrophysical sources [2], it is plausible but not probable that gravitational waves will be detected with the first generation of interferometers. The original conception of LIGO included an upgrade of LIGO to sensitivities at which it is probable to detect

a rich variety of gravitational waves [2]. The LIGO Scientific Collaboration (LSC) [3] is currently planning this upgrade to begin in 2006. This second stage includes: (i) improvement of the seismic isolation system to push the seismic wall downward in frequency to 10 Hz, (ii) improvement of the suspension system to lower the noise in the band between ~ 10 Hz and ~ 200 Hz, (iii) increase (decrease) of light power (shot noise) circulating in the arm cavities ($\sim$1 MWatt), (iv) improvement in the optics so that they can handle the increased laser power, and (v) introduction of an extra mirror, called a signal-recycling (SR) mirror, at the dark-port output. This upgraded configuration of LIGO ("advanced interferometer") is sometimes called LIGO-II and its design is sketched in Fig. 3.1.

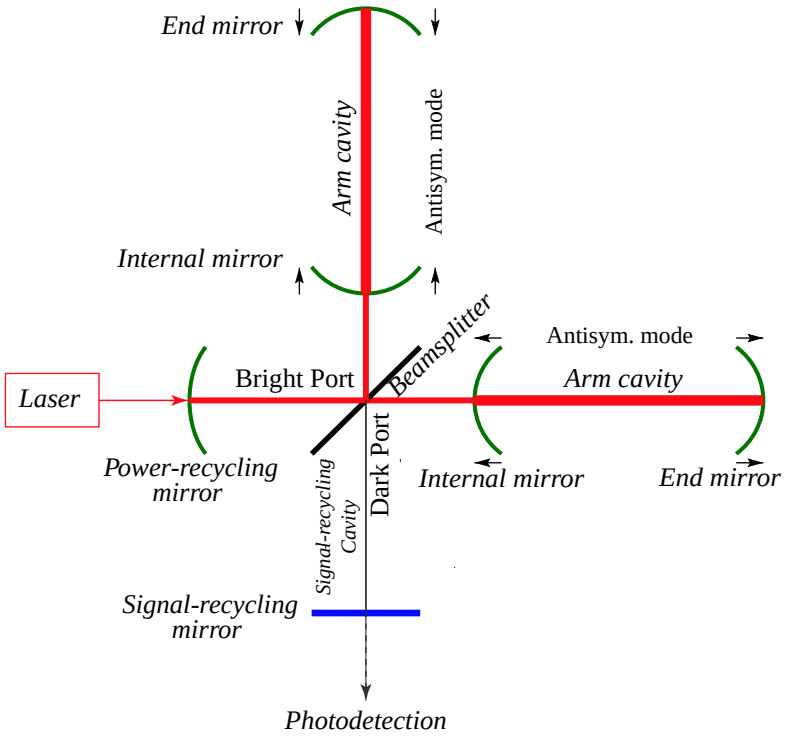

Figure 3.1: Schematic diagram of a signal recycled interferometer such as LIGO-II. The antisymmetric mode of motion of the four arm-cavity mirrors (marked by arrows) is monitored by laser interferometry. A signal-recycling mirror is used to feed the signal light back into the arm cavities, while a power-recycling mirror is introduced to feed back into the arm cavities the unused laser light coming out the bright port.

The SR mirror (see Fig. 3.1) sends the signal coming out the dark port back into the arm cavities; in this sense it *recycles* the *signal*. [1] The optical system composed of the SR cavity and the

[1] The configuration of LIGO-II will also include a power-recycling (PR) mirror between the laser and the beamsplitter (see Fig. 3.1). This mirror *recycles* back into the arm cavities the unused laser light coming out the bright port and increases the light power at the beamsplitter. Besides this effect, the presence of the PR mirror does not affect the derivation of the quantum noise at the dark-port output. Therefore, although in our analysis we assume high light power, we do not need to take into account the PR mirror in deducing the interferometer's input-output relation.

arm cavities forms a composite resonant cavity, whose eigenfrequencies and quality factors can be controlled by the position and reflectivity of the SR mirror. Near its eigenfrequencies (resonances), the device can gain sensitivity. In fact, the initial motivation for introducing the SR cavity was based on the idea of using this feature to reshape the noise curves, enabling the interferometer to work either in broadband or in narrowband configurations, and improving in this way the observation of specific GW astrophysical sources [2]. Historically, the first idea for a narrowband configuration, so-called *synchronous* or *resonant recycling*, was due to Drever [4] and was subsequently analyzed by Vinet et al. [5]. It used a different optical topology from Fig. 3.1. The original idea for the optical topology of Fig. 3.1 was due to Meers [6], who proposed its use for *dual recycling* – a scheme which by recycling the signal light *increases* the storage time of the signal inside the interferometer and lowers the shot noise. Later, Mizuno et al. [7, 8, 9] proposed another scheme called Resonant Sideband Extraction (RSE), which also uses the optical topology of Fig. 3.1 but adjusts the SR mirror so that the storage time of the signal inside the interferometer *decreases* while the observation bandwidth *increases*. In general, by choosing appropriate detunings [2] of the SR cavity, the optical configuration can be in either of the two regimes, or in between. These schemes have been experimentally tested by Freise et al. [10] with the 30 m laser interferometer in Garching (Germany), and by Mason [11] on a table-top experiment at Caltech (USA).

All the above-mentioned theoretical analyses and experiments of SR interferometers [4, 5, 6, 7, 8, 9, 10, 11] refer to configurations with low laser power, for which the radiation pressure on the arm-cavity mirrors is negligible and the noise spectra are dominated by shot noise. However, when the laser power is increased, the shot noise decreases while the effect of radiation-pressure fluctuation increases. LIGO-II has been planned to work at a laser power for which the two effects are comparable in the observation band 10–200 Hz [3]. Therefore, to correctly describe the quantum optical noise in LIGO-II, the results so far obtained in the literature [4, 5, 6, 7, 8, 9, 10, 11] must be complemented by a thorough investigation of the influence of the radiation-pressure force on the mirror motion.

Until recently the LIGO-II noise curves were computed using a semiclassical approach [3], which, although capable of estimating the shot noise, is unable to take into account correctly the effects of radiation-pressure fluctuations. Very recently, building on earlier work of Kimble, Levin, Matsko, Thorne and Vyatchanin (KLMTV for short) [12], which describes the initial optical configuration of LIGO/TAMA/VIRGO interferometers (so-called conventional interferometers) within a full quantum-mechanical approach, we investigated the SR optical configuration (Fig. 3.1) (see Chapter 2). Our analysis revealed important new properties of SR interferometers, including (i) the presence of correlations between shot noise and radiation-pressure noise, (ii) the possibility of beating the

[2] By detuning of the SR cavity we mean the phase gained by the carrier frequency in the SR cavity, see Sec. 3.3.2 for details.

standard quantum limit (SQL) by a modest amount, roughly a factor of two over a bandwidth of $\Delta f \sim f$ [3] and (iii) the presence of instabilities in the optical-mechanical system formed by the optical fields and the arm-cavity mirrors. We also noticed in Chapter 2 that the way the SQL is beaten in SR interferometer is quite different from standard quantum-nondemolition (QND) techniques [15] based on building up correlations between shot noise and radiation-pressure noise by (i) injecting squeezed vacuum into an interferometer's dark port [16] and/or (ii) introducing two kilometer-long filter cavities into the interferometer's output port [17, 12] and applying homodyne detection on the filtered light. Indeed, our analyses suggest that the improvement in the noise curves comes largely from the resonant features introduced by the SR cavity: whereas the amplitude of the classical output signal is amplified near the resonances, the output quantum fluctuation is not strongly affected by them. This way of using resonances to beat the SQL was first proposed by Braginsky, Khalili and colleagues in their scheme of "optical bar" GW detectors [18], where similarly the test mass is effectively an oscillator whose restoring force is provided by in-cavity optical fields. For an "optical bar" the free-mass SQL is irrelevant and we can beat the free-mass SQL using classical techniques of position monitoring [18].

In Chapter 2, our analysis was mainly focused on determining the input–output relations for the electromagnetic quadrature fields in a SR interferometer, and evaluating the corresponding noise spectral density. The resonant features of the whole device were discussed only briefly. In this chapter we give a detailed description of the dynamics of the system formed by the optical fields and the mirrors, we discuss the origin of the resonances and their possible instabilities, and we analyze the suppression of the instabilities by an appropriate control system. In our analysis we have found the Braginsky-Khalili formalism for linear quantum measurements [19] very powerful and intuitive, and we use it throughout this chapter.

This Chapter is divided into two parts: the formalism and its application. In Sec. 3.2 we introduce the force-susceptibility formalism and discuss some general features of linear quantum-measurement devices. In particular, after briefly commenting in Sec. 3.2.1 on general quantum-measurement systems, we derive in Sec. 3.2.2 the equations of motion for *linear* quantum-measurement devices; in Sec. 3.2.3 we write down a set of conditions on the susceptibilities of linear quantum-measurement systems; in Sec. 3.2.4 we use these conditions to construct an effective description of a quantum-measurement process which allows us to identify in a straightforward way the shot noise and the radiation-pressure noise. In the subsequent sections we apply the formalism developed in Sec. 3.2 to SR interferometers. In Sec. 3.3 we show that SR interferometers can be described by the force-susceptibility formalism and we derive their equations of motion, pointing out the existence of a "ponderomotive rigidity." In Sec. 3.4 we discuss in detail the oscillatory behavior of the system

[3] This performance refers only to the quantum optical noise. The total noise, which includes also all the other sources of noise, such as seismic and thermal noise, can beat the SQL only if thermoelastic noise [13] can also be pushed below the SQL.

induced by the ponderomotive rigidity, its resonances and instabilities. In Sec. 3.5 we describe the suppression of the instability by a feedback control system which does not compromise the sensitivity. Finally, Sec. 3.6 summarizes our main conclusions. As a foundation for our linear analysis of SR interferometers we summarize in the Appendix (Sec. 3.7) some general properties of linear quantum-mechanical systems.

3.2 Quantum-measurement systems

3.2.1 General conditions defining a measurement system

Following Braginsky and Khalili [19], we define a *measurement process* as a transformation from some original classical observable which is *unknown*, e.g., the gravitational-wave amplitude, into another classical observable which is *known*, e.g., the data stored in the computer. Generally, the system which implements this process is composed of a probe $\mathcal{P}$, which is directly coupled to the classical observable to be measured (for interferometers this is the antisymmetric mode of motion of the four arm-cavity mirrors, see Sec. 3.3.1), and the detector $\mathcal{D}$, which couples to the probe and produces the output observable (for interferometers this is the optical system and the photodetector). A measurement system is drawn schematically in Fig. 3.2. Because the probe and the detector are quantum mechanical systems, the overall device is called a *quantum-measurement device*. The output observable $\hat{Z} = \mathcal{S} + \hat{\mathcal{Q}}$ contains a classical part $\mathcal{S}$, which depends on the classical observable G to be measured, and some quantum noise $\hat{\mathcal{Q}}$ due to the probe, the detector and their mutual interaction.

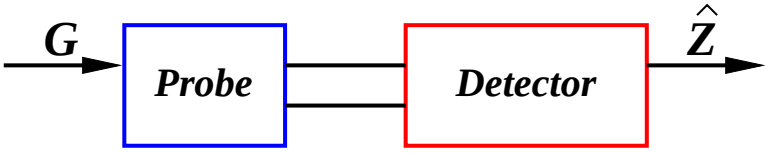

Figure 3.2: Schematic diagram of a measurement device. G is the classical observable acting on the probe that we want to measure, and $\hat{Z}$ is the detector's observable which describes the output of the measurement system.

According to the statistical interpretation of quantum mechanics [21], the output of a quantum-measurement process at different times should be *simultaneously measurable*. One sufficient condition for *simultaneous measurability* is that the Heisenberg operators of the output observable, $\hat{Z}(t)$, satisfy [4]

$$\left[\hat{Z}(t_1), \hat{Z}(t_2)\right] = 0 \quad \forall t_1, t_2\,. \tag{3.1}$$

[4] We refer to this condition as sufficient since for observables that do not satisfy this condition, there may still exist a subspace of the Hilbert space of the system in which these observables are simultaneously measurable.

Henceforth, we shall regard Eq. (3.1) as the *condition of simultaneous measurability*. Although the condition (3.1) was originally introduced by Braginsky et al. [15, 19] as the definition of quantum-nondemolition (QND) observables (see also Refs. [22, 23, 24]), we introduce and use it for different purposes, as will become clear in the following. If the condition (3.1) is satisfied, then any sample of data $\left\{\hat{Z}(t_1), \hat{Z}(t_2), \ldots, \hat{Z}(t_n)\right\}$ can be stored directly as bits of classical data in a classical storage medium, and any noise from subsequent processing of the signal can be made arbitrarily small, i.e., *all quantum noises* are included in the quantum fluctuations of $\hat{Z}(t)$. We want to discuss the *simultaneous measurability* condition (3.1) more deeply by pointing out the following relation, which was also in part discussed by Unruh [22] and Caves, Thorne, Drever, Sandberg and Zimmermann in Sec. IV of Ref. [23], and reviewed subsequently in Ref. [24], although from a different point of view.

Simultaneous-Measurability – Zero-Response Relation: *For a Quantum Measurement Device (QMD), the simultaneous measurability condition for the output $\hat{Z}(t)$, i.e., $[\hat{Z}(t_1), \hat{Z}(t_2)] = 0 \quad \forall t_1, t_2$, is equivalent to requiring that if the device is coupled to an external system via an interaction Hamiltonian of the form $V(\hat{Z}, \hat{\mathcal{E}})$ where V is an arbitrary function and $\hat{\mathcal{E}}$ belongs to the external system, then the back action on the QMD does <u>not</u> alter the evolution of the output observable $\hat{Z}$.*

Proof of necessity. [5] Let us suppose that our QMD with output $\hat{Z}$ evolves under a Hamiltonian $\hat{H}_{\rm QMD}$, and that $[\hat{Z}(t), \hat{Z}(t')] = 0$ for all t, t'. Now let us couple it to an arbitrary external system with Hamiltonian $\hat{H}_{\rm EXT}$ via a generic interaction term $V(\hat{Z}, \hat{\mathcal{E}})$ as specified above, where $\hat{\mathcal{E}}$ is an observable of the external system. The total Hamiltonian is

$$\hat{H} = \left(\hat{H}_{\rm QMD} + \hat{H}_{\rm EXT}\right) + V(\hat{Z}, \hat{\mathcal{E}})\,. \tag{3.2}$$

If we treat the two terms in the bracket as the zeroth-order Hamiltonian and the interaction Hamiltonian $V(\hat{Z}, \hat{\mathcal{E}})$ as a perturbation, by applying the results derived in the Appendix (Sec. 3.7) [see Eq. (3.130)] we can write the Heisenberg operator of the output variable $\hat{Z}$ as,

$$\begin{aligned}\hat{Z}_{\rm pert}(t) = \hat{Z}(t) + \frac{i}{\hbar}\int_{-\infty}^{t} dt_1 \left[V(\hat{Z}(t_1), \hat{\mathcal{E}}(t_1)), \hat{Z}(t)\right] + \\ \left(\frac{i}{\hbar}\right)^2 \int_{-\infty}^{t} dt_1 \int_{-\infty}^{t_1} dt_2 \left[V(\hat{Z}(t_2), \hat{\mathcal{E}}(t_2)), \left[V(\hat{Z}(t_1), \hat{\mathcal{E}}(t_1)), \hat{Z}(t)\right]\right] + \cdots\,,\end{aligned} \tag{3.3}$$

with higher-order terms of the form [see Eq. (3.130)]:

$$\left[V(\hat{Z}(t_n), \hat{\mathcal{E}}(t_n)), \left[\cdots, \left[V(\hat{Z}(t_2), \hat{\mathcal{E}}(t_2)), \left[V(\hat{Z}(t_1), \hat{\mathcal{E}}(t_1)), \hat{Z}(t)\right]\right]\cdots\right]\right]\,. \tag{3.4}$$

Here $\hat{Z}(t)$ and $\hat{\mathcal{E}}(t)$ evolve under the Hamiltonians $\hat{H}_{\rm QMD}$ and $\hat{H}_{\rm EXT}$, respectively. Because they

[5] A similar calculation was carried out by Caves et al. in Sec. IV of Ref. [23].

belong to two different Hilbert spaces we have $[\hat{Z}(t), \hat{\mathcal{E}}(t')] = 0$ for all t, t'. By assumption, we also have $[\hat{Z}(t_1), \hat{Z}(t_2)] = 0 \quad \forall t_1, t_2$. Using these two facts, we obtain $[V(\hat{Z}(t_1), \hat{\mathcal{E}}(t_1)), \hat{Z}(t_2)] = 0 \quad \forall t_1, t_2$, and then using Eq. (3.3) we derive $\hat{Z}_{\rm pert}(t) = \hat{Z}(t)$. This means that the evolution of $\hat{Z}$ is not affected by the kind of external coupling we introduced.

Proof of sufficiency. Let us suppose the evolution of $\hat{Z}$ is not affected by <u>any</u> external system of the form specified above. Then, in particular, it must be true for the simple interaction Hamiltonian $V(\hat{Z}, \hat{\mathcal{E}}) = -\alpha \hat{Z}\, \mathcal{E}$, where α is some coupling constant which can vary continuously, e.g., in the interval $(0, 1]$, and we choose a classical external coupling $\mathcal{E}$. In this particular case Eq. (3.3) becomes

$$\hat{Z}_{\rm pert}(t) = \hat{Z}(t) - \alpha \, \frac{i}{\hbar} \int_{-\infty}^{t} dt_1 \left[\hat{Z}(t_1), \hat{Z}(t)\right] \, \mathcal{E}(t_1) + O(\alpha^2) \,, \tag{3.5}$$

with higher-order terms of the form: $\alpha^n \, [\hat{Z}(t_n), [\cdots, [\hat{Z}(t_2), [\hat{Z}(t_1), \hat{Z}(t)]] \cdots]]$. By assumption the LHS of Eq. (3.5) does not change when we vary α. The RHS of Eq. (3.5) is a power series in α, and using the uniqueness of the Taylor expansion, we deduce that all the terms beyond the zeroth order should vanish separately. In particular, the first-order term should vanish and we conclude that $[\hat{Z}(t), \hat{Z}(t')] = 0$ for all t, t'. □

Let us comment on two interesting aspects of the Simultaneous-Measurability – Zero-Response Relation given above.

- This relation links the abstract quantum mechanical idea of *simultaneous measurability* to the classical dynamics of the measurement device, yielding a simple criterion for the quantum-classical transition: the observable which corresponds to the classical output variable should have no response to external perturbations directly coupled to it. [6] We shall use this criterion in our analysis of linear systems in Sec. 3.2.3.

- This relation is also interesting conceptually. In practice, the result of every measurement is read out by coupling the measurement device to another system, and the boundary between the "measurement" (still part of the QMD) and the "data analysis" (external to the QMD) occurs at a "stage" at which no possible direct coupling to the output observable could change the evolution of the output observable itself. Otherwise at that stage the "external coupling" should still be considered as part of the measurement device.

Before ending this section, let us compare the point of view followed in this section to the one pursued in previous QND analyses [22, 23, 24], especially Sec. IV of Ref. [23]. The authors of Refs. [23, 24] followed two steps in their discussion. First, they searched for a class of observables $\hat{A}(t)$ of a quantum-mechanical system that can be monitored without adding fundamental noise,

[6] By directly coupling to $\hat{Z}$ we mean the interaction Hamiltonian is of the form $V(\hat{Z}, \hat{\mathcal{E}})$, since only this form guarantees that $\hat{Z}$ is the only observable of the device that influences the interaction.

deducing a condition for $\hat{A}(t)$ that coincides with Eq. (3.1). They called such observables QND observables. Secondly, they found appropriate interaction Hamiltonians describing the coupling between $\hat{A}(t)$ and a measuring apparatus that do not disturb the evolution of $\hat{A}(t)$ during the measurement process. However, in Refs. [23, 24] there is no clear distinction between what we call the detector and the external measurement system; these two systems are referred to together as the measuring apparatus. Thus, the observable $\hat{A}(t)$ does not necessarily coincide with the output $\hat{Z}(t)$ of our probe-detector system, and for this reason we prefer not to call it a QND observable in the sense of Refs. [22, 23, 24].

As a final remark, we note that whereas in Refs. [23, 24] the measuring apparatus and the interaction Hamiltonian are indispensable parts of a measurement process, in this chapter, by distinguishing the detector from the external system, we use the latter only as part of a *gedanken* experiment, by which we clarify the relation between simultaneous measurability and the response to external couplings, which will lead to useful properties of linear quantum-measurement devices in Sec. 3.2.3.

3.2.2 Equations of motion of a linear quantum-measurement system: the force-susceptibility formalism

Starting in this section we shall focus on linear measurement systems. We shall see in Sec. 3.3 that GW interferometers belong to this class of devices. Our analysis has been inspired by the formalism of linear quantum-measurement theory introduced by Braginsky and Khalili (Chaps. V, VI and VII of Ref. [19]) and is based on the force-susceptibility description of linearly coupled systems under linearly applied classical forces (see, e.g., Sec. 6.4 of Ref. [19]).

In a *linear measurement process*, the device acts linearly and is linearly coupled to the classical observable to be measured (see the Appendix for a precise definition of linear systems). We suppose that the device can be artificially divided into two linearly coupled, but otherwise independent subsystems: the probe, which is subject to the external classical force we want to measure, and the detector, which yields a classical output. More specifically, in our Hamiltonian system the probe is coupled to the external classical force G by $-\hat{y}\,G$, where $\hat{y}$ is some linear observable of the probe, while the probe and the detector are coupled by a term $-\hat{x}\,\hat{F}$, where $\hat{x}$ is a generalized (linear) displacement of the probe, and $\hat{F}$ is a linear observable of the detector which describes its back-action force on the probe. In general, the observable $\hat{x}$ to which the external force is coupled and the observable $\hat{y}$ that the detector directly measures might not be the same. However, in our idealized model of GW interferometers (Sec. 3.3 below), $\hat{x}$ and $\hat{y}$ are actually the same observable, namely, the generalized coordinate of the antisymmetric mode of motion of the four arm-cavity mirrors (see Fig. 3.1 and Sec. 3.3.1), and $\hat{F}$ is the radiation-pressure force acting on this mode. Henceforth, we

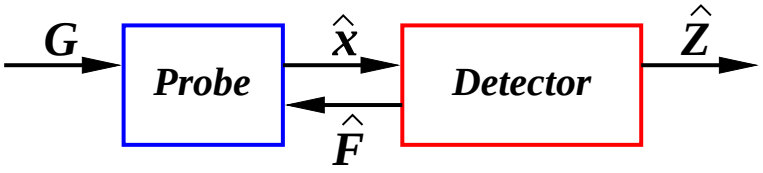

Figure 3.3: Schematic diagram of a linear measurement system. G is the external classical force acting on the probe that we want to measure, $\hat{x}$ is the linear observable of the probe, $\hat{F}$ is the linear observable of the detector which describes the back-action force on the probe, and $\hat{Z}$ is the linear observable of the detector which describes the output of the overall measurement system.

shall impose $\hat{y} \equiv \hat{x}$. Finally, we denote by $\hat{Z}$ the linear observable of the detector which describes the output of the entire device. A sketchy representation of the measurement device is drawn in Fig. 3.3. The linear observables $\hat{x}$ describing the probe $\mathcal{P}$ and $\hat{Z}$, $\hat{F}$ describing the detector $\mathcal{D}$ belong to two different Hilbert spaces $\mathcal{H}_{\mathcal{P}}$ and $\mathcal{H}_{\mathcal{D}}$, respectively, and the Hilbert space of the combined system is $\mathcal{H}_{\mathcal{P}} \otimes \mathcal{H}_{\mathcal{D}}$. The Hamiltonian is given by

$$\hat{H} = \left[\left(\hat{H}_{\mathcal{P}} - \hat{x}\, G\right) + \hat{H}_{\mathcal{D}}\right] - \hat{x}\, \hat{F}\,. \tag{3.6}$$

We shall now derive the equations of motion of the system composed of the linear observables $\hat{x}$, $\hat{Z}$ and $\hat{F}$. As a first step in our calculation, we regard the Hamiltonians $\hat{H}_{\mathcal{P}} - \hat{x}\, G$ and $\hat{H}_{\mathcal{D}}$ as zeroth order Hamiltonians for the subsystems $\mathcal{P}$ and $\mathcal{D}$, respectively, and we treat $-\hat{x}\, \hat{F}$ as a linear coupling between $\mathcal{P}$ and $\mathcal{D}$. Working in the Heisenberg picture, we obtain the following equations [see Theorem 4 of the Appendix and Eqs. (3.133), (3.134)]:

$$\hat{Z}^{(1)}(t) = \hat{Z}^{(0)}(t) + \frac{i}{\hbar}\int_{-\infty}^{t} dt'\, C_{Z^{(0)}F^{(0)}}(t,t')\, \hat{x}^{(1)}(t')\,, \tag{3.7}$$

$$\hat{F}^{(1)}(t) = \hat{F}^{(0)}(t) + \frac{i}{\hbar}\int_{-\infty}^{t} dt'\, C_{F^{(0)}F^{(0)}}(t,t')\, \hat{x}^{(1)}(t')\,, \tag{3.8}$$

$$\hat{x}^{(1)}(t) = \hat{x}^{(G)}(t) + \frac{i}{\hbar}\int_{-\infty}^{t} dt'\, C_{x^{(G)}x^{(G)}}(t,t')\, \hat{F}^{(1)}(t')\,. \tag{3.9}$$

Here $C_{AB}(t,t')$ is a complex number (C-number), called the (time-domain) susceptibility, and is defined by Eq. (3.132) of the Appendix, i.e.,

$$C_{AB}(t,t') \equiv \left[\hat{A}(t),\, \hat{B}(t')\right]\,. \tag{3.10}$$

[Henceforth, we shall often use the expressions *different-time commutator* and *time-domain susceptibility* interchangeably.] The superscript (1) in Eqs. (3.7)–(3.9) denotes time evolution under the total Hamiltonian $\hat{H}$ [Eq. (3.6)], the superscript (0) on $\hat{F}(t)$ and $\hat{Z}(t)$ denotes time evolution under the free Hamiltonian of the detector $\hat{H}_{\mathcal{D}}$, while the superscript (G) on $\hat{x}(t)$ refers to the time

evolution under the Hamiltonian $\hat{H}_{\mathcal{P}} - \hat{x}\, G$, which describes the probe under the sole influence of $G(t)$.

As a second step, we want to relate $\hat{x}^{(G)}(t)$ to $\hat{x}^{(0)}(t)$, which evolves under the free probe Hamiltonian $\hat{H}_{\mathcal{P}}$. Using Theorem 3 in the Appendix and Eqs. (3.131), (3.132), we deduce

$$\hat{x}^{(G)}(t) = \hat{x}^{(0)}(t) + \frac{i}{\hbar}\int_{-\infty}^{t} dt'\, C_{x^{(0)}x^{(0)}}(t,t')\, G(t')\,. \tag{3.11}$$

Noticing from Eq. (3.11) that $\hat{x}^{(G)}$ differs from $\hat{x}^{(0)}$ by a time dependent C-number, we get $C_{x^{(G)}x^{(G)}}(t,t') = C_{x^{(0)}x^{(0)}}(t,t')$. Using this fact and inserting Eq. (3.11) into Eq. (3.9), we can relate the Heisenberg operators evolving under the full Hamiltonian $\hat{H}$ to those evolving under the free Hamiltonians of the probe and the detector $\hat{H}_{\mathcal{P}}$ and $\hat{H}_{\mathcal{D}}$ separately:

$$\hat{Z}^{(1)}(t) = \hat{Z}^{(0)}(t) + \frac{i}{\hbar}\int_{-\infty}^{t} dt'\, C_{Z^{(0)}F^{(0)}}(t,t')\,\hat{x}^{(1)}(t')\,, \tag{3.12}$$

$$\hat{F}^{(1)}(t) = \hat{F}^{(0)}(t) + \frac{i}{\hbar}\int_{-\infty}^{t} dt'\, C_{F^{(0)}F^{(0)}}(t,t')\,\hat{x}^{(1)}(t')\,, \tag{3.13}$$

$$\hat{x}^{(1)}(t) = \hat{x}^{(0)}(t) + \frac{i}{\hbar}\int_{-\infty}^{t} dt'\, C_{x^{(0)}x^{(0)}}(t,t')\,[G(t') + \hat{F}^{(1)}(t')]\,. \tag{3.14}$$

A quantity of special interest for us is the displacement induced on a free probe (without any influence of the detector) by $G(t)$, namely, the second term on the RHS of Eq. (3.11). For a GW interferometer this displacement is $L\,h(t)$, where L is the arm-cavity length and $h(t)$ is the differential strain induced by the gravitational wave on the free arm-cavity mirrors (the difference in strain between the two arms). In our notation we denote this quantity by

$$L\,h(t) = \frac{i}{\hbar}\int_{-\infty}^{t} dt'\, C_{x^{(0)}x^{(0)}}(t,t')\, G(t')\,, \tag{3.15}$$

and for a GW interferometer $G(t) = (m/4)\,L\,\ddot{h}(t)$, where $m/4$ is the reduced mass of the antisymmetric mode of motion of the four arm-cavity mirrors (see Secs. 3.3.1 and III B). [Note that each mirror has mass m.]

Henceforth, we shall assume that both the probe and the detector have time independent Hamiltonians, i.e., both $\hat{H}_{\mathcal{D}}$ and $\hat{H}_{\mathcal{P}}$ are time independent. In this case, as shown in the Appendix, the susceptibilities that appear in Eqs. (3.12)–(3.14) depend only on $t-t'$. By transforming them into the Fourier domain, denoting by $h(\Omega)$ the Fourier transform of $h(t)$ and introducing the Fourier-domain susceptibility

$$R_{AB}(\Omega) \equiv \frac{i}{\hbar}\int_{0}^{+\infty} d\tau\, e^{i\Omega\tau}\, C_{AB}(0,-\tau)\,, \tag{3.16}$$

we derive

$$\hat{Z}^{(1)}(\Omega) = \hat{Z}^{(0)}(\Omega) + R_{ZF}(\Omega)\,\hat{x}^{(1)}(\Omega)\,, \tag{3.17}$$

$$\hat{F}^{(1)}(\Omega) = \hat{F}^{(0)}(\Omega) + R_{FF}(\Omega)\,\hat{x}^{(1)}(\Omega)\,, \tag{3.18}$$

$$\hat{x}^{(1)}(\Omega) = \hat{x}^{(0)}(\Omega) + L\,h(\Omega) + R_{xx}(\Omega)\,\hat{F}^{(1)}(\Omega)\,. \tag{3.19}$$

Here and below, to simplify the notation we denote $R_{ZF} \equiv R_{Z^{(0)}F^{(0)}}$, $R_{FF} \equiv R_{F^{(0)}F^{(0)}}$, $R_{xx} \equiv R_{x^{(0)}x^{(0)}}$. By solving Eqs. (3.17)–(3.19) for the full-evolution operators in terms of the free-evolution ones, we finally get:

$$\hat{x}^{(1)}(\Omega) = \frac{1}{1 - R_{xx}(\Omega)\,R_{FF}(\Omega)}\,\left[\hat{x}^{(0)}(\Omega) + L\,h(\Omega) + R_{xx}(\Omega)\,\hat{F}^{(0)}(\Omega)\right]\,, \tag{3.20}$$

$$\hat{F}^{(1)}(\Omega) = \frac{1}{1 - R_{xx}(\Omega)\,R_{FF}(\Omega)}\,\left[\hat{F}^{(0)}(\Omega) + R_{FF}(\Omega)\,\left(\hat{x}^{(0)}(\Omega) + L\,h(\Omega)\right)\right]\,, \tag{3.21}$$

$$\hat{Z}^{(1)}(\Omega) = \hat{Z}^{(0)}(\Omega) + \frac{R_{ZF}(\Omega)}{1 - R_{xx}(\Omega)\,R_{FF}(\Omega)}\,\left[\hat{x}^{(0)}(\Omega) + L\,h(\Omega) + R_{xx}(\Omega)\,\hat{F}^{(0)}(\Omega)\right]\,. \tag{3.22}$$

Let us point out that if the kernel relating the full-evolution operators to the free-evolution ones, i.e., $1/(1 - R_{xx}\,R_{FF})$, contains poles both in the lower *and in the upper* complex plane [with our definition of Fourier transform given by Eq. (3.135)], then by applying the standard inverse Fourier transform to Eqs. (3.20)–(3.22), we get that $\hat{x}^{(1)}(t)$, $\hat{F}^{(1)}(t)$ and $\hat{Z}^{(1)}(t)$ depend on the gravitational-wave field and the free-evolution operators $\hat{x}^{(0)}(t)$, $\hat{F}^{(0)}(t)$ and $\hat{Z}^{(0)}(t)$ both in the past *and in the future*. However, these are not the correct solutions for the real motion. This situation is a very common one in physics and engineering (it occurs for example in the theory of linear electronic networks [20] and the theory of plasma waves [25]), and the cure for it is well known: in order to obtain the (correct) full-evolution operators $\hat{x}^{(1)}(t)$, $\hat{F}^{(1)}(t)$ and $\hat{Z}^{(1)}(t)$ that only depend on the past, *we have to alter the integration contour in the inverse-Fourier transform, going above all the poles in the complex plane*. [In the language of plasma physics we have to use the *Landau contours*.] This procedure, which can be justified rigorously using Laplace transforms [26], makes $\hat{x}^{(1)}(t)$, $\hat{F}^{(1)}(t)$ and $\hat{Z}^{(1)}(t)$ for many systems (including LIGO-II interferometers) infinitely sensitive to driving forces in the infinitely distant past. The reason is simple and well known in other contexts: such quantum-measurement systems possess instabilities, which can be deduced from the homogeneous solutions of Eqs. (3.20)–(3.22), whose eigenfrequencies are given by the equation $1 - R_{xx}(\Omega)\,R_{FF}(\Omega) = 0$. The zeros of the equation $1 - R_{xx}(\Omega)\,R_{FF}(\Omega) = 0$ are generically complex and for unstable systems they have positive imaginary parts, corresponding to homogeneous solutions that grow exponentially toward the future.

3.2.3 Conditions defining a linear measurement system in terms of susceptibilities

As we pointed out in Sec. 3.2.1, in order to be identified as the output of the measurement system, the observable $\hat{Z}$ should satisfy $[\hat{Z}(t_1), \hat{Z}(t_2)] = 0,\ \forall\, t_1,\, t_2$, i.e., the condition of *simultaneous measurability*. In that section, we have also proved the equivalence between this condition and the condition that any external coupling to the measurement system through $\hat{Z}$ should not change the evolution of $\hat{Z}$ itself. In the following we shall take advantage of this equivalence: By imagining that we couple the linear measurement system to some external system through $\hat{Z}$ and by looking at (possible) changes in $\hat{Z}$'s evolution, we shall obtain a set of conditions for the susceptibilities involving $\hat{Z}$.

Let us first restrict ourselves to the simplest possible external coupling, $\hat{V} = -\hat{Z}\,\mathcal{E}$, where $\mathcal{E}$ is a classical external force. The total Hamiltonian (3.6) becomes

$$\hat{H} = \Big[\Big(\hat{H}_{\mathcal{P}} - \hat{x}\,G\Big) + \hat{H}_{\mathcal{D}}\Big] - \hat{x}\,\hat{F} - \hat{Z}\,\mathcal{E} = \Big[\Big(\hat{H}_{\mathcal{P}} - \hat{x}\,G\Big) + \Big(\hat{H}_{\mathcal{D}} - \hat{Z}\,\mathcal{E}\Big)\Big] - \hat{x}\,\hat{F}\,. \tag{3.23}$$

To derive the equations of motion for the Hamiltonian (3.23) we apply the procedure used in Sec. 3.2.2 to deduce the equations of motion for the Hamiltonian (3.6). First, we consider $(\hat{H}_{\mathcal{P}} - \hat{x}\,G)$ and $(\hat{H}_{\mathcal{D}} - \hat{Z}\,\mathcal{E})$ as zeroth order Hamiltonians and relate the operators $\hat{Z}^{(1)}_{\rm pert}$, $\hat{F}^{(1)}_{\rm pert}$ and $\hat{x}^{(1)}_{\rm pert}$, which evolve under the full Hamiltonian (3.23), to the operator $\hat{x}^{(G)}$, which evolves under the Hamiltonian $(\hat{H}_{\mathcal{P}} - \hat{x}\,G)$, and the operators $\hat{Z}^{(\mathcal{E})}$ and $\hat{F}^{(\mathcal{E})}$, evolving under the Hamiltonian $(\hat{H}_{\mathcal{D}} - \hat{Z}\,\mathcal{E})$,

$$\hat{Z}^{(1)}_{\rm pert}(t) = \hat{Z}^{(\mathcal{E})}_{\rm pert}(t) + \frac{i}{\hbar}\int_{-\infty}^{t} dt'\, C_{Z^{(\mathcal{E})}F^{(\mathcal{E})}}(t,t')\,\hat{x}^{(1)}_{\rm pert}(t')\,, \tag{3.24}$$

$$\hat{F}^{(1)}_{\rm pert}(t) = \hat{F}^{(\mathcal{E})}_{\rm pert}(t) + \frac{i}{\hbar}\int_{-\infty}^{t} dt'\, C_{F^{(\mathcal{E})}F^{(\mathcal{E})}}(t,t')\,\hat{x}^{(1)}_{\rm pert}(t')\,, \tag{3.25}$$

$$\hat{x}^{(1)}_{\rm pert}(t) = \hat{x}^{(G)}(t) + \frac{i}{\hbar}\int_{-\infty}^{t} dt'\, C_{x^{(G)}x^{(G)}}(t,t')\,\hat{F}^{(1)}_{\rm pert}(t')\,. \tag{3.26}$$

Second, we relate the operators $\hat{x}^{(G)}$, $\hat{Z}^{(\mathcal{E})}$ and $\hat{F}^{(\mathcal{E})}$ to the operators $\hat{x}^{(0)}$, $\hat{Z}^{(0)}$ and $\hat{F}^{(0)}$ which evolve under $\hat{H}_{\mathcal{P}}$ and $\hat{H}_{\mathcal{D}}$:

$$\hat{Z}^{(\mathcal{E})}_{\rm pert}(t) = \hat{Z}^{(0)}(t) + \frac{i}{\hbar}\int_{-\infty}^{t} dt'\, C_{Z^{(0)}Z^{(0)}}(t,t')\,\mathcal{E}(t')\,, \tag{3.27}$$

$$\hat{F}^{(\mathcal{E})}_{\rm pert}(t) = \hat{F}^{(0)}(t) + \frac{i}{\hbar}\int_{-\infty}^{t} dt'\, C_{F^{(0)}Z^{(0)}}(t,t')\,\mathcal{E}(t')\,, \tag{3.28}$$

$$\hat{x}^{(G)}(t) = \hat{x}^{(0)}(t) + \frac{i}{\hbar}\int_{-\infty}^{t} dt'\, C_{x^{(0)}x^{(0)}}(t,t')\,G(t')\,. \tag{3.29}$$

Noticing that $\hat{Z}^{(\mathcal{E})}_{\rm pert}$, $\hat{F}^{(\mathcal{E})}_{\rm pert}$ and $\hat{x}^{(G)}$ differ from $\hat{Z}^{(0)}$, $\hat{F}^{(0)}$ and $\hat{x}^{(0)}$ only by time dependent C-numbers,

we obtain the following relations: $C_{Z^{(\varepsilon)}F^{(\varepsilon)}}(t,t') = C_{Z^{(0)}F^{(0)}}(t,t')$, $C_{F^{(\varepsilon)}F^{(\varepsilon)}}(t,t') = C_{F^{(0)}F^{(0)}}(t,t')$ and $C_{x^{(G)}x^{(G)}}(t,t') = C_{x^{(0)}x^{(0)}}(t,t')$. Then, by inserting Eqs. (3.27)–(3.29) into Eqs. (3.24)–(3.26), we deduce the equations of motion of $\hat{Z}$, $\hat{F}$ and $\hat{x}$ under the Hamiltonian (3.23):

$$\hat{Z}^{(1)}_{\rm pert}(t) = \hat{Z}^{(0)}(t) + \frac{i}{\hbar}\int_{-\infty}^{t} dt' \left[C_{Z^{(0)}Z^{(0)}}(t,t')\,\mathcal{E}(t') + C_{Z^{(0)}F^{(0)}}(t,t')\,\hat{x}^{(1)}_{\rm pert}(t')\right], \quad (3.30)$$

$$\hat{F}^{(1)}_{\rm pert}(t) = \hat{F}^{(0)}(t) + \frac{i}{\hbar}\int_{-\infty}^{t} dt' \left[C_{F^{(0)}Z^{(0)}}(t,t')\,\mathcal{E}(t') + C_{F^{(0)}F^{(0)}}(t,t')\,\hat{x}^{(1)}_{\rm pert}(t')\right], \quad (3.31)$$

$$\hat{x}^{(1)}_{\rm pert}(t) = \hat{x}^{(0)}(t) + \frac{i}{\hbar}\int_{-\infty}^{t} dt'\, C_{x^{(0)}x^{(0)}}(t,t') \left[G(t') + \hat{F}^{(1)}_{\rm pert}(t')\right]. \quad (3.32)$$

From Eqs. (3.30)–(3.32) we infer that there are two ways the external force $\mathcal{E}$ can influence the evolution of $\hat{Z}^{(1)}_{\rm pert}$: (i) $\mathcal{E}$ can affect $\hat{Z}^{(1)}_{\rm pert}$ directly, through the first term in the bracket of Eq. (3.30), unless $C_{Z^{(0)}Z^{(0)}}(t,t') = 0$ for all $t > t'$ (and thus for all pairs of t and t'); and (ii) $\mathcal{E}$ can influence the evolution of $\hat{Z}^{(1)}_{\rm pert}$ indirectly, affecting the evolution of $\hat{F}^{(1)}_{\rm pert}$ [first term in the bracket of Eq. (3.31)], and through it the evolution of $\hat{x}^{(1)}_{\rm pert}$ and $\hat{Z}^{(1)}_{\rm pert}$ [second terms in the brackets of Eqs. (3.32), (3.30)], unless $C_{F^{(0)}Z^{(0)}}(t,t') = 0$ for all $t > t'$.

Now we are ready to deduce the conditions that must be satisfied in order that the evolution of $\hat{Z}$ not be changed by the external coupling $\mathcal{E}$. In principle the two ways $\mathcal{E}$ affects the evolution of $\hat{Z}$ may cancel each other. However, noticing the fact that case (i) does not depend on the probe (only $C_{Z^{(0)}Z^{(0)}}$ matters), but case (ii) does ($C_{x^{(0)}x^{(0)}}$ also matters), we see that the cancellation will not always occur if we assume that, *whatever probe the detector is coupled to*, $\hat{Z}$ always corresponds to the output of the measurement process. Thus *both* conditions must be satisfied: $C_{Z^{(0)}Z^{(0)}} = 0$ and $C_{F^{(0)}Z^{(0)}} = 0$.

This argument for both conditions can be made more clear by assigning an "effective mass" μ to the probe and consider a continuous family of probes labeled by μ (for interferometers the family of probes are the family of mirrors with different masses). The susceptibility of the coordinate $\hat{x}$ depends on the effective mass as

$$C_{x^{(0)}x^{(0)}} \propto \frac{1}{\mu}, \quad (3.33)$$

which simply says that the probe's response to external forces decreases as its effective mass increases. Because $\hat{Z}^{(0)}$ and $\hat{F}^{(0)}$ are operators evolving under the free Hamiltonian of the detector, they do not depend on μ. Now consider two cases: First, the limiting case of $\mu \to \infty$. Then $C_{x^{(0)}x^{(0)}} \to 0$ and from Eq. (3.32) we get $\hat{x}^{(1)}_{\rm pert}(t) = \hat{x}^{(0)}(t)$. As a consequence, $\mathcal{E}$ affects the evolution of $\hat{Z}^{(1)}_{\rm pert}$ only through the first term in the bracket of Eq. (3.30) [see case (i) above], unless $C_{Z^{(0)}Z^{(0)}}(t,t') = 0$ for all pairs of t and t'. Second, consider the case of finite mass μ, and then conclude that $\mathcal{E}$ will affect the evolution of $\hat{Z}^{(1)}_{\rm pert}$ only through the second term in the bracket of Eq. (3.30) [see case (ii) above], unless $C_{F^{(0)}Z^{(0)}}(t,t') = 0$ for all $t > t'$.

In conclusion we have found that if, whatever the probe is, $\hat{Z}$ always corresponds to the output of the linear measurement device, then the following conditions must be satisfied

$$\text{LQM}: \begin{cases} C_{Z^{(0)}Z^{(0)}}(t,t') & \equiv [\hat{Z}^{(0)}(t), \hat{Z}^{(0)}(t')] & = 0 \qquad \forall\, t, t' \\ C_{F^{(0)}Z^{(0)}}(t,t') & \equiv [\hat{F}^{(0)}(t), \hat{Z}^{(0)}(t')] & = 0 \qquad \forall\, t > t' \,. \end{cases} \tag{3.34}$$

In the frequency domain these conditions read

$$R_{ZZ}(\Omega) = 0 = R_{FZ}(\Omega)\,. \tag{3.35}$$

It is possible to show that LQM [Eqs. (3.34)] are also sufficient conditions for the simultaneous measurability condition (3.1) be satisfied independently of the probe's nature; imagine coupling our linear measurement system to an external system with an arbitrary Hamiltonian $H_{\rm EXT}$ via a generic coupling $V(\hat{Z}, \hat{\mathcal{E}})$, $\hat{\mathcal{E}}$ being an external observable, and check whether the evolution of $\hat{Z}$ is affected by this coupling. The check can be achieved by writing the total Hamiltonian as

$$\hat{H} = \Big[\Big(\hat{H}_{\mathcal{P}} - \hat{x}\, G\Big) + \Big(\hat{H}_{\mathcal{D}} - \hat{Z}\,\hat{\mathcal{E}} + \hat{H}_{\rm EXT}\Big)\Big] - \hat{x}\,\hat{F}\,, \tag{3.36}$$

and re-doing all the steps followed earlier in this section. It is helpful to notice that the evolutions of $\hat{Z}$ and $\hat{F}$ under $\hat{H}_{\mathcal{D}} - \hat{Z}\hat{\mathcal{E}} + \hat{H}_{\rm EXT}$ are the same as those under $\hat{H}_{\mathcal{D}}$, once the condition LQM, or Eqs. (3.34), is satisfied. The result, after a long calculation is that conditions (3.34) are sufficient to guarantee that the evolution of $\hat{Z}$ is unaffected by the coupling. The technical details of the proof are left as an exercise for the reader.

3.2.4 Effective description of measurement systems

It is common to normalize the output observable $\hat{Z}$ to unit signal — e.g., in the case of GW interferometer, it is common to set to unity the coefficient in front of the (classical) observable $L\,h$ we want to measure so the normalized output $\hat{Z}$ has the form:

$$\hat{\mathcal{O}} = \hat{\mathcal{N}} + L\,h\,, \tag{3.37}$$

where $\hat{\mathcal{N}}$ is the so-called *signal-referred* quantum noise. The observable $\hat{\mathcal{O}}$ can be easily deduced in the frequency domain by renormalizing Eq. (3.22),

$$\begin{aligned} \hat{\mathcal{O}}(\Omega) &= \frac{1 - R_{xx}(\Omega)\, R_{FF}(\Omega)}{R_{ZF}(\Omega)}\, \hat{Z}^{(1)}(\Omega) \\ &= \frac{\hat{Z}^{(0)}(\Omega)}{R_{ZF}(\Omega)} + R_{xx}(\Omega)\left[\hat{F}^{(0)}(\Omega) - R_{FF}(\Omega)\,\frac{\hat{Z}^{(0)}(\Omega)}{R_{ZF}(\Omega)}\right] + \hat{x}^{(0)}(\Omega) + L\,h(\Omega)\,, \end{aligned} \tag{3.38}$$

that is,

$$\hat{\mathcal{O}}(\Omega) = \hat{\mathcal{Z}}(\Omega) + R_{xx}(\Omega)\,\hat{\mathcal{F}}(\Omega) + \hat{x}^{(0)}(\Omega) + L\,h(\Omega)\,. \tag{3.39}$$

Here we have introduced two linear observables $\hat{\mathcal{Z}}$ and $\hat{\mathcal{F}}$ defined in the Hilbert space $\mathcal{H}_{\mathcal{D}}$ of the detector,

$$\hat{\mathcal{Z}}(\Omega) \equiv \frac{\hat{Z}^{(0)}(\Omega)}{R_{ZF}(\Omega)}\,, \qquad \hat{\mathcal{F}}(\Omega) \equiv \hat{F}^{(0)}(\Omega) - R_{FF}(\Omega)\,\frac{\hat{Z}^{(0)}(\Omega)}{R_{ZF}(\Omega)}\,. \tag{3.40}$$

In the time domain the output observable $\hat{\mathcal{O}}(t)$ reads

$$\hat{\mathcal{O}}(t) = \int_{-\infty}^{+\infty} dt'\,K(t-t')\,\hat{Z}^{(1)}(t') \tag{3.41}$$

where

$$K(t) = \int_{-\infty}^{+\infty} \frac{1 - R_{xx}(\Omega)\,R_{FF}(\Omega)}{R_{ZF}(\Omega)}\,e^{-i\,\Omega\,t}\,\frac{d\Omega}{2\pi}\,. \tag{3.42}$$

Thus

$$\hat{\mathcal{O}}(t) = \hat{\mathcal{Z}}(t) + \frac{i}{\hbar}\int_{-\infty}^{t} dt' C_{x^{(0)}x^{(0)}}(t,t')\,\hat{\mathcal{F}}(t') + \hat{x}^{(0)}(t) + L\,h(t)\,. \tag{3.43}$$

Using the two properties given by Eqs. (3.138) of the Appendix, and applying the conditions LQM [Eqs. (3.34)], we obtain the following commutation relations for the observables $\hat{\mathcal{Z}}(t)$ and $\hat{\mathcal{F}}(t)$ in the Fourier domain

$$\left[\hat{\mathcal{Z}}(\Omega), \hat{\mathcal{Z}}^{\dagger}(\Omega')\right] = 0 = \left[\hat{\mathcal{F}}(\Omega), \hat{\mathcal{F}}^{\dagger}(\Omega')\right]\,, \qquad \left[\hat{\mathcal{Z}}(\Omega), \hat{\mathcal{F}}^{\dagger}(\Omega')\right] = -2\pi\,i\hbar\,\delta(\Omega - \Omega')\,, \tag{3.44}$$

or in the time domain: [7]

$$\left[\hat{\mathcal{Z}}(t), \hat{\mathcal{Z}}(t')\right] = 0 = \left[\hat{\mathcal{F}}(t), \hat{\mathcal{F}}(t')\right] \qquad \forall\, t, t'\,, \tag{3.45}$$

$$\left[\hat{\mathcal{Z}}(t), \hat{\mathcal{F}}(t')\right] = -i\hbar\,\delta(t-t') \qquad \forall\, t, t'\,. \tag{3.46}$$

It is interesting to notice that, because the observables $\hat{\mathcal{Z}}(t)$ and $\hat{\mathcal{F}}(t)$ satisfy the commutation relations (3.45), they can be regarded at different times as describing different degrees of freedom. Moreover, because of Eq. (3.46), the observables $\hat{\mathcal{Z}}(t)$ and $\hat{\mathcal{F}}(t)$ can be seen at each instant of time as the *canonical* momentum and coordinate of different *effective* monitors (probe-detector measuring devices). Therefore, $\hat{\mathcal{Z}}(t)$ and $\hat{\mathcal{F}}(t)$ define an infinite set of effective monitors, indexed by t, similar to the successive independent monitors of von Neumann's model [21] for quantum-measurement processes investigated by Caves, Yuen and Ozawa [27]. However, by contrast with von Neumann's model, the monitors defined by $\hat{\mathcal{Z}}(t)$ and $\hat{\mathcal{F}}(t)$ at different t's are *not* necessarily independent. They

[7] Note that, if we use the commutator of $\hat{\mathcal{Z}}$ and $\hat{\mathcal{F}}$ to evaluate the susceptibilities, we find naively that $R_{\mathcal{F}\mathcal{Z}}$ and $R_{\mathcal{Z}\mathcal{F}}$ are proportional to $\int_0^\infty d\tau\delta(\tau)$, which is not a well defined quantity. However, introducing an upper cut-off Λ in the frequency domain we can write $\delta(\tau)$ as $\delta(\tau) = \sin\Lambda\tau/\pi\tau$ for $\Lambda \to +\infty$, which is symmetric around the origin. With this prescription $\int_0^{+\infty} d\tau\delta(\tau) = 1/2$, and the susceptibilities: $R_{\mathcal{Z}\mathcal{Z}} = R_{\mathcal{F}\mathcal{F}} = 0, R_{\mathcal{F}\mathcal{Z}} = 1/2, R_{\mathcal{Z}\mathcal{F}} = -1/2$.

may, in fact, have nontrivial statistical correlations, embodied in the relations

$$\langle \hat{\mathcal{Z}}(t)\,\hat{\mathcal{Z}}(t')\rangle \neq \text{const}\times\delta(t-t')\,,\quad \langle \hat{\mathcal{F}}(t)\,\hat{\mathcal{F}}(t')\rangle \neq \text{const}\times\delta(t-t')\,,\quad \langle \hat{\mathcal{Z}}(t)\,\hat{\mathcal{F}}(t')\rangle \neq \text{const}\times\delta(t-t')\,, \tag{3.47}$$

where "$\langle\quad\rangle$" denotes the expectation value in the quantum state of the system. These correlations can be built up automatically by the internal dynamics of the detector – for example they are present in LIGO-type GW interferometers (see Ref. [12] and Chapter 2).

Let us now comment on the origin of the various terms appearing in Eq. (3.43):

- The first term $\hat{\mathcal{Z}}(t)$ describes the quantum fluctuations in the monitors' readout variable [see also Eq. (3.40)] which are independent of the probe. In particular, $\hat{\mathcal{Z}}$ does not depend on the effective mass μ of the probe. Henceforth, we refer to $\hat{\mathcal{Z}}$ as the *effective* output fluctuation. For an interferometer, the quantum noise embodied in $\hat{\mathcal{Z}}$ is the well-known shot noise.

- The second term in Eq. (3.43) is the effective response of the output at time t to the monitor's back-action force at earlier times $t' < t$. Since $C_{x^{(0)}x^{(0)}} \propto 1/\mu$ this part of the output depends on the effective mass of the probe. For GW interferometers the back action is caused by radiation-pressure fluctuations acting on the four arm-cavity mirrors. In the following we refer to $\hat{\mathcal{F}}$ as the *effective* back-action or radiation-pressure force. The noise embodied in $\hat{\mathcal{F}}$ is called the back-action noise. [In the case of GW interferometers, it is also called the radiation-pressure noise, since the back-action is just the radiation-pressure force.]

- The third term in Eq. (3.43) is the free-evolution operator of the probe's coordinate. In principle, this is also a noise term. However, in many cases the free-evolution of the probe coordinate is confined to a certain uninteresting frequency range, so if we make measurements outside this range, the noise due to the free evolution of the probe will not affect the measurement. We shall see in Sec. 3.3.2 that this will be the case for GW interferometers, as has been pointed out and discussed at length by Braginsky, Gorodetsky, Khalili, Matsko, Thorne and Vyatchanin (BGKMTV for short) [28].

- The last term in Eq. (3.43) is the displacement induced on the probe by the classical observable we want to measure.

Within the effective description of the measurement's renormalized output [Eq. (3.43)], it is instructive to analyze how the simultaneous measurability condition, $[\hat{\mathcal{O}}(t_1), \hat{\mathcal{O}}(t_2)] = 0 \quad \forall t_1, t_2$, is enforced by the probe-detector interaction. To evaluate explicitly the commutation relations of the observable $\hat{\mathcal{O}}$, we notice that in Eq. (3.43) the first two terms always commute with the third term,

because they belong to the two different Hilbert spaces $\mathcal{H}_{\mathcal{D}}$ and $\mathcal{H}_{\mathcal{P}}$. The other terms give

$$\left[\hat{\mathcal{O}}(t_1), \hat{\mathcal{O}}(t_2)\right] = \left[\hat{\mathcal{Z}}(t_1) + \frac{i}{\hbar}\int_{-\infty}^{t_1} dt_1' C_{x^{(0)}x^{(0)}}(t_1, t_1')\,\hat{\mathcal{F}}(t_1'),\quad \hat{\mathcal{Z}}(t_2) + \frac{i}{\hbar}\int_{-\infty}^{t_2} dt_2' C_{x^{(0)}x^{(0)}}(t_2, t_2')\,\hat{\mathcal{F}}(t_2')\right] + \left[\hat{x}^{(0)}(t_1), \hat{x}^{(0)}(t_2)\right] . \tag{3.48}$$

Hence, the two-time commutator of $\hat{\mathcal{O}}(t)$ is the sum of two terms: the first term depends solely on detector observables, while the second term is just the two-time commutator of the free-probe coordinate $\hat{x}^{(0)}(t)$. Using the commutation relations of $\hat{\mathcal{Z}}(t)$ and $\hat{\mathcal{F}}(t)$ given by Eqs. (3.45), (3.46) it is straightforward to deduce that in Eq. (3.48) the detector commutator exactly cancels the probe commutator. This clean cancellation is a very interesting property of probe-detector kinds of quantum-measurement systems and has been recently pointed out and discussed at length by BGKMTV in Ref. [28].

3.3 Dynamics of signal recycled interferometers: equations of motion

In this section we investigate the dynamics of a SR interferometer, showing that it is a probe-detector linear quantum-measurement device as defined and investigated in Sec. 3.2.

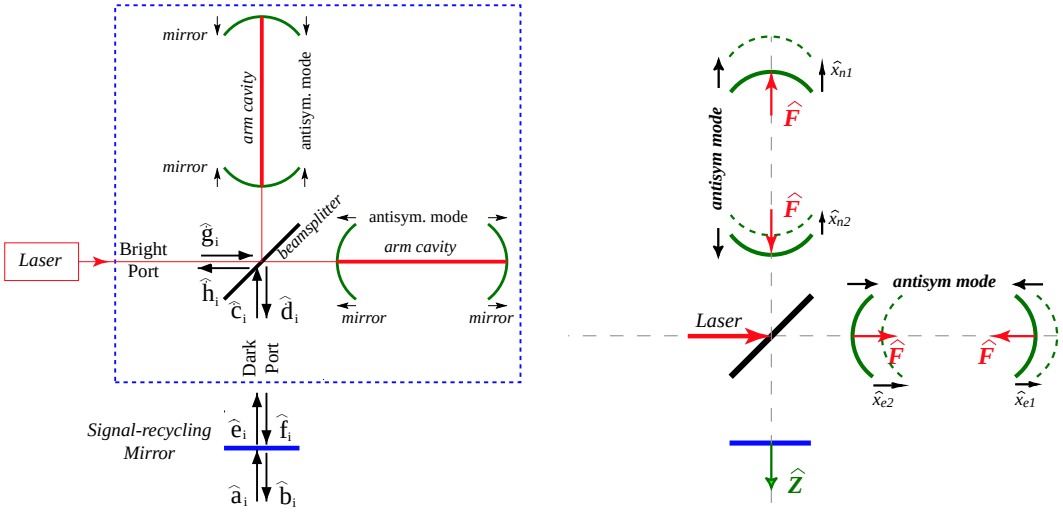

Figure 3.4: On the left panel we draw a SR interferometer, showing the antisymmetric mode of mirror motion (marked by arrows), the dark-port and SR optical fields $\hat{a}_i, \ldots, \hat{f}_i$ and the bright-port fields $\hat{g}_i, \hat{h}_i$, $i = 1, 2$. The conventional-interferometer optical scheme is contained inside the dashed box. On the right panel we identify the variables, $\hat{x} \equiv \hat{x}_{\rm antisym} = (\hat{x}_{n1} - \hat{x}_{n2}) - (\hat{x}_{e1} - \hat{x}_{e2})$, $\hat{Z}$ and $\hat{F}$, describing the dynamics of the SR interferometer.

3.3.1 Identifying the dynamical variables and their interactions

In gravitational-wave interferometers composed of equal-length arms (the optical configuration adopted by LIGO/VIRGO/GEO/TAMA), laser interferometry is used to monitor the displacement of the antisymmetric mode of the four arm-cavity mirrors induced by the passage of a gravitational wave (see Fig. 3.4).

Recently Kimble, Levin, Matsko, Thorne and Vyatchanin (KLMTV for short) [12] described a conventional (LIGO-I type) interferometer using a full quantum mechanical approach (see the optical scheme inside the dashed box in the left panel of Fig. 3.4). KLMTV [12] showed (as has long been known [29]) that in this kind of interferometer the antisymmetric mode of motion of the four arm-cavity mirrors and the dark-port sideband fields ($\hat{c}_i$ and $\hat{d}_i$ [8] in Fig. 3.4) are decoupled from other degrees of freedom, i.e., from other modes of motion of the four arm-cavity mirrors and from the bright-port sideband fields ($\hat{g}_i$ and $\hat{h}_i$ in Fig. 3.4). As a consequence, the dynamics relevant to the output signal and the corresponding noise are described only by the antisymmetric mode of motion of the four arm-cavity mirrors and the dark-port sideband fields (see Appendix B of KLMTV [12] for details). This result remains valid for SR interferometers (see Chapter 2): we only need to include in the analysis all the optical fields inside the SR cavity, such as $\hat{c}_i$, $\hat{d}_i$, $\hat{e}_i$ and $\hat{f}_i$ [but not $\hat{g}_i$ or $\hat{h}_i$], and those outside the SR cavity, such as $\hat{a}_i$ and $\hat{b}_i$.

The coordinate of the antisymmetric mode of motion is defined by KLMTV [see Fig. 3 and Eq. (12) of Ref. [12], and the right panel of Fig. 3.4 of this chapter] as

$$\hat{x}_{\rm antisym} \equiv (\hat{x}_{n1} - \hat{x}_{n2}) - (\hat{x}_{e1} - \hat{x}_{e2})\,, \tag{3.49}$$

and we identify it with the dynamical variable $\hat{x}$ introduced in Sec. 3.2.2 [see Eq. (3.9)]. The output of the detector can be constructed from two independent output observables, the two quadratures $\hat{b}_1$ and $\hat{b}_2$ of the outgoing electromagnetic field immediately outside the SR mirror (see the left panel of Fig. 3.4). If a homodyne-detection read-out scheme is implemented, then the output is a linear combination of the two quadratures, that is

$$\hat{b}_\zeta \equiv \sin\zeta\,\hat{b}_1 + \cos\zeta\,\hat{b}_2\,, \quad \zeta = {\rm const}\,, \tag{3.50}$$

which is a generic quadrature field. [9] We thus identify the dynamical variable $\hat{Z}$ introduced in Sec. 3.2.2 [Eq. (3.7)] as

$$\hat{Z}_\zeta \equiv \hat{b}_\zeta\,. \tag{3.51}$$

[8] Here $\hat{a}_i$, $\hat{b}_i$, $\hat{c}_i$, ... with $i = 1, 2$ stand for the two quadrature operators of the electromagnetic field. This formalism was developed by Caves and Schumaker [30], adopted by KLMTV [12] and the authors (Chapter 2).

[9] Rigorously speaking, the output is the photocurrent, which in the homodyne detection scheme is almost precisely proportional to the output quadrature field, but not quite so; see Ref. [28] and Sec. 2.7 of this thesis for more discussion on this point.

In particular, when $\zeta = \pi/2$ and $\zeta = 0$ we have $\hat{Z}_1 \equiv \hat{b}_1$ and $\hat{Z}_2 \equiv \hat{b}_2$.

The radiation-pressure force acting on the arm-cavity mirrors, and coupled to the antisymmetric mode, can be directly related to the dark-port quadrature fields. This result was explicitly derived in Appendix B of KLMTV [12]. As a foundation for subsequent calculations, we shall summarize the main steps of their derivation: The force acting on each arm-cavity mirror is $2W/c$, where W is the power circulating in each arm cavity, which is proportional to the square of the amplitude of the electric field propagating toward the mirror. In the arm cavities, the electric field can be decomposed into two parts: the carrier and the sideband fields. Introducing the carrier amplitude C and the sideband quadrature operators $\hat{s}_{1,2}$, we have

$$\hat{E}(t) = C\cos\omega_0 t + \cos\omega_0 t\,\left[\int_0^{+\infty}\frac{d\Omega}{2\pi}\,e^{-i\,\Omega t}\,\hat{s}_1 + \text{h.c.}\right] + \sin\omega_0 t\,\left[\int_0^{+\infty}\frac{d\Omega}{2\pi}\,e^{-i\,\Omega t}\,\hat{s}_2 + \text{h.c.}\right]\,, \quad (3.52)$$

where h.c. stands for Hermitian conjugate. (Note that by writing the carrier field as $C\cos\omega_0 t$, we have adopted the convention used by KLMTV [12].) Taking the square of $\hat{E}(t)$, we obtain

$$\begin{aligned}\hat{E}^2(t) &= [\text{DC component}] + [\text{high frequency component } (>\omega_0)] \\ &+ C\,\left[\int_0^{+\infty}\frac{d\Omega}{2\pi}\,e^{-i\,\Omega t}\,\hat{s}_1 + \text{h.c.}\right] + (\text{quadratic terms in } \hat{s}_1,\,\hat{s}_2)\,, \end{aligned} \quad (3.53)$$

where we have used the fact that in the integral $\Omega < \omega_0$. The DC and $\omega_0 \sim 10^{15}\,\text{sec}^{-1}$ components are not in the detection band of GW interferometers, $10\,\text{Hz} \le \Omega/2\pi \le 10^4\,\text{Hz}$; in practice they will be counteracted by control systems. We also ignore the quadratic terms in Eq. (3.53), since they are much smaller than the linear terms. Thus, modulo a factor of proportionality, we obtain in the Fourier domain the following expression for the radiation-pressure force acting on each mirror:

$$\hat{F}_{\text{RP}}(\Omega) \propto C\,\hat{s}_1(\Omega)\,. \quad (3.54)$$

As shown in Appendix B of Ref. [12], the in-cavity quadrature field $\hat{s}_1$ is a combination of the incoming quadratures from both the dark and the bright ports. However, the contribution from the bright-port fields do not couple to the antisymmetric mode, so the force acting on the antisymmetric mode is due only to the incoming fields from the dark port. More specifically, in Appendix B.4 of Ref. [12], KLMTV related the in-cavity carrier amplitude C and the sideband quadrature $\hat{s}_1$ (which they denoted by $\hat{j}_1$ [10]) to the input carrier amplitude and ingoing dark-port quadrature $\hat{c}_1$ (which they denoted by $\hat{a}_1$). Although they did not give the explicit expression we need here for $\hat{F}_{\text{RP}}$, it is straightforward to recover it. Using the arrows indicated in the right panel of Fig. 3.4 as positive

[10] We ignore the effect of the arm-cavity optical losses, thus in this case the quadratures $\hat{j}_i$ and $\hat{k}_i$ in Ref. [12] are equal.

directions, we find [11]

$$\hat{F}_{\rm RP} = \sqrt{\frac{2I_0\hbar\omega_0}{(\Omega^2+\gamma^2)\,L^2}}\,e^{i\,\beta}\,\hat{c}_1, \tag{3.55}$$

where ω_0 is the carrier laser frequency, I_0 is the carrier light power entering the beamsplitter, $2\beta = 2\arctan\Omega/\gamma$ is the net phase gained by the sideband frequency Ω while in the arm cavity, $\gamma = Tc/4L$ is the half bandwidth of the arm cavity (T is the power transmissivity of the input mirrors and L is the length of the arm cavity). We identify the force $\hat{F}_{\rm RP}$ with the dynamical variable $\hat{F}$ introduced in Sec. 3.2.2 [see Eq. (3.8)]:

$$\hat{F} \equiv \hat{F}_{\rm RP} = \sqrt{\frac{2I_0\hbar\omega_0}{(\Omega^2+\gamma^2)\,L^2}}\,e^{i\,\beta}\,\hat{c}_1\,. \tag{3.56}$$

Applying Newton's law to the four mirrors, we deduce

$$m\,\ddot{\hat{x}} = 4\hat{F} + \text{other forces}\,, \tag{3.57}$$

where "other forces" refer to forces not due to the optical-mechanical interaction, e.g., the force due to the gravitational wave and thermal forces. By identifying the reduced mass of the antisymmetric mode as $m/4$, we obtain that the coupling term in the total Hamiltonian (3.6) is $-\hat{x}\,\hat{F}$. [The reduced mass coincides with the effective mass of the probe μ introduced in Sec. 3.2.]

Note that, by assuming the four forces acting on the arm-cavity mirrors are equal, we have made the approximation used by KLMTV [12] of disregarding the motion of the mirrors during the light's round-trip time (quasi-static approximation). [12]

3.3.2 Free evolutions of test mass and optical field

In this section we derive the dynamics of the free probe and the detector, i.e., that of the antisymmetric mode of motion of the arm-cavity mirrors when there is no light in the arm cavities, and that of the optical fields when the arm-cavity mirrors are held fixed. The full, coupled dynamics will be discussed in the following section.

The mirror-endowed test masses are suspended from seismic isolation stacks and have free oscillation frequency $\sim$1 Hz. However, since we are interested in frequencies above $\sim$10 Hz (below these frequencies the seismic noise is dominant), we can approximate the antisymmetric-mode coordinate as the coordinate of a free particle with (reduced) mass $m/4$ — as is also done by KLMTV [12].

[11] This result can be obtained from Eq. (B21) of KLMTV [12] using the fact that $\hat{x}_{\rm BA} = -4/m\Omega^2\,\hat{F}_{\rm RP}$. Since in this chapter we ignore optical losses, in Eq. (B21) we can replace β_* and $\mathcal{K}_*$ by β and $\mathcal{K}$ and ignore the noise operator $\hat{n}_1$.

[12] The description of a SR interferometer beyond the quasi-static approximation [31, 32] introduces nontrivial corrections to the back-action force, proportional to the power transmissivity of the input arm-cavity mirrors. Since the power transmissivity expected for LIGO-II is very small, we expect a small modification of our results, but an explicit calculation is much needed to quantify this effect.

Hence, its free evolution is given by

$$\hat{x}^{(0)}(t) = \hat{x}_s + \frac{4}{m}\,\hat{p}_s\,t\,, \tag{3.58}$$

where $\hat{x}_s$ and $\hat{p}_s$ are the Schrödinger operators of the canonical coordinate and momentum of the mode. Inserting Eq. (3.58) into Eqs. (3.10), (3.16) and using the usual commutation relations $[\hat{x}_s, \hat{p}_s] = i\hbar$, it is straightforward to derive

$$R_{xx} = -\frac{4}{m\Omega^2}\,. \tag{3.59}$$

As discussed in detail by BGKMTV [28], since at frequencies below $\lesssim 10$ Hz the data will be filtered out, the free evolution observable $\hat{x}^{(0)}(t)$, whose Fourier component has support only at zero frequency (in a real interferometer it has support at the pendulum frequency ~ 1 Hz), does not contribute to the output noise. For this reason, henceforth, we shall disregard the free-evolution observable $\hat{x}^{(0)}(t)$ in the equations of motion describing the dynamics of GW interferometers.

Concerning the free detector (the light with fixed mirrors), we can solve its dynamics by expressing the various quantities in terms of the quadrature operators of the input field at the SR mirror, $\hat{a}_i$, $i = 1, 2$ (see Fig. 3.4). For LIGO-II the input field will be in the vacuum state. All the quantum fluctuations affecting the output optical field $\hat{b}_i$ are due to the vacuum fluctuations $\hat{a}_i$ entering the interferometer from the SR mirror.

Through Eqs. (3.51), (3.56), we have already expressed $\hat{Z}$ and $\hat{F}$ in terms of the quadrature fields $\hat{b}_\zeta$ and $\hat{c}_1$; thus we need now to relate the latter to $\hat{a}_i$, $i = 1, 2$, This can be done using Eqs. (2.11),(2.15)–(2.19) of this thesis (in Chapter 2), in the case of fixed mirrors. First, for the input-output relation at the beam splitter (see Fig. 3.4) we have

$$\hat{d}_1 = \hat{c}_1\, e^{2i\beta}\,, \qquad \hat{d}_2 = \hat{c}_2\, e^{2i\beta}\,, \tag{3.60}$$

which is obtained from Eq. (2.11) of this thesis (in Chapter 2), or Eq. (16) of Ref. [12] in the limit $I_0 \to 0$ and $h \to 0$, i.e., when we neglect the effects of mirror motion under radiation pressure and gravitational waves. Second, propagating the quadrature fields inside the SR cavity, we obtain [see Eqs. (2.16), (2.17)]

$$\hat{f}_1 = (\hat{d}_1\,\cos\phi - \hat{d}_2\,\sin\phi)\,, \qquad \hat{f}_2 = (\hat{d}_1\,\sin\phi + \hat{d}_2\,\cos\phi)\,, \tag{3.61}$$

$$\hat{e}_1 = (\hat{c}_1\,\cos\phi + \hat{c}_2\,\sin\phi)\,, \qquad \hat{e}_2 = (-\hat{c}_1\,\sin\phi + \hat{c}_2\,\cos\phi)\,, \tag{3.62}$$

where $\phi \equiv [\omega_0 l/c]_{\mathrm{mod}\,2\pi}$ is the phase gained by the carrier frequency ω_0 traveling one-way in the SR cavity, and for simplicity we have neglected the tiny additional phase $\Phi \equiv \Omega l/c$ gained by the

sideband frequency $\Omega/2\pi$ in the SR cavity. [The length of the SR cavity is typically $l \sim 10\,\mathrm{m}$, hence $\Phi \ll 1$.] From the reflection/transmission relations at the SR mirror we derive [see Eqs. (2.18), (2.19)]

$$\hat{e}_1 = \tau\,\hat{a}_1 + \rho\,\hat{f}_1\,, \qquad \hat{e}_2 = \tau\,\hat{a}_2 + \rho\,\hat{f}_2\,, \tag{3.63}$$

$$\hat{b}_1 = \tau\,\hat{f}_1 - \rho\,\hat{a}_1\,, \qquad \hat{b}_2 = \tau\,\hat{f}_2 - \rho\,\hat{a}_2\,, \tag{3.64}$$

where τ and ρ are the transmissivity and reflectivity of the SR mirror, with $\tau^2 + \rho^2 = 1$. [13] Solving Eqs. (3.60)–(3.64) and using Eq. (3.51), we obtain for the free-evolution operators

$$\hat{Z}_1^{(0)}(\Omega) \equiv \Big[\hat{b}_1(\Omega)\Big]_{\substack{\text{mirrors}\\ \text{fixed}}} = \frac{e^{2i\beta}}{M_0}\left\{\left[\left(1+\rho^2\right)\,\cos 2\phi - 2\rho\,\cos 2\beta\right]\,\hat{a}_1 - \tau^2\,\sin 2\phi\,\hat{a}_2\right\}, \tag{3.65}$$

$$\hat{Z}_2^{(0)}(\Omega) \equiv \Big[\hat{b}_2(\Omega)\Big]_{\substack{\text{mirrors}\\ \text{fixed}}} = \frac{e^{2i\beta}}{M_0}\left\{\tau^2\,\sin 2\phi\,\hat{a}_1 + \left[\left(1+\rho^2\right)\,\cos 2\phi - 2\rho\,\cos 2\beta\right]\,\hat{a}_2\right\}, \tag{3.66}$$

$$\big[\hat{c}_1(\Omega)\big]_{\substack{\text{mirrors}\\ \text{fixed}}} = \frac{\tau\left[\left(1-\rho\,e^{2i\beta}\right)\,\cos\phi\,\hat{a}_1 - \left(1+\rho\,e^{2i\beta}\right)\,\sin\phi\,\hat{a}_2\right]}{M_0}, \tag{3.67}$$

where we have defined,

$$M_0(\Omega) \equiv 1 + \rho^2\,e^{4i\beta} - 2\rho\,\cos 2\phi\,e^{2i\beta} = \left(1 + 2\rho\,\cos 2\phi + \rho^2\right)\,\frac{(\Omega-\Omega_+)\,(\Omega-\Omega_-)}{(\Omega+i\gamma)^2}\,, \tag{3.68}$$

and

$$\Omega_\pm = \frac{1}{1+2\rho\,\cos 2\phi + \rho^2}\,\left[\pm 2\rho\,\gamma\,\sin 2\phi - i\gamma\,(1-\rho^2)\right]\,. \tag{3.69}$$

Note that $\hat{Z}_\zeta^{(0)}$ can be computed from Eqs. (3.65), (3.66) by taking the linear combination of $\hat{Z}_1^{(0)}$ and $\hat{Z}_2^{(0)}$, in the manner of Eqs. (3.50), (3.51). From Eqs. (3.56) and (3.67) we obtain for the free-evolution radiation-pressure force: [14]

$$\hat{F}^{(0)}(\Omega) = \tau\,\sqrt{\frac{2I_0\hbar\omega_0}{(\Omega^2+\gamma^2)\,L^2}}\,\frac{e^{i\,\beta}}{M_0}\,\left[\left(1-\rho\,e^{2i\beta}\right)\,\cos\phi\,\hat{a}_1 - \left(1+\rho\,e^{2i\beta}\right)\,\sin\phi\,\hat{a}_2\right]\,. \tag{3.70}$$

Using Eqs. (3.65), (3.66) and (3.70), and the fact that ζ is frequency independent, we have explicitly checked that the susceptibilities of the free-evolution operators, $\hat{Z}_\zeta^{(0)}$ and $\hat{F}^{(0)}$, satisfy the necessary and sufficient conditions LQM, given in Sec. 3.2.3, which define a linear quantum-measurement system with output $\hat{Z}$. More specifically, using the commutation relations among the

[13] For simplicity we ignore the effects of optical losses which were discussed in Sec. 2.5 of this thesis.

[14] Note that if we take the limit $\tau \to 0$, $\hat{F}^{(0)}(\Omega)$ does not go to zero but $\sim \delta(\Omega \pm \gamma\,\tan\phi)$. Thus the main contribution of the fluctuating force comes from frequencies close to $\Omega = \pm\gamma\,\tan\phi$, which are the optical resonances of the interferometer with arm-cavity mirrors fixed.

quadrature fields $\hat{a}_1$ and $\hat{a}_2$ [Eqs. (7a), (7b) of Ref. [12]], namely,

$$[\hat{a}_1, \hat{a}^\dagger_{2'}] = -[\hat{a}_2, \hat{a}^\dagger_{1'}] = 2\pi\, i\, \delta(\Omega - \Omega')\,, \tag{3.71}$$

$$[\hat{a}_1, \hat{a}^\dagger_{1'}] = 0 = [\hat{a}_1, \hat{a}_{1'}]\,, \qquad [\hat{a}_2, \hat{a}^\dagger_{2'}] = 0 = [\hat{a}_2, \hat{a}_{2'}]\,, \tag{3.72}$$

we have derived that

$$R_{Z_\zeta Z_\zeta} = 0 = R_{F Z_\zeta}\,; \tag{3.73}$$

and we have also derived that

$$R_{FF}(\Omega) = \frac{2I_0\,\omega_0}{L^2}\,\frac{\rho\,\sin 2\phi}{1 + 2\rho\,\cos 2\phi + \rho^2}\,\frac{1}{(\Omega - \Omega_+)\,(\Omega - \Omega_-)}\,, \tag{3.74}$$

$$R_{Z_1 F}(\Omega) = -i\,\sqrt{\frac{2I_0\,\omega_0}{\hbar\,L^2}}\,\frac{\tau\,\sin\phi}{1 + 2\rho\,\cos 2\phi + \rho^2}\,\frac{(1-\rho)\,\Omega + i(1+\rho)\,\gamma}{(\Omega - \Omega_+)\,(\Omega - \Omega_-)}\,, \tag{3.75}$$

$$R_{Z_2 F}(\Omega) = i\,\sqrt{\frac{2I_0\,\omega_0}{\hbar\,L^2}}\,\frac{\tau\,\cos\phi}{1 + 2\rho\,\cos 2\phi + \rho^2}\,\frac{(1+\rho)\,\Omega + i(1-\rho)\,\gamma}{(\Omega - \Omega_+)\,(\Omega - \Omega_-)}\,, \tag{3.76}$$

$$R_{Z_\zeta F}(\Omega) = R_{Z_1 F}(\Omega)\,\sin\zeta + R_{Z_2 F}(\Omega)\,\cos\zeta\,. \tag{3.77}$$

In actuality the commutation relations (3.71), (3.72) are approximate expressions for $\Omega \ll \omega_0$. However, this is a good approximation since the sideband frequency $\Omega/2\pi$ varies over the range $10 - 10^4\,\mathrm{Hz}$, which is ten orders of magnitude smaller than $\omega_0/2\pi \sim 10^{14}\,\mathrm{Hz}$. If we had used the exact commutation relations (see Caves and Schumaker [30] or Eqs. (2.4), (2.5) of this thesis), we would still have $R_{F Z_\zeta} = 0$, [15] but we would have correction terms in the other susceptibilities. In particular, $R_{Z_\zeta Z_\zeta}$ would not vanish, but would instead be on the order of Ω/ω_0. These issues are discussed in Sec. 2.7 of this thesis.

Before ending this section we want to discuss the resonant features of the free-evolution optical fields, which originally motivated the Signal Recycling (SR) [4, 5, 6] and Resonant Sideband Extraction (RSE) schemes [7, 8, 9]. By definition a resonance is an infinite response to a driving force acting at a certain (complex) frequency. Mathematically, it corresponds to a pole of the Fourier-domain susceptibility at that (complex) frequency. From Eqs. (3.74)–(3.77) we deduce that R_{FF} and $R_{Z_\zeta F}$ have only two poles $\Omega_\pm$, given by Eq. (3.69), which are the two complex resonant frequencies of the free optical fields, Eqs. (3.65), (3.66). The corresponding eigenmodes are of the form $e^{-t/\tau_{\mathrm{decay}}}\,e^{-i\,\Omega_{\mathrm{osc}}\,t}$, with oscillation frequency

$$\Omega_{\mathrm{osc}\pm} = \Re(\Omega_\pm) = \pm\frac{2\rho\,\gamma\,\sin 2\phi}{1 + 2\rho\,\cos 2\phi + \rho^2}\,, \tag{3.78}$$

[15] It is quite straightforward to understand why $R_{F Z_\zeta}$ must be zero. In fact $\hat{Z}_\zeta$ is the amplitude of an outgoing wave; thus, the operator $\hat{Z}_\zeta$ at an earlier time cannot be causally correlated with $\hat{F}$ at any later time, and as a consequence $[\hat{F}^{(0)}(t_1), \hat{Z}^{(0)}_\zeta(t_2)] = 0$ for $t_1 > t_2$.

and decay time

$$\tau_{\rm decay} = -\frac{1}{\Im(\Omega_{\pm})} = \frac{1 + 2\rho\,\cos 2\phi + \rho^2}{\gamma\,(1-\rho^2)}\,. \tag{3.79}$$

This oscillation frequency and decay time give information on the frequency of perturbations to which the optical fields are most sensitive, and on the time these perturbations last in the interferometer before leaking out. Let us focus on several limiting cases:

(i) For $\rho = 0$, i.e., the case of a conventional (LIGO-I type) of interferometer, we have $\Omega_{\rm osc} = 0$ and $\tau_{\rm decay} = 1/\gamma$. Thus, there is no oscillation, while the decay time $1/\gamma$ of the entire interferometer is just the storage time of the arm cavity.

(ii) For $\rho \to 1$, i.e., when the SR optical system is nearly closed, we have $\Omega_{\rm osc} = \pm\gamma\tan\phi$ and $\tau_{\rm decay} \to +\infty$, which corresponds to a pure oscillation. Noticing that for sideband fields with frequency $\Omega/2\pi$, the phase gained in the arm cavity is $2\beta = 2\arctan\Omega/\gamma$ and the phase gained during a round trip in the SR cavity is $2\phi = 2\omega_0 l/c$, we obtain that $\Omega_{\rm osc}$ is just the frequency at which the total round-trip phase in the entire cavity (arm cavity + SR cavity) is $2\pi n$, with n an integer.

(iii) For $0 < \rho < 1$ and $\phi = 0$, we get $\Omega_{\rm osc} = 0$ and $\tau_{\rm decay} = (1+\rho)/[\gamma\,(1-\rho)] > 1/\gamma$. This is the so-called tuned SR configuration [4, 5, 6], where the sideband fields remain in the inteferometer for a time longer than the storage time of the arm cavities [cf. (i)].

(iv) For $0 < \rho < 1$ and $\phi = \pi/2$, we get $\Omega_{\rm osc} = 0$ and $\tau_{\rm decay} = (1-\rho)/[\gamma\,(1+\rho)] < 1/\gamma$. This is the so-called tuned RSE configuration [7, 8, 9], where the sideband fields remain in the interferometer for a time shorter than the storage time of the arm cavities [cf. (i)].

3.3.3 Coupled evolution of test mass and optical field: ponderomotive rigidity

In Sec. 3.2.2 we have solved the equations of motion for a generic quantum-measurement device by expressing the full-evolution operators in terms of the free-evolution operators [see Eqs. (3.20)–(3.22)]. Using the free-evolution optical-field operators (3.65), (3.66) and (3.70) and the optical-field susceptibilities (3.74)–(3.77), along with the susceptibility of the antisymmetric mode (3.59), [16] we can now obtain the full evolution of the antisymmetric mode $\hat{x}^{(1)}$ and that of the output optical field $\hat{Z}^{(1)}_{\zeta}$ for a SR interferometer. In Chapter 2, we evaluated the output quadrature fields by a slightly different method, introduced by KLMTV [12]. However, the approach followed in this chapter provides the output field in a more straightforward way, and gives a clearer understanding

[16] As was discussed at the beginning of Sec. 3.3.2, the free-evolution operator $\hat{x}^{(0)}$ describing the antisymmetric mode is irrelevant since it will be filtered out during the data analysis.

of the interferometer dynamics. Moreover, we think this method is more convenient when the optical configuration of the interferometer is rather complex.

We start by investigating the interaction between the probe and the detector. The equations that couple the various quantities $\hat{x}$, $\hat{F}$ and $\hat{Z}$ are [Eqs. (3.17)–(3.19)]:

$$\hat{Z}_\zeta^{(1)}(\Omega) = \hat{Z}_\zeta^{(0)}(\Omega) + R_{Z_\zeta F}(\Omega)\,\hat{x}^{(1)}(\Omega)\,, \tag{3.80}$$

$$\hat{F}^{(1)}(\Omega) = \hat{F}^{(0)}(\Omega) + R_{FF}(\Omega)\,\hat{x}^{(1)}(\Omega)\,, \tag{3.81}$$

$$\hat{x}^{(1)}(\Omega) = R_{xx}(\Omega)\,[G(\Omega) + \hat{F}^{(1)}(\Omega)]\,. \tag{3.82}$$

In these equations, we have made explicit the dependence on the gravitational force $G(\Omega) = -(m/4)\,\Omega^2\,h(\Omega)$ [see also Eq. (3.15)] and have neglected the free evolution operator $\hat{x}^{(0)}$ (see the discussion at the beginning of Sec. 3.3.2).

Equation (3.82) is the equation of motion of the antisymmetric mode under the GW force G and the radiation-pressure force $\hat{F}$, with response function R_{xx}. Equations (3.80) and (3.81) are the equations of motion of the optical fields $\hat{Z}_\zeta$ and $\hat{F}$ under the modulation of the antisymmetric mode of motion of the four arm-cavity mirrors $\hat{x}$, with response functions $R_{Z_\zeta F}(\Omega)$ and $R_{FF}(\Omega)$, respectively.

The optical-mechanical interaction in a conventional interferometer ($\rho = 0$ and $\phi = 0$) was analyzed by KLMTV in Ref. [12]. Here we summarize only the main features. Inside the arm cavity the electric field is [see Eq. (3.52)]

$$\begin{aligned}\hat{E}(t) &\propto C\cos\omega_0 t + \hat{S}_1(t)\cos\omega_0 t + \hat{S}_2(t)\sin\omega_0 t\,,\\ &\approx C\left[1+\frac{\hat{S}_1(t)}{C}\right]\cos\left[\omega_0 t - \frac{\hat{S}_2(t)}{C}\right]\,,\end{aligned} \tag{3.83}$$

with

$$\hat{S}_j(t) = \int_0^{+\infty}\frac{d\Omega}{2\pi}\,e^{-i\,\Omega\,t}\,\hat{s}_j + \text{h.c.}\,, \qquad j = 1, 2\,, \tag{3.84}$$

where in Eq. (3.83) we have assumed that the sideband amplitudes are much smaller than the carrier amplitude. From Eq. (3.83) we infer that the sideband fields $\hat{S}_1$ and $\hat{S}_2$ modulate the amplitude and the phase of the carrier field. If the arm-cavity mirrors are not moving, then it is easy to deduce that $\hat{b}_1 \propto \hat{s}_1 \propto \hat{a}_1$ and $\hat{b}_2 \propto \hat{s}_2 \propto \hat{a}_2$ (see Fig. 3.4). Thus, given our conventions for the quadratures, we can refer to $\hat{s}_1$, $\hat{a}_1$ and $\hat{b}_1$ as amplitude quadratures, and $\hat{s}_2$, $\hat{a}_2$ and $\hat{b}_2$ as phase quadratures in the present case of a conventional interferometer. When the arm-cavity mirrors move, their motion modulates the phase of the carrier field, pumping part of it into the phase quadrature $\hat{S}_2(t)$, and thus into $\hat{b}_2$ [see Appendix B of Ref. [12], especially Eq. (B9a)]. As a consequence $R_{Z_2F} \neq 0$ but $R_{Z_1F} = 0$. On the other hand, the radiation-pressure force acting on the arm-cavity mirrors is determined by

the amplitude modulation $\hat{S}_1(t)$ and does not respond to the motion of the arm-cavity mirrors; thus $R_{FF} = 0$.

Let us now analyze a SR interferometer. As pointed out above, the antisymmetric mode of motion of the arm-cavity mirrors, $\hat{x}$, only appears in the phase quadrature $\hat{d}_2$. [Note that now $\hat{c}_i$ and $\hat{d}_i$ take the place of $\hat{a}_i$ and $\hat{b}_i$ in the above analysis of conventional interferometers.] Schematically,

$$\begin{pmatrix} \hat{c}_1 \\ \hat{c}_2 \end{pmatrix} \overset{\text{arm cavity}}{\longrightarrow} e^{i\,(\text{phase})} \begin{pmatrix} \hat{c}_1 \\ \hat{c}_2 \end{pmatrix} + \begin{pmatrix} 0 \\ \hat{x} \end{pmatrix} \Leftrightarrow \begin{pmatrix} \hat{d}_1 \\ \hat{d}_2 \end{pmatrix} . \tag{3.85}$$

Because of the presence of the SR mirror, part of the field coming out from the beamsplitter is reflected by the SR mirror and fed back into the arm cavities. Due to the propagation inside the SR cavity, the outgoing amplitude/phase quadrature fields at the beamsplitter, $\hat{d}_{1,2}$, get rotated [see Eqs. (3.61), (3.62)]. Moreover, whereas part of the light leaks out from the SR mirror, contributing to the output field, some vacuum fields leak into the SR cavity from outside [see Eqs. (3.63), (3.64)]. When the light reflected by the SR mirror, along with the vacuum fields that have leaked in, reaches the beamsplitter again, the rotation angle is 2ϕ. Schematically, we can write

$$\begin{pmatrix} \hat{d}_1 \\ \hat{d}_2 \end{pmatrix} \overset{\text{SR cavity}}{\longrightarrow} \rho \begin{pmatrix} \cos 2\phi & -\sin 2\phi \\ \sin 2\phi & \cos 2\phi \end{pmatrix} \begin{pmatrix} \hat{d}_1 \\ \hat{d}_2 \end{pmatrix} + \tau \begin{pmatrix} \text{vacuum fields} \\ \text{from outside} \end{pmatrix} \Leftrightarrow \begin{pmatrix} \hat{c}_1 \\ \hat{c}_2 \end{pmatrix} , \tag{3.86}$$

where ρ and τ are the amplitude reflectivity and transmissivity of the SR mirror.

In the particular case of $\phi = 0$ or $\pi/2$, namely, the *tuned* SR/RSE configurations [6, 7, 8, 9], the rotation matrix in Eq. (3.86) is diagonal. Since $\hat{x}$ appears only in $\hat{d}_2$ [see Eq. (3.85)], the fact that the propagation matrix is diagonal guarantees that $\hat{x}$ remains only in the quadratures $\hat{d}_2$ and $\hat{c}_2$. As a result, the radiation-pressure force, which is proportional to $\hat{c}_1$ [see Eq. (3.56)], is not affected by the antisymmetric mode of motion, and $R_{FF} = 0$ [see Eq. (3.74)] as in conventional interferometers. Moreover, since the quadratures at the beamsplitter $\hat{d}_{1,2}$ are rotated by an angle of ϕ when they reach the SR mirror [see Eq. (3.61)], the information on the motion of the arm-cavity mirrors is contained only in the output quadrature $\hat{b}_2$ for $\phi = 0$ and $\hat{b}_1$ for $\phi = \pi/2$. Therefore $R_{Z_1F} = 0$ for $\phi = 0$ and $R_{Z_2F} = 0$ for $\phi = \pi/2$, as obtained directly from Eqs. (3.75), (3.76).

For a generic configuration with $\phi \neq 0$ or $\pi/2$, which is often referred to as the *detuned* case [6], $\hat{x}$ appears in both the quadratures $\hat{c}_{1,2}$ as a consequence of the nontrivial rotation in Eq. (3.86). Thus the radiation-pressure force and both the output quadratures respond to $\hat{x}$, i.e., $R_{FF} \neq 0$ and $R_{Z_\zeta F} \neq 0$ for all ζ, as can be seen from Eqs. (3.74)–(3.76).

Before ending this section let us make some remarks. When $R_{FF} = 0$, as occurs in conventional interferometers and the tuned SR/RSE configurations, we infer from Eqs. (3.59), (3.81) and (3.82)

that

$$-\frac{m}{4}\,\Omega^2\,\hat{x}^{(1)}(\Omega) = G(\Omega) + \hat{F}^{(0)}(\Omega)\,. \tag{3.87}$$

This means that the antisymmetric mode of motion of the four arm-cavity mirrors behaves as a free test mass subject to the GW force $G(\Omega)$ and the fluctuating radiation-pressure force $\hat{F}^{(0)}$. It is well known that for such systems the Heisenberg uncertainty principle imposes a limiting noise spectral density $S_h^{\rm SQL} = 8\hbar/(m\Omega^2 L^2)$ for the dimensionless gravitational-wave signal $h(t) = \Delta L/L$ [33]. This limiting noise spectral density is called the standard quantum limit (SQL) for GW interferometers, and LIGO/VIRGO/GEO/TAMA interferometers can beat this SQL only if correlations among the optical fields are introduced (Refs. [16, 17, 12] and Chapter 2).

When $R_{FF} \neq 0$, Eqs. (3.59), (3.81) and (3.82) give

$$-\frac{m}{4}\,\Omega^2\,\hat{x}^{(1)}(\Omega) = G(\Omega) + \hat{F}^{(0)}(\Omega) + R_{FF}(\Omega)\,\hat{x}^{(1)}(\Omega)\,. \tag{3.88}$$

Thus the antisymmetric mode of motion of the four arm-cavity mirrors is not only disturbed randomly by the fluctuating force $\hat{F}^{(0)}$, but also, and more fundamentally, is subject to a linear restoring force with a frequency-dependent rigidity (or "spring constant") $K(\Omega) = -R_{FF}(\Omega) \neq 0$, generally called a *ponderomotive rigidity* [18]. This phenomenon was originally analyzed in "optical-bar" GW detectors by Braginsky, Khalili and colleagues, where the ponderomotive rigidity affects the internal mirror, i.e., an intra-cavity meter which couples the two resonators with end-mirror–endowed test masses [18]. Hence, SR interferometers do not monitor the displacements of a free test mass but instead that of a test mass subject to a force field $\hat{F}_{\rm res}(\Omega) = -K(\Omega)\,\hat{x}^{(1)}(\Omega)$. This suggests that the SQL, derived from the monitoring of a free test mass, is irrelevant for detuned SR interferometers. Indeed, in Chapter 2, we found that there exists a region of the parameter space ρ, ϕ and I_0 for which the quantum noise curves can beat the SQL by roughly a factor of two over a bandwidth $\Delta f \sim f$.

3.4 Dynamics of signal recycled interferometers: resonances and instabilities

In the previous section we have shown that in a SR interferometer the four arm-cavity mirrors are subject to a frequency dependent restoring force. Thus we expect the mirrors' motion be characterized by resonances and possible instabilities. In Chapter 2, we have identified those resonances by evaluating the input-output relation for the quadrature fields $\hat{b}_i$ $(\hat{a}_i, h)$. In this section, by using the dynamics of the whole system composed of the optical fields and the mirrors, we shall investigate in more detail the features of those resonances and instabilities.

3.4.1 Physical origins of the two pairs of resonances

Let us first seek a qualitative understanding of the resonances. In Fig. 3.5 we draw the amplitude and the phase of the ponderomotive rigidity R_{FF}, given by Eq. (3.74), for a typical choice of LIGO-II parameters: $\phi = \pi/2 - 0.47$, $\rho = 0.9$ and $I_0 \simeq 10^4\,\mathrm{W}$. The amplitude and phase of R_{FF} resemble those of the response function of a damped harmonic oscillator, except for the fact that the phase of R_{FF} is reversed. From Fig. 3.5 we infer that when the frequency $f = \Omega/2\pi$ is small, $|R_{FF}|$ is almost constant, while the phase is nearly $-180°$. Thus in this frequency region the spring constant is approximately a constant positive number $\sim K(\Omega = 0) = -R_{FF}(\Omega = 0) > 0$. However, $K(\Omega = 0)$ is positive only if $0 < \phi < \pi/2$, while for $\pi/2 < \phi < \pi$ the spring constant at low frequencies is negative. As a consequence, for $\pi/2 < \phi < \pi$, there is a non-oscillating instability, namely, a pair of complex-conjugate purely imaginary resonant frequencies. [Note that because the SR-interferometer dynamics is invariant under the transformation $\phi \to \phi + \pi$ (Chapter 2), we can restrict ourselves to $0 \le \phi \le \pi$.]

For larger $f = \Omega/2\pi$, $K(\Omega) = -R_{FF}(\Omega)$ has a resonant peak centered at $\Omega = \Omega_{\mathrm{osc}}$, with width $\sim 1/\tau_{\mathrm{decay}}$ [see Eqs. (3.78), (3.79)].

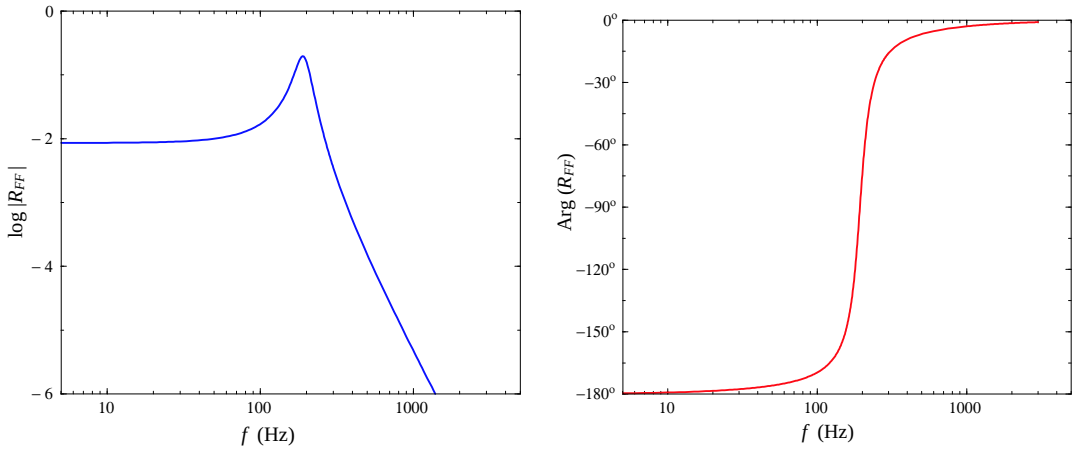

Figure 3.5: Amplitude (on the left panel) and phase (on the right panel) of R_{FF} as a function of the sideband frequency $f = \Omega/2\pi$ for $\phi = \pi/2 - 0.47$, $\rho = 0.9$ and $I_0 \simeq 10^4$ W. Note that the amplitude of R_{FF} is shown in arbitrary unit.

Hence, the dynamics of the system composed of the optical field and the arm-cavity mirrors in a SR interferometer is analogous to the dynamics of a massive spring, with an internal mode, attached to a test mass. When the test mass moves at low frequency, i.e., $\Omega \ll \Omega_{\mathrm{osc}}$, the internal configuration of the spring has time to keep up with its motion and it remains uniform, providing a linear restoring force which induces a pair of resonances at frequencies $\Omega_{\mathrm{mech}} = \pm\sqrt{4K(\Omega \ll \Omega_{\mathrm{osc}})/m} \sim \pm\sqrt{4K(\Omega = 0)/m}$.

When the test mass moves at high frequency, the internal mode of the spring is excited, providing

another pair of resonances to the system. Inserting the equation of motion (3.82) of $\hat{x}$ and the expression for R_{FF}, Eq. (3.74), into the equation of motion (3.81) of $\hat{F}$, we obtain

$$-(\Omega-\Omega_+)\,(\Omega-\Omega_-)\,\hat{F}^{(1)}(\Omega) = \text{driving terms} + \frac{4}{m\Omega^2}\,\frac{2I_0\omega_0}{L^2}\,\frac{\rho\sin 2\phi}{1+2\rho\cos 2\phi+\rho^2}\,\hat{F}^{(1)}(\Omega)\,. \quad (3.89)$$

In the absence of the SR mirror, i.e., for $\rho = 0$, the term proportional to $\hat{F}^{(1)}$ on the RHS of Eq. (3.89) vanishes, and the optical field is characterized by the two resonant frequencies $\Omega_\pm$ given by Eq. (3.69). By contrast, when the SR mirror is present, the term proportional to $\hat{F}^{(1)}$ on the RHS of Eq. (3.89) shifts the resonant frequencies away from the values $\Omega_\pm$.

In conclusion, the dynamics of SR interferometers is characterized by two (pairs of) resonances with different origin: the (pair of) resonances at low frequency have a "mechanical" origin, coming from the linear restoring force due to the ponderomotive rigidity; the (pair of) resonances at higher frequency have an "optical" origin. Because of the motion of the arm-cavity mirrors the optical resonant frequencies get shifted away from the free-evolution SR resonant frequencies $\Omega_\pm$. In this sense we can regard the SR interferometer as an "optical spring" [See Fig. 3.6].

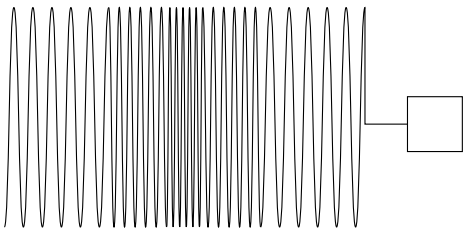

Figure 3.6: The SR-interferometer dynamics resembles the dynamics of a massive spring with one internal oscillation mode (and damping) attached to a test mass. The overall dynamical system is characterized by two pairs of resonances.

3.4.2 Quantitative investigation of the resonances

Equations (3.80)–(3.82) describe the coupled evolution of the dynamical variables $\hat{x}$, $\hat{F}$ and $\hat{Z}$:

$$\hat{x}^{(1)}(\Omega) = \frac{R_{xx}(\Omega)}{1-R_{xx}(\Omega)\,R_{FF}(\Omega)}\,\Big[G(\Omega)+\hat{F}^{(0)}(\Omega)\Big]\,, \quad (3.90)$$

$$\hat{F}^{(1)}(\Omega) = \frac{1}{1-R_{xx}(\Omega)\,R_{FF}(\Omega)}\,\Big[\hat{F}^{(0)}(\Omega)+R_{FF}(\Omega)\,R_{xx}(\Omega)G(\Omega)\Big]\,, \quad (3.91)$$

$$\hat{Z}_\zeta^{(1)}(\Omega) = \hat{Z}_\zeta^{(0)}(\Omega) + \frac{R_{Z_\zeta F}(\Omega)\,R_{xx}(\Omega)}{1-R_{xx}(\Omega)\,R_{FF}(\Omega)}\,\Big[G(\Omega)+\hat{F}^{(0)}(\Omega)\Big]\,. \quad (3.92)$$

Let us first analyze these equations in the low–laser-power limit, which has long been considered in the literature for the SR/RSE schemes [4, 5, 6, 7, 8, 9] and has recently been tested experimentally

[10, 11]. For LIGO-II [3] low–laser-power limit corresponds to $I_0 \ll 10^4\,\mathrm{W}$. Using Eqs. (3.74)–(3.77), and the fact that $\hat{Z}_\zeta^{(0)}$ does not depend on I_0, and $\hat{F}^{(0)} \propto \sqrt{I_0}$ [see Eqs. (3.65), (3.66) and (3.70)], we deduce that $R_{FF} \propto I_0$ and $R_{Z_\zeta F} \propto \sqrt{I_0}$. Therefore, for very low laser power, if we restrict ourselves only to terms up to the order of $\sqrt{I_0}$, we can reduce Eq. (3.92) to

$$\left[\hat{Z}_\zeta^{(1)}(\Omega)\right]_{\text{low power}} = \hat{Z}_\zeta^{(0)}(\Omega) + R_{Z_\zeta F}(\Omega)\, R_{xx}(\Omega)\, G(\Omega)\,, \tag{3.93}$$

which says that the response of $\hat{Z}_\zeta^{(1)}$ to the GW force G is given by the product of R_{xx}, the response of $\hat{x}$ to G, times $R_{Z_\zeta F}$, the response of $\hat{Z}_\zeta$ to $\hat{F}$. Hence, for low laser power the dynamics is characterized by four *decoupled* resonant frequencies: two of them, $\Omega^2 = 0$ (degenerate), are those of the free test mass as embodied in R_{xx}; the other two, $\Omega = \Omega_\pm$ [see Eq. (3.69)], are those of the free-evolution optical fields as embodied in $R_{Z_\zeta F}$. As was discussed in Sec. 3.2.2, when the imaginary part of the resonant frequency is negative (positive) the mode is stable (unstable). Therefore the decoupled "mechanical" resonances $\Omega^2 = 0$ are marginally stable, while the decoupled "optical" resonances $\Omega_\pm$ are stable. [We remind the reader that $\Im(\Omega_\pm) < 0$.]

If we increase the laser power sufficiently, the effect of the radiation pressure is no longer negligible, and from Eqs. (3.90)–(3.92) we derive the following condition for the resonances:

$$\frac{R_{xx}(\Omega)\, R_{Z_\zeta F}(\Omega)}{1 - R_{xx}(\Omega)\, R_{FF}(\Omega)} \to +\infty \tag{3.94}$$

which simplifies to

$$\Omega^2\,(\Omega - \Omega_+)\,(\Omega - \Omega_-) + \frac{I_0\,\gamma^3}{2I_{\mathrm{SQL}}}\,(\Omega_+ - \Omega_-) = 0\,. \tag{3.95}$$

In these equations we have adopted as a reference light power $I_{\mathrm{SQL}} \equiv m\,L^2\,\gamma^4/4\omega_0$, introduced by KLMTV [12]; this is the light power at the beamsplitter needed by a conventional interferometer to reach the SQL at $\Omega = \gamma$. Because of the presence of the term proportional to I_0 in Eq. (3.95), $\Omega^2 = 0$ and $\Omega = \Omega_\pm$ are no longer the resonant frequencies of the coupled SR dynamics.

If the laser power is not very high, we expect the roots of Eq. (3.95) to differ only slightly from the decoupled ones. Let us then apply a perturbative analysis. Concerning the double roots $\Omega^2 = \Omega_0^2 = 0$, working at leading order in the frequency shift $\Delta\Omega_0 = \Omega - \Omega_0 = \Omega$, we derive

$$(\Delta\Omega_0)^2 = -\frac{I_0\,\gamma^3}{2I_{\mathrm{SQL}}}\,\frac{(\Omega_+ - \Omega_-)}{\Omega_+\,\Omega_-} = \frac{I_0}{I_{\mathrm{SQL}}}\,\frac{(2\rho\,\gamma^2\,\sin 2\phi)\,(1 + 2\rho\,\cos 2\phi + \rho^2)}{4\rho^2\,\sin^2 2\phi + (1-\rho^2)^2}\,. \tag{3.96}$$

If the SR detuning phase lies in the range $0 < \phi < \pi/2$, then $(\Delta\Omega_0)^2$ is always positive. Hence, at leading order, the initial double zero resonant frequency $\Omega^2 = 0$ splits into two real resonant frequencies having opposite signs and proportional to $(I_0/I_{\mathrm{SQL}})^{1/2}\,\gamma$. The imaginary parts of these resonant frequencies appear only at the next to leading order, and it turns out (as discussed later

on in this section) that they always increase (becoming more positive) as $I_0/I_{\rm SQL}$ grows, generating instabilities.

If the SR detuning phase lies in the range $\pi/2 < \phi < \pi$, then at leading order $(\Delta\Omega_0)^2$ is negative, and we get two complex-conjugate purely imaginary roots. The system is therefore characterized by a non-oscillating instability.

Regarding the roots $\Omega = \Omega_\pm$, we can expand Eq. (3.95) with respect to $\Delta\Omega_\pm = \Omega - \Omega_\pm$. A simple calculation gives

$$\Delta\Omega_\pm = \mp \frac{I_0\,\gamma^3}{2I_{\rm SQL}}\,\frac{1}{(\Omega_\pm)^2}\,. \tag{3.97}$$

Using Eq. (3.69) we find that

$$\Re(\Delta\Omega_\pm) = \mp \frac{I_0\,\gamma}{2I_{\rm SQL}}\,\frac{[4\rho^2\,\sin^2 2\phi - (1-\rho^2)^2]\,(1+2\rho\,\cos 2\phi + \rho^2)^2}{[4\rho^2\,\sin^2 2\phi + (1-\rho^2)^2]^2}\,, \tag{3.98}$$

$$\Im(\Delta\Omega_\pm) = -\frac{I_0}{I_{\rm SQL}}\,\frac{[2\rho\,\gamma\,\sin 2\phi\,(1-\rho^2)]\,(1+2\rho\,\cos 2\phi + \rho^2)^2}{[4\rho^2\,\sin^2 2\phi + (1-\rho^2)^2]^2}\,. \tag{3.99}$$

This says that, if the SR detuning phase lies in the range $0 < \phi < \pi/2$, then $\Im(\Delta\Omega_\pm)$ always decreases (becoming more negative) as $I_0/I_{\rm SQL}$ increases. Hence, the imaginary parts of the resonant frequencies are pushed away from the real Ω axis, i.e., the system remains stable. On the other hand, $\Re(\Delta\Omega_\pm)$ may either increase or decrease as $I_0/I_{\rm SQL}$ grows. If $\pi/2 < \phi < \pi$ then the imaginary parts become less negative as the laser power increases, so the system becomes less stable.

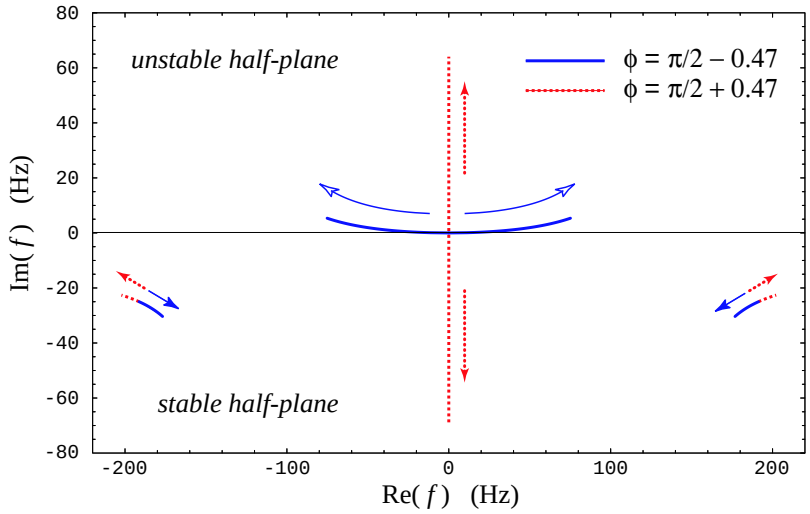

Figure 3.7: Shift of the resonances in a SR interferometer induced by the radiation pressure force as I_0 increases from $\sim$0 up to $I_{\rm SQL}$. This figure is drawn for a SR mirror reflectivity $\rho = 0.9$.

Note that, although turning up the laser power drives the optical resonant frequencies away from their nonzero values $\Omega_\pm$, their changes are very small or comparable to their original values.

By contrast, the mechanical resonant frequencies move away from zero; hence their motion is very significant. In this sense, as the laser power increases, the mechanical (test-mass) resonant frequencies move faster than the optical ones. This fact can also be understood by observing that $\Delta\Omega_0$ is proportional to the square root of I_0, while $\Delta\Omega_\pm$ is proportional to I_0 itself. For the optical configurations of interest for LIGO-II, we found in Chapter 2 that when we increase the laser power from $I_0 = 0$ to $I_0 = I_{\rm SQL}$, the optical resonant frequencies stay more or less close to their original values while the mechanical ones, which start from zero at $I_0 = 0$, move into the observation band of LIGO-II as $I_0 \to I_{\rm SQL}$.

To get a more intuitive idea of the shift in the resonant frequencies for high laser power, we have explored the resonant features numerically. In Fig. 3.7 we plot the trajectories of the resonant frequencies when I_0 varies from ~ 0 to $I_{\rm SQL}$ (the arrows indicate the directions of increasing power), for two choices of SR parameters: $\rho = 0.9$, and $\phi = \pi/2 \mp 0.47$, for which the decoupled resonant frequencies $\Omega_\pm$ coincide. The behaviors of the optical resonant frequencies under an increase of the power agree with the conclusion of the perturbative analysis deduced above. For $\phi = \pi/2 - 0.47$, or more generally for $0 < \phi < \pi/2$, the imaginary part of the optical resonant frequency becomes more negative when the laser power increases, and the resonance becomes more stable; for $\phi = \pi/2 - 0.47$, or generically for $\pi/2 < \phi < \pi$, the imaginary part becomes slightly less negative when the laser power increases. The behavior of the mechanical resonance is particularly interesting. For $\phi = \pi/2 - 0.47$, or generically for $0 < \phi < \pi/2$, and for very low laser power I_0 the two resonant frequencies separate along the real axis, as anticipated by the perturbative analysis. Moreover, as I_0 increases they both gain a positive imaginary part. However, since the trajectory is tangent to the real axis, the growth of the imaginary parts is much smaller than the growth of the real parts. For $\phi = \pi/2 + 0.47$, or more generally for $\pi/2 < \phi < \pi$, the two resonant frequencies separate along the imaginary axis, moving in that direction as I_0 increases.

We finally note that whenever the SR detuning ϕ is different from 0 and $\pi/2$, the mechanical resonance is always unstable. We shall discuss this issue in more detail in the next section.

3.4.3 Characterization of mechanical instabilities

As discussed in the previous section, the coupled mechanical resonant frequencies always have a positive imaginary part, corresponding to an instability. The growth rate of this unstable mode is proportional to the positive imaginary part of the resonant frequency. The time constant, or e-folding time of the mode, is $1/\Im(\Omega)$. Hence, the larger the $\Im(\Omega)$ the more unstable the system is.

In order to quantify the consequences of the instability, we have solved numerically the condition of resonances, Eq. (3.95). In the left panel of Fig. 3.8, we plot the imaginary parts of the four resonant frequencies, in units of $\gamma = Tc/4L$ (the bandwidth of the arm cavity, see Sec. 3.3.1), as a function of the detuning phase $0 < \phi < \pi$ of the SR cavity, fixing $I_0 = I_{\rm SQL} \simeq 10^4\,{\rm W}$ and $\rho = 0.9$. For an

interferometer with arm-cavity length $L = 4\,\mathrm{km}$, and internal-mirror power reflectivity $T = 0.033$, which is the value anticipated by the LIGO-II community [3], we get $\gamma = 619\,\mathrm{s}^{-1}$. Hence, the storage time of the arm cavity is $1/\gamma \simeq 1.6\,\mathrm{ms}$.

From the left panel of Fig. 3.8 we infer that the imaginary parts of the two coupled optical resonant frequencies (shown with a solid line) coincide over the entire range $0 < \phi < \pi$. The imaginary parts of the two coupled mechanical resonant frequencies (drawn by a long-dashed line) also coincide for $0 < \phi < \pi/2$, but they have opposite imaginary parts for $\pi/2 < \phi < \pi$ (see also Fig. 3.7 for two special choices of ϕ). From the various plots we conclude that the region characterized by the weakest instability is $\phi \lesssim \pi/2$. It is important to note that for these values of the detuning phase the noise curves of a SR interferometer have two distinct valleys that beat the SQL (see Sec. 2.4 of this thesis). [17] In Chapter 2 the authors pointed out that the positions of the valleys of the noise curves coincide roughly with the real parts of the system's coupled mechanical and optical resonant frequencies. By taking into account Fig. 3.5 and the dynamics of the system, discussed in Sec. 3.4.1, we can make the following remark. The "spring constant" $K(\Omega)$ is real only for $\Omega \ll \Omega_{\pm}$. For larger Ω's, its imaginary part contributes to that of the resonant frequency, and thus to the instability. Therefore, the farther the coupled mechanical resonant frequency is from the decoupled optical resonant frequency ($\Omega_{\pm}$), the less unstable it is. However, the distance between the coupled mechanical resonant frequency and the decoupled optical resonant frequency ($\Omega_{\pm}$) is directly related to the distance between the coupled mechanical and coupled optical resonant frequencies. Therefore, the more separate the two coupled resonances are, i.e., the farther apart the two valleys of the noise curve are, the more stable the mechanical resonance is.

In Chapter 2, by analyzing the case of very highly reflecting SR mirrors ($\rho \to 1$) the authors found interesting noise curves for the detuning range $\mathcal{D} = \{\phi : \arctan[(4I_0/I_{\mathrm{SQL}})^{1/3}] < \phi < \pi/2\}$ [see Sec. 2.4.1 of this thesis, and, in particular, Eq. (2.64)]. In the right panel of Fig. 3.8, we blow up the left panel around this region $\mathcal{D}$ and plot various curves obtained by varying the SR reflectivity $\rho = 0.8, 0.9, 0.95$ and 0.98. We observe that, for this parameter set, the largest growth rate is $\sim 0.2\gamma \sim 124\,\mathrm{s}^{-1}$, corresponding to an e-folding time of 8 ms, which is five times larger than the arm-cavity storage time.

Finally, we notice that the kind of instability we have found in SR interferometers has an origin similar to the dynamical instability induced in a detuned Fabry-Perot cavity by the radiation-pressure force acting on the mirrors [34, 31, 32].

[17] In this chapter we are only concerned with the quantum noise. Thermal noise also contributes significantly to the total interferometer noise; for the current baseline design it is estimated to be slightly above the SQL [13], but design modifications are being explored [14] which would reduce it to about half the SQL in amplitude.

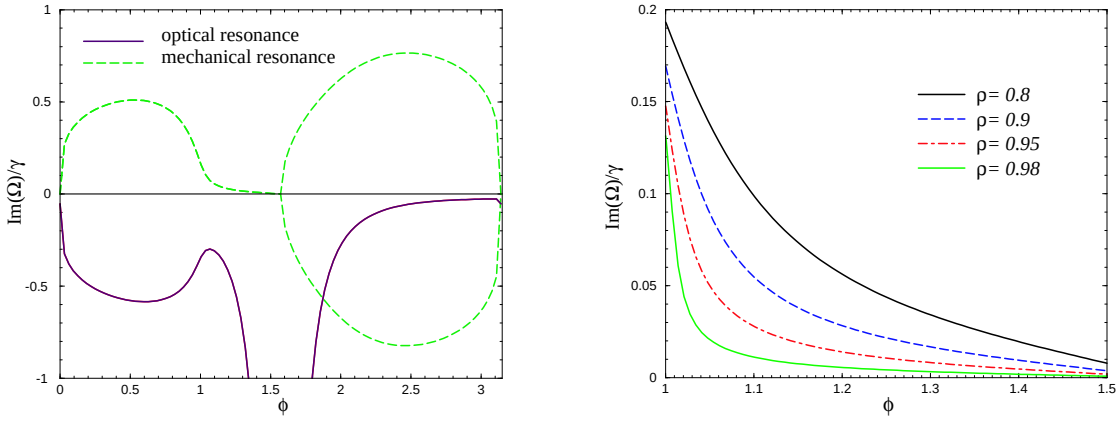

Figure 3.8: The growth of instabilities for highly reflecting SR mirrors. In the left panel we plot the imaginary part of the resonant frequencies, obtained solving Eq. (3.95), versus the SR detuning phase ϕ, for $\rho = 0.9$ and $I_0 = I_{\rm SQL} \simeq 10^4\,{\rm W}$. On the right panel we blow up the plot shown in the left panel for the detuning region $\mathcal{D} = \{\phi : \arctan[(4I_0/I_{\rm SQL})^{1/3}] < \phi < \pi/2\}$, fixing $\rho = 0.8, 0.9, 0.95, 0.98$ and $I_0 = I_{\rm SQL} \simeq 10^4\,{\rm W}$. This range of physical parameters corresponds to interesting LIGO-II noise curves (see Chapter 2).

3.5 Control systems for signal recycled interferometers

In this section we discuss how to suppress the instabilities present in SR interferometers by a suitable servo system. Since the control system must sense the mirror motion inside the observation band and act on (usually damp) it, there is an issue to worry about: If the dynamics is changed by the control system, it is not clear *a priori* whether the resonant dips (or at least the mechanical one which corresponds to the unstable resonance), which characterize the noise curves in the uncontrolled SR interferometer (see Chapter 2), will survive. In the following we shall show the existence of control systems that suppress the instability without altering the noise curves of uncontrolled interferometers, thereby relieving ourselves from the above worry.

3.5.1 Generic feedback control systems: changing the dynamics without affecting the noise

We shall identify a broad category of control systems for which, if the instability can be suppressed, the noise curves are not altered. We suppose that the output signal $\hat{Z}$ is sent through a linear filter $K_{\mathcal{C}}$ and then applied to the antisymmetric mode of the arm-cavity mirrors (see the schematic drawing in Fig. 3.9). This operation corresponds to modifying the Hamiltonian (3.6) into the form

$$\hat{H} = [(\hat{H}_{\mathcal{P}} - \hat{x}\,G) + \hat{H}_{\mathcal{D}}] - \hat{x}\,\hat{F} - \hat{x}\,\hat{\mathcal{C}}\,, \tag{3.100}$$

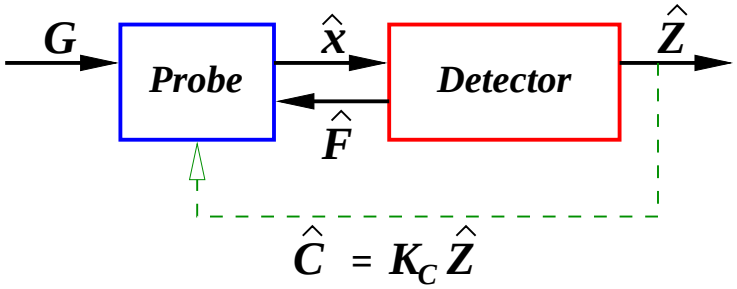

Figure 3.9: Scheme of the control system introduced to quench the instabilities present in a SR interferometer. The output $\hat{Z}$, which contains the GW signal and the quantum noise, is sent through a linear filter with output $\hat{\mathcal{C}} = K_{\mathcal{C}}\,\hat{Z}$, and is then fed back onto the probe, i.e., the antisymmetric mode of motion of the four arm-cavity mirrors.

where $\hat{\mathcal{C}}$ is a detector observable whose free Heisenberg operator (evolving under $H_{\mathcal{D}}$) at time t is given, as required by causality, by an integration over $t' < t$,

$$\hat{\mathcal{C}}^{(0)}(t) = \int_{-\infty}^{t} dt'\, K_{\mathcal{C}}(t-t')\,\hat{Z}^{(0)}(t')\,. \tag{3.101}$$

Physically the filter kernel $K_{\mathcal{C}}(\tau)$ should be a function defined for $\tau > 0$ and should decay to zero when $\tau \to +\infty$. However, in order to apply Fourier analysis, we can extend its definition to $\tau < 0$ by imposing $K_{\mathcal{C}}(\tau < 0) \equiv 0$, thereby obtaining

$$\hat{\mathcal{C}}^{(0)}(t) = \int_{-\infty}^{+\infty} dt'\, K_{\mathcal{C}}(t-t')\,\hat{Z}^{(0)}(t'). \tag{3.102}$$

Therefore, in the Fourier domain we have

$$\hat{\mathcal{C}}^{(0)}(\Omega) = K_{\mathcal{C}}(\Omega)\hat{Z}^{(0)}(\Omega), \tag{3.103}$$

where $K_{\mathcal{C}}(\Omega)$ is the Fourier transform of $K_{\mathcal{C}}(\tau)$. It is straightforward to show that the two time-domain properties $K_{\mathcal{C}}(\tau < 0) = 0$ and $K_{\mathcal{C}}(\tau \to +\infty) \to 0$ correspond in the Fourier domain to the requirement that $K_{\mathcal{C}}(\Omega)$ have poles only in the lower-half Ω plane.

Working in the Fourier domain and assuming that the readout scheme is homodyne detection with detection phase $\zeta = \text{const}$, we derive a set of equations of motion similar to Eqs. (3.80)–(3.82),

$$\hat{Z}_{\zeta}^{(1)}(\Omega) = \hat{Z}_{\zeta}^{(0)}(\Omega) + \left[R_{Z_\zeta F}(\Omega) + R_{Z_\zeta \mathcal{C}_\zeta}(\Omega)\right]\,\hat{x}^{(1)}(\Omega)\,, \tag{3.104}$$

$$\hat{F}^{(1)}(\Omega) = \hat{F}^{(0)}(\Omega) + \left[R_{FF}(\Omega) + R_{F\mathcal{C}_\zeta}(\Omega)\right]\,\hat{x}^{(1)}(\Omega)\,, \tag{3.105}$$

$$\hat{x}^{(1)}(\Omega) = R_{xx}(\Omega)\,[G(\Omega) + \hat{F}^{(1)}(\Omega) + \hat{\mathcal{C}}_{\zeta}^{(1)}(\Omega)]\,, \tag{3.106}$$

$$\hat{\mathcal{C}}_{\zeta}^{(1)}(\Omega) = \hat{\mathcal{C}}_{\zeta}^{(0)}(\Omega) + \left[R_{\mathcal{C}_\zeta F}(\Omega) + R_{\mathcal{C}_\zeta \mathcal{C}_\zeta}(\Omega)\right]\,\hat{x}^{(1)}(\Omega)\,. \tag{3.107}$$

Each of Eqs. (3.104), (3.105) and (3.107) has two response terms due to the two coupling terms between the probe and the detector in the total Hamiltonian (3.100). However, some of the responses are actually zero. In particular, inserting Eq. (3.101) into $[\hat{F}^{(0)}(t), \hat{\mathcal{C}}_\zeta^{(0)}(t')]$ and using the fact that $[\hat{F}^{(0)}(t), \hat{Z}_\zeta^{(0)}(t')] = 0$ for $t > t'$ [see Eq. (3.34)], we find $R_{FC_\zeta}(\Omega) = 0$. Combining Eq. (3.101) with the fact that $[\hat{Z}_\zeta^{(0)}(t), \hat{Z}_\zeta^{(0)}(t')] = 0$ for all t, t' [see Eq. (3.34)], we have $R_{Z_\zeta \mathcal{C}_\zeta}(\Omega) = 0 = R_{\mathcal{C}_\zeta \mathcal{C}_\zeta}(\Omega)$. Moreover, the fact that $K_\mathcal{C}(t - t') = 0 = C_{Z^{(0)}F^{(0)}}(t, t')$ for $t < t'$ gives the equality $R_{\mathcal{C}_\zeta F}(\Omega) = K_\mathcal{C}(\Omega)\, R_{Z_\zeta F}(\Omega)$. Imposing these conditions, we deduce a simplified set of equations of motion:

$$\hat{Z}_\zeta^{(1)}(\Omega) = \hat{Z}_\zeta^{(0)}(\Omega) + R_{Z_\zeta F}(\Omega)\, \hat{x}^{(1)}(\Omega)\,, \tag{3.108}$$

$$\hat{F}^{(1)}(\Omega) = \hat{F}^{(0)}(\Omega) + R_{FF}(\Omega)\, \hat{x}^{(1)}(\Omega)\,, \tag{3.109}$$

$$\hat{x}^{(1)}(\Omega) = R_{xx}(\Omega)\, [G(\Omega) + \hat{F}^{(1)}(\Omega) + \hat{\mathcal{C}}_\zeta^{(1)}(\Omega)]\,, \tag{3.110}$$

$$\hat{\mathcal{C}}_\zeta^{(1)}(\Omega) = K_\mathcal{C}(\Omega)\, \hat{Z}^{(1)}(\Omega)\,. \tag{3.111}$$

Solving Eqs. (3.108)–(3.111), we obtain

$$\hat{x}^{(1)}(\Omega) = \frac{R_{xx}}{1 - R_{xx}\, \left(R_{FF} + R_{Z_\zeta F}\, K_\mathcal{C}\right)} \left[G(\Omega) + \hat{F}^{(0)}(\Omega) + K_\mathcal{C}(\Omega)\, \hat{Z}_\zeta^{(0)}(\Omega)\right]\,, \tag{3.112}$$

$$\hat{Z}_\zeta^{(1)}(\Omega) = \frac{1 - R_{xx}\, R_{FF}}{1 - R_{xx}\, \left(R_{FF} + R_{Z_\zeta F}\, K_\mathcal{C}\right)} \left\{ \hat{Z}_\zeta^{(0)}(\Omega) + \frac{R_{Z_\zeta F}\, R_{xx}}{1 - R_{xx}\, R_{FF}} \left[G(\Omega) + \hat{F}^{(0)}(\Omega)\right] \right\}\,, \tag{3.113}$$

$$\hat{F}^{(1)}(\Omega) = \frac{1 - K_\mathcal{C}\, R_{xx}\, R_{Z_\zeta F}}{1 - R_{xx}\, \left(R_{FF} + R_{Z_\zeta F}\, K_\mathcal{C}\right)} \left\{ \hat{F}^{(0)}(\Omega) + \frac{R_{FF}\, R_{xx}}{1 - K_\mathcal{C}\, R_{xx}\, R_{Z_\zeta F}} \left[G(\Omega) + K_\mathcal{C}\, \hat{Z}^{(0)}(\Omega)\right] \right\}. \tag{3.114}$$

From the above equations (3.112)–(3.114), we infer that the stability condition for the controlled system is determined by the positions of the roots of $[1 - R_{xx}(R_{FF} + R_{Z_\zeta F} K_\mathcal{C})]$. Therefore, by choosing the filter kernel $K_\mathcal{C}$ appropriately, it may be possible that all the roots have negative imaginary part, in which case the system will be stable.

Before working out a specific control kernel $K_\mathcal{C}$ that suppresses the instability, let us notice that different choices of $K_\mathcal{C}$ give outputs (3.113) that differ only by an overall frequency-dependent normalization factor. This factor does not influence the interferometer's noise, since from Eq. (3.113) we can see that the relative magnitudes of the signal (term proportional to G) and the noise (terms proportional to $\hat{Z}_\zeta^{(0)}$ and $\hat{F}^{(0)}$) depend only on the quantities inside the brackets $\{\quad\}$ and not on the factor multiplying the bracket [see Chapter 2 for a detailed discussion of the noise spectral density]. Therefore if this control system can suppress the instability, the resulting well-behaved controlled SR interferometer will have the same noise as evaluated in Chapter 2 for the uncontrolled SR interferometer. This important fact can be easily understood by observing that, because the whole output (the GW signal h and the noise N) is fed back onto the arm-cavity mirrors, h and

N are suppressed in the same way by the control system, and thus their relative magnitude at any frequency Ω is the same as if the SR interferometer had been uncontrolled.

3.5.2 An example of a servo system: effective damping of the test-mass

Physically, it is quite intuitive to think of the feedback system as a system that effectively "damps" the test-mass motion. When the control system is present, the equation of motion for the anti-symmetric mode can be obtained from Eqs. (3.110), (3.108) and (3.111). It reads [as compared to Eq. (3.82)]:

$$\hat{x}^{(1)}(\Omega) = \frac{R_{xx}}{1 - K_{\mathcal{C}}\, R_{xx}\, R_{Z_\zeta F}} \left[G(\Omega) + \hat{F}^{(1)}(\Omega) + K_{\mathcal{C}}\, \hat{Z}^{(0)}_{\zeta}(\Omega) \right] . \tag{3.115}$$

Denoting by $R^{\mathcal{C}}_{xx}$ the response of $\hat{x}^{(1)}$ to G and $\hat{F}^{(1)}$ when the servo system is present, i.e.,

$$R^{\mathcal{C}}_{xx} = \frac{R_{xx}}{1 - K_{\mathcal{C}}\, R_{xx}\, R_{Z_\zeta F}} , \tag{3.116}$$

we can rewrite the overall normalization factor which appears in Eqs. (3.112)–(3.114) as

$$\frac{1}{1 - R_{xx}\, \left(R_{FF} + R_{Z_\zeta F}\, K_{\mathcal{C}} \right)} = \frac{R^{\mathcal{C}}_{xx}}{R_{xx}}\, \frac{1}{1 - R^{\mathcal{C}}_{xx}\, R_{FF}} . \tag{3.117}$$

A sufficient condition for stability is that both $R^{\mathcal{C}}_{xx}/R_{xx}$ and $1/(1 - R^{\mathcal{C}}_{xx} R_{FF})$ have poles only in the lower-half complex plane. [Note that when the servo system is present $R^{\mathcal{C}}_{xx}$ replaces R_{xx} in the stability condition of the system, see Sec. 3.2.2, Eqs. (3.20)–(3.22) and discussions after them.]

We have found it natural to choose for $R^{\mathcal{C}}_{xx}(\Omega)$ the susceptibility of a damped oscillator (with effective mass $m/4$), having both poles in the lower-half Ω plane at $\Omega = -i\lambda$, i.e., [18]

$$R^{\mathcal{C}}_{xx}(\Omega) = -\frac{4}{m}\, \frac{1}{(\Omega + i\lambda)^2} , \tag{3.119}$$

with λ a real parameter. This choice automatically ensures that $R^{\mathcal{C}}_{xx}/R_{xx}$ has poles only in the lower-half complex plane. Moreover, by choosing λ appropriately we can effectively push the roots of $(1 - R^{\mathcal{C}}_{xx}\, R_{FF})$ in Eq. (3.117) to the lower-half Ω plane, as shown in Fig. 3.10 for $\rho = 0.9$, $\phi = \pi/2 - 0.47$, $\lambda = 0.05\,\gamma$ and I_0 from ~ 0 up to $I_{\rm SQL}$.

However, we also need to check that $K_{\mathcal{C}}(\Omega)$ has poles only in the lower-half Ω plane. Using

[18] In the time domain this choice of $R^{\mathcal{C}}_{xx}(\Omega)$ corresponds to the equation of motion

$$\frac{m}{4}\ddot{x} = -\frac{m\lambda}{2}\dot{x} - \frac{m\lambda^2}{4}x + \text{forces} . \tag{3.118}$$

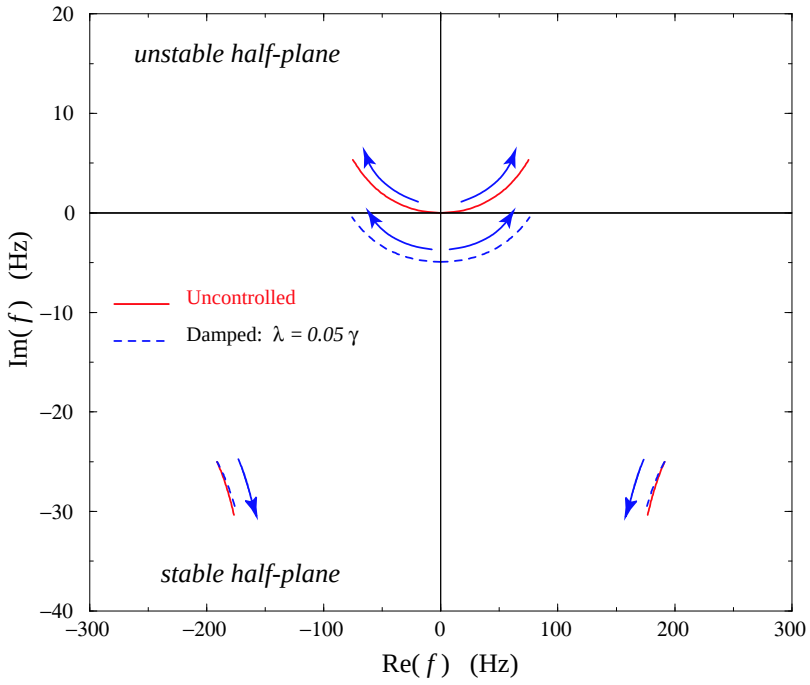

Figure 3.10: Effective damping due to a servo system with control kernel given by Eq. (3.120). We have fixed: $\lambda = 0.05\,\gamma$, $\rho = 0.9$, $\phi = \pi/2 - 0.47$ and I_0 from ~ 0 up to $I_{\rm SQL} \simeq 10^4\,{\rm W}$. The arrows indicate the directions of increasing light power I_0. The originally unstable mechanical resonance (solid line) is pushed downward in the complex Ω-plane, and stabilized (dashed line). The figure also shows the effect of the control system on the stable optical resonances.

Eqs. (3.116), (3.119) we obtain the following explicit expression for the kernel:

$$\begin{aligned} K_{\mathcal{C}}(\Omega) &= \frac{1}{R_{Z_\zeta F}}\left(\frac{1}{R_{xx}} - \frac{1}{R^{\mathcal{C}}_{xx}}\right) \\ &= \frac{m\lambda}{2\,\tau}\sqrt{\frac{\hbar L^2}{2I_0\omega_0}}\left(\Omega + \frac{i\lambda}{2}\right)\frac{(1+2\rho\cos 2\phi+\rho^2)(\Omega-\Omega_-)(\Omega-\Omega_+)}{(\Omega+i\gamma)\cos(\phi+\zeta)+\rho(\Omega-i\gamma)\cos(\phi-\zeta)}\,. \end{aligned} \tag{3.120}$$

For $\zeta = 0$ or $\zeta = \pi/2$, i.e., when either of the two quadratures $\hat{b}_1$ or $\hat{b}_2$ is measured, the control kernel (3.120) indeed has poles only in the lower-half complex plane. More generally, we have shown that if $0 < \phi < \pi/2$, the control kernel (3.120) has poles in the lower-half complex plane for all $\pi/2 \le \zeta \le \pi$, regardless of the value of ρ, but it may become unphysical in the region $0 < \zeta < \pi/2$. However, for the unphysical values of ζ there are various feasible ways out. For example, we could change $R^{\mathcal{C}}_{xx}$ by replacing m in Eq. (3.119) with a slightly smaller quantity $m_{\mathcal{C}}$. In this case

$$\left(\frac{1}{R_{xx}} - \frac{1}{R^{\mathcal{C}}_{xx}}\right) = -\frac{m}{4}\left[\Omega\left(1-\sqrt{\frac{m_{\mathcal{C}}}{m}}\right) - i\lambda\sqrt{\frac{m_{\mathcal{C}}}{m}}\right]\left[\Omega\left(1+\sqrt{\frac{m_{\mathcal{C}}}{m}}\right) + i\lambda\sqrt{\frac{m_{\mathcal{C}}}{m}}\right]. \tag{3.121}$$

By choosing $m_{\mathcal{C}}$ appropriately, we can use the first factor in Eq. (3.121), which has a root in the

upper-half complex plane, to cancel the bad pole coming from $R_{Z_\zeta F}$ in Eq. (3.120), so that $K_{\mathcal{C}}$ will have poles only in the lower-half complex plane. Finally, we must adjust λ so that the effective damping suppress the instability.

Of course, the servo electronics employed to implement the control system will inevitably introduce some noise into the interferometer. In our investigation we have not modelled this noise. However, LIGO experimentalists have seen no fundamental noise limit in implementing control kernels of the kind we discussed, and deem it technically possible to suppress any contribution coming from the electronics to within 10% of the total predicted quantum noise [35, 36]. This issue deserves a more careful study and it will be tackled elsewhere.

In this chapter we have restricted ourselves to the readout scheme of frequency independent homodyne detection, in which only one (frequency independent) quadrature b_ζ is measured. The issue of control-system design when other readout schemes are present, e.g., the so-called radio-frequency modulation-demodulation design, is yet to be addressed.

Finally, for simplicity we have limited our discussion to lossless SR interferometers. When optical losses are taken into account, we have found that the instability problem is still present (Chapter 2) and we have checked that those instabilities can be cured by the same type of control system as was discussed above for lossless SR interferometers.

3.6 Conclusions

Using the formalism of linear quantum-measurement theory, extended by Braginsky and Khalili [19] to GW detectors, we have described the optical-mechanical dynamics of SR interferometers such as LIGO-II [3]. This analysis has allowed us to work out various significant features of such interferometers, which previous investigations [4, 5, 6, 7, 8] could not reveal.

We have found that when the (carrier) laser frequency is detuned in the SR cavity, the arm-cavity mirrors are not only perturbed by a random fluctuating force but are also subject to a linear restoring force with a specific frequency-dependent rigidity. This phenomenon is not unique to SR interferometers; it is a generic feature of detuned cavities [34, 18, 31, 32] and was originally used by Braginsky, Khalili and colleagues in designing the "optical bar" GW detectors [18].

Our analysis has revealed that, for SR interferometers, the dynamics of the whole optical-mechanical system, composed of the arm-cavity mirrors and the optical field, resembles that of a free test mass (mirror motion) connected to a massive spring (optical fields). When the test mass and the spring are not connected (e.g., for very low laser power) they have their own eigenmodes, namely, the uniform translation mode for the free test mass (free antisymmetric mode), and the longitudinal-wave mode for the spring (decoupled SR optical resonance). However, as soon as the free test mass is connected to the massive spring (e.g, for LIGO-II laser power), the two free modes

get shifted in frequency, so the entire coupled system can resonate at two pairs of finite frequencies (coupled mechanical and optical resonances). From this point of view a SR interferometer behaves like an "optical spring" detector. For LIGO-II parameters, both resonant frequencies can lie in the observation band $10\,\mathrm{Hz} < f < 10\,\mathrm{kHz}$ and they are responsible for the beating of the SQL in SR interferometers (see Chapter 2).

The formalism used in the present Chapter has allowed us to analyze in more detail the features of the instabilities in SR interferometers, pointed out in Chapter 2. Most importantly, we have shown the possibility of using a feedback control system to cure such instabilities without compromising the performance of the interferometer. However, before any practical implementation, a much more careful and precise study should be carried out, including various readout schemes.

Finally, the general discussion based on the Braginsky-Khalili force-susceptibility formalism, given in the first part of this chapter (Sec. 3.2), and the application to a specific type of GW interferometer, the LIGO-II SR interferometer, given in the second part of it (Secs. 3.3–3.5), may provide, along with Ref. [12] and Chapter 2, a framework for future investigations of quantum noise in advanced, more complex, optical configurations.

3.7 Appendix. Basic properties of linear systems

In this Appendix, to clarify the formalism used in Sec. 3.2, we summarize some well-known basic properties of linear systems linearly coupled to each other or to external classical forces. Much of this material can be found in Sakurai [37], and for its application to quantum-measurement processes in Braginsky and Khalili [19] and Caves et al. [23].

Definition 1 (Linear systems) *Any system whose Hamiltonian is at most quadratic in its canonical coordinates and momenta is a linear system.*

Definition 2 (Linear observables) *Any linear combination (either time dependent or time independent) of the canonical coordinates and momenta of a linear system, plus a possible complex number (C-number), is a linear observable of the system.*

Denoting all the canonical coordinates and momenta by $\hat{\mathcal{C}}_i$ with $i = 1, 2, \cdots$, the Hamiltonian of a linear system can be written as

$$\hat{H}(t) = \sum_{i,j} L_2^{ij}(t)\,\hat{\mathcal{C}}_i\,\hat{\mathcal{C}}_j + \sum_i L_1^i(t)\,\hat{\mathcal{C}}_i + L_0(t)\,, \tag{3.122}$$

where $L_2^{ij}(t)$ is symmetric in i and j. The equations of motion of the canonical observables in the Heisenberg picture read [we use the fact that $\hat{\mathcal{C}}_{jH}$ does not depend explicitly on time]:

$$\begin{aligned} i\hbar\frac{d}{dt}\hat{\mathcal{C}}_{jH}(t) &= \left[\hat{\mathcal{C}}_{jH}(t), \hat{H}_H(t)\right], \\ &= \hat{U}^\dagger(-\infty,t)\,\left[\hat{\mathcal{C}}_{jS}, \hat{H}_S(t)\right]\,\hat{U}(-\infty,t)\,, \\ &= \hat{U}^\dagger(-\infty,t)\left[\sum_{l,m} 2\,L_2^{lm}(t)\,C_{jl}\,\hat{\mathcal{C}}_{mS} + \sum_l L_1^l(t)\,C_{jl}\right]\hat{U}(-\infty,t)\,, \\ &= \sum_{l,m} 2\,L_2^{lm}(t)\,C_{jl}\,\hat{\mathcal{C}}_{mH}(t) + \sum_l L_1^l(t)\,d_{jl}\,. \end{aligned} \tag{3.123}$$

Here the subscripts S and H stand for Schrödinger and Heisenberg pictures respectively, $C_{jl} \equiv [\hat{\mathcal{C}}_{jS}, \hat{\mathcal{C}}_{lS}]$ is the commutator between the canonical operators, which is a C-number, and $\hat{U}(-\infty,t)$ is the time-evolution operator which satisfies the Schrödinger equation

$$i\hbar\frac{d}{dt}\hat{U}(-\infty,t) = \hat{H}_S\,\hat{U}(-\infty,t) \tag{3.124}$$

with initial condition $\hat{U}(-\infty,-\infty) = 1$. The solution to Eq. (3.123) is of the form

$$\hat{\mathcal{C}}_{jH}(t) = \sum_k \alpha_{jk}(t)\,\hat{\mathcal{C}}_{kH}(-\infty) + \beta_j(t) = \sum_k \alpha_{jk}(t)\,\hat{\mathcal{C}}_{kS} + \beta_j(t)\,, \tag{3.125}$$

where $\alpha_{jk}(t)$ and $\beta_j(t)$ are time dependent C-numbers.

For any linear observable A it follows from linearity that $\hat{A}_H(t) = \sum_j a_j(t)\,\hat{\mathcal{C}}_{jH}(t) + b(t)$, which, along with Eq. (3.125), leads to:

$$\hat{A}_H(t) = \sum_j a_j(t)\,\hat{\mathcal{C}}_{jH}(t) + b(t) = \sum_{j,k} a_j(t)\,\alpha_{jk}(t)\,\hat{\mathcal{C}}_{kS} + \sum_j a_j(t)\beta_j(t) + b(t)\,. \tag{3.126}$$

This provides the following theorem:

Theorem 1 *At any time the operator of a linear observable in the Heisenberg picture can always be written as a linear combination of operators of the (time-independent) canonical variables in the Schrödinger picture plus a possible C-number.*

Applying the above theorem to any two linear observables A and B, recalling that $C_{jk} \equiv [\hat{\mathcal{C}}_{jS}, \hat{\mathcal{C}}_{kS}]$ is a C-number and the commutator between a C-number and any operator is zero, we find

$$\left[\hat{A}_H(t), \hat{B}_H(t')\right] = \sum_{j,k} \gamma_j^A(t)\,\gamma_k^B(t')\,C_{jk}\,, \tag{3.127}$$

which is a C-number. Therefore, the following theorem holds:

Theorem 2 *In the Heisenberg picture, the commutator of the operators of any two linear observables at two times is a C-number.*

We are interested in the evolution of a linear system subject to a classical external linear force or linearly coupled to another independent linear system. A force-susceptibility kind of formulation can be introduced in these cases (as is done by Braginsky and Khalili, see Sec. 6.4 of Ref. [19]). We shall describe the system using a perturbative approach. Thus we write the total Hamiltonian in the Schrödinger picture as $\hat{H}_S = \hat{H}_{0S} + \hat{V}_S(t)$, where $\hat{V}_S(t)$ is treated as a perturbation with respect to the zeroth order Hamiltonian $\hat{H}_{0S}$. It is generally convenient to introduce the so-called Interaction picture (see, e.g., Sections 5.5 and 5.6 of Ref. [37]), in which the evolution operator $\hat{U}_I$ is defined by the relation $\hat{U}(-\infty, t) \equiv \hat{U}_0(-\infty, t)\,\hat{U}_I(-\infty, t)$, where $\hat{U}_0(-\infty, t)$ is the evolution operator associated with $\hat{H}_{0S}$ and $\hat{U}$ is defined by Eq. (3.124). Then, $\hat{U}_I(-\infty, t)$ satisfies the equations

$$i\hbar\frac{d}{dt}\hat{U}_I(-\infty, t) = \hat{V}_I(t)\,\hat{U}_I(-\infty, t)\,, \qquad \hat{U}_I(-\infty, -\infty) = 1\,, \tag{3.128}$$

with $\hat{V}_I(t) \equiv \hat{U}_0^\dagger(-\infty,t)\,\hat{V}_S(t)\,\hat{U}_0(-\infty,t)$. The solution of Eq. (3.128) can be written as a perturbative expansion,

$$\begin{aligned}\hat{U}_I(-\infty,t) &= 1+\frac{1}{i\hbar}\int_{-\infty}^{t} dt_1\hat{V}_I(t_1)+\left(\frac{1}{i\hbar}\right)^2\int_{-\infty}^{t}dt_1\int_{-\infty}^{t_1}dt_2\hat{V}_I(t_1)\hat{V}_I(t_2)+\cdots,\\ &= \sum_{n=0}^{\infty}\frac{1}{n!}\left(\frac{1}{i\hbar}\right)^n T\left\{\left[\int_{-\infty}^{t}dt_1\hat{V}_I(t_1)\right]^n\right\},\end{aligned} \tag{3.129}$$

where T denotes the time-ordered product [38]. The Heisenberg operator associated with any observable A, evolving under the full Hamiltonian $\hat{H}$, is linked to the corresponding Heisenberg operator evolving under the Hamiltonian $\hat{H}_0$ by the relation $\hat{A}_H(t) = \hat{U}_I^\dagger(-\infty,t)\hat{A}_H^{(0)}(t)\hat{U}_I(-\infty,t)$, where the superscript (0) on the observable A denotes that the evolution is due to $\hat{H}_0$. Inserting Eq. (3.129) into the above equation, we get

$$\begin{aligned}&\hat{A}_H(t) = \hat{A}_H^{(0)}(t)+\frac{i}{\hbar}\int_{-\infty}^{t}dt_1\left[\hat{V}_I(t_1),\hat{A}_H^{(0)}(t)\right]+\left(\frac{i}{\hbar}\right)^2\int_{-\infty}^{t}dt_1\int_{-\infty}^{t_1}dt_2\left[\hat{V}_I(t_2),\left[\hat{V}_I(t_1),\hat{A}_H^{(0)}(t)\right]\right]\\ &+\cdots+\left(\frac{i}{\hbar}\right)^n\int_{-\infty}^{t}dt_1\int_{-\infty}^{t_1}dt_2\cdots\int_{-\infty}^{t_{n-1}}dt_n\left[\hat{V}_I(t_n),\left[\cdots,\left[\hat{V}_I(t_2),\left[\hat{V}_I(t_1),\hat{A}_H^{(0)}(t)\right]\right]\cdots\right]\right]\\ &+\cdots.\end{aligned} \tag{3.130}$$

For a linear system subject to an external classical linear force $G(t)$, the interaction term is $\hat{V}_I(t) = -\hat{x}_H^{(0)}G(t)$. Plugging this expression into Eq. (3.130) and using Theorem 2, it is straightforward to deduce that the second and all higher-order terms in Eq. (3.130) vanish and the first order perturbation gives the exact solution. Hence, we obtain the following theorem:

Theorem 3 *Consider a linear system subject to a classical generalized force $G(t)$, whose Hamiltonian is given by $\hat{H} = \hat{H}_0 - \hat{x}\,G(t)$, where $\hat{x}$ is a linear observable. Then, for any linear observable $\hat{A}$, the Heisenberg operator $\hat{A}_H(t)$ can be written as the sum of its free-evolution part, $\hat{A}_H^{(0)}(t)$, plus a term which is due to the presence of the external force, i.e.,*

$$\hat{A}_H(t) = \hat{A}_H^{(0)}(t)+\frac{i}{\hbar}\int_{-\infty}^{t}dt'\,C_{Ax}(t,t')\,G(t'), \tag{3.131}$$

where $C_{Ax}(t,t')$ is a C-number, called the (time-domain) susceptibility, given explicitly by

$$C_{Ax}(t,t') \equiv [\hat{A}_H^{(0)}(t),\hat{x}_H^{(0)}(t')]. \tag{3.132}$$

Let us now suppose that we have two independent linear systems $\mathcal{P}$ (e.g., the probe) and $\mathcal{D}$ (e.g., the detector), which by definition are described by two different Hilbert spaces $\mathcal{H}_\mathcal{P}$ and $\mathcal{H}_\mathcal{D}$. We introduce the Hilbert space $\mathcal{H} = \mathcal{H}_\mathcal{P}\otimes\mathcal{H}_\mathcal{D}$ and define for any operator $\hat{x}$ of the system $\mathcal{P}$ the corresponding operator acting on $\mathcal{H}$ as $\hat{x}\otimes\hat{1}$, while for any operator $\hat{F}$ of the system $\mathcal{D}$ we introduce

the operator $\hat{1}\otimes\hat{F}$ which acts on $\mathcal{H}$. Henceforth, we shall limit ourselves to interaction terms V, in the total Hamiltonian $\hat{H}=\hat{H}_{\mathcal{P}}+\hat{H}_{\mathcal{D}}+\hat{V}$, of the form: $\hat{V}=-\hat{x}\otimes\hat{F}$, with $\hat{x}$ and $\hat{F}$ acting on $\mathcal{P}$ and $\mathcal{D}$, respectively. Using Eq. (3.130) with $\hat{V}_I(t)=-\hat{x}_H^{(0)}(t)\hat{F}_H^{(0)}(t)$, noticing that (i) the zeroth order Heisenberg operators of two observables living in different Hilbert spaces commute and (ii) the zeroth order Heisenberg operators of two linear observables living in the same Hilbert space have a C-number commutator, we derive the following theorem:

Theorem 4 *Consider two independent linear systems $\mathcal{P}$ and $\mathcal{D}$, and two linear observables, $\hat{x}$ of $\mathcal{P}$ and $\hat{F}$ of $\mathcal{D}$. Suppose that the two systems are coupled by a term $-\hat{x}\otimes\hat{F}$, i.e., the Hamiltonian of the composite system $\mathcal{P}+\mathcal{D}$ reads $\hat{H}=\hat{H}_{\mathcal{P}}+\hat{H}_{\mathcal{D}}-\hat{x}\otimes\hat{F}$. Then, for any linear observable $\hat{A}$ of the system $\mathcal{P}$ and $\hat{B}$ of the system $\mathcal{D}$, their full Heisenberg evolutions are given by*

$$\hat{A}_H(t)=\hat{A}_H^{(0)}(t)+\frac{i}{\hbar}\int_{-\infty}^{t}dt' C_{Ax}(t,t')\,\hat{F}_H(t')\,,\qquad \hat{B}_H(t)=\hat{B}_H^{(0)}(t)+\frac{i}{\hbar}\int_{-\infty}^{t}dt' C_{BF}(t,t')\,\hat{x}_H(t')\,, \tag{3.133}$$

where $\hat{A}_H^{(0)}$ and $\hat{B}_H^{(0)}$ stand for the free Heisenberg evolutions, and the susceptibilities are defined by

$$C_{Ax}(t,t')\equiv[\hat{A}_H^{(0)}(t),\hat{x}_H^{(0)}(t')]\,,\qquad C_{BF}(t,t')\equiv[\hat{B}_H^{(0)}(t),\hat{F}_H^{(0)}(t')]\,. \tag{3.134}$$

In the case where the zeroth order Hamiltonian is time independent, it is easy and convenient to express the above formalism in the Fourier domain. We first notice that for a time independent $\hat{H}_0$, $\hat{U}_0(t,t+\tau)=e^{-i\hat{H}_0\tau/\hbar}$ and for any two linear observables $\hat{A}_1$ and $\hat{A}_2$ we have $C_{A_1A_2}(t+\tau,t'+\tau)=C_{A_1A_2}(t,t')$, i.e., $C_{A_1A_2}(t,t')$ depends only on $t-t'$. Defining the Fourier transform of any observable $\hat{A}(t)$ as

$$\hat{A}(\Omega)\equiv\int_{-\infty}^{+\infty}dt\,e^{i\Omega t}\,\hat{A}(t)\,, \tag{3.135}$$

Eq. (3.131) becomes $\hat{A}_H(\Omega)=\hat{A}_H^{(0)}(\Omega)+R_{Ax}(\Omega)\,G(\Omega)$ while Eq. (3.133) can be recast in the form

$$\hat{A}_H(\Omega)=\hat{A}_H^{(0)}(\Omega)+R_{Ax}(\Omega)\,\hat{F}_H(\Omega)\,,\qquad \hat{B}_H(\Omega)=\hat{B}_H^{(0)}(\Omega)+R_{BF}(\Omega)\,\hat{x}_H(\Omega)\,, \tag{3.136}$$

where $R_{AB}(\Omega)$ is the susceptibility in the Fourier-domain, given by

$$R_{AB}(\Omega)=\frac{i}{\hbar}\int_{-\infty}^{+\infty}d\tau\,e^{i\Omega\tau}\,\Theta(\tau)C_{AB}(0,-\tau)=\frac{i}{\hbar}\int_{0}^{+\infty}d\tau\,e^{i\Omega\tau}\,C_{AB}(0,-\tau)\,, \tag{3.137}$$

with $\Theta(\tau)$ the step function. For future reference, let us point out two properties which $R_{AB}(\Omega)$ satisfies and that we use repeatedly in Sec. 3.2:

$$R_{AB}^*(\Omega)=R_{AB}(-\Omega)\,,\qquad \left[\hat{A}_H^{(0)}(\Omega_1),\hat{B}_H^{(0)}(\Omega_2)\right]=-2\pi i\hbar\delta(\Omega_1+\Omega_2)\,[R_{AB}(\Omega_1)-R_{BA}(\Omega_2)]\,. \tag{3.138}$$

To deduce the first identity in Eq. (3.138), we consider the complex (Hermitian) conjugate of Eq. (3.137) and use the Hermiticy of $\hat{A}_H^{(0)}(t)$ and $\hat{B}_H^{(0)}(t)$. For the second identity in Eq. (3.138), we take the double Fourier transform of $[\hat{A}_H^{(0)}(t_1), \hat{B}_H^{(0)}(t_2)]$ with respect to t_1 and t_2, and then using Eq. (3.137) we find that the region corresponding to $t_1 > t_2$ in the double integral yields the R_{AB} term of Eq. (3.138), while the region corresponding to $t_1 < t_2$ gives the R_{BA} term.

3.8 Bibliography

[1] A. Abramovici, W. E. Althouse, R. W. P. Drever, Y. Gursel, S. Kawamura, F. J. Raab, D. Shoemaker, L. Sievers, R. E. Spero, K. S. Thorne, R. E. Vogt, R. Weiss, S. E. Whitcomb, and M. E. Zucker, Science **256**, 325 (1992); B. Caron et al., Class. Quantum Grav. **14**, 1461 (1997); H. Lück et al., Class. Quantum Grav. **14**, 1471 (1997); M. Ando et al., *"Stable operation of a 300 m laser interferometer with sufficient sensitivity to detect gravitational-wave events within our galaxy,"* astro-ph/0105473.

[2] See, e.g., A. Abramovici et al. in Ref. [1]; K. S. Thorne, in *Proceedings of the Snowmass 95 Summer Study on Particle and Nuclear Astrophysics and Cosmology*, eds. E. W. Kolb and R. Peccei (World Scientific, Singapore, 1995), p. 398, gr-qc/9506085; K. S. Thorne, *"The scientific case for mature LIGO interferometers,"* (LIGO Document Number P000024-00-R, www.ligo.caltech.edu/docs/P/P000024-00.pdf).

[3] E. Gustafson, D. Shoemaker, K. A. Strain and R. Weiss, *"LSC White paper on detector research and development,"* (LIGO Document Number T990080-00-D, www.ligo.caltech.edu/docs/T/T990080-00.pdf).

[4] R. W. P. Drever, in *Gravitational Radiation*, edited by N. Deruelle and T. Piran (North-Holland, Amsterdam, 1983), pp 321-338, and in *The Detection of Gravitational Waves*, edited by D. G. Blair, (Cambridge University Press, Cambridge, England, 1991).

[5] J. Y. Vinet, B. Meers, C. N. Man and A. Brillet, Phys. Rev. D **38**, 433 (1998).

[6] B. J. Meers, Phys. Rev. D **38**, 2317 (1998).

[7] J. Mizuno, K. A. Strain, P. G. Nelson, J. M. Chen, R. Schilling, A. Rüdiger, W. Winkler and K. Danzmann, Phys. Lett. A **175**, 273 (1993).

[8] J. Mizuno, *"Comparison of optical configurations for laser interferometric gravitatioanl-wave detectors,"* Ph.D. thesis, Max-Planck-Institut für Quantenoptik, Garching, Germany, 1995.

[9] G. Heinzel, *"Advanced optical techniques for laser interferometric gravitational-wave detectors,"* Ph.D. thesis, Max-Planck-Institut für Quantenoptik, Garching, Germany, 1999.

[10] A. Freise, G. Heinzel, K. A. Strain, J. Mizuno, K. D. Skeldon, H. Lück, B. Wilke, R. Schilling, A. Rüdiger, W. Wingler and K. Danzmann, Phys. Lett. A **277**, 135 (2000), gr-qc/0006026.

[11] J. Mason, *"Signal Extraction and Optical Design for an Advanced Gravitational Wave Interferometer,"* Ph.D. thesis, California Institute of Technology, Pasadena, CA, 2001. (LIGO document P010010-00-R, www.ligo.caltech.edu/docs/P/P010010-00.pdf).

[12] H. J. Kimble, Yu. Levin, A. B. Matsko, K. S. Thorne and S. P. Vyatchanin, *"Conversion of conventional gravitational-wave interferometers into QND interferometers by modifying input and/or output optics,"* submitted to Phys. Rev. D; gr-qc/0008026.

[13] V. B. Braginsky, M. L. Gorodetsky and S. P. Vyatchanin, Phys. Lett. A **264**, 1 (1999); Y. T. Liu and K. S. Thorne, Phys. Rev. D **62** (2000) 122002.

[14] V. B. Braginsky, E. D'Ambrosio, R. O'Shaughnessy, S.E. Strigen, K. S. Thorne and S.P. Vyatchanin (in preparation).

[15] V. B. Braginsky, Sov. Phys. JETP **26**, 831 (1968); V. B. Braginsky and Yu. I. Vorontsov, Sov. Phys. Uspekhi **17**, 644 (1975); V. B. Braginsky, Yu. I. Vorontsov and F. Ya. Kahili, Sov. Phys. JETP **46**, 705 (1977).

[16] W. G. Unruh, in *Quantum Optics, Experimental Gravitation, and Measurement Theory*, edited by P. Meystre and M. O. Scully (Plenum, 1982), p. 647; C. M. Caves, Phys. Rev. D **23**, 1693 (1981); M.T. Jaekel and S. Reynaud, Europhys. Lett. **13**, 301 (1990).

[17] S.P. Vyatchanin and A. B. Matsko, JETP **77**, 218 (1993); S.P. Vyatchanin and E.A. Zubova, Phys. Lett. A **203**, 269 (1995); S.P. Vyatchanin and A. B. Matsko, JETP **82**, 1007 (1996); ibid. JETP **83**, 690 (1996); S.P. Vyatchanin, Phys. Lett. A **239**, 201 (1998).

[18] V. B. Braginsky, M.L. Gorodetsky and F. Ya. Khalili, Phys. Lett. A **232**, 340 (1997); V. B. Braginsky and F. Ya. Khalili, Phys. Lett. A **257**, 241 (1999).

[19] V. B. Braginsky and F. Ya. Khalili, *Quantum measurement*, edited by K. S. Thorne (Cambridge University Press, Cambridge, England, 1992).

[20] See, e.g., R.C. Dorf, *Modern Control Systems*, (Addison-Wesley, Reading Massachusetts, 1990), Chaps. 7 and 8.

[21] J. von Neumann, *Mathematical foundations of quantum mechanics*, trans. by R.T. Beyer (Princeton University Press, 1955).

[22] W. G. Unruh, Phys. Rev. D **19**, 2888 (1979).

[23] C. M. Caves, K. S. Thorne, R.W.P. Drever, V.D. Sandberg and M. Zimmermann, Rev. Mod. Phys. **52**, 341 (1980).

[24] V. B. Braginsky, Yu. I. Vorontsov and K. S. Thorne, Science **209**, 547 (1980); V. B. Braginsky and F. Ya. Khalili, Rev. Mod. Phys. **68**, 1 (1996).

[25] See, e.g., S. Ichimaru, *Basic Principles of Plasma Physics*, (Benjamin, Reading Massachusetts 1973).

[26] See, e.g., J. Mathews and R. L. Walker, *Mathematical Methods of Physics*, (Addison-Wesley, Reading Massachusetts, 1970).

[27] H. P. Yuen, Phys. Rev. Lett. **51**, 719 (1983); C. M. Caves, Phys. Rev. Lett. **54**, 2465 (1985); M. Ozawa, Phys. Rev. Lett. **60**, 385 (1988); Phys. Rev. A **41**, 1735 (1990); J. Maddox, Nature **331**, 559 (1988).

[28] V. B. Braginsky, M.L. Gorodetsky, F. Ya. Khalili, A. B. Matsko, K. S. Thorne, S.P. Vyatchanin, *"Noise in gravitational-wave detectors is not influenced by test-mass quantization,"* (in preparation).

[29] A.F. Pace, M.J. Collett and D.F. Walls, Phys. Rev. D **47**, 3173 (1993).

[30] C. M. Caves and B.L. Schumaker, Phys. Rev. A **31**, 3068 (1985); B.L. Schumaker and C. M. Caves, Phys. Rev. A **31**, 3093 (1985).

[31] B. Meers and N. Mac Donald, Phys. Rev. A **40**, 40 (1989); A. Pai, S. V. Dhurandhar, P. Hello and J-Y. Vinet, Europhys. Phys. J. D **8**, 333 (2000), gr-qc/0011099.

[32] M. Rakhmanov, *"Dynamics of laser interferometric gravitational wave detectors,"* Ph.D. thesis, California Institute of Technology, Pasadena, CA, 2000.

[33] K. S. Thorne, in *Three Hundred Years of Gravitation*, edited by S. W. Hawking and W. Israel, (Cambridge University Press, Cambridge, England, 1987), p. 330 and references therein.

[34] A. Dorsel, J. D. McCullen, P. Meystre, E. Vignes and H. Walther, Phys. Rev. Lett. **51**, 1550 (1983); N. Deruelle and P. Tourrenc, in *Gravitation, Geometry and Relativistic Physics* (Springer, Berlin, 1984); P. Meystre, E.M. Wright, J. D. McCullen and E. Vignes, J. Opt. Soc. Am. **2**, 1830 (1985); J.M. Aguirregabria and L. Bel, Phys. Rev. D **36**, 3768 (1987); L. Bel, J. L. Boulanger and N. Deruelle, Phys. Rev. A **7**, 37 (1988).

[35] K. A. Strain (private communication).

[36] N. Mavalvala (private communication).

[37] See, e.g., Chaps. 2 and 5 of J.J. Sakurai, *Modern quantum mechanics*, edited by S.F. Tuan (Benjamin/Cummings Publishing Company, 1985).

[38] See, e.g., E. Merzbacher, *Quantum mechanics*, 2nd ed. (Wiley, New York), especially Secs. 15.8–15.10.

Chapter 4

Scaling law in signal recycled laser-interferometer gravitational-wave detectors

By mapping the signal-recycling (SR) optical configuration to a three-mirror cavity, and then to a single detuned cavity, we express SR optomechanical dynamics, input–output relation and noise spectral density in terms of *only* three characteristic parameters: the (free) optical resonant frequency and decay time of the entire interferometer, and the laser power circulating in arm cavities. These parameters, and therefore the properties of the interferometer, are invariant under an appropriate scaling of SR-mirror reflectivity, SR detuning, arm-cavity storage time and input power at beamsplitter. Moreover, so far the quantum-mechanical description of laser-interferometer gravitational-wave detectors, including radiation-pressure effects, was only obtained at linear order in the transmissivity of arm-cavity internal mirrors. We relax this assumption and discuss how the noise spectral densities change.

Originally published as A. Buonanno and Y. Chen, Phys. Rev. D **67**, 062002 (2003).

4.1 Introduction

A network of broadband ground-based laser interferometers, aimed at detecting gravitational waves (GWs) in the frequency band $10 - 10^4$ Hz, is already operating. This network is composed of GEO, the Laser Interferometer Gravitational-wave Observatory (LIGO), TAMA and VIRGO (whose operation will begin in 2004) [1]. The LIGO Scientific Collaboration (LSC) [2] is currently planning an upgrade of LIGO starting from 2008, called advanced LIGO or LIGO-II. Besides the improvement of the seismic isolation and suspension systems, and the increase (decrease) of light power (shot noise) circulating in arm cavities, the LIGO community has planned to introduce an extra mirror, called a signal-recycling mirror (SRM) [3, 4], at the dark-port output (see Fig. 4.1). The optical system composed of SR cavity and arm cavities forms a composite resonant cavity, whose

eigenfrequencies and quality factors can be controlled by the position and reflectivity of the SR mirror. These eigenfrequencies (resonances) can be exploited to reshape the noise curves, enabling the interferometer to work either in broadband or in narrowband configurations, and improving in this way the observation of specific GW astrophysical sources [5].

The initial theoretical analyses [3, 4] and experiments [6] of SR interferometers refer to configurations with low laser power, for which the radiation pressure on the arm-cavity mirrors is negligible and the quantum-noise spectra are dominated by shot noise. When the laser power is increased, the shot noise decreases while the effect of radiation-pressure fluctuation increases. LIGO-II has been planned to work at a laser power for which the two effects are comparable in the observational band 40–200 Hz [2]. Thus, to correctly describe the quantum optical noise in LIGO-II, the results have been complemented by a thorough investigation of the influence of radiation-pressure force on mirror motion (see Ref. [7] and Chapters 2 and 3 of this thesis). The analyses revealed that SR interferometers behave as an "optical spring." The dynamics of the whole optomechanical system, composed of arm-cavity mirrors and optical field, resembles that of a free test mass (mirror motion) connected to a massive spring (optical fields). When the test mass and the spring are not connected (e.g., for very low laser power) they have their own eigenmodes: the uniform translation mode for the free mode and the longitudinal-wave mode for the spring. However, for LIGO-II laser power the test mass is connected to the massive spring and the two free modes get shifted in frequency, so the entire coupled system can resonate at two pairs of finite frequencies. Near these resonances the noise curve can beat the free mass standard quantum limit (SQL) for GW detectors [8]. Indeed, the SQL is not by itself an absolute limit, it depends on the dynamical properties of the test object (or probe) which we monitor. This phenomenon is not unique to SR interferometers; it is a generic feature of detuned cavities [9, 10] and was used by Braginsky, Khalili and colleagues in conceiving the "optical bar" GW detectors [11]. However, because the optomechanical system is by itself dynamically unstable, and a careful and precise study of the control system should be carried out (Chapter 3).

The quantum mechanical analysis of SR interferometers given in Chapters 2 and 3, was built on results obtained by Kimble, Levin, Matsko, Thorne and Vyatchanin (KLMTV) [7] for conventional interferometers, i.e., without SRM. For this reason, both the SR input–output relation (Chapter 2) and the SR optomechanical dynamics (Chapter 3) were expressed in terms of parameters characterizing conventional interferometers, such as the storage time in the arm cavities, instead of parameters characterizing SR interferometers as a whole, such as the resonant frequencies and the storage time of the entire interferometer. Therefore, the analysis given in Chapters 2 and 3 is not fully suitable for highlighting the physics in SR interferometers.

In this chapter, we first map the SR interferometer into a three-mirror cavity, as originally done by Mizuno [12], though in the low power limit and neglecting radiation-pressure effects, and by Rachmanov [13] in classical regimes. Then, as first suggested by Mizuno [12], we regard the very

short SR cavity (formed by SRM and ITM) as one (effective) mirror and we express input–output relation and noise spectral density (Chapter 2), and optomechanical dynamics (Chapter 3) as well, in terms of three *characteristic* parameters that have more direct physical meaning: the *free* optical resonant frequency and decay time of the entire SR interferometer, and the laser power circulating in arm cavities. By free optical resonant frequency and decay time we mean the real and inverse imaginary part of the (complex) optical resonant frequency when all the test-mass mirrors are *held fixed.* These parameters can then be represented in terms of the more *practical* parameters: the power transmissivity of ITM, the amplitude reflectivity of SRM, SR detuning and the input power. An appropriate scaling of the practical parameters can leave the characteristic parameters invariant.

In addition, in investigating SR interferometers (Chapters 2 and 3) the authors restricted the analyses to linear order in the transmissivity of arm-cavity internal mirrors, as also done by KLMTV [7] for conventional interferometers. In this chapter we relax this assumption and discuss how results change.

The outline of this chapter is as follows. In Sec. 4.2 we explicitly work out the mapping between a SR interferometer and a three-mirror cavity, expressing the free oscillation frequency, decay time and laser power circulating in arm cavity, i.e., the characteristic parameters, in terms of SR-mirror reflectivity, SR detuning and arm-cavity storage time, which are the parameters used in the original description (Chapter 2). An interesting scaling law among the practical parameters is then obtained. In Secs. 4.3 and 4.4.1 the input–output relations, noise spectral density and optomechanical dynamics are expressed in terms of those characteristic parameters. In Sec. 4.4.2 we map the SR interferometer to a single detuned cavity of the kind analyzed by Khalili [10]. In Sec. 4.4.3 we show that correlations between shot noise and radiation-pressure noise in SR interferometers are equivalent to a change of the optomechanical dynamics, as discussed in a more general context by Syrtsev and Khalili [14]. In Sec. 4.4.4, using fluctuation-dissipation theorem, we explain why optical spring detectors have *very low* intrinsic noise, and are then preferable to mechanical springs in measuring very tiny forces. In Sec. 4.5 we derive the input–output relation of SR interferometers at all orders in the transmissivity of internal test-mass mirrors. Finally, Sec. 4.6 summarizes our main conclusions. Appendix 4.7 contains definitions and notations, Appendix 4.8 discusses the Stokes relations in our optical system and in Appendix 4.9 we give the input–output relation including also next-to-leading order terms in the transmissivity of arm-cavity internal mirrors.

In this manuscript we shall be concerned only with quantum noise, though in realistic interferometers seismic and thermal noises are also present. Moreover, we shall neglect optical losses [see Sec. 2.5 of this thesis where optical losses in SR interferometers were discussed].

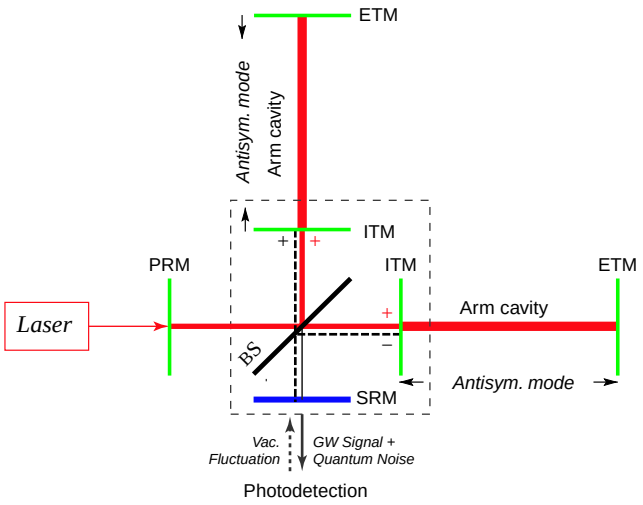

Figure 4.1: We draw a signal- (and power-) recycled LIGO interferometer. The laser light enters the interferometer from the left (bright port), through the power-recycling mirror (PRM), and gets split by a 50/50 beamsplitter (BS) into the two identical (in absence of gravitational waves) arm cavities. Each of the arm cavities is formed by the internal test-mass mirror (ITM) and the end test-mass mirror (ETM). No light leaves the interferometer from below the BS (dark port), except the lights induced by the antisymmetric motion of the test-mass mirrors, e.g., due to a passing-by gravitational wave, or due to vacuum fluctuations that originally enter the interferometer from the dark port. A SRM is placed at the dark port, forming a SR cavity (marked by thick dashed lines) with the ITMs.

4.2 Derivation of scaling law

4.2.1 Equivalent three-mirror–cavity description of signal-recycled interferometer

In Fig. 4.1, we draw a signal- and power- recycled LIGO interferometer. The Michelson-type optical configuration makes it natural to decompose the optical fields and the mechanical motion of the mirrors into modes that are either symmetric (i.e., equal amplitude) or antisymmetric (i.e., equal in magnitude but opposite in signs) in the two arms, as done in Ref. [7] and Chapters 2 and 3, and briefly explained in the following. In order to understand this decomposition more easily, let us for the moment ignore the power-recycling mirror (PRM) and the signal-recycling mirror (SRM).

First, let us suppose all mirrors are held fixed in their equilibrium positions. The laser light, which enters the interferometer from the left of the beamsplitter (BS), excites stationary, monochromatic carrier light inside the two identical arm cavities with equal amplitudes (marked with two + signs in Fig. 4.1) and thereby drives the symmetric mode. To maximize the carrier amplitude inside the arm cavities, the arm lengths are chosen to be on resonance with the laser frequency. When the carrier lights leave the two arms and recombine at the BS, they have the same magnitude and sign, and, as a consequence, leak out the interferometer only from the left port of the BS. No carrier light leaks

out from the port below the BS. For this reason, the left port is called the bright port, and the port below the BS is called the dark port. Obviously, were there any other light that enters the bright port, it would only drive the symmetric mode, which would then leak out only from the bright port. Similarly, lights that enter from the dark port would only drive the antisymmetric optical mode, which have opposite signs at the BS (marked in Fig. 4.1) and would leak out the interferometer only from the dark port.

Now suppose the mirrors (ITMs and ETMs) move in an antisymmetric (mechanical) mode (shown by arrows in Fig. 4.1) such that the two arm lengths change in opposite directions — for example, driven by a gravitational wave. This kind of motion would pump the (symmetric) carriers in the two arms into sideband lights with opposite signs, which lie in the antisymmetric mode, and would leak out the interferometer from the dark port (and thus can be detected). On the contrary, symmetric mirror motions that change the two arm lengths in the same way would induce sidebands in the symmetric mode, which would leave the interferometer from the bright port. Moreover, sideband lights inside the arm cavities, combined with the strong carrier lights, exert forces on the test masses. Since the carrier lights in the two arms are symmetric, sidebands in the symmetric (antisymmetric) optical mode drive only the symmetric (antisymmetric) mechanical modes. In this way, we have two effectively decoupled systems in our interferometer: (i) ingoing and outgoing bright-port optical fields, symmetric optical and mechanical modes, and (ii) ingoing and outgoing dark-port optical fields, antisymmetric optical and mechanical modes.

When the PRM and SRM are present, since each of them only affects one of the bright/dark ports, the decoupling between the symmetric and antisymmetric modes is still valid. Nevertheless, the behavior of each of the subsystems becomes richer. The PRM, along with the two ITMs, forms a power recycling cavity (for symmetric optical modes, shown by solid lines in Fig. 4.1). In practice, in order to increase the carrier amplitude inside the arm cavities [3], this cavity is always set to be on resonance with the input laser light. More specifically, if the input laser power at the PRM is $I_{\rm in}$, then the power input at the BS is $I_0 = 4I_{\rm in}/T_{\rm p}$, and the circulating power inside the arms is $I_c = 2I_0/T$, where $T_{\rm p}$ and T are the power transmissivities of the PRM and the ITM. The SRM, along with the two ITMs, forms a SR cavity (for the antisymmetric optical modes, shown by dashed lines in Fig. 4.1). By adjusting the length and finesse of this cavity, we can modify the resonant frequency and storage time of the antisymmetric optical mode [4], and affect the optomechanical dynamics of the entire interferometer (Chapter 3). These changes will reshape the noise curves of SR interferometers, and can allow them to beat the SQL (Chapter 2).

Henceforth, we focus on the subsystem made up of dark-port fields and antisymmetric optical and mechanical modes, in which the detected GW signal and quantum noises reside. In light of the above discussions, it is convenient to identify the two arm cavities as one effective arm cavity, and map the entire interferometer to a three-mirror cavity, as shown in Fig. 4.2. In particular, the SR

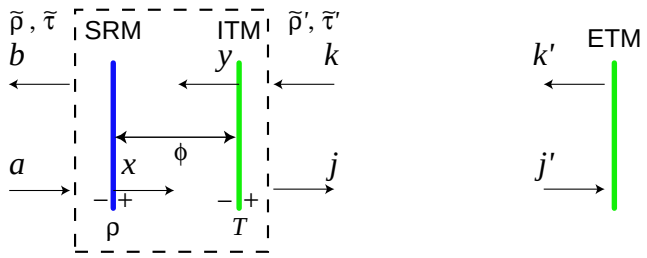

Figure 4.2: We draw the three-mirror cavity which is equivalent to a SR interferometer in describing the antisymmetric optical/mechanical modes and dark-port optical fields. The SR cavity, which is mapped into a two-mirror cavity (in dashed box), can be viewed as an effective mirror, with four effective reflectivities and transmissivities, $\widetilde{\rho}'$, $\widetilde{\tau}'$ (for fields entering from the right side), and $\widetilde{\rho}$, $\widetilde{\tau}$ (for fields entering from the left side). The input and output fields, a and b, corresponds to those at the dark-port of the real SR interferometer.

cavity, formed by the SRM and ITMs is mapped into a two-mirror cavity (inside the dashed box of Fig. 4.2) or *one effective* ITM. The antisymmetric mechanical motions of the two *real* arm cavities is equal or opposite in sign to those of this system. The input and output fields at the dark port corresponds to those of the three-mirror cavity, a and b (shown in Fig. 4.2). Because of the presence of the BS in real interferometer (and the absence in effective one), the optical fields inside the two real arms is $\pm 1/\sqrt{2}$ times the fields in the effective cavity composed of the effective ITM and ETM. As a consequence, fields in this effective cavity are $\sqrt{2}$ times as sensitive to mirror motions as those in the real arms, and the effective power in the effective cavity must be

$$I_{\rm arm} = 2I_c\,. \tag{4.1}$$

Therefore, both the carrier amplitude and the sideband amplitude in the effective cavity are $\sqrt{2}$ times stronger than the ones in each real arm. In order to have the same effects on the motion of the mirrors, we must impose the effective ETM and ITM to be twice as massive as the real ones, i.e.

$$m_{\rm arm} = 2m\,. \tag{4.2}$$

We denote by T and $R = 1 - T$ the power transmissivity and reflectivity of the ITMs, $L = 4$ km is the arm length, and we assume the ETMs to be perfectly reflecting. The arm length is on resonance with the carrier frequency $\omega_0 = 1.8 \times 10^{15}\,\mathrm{sec}^{-1}$, i.e., $\omega_0 L/c = N\pi$, with N an integer. We denote by ρ and l the reflectivity of the SRM and the length of the SR cavity, and $\phi = [\omega_0 l/c]_{\mathrm{mod}\,2\pi}$ the phase gained by lights with carrier frequency upon one trip across the SR cavity. We assume the SR cavity to be very short (~ 10 m) compared with the arm-cavity length. Thus, we disregard the phase gained by lights with sideband frequency while traveling across the SR cavity, i.e., $\Omega\, l/c \to 0$. The three-mirror cavity system can be broken into two parts. The effective arm cavity, which is the

region to the right of the SR cavity, including the ETM (but *excluding* the ITM), where the light interacts with the mechanical motion of the ETM. This region is completely characterized by the circulating power I_c, the arm length L and the mirror mass m. The (very short) SR cavity, made up of the SRM and the ITM, which does not move. This part is characterized by T, ρ and ϕ.

Henceforth, we assume the radiation pressure forces acting on the ETM and ITM to be equal, and the contribution of the radiation-pressure–induced motion of the two mirrors to the output light, or the radiation-pressure noises due to the two mirrors, to be equal. [These assumptions introduce errors on the order of $\max\{\Omega L/c,\, T\}$.] As a consequence, we can equivalently hold the ITM fixed and assume the ETM has a reduced mass of

$$\mu_{\rm arm} = \frac{1}{2} m_{\rm arm}\,. \tag{4.3}$$

4.2.2 The scaling law in generic form

As first noticed by Mizuno [12], when the SR cavity is very short, we can describe it as a single effective mirror with frequency-independent (but complex) effective transmissivities and reflectivities (see Fig. 4.2) $\widetilde{\rho}$, $\widetilde{\tau}$ (for fields entering from the left) and $\widetilde{\rho}'$, $\widetilde{\tau}'$ (for fields entering from the right), and write the following equations for the annihilation (and creation, by taking Hermitian conjugates) operators of the electric field [see Appendix 4.7 for notations and definitions]:

$$j_\pm(\Omega) = \widetilde{\rho}'\, k_\pm(\Omega) + \widetilde{\tau}\, a_\pm(\Omega)\,, \qquad b_\pm(\Omega) = \widetilde{\tau}'\, k_\pm(\Omega) + \widetilde{\rho}\, a_\pm(\Omega)\,. \tag{4.4}$$

Among these four complex coefficients, $\widetilde{\rho}'$, the effective reflectivity from inside the arms, determines the (free) optical resonant frequency $\omega_0 + \widetilde{\Omega}$ of the system through the relation:

$$\widetilde{\rho}'\, e^{2i\widetilde{\Omega}L/c} = 1\,. \tag{4.5}$$

[Note that the carrier frequency ω_0 is assumed to be on resonance in the arm cavity, i.e., $\omega_0 L/\pi c =$ integer.] It turns out that if we keep fixed the arm-cavity circulating power I_c, the mirror mass m and the arm-cavity length L, the input–output relation $(\widetilde{a} - \widetilde{b})$ of the two-port system (4.4) is completely determined by $\widetilde{\rho}'$ alone or equivalently by the (complex) free optical resonant frequency $\widetilde{\Omega}$. To show this, we first redefine the ingoing and outgoing dark-port fields as

$$\widetilde{a}_\pm(\Omega) = \frac{\widetilde{\tau}}{|\widetilde{\tau}|}\, a_\pm(\Omega)\,, \qquad \widetilde{b}_\pm(\Omega) = \frac{\widetilde{\tau}^*}{|\widetilde{\tau}|}\, b_\pm(\Omega)\,. \tag{4.6}$$

This redefinition is always possible since we can freely choose another (common) reference point for the input and output fields. Secondly, using the Stokes relations given in the Appendix 4.8, we

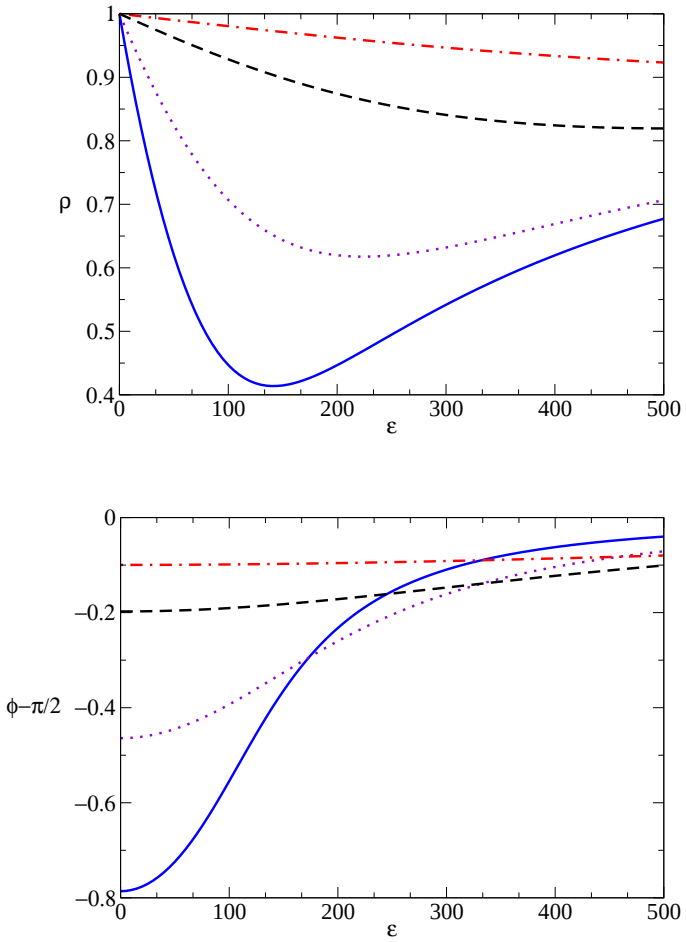

Figure 4.3: We plot ρ and $\phi - \pi/2$ versus ϵ for $\lambda = 2\pi \times 100\,\mathrm{Hz}$ (solid line), $2\pi \times 200\,\mathrm{Hz}$ (dotted line), $2\pi \times 500\,\mathrm{Hz}$ (dashed line) and $2\pi \times 1000\,\mathrm{Hz}$ (dashed-dotted line), having fixed $T = 0.033$.

derive the following equations:

$$j_{\pm}(\Omega) = \widetilde{\rho}'\, k_{\pm}(\Omega) + |\widetilde{\tau}|\, \widetilde{a}_{\pm}(\Omega) = \widetilde{\rho}'\, k_{\pm}(\Omega) + \sqrt{1 - |\widetilde{\rho}'|^2}\, \widetilde{a}_{\pm}(\Omega)\,, \tag{4.7}$$

$$\widetilde{b}_{\pm}(\Omega) = |\widetilde{\tau}|\, k_{\pm}(\Omega) - \widetilde{\rho}'^{*}\, \widetilde{a}_{\pm}(\Omega) = \sqrt{1 - |\widetilde{\rho}'|^2}\, k_{\pm}(\Omega) - \widetilde{\rho}'^{*}\, \widetilde{a}_{\pm}(\Omega)\,, \tag{4.8}$$

from which we infer that the output fields $\widetilde{b}_{\pm}(\Omega)$ depend only on $\widetilde{\rho}'$ or equivalently on $\widetilde{\Omega}$. Thus, if we vary the interferometer characteristic parameters T, ρ and ϕ such that $\widetilde{\rho}'$ is preserved, the input–output relation do not change. We refer to the transformation among the interferometer parameters having this property as the *scaling law*.

4.2.3 The scaling law in terms of interferometer parameters

In this section we give the explicit expression of the scaling law in terms of the practical parameters of the SR interferometer. We start by deriving the effective transmissivities and reflectivities $\widetilde{\rho}$, $\widetilde{\tau}$,

$\widetilde{\rho}'$ and $\widetilde{\tau}'$ in terms of T, $R = 1 - T$, ρ and ϕ. By imposing transmission and reflection conditions at the ITM and SRM, and propagating the fields between these mirrors (see Fig. 4.2), we get the following equations:

$$\tau\,\widetilde{a}_{\pm}(\Omega) + \rho\,e^{i\phi}\,y_{\pm}(\Omega) = x_{\pm}(\Omega)\,, \qquad \sqrt{T}\,k_{\pm}(\Omega) - \sqrt{R}\,e^{i\phi}\,x_{\pm}(\Omega) = y_{\pm}(\Omega)\,, \tag{4.9}$$

$$-\rho\,\widetilde{a}_{\pm}(\Omega) + \tau\,e^{i\phi}\,y_{\pm}(\Omega) = \widetilde{b}_{\pm}(\Omega)\,, \qquad \sqrt{R}\,k_{\pm}(\Omega) + \sqrt{T}\,e^{i\phi}\,x_{\pm}(\Omega) = j_{\pm}(\Omega)\,, \tag{4.10}$$

where the reflection and transmission coefficients of ITM and SRM are chosen to be real, with signs $\{+\sqrt{T}, -\sqrt{R}\}$, $\{+\tau, -\rho\}$ for light that impinges on a mirror from outside the SR cavity; and $\{+\sqrt{T}, +\sqrt{R}\}$, $\{+\tau, +\rho\}$ for light that impinges on a mirror from inside the SR cavity. Solving Eq. (4.9) for $x_{\pm}$ and $y_{\pm}$ in terms of $\widetilde{a}_{\pm}$ and $\widetilde{b}_{\pm}$, plugging these expressions into Eq. (4.10) and comparing with Eq. (4.4) we obtain:

$$\widetilde{\rho}' = \frac{\sqrt{R} + \rho\,e^{2i\phi}}{1 + \sqrt{R}\,\rho\,e^{2i\phi}}\,, \qquad \widetilde{\rho} = -\frac{\rho + \sqrt{R}\,e^{2i\phi}}{1 + \sqrt{R}\,\rho\,e^{2i\phi}}\,, \qquad \widetilde{\tau}' = \widetilde{\tau} = \frac{\tau\sqrt{T}e^{i\phi}}{1 + \sqrt{R}\,\rho\,e^{2i\phi}}\,. \tag{4.11}$$

It can be easily verified that these coefficients satisfy the Stokes relations (4.129)–(4.130). The scaling law can be obtained by imposing that $\widetilde{\rho}'$ does not vary. This gives

$$\frac{\sqrt{R} + \rho\,e^{2i\phi}}{1 + \sqrt{R}\,\rho\,e^{2i\phi}} = \text{const}\,. \tag{4.12}$$

Using Eq. (4.5), we derive the (complex) free optical resonant frequency in terms of T, ρ and ϕ:

$$\widetilde{\Omega} = \frac{ic}{2L}\log\frac{\sqrt{R} + \rho\,e^{2i\phi}}{1 + \sqrt{R}\,\rho\,e^{2i\phi}} \equiv -\lambda - i\,\epsilon\,, \tag{4.13}$$

where we trade $\widetilde{\Omega}$ for two real numbers, the resonant frequency λ and decay rate (inverse decay time) ϵ. For any choice of T, the parameters ρ and ϕ can be expressed in terms of λ and ϵ by solving Eq. (4.13) in terms of $\rho\,e^{2i\phi}$. The result is

$$\rho\,e^{2i\phi} = \frac{e^{-2\epsilon L/c}e^{2i\lambda L/c} - \sqrt{R}}{1 - \sqrt{R}e^{-2\epsilon L/c}e^{2i\lambda L/c}}\,. \tag{4.14}$$

In Fig. 4.3 we plot ρ (upper panel) and $\phi - \pi/2$ (lower panel) as functions of ϵ for four typical values of λ: $2\pi\times100\,\text{Hz}$ (solid lines), $2\pi\times200\,\text{Hz}$ (dotted lines), $2\pi\times500\,\text{Hz}$ (dashed lines) and $2\pi\times1000\,\text{Hz}$ (dashed-dotted lines), while fixing $T = 0.033$. In Fig. 4.4, we plot ρ and $\phi - \pi/2$ as functions of T, as obtained from Eq. (4.14), for three sets of optical resonances: $(\lambda, \epsilon) = (2\pi \times 194.5\,\text{Hz}, 2\pi \times 25.4\,\text{Hz})$, plotted in solid lines, which goes through the point $(T, \rho, \phi) = (0.033, 0.9, \pi/2 - 0.47)$ (marked by a square), which is the configuration selected in Chapters 2 and 3; $(\lambda, \epsilon) = (2\pi\times228.1\,\text{Hz}, 2\pi\times69.1\,\text{Hz})$, plotted in dotted lines, which goes through the point $(T, \rho, \phi) = (0.005, 0.96, \pi/2 - 0.06)$ (marked by

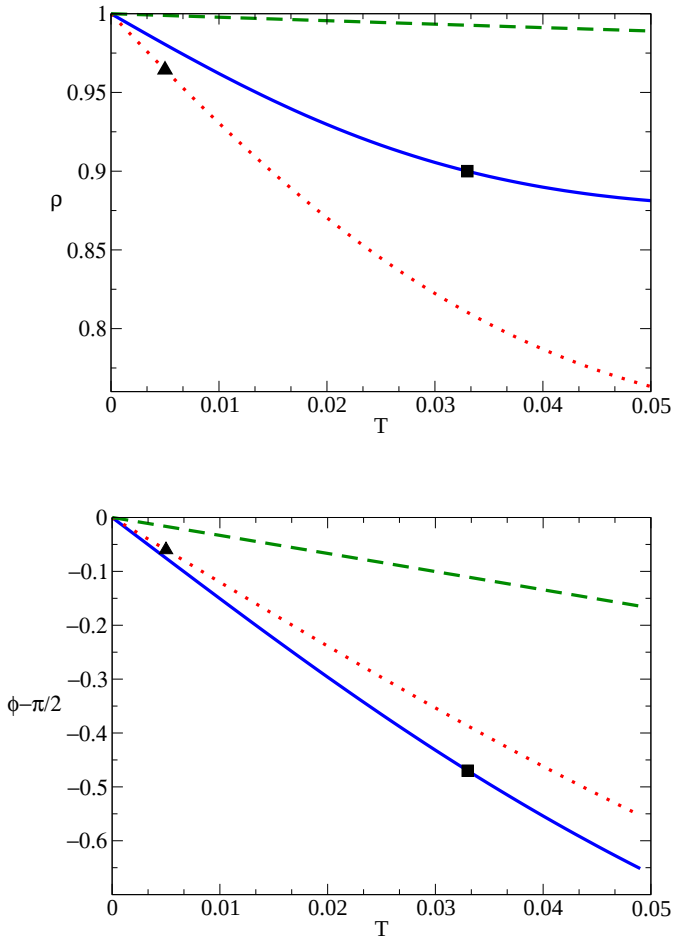

Figure 4.4: We plot ρ and $\phi - \pi/2$ versus T for three sets of optical resonances: $(\lambda, \epsilon) = (2\pi \times 194.48\,\mathrm{Hz}, 2\pi \times 25.42\,\mathrm{Hz})$ (solid lines), $(\lambda, \epsilon) = (2\pi \times 228.10\,\mathrm{Hz}, 2\pi \times 69.13\,\mathrm{Hz})$ (dotted lines) and $(\lambda, \epsilon) = (2\pi \times 900\,\mathrm{Hz}, 2\pi \times 30\,\mathrm{Hz})$ (dashed-dotted lines). We mark with a square and a triangle the special configurations selected in Chapters 2 and 3, with $(T, \rho, \phi) = (0.033, 0.9, \pi/2 - 0.47)$, and the current LIGO-II reference design [15], with $(T, \rho, \phi) = (0.005, 0.96, \pi/2 - 0.06)$, respectively.

a triangle), which is the current LIGO-II reference design [15]; and $(\lambda, \epsilon) = (2\pi \times 900\,\mathrm{Hz}, 2\pi \times 30\,\mathrm{Hz})$, plotted in dashed-dotted lines, which is an example of a configuration with narrowband sensitivity around a high frequency. As T, ρ and ϕ vary along these curves, the input-output relation is preserved.

As done in Chapter 2, we now expand all the quantities in T and keep only the first nontrivial order. [The accuracy of this procedure will be discussed in Sec. 4.5.] For the crucial quantity $\widetilde{\rho}'$ a straightforward calculations gives

$$\widetilde{\rho}' = 1 - \frac{T}{2} \frac{1 - \rho\, e^{2i\phi}}{1 + \rho\, e^{2i\phi}}\,. \tag{4.15}$$

So the scaling law at linear leading order in T is

$$T\,\frac{1-\rho\,e^{2i\phi}}{1+\rho\,e^{2i\phi}} = \text{const.}\,. \tag{4.16}$$

Moreover, applying Eq. (4.15) to Eq. (4.5), we derive the following expression for the (free) optical resonant frequency at leading order in T:

$$\widetilde{\Omega} = \frac{1}{i}\,\frac{1-\rho\,e^{2i\phi}}{1+\rho\,e^{2i\phi}}\,\frac{Tc}{4L} = \frac{-2\rho\sin 2\phi - i(1-\rho^2)}{1+\rho^2+2\rho\cos 2\phi}\,\gamma\,, \tag{4.17}$$

where $\gamma = Tc/4L$ is the half-bandwidth of the arm cavity. The frequency $\widetilde{\Omega}$ coincides with the frequency Ω_- introduced in Chapter 3. [Since in Chpater 3 we used the quadrature formalism, we had to introduce another (free) optical resonant frequency which they denoted by $\Omega_+ = -\Omega_-^*$. See discussion around Eq. (4.118) in Appendix 4.7.] Thus, at linear order in T we have:

$$\lambda = \frac{2\rho\,\gamma\,\sin 2\phi}{1+\rho^2+2\rho\cos 2\phi}\,, \qquad \epsilon = \frac{(1-\rho^2)\,\gamma}{1+\rho^2+2\rho\cos 2\phi}\,. \tag{4.18}$$

Finally, using Eqs. (4.129) and Eq. (4.15) we obtain the coefficients redefining the fields $a_\pm(\Omega)$ and $b_\pm(\Omega)$ in Eq. (4.6):

$$\frac{\widetilde{\tau}}{|\widetilde{\tau}|} = \frac{(1+\rho)\cos\phi + i(1-\rho)\sin\phi}{\sqrt{1+2\rho\cos 2\phi+\rho^2}}\,. \tag{4.19}$$

4.3 Input–output relation and noise spectral density in terms of characteristic parameters

4.3.1 Input–output relation

In this section we shall express the input–output relation of SR interferometer (at leading order in T) *only* in terms of the (free) optical resonant frequency, $\widetilde{\Omega} = -\lambda - i\,\epsilon$, and the parameter ι_c, defined by

$$\iota_c = \frac{8\omega_0\,I_c}{m\,L\,c}\,, \tag{4.20}$$

where the circulating power I_c is related to the input power at BS I_0 by

$$I_c = \frac{2}{T} I_0\,. \tag{4.21}$$

Using Eq. (4.19) and the results derived in Appendix 4.7 [see Eqs. (4.114), (4.116) and (4.117)] we transform Eqs. (4.6), which are given in terms of annihilation and creation operators, into equations

for quadrature fields:

$$\begin{pmatrix} \widetilde{a}_1 \\ \widetilde{a}_2 \end{pmatrix} = \frac{1}{\sqrt{1+2\rho\cos 2\phi+\rho^2}} \begin{pmatrix} (1+\rho)\cos\phi & -(1-\rho)\sin\phi \\ (1-\rho)\sin\phi & (1+\rho)\cos\phi \end{pmatrix} \begin{pmatrix} a_1 \\ a_2 \end{pmatrix} , \tag{4.22}$$

and

$$\begin{pmatrix} \widetilde{b}_1 \\ \widetilde{b}_2 \end{pmatrix} = \frac{1}{\sqrt{1+2\rho\cos 2\phi+\rho^2}} \begin{pmatrix} (1+\rho)\cos\phi & (1-\rho)\sin\phi \\ -(1-\rho)\sin\phi & (1+\rho)\cos\phi \end{pmatrix} \begin{pmatrix} b_1 \\ b_2 \end{pmatrix} . \tag{4.23}$$

Inserting the above expressions into Eqs. (2.20)–(2.24) in Chapter 2, and using Eqs. (4.18)–(4.21), we get the input–output relation depending only on the characteristic or scaling invariant quantities λ, ϵ and ι_c:

$$\begin{pmatrix} \widetilde{b}_1 \\ \widetilde{b}_2 \end{pmatrix} = \frac{1}{\widetilde{M}^{(1)}} \left\{ \begin{pmatrix} \widetilde{C}_{11}^{(1)} & \widetilde{C}_{12}^{(1)} \\ \widetilde{C}_{21}^{(1)} & \widetilde{C}_{22}^{(1)} \end{pmatrix} \begin{pmatrix} \widetilde{a}_1 \\ \widetilde{a}_2 \end{pmatrix} + \begin{pmatrix} \widetilde{D}_1^{(1)} \\ \widetilde{D}_2^{(1)} \end{pmatrix} \frac{h}{h_{\rm SQL}} \right\} , \tag{4.24}$$

where we define:

$$\widetilde{M}^{(1)} = \left[\lambda^2 - (\Omega+i\epsilon)^2\right]\, \Omega^2 - \lambda\,\iota_c\,, \tag{4.25}$$

and

$$\widetilde{C}_{11}^{(1)} = \widetilde{C}_{22}^{(1)} = \Omega^2(\Omega^2-\lambda^2+\epsilon^2) + \lambda\,\iota_c\,, \qquad \widetilde{C}_{12}^{(1)} = -2\epsilon\,\lambda\,\Omega^2\,, \qquad \widetilde{C}_{21}^{(1)} = 2\epsilon\,\lambda\,\Omega^2 - 2\epsilon\,\iota_c\,, \tag{4.26}$$

$$\widetilde{D}_1^{(1)} = -2\lambda\,\sqrt{\epsilon\,\iota_c}\,\Omega\,, \qquad \widetilde{D}_2^{(1)} = 2(\epsilon - i\Omega)\,\Omega\,\sqrt{\epsilon\,\iota_c}\,, \tag{4.27}$$

and

$$h_{\rm SQL} \equiv \sqrt{\frac{8\hbar}{m\Omega^2 L^2}}\,, \tag{4.28}$$

is the free-mass SQL for the gravitational strain $h(\Omega)$ in LIGO detectors [8]. The quantity ι_c has the dimension of a frequency to the third power (Ω^3). Since it is proportional to the laser power circulating in the arm cavity, it provides a measure of radiation-pressure strength. In order that radiation pressure influence interferometer dynamics in the frequency range interesting for LIGO, we need

$$\iota_c \gtrsim \Omega_{\rm GW}^3 \qquad \Rightarrow \qquad I_c \gtrsim \frac{m\,L\,c\,\Omega_{\rm GW}^3}{8\omega_0}\,, \tag{4.29}$$

which gives $I_c \gtrsim 100$ kW for typical LIGO-II–parameters and $\Omega_{\rm GW} = 2\pi \times 100\,{\rm Hz}$. The input–output relation (4.24) is more explicit in representing interferometer properties than that given in Chapter 2, and can be quite useful in the process of optimizing the SR optical configuration. From the last term of Eq. (4.24) we observe that as long as the SR oscillation frequency $\lambda \neq 0$, both quadrature fields contain the GW signal. Moreover, the resonant structure, discussed in Chapter 2, is readily displayed in the denominator of Eq. (4.24), given by Eq. (4.25). As we shall see in

Sec. 4.4, the shot noise and radiation-pressure noise, and the fact they are correlated, can also be easily worked out from Eq. (4.24).

In Chapter 3 we found that one of the SR resonant frequencies, obtained by imposing $\widetilde{M}^{(1)} = 0$, has always a positive imaginary part, corresponding to an instability. This instability has an origin similar to the dynamical instability induced in a detuned Fabry-Perot cavity by the radiation-pressure force acting on the mirrors [9, 11]. To suppress it, we proposed (in Chapter 3) a feedback control system that does not compromise the GW interferometer sensitivity. Although the model we used to describe the servo system may be realistic for an all-optical control loop, this might not be the case if an electronic servo system is implemented. However, results obtained in Ref. [16] would suggest it does. In any case, a more thorough studying should be pursued to fully clarify this issue. In this chapter, we always assume that an appropriate control system of the kind proposed in Chapter 3 is used.

Finally, when $\lambda = 0$ (which corresponds to either $\rho = 0$, or $\rho \neq 0$, $\phi = 0, \pi/2$) Eq. (4.24) simplifies to

$$\begin{pmatrix} \widetilde{b}_1 \\ \widetilde{b}_2 \end{pmatrix} = e^{2i\beta'} \begin{pmatrix} 1 & 0 \\ -\mathcal{K}' & 1 \end{pmatrix} \begin{pmatrix} \widetilde{a}_1 \\ \widetilde{a}_2 \end{pmatrix} + e^{i\beta'} \sqrt{2\mathcal{K}'} \begin{pmatrix} 0 \\ 1 \end{pmatrix} \frac{h}{h_{\rm SQL}} \,, \tag{4.30}$$

which exactly coincides with Eq. (16) of Ref. [7] for a conventional interferometer, but where

$$\beta' = \arctan\left(\frac{\Omega}{\epsilon}\right) \,, \qquad \mathcal{K}' = \frac{2\,\epsilon\,\iota_c}{\Omega^2\,(\Omega^2+\epsilon^2)} \,. \tag{4.31}$$

The simple relations (4.30) and (4.31) nicely unify the SR optical configuration $\phi = 0, \pi/2$ (denoted by ESR/ERSE in Chapter 2) with the conventional-interferometer optical configuration.

4.3.2 Noise spectral density

The noise spectral density can be calculated as follows (see Ref. [7] and Chapter 2). Assuming that the quadrature $\widetilde{b}_\zeta = \widetilde{b}_1 \sin\zeta + \widetilde{b}_2 \cos\zeta$ is measured, and using Eq. (4.24), we can express the interferometer noise as an equivalent GW Fourier component:

$$h_n \equiv h_{\rm SQL}\, \Delta\widetilde{b}_\zeta \,, \tag{4.32}$$

where

$$\Delta\widetilde{b}_\zeta = \frac{(\widetilde{C}^{(1)}_{11} \sin\zeta + \widetilde{C}^{(1)}_{21} \cos\zeta)\,\widetilde{a}_1 + (\widetilde{C}^{(1)}_{12} \sin\zeta + \widetilde{C}^{(1)}_{22} \cos\zeta)\,\widetilde{a}_2}{\widetilde{D}^{(1)}_1 \sin\zeta + \widetilde{D}^{(1)}_2 \cos\zeta} \,. \tag{4.33}$$

Then the (single-sided) spectral density $S_h^\zeta(f)$, with $f = \Omega/2\pi$, associated with the noise h_n can be computed by the formula [see Eq. (22) of Ref. [7]]:

$$2\pi\,\delta(\Omega-\Omega')\,S_h^\zeta(f) = \langle {\rm in}| h_n(\Omega)\,h_n^\dagger(\Omega') + h_n^\dagger(\Omega')\,h_n(\Omega)|{\rm in}\rangle \,. \tag{4.34}$$

Assuming that the input of the whole SR interferometer is in its vacuum state, i.e., $|\mathrm{in}\rangle = |0_{\tilde{a}}\rangle$, and using

$$\langle 0_{\tilde{a}}|\widetilde{a}_i(\Omega)\,\widetilde{a}_j^\dagger(\Omega') + \widetilde{a}_j^\dagger(\Omega')\,\widetilde{a}_i(\Omega)|0_{\tilde{a}}\rangle = 2\pi\,\delta(\Omega-\Omega')\,\delta_{ij}\,, \tag{4.35}$$

we find that Eq. (4.34) can be recast in the simple form (note that $\widetilde{C}_{ij}^{(1)} \in \Re$):

$$S_h^\zeta = h_{\mathrm{SQL}}^2\,\frac{\left(\widetilde{C}_{11}^{(1)}\,\sin\zeta + \widetilde{C}_{21}^{(1)}\,\cos\zeta\right)^2 + \left(\widetilde{C}_{12}^{(1)}\,\sin\zeta + \widetilde{C}_{22}^{(1)}\,\cos\zeta\right)^2}{\left|\widetilde{D}_1^{(1)}\,\sin\zeta + \widetilde{D}_2^{(1)}\,\cos\zeta\right|^2}\,. \tag{4.36}$$

Plugging into the above expression Eqs. (4.26), (4.27) we get the very explicit (and very simple!) expression for the noise spectral density:

$$\begin{aligned} S_h^\zeta \;=\; & \frac{\Omega^2 h_{\mathrm{SQL}}^2}{4\epsilon\iota_c\left[\Omega^2\cos^2\zeta + (\epsilon\cos\zeta - \lambda\sin\zeta)^2\right]}\Bigg\{\left[(\Omega+\lambda)^2+\epsilon^2\right]\left[(\Omega-\lambda)^2+\epsilon^2\right] + \frac{2\iota_c}{\Omega^2}\big[\Omega^2(\lambda-\epsilon\sin 2\zeta) \\ - \;& \lambda(\epsilon^2+\lambda^2+2\epsilon^2\cos 2\zeta) - \epsilon(\epsilon^2-\lambda^2)\sin 2\zeta\big] + \frac{\iota_c^2}{\Omega^4}\left[2\epsilon^2(1+\cos 2\zeta) - 2\epsilon\lambda\sin 2\zeta + \lambda^2\right]\Bigg\}\,. \end{aligned} \tag{4.37}$$

4.4 Optomechanical dynamics in terms of characteristic parameters

The scaling laws (4.14), (4.16) could have been equivalently derived by imposing the invariance of the optomechanical dynamics (see Chapter 3). In this section we express all the relevant quantities characterizing the SR optomechanical dynamics in terms of the scaling invariant parameters λ, ϵ and ι_c.

4.4.1 Radiation-pressure force

In Chapter 2 we assumed that SR interferometers can be artificially divided into two linearly coupled, but otherwise independent subsystems: the probe $\mathcal{P}$, which is subject to the external classical GW force G and the detector $\mathcal{D}$, which yields a classical output Z. The Hamiltonian of the overall system is given by [see Sec. 2.2.2 for notations and definitions]:

$$H = H_{\mathcal{P}} + H_{\mathcal{D}} - x\,(F+G)\,, \tag{4.38}$$

where x is the operator describing the antisymmetric mode of motion of four arm-cavity mirrors and F is the radiation-pressure or back-action force the detector applies on the probe. In the Heisenberg picture, using the superscript (1) for operators evolving under the total Hamiltonian H, and superscript (0) for operators evolving under the free Hamiltonian of the detector $H_{\mathcal{D}}$, the

equations of motion in Fourier domain read (Chapter 2):

$$Z^{(1)}(\Omega) = Z^{(0)}(\Omega) + R_{ZF}(\Omega)\, x^{(1)}(\Omega)\,, \tag{4.39}$$

$$F^{(1)}(\Omega) = F^{(0)}(\Omega) + R_{FF}(\Omega)\, x^{(1)}(\Omega)\,, \tag{4.40}$$

$$x^{(1)}(\Omega) = L\, h(\Omega) + R_{xx}(\Omega)\, F^{(1)}(\Omega)\,. \tag{4.41}$$

where $R_{xx}(\Omega) = -4/m/\Omega^2$, $h(\Omega)$ is the gravitational strain [see Eq. (3.15) in Chapter 3] related to the GW force in Fourier domain by $G(\Omega) = -(m/4)\, L\, \Omega^2\, h(\Omega)$, while the various Fourier-domain susceptibilities are defined by

$$R_{AB}(\Omega) \equiv \frac{i}{\hbar} \int_0^{+\infty} d\tau\, e^{i\Omega\tau}\, [A(0), B(-\tau)]\,, \tag{4.42}$$

where $[A(t), B(t')]$ is the commutator between operators A and B. As discussed in Sec. 4.1, LIGO-II has been planned to work at a laser power for which shot noise and radiation-pressure noise are comparable in the observational band 40–200 Hz. In Sec. 2.3.1 of this thesis, the radiation-pressure force was explicitly derived. Here, we want to express it, and the other crucial quantities entering the equations of motion (4.39)–(4.41) in terms of the characteristic parameters λ, ϵ and

$$\mathcal{I}_c = m\, \iota_c = \frac{8\omega_0\, I_c}{L\, c}\,. \tag{4.43}$$

Using Eqs. (4.18) a straightforward calculation gives the rather simple expressions:

$$F^{(0)}(\Omega) = \sqrt{\frac{\epsilon \mathcal{I}_c\, \hbar}{2}}\, \frac{(i\Omega - \epsilon)\, \widetilde{a}_1(\Omega) + \lambda\, \widetilde{a}_2(\Omega)}{(\Omega - \lambda + i\epsilon)\, (\Omega + \lambda + i\epsilon)}\,, \tag{4.44}$$

$$Z_1^{(0)}(\Omega) = \frac{(\lambda^2 - \epsilon^2 - \Omega^2)\, \widetilde{a}_1(\Omega) + 2\lambda\, \epsilon\, \widetilde{a}_2(\Omega)}{(\Omega - \lambda + i\epsilon)\, (\Omega + \lambda + i\epsilon)}\,, \tag{4.45}$$

$$Z_2^{(0)}(\Omega) = \frac{-2\lambda\, \epsilon\, \widetilde{a}_1(\Omega) + (\lambda^2 - \epsilon^2 - \Omega^2)\, \widetilde{a}_2(\Omega)}{(\Omega - \lambda + i\epsilon)\, (\Omega + \lambda + i\epsilon)}\,, \tag{4.46}$$

$$R_{Z_1 F}(\Omega) = \sqrt{\frac{\epsilon \mathcal{I}_c}{2\hbar}}\, \frac{\lambda}{(\Omega - \lambda + i\epsilon)\, (\Omega + \lambda + i\epsilon)}\,, \tag{4.47}$$

$$R_{Z_2 F}(\Omega) = -\sqrt{\frac{\epsilon \mathcal{I}_c}{2\hbar}}\, \frac{(\epsilon - i\Omega)}{(\Omega - \lambda + i\epsilon)\, (\Omega + \lambda + i\epsilon)}\,. \tag{4.48}$$

The optical pumping field in detuned Fabry-Perot resonator converts the free test mass into an optical spring having very low intrinsic noise [11]. The ponderomotive rigidity $K_{\rm pond.\,rig.}$, which characterizes the optomechanical dynamics in SR interferometers, is also responsible of the beating

of the free mass SQL [see Sec. 3.3.3 of this thesis] and its explicit expression is given by

$$K_{\rm pond}(\Omega) = -R_{FF}(\Omega) = -\frac{\mathcal{I}_c}{4}\,\frac{\lambda}{(\Omega-\lambda+i\epsilon)\,(\Omega+\lambda+i\epsilon)}\,. \tag{4.49}$$

As long as the free optical resonant frequency λ differs from zero, $K_{\rm pond}$ is always non-vanishing. Moreover, in order to have a (nearly) real mechanical resonant frequency at low frequency, we require $\lambda < 0$ [as can be obtained by imposing $K_{\rm pond}(\Omega = 0) > 0$.]

4.4.2 Equivalence between noise correlations and change of dynamics

As derived in Chapters 2 and 3, the output of SR interferometers, when the first or second quadrature of the outgoing dark-port field is measured, can also be written as

$$\mathcal{O}_i(\Omega) = \mathcal{Z}_i(\Omega) + R_{xx}(\Omega)\,\left[\mathcal{F}_i(\Omega) + G(\Omega)\right]\,, \qquad i = 1,2 \tag{4.50}$$

where:

$$\mathcal{Z}_i(\Omega) = \frac{Z_i^{(0)}(\Omega)}{R_{Z_iF}(\Omega)}\,, \quad \mathcal{F}(\Omega) = F^{(0)}(\Omega) - R_{FF}(\Omega)\frac{Z_i^{(0)}(\Omega)}{R_{Z_iF}(\Omega)}\,, \qquad i = 1,2\,. \tag{4.51}$$

Expressing these quantities in scaling-invariant form [here the first or second quadrature refers to $\widetilde{b}_1$ or $\widetilde{b}_2$, so the $Z_{1,2}$ discussed here are related to those in Chapter 2 by the rotation (4.23)], we get:

$$\mathcal{Z}_1(\Omega) = \sqrt{\frac{2\hbar}{\epsilon\mathcal{I}_c}}\,\frac{1}{\lambda}\,\left[(\lambda^2-\epsilon^2-\Omega^2)\,\widetilde{a}_1(\Omega) + 2\epsilon\,\lambda\,\widetilde{a}_2(\Omega)\right]\,, \tag{4.52}$$

$$\mathcal{Z}_2(\Omega) = \sqrt{\frac{2\hbar}{\epsilon\mathcal{I}_c}}\,\frac{1}{(\epsilon-i\Omega)}\,\left[2\epsilon\,\lambda\,\widetilde{a}_1(\Omega) - (\lambda^2-\epsilon^2-\Omega^2)\,\widetilde{a}_2(\Omega)\right]\,, \tag{4.53}$$

and

$$\mathcal{F}_1(\Omega) = \sqrt{\frac{\mathcal{I}_c\,\hbar}{8\,\epsilon}}\,\widetilde{a}_1(\Omega)\,, \tag{4.54}$$

$$\mathcal{F}_2(\Omega) = \sqrt{\frac{\mathcal{I}_c\,\hbar}{8\,\epsilon}}\,\frac{1}{(\epsilon-i\Omega)}\,\left[2\epsilon\,\widetilde{a}_1(\Omega) - \lambda\,\widetilde{a}_2(\Omega))\right]\,. \tag{4.55}$$

The form of Eq. (4.50), along with the fact that the operators $\mathcal{Z}_i(\Omega)$ and $\mathcal{F}_i(\Omega)$ are proportional to $1/\sqrt{I_c}$ and $\sqrt{I_c}$, made it natural to refer to them (see Chapter 3) as *effective* output fluctuation and *effective* radiation-pressure force. The quantum noise embodied in $\mathcal{Z}_i(\Omega)$ is the shot noise, while the quantum noise described by $\mathcal{F}_i(\Omega)$ is the radiation-pressure or back-action noise. The operators $\mathcal{Z}_i(\Omega)$, $\mathcal{F}_i(\Omega)$ satisfy the following commutation relations (see Ref. [8] and Chapters 2 and 3):

$$[\mathcal{Z}_i(\Omega), \mathcal{Z}_i^\dagger(\Omega')] = 0 = [\mathcal{F}_i(\Omega), \mathcal{F}_i^\dagger(\Omega')]\,, \qquad [\mathcal{Z}_i(\Omega), \mathcal{F}_i^\dagger(\Omega')] = -2\pi\,i\,\hbar\,\delta(\Omega-\Omega')\,, \qquad i = 1,2\,. \tag{4.56}$$

If the output quadrature i is measured, the noise spectral density (4.36), written in terms of the operators $\mathcal{Z}_i$ and $\mathcal{F}_i$, reads [8]:

$$S_{h,i}(\Omega) = \frac{1}{L^2}\left\{S_{\mathcal{Z}_i\mathcal{Z}_i}(\Omega) + 2\mathcal{R}_{xx}(\Omega)\,\Re\left[S_{\mathcal{F}_i\mathcal{Z}_i}(\Omega)\right] + \mathcal{R}^2_{xx}(\Omega)\,S_{\mathcal{F}_i\mathcal{F}_i}(\Omega)\right\}, \tag{4.57}$$

where the (one-sided) cross spectral density of two operators is expressible, by analogy with Eq. (4.34), as

$$2\pi\,\delta\left(\Omega-\Omega'\right)\,S_{\mathcal{A}\mathcal{B}}(\Omega) = \langle 0_{\tilde{a}}|\mathcal{A}(\Omega)\mathcal{B}^\dagger(\Omega') + \mathcal{B}^\dagger(\Omega')\mathcal{A}(\Omega)|0_{\tilde{a}}\rangle\,. \tag{4.58}$$

In Eq. (4.57), the terms containing $S_{\mathcal{Z}_i\mathcal{Z}_i}$, $S_{\mathcal{F}_i\mathcal{F}_i}$ and $\Re\left[S_{\mathcal{F}_i\mathcal{Z}_i}\right]$ should be identified as shot noise, radiation-pressure noise and a term proportional to the correlation between the two noises, respectively [8]. The noise spectral densities expressed in terms of the scaling invariant quantities λ, ϵ and $\mathcal{I}_c$ are rather simple and read:

$$S_{\mathcal{Z}_1\mathcal{Z}_1}(\Omega) = \frac{2\hbar}{\mathcal{I}_c}\,\frac{\left[(\Omega+\lambda)^2+\epsilon^2\right]\left[(\Omega-\lambda)^2+\epsilon^2\right]}{\epsilon\,\lambda^2}, \tag{4.59}$$

$$S_{\mathcal{Z}_2\mathcal{Z}_2}(\Omega) = \frac{2\hbar}{\mathcal{I}_c}\,\frac{\left[(\Omega+\lambda)^2+\epsilon^2\right]\left[(\Omega-\lambda)^2+\epsilon^2\right]}{\epsilon\,(\epsilon^2+\Omega^2)}, \tag{4.60}$$

$$S_{\mathcal{F}_1\mathcal{F}_1}(\Omega) = \frac{\hbar\mathcal{I}_c}{8\,\epsilon}, \tag{4.61}$$

$$S_{\mathcal{F}_2\mathcal{F}_2}(\Omega) = \frac{\hbar\mathcal{I}_c}{8\,\epsilon}\,\frac{(4\epsilon^2+\lambda^2)}{\epsilon^2+\Omega^2}, \tag{4.62}$$

$$S_{\mathcal{Z}_1\mathcal{F}_1}(\Omega) = \hbar\,\frac{(\lambda^2-\epsilon^2-\Omega^2)}{2\epsilon\,\lambda}, \tag{4.63}$$

$$S_{\mathcal{Z}_2\mathcal{F}_2}(\Omega) = \hbar\,\frac{\lambda\,(\lambda^2+3\epsilon^2-\Omega^2)}{2\epsilon\,(\epsilon^2+\Omega^2)}. \tag{4.64}$$

Note that in our case $S_{\mathcal{F}_i\mathcal{Z}_i}$ is real, thus $S_{\mathcal{F}_i\mathcal{Z}_i} = S_{\mathcal{Z}_i\mathcal{F}_i}$. It is straightforward to check that the following relation is also satisfied:

$$S_{\mathcal{Z}_i\mathcal{Z}_i}(\Omega)\,S_{\mathcal{F}_i\mathcal{F}_i}(\Omega) - S_{\mathcal{Z}_i\mathcal{F}_i}(\Omega)\,S_{\mathcal{F}_i\mathcal{Z}_i}(\Omega) = \hbar^2\,, \qquad i=1,2\,. \tag{4.65}$$

Since in SR interferometers $S_{\mathcal{Z}_i\mathcal{F}_i} \neq 0$, the noise spectral density $S_{h,i}$ is not limited by the free-mass SQL for GW interferometers ($S_{\rm SQL} \equiv h^2_{\rm SQL}$), as derived and discussed in Chapters 2 and 3.

We want to show now that cross correlations between shot noise and radiation-pressure noise are equivalent to some modification of the optomechanical dynamics of the system composed of probe and detector, as originally pointed out by Syrtsev and Khalili in Sec. III of Ref. [14]. More specifically, we shall show that for linear quantum measurement devices, at the cost of modifying

the optomechanical dynamics, the measurement process can be described in terms of new operators $\mathcal{Z}'$ and $\mathcal{F}'$ with zero cross correlation.

In Chapter 2 the authors found that the most generic transformation which preserves the commutation relations (4.56) is of the form [see Eq. (2.25) in Chapter 2]:

$$\begin{pmatrix} \mathcal{Z}_i'(\Omega) \\ \mathcal{F}_i'(\Omega) \end{pmatrix} = e^{i\alpha} \begin{pmatrix} L_{11} & L_{12} \\ L_{21} & L_{22} \end{pmatrix} \begin{pmatrix} \mathcal{Z}_i(\Omega) \\ \mathcal{F}_i(\Omega) \end{pmatrix}, \tag{4.66}$$

with α, $L_{ij} \in \Re$ and $\det L_{ij} = 1$. Under this transformation the output (4.50) becomes:

$$\mathcal{O}_i(\Omega) = e^{-i\alpha}\,[L_{22} - R_{xx}(\Omega)\,L_{21}]\;\mathcal{Z}_i'(\Omega) + e^{-i\alpha}\,[-L_{12} + R_{xx}(\Omega)\,L_{11}]\;\mathcal{F}_i'(\Omega) + R_{xx}(\Omega)\,G(\Omega)\,. \tag{4.67}$$

By imposing that the system responds in the same way to electromagnetic and gravitational forces, $\mathcal{F}'(\Omega)$ and $G(\Omega)$, we find the two conditions: $e^{i\alpha} = \pm 1$ and $R_{xx}(\Omega)\,(L_{11} \mp 1) = L_{12}$. The transformation we have to apply so that the correlations between new fields $\mathcal{Z}_i'(\Omega)$ and $\mathcal{F}_i'(\Omega)$ are zero, give the following set of equations:

$$L \begin{pmatrix} S_{\mathcal{Z}_i\mathcal{Z}_i}(\Omega) & S_{\mathcal{Z}_i\mathcal{F}_i}(\Omega) \\ S_{\mathcal{F}_i\mathcal{Z}_i}(\Omega) & S_{\mathcal{F}_i\mathcal{F}_i}(\Omega) \end{pmatrix} L^t = \begin{pmatrix} S_{\mathcal{Z}_i'\mathcal{Z}_i'}(\Omega) & 0 \\ 0 & S_{\mathcal{F}_i'\mathcal{F}_i'}(\Omega) \end{pmatrix}. \tag{4.68}$$

When $S_{\mathcal{Z}\mathcal{F}} = S_{\mathcal{F}\mathcal{Z}} \in \Re$, as it happens in SR interferometers, the above conditions can be solved in infinite ways. A simple solution, suggested by Syrtsev and Khalili [14], is obtained by taking $\alpha = 0$ and $L_{11} = 1$. In this case, a straightforward calculation gives: $L_{12} = 0$, $L_{21} = -S_{\mathcal{Z}_i\mathcal{F}_i}/S_{\mathcal{Z}_i\mathcal{Z}_i}$ and $L_{22} = 1$. The output becomes:

$$\mathcal{O}_i'(\Omega) = \mathcal{Z}_i'(\Omega) + \chi_i^{\rm eff}(\Omega)\;[\mathcal{F}_i'(\Omega) + G(\Omega)]\;, \qquad \mathcal{O}_i'(\Omega) = \mathcal{O}_i(\Omega)\,\frac{R_{xx}(\Omega)}{\chi_i^{\rm eff}(\Omega)}\,, \tag{4.69}$$

where $\chi_i^{\rm eff}$, the *effective* susceptibility, is given by

$$\chi_i^{\rm eff}(\Omega) = \frac{R_{xx}(\Omega)}{1 + R_{xx}(\Omega)\,S_{\mathcal{Z}_i\mathcal{F}_i}(\Omega)/S_{\mathcal{Z}_i\mathcal{Z}_i}(\Omega)}\,. \tag{4.70}$$

The spectral densities of the new operators $\mathcal{Z}_i'$ and $\mathcal{F}_i'$ are

$$S_{\mathcal{Z}_i'\mathcal{Z}_i'}(\Omega) = S_{\mathcal{Z}_i\mathcal{Z}_i}(\Omega)\,, \qquad S_{\mathcal{F}_i'\mathcal{F}_i'}(\Omega) = S_{\mathcal{F}_i\mathcal{F}_i}(\Omega) - \frac{S^2_{\mathcal{Z}_i\mathcal{F}_i}(\Omega)}{S_{\mathcal{Z}_i\mathcal{Z}_i}(\Omega)}\,, \qquad i = 1, 2\,, \tag{4.71}$$

with

$$S_{\mathcal{F}_1'\mathcal{F}_1'}(\Omega) = \frac{\hbar\mathcal{I}_c}{2}\,\frac{\epsilon\,\lambda^2}{[(\Omega+\lambda)^2+\epsilon^2]\,[(\Omega-\lambda)^2+\epsilon^2]}\,, \tag{4.72}$$

$$S_{\mathcal{F}_2'\mathcal{F}_2'}(\Omega) = \frac{\hbar\mathcal{I}_c}{2}\,\frac{\epsilon(\epsilon^2+\Omega^2)}{[(\Omega+\lambda)^2+\epsilon^2]\,[(\Omega-\lambda)^2+\epsilon^2]}\,. \tag{4.73}$$

These new operators satisfy the condition [see Eq. (4.65)]:

$$S_{\mathcal{Z}_i'\mathcal{Z}_i'}(\Omega)\,S_{\mathcal{F}_i'\mathcal{F}_i'}(\Omega) = \hbar^2\,, \qquad i=1,2\,. \tag{4.74}$$

4.4.3 Equivalence to a single detuned cavity and frequency-dependent rigidity

At the end of Sec. 4.2.2 we discussed under which assumptions radiation-pressure effects were included in the description of SR interferometers in Chapters 2 and 3. There, the authors assumed that radiation pressure forces acting on ETM and ITM are equal, and disregarded ETM and ITM motions during the light round-trip time in arm cavities. In this case the ITM and SRM can be considered fixed, and as shown in Sec. 4.2.1 it is possible to map the SR optical configuration to a three-mirror cavity with only the ETM movable. We shall see explicitly in this section that, since the very short SR cavity can be regarded as a single effective mirror, we can further map the SR interferometer to a single-detuned cavity with only the ETM movable, which is exactly the system that Khalili discussed in Ref. [10]. [More specifically, the single-detuned cavity has (complex) free optical resonant frequency $\omega_0-\lambda-i\epsilon$, ETM mass $\mu_{\rm arm}=m_{\rm arm}/2=m$, and circulating power $I_{\rm arm}=2I_c$. See Eqs. (4.1), (4.2) and (4.3).]

If the output quadrature i is measured, the noise spectral density expressed in terms of the operators $\mathcal{Z}_i'$ and $\mathcal{F}_i'$, can be written as

$$S_{h,i}(\Omega) = \frac{R_{xx}^2(\Omega)}{L^2}\,\left[\left[\chi_i^{\rm eff}(\Omega)\right]^{-2}\,S_{\mathcal{Z}_i'\mathcal{Z}_i'}(\Omega)+S_{\mathcal{F}_i'\mathcal{F}_i'}(\Omega)\right]\,. \tag{4.75}$$

In order to make explicit the connection with Ref. [10], we evaluate the noise spectral density for $x_{\rm GW}\equiv L\,h/2$ and we denote it by $S_{x_{\rm GW}}$. It reads:

$$S_{x_{\rm GW},i}(\Omega) = \frac{1}{\mu_{\rm arm}^2\,\Omega^4}\,\left\{\left[\frac{\chi_i^{\rm eff}(\Omega)}{4}\right]^{-2}\,\frac{S_{\mathcal{Z}_i'\mathcal{Z}_i'}(\Omega)}{4}+4S_{\mathcal{F}_i'\mathcal{F}_i'}(\Omega)\right\}\,, \tag{4.76}$$

where as discussed above $\mu_{\rm arm}=m_{\rm arm}/2=m$. By rewriting the generalized susceptibility into the form,

$$\frac{\chi_i^{\rm eff}(\Omega)}{4} = \frac{1}{-\mu_{\rm arm}\,\Omega^2+4\,K_i^{\rm eff}(\Omega)}\,, \qquad i=1,2\,, \tag{4.77}$$

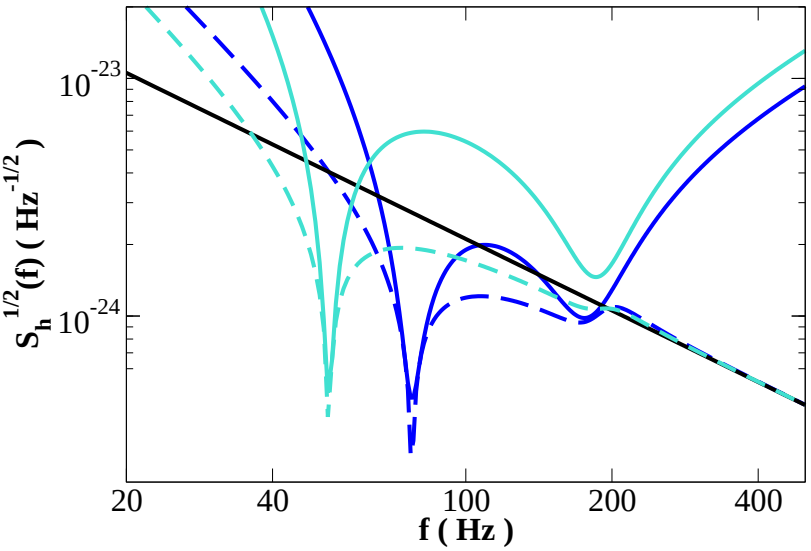

Figure 4.5: Plot of $\sqrt{S_{h,2}}$ (continuous lines) and $\sqrt{S_{h,2}^{\rm min}}$ (dashed lines) versus frequency f for $T = 0.033$, $\epsilon = 2\pi \times 25.0\,{\rm Hz}$, $\lambda = 2\pi \times 191.3\,{\rm Hz}$, and two different values of the laser power circulating in the arm cavities: $I_c = 300$ kW (lighter-color lines) and $I_c = 600$ kW (darker-color lines). The free-mass SQL line (black straight line) is also shown for comparison.

we introduce, as Khalili also did [10], the *effective* rigidity $K_i^{\rm eff}(\Omega)$, defined by

$$K_i^{\rm eff}(\Omega) \equiv \frac{S_{\mathcal{Z}_i\mathcal{F}_i}(\Omega)}{S_{\mathcal{Z}_i\mathcal{Z}_i}(\Omega)}\,. \tag{4.78}$$

More explicitly,

$$K_1^{\rm eff}(\Omega) = \frac{\mathcal{I}_c\lambda}{4}\,\frac{-\epsilon^2+\lambda^2-\Omega^2}{[(\Omega-\lambda)^2+\epsilon^2]\,[(\Omega+\lambda)^2+\epsilon^2]}\,, \tag{4.79}$$

$$K_2^{\rm eff}(\Omega) = \frac{\mathcal{I}_c\lambda}{4}\,\frac{3\,\epsilon^2+\lambda^2-\Omega^2}{[(\Omega-\lambda)^2+\epsilon^2]\,[(\Omega+\lambda)^2+\epsilon^2]}\,. \tag{4.80}$$

Those expressions, in particular Eqs. (4.76), (4.80) agree with those derived by Khalili [10] for single detuned cavity [see Eqs. (19) and (21) in Ref. [10]] if we make the following identifications (this chapter $\rightarrow$ Khalili): $\lambda \rightarrow \delta$, $\epsilon \rightarrow \gamma$, $2L\,I_{\rm arm}/c \equiv 4L\,I_c/c \rightarrow \mathcal{E}$ (energy stored in the single cavity), $\chi_i^{\rm eff}/4 \rightarrow \chi$, and $4K_i^{\rm eff} \rightarrow K$. Note that in Ref. [10] it is always assumed that the second quadrature is measured.

The description of the measurement system in terms of the uncorrelated fields, $\mathcal{Z}_i'$ and $\mathcal{F}_i'$, yields another way of understanding why in SR interferometers the free mass SQL, $S_h^{\rm SQL} \equiv h_{\rm SQL}^2$, loses its significance. Indeed, by using Eq. (4.74), we get $S_{\mathcal{Z}_i'\mathcal{Z}_i'} = \hbar^2/S_{\mathcal{F}_i'\mathcal{F}_i'}$. Plugging this expression into

Eq. (4.75), minimizing with respect to $S_{\mathcal{F}'_i\mathcal{F}'_i}$, we obtain,

$$S^{\rm min}_{\mathcal{F}'_2\mathcal{F}'_2}(\Omega) = \frac{\hbar}{|1 + R_{xx}(\Omega)\, K^{\rm eff}_2(\Omega)|}\, \frac{1}{R_{xx}(\Omega)}\,, \tag{4.81}$$

and the minimal noise spectral density is,

$$S^{\rm min}_{h,i}(\Omega) = \frac{2\hbar}{L^2}\, \left|\frac{R^2_{xx}(\Omega)}{\chi^{\rm eff}_i(\Omega)}\right| = S^{\rm SQL}_h \left|\frac{R_{xx}(\Omega)}{\chi^{\rm eff}_i(\Omega)}\right|\,, \tag{4.82}$$

which can be formally regarded as a non-free-mass SQL for the *effective* dynamics described by $\chi^{\rm eff}_i$. To give an example, in Fig. 4.5 we plot the square root of the noise spectral densities $S_{h,2}$ and $S^{\rm min}_{h,2}$ versus frequency f having fixed $\epsilon = 2\pi \times 25.0\,{\rm Hz}$, $\lambda = 2\pi \times 191.3\,{\rm Hz}$, for two different values of the laser power circulating in the arm cavities: $I_c = 300$ kW and $I_c = 600$ kW. For comparison we also plot the free-mass SQL line. As we can see from the plot, $S^{\rm min}_{h,2}$ can go quite below the free-mass SQL.

The effective dynamics can be also used to optimize the performance of SR interferometers [10]. The roots of the following equation,

$$K^{\rm eff}_i(\Omega) - \frac{m}{4}\,\Omega^2 = 0\,, \tag{4.83}$$

corresponds to resonances produced by the effective rigidity, at which $\chi^{\rm eff} \to \infty$ and, using Eq. (4.82),

$$S^{\rm min}_{h,i}(\Omega) \to 0\,. \tag{4.84}$$

As observed by Khalili [10], we could expect that the more the roots of Eq. (4.83) coincide, the more broadband the noise curve will be. For example, we could expect that interferometer configurations with double or triple zeros be optimal. However, as we shall see, those configurations are not much better than some of the three-single-zero cases.

Assuming the second quadrature ($i = 2$) is observed, we obtain for the triple-zero case [see also Eqs. (29), (30) and (31) in Ref. [10]]:

$$\iota_c = 2\left(\frac{9\sqrt{177} - 113}{49}\right)\,\lambda^3\,, \qquad \epsilon = \frac{\sqrt{280 - 21\,\sqrt{177}}}{7}\,\lambda\,, \qquad \Omega_{\rm triple\,zero} = \sqrt{\frac{2(-11 + \sqrt{177})}{7}}\,\lambda\,. \tag{4.85}$$

In Fig. 4.6 we plot the square root of the noise spectral density $S_{h,2}$ versus frequency f for the triple-zero case having fixed $\Omega_{\rm triple\,zero} = 2\pi \times 100$ Hz, i.e., the (free) oscillation frequency $\lambda = 2\pi \times 123.3\,{\rm Hz}$ and $\epsilon = 2\pi \times 13.8\,{\rm Hz}$. The SQL line is also plotted. For comparison we also show the noise spectral density $S_{h,2}$ corresponding to a solution of Eq. (4.83) with three-single zeros: $\lambda = 2\pi \times 191.3\,{\rm Hz}$, $\epsilon = 2\pi \times 25.0\,{\rm Hz}$ and $I_c = 590$ kW. As mentioned, the spectral density in the triple-zero case is not

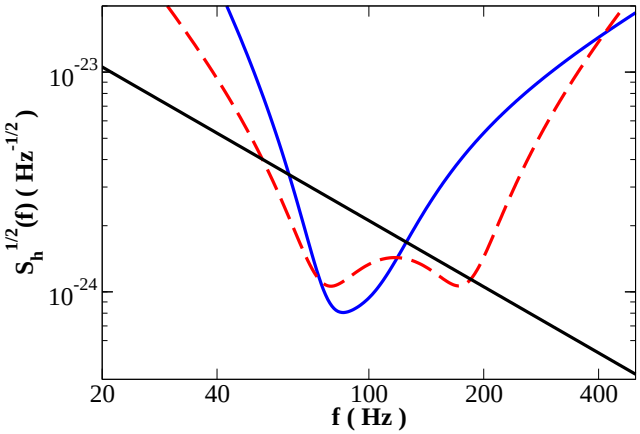

Figure 4.6: Plot of the square root of the noise spectral density S_h versus frequency f for (i) triple-zero case (continuous line) with $\lambda = 2\pi \times 123.2\,\mathrm{Hz}$, $\epsilon = 2\pi \times 13.8\,\mathrm{Hz}$, and $I_c = 320$ kW and (ii) three-single-zero case (dashed line) with $\lambda = 2\pi \times 191.3\,\mathrm{Hz}$, $\epsilon = 2\pi \times 25.0\,\mathrm{Hz}$ and $I_c = 590$ kW. For comparison we also show the free-mass SQL line (black straight line).

significantly broadband, especially if compared with the three-single-zero case.

This result originates from the *non-universal* nature of the curve $S_{h,i}^{\min}$. The SQL (4.28) does not change if we adjust (by varying the circulating power) the balance between shot noise and radiation-pressure noise and find the interferometer parameters whose noise curve can touch it. By contrast, the curve $S_{h,i}^{\min}$ changes when we adjust (by varying the circulating power or the optical resonant frequencies) the effective shot and radiation-pressure noises, $S_{\mathcal{Z}_i'\mathcal{Z}_i'}$ and $S_{\mathcal{F}'_i\mathcal{F}'_i}$. [The change of $S_{h,2}^{\min}$ as I_c is varied can be also seen from Fig. 4.5.] As a consequence, the fact that $S_{h,i}^{\min}$ is low and broad-band for a certain configuration cannot guarantee the noise curve will also be optimal. In particular, in the triple-zero case, Eq. (4.83) already fixes all the interferometer parameters, leaving no freedom for the noise curve to really take advantage of the triple zeros. The fact that only a *non-universal* minimum noise spectral density exists in SR interferometers arises in part because of the double role played by the carrier light. Indeed, the latter provides the means for measurement, and therefore determines the balance between shot and radiation-pressure noises, but it also directly affects the optomechanical dynamics of the system, originating the optical-spring effect.

Finally, Braginsky, Khalili and Volikov [17] have recently proposed a table-top quantum-measurement experiment to (i) investigate the ponderomotive rigidity effect present in single detuned cavity and (ii) beat the free mass SQL. Although the table-top experiment will concern physical parameters very different from LIGO-II, e.g., the test mass $m \sim 2 \times 10^{-2}$ g, $L \sim 1$ cm, $\Omega \sim 10^4\, s^{-1}$, $I_c \sim$ 1-10 W, however, because of the equivalence we have explicitly demonstrated between SR interferometers and single detuned cavities, the results of the table-top experiment could shed new light and investigate

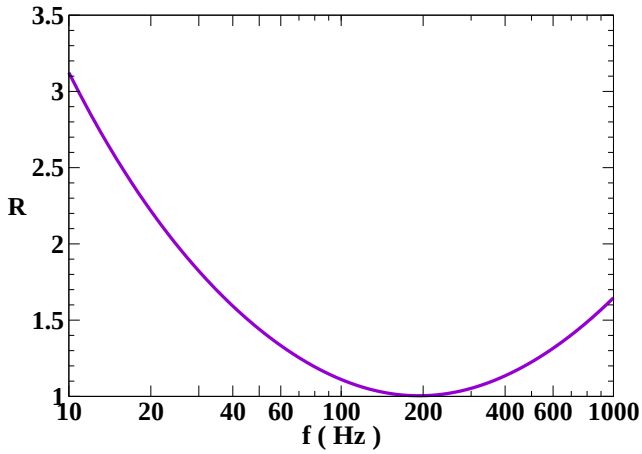

Figure 4.7: Plot of $R \equiv S_x(f)/(2\hbar\,|\Im[\chi(f)]|)$ versus f when $\lambda = 2\pi \times 191.3\,\mathrm{Hz}$, $\epsilon = 2\pi \times 25.0\,\mathrm{Hz}$ and $I_c = 590$ kW.

various features of SR optomechanical configurations relevant for LIGO-II.

4.4.4 Optical spring equivalent to mechanical spring but at zero temperature

When proposing the optical-bar GW detectors [11], Braginsky, Gorodetsky and Khalili pointed out that detuned optical pumping field in Fabry-Perot resonator can convert the free test mass into an optical spring having *very low* intrinsic noise. In this section we illustrate why this happens in SR interferometers and why optical springs are indeed preferable to mechanical springs in measuring very tiny forces.

The Heisenberg operator in Fourier domain $x^{(1)}(\Omega)$ describing the antisymmetric mode of motion of SR interferometer, satisfies the following equation [see Eqs. (4.39), (4.41) above and also Eq. (2.20) in Chapter 2]:

$$x^{(1)}(\Omega) = \chi(\Omega)\, F^{(0)}(\Omega)\,, \qquad \chi(\Omega) = \frac{R_{xx}(\Omega)}{1 - R_{xx}(\Omega)\, R_{FF}(\Omega)}\,. \tag{4.86}$$

Using Eq. (4.49) we get:

$$\chi(\Omega) = \frac{4}{m}\, \frac{\lambda^2 + (\epsilon - i\Omega)^2}{\lambda\, \iota_c - \Omega^2\, [\lambda^2 + (\epsilon - i\Omega)^2]}\,. \tag{4.87}$$

The noise spectral density associated with x is

$$S_x(\Omega) = |\chi(\Omega)|^2\, S_F(\Omega)\,, \tag{4.88}$$

where:

$$\pi\,\delta\,(\Omega-\Omega')\;S_x(\Omega)=\langle 0_{\tilde{a}}|\,x^{(1)}(\Omega)x^{(1)\,\dagger}(\Omega')|0_{\tilde{a}}\rangle\,,\qquad \pi\,\delta\,(\Omega-\Omega')\;S_F(\Omega)=\langle 0_{\tilde{a}}|\,F^{(0)}(\Omega)F^{(0)\,\dagger}(\Omega')|0_{\tilde{a}}\rangle\,. \tag{4.89}$$

More explicitly,

$$S_F(\Omega)=\frac{\mathcal{I}_c\,\hbar}{2}\,\frac{\epsilon\,(\lambda^2+\epsilon^2+\Omega^2)}{[(\Omega-\lambda)^2+\epsilon^2]\,[(\Omega+\lambda)^2+\epsilon^2]}\,. \tag{4.90}$$

For the optical spring, which is made up of electromagnetic oscillators in their ground states (the vacuum state), we have [see e.g., Chapter 6 in Ref. [8] [1]]:

$$S_x(\Omega)\geq 2\hbar\,|\Im[\chi(\Omega)]|\,, \tag{4.91}$$

which can be regarded as a zero-temperature version of the fluctuation-dissipation theorem. For a mechanical system, e.g., a mechanical spring, with the same susceptibility, but in thermal equilibrium at temperature $T\gg\hbar\Omega/k$, where k is the Boltzmann constant, the standard version of fluctuation-dissipation theorem says,

$$S_x(\Omega)=4\frac{k\,T}{\Omega}\,|\Im[\chi(\Omega)]|\,. \tag{4.92}$$

If we assume $\Omega\sim 2\pi\times 100\,\mathrm{Hz}$, $\hbar\Omega/k\sim 5\times 10^{-9}\,\mathrm{Kelvin}$, the condition $T\gg\hbar\Omega/k$ is always valid for any practical mechanical system. As a consequence,

$$S_x^{\mathrm{mech.\,spring}}(\Omega)\sim\frac{k\,T}{\hbar\,\Omega}\,S_x^{\mathrm{opt.\,spring}}(\Omega)\,. \tag{4.93}$$

At $T=300K$, $\Omega/2\pi=100$ Hz, we get $S_x^{\mathrm{mech.\,spring}}\sim 10^{11}\,S_x^{\mathrm{opt.\,spring}}$. Thus, because of the very large coefficient $kT/\hbar\Omega$ in Eq. (4.93), fluctuating noise in an optical spring is always much smaller than in a mechanical spring!

For SR interferometers described in this chapter, the fluctuating noise S_x does not saturate the inequality in Eq. (4.91). This can be inferred from Fig. 4.7 where we plot $R\equiv S_x(f)/(2\hbar\,|\Im[\chi(f)]|)$ versus f, where S_x has been obtained from Eqs. (4.87), (4.88) and (4.90), for the following choice of the physical parameters: $m=30$ kg, $T=0.033$, $\gamma=2\pi\times 98.5\,\mathrm{Hz}$, with $\lambda=2\pi\times 191.3\,\mathrm{Hz}$, $\epsilon=2\pi\times 25.0\,\mathrm{Hz}$ and $I_c=560$ kW. The minimum of R is at the frequency corresponding to the (free) oscillation frequency of the SR interferometer, i.e., $f_{\mathrm{min}}=\lambda/(2\pi)=191.3$ Hz.

[1] Note that the factor 2 in the RHS of Eqs. (4.91), (4.92) is due to the fact that we use one-sided spectral densities while Braginsky and Khalili [8] use two-sided spectral densities.

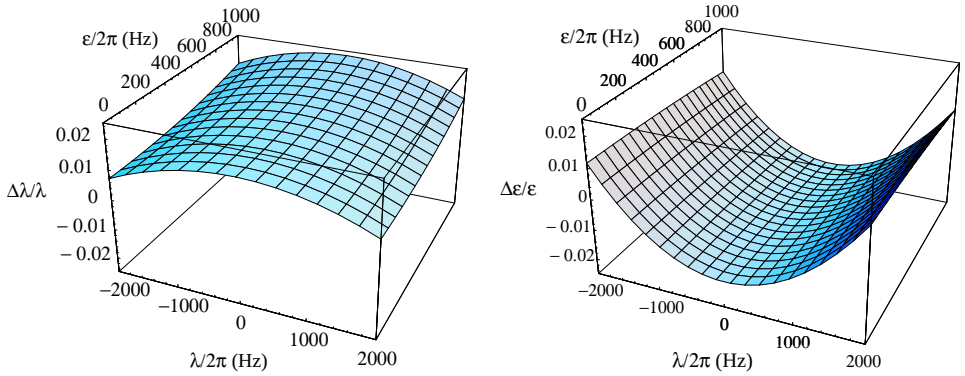

Figure 4.8: We plot the fractional error $\Delta\lambda/\lambda$ (in left panel) and $\Delta\epsilon/\epsilon$ (in right panel) as a function of λ and ϵ. The quantities $\Delta\lambda$ and $\Delta\epsilon$ are the difference between the value of λ and ϵ obtained from the first-order-T free optical frequency (4.94) and the exact one (4.13). [$T = 0.033$ is assumed]

4.5 Input–output relation at all orders in transmissivity of internal test-mass mirrors

To simplify the calculation and the modeling of GW interferometers, KLMTV [7] calculated the input–output relation of a conventional interferometer at leading order in T and $\Omega\, L/c$. By taking only the leading order terms in T, they ignored the radiation-pressure forces acting on the ITM due to the electromagnetic field present in the cavity made up of ITM and BS. By limiting their analysis to the leading order in $\Omega L/c$, they assumed the radiation-pressure forces acting on the ITM and ETM are equal. In conventional interferometers, T alone determines the half-bandwidth γ of the arm cavities (through $\gamma = Tc/4L$), which fully characterizes the interferometer [see Eq. (16) in Ref. [7] and Eqs. (4.30), (4.31) above]. Moreover, since $\Omega_{\rm GW}$ is comparable to γ and $T \sim 0.005 - 0.033$, the two small quantities, $\Omega L/c$ and T are on the same order, and the accuracy in expanding the input–output relation in these two parameters is rather under control. [Note that if $\gamma \sim 2\pi \times 100\,$Hz, we have $T \sim 0.033$.]

In describing SR interferometers, we build on the leading-order results of Ref. [7]. However, in SR interferometers the accuracy of expanding in T can be quite obscure, because T is not the only small quantity characterizing SR-interferometer performances — for example the SRM transmissivity can also be a small quantity. Thus, to clarify the accuracy of the expansion in T, we now derive the input–output relation at all orders in T, and compare with the leading order result (4.24) (Chapter 2). The calculation is much easier if we view the SR cavity as a single effective mirror, as done in Sec. 4.2. However, in doing so, we still use the assumptions mentioned at the beginning of this section. See also the end of Sec. 4.2.1.

4.5.1 Free optical resonant frequencies

It is interesting to investigate the error in the prediction of the (free) optical resonant frequency introduced by using only the leading order terms in T and $\Omega L/c$. For a generic set of T, ρ and ϕ, it can be quite complicated to characterize that error. For example, when $\rho > \sqrt{R}$ and $\phi \sim \pi/2$, $\widetilde{\rho}'$ is near -1 (in the complex plane) and the expansion (4.15) around $\widetilde{\rho}' = 1$ totally breaks down. However, we are only concerned with those parameters meaningful for a GW detector, and thus we limit our analysis to the region where $|\widetilde{\Omega}| = \sqrt{\lambda^2 + \epsilon^2} \sim \Omega_{\rm GW} < 10^4\,{\rm s}^{-1}$, corresponding to $|\widetilde{\Omega}L/c| \lesssim 0.1$. In this way $|\widetilde{\rho}' - 1|$ is always relatively small. To test the accuracy, we fix T, and for each $\widetilde{\Omega} = -\lambda - i\epsilon$, we solve Eq. (4.13) for ρ and ϕ. Then, we insert these values into Eq. (4.17) to get the first-order-T expression for $\widetilde{\Omega}$, which we denote by $\widetilde{\Omega}^{(1)}$. The result is

$$\begin{aligned}\widetilde{\Omega}^{(1)} &= \frac{c}{L}\left(\frac{1+\sqrt{R}}{2}\right)^2 \tan\left(\frac{\widetilde{\Omega}L}{c}\right), \\ &= \widetilde{\Omega}\left[1 - \frac{T}{2} + \mathcal{O}(T^2)\right]\left[1 + \frac{1}{3}\left(\frac{\widetilde{\Omega}L}{c}\right)^2 + \mathcal{O}\left(\frac{\widetilde{\Omega}^4 L^4}{c^4}\right)\right]. \end{aligned} \tag{4.94}$$

From this equation we infer that since $|\widetilde{\Omega}L/c| \lesssim 0.1$, and T is smaller than a few percents, the error in the (free) optical resonant frequency is not very significant (less than a few percents). In Fig. 4.8 we plot the fractional differences (denoted by $\Delta\lambda/\lambda$ and $\Delta\epsilon/\epsilon$) between the real and imaginary parts of $\widetilde{\Omega}^{(1)}$ and $\widetilde{\Omega}$, as functions of ϵ and λ for $T = 0.033$. The fractional differences are always smaller than 2.5%.

4.5.2 Input–output relation and noise spectral density

Using the formalism of Sec. 4.2 and Appendix 4.7, it is rather easy to derive the exact input–output relation in terms of λ, ϵ and ι_c. The input–output relation (j-k) of the arm cavity composed of the effective ITM and ETM is

$$\begin{pmatrix} k_1 \\ k_2 \end{pmatrix} = e^{2i\Omega L/c}\begin{pmatrix} 1 & 0 \\ -\mathcal{K}_{\rm arm} & 1 \end{pmatrix}\begin{pmatrix} j_1 \\ j_2 \end{pmatrix} + e^{i\Omega L/c}\sqrt{2\mathcal{K}_{\rm arm}}\,\frac{h}{h^{\rm arm}_{\rm SQL}}\begin{pmatrix} 0 \\ 1 \end{pmatrix}, \tag{4.95}$$

where

$$\mathcal{K}_{\rm arm} = \frac{8I_{\rm arm}\omega_0}{\mu_{\rm arm}\Omega^2 c^2} = \frac{16 I_c \omega_0}{m\Omega^2 c^2}, \quad h^{\rm arm}_{\rm SQL} = \sqrt{\frac{8\hbar}{\mu_{\rm arm}\Omega^2 L^2}} = \sqrt{\frac{8\hbar}{m\Omega^2 L^2}}. \tag{4.96}$$

Writing Eqs. (4.7) and (4.8) in terms of quadratures, that is

$$\begin{pmatrix} j_1 \\ j_2 \end{pmatrix} = \sqrt{1-|\widetilde{\rho}'|^2}\begin{pmatrix} \widetilde{a}_1 \\ \widetilde{a}_2 \end{pmatrix} + |\widetilde{\rho}'|\begin{pmatrix} \cos\psi & -\sin\psi \\ \sin\psi & \cos\psi \end{pmatrix}\begin{pmatrix} k_1 \\ k_2 \end{pmatrix}, \tag{4.97}$$

and

$$\begin{pmatrix} \widetilde{b}_1 \\ \widetilde{b}_2 \end{pmatrix} = \sqrt{1-|\widetilde{\rho}'|^2} \begin{pmatrix} k_1 \\ k_2 \end{pmatrix} - |\widetilde{\rho}'| \begin{pmatrix} \cos\psi & \sin\psi \\ -\sin\psi & \cos\psi \end{pmatrix} \begin{pmatrix} \widetilde{a}_1 \\ \widetilde{a}_2 \end{pmatrix}, \tag{4.98}$$

where $\psi = \arg(\widetilde{\rho}')$, and using Eq. (4.11), we obtain the input–output relation $(\widetilde{a} - \widetilde{b})$ of the three-mirror cavity, and thus that of the equivalent SR interferometer. They can be represented in the same form as Eq. (4.24), with $\widetilde{M}^{(1)}$, $\widetilde{C}_{ij}^{(1)}$, and $\widetilde{D}_i^{(1)}$ replaced by

$$\begin{aligned} \widetilde{M}^{\rm ex} = \frac{\Omega^2 c^2 e^{-2i\Omega L/c}}{4L^2} \Bigg\{ & \left[1 - e^{2i(\Omega+\lambda+i\epsilon)L/c}\right] \left[1 - e^{2i(\Omega-\lambda+i\epsilon)L/c}\right] \\ & + i\frac{\iota_c L}{\Omega^2 c} \left[e^{2i(\Omega+\lambda+i\epsilon)L/c} - e^{2i(\Omega-\lambda+i\epsilon)L/c}\right] \Bigg\}, \end{aligned} \tag{4.99}$$

and

$$\begin{aligned} \widetilde{C}_{11}^{\rm ex} = \widetilde{C}_{22}^{\rm ex} &= \frac{\Omega^2 c^2}{4L^2} \Bigg\{ \left[1 - 2e^{-2\epsilon L/c}\cos(2\lambda L/c)\cos(2\Omega L/c) + e^{-4\epsilon L/c}\cos(4\lambda L/c)\right] \\ &\quad + \frac{\iota_c L}{\Omega^2 c} e^{-4\epsilon L/c}\sin(4\lambda L/c) \Bigg\}, \end{aligned} \tag{4.100}$$

$$\begin{aligned} \widetilde{C}_{12}^{\rm ex} &= \frac{\Omega^2 c^2}{4L^2} \Bigg\{ -2e^{-2\epsilon L/c}\sin(2\lambda L/c)\left[\cos(2\Omega L/c) - e^{-2\epsilon L/c}\cos(2\lambda L/c)\right] \\ &\quad + \frac{2\iota_c L}{\Omega^2 c} e^{-4\epsilon L/c}\sin^2(2\lambda L/c) \Bigg\}, \end{aligned} \tag{4.101}$$

$$\begin{aligned} \widetilde{C}_{21}^{\rm ex} &= \frac{\Omega^2 c^2}{4L^2} \Bigg\{ 2e^{-2\epsilon L/c}\sin(2\lambda L/c)\left[\cos(2\Omega L/c) - e^{-2\epsilon L/c}\cos(2\lambda L/c)\right] \\ &\quad - \frac{2\iota_c L}{\Omega^2 c}\left[1 - e^{-4\epsilon L/c}\cos^2(2\lambda L/c)\right] \Bigg\}, \end{aligned} \tag{4.102}$$

$$\widetilde{D}_1^{\rm ex} = \frac{\Omega^2 c^2}{4L^2}\left[-2e^{-2\epsilon L/c}e^{i\Omega L/c}\sin(2\lambda L/c)\right]\sqrt{\frac{(1-e^{-4\epsilon L/c})\iota_c L}{\Omega^2 c}}, \tag{4.103}$$

$$\widetilde{D}_2^{\rm ex} = \frac{\Omega^2 c^2}{4L^2}\left[2e^{-i\Omega L/c} - 2e^{-2\epsilon L/c}e^{i\Omega L/c}\cos(2\lambda L/c)\right]\sqrt{\frac{(1-e^{-4\epsilon L/c})\iota_c L}{\Omega^2 c}}. \tag{4.104}$$

In order to compare with the results obtained in Chapters 2 and 3, we have also to relate $\widetilde{a}$, $\widetilde{b}$ to a and b. The exact transformations [to be compared with Eqs. (4.22), (4.23)] are

$$\begin{pmatrix} \widetilde{a}_1 \\ \widetilde{a}_2 \end{pmatrix} = \frac{1}{\sqrt{1 + 2\rho\sqrt{R}\cos 2\phi + \rho^2 R}} \begin{pmatrix} (1+\rho\sqrt{R})\cos\phi & -(1-\rho\sqrt{R})\sin\phi \\ (1-\rho\sqrt{R})\sin\phi & (1+\rho\sqrt{R})\cos\phi \end{pmatrix} \begin{pmatrix} a_1 \\ a_2 \end{pmatrix}, \tag{4.105}$$

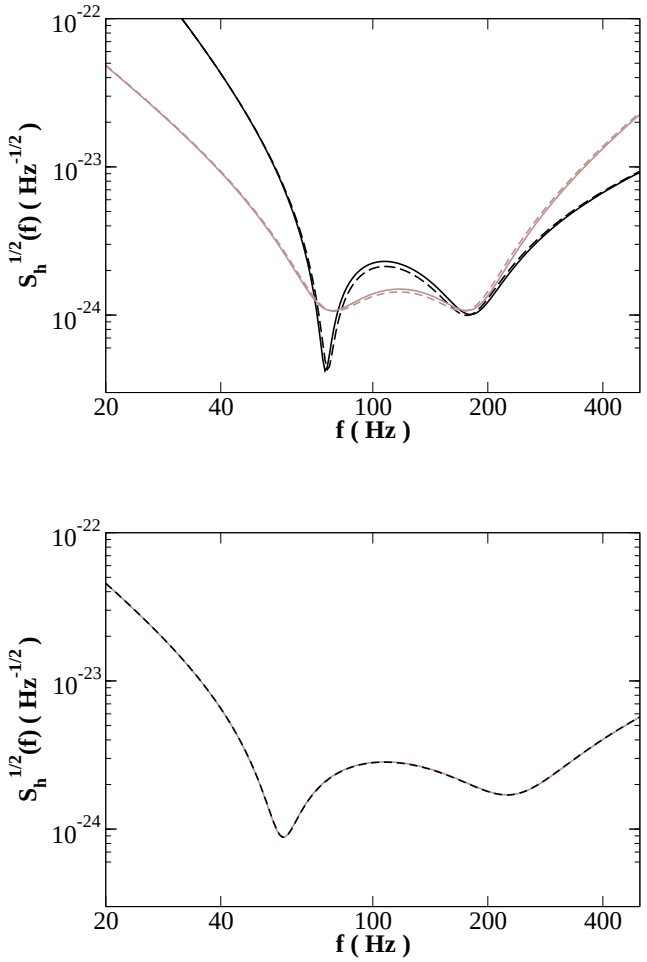

Figure 4.9: Comparison of first-order T-expanded (dashed line) and exact (continuous line) noise spectral density $\sqrt{S_h}$ versus frequency f. In the upper panel we use the parameters $T = 0.033$, $\rho = 0.9$ and $\phi = \pi/2 - 0.47$, $m = 30\,\mathrm{kg}$, and $I_c = 592\,\mathrm{kW}$ and show the curves for the two orthogonal quadratures $\widetilde{b}_1$ (lighter-color lines) and $\widetilde{b}_2$ (darker-color lines). In the lower panel we use $T = 0.005$, $\rho = 0.964$, $\phi = \pi/2 - 0.06$, $m = 40\,\mathrm{kg}$, $I_c = 840\,\mathrm{kW}$, and $\zeta = 1.13\pi$.

and

$$\begin{pmatrix} \widetilde{b}_1 \\ \widetilde{b}_2 \end{pmatrix} = \frac{1}{\sqrt{1+2\rho\sqrt{R}\cos 2\phi+\rho^2 R}} \begin{pmatrix} (1+\rho\sqrt{R})\cos\phi & (1-\rho\sqrt{R})\sin\phi \\ -(1-\rho\sqrt{R})\sin\phi & (1+\rho\sqrt{R})\cos\phi \end{pmatrix} \begin{pmatrix} b_1 \\ b_2 \end{pmatrix} . \quad (4.106)$$

As an example, we compare in the upper panel of Fig. 4.9 the exact and first-order T-expanded noise spectral densities for the two orthogonal quadratures $\widetilde{b}_1$ and $\widetilde{b}_2$, having fixed $T = 0.033$, $\rho = 0.9$, $\phi = \pi/2 - 0.47$, $m = 30\,\mathrm{kg}$ and $I_c = 592\,\mathrm{kW}$ (which corresponds to $I_0 = I_{\mathrm{SQL}}$ at BS) as used in Chapters 2 and 3. The T-expanded noise spectral density is given by Eq. (4.37), where we used for λ, ϵ and the redefined output quadratures Eqs. (4.18), (4.19). The exact noise spectral density is obtained from Eq. (4.36) by replacing $\widetilde{M}^{(1)}$, $\widetilde{C}_{ij}^{(1)}$, and $\widetilde{D}_i^{(1)}$ with $\widetilde{M}^{\mathrm{ex}}$, $\widetilde{C}_{ij}^{\mathrm{ex}}$, and $\widetilde{D}_i^{\mathrm{ex}}$. From Fig. 4.9, we see that there is a discernible difference. In the lower panel of Fig. 4.9, we compare the exact and first-order T-expanded noise spectral densities using the reference-design parameters of LIGO-II [15]: $T = 0.005$, $\rho = 0.964$, $\phi = \pi/2 - 0.06$, $m = 40\,\mathrm{kg}$, $I_c = 840\,\mathrm{kW}$, and $\zeta = 1.13\pi$. In this case, the two curves agree nicely with each other, presumably, because T is rather small. In the general case, if we want to trust the leading order calculation, it is not obvious how small T can be, since ρ and ϕ have to change along with T to preserve the invariance of interferometer performance. For this reason, it is more convenient to seek an expansion that is also scaling invariant, i.e., whose accuracy only depends on the scaling-invariant properties of the interferometer. To this respect, the set of quantities $\lambda L/c$, $\epsilon L/c$, $\iota_c^{1/3} L/c$ and $\Omega L/c$, which are all small and on the same order, is a good choice. It is then meaningful to expand with respect to these quantities and take the leading order terms. We denote the noise spectral density obtained in this way by first-order λ-ϵ-$\iota_c^{1/3}$-expanded noise spectral density. [This technique of identifying and expanding in small quantities of the same order can be very convenient and powerful in the analysis of complicated interferometer configurations, e.g., the speed meter interferometer [18].] Not surprisingly, doing so gives us right away the scaling-invariant input–output relation (4.24). In the upper and lower panels of Fig. 4.10 we compare the exact and first-order λ-ϵ-$\iota_c^{1/3}$-expanded noise spectral densities for the two orthogonal quadratures $\widetilde{b}_{1,2}$, with the same parameters used in Fig. 4.9, i.e., $T = 0.033$, $\rho = 0.9$ and $\phi = \pi/2 - 0.47$, $m = 30\,\mathrm{kg}$, and $I_c = 592\,\mathrm{kW}$ (upper panel) and $T = 0.005$, $\rho = 0.964$, $\phi = \pi/2 - 0.06$, $m = 40\,\mathrm{kg}$, $I_c = 840\,\mathrm{kW}$, and $\zeta = 1.13\pi$ (lower panel). The first-order λ-ϵ-$\iota_c^{1/3}$-expanded noise spectral density is obtained using for λ, ϵ and the redefined output quadratures Eqs. (4.13), (4.105). The agreement between the exact and first-order λ-ϵ-$\iota_c^{1/3}$-expanded noise spectral densities is much better than the agreement between the exact and T-expanded noise spectral densities, given in Fig. 4.9.

When either $\lambda L/c$, $\epsilon L/c$, $\iota_c^{1/3} L/c$ or $\Omega L/c$ is not small enough, the first-order λ-ϵ-$\iota_c^{1/3}$ expansion fails. An interesting example of astrophysical relevance is the configuration with large λ and small ϵ, which has narrowband sensitivities centered around a high (optical) resonant frequency. In the upper panel of Fig. 4.11 we compare the first-order λ-ϵ-$\iota_c^{1/3}$-expanded noise spectral density with

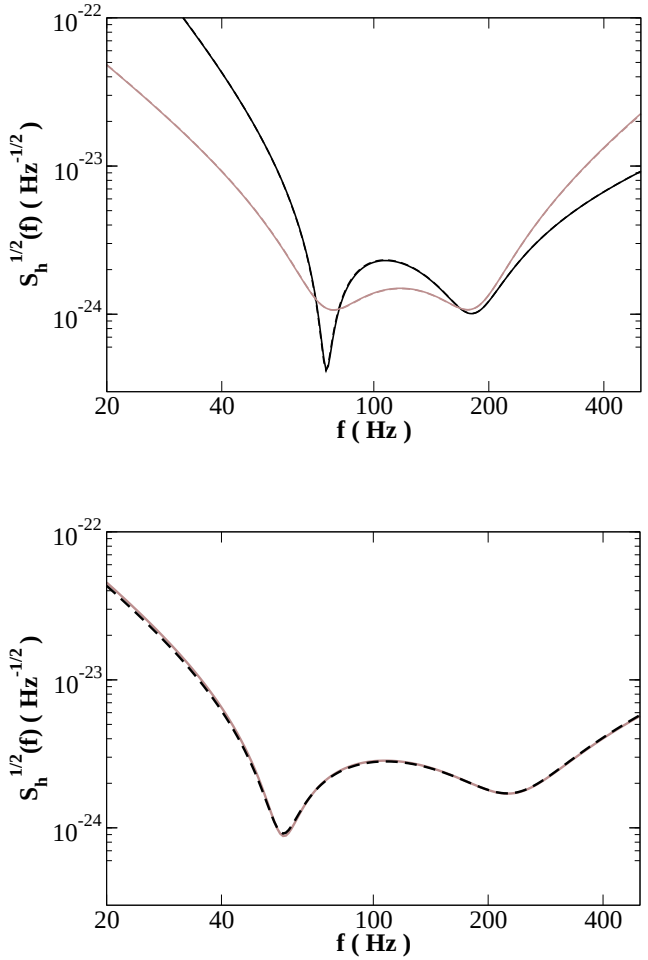

Figure 4.10: Comparison of first-order λ-ϵ-$\iota_c^{1/3}$-expanded (dashed line) and exact (continuous line) noise spectral density $\sqrt{S_h}$ versus frequency f. In the upper panel we use $T = 0.033$, $\rho = 0.9$ and $\phi = \pi/2 - 0.47$, $m = 30\,\mathrm{kg}$, and $I_c = 592\,\mathrm{kW}$, and show the curves for the two orthogonal quadratures $\widetilde{b}_1$ (lighter-color lines) and $\widetilde{b}_2$ (darker-color lines). In the lower panel we use $T = 0.005$, $\rho = 0.964$, $\phi = \pi/2 - 0.06$, $m = 40\,\mathrm{kg}$, $I_c = 840\,\mathrm{kW}$, and $\zeta = 1.13\pi$.

the exact one, for the two quadratures $\widetilde{b}_{1,2}$ having fixed: $\lambda = 2\pi \times 900\,\mathrm{Hz}$, $\epsilon = 20\,\mathrm{Hz}$, $m = 30\,\mathrm{kg}$ and $I_c = 600\,\mathrm{kW}$. Near the lower optomechanical resonant frequency, the first-order λ-ϵ-$\iota_c^{1/3}$ expansion deviates from the exact one by significant amounts. However, it is sufficient to expand up to the second order in $\lambda L/c$, $\epsilon L/c$, $\iota_c^{1/3} L/c$ and $\Omega L/c$ to get a much better agreement, as we infer from the lower panel of Fig. 4.11. [The input–output relation expanded at second order is given in Appendix 4.9.]

4.6 Conclusions

In this chapter we showed that, under the assumptions used to describe SR interferometers (see Chapters 2 and 3), i.e., radiation pressure forces acting on ETMs and ITMs equal, and ETM and ITM motions neglected during the light round-trip time in arm cavities, the SR cavity can be viewed as a single effective (fixed) mirror located at the ITM position. We then explicitly map the SR optical configuration to a three-mirror cavity [12, 13] [see e.g., Sec. 4.2] or even a single detuned cavity [10] [see Sec. 4.4.2]. The mapping has revealed an interesting scaling law present in SR interferometers. By varying the SRM reflectivity ρ, the SR detuning ϕ and the ITM transmissivity T in such a way that the circulating power I_c and the (free) optical resonant frequency (or more specifically its real and imaginary parts λ and ϵ) remain fixed [see Eq. (4.18)], the input–output relation and the optomechanical dynamics remain invariant.

We expressed the input–output relation (4.24), noise spectral density (4.36) and all quantities characterizing the optomechanical dynamics, such as the radiation-pressure force (4.44) and ponderomotive rigidity (4.49), in terms of the scaling invariant quantities or characteristic parameters. The various formulas are much simpler than the ones obtained in the original description (see Chapters 2 and 3). The scaling invariant formalism will be certainly useful in the process of optimizing the SR optical configuration of LIGO-II and for investigating advanced LIGO configurations. Moreover, the equivalance we explicitly showed between SR interferometer and single detuned cavity, could also make the table-top experiments of the kind recently suggested in Ref. [17] more relevant to the development of LIGO-II.

In this chapter we also evaluated the input–output relation for SR interferometers at all orders in the transmissivity of ITMs [see Sec. 4.5]. So far, the calculations were limited to the leading order. We found that the differences between leading-order and all-order noise spectral densities for broadband configurations of advanced LIGO do not differ much [see Fig. 4.9]. However for narrowband configurations, which have an astrophysical interest, the differences can be quite noticeable [see upper panel of Fig. 4.11]. In any case, we showed that by using the (very simple) next-to-leading-order input–output relation, explicitly derived in Appendix 4.9, we can recover the all-order results with very high accuracy [see lower panel of Fig. 4.11].

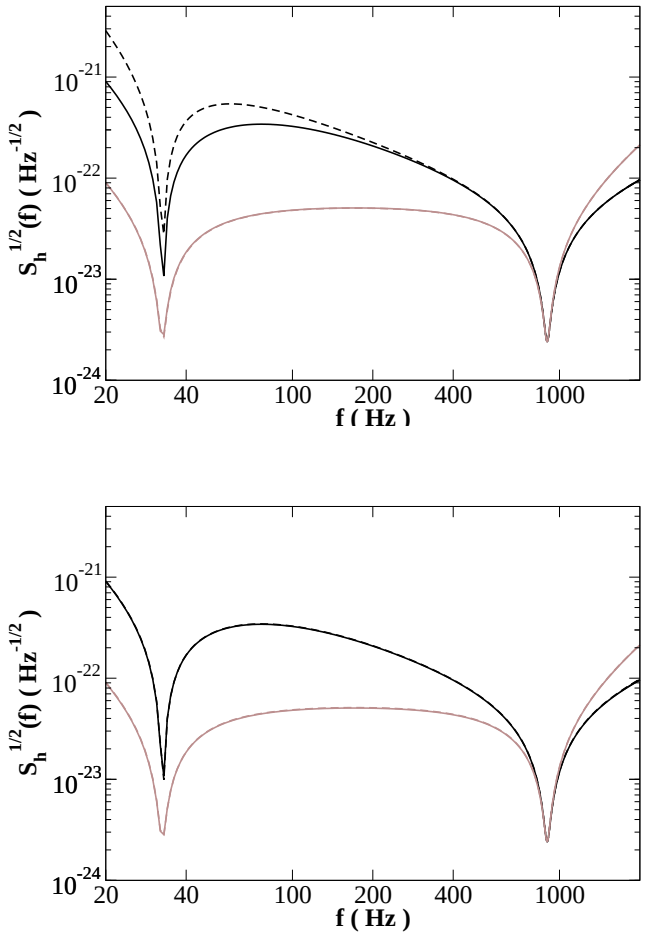

Figure 4.11: For the two orthogonal quadratures $\widetilde{b}_1$ (lighter-color lines) and $\widetilde{b}_2$ (darker-color lines) we compare the first-order λ-ϵ-$\iota_c^{1/3}$-expanded noise spectral density (dashed line) with the exact (continuous line) noise spectral density (in upper panel) and the second-order λ-ϵ-$\iota_c^{1/3}$-expanded noise spectral density (dashed line) with the exact (continuous line) noise spectral density (in lower panel). For all the cases we fix $\lambda = 2\pi \times 900\,\mathrm{Hz}$, $\epsilon = 2\pi \times 20\,\mathrm{Hz}$, $m = 30\,\mathrm{kg}$ and $I_c = 600\,\mathrm{kW}$.

Finally, it will be rather interesting to investigate how the results change if we relax the assumption of disregarding (i) the motion of ITMs and ETMs during the light round-trip time in arm cavities and (ii) the radiation-pressure forces on ITMs due to light power present in the cavity composed of ITM and BS. This analysis is left for future work.

4.7 Appendix. Useful relations in the quadrature formalism

As in Ref. [7] we describe the interferometer's light by the electric field evaluated on the optic axis, i.e., on the center of light beam. Correspondingly, the electric fields that we write down will be functions of time only. All dependence on spatial position will be suppressed from our formulae.

The input field at the bright port of the beam splitter, which is assumed to be infinitesimally thin, is a carrier field, described by a coherent state with power I_0 and (angular) frequency ω_0. We denote by $f_{\rm GW} = \Omega/2\pi$ the GW frequency, which lies in the range $10 - 10^4$ Hz. The interaction of a gravitational wave with the optical system produces sideband frequencies $\omega_0 \pm \Omega$ in the electromagnetic field at the dark-port output. We describe the quantum optics inside the interferometer using the two-photon formalism developed by Caves and Schumaker [19]. The quantized electromagnetic field in the Heisenberg picture evaluated at some fixed point on the optic axis is [7]:

$$E(t) = \sqrt{\frac{2\pi\hbar\,\omega_0}{\mathcal{A}\,c}}\, e^{-i\omega_0\, t} \int_0^{+\infty} (a_+(\Omega)\, e^{-i\Omega t} + a_-(\Omega)\, e^{i\Omega t})\, \frac{d\Omega}{2\pi} + \text{h.c.}\,, \tag{4.107}$$

where h.c. means Hermitian conjugate and we denoted $a_+(\Omega) \equiv a_{\omega_0+\Omega}$ and $a_-(\Omega) \equiv a_{\omega_0-\Omega}$. Here $\mathcal{A}$ is the effective cross sectional area of the laser beam and c is the speed of light. The annihilation and creation operators $a_\pm(\Omega)$ in Eq. (4.107) satisfy the commutation relations:

$$[a_+, a_{+'}^\dagger] = 2\pi\,\delta(\Omega - \Omega')\,, \quad [a_-, a_{-'}^\dagger] = 2\pi\,\delta(\Omega - \Omega')\,, \tag{4.108}$$

$$[a_+, a_{+'}] = 0 = [a_-, a_{-'}]\,, \quad [a_+^\dagger, a_{+'}^\dagger] = 0 = [a_-^\dagger, a_{-'}^\dagger]\,, \quad [a_+, a_{-'}] = 0 = [a_+, a_{-'}^\dagger]\,. \tag{4.109}$$

Following the Caves-Schumaker two-photon formalism [19], we introduce the amplitudes of the two-photon modes as

$$a_1 = \frac{a_+ + a_-^\dagger}{\sqrt{2}}\,, \qquad a_2 = \frac{a_+ - a_-^\dagger}{\sqrt{2}i}\,; \tag{4.110}$$

a_1 and a_2 are called quadrature fields and they satisfy the commutation relations:

$$\begin{aligned} &[a_1, a_{2'}^\dagger] = -[a_2, a_{1'}^\dagger] = 2\pi i\delta(\Omega - \Omega')\,, \\ &[a_1, a_{1'}^\dagger] = 0 = [a_1, a_{1'}]\,, \qquad [a_2, a_{2'}^\dagger] = 0 = [a_2, a_{2'}]\,. \end{aligned} \tag{4.111}$$

The electric field (4.107) in terms of the quadratures reads:

$$E(a_i; t) = \cos(\omega_0\, t)\, E_1(a_1; t) + \sin(\omega_0\, t)\, E_2(a_2; t)\,, \tag{4.112}$$

where:

$$E_j(a_j; t) = \sqrt{\frac{4\pi\hbar\,\omega_0}{\mathcal{A}\,c}} \int_0^{+\infty} (a_j\, e^{-i\Omega t} + a_j^\dagger\, e^{i\Omega t})\, \frac{d\Omega}{2\pi} \qquad j = 1, 2\,. \tag{4.113}$$

Any linear relation among the fields $a_\pm(\Omega)$ of the kind:

$$b_\pm(\Omega) = f_\pm(\Omega)\, a_\pm(\Omega)\,, \qquad f_+(\Omega) \equiv f(\omega_0+\Omega)\,, \qquad f_-(\Omega) \equiv f(\omega_0-\Omega)\,, \tag{4.114}$$

can be transformed into the following relation among the quadrature fields:

$$\left(\begin{array}{c} b_1 \\ b_2 \end{array}\right) = \frac{1}{2}\left(\begin{array}{cc} (f_+ + f_-^*) & i\,(f_+ - f_-^*) \\ -i\,(f_+ + f_-^*) & (f_+ + f_-^*) \end{array}\right)\left(\begin{array}{c} a_1 \\ a_2 \end{array}\right). \tag{4.115}$$

In general, the above equation can be very complicated. In this chapter we restrict ourselves to two special cases. The first case is when $|f_+| = |f_-|$ and we write

$$f_\pm(\Omega) = F(\Omega)\, e^{i\Psi_\pm(\Omega)} \quad \forall\, \Omega\, > 0\,, \tag{4.116}$$

and Eq. (4.115) becomes:

$$\left(\begin{array}{c} b_1 \\ b_2 \end{array}\right) = F(\Omega)\, e^{i(\Psi_+ - \Psi_-)/2}\left(\begin{array}{cc} \cos\frac{\Psi_+ + \Psi_-}{2} & -\sin\frac{\Psi_+ + \Psi_-}{2} \\ \sin\frac{\Psi_+ + \Psi_-}{2} & \cos\frac{\Psi_+ + \Psi_-}{2} \end{array}\right)\left(\begin{array}{c} a_1 \\ a_2 \end{array}\right). \tag{4.117}$$

It is easily checked that the input–output relation for the following processes: (i) free propagation in space, (ii) reflection and transmission from a thin mirror, (iii) reflection and transmission from one (or more) Fabry-Perot cavity for which ω_0 is either resonant or antiresonant, and (iv) reflection and transmission from one (or more) FP cavity whose bandwidth is much larger than the range of values of Ω we are interested in [in this case $f(\Omega)$ can be considered as a constant (complex) number] are all special cases (or linear combinations) of the relation (4.117).

The second case of interest for us is when there is *one* resonance at $\omega_0 + \Omega_{\rm r}$, with $\Omega_{\rm r}$ complex. In this case $f(\Omega)$ is of the form:

$$f(\omega) = \frac{g(\omega)}{\omega - \omega_0 - \Omega_{\rm r}}\,, \tag{4.118}$$

where $g(\omega)$ does not have poles. For $\Omega > 0$, we have

$$f_+ = \frac{g(\omega_0+\Omega)}{\Omega - \Omega_{\rm r}}\,, \qquad f_-^* = -\frac{g^*(\omega_0-\Omega)}{\Omega + \Omega_{\rm r}^*}\,, \tag{4.119}$$

and thus

$$f_+ + f_-^* = \frac{(\Omega+\Omega_{\rm r}^*)\, g(\omega_0+\Omega) - (\Omega-\Omega_{\rm r})\, g^*(\omega_0-\Omega)}{(\Omega-\Omega_{\rm r})\,(\Omega+\Omega_{\rm r}^*)}\,, \tag{4.120}$$

$$f_+ - f_-^* = \frac{(\Omega+\Omega_{\rm r}^*)\, g(\omega_0+\Omega) + (\Omega-\Omega_{\rm r})\, g^*(\omega_0-\Omega)}{(\Omega-\Omega_{\rm r})\,(\Omega+\Omega_{\rm r}^*)}\,. \tag{4.121}$$

Since the quadrature field at Ω mixes the frequencies $\omega_0+\Omega$ and $\omega_0-\Omega$, the single resonant frequency

$\Omega_{\rm r}$ appears in the above equation as a pair of resonant frequencies $\{\Omega_{\rm r}, -\Omega_{\rm r}^*\}$.

Figure 4.12: A two-port linear optical system can always be expressed in terms of four effective transmissivities and reflectivities, $\widetilde{\rho}'$, $\widetilde{\tau}'$ (for fields entering from the right side), and $\widetilde{\rho}$, $\widetilde{\tau}$ (for fields entering from the left side). By taking the complex conjugates of the field amplitudes and inverting their propagation directions, a new set of fields related by the same set of transmissivities and reflectivities is obtained.

4.8 Appendix. The Stokes relations

The transmission and reflection coefficients of a system of mirrors, or more generally of a two-port linear optical system, can always be expressed in terms of four effective transmissivities and reflectivities: $\widetilde{\rho}$, $\widetilde{\tau}$, $\widetilde{\rho}'$ and $\widetilde{\tau}'$ [see Fig. 4.12]. These quantities are generally frequency dependent (complex) numbers. For the fields shown in Fig. 4.12, we have:

$$j_\omega = \widetilde{\rho}' k_\omega + \widetilde{\tau} a_\omega \,, \tag{4.122}$$

$$b_\omega = \widetilde{\tau}' k_\omega + \widetilde{\rho} a_\omega \,. \tag{4.123}$$

Imposing that the two-port linear optical system satisfies the conservation of energy, we have:

$$|\widetilde{\rho}|^2 + |\widetilde{\tau}|^2 = 1 \,, \quad |\widetilde{\rho}'|^2 + |\widetilde{\tau}'|^2 = 1 \,. \tag{4.124}$$

If we take the complex conjugates of all the complex amplitudes and revert their propagation directions, the resulting configuration is also a solution of the optical system, in the sense that the new fields are also related by the same sets of effective transmissivities and reflectivities. Thus, the system is invariant under time reversal. By applying explicitly this symmetry, it is straightforward to derive:

$$\widetilde{\rho}\,\widetilde{\rho}^* + \widetilde{\tau}'\,\widetilde{\tau}^* = 1 \,, \qquad \widetilde{\rho}^*\,\widetilde{\tau} + \widetilde{\tau}^*\,\widetilde{\rho}' = 0 \,, \tag{4.125}$$

$$\widetilde{\rho}'\,\widetilde{\rho}'^* + \widetilde{\tau}\,\widetilde{\tau}'^* = 1 \,, \qquad \widetilde{\rho}'^*\,\widetilde{\tau}' + \widetilde{\tau}'^*\,\widetilde{\rho} = 0 \,. \tag{4.126}$$

Equations (4.124)–(4.126) are the well-known Stokes relations [20]. If we rewrite the transmissivity and reflectivity coefficients as

$$\widetilde{\rho} = |\widetilde{\rho}|\, e^{i\mu}\,, \qquad \widetilde{\tau} = |\widetilde{\tau}|\, e^{i\nu}\,, \tag{4.127}$$

$$\widetilde{\rho}' = |\widetilde{\rho}'|\, e^{i\mu'}\,, \qquad \widetilde{\tau}' = |\widetilde{\tau}'|\, e^{i\nu'}\,, \tag{4.128}$$

and insert them into the Stokes relations (4.125)–(4.126), we obtain

$$|\widetilde{\rho}| = |\widetilde{\rho}'|\,, \qquad |\widetilde{\tau}| = |\widetilde{\tau}'|\,, \qquad |\widetilde{\rho}|^2 + |\widetilde{\tau}|^2 = 1\,; \tag{4.129}$$

$$e^{i\nu} = e^{i\nu'}\,, \qquad e^{i(\mu+\mu')} = -e^{2i\nu}\,. \tag{4.130}$$

4.9 Appendix. Input–output relations at second order in transmissivity of internal test masses

The input–output relation expanded up to second order in $\lambda L/c$, $\epsilon L/c$, $\iota_c^{1/3} L/c$ and $\Omega L/c$ can be obtained in a straightforward way by expanding Eqs. (4.99)–(4.104). The new coefficients $\widetilde{M}^{(2)}$, $\widetilde{C}_{ij}^{(2)}$ and $\widetilde{D}_i^{(2)}$ are very simple. In fact, they can be represented in terms of the first-order ones, $\widetilde{M}^{(1)}$, $\widetilde{C}_{ij}^{(1)}$ and $\widetilde{D}_i^{(1)}$ given by Eqs. (4.25)–(4.27), through the following formulas (truncated at the next-to-leading order):

$$\widetilde{M}^{(2)} = (1 - 2\epsilon L/c)\widetilde{M}^{(1)}\,, \tag{4.131}$$

$$\begin{pmatrix} \widetilde{C}_{11}^{(2)} & \widetilde{C}_{12}^{(2)} \\ \widetilde{C}_{21}^{(2)} & \widetilde{C}_{22}^{(2)} \end{pmatrix} = (1 - 2\epsilon L/c) \begin{pmatrix} 1 & \lambda L/c \\ -\lambda L/c & 1 \end{pmatrix} \begin{pmatrix} \widetilde{C}_{11}^{(1)} & \widetilde{C}_{12}^{(1)} \\ \widetilde{C}_{21}^{(1)} & \widetilde{C}_{22}^{(1)} \end{pmatrix} \begin{pmatrix} 1 & \lambda L/c \\ -\lambda L/c & 1 \end{pmatrix}, \tag{4.132}$$

and

$$\begin{pmatrix} \widetilde{D}_1^{(2)} \\ \widetilde{D}_2^{(2)} \end{pmatrix} = (1 - 2\epsilon L/c) \begin{pmatrix} 1 & \lambda L/c \\ -\lambda L/c & 1 \end{pmatrix} \begin{pmatrix} \widetilde{D}_1^{(1)} \\ \widetilde{D}_2^{(1)} \end{pmatrix}. \tag{4.133}$$

It is quite remarkable that, at second order, the optomechanical resonances, determined by $\widetilde{M}^{(2)} = 0$, remain unchanged with respect to the first order result obtained imposing $\widetilde{M}^{(1)} = 0$. Apart from a (frequency-independent) rotation of the quadrature phases, the input–output relation at next-to-leading order are very similar to the leading-order one.

4.10 Bibliography

[1] A. Abramovici et al., Science **256**, 325 (1992); B. Caron et al., Class. Quantum Grav. **14**, 1461 (1997); H. Lück et al., Class. Quantum Grav. **14**, 1471 (1997); M. Ando et al., Phys. Rev. Lett. **86**, 3950 (2001).

[2] E. Gustafson, D. Shoemaker, K. A. Strain and R. Weiss, *"LSC white paper on detector research and development,"* LIGO Document Number T990080-00-D, `www.ligo.caltech.edu/docs/T/T990080-00.pdf`.

[3] R. W. P. Drever, in *The Detection of Gravitational Waves*, ed. by D. G. Blair, (Cambridge University Press, Cambridge, England, 1991).

[4] J. Y. Vinet, B. J. Meers, C.N. Man and A. Brillet, Phys. Rev. D **38**, 433 (1998); B. J. Meers Phys. Rev. D **38**, 2317 (1998); J. Mizuno et al. Phys. Lett. A **175**, 273 (1993); G. Heinzel, *"Advanced optical techniques for laser-interferometric gravitational-wave detectors,"* Ph.D. thesis, Max-Planck-Institut für Quantenoptik, Garching, 1999.

[5] K. S. Thorne, "The scientific case for mature LIGO interferometers," LIGO Document Number P000024-00-R, `www.ligo.caltech.edu/docs/P/P000024-00.pdf`; C. Cutler and K. S. Thorne, "An overview of gravitational-wave sources," `gr-qc/0204090`.

[6] A. Freise et al. Phys. Lett. A **277**, 135 (2000); J. Mason, *"Signal Extraction and Optical Design for an Advanced Gravitational Wave Interferometer,"* Ph.D. thesis, California Institute of Technology, Pasadena, CA, 2001, LIGO document P010010-00-R, `www.ligo.caltech.edu/docs/P/P010010-00.pdf`.

[7] H.J. Kimble, Yu. Levin, A.B. Matsko, K.S. Thorne and S.P. Vyatchanin, Phys. Rev. D **65**, 022002 (2002).

[8] V.B. Braginsky and F.Ya. Khalili, *Quantum Measurement*, edited by K.S. Thorne (Cambridge University Press, Cambridge, England, 1992).

[9] A. Dorsel, J. D. McCullen, P. Meystre, E. Vignes and H. Walther, Phys. Rev. Lett. **51**, 1550 (1983); N. Deruelle and P. Tourrenc, in *Gravitation, Geometry and Relativistic Physics* (Springer, Berlin, 1984); P. Meystre, E.M. Wright, J. D. McCullen and E. Vignes, J. Opt. Soc. Am. **2**, 1830 (1985); J. M. Aguirregabria and L. Bel, Phys. Rev. D **36**, 3768 (1988); L. Bel, J. L. Boulanger and N. Deruelle, Phys. Rev. A **7**, 37 (1988); B. Meers and N. Mac Donald, *Phys. Rev. A* **40**, 40 (1989); A. Pai, S. V. Dhurandhar, P. Hello and J. Y. Vinet, Europhys. Phys. J. D **8**, 333 (2000).

[10] F. Ya. Khalili, Phys. Lett. A **288**, 251 (2001).

[11] V. B. Braginsky, M. L. Gorodetsky and F. Ya. Khalili, Phys. Lett. A **232**, 340 (1997); V. B. Braginsky and F. Ya. Khalili, Phys. Lett. A **257**, 241 (1999).

[12] J. Mizuno, *"Comparison of optical configurations for laser-interferometer gravitational-wave detectors,"* Ph.D. thesis, Max-Planck-Institut für Quantenoptik, Garching, 1995.

[13] M. Rachmanov, *"Dynamics of laser interferometric gravitational wave detectors,"* Ph.D. thesis, California Institute of Technology, Pasadena, CA, 2000.

[14] A. V. Syrtsev and F. Ya. Khalili, JETP **79**, 3 1994.

[15] The reference design of LIGO-II is obtained by optimizing the *total* noise spectral density, which also includes seismic and thermal noises, with respect to GWs from binary black holes. See `www.ligo.caltech.edu/~ligo2/scripts/l2refdes.htmu` for details.

[16] J. M. Courty, F. Grassia and S. Reynaud, Europhys. Lett. **46**, 31 (1999); F. Grassia, J. M. Courty, S. Reynaud and P. Touboul, Eur. Phys. J D **8**, 101 (2000).

[17] V. B. Braginsky, F. Ya. Khalili and P. S. Volikov, Phys. Lett. A **287**, 31 (2001).

[18] P. Purdue, Phys. Rev. D **66**, 022001 (2002) ; P. Purdue and Y. Chen, Phys. Rev. D **66**, 122004 (2002), Chapter 6 of this thesis.

[19] C. M. Caves and B.L. Schumaker, Phys. Rev. A **31**, 3068 (1985); B.L. Schumaker and C. M. Caves, Phys. Rev. A **31**, 3093 (1985).

[20] R. Blandford and K. S Thorne, *"Applications of Classical Physics,"* (unpublished textbook), Chapter 8, `www.its.caltech.edu/~rblandfo/ph136/ph136.html`.

Chapter 5

Quantum noise in laser-interferometer gravitational-wave detectors with a heterodyne readout scheme

We analyze and discuss the quantum noise in signal-recycled laser interferometer gravitational-wave detectors, such as Advanced LIGO, using a heterodyne readout scheme and taking into account the optomechanical dynamics. Contrary to homodyne detection, a heterodyne readout scheme can simultaneously measure more than one quadrature of the output field, providing an additional way of optimizing the interferometer sensitivity, but at the price of additional noise. Our analysis provides the framework needed to evaluate whether a homodyne or heterodyne readout scheme is more optimal for second generation interferometers from an astrophysical point of view. As a more theoretical outcome of our analysis, we show that as a consequence of the Heisenberg uncertainty principle the heterodyne scheme cannot convert conventional interferometers into (broadband) quantum non-demolition interferometers.

A. Buonanno, Y. Chen and N. Mavalvala, gr-qc/0302041, accepted for publication in Phys. Rev. D

5.1 Introduction

Long-baseline laser-interferometer gravitational-wave (GW) detectors have begun operation in the United States (LIGO [1]), Europe (VIRGO [2] and GEO 600 [3]) and Japan (TAMA 300 [4]). Even as the first detectors begin the search for gravitational radiation, development of the next generation detectors, such as Advanced LIGO (or LIGO-II), is underway. With planned improvements in the seismic noise reduction — via active vibration isolation [5], and in the limits set by thermal noise — via the improved mechanical quality of the optics and clever suspension strategies [6], the sensitivity of second generation detectors is expected to be quantum-noise-limited in much of the detection band from 10 to 10^4 Hz.

The optical configuration of all current GW detectors includes a Michelson interferometer. Two 4 km-long Fabry-Perot cavities are inserted into the arms of the Michelson interferometer; the optical field builds up in the cavities and samples the GW-induced phase shift multiple times. The arm cavities, thus, increase the phase sensitivity of the detector. The Michelson-based optical configuration makes it natural to decompose the optical fields and the mechanical motion of the arm-cavity mirrors into modes that are either symmetric (i.e., equal amplitude) or antisymmetric (i.e., equal in magnitude but opposite in signs) in the two arms, as explained in detail, for example, in Ref. [7] and Chapters 2 – 4. No light leaves the interferometer from below the beam-splitter (BS) or dark port, except the lights induced by the antisymmetric motion of the arm-cavity test-mass mirrors, e.g., due to a passing-by gravitational wave, or due to vacuum fluctuations that originally enter the interferometer from the dark port. Since GW interferometers operate on a dark fringe, the intensity of the light exiting the antisymmetric port is quadratic in the GW amplitude, and therefore insensitive to it, to first order. The standard way to circumvent this is to interfere the signal field with a relatively strong local oscillator (LO) field, such that the intensity of the total optical field, detected at the beat frequency, varies linearly with the GW amplitude. The various methods of measuring the GW-induced signal at the antisymmetric port are referred to as *readout schemes.*

Previously (in Ref. [7] and Chapters 2 – 4), the quantum noise in Advanced LIGO was calculated assuming a homodyne readout scheme, in which the LO field oscillates at exactly the same frequency as the incident laser. The homodyne readout scheme can pose significant technical challenges for laser noise. In this chapter we consider heterodyne readout schemes, in which the LO has different frequencies from the carrier. The heterodyne readout is usually implemented, as in initial LIGO (or LIGO-I), by using phase modulated light: the light incident on the interferometer consists of a carrier and radio frequency (RF) phase modulation (PM) sidebands [1]. Using the Schnupp asymmetry [9], the PM sidebands are transmitted to the photodetector as efficiently as possible, while the carrier still returns to the bright port. The transmitted sidebands then act as a LO against which the GW signal can beat. Demodulation at the modulation frequency converts the signal back down into the baseband. This technique circumvents laser technical noise by upconverting the signal detection to frequencies where the laser light is shot-noise-limited (a few MHz). *Here we do not concern ourselves with technical noise on the laser; we consider only the fundamental quantum noise on the light.* When the RF modulation-demodulation readout scheme is implemented, more than one quadrature of the interferometer output will be available for measurement, providing an additional tool for the optimization of the sensitivity, which is not available in homodyne detection.

However, an *additional* quantum noise contribution, as compared with the homodyne readout scheme, usually appears in this scheme during the photodetection process — as was realized

[1] Because all cases of heterodyning we consider in this work are carried out at radio frequencies, we refer to this readout as *RF modulation-demodulation.*

by Gea-Banacloche and Luechs in Ref. [8] where they evaluated the compatibility of squeezing and modulation-demodulation readout schemes in simple Michelson interferometers, and also by Schnupp, using more general considerations [9]. This additional contribution is due to vacuum fluctuations in frequency bands that are twice the modulation frequency away from the carrier. Subsequently, the heterodyne scheme was investigated in more detail by Niebauer et al. [10] and Meers and Strain [11]. These works [8, 9, 10, 11] focused exclusively on the detection of the output *phase* quadrature with *phase* modulated LO light (at the output port), which is appropriate for conventional GW interferometers with low circulating power, and hence negligible back action noise, but not for the advanced GW interferometers considered here.

The main purpose of this chapter is to further generalize the results obtained in Refs. [8, 9, 10, 11], by including the possibility of detecting *generic* quadratures with LO light that are *mixtures* of phase and amplitude modulation to the carrier, and applying them to advanced GW interferometers, such as Advanced LIGO. In particular, we provide expressions and examples of the quantum noise, taking into account explicitly both the variable-quadrature optimization and the additional heterodyne noise. This lays the foundation for optimization of the detector sensitivity for specific astrophysical sources and for comparison between heterodyne and homodyne schemes from an astrophysical point of view. The results of these investigations will be reported elsewhere [12].

Recently, Somiya [13] showed independently the possibility of measuring different quadratures through heterodyne detection, and investigated the consequences for both conventional and signal-recycled interferometers. However, the additional heterodyne noise was not explicitly taken into account — it was hoped that, in certain sophisticated heterodyne schemes, the additional heterodyne noise becomes negligible, while the variable-quadrature optimization remains possible. However, as we show in this , the additional heterodyne noise is a direct consequence of the Heisenberg uncertainty principle, and will always exist as long as more than one quadrature is available for simultaneous measurement. Moreover, the Heisenberg uncertainty principle gives rise to a quantum limit to the additional heterodyne noise, which is frequency independent unless a frequency-dependent squeezing is implemented. This frequency-independent quantum limit will seriously constrain the power of the variable-quadrature optimization of heterodyne schemes in achieving (broadband) quantum non-demolition (QND) performances. In fact, for conventional interferometers, all quantum-limited heterodyne detection can be shown to be equivalent to a frequency-independent homodyne detection performed on an otherwise identical conventional interferometer with lower input laser power.

This Chapter is organized as follows: in Section 5.2 we describe the modulation/demodulation process and derive the demodulated output of signal-recycled interferometers in terms of quadrature operators and arbitrary heterodyne field amplitudes — taking the simplest sine-wave modulation/demodulation scheme as an example; in Section 5.3 we derive the expressions of the quantum noise spectral density in this scheme, and apply them to initial and Advanced LIGO interferome-

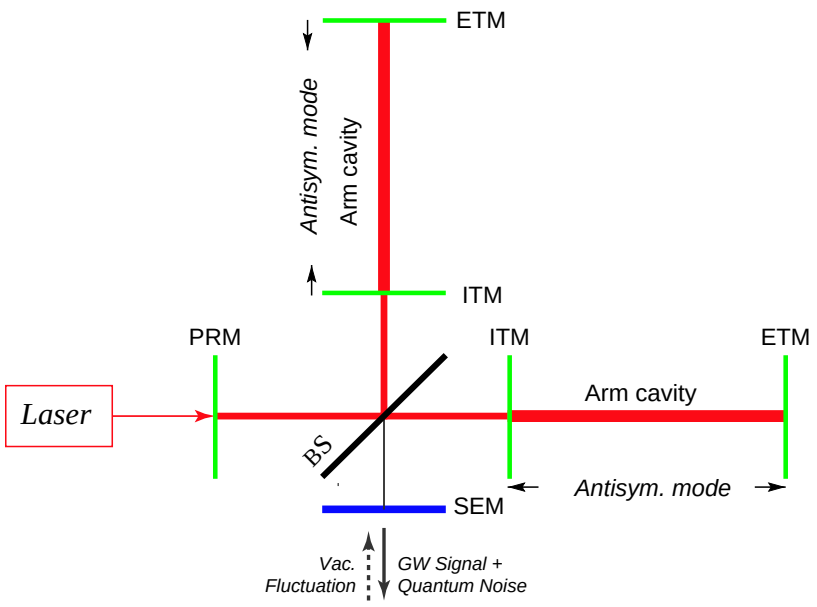

Figure 5.1: We draw a signal- (and power-) recycled LIGO interferometer. The laser light enters the interferometer from the left (bright port), through the power-recycling mirror (PRM), and gets split by a 50/50 beamsplitter into the two identical (in absence of gravitational waves) arm cavities. Each of the arm cavities is formed by the input test-mass (ITM) and the end test-mass (ETM) mirrors. A signal extracting mirror (SEM) is placed at the dark port, forming a signal extracting (SE) cavity with the ITMs.

ters; in Section 5.4.1 we analyze a completely general modulation/demodulation scheme, derive a quantum limit for heterodyne measurements and discuss the consequence of this quantum limit for conventional interferometers. Finally, in Section 5.5, we present our conclusions.

5.2 The radio-frequency modulation-demodulation scheme in advanced LIGO

5.2.1 Overview of Advanced LIGO optical configuration

The Michelson interferometer is operated on the dark fringe to minimize static laser power, and hence the shot noise associated with this light, at the antisymmetric (dark) port. Since most of the light returns toward the laser, a partially transmitting mirror, the power-recycling mirror (PRM) is placed between the laser and the beam splitter to 'recycle' the light back into the interferometer [14] (see Fig. 5.1). The optical configuration currently planned to achieve quantum-limited performance in Advanced LIGO uses the Resonant Sideband Extraction (RSE) technique [15], in addition to power-recycling. In RSE, an additional partially transmitting mirror, the signal extraction mirror (SEM), is placed between the antisymmetric port of the beamsplitter and photodetector (see Fig 5.1).

The optical properties (reflectivity, loss) of this signal extraction mirror and its microscopic

position (in fractions of the wavelength of the laser light, $1.064\,\mu$m) can significantly influence the frequency response of the interferometer [16, 15]. When the signal extraction cavity (SEC) — comprising the SEM and the input test-mass (ITM) mirrors of the arm cavities — is exactly resonant or anti-resonant at the laser frequency, the bandwidth of the entire detector can be increased or decreased by altering the reflectivity of the SEM. These two special cases are referred to as resonant sideband extraction (RSE) [15] and signal recycling (SR) [16], respectively.

As the signal cavity is slightly offset (detuned) from resonance (RSE) or antiresonance (SR), the frequency at which the peak optical response of the detector occurs can be shifted to frequencies where other noise sources are not dominant. Note that, unlike conventional interferometers and tuned RSE/SR interferometers, the frequency responses of detuned configurations are no longer symmetric around the carrier frequency, with only one resonant peak located either higher or lower than the carrier frequency. As a consequence, although the interferometer will respond resonantly to GW's with a certain nonzero frequency, only one of the two (upper and lower) sidebands the GW generates symmetrically around the carrier frequency is on resonance. More generally, the upper and lower GW sidebands contribute asymmetrically to the total output field, which makes the GW signal appear simultaneously in both quadratures of the output field (see Chapters 2 – 4). Detuned configurations are neither RSE nor SR in the original sense, but roughly speaking, such a configuration can be classified as either RSE or SR by looking at whether the bandwidth of the entire interferometer is broader or narrower than that of the arm cavity. Historically, since SR was invented earlier than RSE, some literature refers to all configurations with a signal mirror as "Signal Recycled."

Since detuned RSE allows us to control the spectral response of the interferometer and optimize for specific astrophysical sources, it has become a strongly favored candidate for Advanced LIGO [2]. A notable consequence is that with the high laser power of Advanced LIGO, the optomechanical coupling induced by detuned RSE/SR significantly modifies the dynamics of the interferometer, introducing an additional resonance at which the sensitivity also peaks (see Chapters 2 – 4).

5.2.2 Modulation and demodulation processes

The RF modulation-demodulation scheme comprises two parts: the modulation-preparation and demodulation-readout processes. In this section we consider only the simplest case, sine wave modulation and demodulation. A more general discussion of modulation/demodulation schemes can be found in Sec. 5.4.

Phase modulated light is incident on the interferometer. It is composed of the carrier at the laser frequency $\omega_0 \sim 2 \cdot 10^{15}\,\mathrm{s}^{-1}$, and a pair of phase modulation sidebands offset from the carrier

[2] RSE, instead of SR, is chosen for Advanced LIGO in order to decrease the required input power [15]. However, as far as quantum noise is concerned, the required circulating power inside the arms will not be influenced by whether SR or RSE is used (see Ref. [15] and Chapter 4.

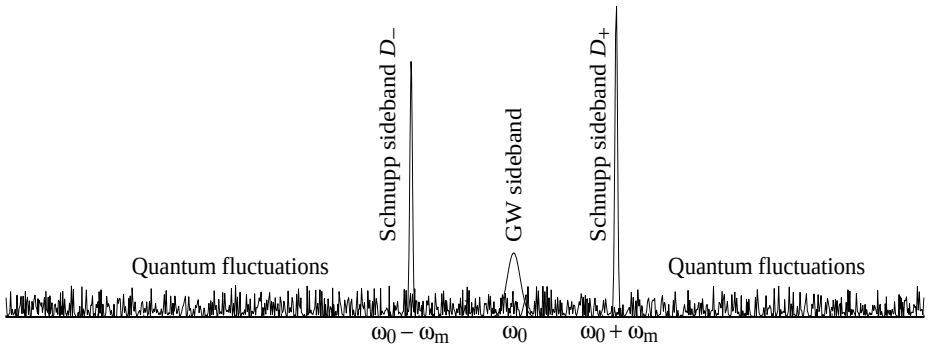

Figure 5.2: The outgoing field at the interferometer output consists of GW sideband signals around ω_0, the Schnupp sideband fields at $\omega_0 \pm \omega_m$ and quantum fluctuations spread out at all frequencies.

by several MHz, so $\omega_m \sim 2\pi \cdot 10^6\,s^{-1} \gg$ GW-sideband frequency $< 2\pi \cdot 10^4\,s^{-1}$. The detection port is kept as dark as possible for the carrier, while the PM sidebands at $\omega_0 \pm \omega_m$ are coupled out as efficiently as possible to act as the local oscillator for the GW-induced carrier field that leaks out. Maximal RF sideband transmission is adjusted in two ways: (i) by a path difference in the arms of the Michelson that is arranged to be highly transmissive for the RF component of the field – the Schnupp asymmetry; and (ii) by matching the transmission of the power-recycling and signal-extracting mirrors so that the effective cavity comprising those two mirrors is critically coupled. In addition to the gravitational-wave readout, the PM sidebands are also useful for controlling the auxiliary degrees of freedom of the interferometer [17].

In Fig. 5.2 we show the outgoing optical field at the interferometer output in the frequency domain, which consists of the GW sidebands, the Schnupp sidebands and quantum fluctuations at the output. The relative amplitudes of the RF sidebands are intentionally shown to be unequal. This is a case of unbalanced heterodyning, and is an intrinsic feature of the detuned RSE interferometer. As described above, when we move to detuned RSE, the SEC is detuned from perfect carrier resonance, such that the resonance peak of the signal cavity coincides with *one* of the GW signal sidebands, at the expense of the other one; consequently, the GW signal appears in both quadratures of the output field. At the same time, this phase shift in the signal cavity moves both RF sidebands off perfect resonance as well, which results in poor output coupling of both RF sidebands. This can be remedied by offsetting the RF sideband frequency – or conversely, the macroscopic length of the SEC – to make *one* of the RF sidebands resonant [18]. Hence, detuned RSE leads to unbalanced heterodyne fields. Although the carrier is phase modulated before entering the interferometer, the heterodyne fields at the output port will no longer act as a pure phase modulation on the carrier.

At the detection port, a standard heterodyne detection procedure is used to extract the GW signal:

$$\text{Outgoing light} \Rightarrow \text{Photodetection} \rightarrow \text{Mixing with } \cos(\omega_m t + \phi_D) \rightarrow \text{Low} - \text{pass filter} \Rightarrow \text{Demodulated output}$$

The photodetection process consists of taking the square of the optical field shown in Fig. 5.2. This operation mixes the GW signal (and quantum fluctuations) located at frequency $\sim \omega_0$ with the RF sideband fields located at frequency $\omega_0 \pm \omega_{\rm m}$. As a consequence the GW signal is measured in the RF band around $\pm\omega_{\rm m}$. By taking the product of (or mixing) the photodetection output with the demodulation function, $\cos(\omega_{\rm m} t + \phi_{\rm D})$, the GW signal is down-converted back to low frequencies. The result is then filtered by a low-pass filter, yielding a *frequency-independent* quadrature that does depend on $\phi_{\rm D}$. However, as we shall see more quantitatively in the following sections, in addition to the GW signal (and quantum fluctuations) centered at $\sim \omega_0$, quantum fluctuations at $\sim \omega_0 \pm 2\omega_{\rm m}$ also enter the demodulated output at the antisymmetric port. This gives rise to an additional noise term that is not present in a homodyne readout scheme.

5.2.3 Demodulated output of LIGO interferometers

The optical field coming out from the interferometer [see Fig. 5.1] can be written as a sum of two parts:

$$E(t) = L(t) + S(t)\,. \tag{5.1}$$

The first term,

$$L(t) = \Big[D_+ e^{i\,(\omega_0+\omega_{\rm m})\,t} + D_- e^{i\,(\omega_0-\omega_{\rm m})\,t} \Big] + \text{h.c.}\,, \tag{5.2}$$

is the (classical) LO light composed of the Schnupp sideband fields at frequencies $\omega_0 \pm \omega_{\rm m}$, with (complex) amplitudes D_+ and D_-, respectively. The magnitude and phase of $D_\pm$ depend on the specific optical configuration. The two quadratures of the LO are generated by either amplitude modulation (first quadrature) or phase modulation (second quadrature) of the input light. The second term in Eq. (5.1) ,

$$\begin{aligned} S(t) &\equiv \int_0^{+\infty} \frac{d\omega}{2\pi} \left[e^{-i\omega t}\, b_\omega + \text{h.c.} \right] , \\ &= \int_{-\Lambda}^{+\Lambda} \frac{d\Omega}{2\,\pi} \left[e^{-i\,(\omega_0 - 2\omega_{\rm m} + \Omega)\,t}\, b_{\omega_0 - 2\omega_{\rm m} + \Omega} + \text{h.c.} \right] \\ &+ \int_{-\Lambda}^{+\Lambda} \frac{d\Omega}{2\,\pi} \left[e^{-i\,(\omega_0 + \Omega)\,t}\, b_{\omega_0 + \Omega} + \text{h.c.} \right] \\ &+ \int_{-\Lambda}^{+\Lambda} \frac{d\Omega}{2\,\pi} \left[e^{-i\,(\omega_0 + 2\omega_{\rm m} + \Omega)\,t}\, b_{\omega_0 + 2\omega_{\rm m} + \Omega} + \text{h.c.} \right] \\ &+ \text{(contributions at irrelevant frequency bands)}\,, \end{aligned} \tag{5.3}$$

contains both the (classical) GW signal and the quantum fluctuations of optical fields near ω_0. Here $\Lambda \lesssim \omega_{\rm m}$ is the demodulation bandwidth [3]. [For simplicity and clarity, we only write out explicitly

[3] Note that both in $L(t)$ and $S(t)$ we disregard the overall factor $\sqrt{2\pi\hbar\omega_0/\mathcal{A}c}$ where $\mathcal{A}$ is the effective cross sectional area of the laser beam and c is the speed of light. This factor does not affect the final expression of the spectral density and for simplicity we neglect it. See Eq. (2.6) in Chapter 2.

the terms that will eventually contribute to the demodulated output.]

The photocurrent from the photodetector is proportional to the square of the optical field,

$$\begin{aligned} i(t) \propto E^2(t) &= L^2(t) + 2L(t)\,S(t) + S^2(t)\,, \\ &= \big[\text{contributions at frequencies } 0,\ \pm 2\omega_{\rm m},\ \pm(2\omega_0 \pm 2\omega_{\rm m}),\ \text{from } L^2(t)\big] \\ &+ 2D_+ \left[\int_{-\Lambda}^{+\Lambda} \frac{d\Omega}{2\pi} e^{i(\omega_{\rm m}-\Omega)t}\, b_{\omega_0+\Omega} + \int_{-\Lambda}^{+\Lambda} \frac{d\Omega}{2\pi} e^{-i(\omega_{\rm m}+\Omega)t}\, b_{\omega_0+2\omega_{\rm m}+\Omega}\right] + \text{h.c.} \\ &+ 2D_- \left[\int_{-\Lambda}^{+\Lambda} \frac{d\Omega}{2\pi} e^{i(\omega_{\rm m}-\Omega)t}\, b_{\omega_0-2\omega_{\rm m}+\Omega} + \int_{-\Lambda}^{+\Lambda} \frac{d\Omega}{2\pi} e^{-i(\omega_{\rm m}+\Omega)t}\, b_{\omega_0+\Omega}\right] + \text{h.c.} \\ &+ [\text{contributions at irrelevant frequency bands}] \\ &+ \big[\text{terms quadratic in } b,\ b^\dagger,\ \text{from } S^2(t)\big]\ . \end{aligned} \tag{5.4}$$

After taking the product of (or mixing) $i(t)$ with $\cos(\omega_{\rm m}t + \phi_{\rm D})$ and applying a low-pass filter with cutoff frequency Λ, we obtain the demodulated output

$$\begin{aligned} i(t)\cos(\omega_{\rm m}t+\phi_{\rm D}) \overset{\text{Low-pass}}{\Longrightarrow} O(\phi_{\rm D};t) &= \int_{-\Lambda}^{+\Lambda} \frac{d\Omega}{2\pi} \left[\left(D_+ e^{-i\phi_{\rm D}} + D_- e^{i\phi_{\rm D}}\right) e^{-i\,\Omega\,t}\, b_{\omega_0+\Omega} + \text{h.c.}\right] \\ &+ \int_{-\Lambda}^{+\Lambda} \frac{d\Omega}{2\pi} \left[D_+ e^{i\phi_{\rm D}} e^{-i\,\Omega\,t}\, b_{\omega_0+2\omega_{\rm m}+\Omega} + \text{h.c.}\right] \\ &+ \int_{-\Lambda}^{+\Lambda} \frac{d\Omega}{2\pi} \left[D_- e^{-i\phi_{\rm D}} e^{-i\,\Omega\,t}\, b_{\omega_0-2\omega_{\rm m}+\Omega} + \text{h.c.}\right]\ , \end{aligned} \tag{5.5}$$

where we assume the local oscillator to be strong enough that the quadratic terms in Eq. (5.4) can be ignored. It is convenient to recast the demodulated output (5.5) in terms of quadrature operators by using the following relation (for $\Lambda \ll \omega$):

$$\int_{-\Lambda}^{+\Lambda} \frac{d\Omega}{2\pi} \left[A e^{-i\,\Omega\,t}\, b_{\omega+\Omega} + A^* e^{i\,\Omega\,t}\, b^\dagger_{\omega+\Omega}\right] = \int_0^{+\Lambda} \frac{d\Omega}{2\pi} \sqrt{2}\, A_0\, e^{-i\,\Omega\,t}\, b^\omega_{\alpha+\frac{\pi}{2}}(\Omega) + \text{h.c.}\,. \tag{5.6}$$

Here $A = A_0\, e^{i\alpha}$ ($A_0,\ \alpha \in \Re$) is an arbitrary complex amplitude, and the quadrature operator $b^\omega_{\alpha+\frac{\pi}{2}}$ is defined as [see also Chapter 2]

$$b^\omega_\zeta(\Omega) = b^\omega_1(\Omega)\sin\zeta + b^\omega_2(\Omega)\cos\zeta\,, \tag{5.7}$$

where

$$b^\omega_1(\Omega) = \frac{b_{\omega+\Omega} + b^\dagger_{\omega-\Omega}}{\sqrt{2}}\,, \qquad b^\omega_2(\Omega) = \frac{b_{\omega+\Omega} - b^\dagger_{\omega-\Omega}}{\sqrt{2}i}\,. \tag{5.8}$$

The superscript ω on the quadrature fields is added to emphasize that the quadratures are defined with respect to the central frequency ω. By applying relation (5.6) to the demodulated output (5.5),

we get

$$O(\phi_{\rm D};t) = \int_0^{+\Lambda} \frac{d\Omega}{2\pi} e^{-i\,\Omega\,t}\sqrt{2}\left[D_0\, b_{\zeta_0}^{\omega_0}(\Omega) + |D_+|\; b_{\zeta_+}^{\omega_0+2\omega_{\rm m}}(\Omega) + |D_-|\; b_{\zeta_-}^{\omega_0-2\omega_{\rm m}}(\Omega)\right] + \text{h.c.}\,, \tag{5.9}$$

in which we have defined,

$$D_0 \equiv \left|D_+\, e^{-i\phi_{\rm D}} + D_-\, e^{i\phi_{\rm D}}\right|\,, \tag{5.10}$$

and

$$\zeta_0 \equiv \frac{\pi}{2} + \arg\left(D_+\, e^{-i\phi_{\rm D}} + D_-\, e^{i\phi_{\rm D}}\right)\,, \tag{5.11}$$

$$\zeta_\pm \equiv \pm\phi_{\rm D} + \frac{\pi}{2} + \arg D_\pm\,. \tag{5.12}$$

In the frequency domain, we have,

$$O(\phi_{\rm D};\Omega) = \sqrt{2}D_0\left[b_{\zeta_0}^{\omega_0}(\Omega) + \frac{|D_+|}{D_0}\, b_{\zeta_+}^{\omega_0+2\omega_{\rm m}}(\Omega) + \frac{|D_-|}{D_0}\, b_{\zeta_-}^{\omega_0-2\omega_{\rm m}}(\Omega)\right]\,, \qquad |\Omega| < \Lambda\,. \tag{5.13}$$

The first term inside the parenthesis, $b_{\zeta_0}^{\omega_0}$ is an output quadrature field around the carrier frequency ω_0, which contains both the GW signal and vacuum fluctuations in the optical fields near the carrier frequency. In Chapters 2 – 4, this quadrature field is related to the input quadrature field at the antisymmetric port via the input-output relations, from which the spectral density of the quantum noise can be derived. Measuring this field is the task of all readout schemes. For example, a homodyne scheme can measure directly an arbitrary frequency-independent quadrature. For this reason, we call the quadrature field $b_{\zeta_0}^{\omega_0}$ the *homodyne quadrature* for distinction. The two additional terms inside the parenthesis are the additional noise, which come from vacuum fluctuations around $\omega_0 \pm 2\omega_m$. The sum of all three terms is what we measure in the heterodyne scheme, which we call the *heterodyne quadrature*.

Quantity	Symbol and Value
Laser frequency	$\omega_0 = 1.8 \times 10^{15}\,\text{sec}^{-1}$
GW sideband frequency	Ω
Input test-mass transmissivity	T
Arm-cavity length	$L = 4\,\text{km}$
Mirror mass	m
Light power at beamsplitter	I_0
SEM amplitude reflectivity and transmissivity	ρ, τ
SEC length	$l \sim 10\,\text{m}$
SEC detuning	$\phi = [\omega_0 l/c]_{\text{mod}\,2\pi}$

Table 5.1: Basic quantities of Advanced LIGO interferometers

5.2.4 Features of the RF modulation-demodulation scheme

As can be inferred from Eq. (5.11), as long as $|D_+| \neq |D_-|$, all homodyne quadratures can be measured through some heterodyne quadrature with the appropriate demodulation phase $\phi_{\rm D}$. The (single-sided) spectral density $S(\Omega)$ associated with the noise h_n can be computed by the formula [see Eq. (22) of Ref. [7]]:

$$2\pi\,\delta(\Omega-\Omega')\,S(\Omega) = \langle {\rm in}|h_n(\Omega)\,h_n^\dagger(\Omega') + h_n^\dagger(\Omega')\,h_n(\Omega)|{\rm in}\rangle\,, \tag{5.14}$$

and if the input state of the whole interferometer is the vacuum state ($|{\rm in}\rangle = |0_a\rangle$), the following relation holds:

$$\langle 0_a|a_i(\Omega)\,a_j^\dagger(\Omega') + a_j^\dagger(\Omega')\,a_i(\Omega)|0_a\rangle = 2\pi\,\delta(\Omega-\Omega')\,\delta_{ij}\,. \tag{5.15}$$

From Eq. (5.13) we see that the noise spectral density in the heterodyne quadrature is a sum of that of the homodyne quadrature, $S_b^{\rm hom}(\phi_{\rm D};\Omega)$, and those of the additional noise terms, $S_b^{\rm add}(\phi_{\rm D};\Omega)$. Since $S_b^{\rm hom}(\phi_{\rm D};\Omega)$ and $S_b^{\rm add}(\phi_{\rm D};\Omega)$ come from different frequency bands, we assume that they are uncorrelated, hence

$$S_b^{\rm het}(\phi_{\rm D};\Omega) = S_b^{\rm hom}(\phi_{\rm D};\Omega) + S_b^{\rm add}(\phi_{\rm D};\Omega)\,. \tag{5.16}$$

Assuming that the fields associated with the additional heterodyne noise are in the vacuum state, we get a white (frequency-independent) spectrum for the additional noise,

$$S_b^{\rm add}(\phi_{\rm D}) = \frac{|D_+|^2+|D_-|^2}{D_0^2} = \frac{|D_+|^2+|D_-|^2}{|D_+e^{-i\phi_{\rm D}} + D_-e^{i\phi_{\rm D}}|^2}\,, \tag{5.17}$$

which usually depends on $\phi_{\rm D}$, unless either D_+ or D_- is zero, which we refer to as the *totally unbalanced* case. In the case of balanced modulation, when $|D_+| = |D_-|$, only one quadrature,

$$\zeta_0^{\rm balanced} = \frac{\pi}{2} + \frac{1}{2}\left(\arg D_+ + \arg D_-\right)\,, \tag{5.18}$$

is measured, with additional noise

$$S_b^{\rm add\,balanced} = \frac{1}{2}\,, \tag{5.19}$$

and with a frequency-independent optimal demodulation phase

$$\phi_{\rm D}^{\rm balanced} = \frac{1}{2}\left[\arg D_+ - \arg D_-\right] + N\pi\,, \quad N = 0,\,\pm1,\,\ldots\,. \tag{5.20}$$

This is the lowest possible additional noise for heterodyne schemes with just one pair of sidebands. The noise spectral density can have different shapes as a function of the homodyne angle (see Ref. [7] and Chapter 2). At different signal sideband frequencies, the optimal homodyne angle

$\zeta_{\rm opt}$ that gives the lowest homodyne noise can be different. In homodyne detection, since both quadratures of the carrier are generally not available, only a single frequency-independent quadrature can be measured [4]. By contrast, in heterodyne detection schemes (except for the balanced case), all quadratures are available for simultaneous measurement, and the final heterodyne noise at each frequency will be the minimum of all quadratures.

5.3 Noise spectral density and the effect of the additional noise

In this section, we write down the noise spectral density for both conventional and RSE interferometers when the RF modulation-demodulation scheme described in Section 5.2 is used.

Symbol	Quantity	Expression
γ	Half bandwidth of arm cavity	$\dfrac{Tc}{4L}$
β	Phase gained by resonant field in arm cavity	$\arctan(\Omega/\gamma)$
$h_{\rm SQL}$	Free-mass standard quantum limit	$\sqrt{\dfrac{8\hbar}{m\Omega^2L^2}}$
$I_{\rm SQL}$	Characteristic input power for conventional interferometer to reach the SQL at $\Omega=\gamma$	$\dfrac{mL^2\gamma^4}{4\omega_0}$
$\mathcal{K}$	Coupling constant for radiation-pressure effects	$\dfrac{2(I_0/I_{\rm SQL})\gamma^4}{\Omega^2(\Omega^2+\gamma^2)}$

Table 5.2: Quantities derived from those listed in Tab. 5.1

5.3.1 Total noise spectral density

The input-output relation for RSE interferometers, including optomechanical effects, were derived in Chapter 2 [see Eqs. (2.20)–(2.24) and (2.26) in Chapter 2]. The output fields in the frequency band of $(\omega_0-\Lambda,\,\omega_0+\Lambda)$ are (in the conventions used in this manuscript)

$$\begin{pmatrix} b_1^{\omega_0} \\ b_2^{\omega_0} \end{pmatrix} = \frac{1}{M}\left[e^{2i\beta}\begin{pmatrix} C_{11} & C_{12} \\ C_{21} & C_{22} \end{pmatrix}\begin{pmatrix} a_1^{\omega_0} \\ a_2^{\omega_0} \end{pmatrix} + \sqrt{2\mathcal{K}}\tau e^{i\beta}\begin{pmatrix} D_1 \\ D_2 \end{pmatrix}\frac{h}{h_{\rm SQL}}\right], \tag{5.21}$$

[4] Unless the output signal is filtered through the kilometer-scale optical filters proposed by Kimble et al. [7].

where

$$M = 1 + \rho^2\, e^{4i\beta} - 2\rho\, e^{2i\beta} \left(\cos 2\phi + \frac{\mathcal{K}}{2} \sin 2\phi \right) , \tag{5.22}$$

$$C_{11} = C_{22} = (1+\rho^2) \left(\cos 2\phi + \frac{\mathcal{K}}{2} \sin 2\phi \right) - 2\rho \cos 2\beta \,, \tag{5.23}$$

$$C_{12} = -\tau^2 \left(\sin 2\phi + \mathcal{K} \sin^2 \phi \right) , \qquad C_{21} = \tau^2 \left(\sin 2\phi - \mathcal{K} \cos^2 \phi \right) , \tag{5.24}$$

$$D_1 = -(1 + \rho\, e^{2i\beta}) \sin\phi \,, \qquad D_2 = -(-1 + \rho\, e^{2i\beta}) \cos\phi \,. \tag{5.25}$$

The quantities $\mathcal{K}$, β, ρ, ϕ, τ and $h_{\rm SQL}$ are defined in the same way as in Chapters 2 and 3. We denote by $h(\Omega)$ the gravitational strain and give a summary of the main quantities in Tables 5.1 and 5.2. We assume that the fields a^{ω_0} incident on the unused input of the antisymmetric port are in the vacuum state for all frequencies. Moreover, the additional heterodyne noise fields $b^{\omega_0 \pm 2\omega_m}$ in Eq. (5.13) must also be in vacuum states, since they are far away from the carrier frequency and are not affected by the ponderomotive squeezing effects of the interferometer. We assume that the higher-order terms of the modulation are not resonant in the interferometer, which is in general the case. Even if the higher-order sidebands are resonance, we would not expect any ponderomotive squeezing since the frequency is too high for the test-mass displacement to respond to an external force. Using Eqs. (5.14)–(5.17) and (5.21), we obtain the total heterodyne noise spectral density in h, as a sum of the corresponding homodyne noise (first term) and the additional heterodyne noise (second term) [see Eqs. (5.10), (5.11) for the definitions of D_0 and ζ_0]:

$$\begin{aligned} & S_h^{\rm het}(\phi_{\rm D};\Omega) \\ = \; & \frac{h_{\rm SQL}^2}{2\mathcal{K}} \frac{1}{\tau^2 \left| D_1 \sin\zeta_0 + D_2 \cos\zeta_0 \right|^2} \Bigg[\left(C_{11} \sin\zeta_0 + C_{21} \cos\zeta_0 \right)^2 + \left(C_{12} \sin\zeta_0 + C_{22} \cos\zeta_0 \right)^2 \\ & \qquad + \frac{|D_+|^2 + |D_-|^2}{\left| D_+ e^{-i\phi_{\rm D}} + D_- e^{i\phi_{\rm D}} \right|^2} |M|^2 \Bigg] . \end{aligned} \tag{5.26}$$

We note that the optimal heterodyne noise spectral density at a given GW signal sideband frequency is the minimum of those obtained varying $\phi_{\rm D}$ (and thus ζ_0).

5.3.2 Conventional interferometers

For the power-recycled Fabry-Perot Michelson optical configuration, the so-called conventional interferometer, the GW signal appears only in the second (or phase) quadrature. Furthermore, barring imperfections, the transmission of the Schnupp sidebands is balanced. In our notation such a scheme is obtained by setting $D_- = -D_+^*$, with $\phi_{\rm D} = \pm\pi/2 + \arg D_+$ which is the optimal demodulation

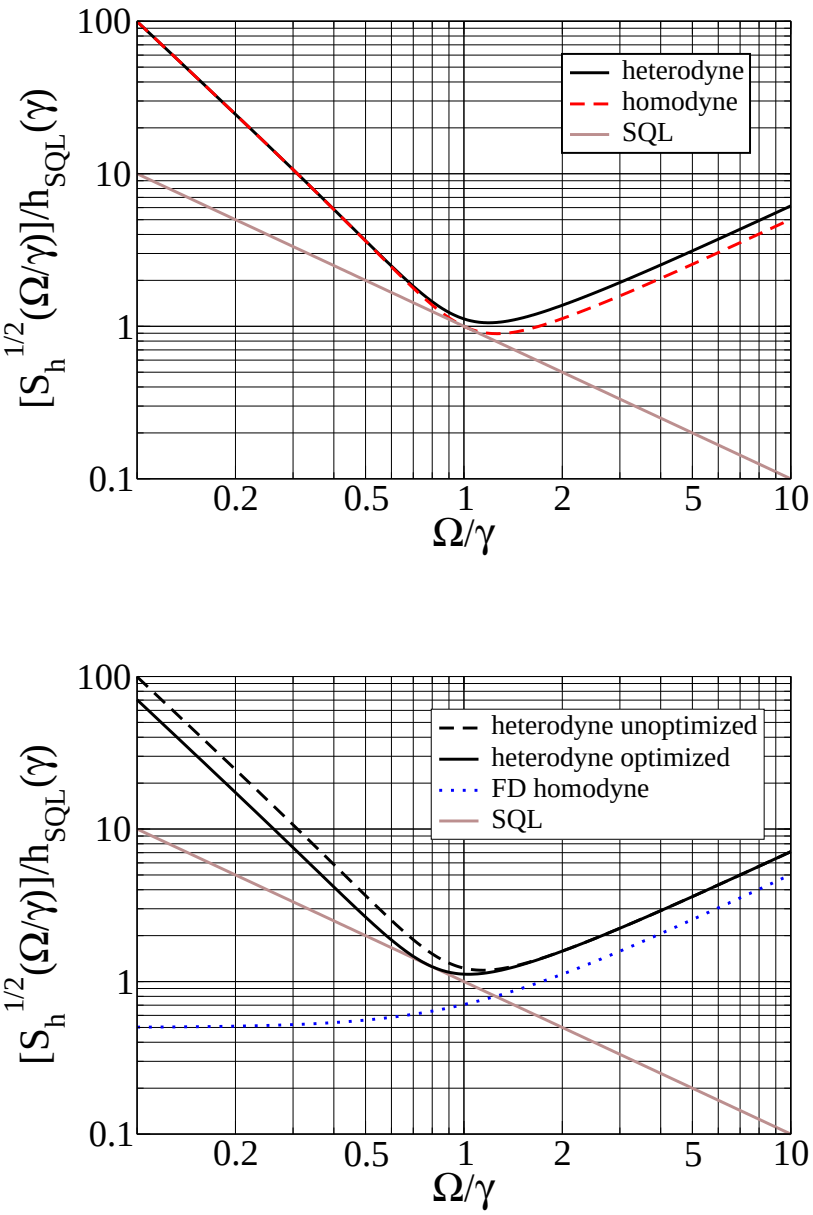

Figure 5.3: In the upper panel we show the square root of noise spectral density, in units of $h_{\rm SQL}(\gamma)$, for a conventional interferometer with $I_0 = I_{\rm SQL}$, using balanced heterodyne modulation (solid curve) and the homodyne (dashed curve) scheme, plotted as functions of Ω/γ. The second quadrature is measured. In the lower panel we plot the noise spectral density of the same interferometer, using unbalanced heterodyne detection, with homodyne angle chosen at the optimal value for the homodyne case, $\zeta(\Omega) = \zeta_{\rm opt\,hom}(\Omega)$ (dashed line), and at the re-optimized value for the heterodyne case $\zeta(\Omega) = \zeta_{\rm opt\,het}(\Omega)$ (solid curve), respectively. The optimal heterodyne noise spectral density *without the additional noise* is also shown (dotted curve), which agrees with the result for frequency-independent homodyne detection [7]. The SQL line is shown in both panels as gray straight lines.

phase for all frequencies [see Eq. (5.20)]. Evaluating Eq. (5.26) in the case $\phi = 0, \tau = 1$, we get

$$S_h^{\text{het conv}} = \frac{h_{\text{SQL}}^2}{2\mathcal{K}} \left(\mathcal{K}^2 + 1 + \frac{1}{2} \right) , \tag{5.27}$$

where the last term inside the parenthesis is the additional heterodyne noise, which is equal to 1/2 the shot noise in homodyne readout scheme (second term), originally derived in Ref. [11]. In the upper panel of Fig. 5.3, we plot the noise curves of a conventional interferometer with $I_0 = I_{\text{SQL}}$, using homodyne and balanced heterodyne detection, respectively, with the second quadrature measured. This is exactly the result in Ref. [10]. More sophisticated modulation schemes that can further lower or eliminate the additional heterodyne noise *in this quadrature* have been investigated by Schnupp [9], Niebauer et al. [10], and Meers and Strain [11].

If, on the contrary, the RF sidebands at the antisymmetric port are not balanced, one can measure arbitrary quadratures by adjusting the demodulation phase [see Sec. 5.2.4]. As proposed by Vyatchanin, Matsko and Zubova [19], and further investigated by Kimble, Levin, Matsko, Thorne and Vyatchanin (KLMTV) [7], measuring different quadratures at different GW signal sideband frequencies can allow conventional interferometers to beat the Standard Quantum Limit (SQL) [20] significantly, thus converting them into a QND interferometer. Somiya [13] proposed that, by using a frequency-dependent demodulation phase, a KLMTV-type, frequency-dependent optimization is achievable in a totally unbalanced modulation scheme. However, the effect of the additional heterodyne noise was not explicitly taken into account and we show in this section that the additional heterodyne noise plays an important role as soon as one approaches the SQL. So much so, that for totally unbalanced heterodyne detection, the SQL cannot be beaten, and for intermediate levels of imbalance the SQL is beaten by very modest amounts.

For simplicity, we first consider a totally unbalanced modulation scheme (which was the case investigated by Somiya [13]), in which only D_+ (or only D_-) is non-zero. From Eq. (5.26), fixing $\tau = 1$, $\rho = 0$ and $\phi = 0$, we have

$$S_h^{\text{het conv}} = \frac{h_{\text{SQL}}^2}{2\mathcal{K}} \left[(\mathcal{K} - \tan\zeta_0)^2 + 1 + \frac{1}{\cos^2\zeta_0} \right] , \tag{5.28}$$

where the last term inside the parenthesis is the additional noise due to heterodyne detection. Using the optimal detection angle in the (frequency dependent) homodyne case [19, 7], $\zeta_{\text{opt hom}} = \arctan\mathcal{K}$, one has

$$S_h = \frac{h_{\text{SQL}}^2}{2\mathcal{K}} \left(\mathcal{K}^2 + 2 \right) \geq \sqrt{2} h_{\text{SQL}}^2 , \tag{5.29}$$

which cannot reach the SQL. Re-optimizing the detection angle, we obtain $\zeta_{\text{opt het}} = \arctan(\mathcal{K}/2)$. This gives

$$\left[S_h^{\text{het conv}} \right]_{\text{opt}} = \frac{h_{\text{SQL}}^2}{2\mathcal{K}} \left(\frac{\mathcal{K}^2}{2} + 2 \right) \geq h_{\text{SQL}}^2 , \tag{5.30}$$

which only touches, but never beats, the SQL. In the lower panel of Fig. 5.3, we plot the noise curve of a conventional interferometer with $I_0 = I_{\rm SQL}$, the heterodyne noise spectral density using $\zeta_{\rm opt\,hom}$ [given by Eq. (5.29)], and the optimal heterodyne noise spectral density [given by Eq. (5.30)]. As can be further verified, having two sidebands with unequal amplitude can allow the interferometer to beat the SQL, but only by very moderate amounts, and in limited frequency bands.

We might still expect to use more sophisticated modulation-demodulation schemes to lower the additional heterodyne noise while retaining the possibility of variable-quadrature optimization. However, as we shall see in Sec. 5.4, such an effort will be significantly limited by the Heisenberg uncertainty principle.

5.3.3 Signal-recycled interferometers

In this section, we give some examples of noise curves of detuned RSE interferometers with a heterodyne readout scheme, and compare them to the homodyne cases.

In the balanced scheme the additional heterodyne noise is the lowest, but only one quadrature can be measured. For this case we show the effect of the additional heterodyne noise on the sensitivity curves in Fig. 5.4. In the upper panel, we plot the noise curves for a detuned RSE interferometer with $T = 0.033$, $\rho = 0.9$, $\phi = \pi/2 - 0.47$, $I_0 = I_{\rm SQL}$ and $m = 30\,{\rm kg}$, (the configuration considered in Chapters 2 and 3) when the first ($\zeta = \pi/2$) and second quadratures ($\zeta = 0$) are measured, by homodyne and balanced heterodyne read-out schemes. In the lower panel, we plot the ratio of the heterodyne noise to the corresponding homodyne ones. The additional heterodyne noise has more features around the two valleys of the noise curves, where the optomechanical dynamics (the RSE transfer function) determines the shape of the curves. Above $\sim$ 200 Hz, the ratio between the square roots of the heterodyne and the homodyne noise spectral densities assumes the constant value $\sqrt{3/2} \sim 1.22$, which is due to the additional heterodyne noise when the shot noise dominates [see Eq. (5.27)].

Practical implementation of the RF sidebands in the interferometer has shown that detuned RSE configurations are likely to be very unbalanced [18, 12]. In the upper panel of Fig. 5.5, we plot the unbalanced heterodyne noise spectral densities for the same interferometer parameters used in Fig. 5.4, with $\zeta_0 = 0$, $\pi/4$, $\pi/2$ and $3\pi/4$, and the optimal heterodyne noise obtained by maximizing over ζ_0 at each sideband frequency. Indeed, in the heterodyne readout scheme we have the advantage of optimizing the detection angle at different frequencies. At each particular signal sideband frequency, the optimal heterodyne noise spectral density is just the minimum of all quadratures. In the lower panel of Fig. 5.5, we compare the optimal heterodyne noise with the homodyne noise at $\zeta = 0$ and $\zeta = \pi/2$. As we see from this example, for the same interferometer configuration, neither the homodyne nor the heterodyne readout can provide a noise spectral density that is the lowest for all GW signal sideband frequencies. To make a more rigorous comparison

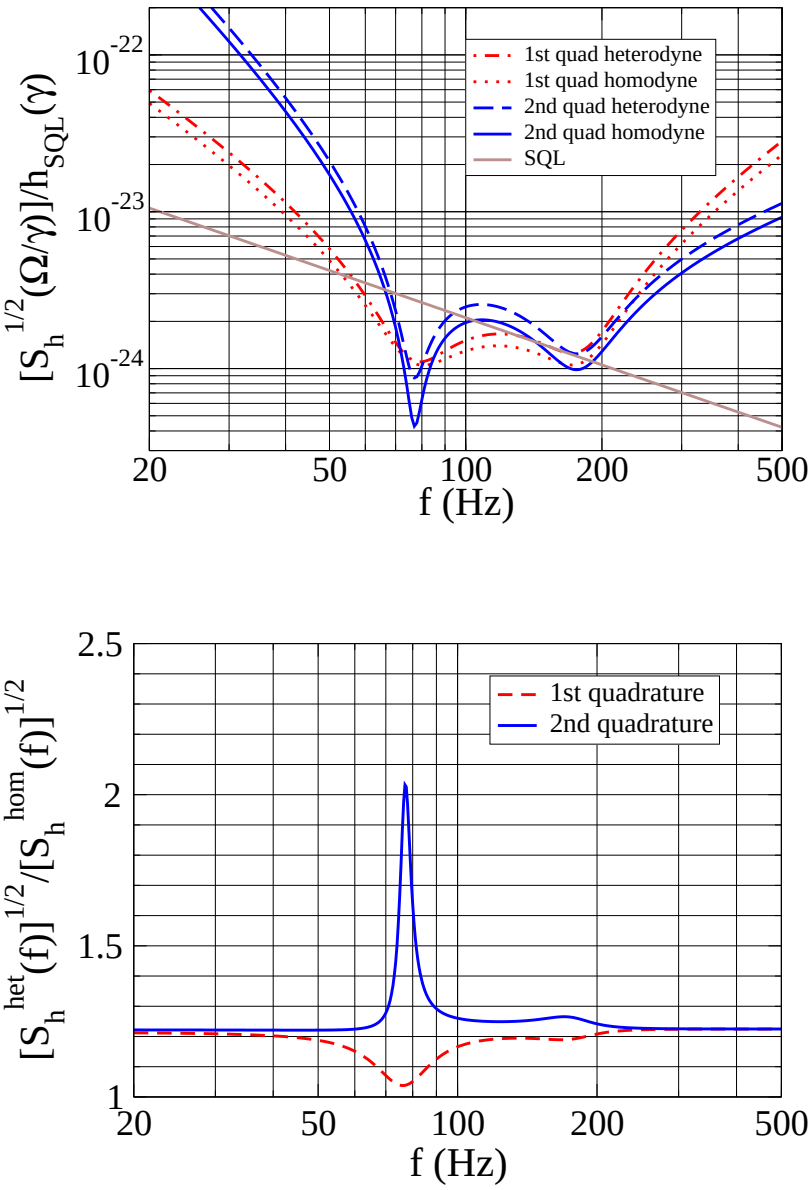

Figure 5.4: A detuned RSE interferometer ($T = 0.033$, $\rho = 0.9$, $\phi = \pi/2 - 0.47$, $m = 30\,\mathrm{kg}$, $I_0 = I_{\mathrm{SQL}}$) using balanced heterodyne detection. In the upper panel we plot the square root of total heterodyne noise spectral density in the first (dash-dot curve) and second (long dashed curve) quadratures, compared with the homodyne ones (dot curve and solid curve, respectively). The SQL line is also shown as a gray straight line. In the lower panel we show the ratio of the square roots of the heterodyne and the homodyne noise spectral densities, for the first (dashed curve) and second (solid curve) quadratures.

between these two schemes a more critical study is required that takes into consideration specific astrophysical GW sources, the experimental feasibility and the other sources of noise, as well. [As an example, current Advanced LIGO design estimates the dominant, thermoelastic component at about the SQL [21]. To lower the thermoelastic contribution below the SQL an interesting and challenging proposal has been analyzed recently [22].] The optimization of homodyne versus heterodyne readout schemes which include those effects is currently under way, and will be reported elsewhere [12].

As shown in Chapter 3, detuned RSE interferometers have an unstable optomechanical resonance. In the parameter regime emphasized in Chapters 2 – 4, the unstable resonance lies within the observation band — which gives a dip in the noise spectrum. Consequently, the control scheme must sense and act on the motion of the system within the observation band. In Chapter 3, an idealized control scheme is conceived for the homodyne readout, which suppresses the instability and leaves the noise spectral density unchanged. The same control issue will need to be addressed with the heterodyne readout scheme as well.

5.4 More general discussion of heterodyne schemes: minimal additional noise and quantum limit

In Sec. 5.2 we discussed the sinusoidal modulation-demodulation scheme, which is the easiest to implement. There exist more sophisticated schemes, such as those proposed by Schnupp, investigated by Niebauer et al. [10], and Meers and Strain [11], that can further optimize the interferometer performances. These authors restricted their analyses to low-power interferometers and focused on the detection of the second (or phase) quadrature. In this section, we extend their discussions to the more general case where all quadratures can be measured. As we shall see, although modulation/demodulation readout schemes offer the advantage of variable-quadrature optimization, they are in general limited in converting non-QND interferometers to (broadband) QND interferometers.

5.4.1 Quantum Limit for the additional heterodyne noise

The field coming out from the dark port can be written, in time domain, as

$$E(t) = [A(t)\cos\omega_0 t + P(t)\sin\omega_0 t] + [E_1(t)\cos\omega_0 t + E_2(t)\sin\omega_0 t] \ , \tag{5.31}$$

where the first term is the transmitted Schnupp sideband fields in the form of a combination of amplitude modulation $[A(t)]$ and phase modulation $[P(t)]$ to the carrier. In Eq. (5.31) we denoted by $E_1(t)$ and $E_2(t)$ the quadrature fields containing GW signal and quantum fluctuations. The

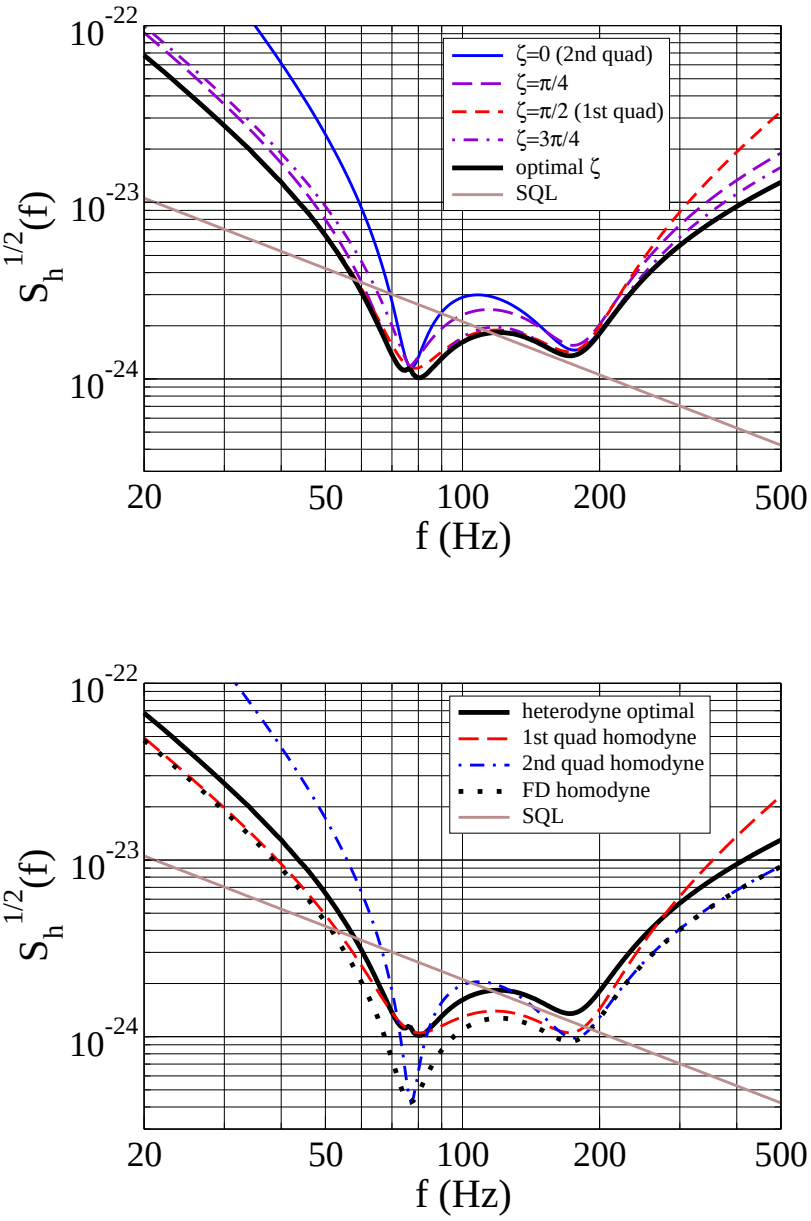

Figure 5.5: A detuned RSE interferometer ($T = 0.033$, $\rho = 0.9$, $\phi = \pi/2 - 0.47$, $m = 30\,\mathrm{kg}$, $I_0 = I_{\mathrm{SQL}}$, same as Fig. 5.4) using totally unbalanced heterodyne detection. In the upper panel we show the noise curves for quadratures with $\zeta = 0$ (solid curve), $\pi/4$ (long dashed curve), $\pi/2$ (short dashed curve) and $3\pi/4$ (dash-dot curve) are shown, together with the final heterodyne noise optimized at all sideband frequencies (thick solid curve). In the lower panel, the final heterodyne noise (thick solid curve) is shown along with the homodyne noise in the first (dashed curve) and second (dash-dot curve) quadratures. The optimal heterodyne noise without the additional noise is also shown (dotted curve) for comparison. The SQL is plotted in both panels as gray straight lines.

output from the photodetector is then

$$i(t) \propto A(t)E_1(t) + P(t)E_2(t)\,. \tag{5.32}$$

The amplitude and phase modulation is in general periodic functions, with the same angular frequency $\omega_{\rm m}$ [$\omega_0 \gg \omega_{\rm m} \gg \Omega_{\rm GW}$]:

$$A(t) = \sum_k A_k e^{-ik\omega_m t}\,, \quad A_k = A^*_{-k}\,; \tag{5.33}$$

$$P(t) = \sum_k P_k e^{-ik\omega_m t}\,, \quad P_k = P^*_{-k}\,. \tag{5.34}$$

$$\tag{5.35}$$

In the frequency domain Eq. (5.32) reads:

$$i(\Omega) \propto \sum_k \left[A_k b_1^{\omega_0}(\Omega - k\omega_{\rm m}) + P_k b_2^{\omega_0}(\Omega - k\omega_{\rm m})\right]\,. \tag{5.36}$$

Denoting the demodulation function with $D(t)$, the demodulated output is

$$O(t) = D(t)i(t) \propto D(t)A(t)E_1(t) + D(t)P(t)E_2(t)\,. \tag{5.37}$$

The demodulation function $D(t)$ should have the same frequency as the modulation functions, therefore:

$$D(t) = \sum_k D_k e^{-ik\omega_m t}\,, \quad D_k = D^*_{-k}\,. \tag{5.38}$$

Note that Eq. (5.37) is a generalization of Eq. (4) of Ref. [11]. Using the above equations, the Fourier transform of the demodulated output (5.37) can be written as

$$\widetilde{O}(\Omega) = \sum_k D^*_k \left[A_k b_1^{\omega_0}(\Omega) + P_k b_2^{\omega_0}(\Omega)\right] + \sum_{p\neq 0}\sum_k D^*_k \left[A_{k+p} b_1^{\omega_0}(\Omega - p\,\omega_m) + P_{k+p} b_2^{\omega_0}(\Omega - p\,\omega_m)\right]\,. \tag{5.39}$$

Let us suppose that the low-frequency component of $\widetilde{O}(\Omega)$ is filtered out, then the first term in Eq. (5.39) gives a frequency-independent quadrature field near ω_0, while the second term gives the additional heterodyne noise that arises from quantum fluctuations near $\omega_0 \pm p\,\omega_{\rm m}$, with $p = \pm 1$, ± 2, ± 3, ... Since $\omega_{\rm m} \gg \Omega_{\rm GW}$, these fields are not affected by ponderomotive squeezing effects in the interferometer arm cavities and will be in the vacuum state. As a consequence, the additional heterodyne noise will also be frequency independent. [Unless frequency-dependent squeezed states are injected into the dark port of the interferometer.] In this way, for any particular quadrature ζ, there is a uniform minimum of the additional heterodyne noise at all frequencies.

Let us now construct for an arbitrary quadrature ζ the optimal demodulation function $D(t)$ and evaluate the minimal additional noise. If we want to measure $b_\zeta^{\omega_0}$, Eq. (5.39) says that we have to impose

$$\left(\sum_k D_k^* A_k, \sum_k D_k^* P_k\right) = (\sin\zeta, \cos\zeta)\,, \tag{5.40}$$

or in the time domain,

$$(\sin\zeta, \cos\zeta) = \left(\frac{1}{T}\int_0^T D(t)A(t)dt, \frac{1}{T}\int_0^T D(t)P(t)dt\right)\,, \tag{5.41}$$

where $T = 2\pi/\omega_{\rm m}$ is the common period of the modulation and demodulation functions. Note that, in order for the quadrature ζ to be measured, Eqs. (5.40) and (5.41) need only be true up to a constant factor. Having written them in the current way, we have in fact chosen a specific normalization for $D(t)$. Using the Parseval theorem and Eq. (5.41), we derive for the spectral density of the additional heterodyne noise:

$$\begin{aligned}
S^{\rm add} &= \sum_{p\neq 0}\left|\sum_k D_k^* A_{k+p}\right|^2 + \sum_{p\neq 0}\left|\sum_k D_k^* P_{k+p}\right|^2\,,\\
&= \sum_{p}\left|\sum_k D_k^* A_{k+p}\right|^2 + \sum_{p}\left|\sum_k D_k^* P_{k+p}\right|^2 - \left|\sum_k D_k^* A_k\right|^2 - \left|\sum_k D_k^* P_k\right|^2\,,\\
&= \frac{1}{T}\int_0^T D^2(t)\left[A^2(t)+P^2(t)\right]dt - \left(\frac{1}{T}\int_0^T D(t)A(t)dt\right)^2 - \left(\frac{1}{T}\int_0^T D(t)P(t)dt\right)^2\,,\\
&= \frac{1}{T}\int_0^T D^2(t)\left[A^2(t)+P^2(t)\right]dt - 1\,.
\end{aligned} \tag{5.42}$$

[Note that Eq. (5.42), which corresponds directly to Eq. (12) of Ref. [11], is also consistent with Eq. (18) of Ref. [11], since Eqs. (5.40) and (5.41) have already imposed a normalization for $D(t)$.] In order to find the $D(t)$ that satisfies Eq. (5.41) and minimize $S^{\rm add}$, we introduce two Lagrange multipliers, λ and μ, and impose,

$$\delta\int dt\left\{\left[(A^2(t)+P^2(t)\right]D^2(t) - 2\lambda A(t)D(t) - 2\mu P(t)D(t)\right\} = 0\,, \tag{5.43}$$

which yields:

$$D(t) = \frac{\lambda A(t) + \mu P(t)}{A^2(t)+P^2(t)}\,. \tag{5.44}$$

[In Eq. (5.43), the factors of 2 in front of λ and μ are added for simplicity.] Inserting Eq. (5.44) back into Eq. (5.41) gives,

$$\mathbf{M}\begin{pmatrix}\lambda\\ \mu\end{pmatrix} = \begin{pmatrix}\sin\zeta\\ \cos\zeta\end{pmatrix}\,, \tag{5.45}$$

where

$$\mathbf{M} = \begin{pmatrix} \frac{1}{T}\int_0^T \frac{A^2(t)}{A^2(t)+P^2(t)}dt & \frac{1}{T}\int_0^T \frac{A(t)P(t)}{A^2(t)+P^2(t)}dt \\ \frac{1}{T}\int_0^T \frac{A(t)P(t)}{A^2(t)+P^2(t)}dt & \frac{1}{T}\int_0^T \frac{P^2(t)}{A^2(t)+P^2(t)}dt \end{pmatrix} . \tag{5.46}$$

The optimal demodulation function for the ζ quadrature is then given by inverting Eq. (5.45) and inserting the resulting λ and μ into Eq. (5.44). The minimal additional noise can be then obtained by inserting the optimal demodulation function into Eq. (5.42):

$$\begin{aligned} S^{\text{add min}}(\zeta) = \begin{pmatrix} \lambda & \mu \end{pmatrix} \mathbf{M} \begin{pmatrix} \lambda \\ \mu \end{pmatrix} - 1 &= \begin{pmatrix} \sin\zeta & \cos\zeta \end{pmatrix} \mathbf{M}^{-1} \begin{pmatrix} \sin\zeta \\ \cos\zeta \end{pmatrix} - 1 \\ &= \begin{pmatrix} \sin\zeta & \cos\zeta \end{pmatrix} (\mathbf{M}^{-1} - \mathbf{I}) \begin{pmatrix} \sin\zeta \\ \cos\zeta \end{pmatrix} . \end{aligned} \tag{5.47}$$

Moreover, we note an interesting property of $\mathbf{M}$:

$$\mathbf{I} - \mathbf{M} = (\det \mathbf{M})\mathbf{M}^{-1} . \tag{5.48}$$

As a consequence,

$$\mathbf{M}^{-1} - \mathbf{I} = \mathbf{M}^{-1}(\mathbf{I} - \mathbf{M}) = (\det \mathbf{M})(\mathbf{M}^{-1})^2, \tag{5.49}$$

so

$$\det\left[\mathbf{M}^{-1} - \mathbf{I}\right] = 1 . \tag{5.50}$$

This implies that, the minimal additional noise can be written in a form

$$S^{\text{add min}}(\zeta) = \begin{pmatrix} \sin\zeta & \cos\zeta \end{pmatrix} \begin{pmatrix} \cos\phi & \sin\phi \\ -\sin\phi & \cos\phi \end{pmatrix} \begin{pmatrix} e^R & \\ & e^{-R} \end{pmatrix} \begin{pmatrix} \cos\phi & -\sin\phi \\ \sin\phi & \cos\phi \end{pmatrix} \begin{pmatrix} \sin\zeta \\ \cos\zeta \end{pmatrix} , \tag{5.51}$$

with ϕ and R frequency-independent, and determined by the eigenvectors and eigenvalues of the matrix $\mathbf{M}^{-1} - \mathbf{1}$, which are determined ultimately by the amplitude and phase modulations. It is interesting to note that this minimal noise spectrum is of exactly the same form as that of a squeezed state.

This phenomenon could in fact be anticipated from quantum mechanics. For the same sideband frequency Ω, the different quadratures do not commute with each other, and have the following commutation relations:

$$\left[b_\zeta^{\omega_0}(\Omega), b_{\zeta'}^{\omega_0\,\dagger}(\Omega')\right] = 2\pi i \sin(\zeta - \zeta')\delta(\Omega - \Omega') . \tag{5.52}$$

As a consequence, quantum fluctuations in the various quadratures are constrained by the Heisenberg

uncertainty principle. As is well known, the squeezed states have the minimum noise spectrum allowed by the uncertainty principle. In modulation/demodulation schemes, all quadratures can be read out, with additional noise:

$$b^{\rm het}(\zeta,\Omega) = b_\zeta^{\omega_0}(\Omega) + n(\zeta,\Omega)\,. \tag{5.53}$$

So, all output observables should commute with each other, and as a consequence

$$\left[b^{\rm het}(\zeta,\Omega), b^{\rm het\dagger}(\zeta',\Omega')\right] = 0\,. \tag{5.54}$$

Since $b_\zeta^{\omega_0}(\Omega)$ and $n(\zeta,\Omega)$ come from different frequency bands of the output field, they must commute with each other, so we must have that the mutual commutators of $n(\zeta,\Omega)$ cancel those of $b_\zeta^{\omega_0}(\Omega)$:

$$\left[n(\zeta,\Omega), n^\dagger(\zeta',\Omega')\right] = -2\pi i \sin(\zeta-\zeta')\delta(\Omega-\Omega')\,. \tag{5.55}$$

Since they do not commute with each other, the additional noise $n(\zeta,\Omega)$ is also subject to the constraint of the Heisenberg uncertainty principle — in the same way as $b_\zeta^{\omega_0}(\Omega)$, since the commutators only differ by a sign [see Eqs. (5.52) and (5.55)]. This explains why the minimum additional heterodyne noise has a spectral density of the same form as the squeezed states. The minimum noise spectrum (5.51) can be regarded as a *quantum limit* for modulation/demodulation schemes.

5.4.2 Impact of the Quantum Limit on conventional interferometers

As discussed in Refs. [19, 7], using an appropriate readout scheme, conventional interferometers can achieve QND performance through a cancellation between shot and radiation-pressure noises. If the quadrature ζ is measured, we have

$$b^{\rm het\,conv}(\zeta,\Omega) = \cos\zeta\left[e^{2i\beta}\left(\tan\zeta - \mathcal{K}\right)a_1^{\omega_0} + e^{2i\beta}a_2^{\omega_0} + e^{i\beta}\sqrt{2\mathcal{K}}\frac{h}{h_{\rm SQL}}\right] + n(\zeta,\Omega)\,, \tag{5.56}$$

and if we choose to measure the quadrature with $\zeta = \zeta_{\rm c} = \arctan\mathcal{K}$ [5] the part of the shot noise [the term proportional to $a_1^{\omega_0}\tan\zeta$ inside the bracket of Eq. (5.56)] cancels the radiation-pressure noise [the term proportional to $\mathcal{K}a_1^{\omega_0}$ inside the bracket of Eq. (5.56)]. The remaining shot noise [obtained from the term proportional to $a_2^{\omega_0}$ inside the bracket of Eq. (5.56)], normalized to unit signal strength, is inversely proportional to $\mathcal{K}$, and it can be made lower (eventually lower than the SQL noise) by taking larger $\mathcal{K}$. However, for larger values of $\mathcal{K}$, $\tan\zeta_{\rm c}$ grows and the corresponding $\cos\zeta_{\rm c}$ decreases. As can be seen from Eq. (5.56) this implies an even smaller signal strength in the detected quadrature, which makes the additional noise, $n(\zeta_{\rm c},\Omega)$, more and more important. In fact,

[5] Note that $\zeta = \zeta_{\rm c}$ is not the optimal quadrature.

more generally the additional noise limits the extent to which the interferometer can beat the SQL. Writing the total heterodyne noise spectral density [of which Eq. (5.28) is a special case], as

$$S_h = \frac{h_{\rm SQL}^2}{2\,\mathcal{K}} \left[(\mathcal{K} - \tan\zeta)^2 + 1 + \frac{S^{\rm add}(\zeta)}{\cos^2\zeta} \right] , \tag{5.57}$$

and following the argument that had led us to Eq. (5.30), we obtain the following lower limit for the heterodyne noise:

$$[S_h(\Omega)]_{\rm opt} \geq \sqrt{S^{\rm add\,min}(\zeta_{\rm opt}(\Omega))}\, h_{\rm SQL}^2 , \tag{5.58}$$

where $\zeta_{\rm opt}(\Omega)$ is the optimal detection quadrature at frequency Ω, which depends also on the shape of $S^{\rm add}(\zeta)$. Equation (5.58) says that, in order to beat the SQL significantly, the additional heterodyne noise at the optimal quadrature has to be much smaller than unity. However, since the additional heterodyne noise is frequency independent, and subject to the quantum limit (5.51), this requirement cannot always be fulfilled if the optimal homodyne quadrature varies significantly with frequency in the observation band. As a consequence, heterodyne schemes will have very limited power in converting conventional interferometers into (broadband) QND interferometers.

Due to the simplicity of the input-output relations of conventional interferometers, we can go a step further and obtain a cleaner result in this case. Let us suppose that the additional heterodyne noise have exactly the form of Eq. (5.51), with generic values of ϕ and e^R, i.e., it is *quantum limited*. Inserting Eq. (5.51) into Eq. (5.57), we find the frequency-dependent optimal detection phase,

$$\tan\zeta_{\rm opt}(\Omega) = \frac{[1 - \tanh^2(R/2)]\,\mathcal{K}(\Omega) + 2\tanh(R/2)\sin 2\phi}{2 + 2\tanh(R/2)\cos 2\phi} , \tag{5.59}$$

and obtain:

$$S_h^{\rm quant\,lim}(\Omega) = \left[\frac{[1 + 2\cos(2\phi)\tanh(R/2) + \tanh^2(R/2)]\,\mathcal{K}^2(\Omega) - 4\sin(2\phi)\tanh(R/2)\,\mathcal{K}(\Omega) + 4}{4\mathcal{K}(\Omega)\,[1 + \cos(2\phi)\tanh(R/2)]} \right] h_{\rm SQL}^2(\Omega) . \tag{5.60}$$

Moreover, the quantum-limited heterodyne noise spectral density (5.60) can be recast into exactly the same form as that of a frequency-independent homodyne detection

$$S_h^{\rm quant\,lim}(\Omega) = \frac{h_{\rm SQL}^2(\Omega)}{2\mathcal{K}_{\rm eff}(\Omega)} \left[(\mathcal{K}_{\rm eff}(\Omega) - \tan\zeta_{\rm eff})^2 + 1 \right] , \tag{5.61}$$

with

$$\tan\zeta_{\rm eff} \equiv \frac{\tanh(R/2)\sin(2\phi)}{1 + \tanh(R/2)\cos(2\phi)} , \quad \mathcal{K}_{\rm eff}(\Omega) \equiv \left[1 - \frac{1 - \tanh^2(R/2)}{2 + 2\tanh(R/2)\cos(2\phi)} \right] \mathcal{K}(\Omega) . \tag{5.62}$$

Note that in the definition of $\mathcal{K}_{\rm eff}$ the quantity multiplying $\mathcal{K}$ (which is less than 1, since $-1 < \tanh(R/2) < +1$) can be absorbed into the input power [see the definition of $\mathcal{K}$ in Table 5.2].

Equations (5.61) and (5.62) therefore relate a conventional interferometer with a quantum limited heterodyne readout scheme to an identical conventional interferometer, but with lower input power and a frequency-independent homodyne readout scheme. As discussed by KLMTV, the latter does not exhibit broadband QND behavior [although fine tunings of parameters can sometimes give a moderate SQL-beating noise spectral density]. This means, that the variable-quadrature optimization provided by heterodyne readout schemes does not enhance the QND performance of conventional interferometers at all.

Nevertheless, as the equivalence also suggests, quantum-limited heterodyne detection does not deteriorate the sensitivity with respect to frequency-independent homodyne detection, except for the lower effective optical power, which can in principle be made as close as possible to the true optical power, as $e^R \to +\infty$. For certain specially designed interferometers, such as the speed-meter interferometers [23] with Michelson [24] or Sagnac [25, 26] topologies, the optimal homodyne angle is largely constant over a broad frequency band. These interferometers already exhibit broadband QND behavior with frequency-independent homodyne detection. In this situation, a heterodyne detection scheme (e.g., the Schnupp square-wave demodulation scheme), optimized for that particular quadrature, can be employed, e.g., for technical reasons, without compromising the sensitivity.

5.5 Conclusions

In this chapter, we applied a quantum optical formalism to a heterodyne readout scheme for advanced GW interferometers such as Advanced LIGO. Our results provide a foundation for the astrophysical optimization of Advanced LIGO interferometers and should be used to decide whether a homodyne or heterodyne readout scheme is more advantageous.

One of the advantages of the heterodyne readout scheme (with the exception of balanced heterodyning), is that all output quadratures are available for measurement, providing a way of optimizing the sensitivity at each frequency. This result cannot be easily achieved in homodyne detection. However, as originally discovered by Gea-Banacloche and Leuchs [8] and by Schnupp [9], and analyzed by Niebauer et al. [10], and Meers and Strain [11] in the low-power limit, heterodyne detection leads to an additional noise term which is a direct and necessary consequence of the Heisenberg uncertainty principle.

In the specific case of detuned RSE interferometers planned for Advanced LIGO, we derived the expressions for the total heterodyne noise spectral density [see Eqs. (5.22)–(5.26), (5.11)], assuming a pair of Schnupp sidebands with arbitrary amplitude ratios. In the balanced case the effect of the additional heterodyne noise is shown in Fig. 5.4. In the more practical very unbalanced [12] configuration, we compared the noise curve in the optimal heterodyne case, obtained by maximizing over the heterodyne phase at each sideband frequency, with some noise curves obtained when the

homodyne readout scheme is used. The results are shown in Fig. 5.5. Neither the homodyne nor the heterodyne readout provides a noise spectral density that is the lowest for all frequencies. Moreover, the differences between the noise curves occur mainly in the frequency band 70–200 Hz where other sources of noise in Advanced LIGO will probably dominate, e.g., thermal noise [21] (unless more sophisticated techniques are implemented [22]). So, before drawing any conclusion on which readout scheme is preferable, the comparison between them must take into account the other sources of noise present in Advanced LIGO and should be addressed with reference to specific astrophysical GW sources, such as neutron-star and/or (stellar mass) black-hole binaries, for which the GW spectrum is a power law with an upper cutoff ranging from $\sim 200\,\mathrm{Hz}$ to several kHz, and also low-mass X-ray binaries which require narrowband configurations (detuned RSE) around $500 - 700$ Hz. In this chapter we have provided a framework in which these optimizations can be carried out. We shall report on the results of the optimization elsewhere [12].

From a more theoretical point of view, we worked out a frequency-independent quantum limit for the additional heterodyne noise [see Eq. (5.51)], which made more explicit the following fact: lowering the additional heterodyne noise while simultaneously retaining the ability to measure more than one quadrature is incompatible in heterodyne detection, which is inherently frequency-independent unless frequency-dependent squeezing techniques are implemented. In particular, this incompatibility seriously limits the extent to which conventional interferometers can beat the SQL using heterodyne readout scheme. Indeed, we show in Sec. 5.4.2 that conventional interferometers with quantum limited heterodyne detection are equivalent to conventional interferometers with frequency-independent homodyne detection and lower optical power. However, for third-generation GW interferometers with speedmeter-type configurations [23, 24, 25, 26], which are already QND interferometers under an appropriate frequency-independent homodyne detection, heterodyne readout schemes can in principle be employed without compromising their sensitivity.

5.6 Bibliography

[1] A. Abramovici et al., *Science* **256**, 325 (1992); `http://www.ligo.caltech.edu`.

[2] B. Caron et al., *Class. Quantum Grav.* **14**, 1461 (1997); `http://www.virgo.infn.it`.

[3] H. Lück et al., *Class. Quantum Grav.* **14**, 1471 (1997); `http://www.geo600.uni-hannover.de`.

[4] M. Ando et al., *Phys. Rev. Lett.* **86**, 3950 (2001); `http://tamago.mtk.nao.ac.jp`.

[5] R. Abbott et al., *Class. Quantum Grav.* **19**, 1591 (2002).

[6] N. A. Robertson et al., *Class. Quantum Grav.* **19**, 4043 (2002).

[7] H. J. Kimble, Yu. Levin, A. B. Matsko, K. S. Thorne and S. P. Vyatchanin, *Phys. Rev. D* **65**, 022002 (2002). *Class. Quantum Grav.* **19** 1569 (2002).

[8] J. Gea-Banacloche and G. Leuchs, *J. Mod. Opt* **34**, 793 (1987).

[9] L. Schnupp, unpublishhed talk presented at the *"European Collabooration Meeting on Interferometric Detection of Gravitational Waves,"* 1988, Sorrento, Italy.

[10] T. Niebauer, R. Schilling, K. Danzmann, A. Rüdiger and W. Winkler, *Phys. Rev. A* **43**, 5022 (1991).

[11] B. J. Meers and K. Strain, *Phys. Rev. A* **44**, 4693 (1991).

[12] A. Buonanno, Y. Chen, P. Fritschel, N. Mavalvala, and K. Strain, (work in progress).

[13] K. Somiya, *"New photodetection method using unbalanced sidebands for squeezed quantum noise in gravitational wave interferometer,"* submitted to *Phys. Rev. D*, `gr-qc/0208029`.

[14] R. W. P. Drever, in "The detection of gravitational waves," ed. by D. G. Blair, (Cambridge University Press, Cambridge, England, 1991).

[15] J. Mizuno, *"Comparison of optical configurations for laser-interferometer gravitational-wave dtectors,"* Ph.D. thesis, Max-Planck-Institut für Quantenoptik, Garching, Germany, 1995.

[16] B. J. Meers, *Phys. Rev. D* **38**, 2317 (1988); J. Y. Vinet, B. Meers, C. N. Man and A. Brillet, *Phys. Rev. D* **38**, 433 (1988).

[17] K. Strain et al., *Phys. Rev. A* **44**, 4693 (1991).

[18] J. Mason and P. Willems, *"Signal extraction and optical design for an advanced gravitational wave detector,"* accepted for publication in *Appl. Opt.* (2002); see also K. A. Strain, G. Muller, T. Delker, D. H. Reitze, D. B. Tanner, J. E. Mason, P. Willems, D. Shaddock, and D. E. McClelland , *"Signal and control in dual recycling laser interferometer gravitational wave detectors,"* submitted to *Appl. Opt.* (2002).

[19] S. P. Vyatchanin and A. B. Matsko, *JETP* **77**, 218 (1993); S. P. Vyatchanin and E. A. Zubova, *Phys. Lett. A* **203**, 269 (1995); S. P. Vyatchanin, *ibid.* **239**, 201 (1998); S. P. Vyatchanin and A.B. Matsko, *JETP* **82**, 1007 (1996); S. P. Vyatchanin and A.B. Matsko, *JETP* **83**, 690 (1996).

[20] V. B. Braginsky and F. Ya. Khalili, *Rev. Mod. Phys.* **68**, 1 (1996).

[21] V. B. Braginsky, M. L. Gorodetsky and S. P. Vyatchanin, *Phys. Lett. A* **264**, 1 (1999); Y. T. Liu and K. S. Thorne, *Phys. rev. D* **62**, 122002 (2000).

[22] E. D'Ambrosio, R. O'Shaughnessy, V. Strigin, K. S. Thorne and S. P. Vyatchanin, (in preparation).

[23] V. B. Braginsky, F. Ya. Khalili, *Phys. Lett. A* **147**, 251 (1990); V. B. Braginsky, M. L. Gorodetsky, F. Ya. Khalili, and K. S. Thorne, *Phys. Rev. D* **61** 044002 (2000).

[24] P. Purdue, *Phys. Rev. D* **66**, 022001 (2002); P. Purdue and Y. Chen, *Phys. Rev. D* **66**, 122004 (2002).

[25] Y. Chen, *"Sagnac interferometer as a speed-meter-type, quantum-nondemolition gravitational-wave detector,"* accepted for publication in *Phys. Rev. D*, `gr-qc/0208051`, Chapter 7 of this thesis.

[26] F. Ya. Khalili, *"Quantum speedmeter and laser interferometric gravitational-wave antennae,"* `gr-qc/0211088`.

Chapter 6

Practical speed meter designs for QND gravitational-wave interferometers

In the quest to develop viable designs for third-generation optical interferometric gravitational-wave detectors (e.g., LIGO-III and EURO), one strategy is to monitor the relative momentum or speed of the test-mass mirrors, rather than monitoring their relative position. A previous paper analyzed a straightforward but impractical design for a *speed-meter interferometer* that accomplishes this. This Chapter describes some practical variants of speed-meter interferometers. Like the original interferometric speed meter, these designs *in principle* can beat the gravitational-wave standard quantum limit (SQL) by an arbitrarily large amount, over an arbitrarily wide range of frequencies. These variants essentially consist of a Michelson interferometer plus an extra "sloshing" cavity that sends the signal back into the interferometer with opposite phase shift, thereby cancelling the position information and leaving a net phase shift proportional to the relative velocity. *In practice*, the sensitivity of these variants will be limited by the maximum light power $W_{\rm circ}$ circulating in the arm cavities that the mirrors can support and by the leakage of vacuum into the optical train at dissipation points. In the absence of dissipation and with squeezed vacuum (power squeeze factor $e^{-2R} \simeq 0.1$) inserted into the output port so as to keep the circulating power down, the SQL can be beat by $h/h_{\rm SQL} \sim \sqrt{W_{\rm circ}^{SQL} e^{-2R}/W_{\rm circ}}$ at all frequencies below some chosen $f_{\rm opt} \simeq 100$ Hz. Here $W_{\rm circ}^{SQL} \simeq 800{\rm kW}(f_{\rm opt}/100{\rm Hz})^3$ is the power required to reach the SQL in the absence of squeezing. [However, as the power increases in this expression, the speed meter becomes more narrow band; additional power and re-optimization of some parameters are required to maintain the wide band. See Sec. 6.3.2.] Estimates are given of the amount by which vacuum leakage at dissipation points will debilitate this sensitivity (see Fig. 6.12); these losses are 10% or less over most of the frequency range of interest ($f \gtrsim 10$ Hz). The sensitivity can be improved, particularly at high freqencies, by using frequency-dependent homodyne detection, which unfortunately requires two 4-kilometer-long filter cavities (see Fig. 6.4).

Originally published as P. Purdue and Y. Chen, Phys. Rev. D, **66** 122004 (2002).

6.1 Introduction

This Chapter is part of the effort to explore theoretically various ideas for a third-generation interferometric gravitational-wave detector. The goal of such detectors is to beat, by a factor of 5 or more, the *standard quantum limit* (SQL)—a limit that constrains interferometers [1] such as LIGO-I which have conventional optical topology [2, 3], but does not constrain more sophisticated "quantum nondemolition" (QND) interferometers [4, 5].

The concepts currently being explored for third-generation detectors fall into two categories: *external readout* and *intracavity readout*. In interferometer designs with external readout topologies, light exiting the interferometer is monitored for phase shifts, which indicate the motion of the test masses. Examples include conventional interferometers and their variants (such as LIGO-I [2, 3], LIGO-II [6], and those discussed in Ref. [7]), as well as the speed-meter interferometers discussed here and in a previous paper [8]. In intracavity readout topologies, the gravitational-wave force is fed via light pressure onto a tiny internal mass, whose displacement is monitored with a local position transducer. Examples include the optical bar, symphotonic state, and optical lever schemes discussed by Braginsky, Khalili, and Gorodetsky [9, 10, 11]. These intracavity readout interferometers may be able to function at much lower light powers than external readout interferometers of comparable sensitivity because the QND readout is performed via the local position transducer (perhaps microwave-technology based), instead of via the interferometer's light; however, the designs are not yet fully developed.

At present, the most complete analysis of candidate designs for third-generation external-readout detectors has been carried out by Kimble, Levin, Matsko, Thorne, and Vyatchanin [7] (KLMTV). They examined three potential designs for interferometers that could beat the SQL: a squeezed-input interferometer, which makes use of squeezed vacuum being injected into the dark port; a variational-output scheme in which frequency-dependent homodyne detection was used; and a squeezed-variational interferometer that combines the features of both. (Because the KLMTV designs measure the relative positions of the test masses, we shall refer to them as *position meters*, particularly when we want to distinguish them from the speed meters that, for example, use variational-output techniques.) Although at least some of the KLMTV position-meter designs have remarkable performance in the lossless limit, all of them are highly susceptible to losses.

In addition, we note that the KLMTV position meters each require four kilometer-scale cavities (two arm cavities + two filter cavities). The speed meters described in this chapter require at least three kilometer-scale cavities [two arm cavities + one "sloshing" cavity (described below)]. If we use a variational-output technique, as KLMTV did, the resulting interferometer will have five kilometer-scale cavities (two arm cavities + one sloshing cavity + two filter cavities). This is shown in Fig. 6.4 below.

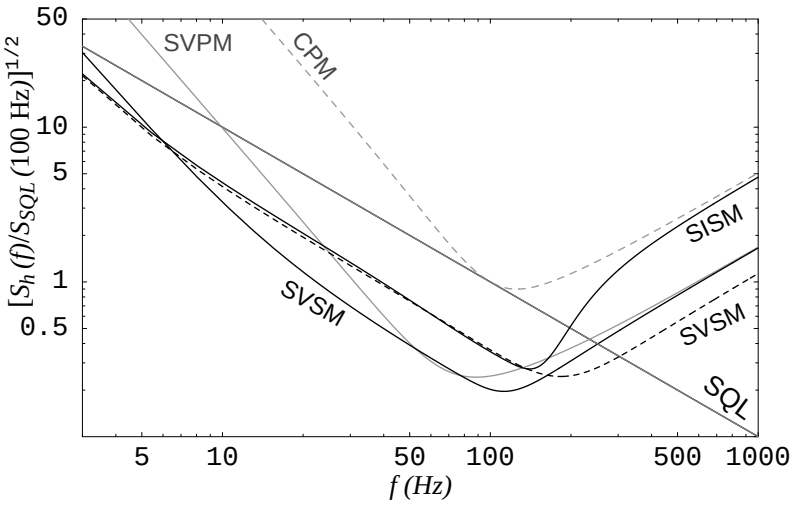

Figure 6.1: Comparison of noise curves (with losses) of several interferometer configurations. Each of these curves has been optimized in a way that is meant to illustrate their relative advantages and disadvantages. The conventional position meter (CPM) [7] has $W_{\rm circ} = 820$ kW and bandwidth $\gamma = cT/4L = 2\pi \times 100$ Hz. The squeezed-input speed meter (SISM)—optmized to agree with the conventional position meter at high frequencies—has power squeeze factor $e^{-2R} = 0.1$, optimal frequency $\omega_{\rm opt} = 2\pi \times 105$ Hz, extraction rate $\delta = 2\omega_{\rm opt}$, and sloshing frequency $\Omega = \sqrt{3}\omega_{\rm opt}$. The squeezed-variational position meter (SVPM) [7] has the same parameters as the conventional position meter, with power squeeze factor $e^{-2R} = 0.1$. There are two squeezed-variational speed-meter curves (SVSM). One (black dashes) uses the same parameters as the squeezed-input speed meter. The other (solid curve) has been optimized to compare more directly with the squeezed-variational position meter; it has $\Omega = 2\pi \times 95$ Hz and $\delta = 2\pi \times 100$ Hz (note that our δ is equivalent to the bandwidth γ used to describe the interferometers in Ref. [7]).

The speed meter described in this chapter can achieve a performance significantly better than a conventional position meter, as shown in Fig. 6.1. (By "conventional," we mean "without any QND techniques." An example is LIGO-I.) The squeezed-input speed meter (SISM) noise curve shown in that Fig. 6.1 beats the SQL by a factor of $\sqrt{10}$ in amplitude and has *fixed-angle* squeezed vacuum injected into the dark port [this allows the interferometer to operate at a lower circulating power than would otherwise be necessary to achieve that level of sensitivity, as described by Eq. (6.3) below]. The squeezed-variational position meter (SVPM), which requires *frequency-dependent* squeezed vacuum and homodyne detection, is more sensitive than the squeezed-input speed meter over much of the frequency range of interest, but the speed meter has the advantage at low frequencies. It should also be noted that the squeezed-variational position meter requires four kilometer-scale cavities (as described in the previous paragraph), whereas the squeezed-input speed meter requires three.

If frequency-dependent homodyne detection is added to the squeezed-input speed meter, the resulting squeezed-variational speed meter (SVSM) can be optimized to beat the squeezed-variational position meter over the entire frequency range. Figure 6.1 contains two squeezed-variational speed meter curves; one is optimized to match the squeezed-input speed meter curve at low frequencies, and

the other is optimized for comparison with the squeezed-variational position-meter curve (resulting in less sensitivity at high frequencies).

The original idea for a speed meter, as a device for measuring the momentum of a single test mass, was conceived by Braginsky and Khalili [12] and was further developed by Braginsky, Gorodetsky, Khalili, and Thorne [13] (BGKT). In their appendix, BGKT sketched a design for an interferometric gravity wave speed meter and speculated that it would be able to beat the SQL. This was verified in Ref. [8] (Paper I), where it was demonstrated that such a device could *in principle* beat the SQL by an arbitrary amount over a wide range of frequencies. However, the design presented in that paper, which we shall call the *two-cavity speed-meter* design, had three significant problems: it required (i) a high circulating power ($\sim$ 8 MW to beat the SQL by a factor of 10 in noise power at 100 Hz and below), (ii) a large amount of power coming out of the interferometer with the signal ($\sim$ 0.5 MW), and (iii) an exorbitantly high input laser power ($\gtrsim$ 300 MW). The present Chapter describes an alternate class of speed meters that effectively eliminate the latter two problems, and techniques for reducing the needed circulating power are discussed. These improvements bring interferometric speed meters into the realm of practicality.

A simple version of the *three-cavity speed-meter* design to be discussed in this chapter is shown in Fig. 6.2. In (an idealized theorist's version of) this speed meter, the input laser light [with electric field denoted $I(\zeta)$ in Fig. 6.2] passes through a power-recycling mirror into a standard Michelson interferometer. The relative phase shifts of the two arms are adjusted so that all of the input light returns to the input port, leaving the other port dark [i.e., the interferometer is operating in the symmetric mode so $D(\eta) = 0$ in Fig. 6.2]. In effect, we have a resonant cavity shaped like $\perp$. When the end mirrors move, they will put a phase shift on the light, causing some light to enter the antisymmetric mode (shaped like $\vdash$) and come out the dark port. So far, this is the same as conventional interferometer designs (but without the optical cavities in the two interferometer arms).

Next, we feed the light coming out of the dark port [$D(\eta)$] into a sloshing cavity [labeled $K(\eta)$ and $L(\zeta)$ in Fig. 6.2]. The light carrying the position information sloshes back into the "antisymmetric cavity" with a phase shift of 180°, cancelling the position information in that cavity and leaving only a phase shift proportional to the relative velocity of the test masses[1]. The sloshing frequency is

$$\Omega = \frac{c\sqrt{T_{\rm s}}}{2L}\,, \tag{6.1}$$

where $T_{\rm s}$ is the power transmissivity of the sloshing mirror, L is the common length of all three cavities, and c is the speed of light. We read the velocity signal [$Q(\eta)$] out at a extraction mirror

[1]The net signal is proportional to the relative velocities of the test masses, assuming that the frequencies ω of the test masses' motion are $\omega \ll \Omega =$ (sloshing frequency). However, the optimal regime of operation for the speed meter is $\omega \sim \Omega$. As a result, the output signal contains a sum over odd time derivatives of position [see the discussion in Sec. 6.3.1]. Therefore, the speed meter monitors not just the relative speed of the test masses, but a mixture of all odd time derivatives of the relative positions of the test masses.

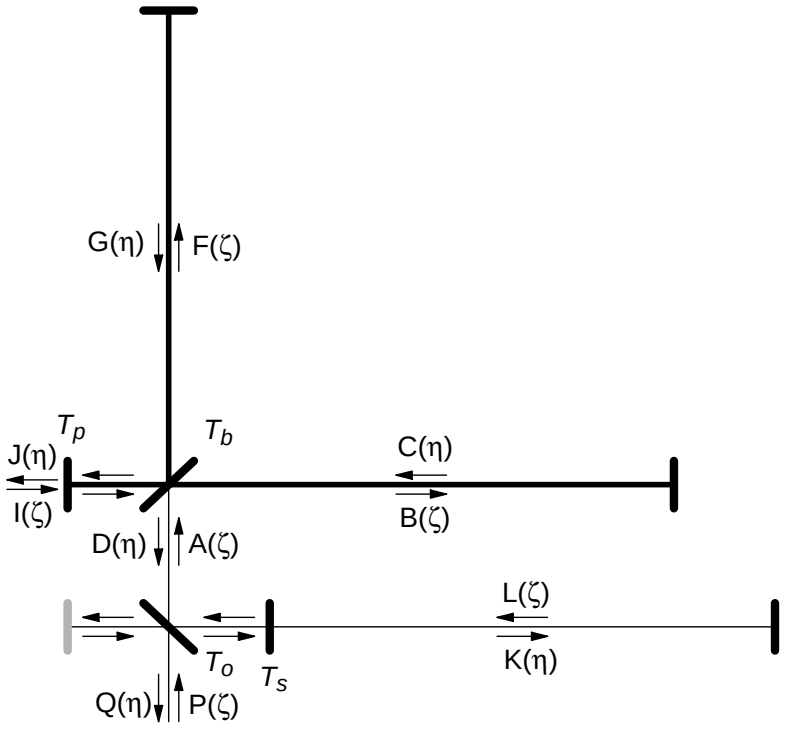

Figure 6.2: Simple version of three-cavity design for speed-meter interferometer. The main laser input port is denoted by $I(\zeta)$, where $\zeta = t - z/c$. The signal is extracted at the bottom mirror [denoted $Q(\eta)$, where $\eta = t + z/c$]. The difference between the one- and two-port versions is the mirror shown in gray.

(with transmissivity $T_{\rm o}$), which gives a signal-light extraction rate of

$$\delta = \frac{cT_{\rm o}}{L}\,. \tag{6.2}$$

We have used the extraction mirror to put the sloshing cavity parallel to one of the arms of the Michelson part of the interferometer, allowing this interferometer to fit into the existing LIGO facilities. The presence of the extraction mirror essentially opens two ports to our system. We can use both outputs, or we can add an additional mirror to close one port (the gray mirror in Fig. 6.2). We will focus on the latter case in this chapter.

The sensitivity h of this interferometer, compared to the SQL, can be expressed as[2]

$$\frac{h}{h_{SQL}} \sim \sqrt{\frac{W_{\rm circ}^{SQL}}{e^{2R}W_{\rm circ}}} \simeq \sqrt{\frac{800\ {\rm kW}}{e^{2R}W_{\rm circ}}}\,, \tag{6.3}$$

where $W_{\rm circ}$ is the power circulating in the arms, $W_{\rm circ}^{SQL} \simeq 800{\rm kW}(f_{\rm opt}/100{\rm Hz})^3$ is the power required to reach the SQL in the absence of squeezing (for the arms of length $L = 4$ km and test masses with mass $m = 40$ kg), and e^{2R} is the power squeeze factor[3]. With no squeezed vacuum, the squeeze factor is $e^{2R} = 1$, so the circulating power $W_{\rm circ}$ must be 8 MW in order to beat the SQL at $f_{\rm opt} \simeq 100$ Hz by a factor of $\sqrt{10}$ in sensitivity. With a squeeze factor of $e^{2R} = 10$, we can achieve the same performance with $W_{\rm circ} \simeq 800$ kW, which is the same as LIGO-II is expected to be.

This performance (in the lossless limit) is the same as that of the two-cavity (Paper I) speed meter for the same circulating power, but the three-cavity design has an overwhelming advantage in terms of required input power. However, there is one significant problem with this design that we must address: the uncomfortably large amount of laser power, equal to $W_{\rm circ}$, flowing through the beam splitter. Even with the use of squeezed vacuum, this power will be too high. Fortunately, there is a method, based on the work of Mizuno [15], that will let us solve this problem:

We add three mirrors into our speed meter (labeled $T_{\rm i}$ in Fig. 6.3); we shall call this the *practical three-cavity speed meter*. Two of the additional mirrors are placed in the excited arms of the interferometer to create resonating Fabry-Perot cavities in each arm (as for conventional interferometers such as LIGO-I). The third mirror is added between the beam splitter and the extraction mirror, in such a way that light with the carrier frequency resonates in the subcavity formed by this mirror and the internal mirrors.

As claimed by Mizuno [15] and tested experimentally by Freise et al. [16] and Mason [17], when the transmissivity of the third mirror decreases from 1, the storage time of sideband fields in the arm

[2]It should be noted that, as the power increases in Eq. (6.3), the speed-meter performance becomes more narrow band. Additional power and a re-optimization of some of the speed meter's parameters are required to maintain the same bandwidth at higher sensitivities. See Sec. 6.3.2 for details.

[3]For an explanation of squeezed vacuum and squeeze factors, see, for example, KLMTV and references cited therein. In particular, their work was based on that of Caves [14] and Unruh [4]. Also, KLMTV state that a likely achievable value for the squeeze factor (in the LIGO-III time frame) is $e^{2R} \simeq 10$, so we use that value in our discussion.

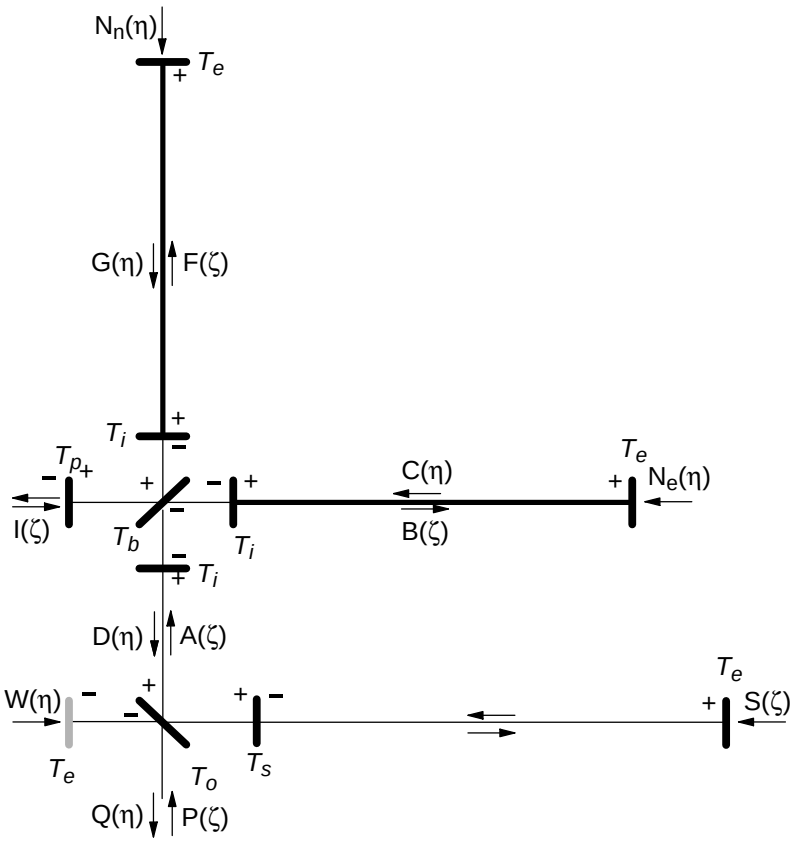

Figure 6.3: Schematic diagram showing the practical version of the three-cavity speed-meter design, which reduces the power flowing through the beam splitter. Three additional mirrors, with transmissivity $T_{\rm i}$, are placed around the beam splitter. The "+" and "−" signs near the mirrors indicate the sign of the reflectivities in the junction conditions for each location. The mirror shown in gray closes the second port of the interferometer.

cavity due to the presence of the internal mirrors will decrease. This phenomenon is called Resonant Sideband Extraction (RSE); consequently, the third mirror is called the RSE mirror. One special case, which is of great interest to us, occurs when the RSE mirror has the same transmissivity as the internal mirrors. In this case, the effect of the internal mirrors on the gravitational-wave sidebands should be exactly cancelled out by the RSE mirror. The three new mirrors then have just one effect: they reduce the carrier power passing through the beam splitter—and they can do so by a large factor.

Indeed, we have confirmed that this is true for our speed meter, as long as the distances between the three additional mirrors (the length of the "RSE cavity") are small (a few meters), so that the phase shifts added to the slightly off-resonance sidebands by the RSE cavity are negligible. We can then adjust the transmissivities of the power-recycling mirror and of the three internal mirrors to

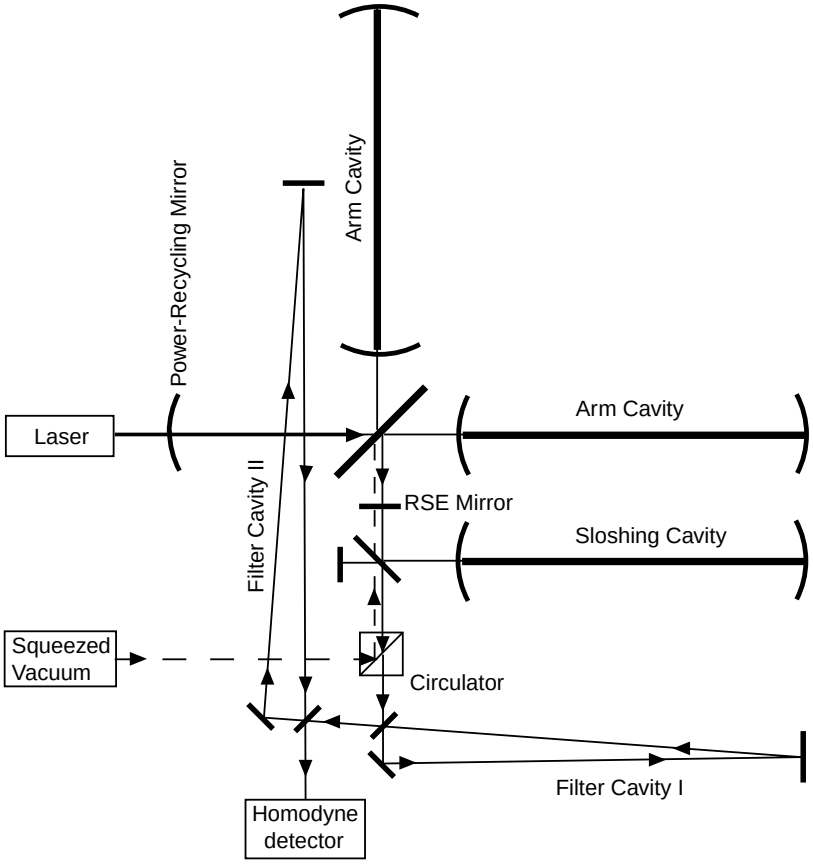

Figure 6.4: Schematic diagram showing the practical three-cavity speed-meter design with squeezed vacuum injected at the dark port and two filter cavities on the output. Note that the circulator is a four-port optical device that separates the injected (squeezed) input and the interferometer's output.

reduce the amount of carrier power passing through the beam splitter to a more reasonable level.

With this design, the high circulating power is confined to the Fabry-Perot arm cavities, as in conventional LIGO designs. There is some question as to the level of power that mirrors will be able to tolerate in the LIGO-III time frame. Assuming that several megawatts is not acceptable, we shall show that the circulating power can be reduced by injecting fixed-angle squeezed vacuum into the dark port, as indicated by Eq. (6.3).

Going a step farther, we shall show that if, in addition to injected squeezed vacuum, we also use frequency-dependent (FD) homodyne detection, the sensitivity of the speed meter is dramatically improved at high frequencies (above $f_{\rm opt} \simeq 100$ Hz); this is shown in Fig. 6.1. The disadvantage of this is that FD homodyne detection requires two filter cavities of the same length as the arm cavities (4 km for LIGO), as shown in Fig. 6.4.

Our analysis of the losses in these scenarios indicates that our speed meters with squeezed vacuum and/or variational-output are much less sensistive to losses than a position meter using

those techniques (as analyzed by KLMTV). Losses for the various speed meters we discuss here are generally quite low and are due primarily to the losses in the optical elements (as opposed to mode-mismatching effects). Without squeezed vacuum, the losses in sensitivity are less than 10% in the range $50 - 105$ Hz, lower at higher frequencies, but higher at low frequencies. Injecting fixed-angle squeezed vacuum into the dark port allows this speed meter to operate at a lower power [see Eq. 6.3], thereby reducing the dominant losses (which are dependent on the circulating power because they come from vacuum fluctations contributing to the back-action). In this case, the losses are less than 4% in the range $25 - 150$ Hz. As before, they are lower at high frequencies, but they increase at low frequencies. Using FD homodyne detection does not change the losses significantly.

This Chapter is organized as follows: In Sec. 6.2 we give a brief description of the mathematical method that we use to analyze the interferometer. In Sec. 6.3.1, we present the results in the lossless case, followed in Sec. 6.3.2 by a discussion of optimization methods. In Sec. 6.3.3, we discuss some of the advantages and disadvantages of this design, including the reasons it requires a large circulating power. Then in Sec. 6.4, we show how the circulating power can be reduced by injecting squeezed vacuum through the dark port of the interferometer and how the use of frequency-dependent homodyne detection can improve the performance at high frequencies. In Section 6.5, we discuss the effect of losses on our speed meter with the various modifications made in Sec. 6.4, and we compare our interferometer configurations with those of KLMTV. Finally, we summarize our results in Sec. 6.6.

6.2 Mathematical description of the interferometer

The interferometers in this chapter are analyzed using the techniques described in Paper I (Sec. II). These methods are based on the formalism developed by Caves and Schumaker [18, 19] and used by KLMTV to examine more conventional interferometer designs. For completeness, we will summarize the main points here.

The electric field propagating in each direction down each segment of the interferometer is expressed in the form

$$E_{\rm field}(\zeta) = \sqrt{\frac{4\pi\hbar\omega_0}{\mathcal{S}c}}A(\zeta)\,. \tag{6.4}$$

Here $A(\zeta)$ is the amplitude (which is denoted by other letters—$B(\zeta)$, $P(\zeta)$, etc.—in other parts of the interferometer; see Fig. 6.2), $\zeta = t - z/c$, ω_0 is the carrier frequency, $\hbar$ is the reduced Planck's constant, and $\mathcal{S}$ is the effective cross-sectional area of the light beam; see Eq. (8) of KLMTV. For light propagating in the negative z direction, $\zeta = t - z/c$ is replaced by $\eta = t + z/c$. We decompose the amplitude into cosine and sine quadratures,

$$A(\zeta) = \mathcal{A}_1(\zeta)\cos\omega_0\zeta + \mathcal{A}_2(\zeta)\sin\omega_0\zeta\,, \tag{6.5}$$

where the subscript 1 always refers to the cosine quadrature, and 2 to sine. Both arms and the sloshing cavity have length $L = 4$ km, whereas all of the other lengths z_i are short compared to L. We choose the cavity lengths to be exact half multiples of the carrier wavelength so $e^{i2\omega_0 L/c} = 1$ and $e^{i2\omega_0 z_i/c} = 1$. There will be phase shifts put onto the sideband light in all of these cavities, but only the phase shifts due to the long cavities are significant.

The aforementioned sidebands are put onto the carrier by the mirror motions and by vacuum fluctuations. We express the quadrature amplitudes for the carrier plus the side bands in the form

$$\mathcal{A}_j(\zeta) = A_j(\zeta) + \int_0^\infty \left[\tilde{a}_j(\omega)e^{-i\omega\zeta} + \tilde{a}_j^\dagger(\omega)e^{i\omega\zeta}\right]\frac{d\omega}{2\pi}\,. \tag{6.6}$$

Here $A_j(\zeta)$ is the carrier amplitude, $\tilde{a}_j(\omega)$ is the field amplitude (a quantum mechanical operator) for the sideband at sideband frequency ω (absolute frequency $\omega_0 \pm \omega$) in the j quadrature, and $\tilde{a}_j^\dagger(\omega)$ is the Hermitian adjoint of $\tilde{a}_j(\omega)$; cf. Eqs. (6)–(8) of KLMTV, where commutation relations and the connection to creation and annihilation operators are discussed. In other portions of the interferometer (Fig. 6.2), $\mathcal{A}_j(\zeta)$ is replaced by, e.g., $\mathcal{C}_j(\zeta)$; $A_j(\zeta)$, by $C_j(\zeta)$; $\tilde{a}_j(\omega)$, by $\tilde{c}_j(\omega)$, etc.

Since each mirror has a power transmissivity and complementary reflectivity satisfying the equation $T + R = 1$, we can write out the junction conditions for each mirror in the system, for both the carrier quadratures and the sidebands [see particularly Eqs. (5) and (12)–(14) in Paper I]. We shall denote the power transmissivities for the sloshing mirror as $T_{\rm s}$, for the extraction (output) mirror as $T_{\rm o}$, the power-recycling mirror as $T_{\rm p}$, for the beam-splitter as $T_{\rm b} = 0.5$, for the internal mirrors as $T_{\rm i}$, and for the end mirrors as $T_{\rm e}$; see Figs. 6.2 and 6.3.

The resulting equations can be solved simultaneously to get expressions for the carrier and sidebands in each segment of the interferometer. Since those expressions may be quite complicated, we use the following assumptions to simplify our results. First, we assume that only the cosine quadrature is being driven (so that the carrier sine quadrature terms are all zero). Second, we assume that the transmissivities obey

$$1 \gg T_{\rm o} \gg T_{\rm s} \gg T_{\rm e} \quad \text{and} \quad 1 \gg \{T_{\rm p}, T_{\rm i}\} \gg T_{\rm e}\,. \tag{6.7}$$

The motivations for these assumptions are that (i) they lead to speed-meter behavior; (ii) as with any interferometer, the best performance is achieved by making the end-mirror transmissivities $T_{\rm e}$ as small as possible; and (iii) good performance requires a light extraction rate comparable to the sloshing rate, $\delta \sim \Omega$ [cf. the first paragraph of Sec. III B in Paper I], which with Eqs. (6.1) and (6.2) implies $T_{\rm o} \sim \sqrt{T_{\rm s}}$ so $T_{\rm o} \gg T_{\rm s}$. Throughout the Chapter, we will be using these assumptions, together with $\omega L/c \ll 1$, to simplify our expressions.

6.3 Speed meter in the lossless limit

For simplicity, in this section we will set $T_e = 0$ (end mirrors perfectly reflecting). We will also neglect the (vacuum-fluctuation) noise coming in the main laser port ($\tilde{i}_{1,2}$) since that noise largely exits back toward the laser and produces negligible noise on the signal light exiting the output port. As a result of these assumptions, the only (vacuum-fluctuation) noise that remains is that which comes in through the output port ($\tilde{p}_{1,2}$). An interferometer in which this is the case and in which light absorption and scattering are unimportant ($R + T = 1$ for all mirrors, as we have assumed) is said to be "lossless." In Sec. 6.5, we shall relax these assumptions; i.e., we shall consider lossy interferometers.

It should be noted that the results and discussion in this section and in Sec. 6.4 apply to both the simple and practical versions of the three-cavity speed meter (Figs. 6.2 and 6.3). The two versions are completely equivalent (in the lossless limit).

6.3.1 Mathematical analysis

The lossless interferometer output for the speed meters in Fig. 6.2 and 6.3, as derived by the analysis sketched in the previous section, is then

$$\tilde{q}_1 = -\frac{\mathcal{L}^*(\omega)}{\mathcal{L}(\omega)}\tilde{p}_1\,, \tag{6.8}$$

$$\tilde{q}_2 = \frac{2i\omega\sqrt{\omega_0\delta W_{\rm circ}}}{\sqrt{\hbar c L}\mathcal{L}(\omega)}\tilde{x} - \frac{\mathcal{L}^*(\omega)}{\mathcal{L}(\omega)}\tilde{p}_2\,. \tag{6.9}$$

Here $\tilde{p}_j(\omega)$ is the side-band field operator [analog of $\tilde{a}_j(\omega)$ in Eq. (6.6)] associated with the dark-port input $P(\zeta)$, and $\tilde{q}_j(\omega)$ associated with the output $Q(\eta)$; see Fig. 6.2. Also, in Eqs. (6.3.1), $\mathcal{L}(\omega)$ is a c-number given by

$$\mathcal{L}(\omega) = \Omega^2 - \omega^2 - i\omega\delta \tag{6.10}$$

[recalling that $\Omega = c\sqrt{T_s}/2L$ is the sloshing frequency, $\delta = cT_o/L$ the extraction rate], the asterisk in $\mathcal{L}^*(\omega)$ denotes the complex conjugate, $\tilde{x}(\omega)$ is the Fourier transform of the relative displacement of the four test masses—i.e., the Fourier transform of the difference in lengths of the interferometer's two arm cavities—and $W_{\rm circ}$ is the circulating power in the each of the interferometer's two arms. Note that the circulating power (derived as in Sec. II B of Paper I) is related to the carrier amplitude B_1 in the arms by[4]

$$W_{\rm circ} = \frac{1}{2}\hbar\omega_0 B_1^2 = \frac{4\hbar\omega_0 I_1^2}{T_i T_p}\,, \tag{6.11}$$

[4]Equation (6.11) refers specifically to the practical version of the three-arm interferometer (Fig. 6.3). The simple (Fig. 6.2) version would be

$$W_{\rm circ} = \frac{1}{2}\hbar\omega_0 B_1^2 = \frac{\hbar\omega_0 I_1^2}{T_p}\,.$$

where I_1 is the input laser amplitude (in the cosine quadrature). Readers who wish to derive the input–output relations (6.3.1) for themselves may find useful guidance in Appendix B of KLMTV [7] and in Secs. II and III of Paper I [8], which give detailed derivations for other interferometer designs.

Notice that the first term in Eq. (6.9) contains $\tilde{x}$ only in the form $\omega\tilde{x}$; this is the velocity signal [actually, the sum of the velocity and higher odd time derivatives of position because of the $\mathcal{L}(\omega)$ in the denominator]. The test masses' relative displacement $\tilde{x}(\omega)$ is given by

$$\tilde{x} = \tilde{x}_e - \tilde{x}_n = L\tilde{h} - \frac{8i\sqrt{\hbar\omega_0\delta W_{\rm circ}}}{m\omega\sqrt{cL}\mathcal{L}(\omega)}\tilde{p}_1\,, \tag{6.12}$$

where $\tilde{x}_e$ is the Fourier transform of the relative displacement of the mirrors of the "east" arm and $\tilde{x}_n$ is the same for the "north" arm. The last term is the back-action produced by fluctuating radiation pressure (derived as in Sec. II B of Paper I).

It is possible to express Eqs. (6.3.1) in a more concise form, similar to Eqs. (16) in KLMTV:

$$\tilde{q}_1 = \Delta\tilde{p}_1 = \tilde{p}_1 e^{2i\psi}\,, \tag{6.13}$$

$$\tilde{q}_2 = \Delta\tilde{p}_2 + \sqrt{2\kappa}\frac{\tilde{h}}{h_{SQL}}e^{i\psi}\,, \quad \Delta\tilde{p}_2 = (\tilde{p}_2 - \kappa\tilde{p}_1)e^{2i\psi}\,. \tag{6.14}$$

Here

$$\tan\psi = -\frac{\Omega^2 - \omega^2}{\omega\delta} \tag{6.15}$$

is a phase shift put onto the light by the interferometer,

$$\kappa = \frac{16\omega_0\delta W_{\rm circ}}{mcL|\mathcal{L}(\omega)|^2} \tag{6.16}$$

is a dimensionless coupling constant that couples the gravity wave signal $\tilde{h}$ into the output $\tilde{q}_2$, and

$$h_{SQL} = \sqrt{\frac{8\hbar}{m\omega^2L^2}} \tag{6.17}$$

is the standard quantum limit for a conventional interferometer such as LIGO-I or VIRGO [1].

In Fig. 6.5, we plot the coupling constant κ as a function of frequency for several values of δ. As the graph shows, κ can be roughly constant for a rather broad frequency band $\omega \lesssim \Omega$, when δ is chosen to be $\sim \Omega$ (as it will be when the interferometer is optimized). Combining this with the fact that $h_{SQL} \propto 1/\omega$, we infer from Eqs. (6.3.1) that the output *signal* at frequencies $\omega \lesssim \Omega$ is proportional to $\omega\tilde{h}$, or equivalently $\omega\tilde{x}$, which is the relative speed of the test masses (as mentioned above).

The terms $\Delta\tilde{p}_1$ and $\Delta\tilde{p}_2$ in Eqs. (6.3.1) represent *quantum noise* (shot noise, radiation-pressure

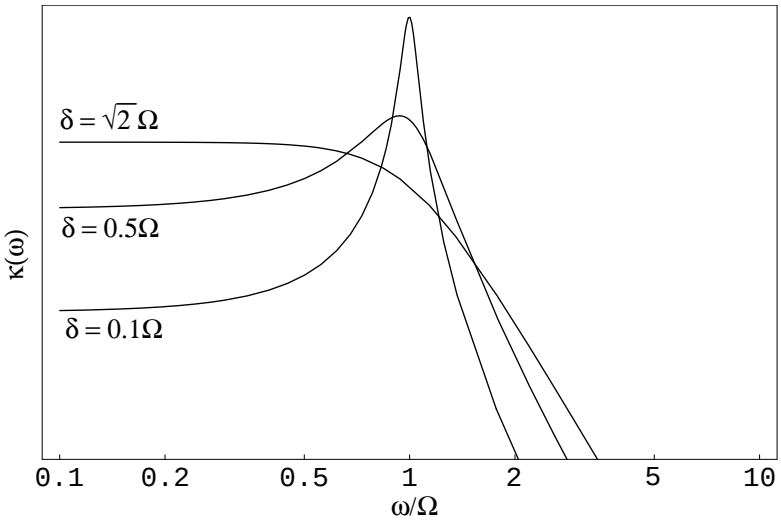

Figure 6.5: The coupling constant $\kappa(\omega)$ in arbitrary (logarithmic) units with ω measured in units of Ω. The three curves correspond to the same light power (such that $\kappa_{\max} = 5$ for the middle curve), but $\delta = 0.1\Omega$, $\delta = 0.5\Omega$, and $\delta = \sqrt{2}\Omega$.

noise, and their correlations). We shall demonstrate below that, in the frequency band $\omega \lesssim \Omega$ where the interferometer samples only the speed, there is no back-action (radiation-pressure) noise. This might not be obvious from Eqs. (6.3.1), especially because they have an identical form (except for the frequency dependence of κ) as the input-output relations of a conventional interferometer, where the term proportional to $\mathcal{K}$ (their version of κ) *is* the radiation-pressure noise. Indeed, if one measures the "sine" quadrature of the output, $\tilde{q}_2$, as is done in a conventional interferometer, this speed meter turns out to be SQL limited, as are conventional interferometers.

Fortunately, the fact that κ is constant (and equal to κ_0) over a broad frequency band will allow the aforementioned cancellation of the back-action, resulting in a QND measurement of speed. To see this, suppose that, instead of measuring the output phase quadrature $\tilde{q}_2$, we use homodyne detection to measure a generic, frequency-independent quadrature of the output:

$$\tilde{q}_\Phi = \Delta\tilde{p}_1 \cos\Phi + (\Delta\tilde{p}_2 + \sqrt{2\kappa}\frac{h}{h_{SQL}}e^{i\psi})\sin\Phi\,, \tag{6.18}$$

where Φ is a fixed homodyne angle. Then from Eqs. (6.3.1), we infer that the noise in the signal, expressed in GW strain units h, is

$$h_n = \frac{h_{SQL}}{\sqrt{2\kappa}}e^{i\psi}[\tilde{p}_1(\cot\Phi - \kappa) + \tilde{p}_2]\,. \tag{6.19}$$

By making $\cot\Phi = \kappa_0 \equiv$ (constant value of κ at $\omega \lesssim \Omega$), the radiation pressure noise in h_n will be cancelled in the broad band where $\kappa = \kappa_0$, thereby making this a QND interferometer.

We assume for now that ordinary vacuum enters the output port of the interferometer; i.e., $\tilde{p}_1$ and

$\tilde{p}_2$ are quadrature amplitudes for ordinary vacuum (we will inject squeezed vacuum in Sec. 6.4.1). This means [Eq. (26) of KLMTV] that their (single-sided) spectral densities are unity and their cross-correlations are zero, which, when combined with Eq. (6.19), implies a spectral density of

$$S_{h_n} = (h_{SQL})^2 \xi^2 \,. \tag{6.20}$$

Here

$$\xi^2 \equiv \frac{(\cot\Phi - \kappa)^2 + 1}{2\kappa} \tag{6.21}$$

is the fractional amount by which the SQL is beaten (in units of squared amplitude). This expression for ξ^2 is the same as that for the speed meters in Paper I [Eq. (35)] and BGKT [Eq. (40)], indicating the theoretical equivalency of these designs. In those papers, an optimization is given for the interferometer. Instead of just using the results of that optimization, we shall carry out a more comprehensive study of it[5].

6.3.2 Optimization

The possible choices of speed meter parameters can be investigated intuitively by examining the behavior of κ. To aid us in our exploration, we choose (as in BGKT and Paper I) to express $|\mathcal{L}(\omega)|^2$ [Eq. (6.10)] as

$$|\mathcal{L}(\omega)|^2 = (\omega^2 - \omega_{\rm opt}^2)^2 + \delta^2(\omega_{\rm opt}^2 + \delta^2/4)\,, \tag{6.22}$$

where

$$\omega_{\rm opt} = \sqrt{\Omega^2 - \delta^2/2}\,, \tag{6.23}$$

is the interferometer's "optimal frequency," i.e., the frequency at which $|\mathcal{L}(\omega)|$ reaches its minimum. Combining with Eq. (6.16), we obtain

$$\kappa = \frac{\Omega_{\rm I}^3\,\delta}{(\omega^2 - \omega_{\rm opt}^2)^2 + \delta^2(\omega_{\rm opt}^2 + \delta^2/4)}\,, \tag{6.24}$$

where

$$\Omega_{\rm I}^3 \equiv \frac{16\omega_0 W_{\rm circ}}{mLc} \tag{6.25}$$

[5]It should be noted that the expressions given in Sec. 6.3.1 are accurate to 6% or better over the frequency range of interest. To achieve 1% accuracy, we expand to the next-highest order. The result can be expressed as a re-definition of the sloshing frequency

$$\Omega^2 \to \Omega'^2 = \Omega^2 - \delta\delta_{\rm s}/2\,,$$

where $\delta_{\rm s} = cT_{\rm s}/2L$. Then κ retains the same functional form:

$$\kappa \to \kappa' = \frac{16\omega_0\delta W_{\rm circ}}{mcL((\Omega'^2 - \omega^2) + \omega^2\delta^2)}\,.$$

As a result, the optimization described in Sec. 6.3.2 applies equally well to κ' and Ω' as to the original κ and Ω.

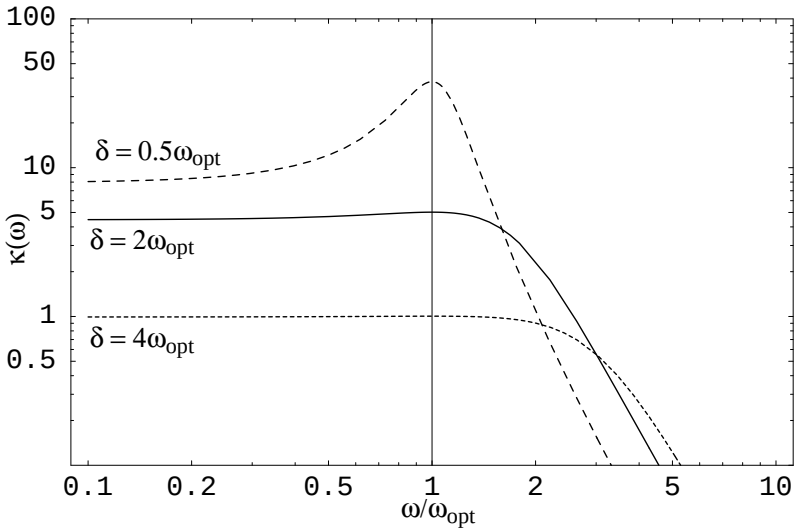

Figure 6.6: The coupling constant $\kappa(\omega)$ with ω measured in units of $\omega_{\rm opt}$. The solid curve is determined by setting $\delta = 2\omega_{\rm opt}$ and $\kappa_{\rm max} = 5$ (this value of $\kappa_{\rm max}$ comes from specifying that we want to beat the SQL by a factor of 10; see Fig. 6.7). If, in addition, we set $\omega_{\rm opt} = 2\pi \times 100$ Hz, then all the parameters have been specified (due to the various relationships between them) and are equal to the values given in Table 6.1. If we maintain the same power but change δ, then the only parameter of Table 6.1 that is affected is $T_{\rm o}$. Examples of such a change are shown for $\delta = 0.5\omega_{\rm opt}$ and $\delta = 4\omega_{\rm opt}$. Note that these two choices of δ are more extreme than would be desirable in practice, but they are shown here to illustrate more clearly the effect on κ of changing the ratio between δ and $\omega_{\rm opt}$.

is a frequency scale related to the circulating power. At $\omega_{\rm opt}$, κ reaches its maximum (see Fig. 6.6)

$$\kappa_{\rm max} = \frac{\Omega_{\rm I}^3}{\delta(\omega_{\rm opt}^2 + \delta^2/4)}\,. \tag{6.26}$$

By setting

$$\cot\Phi = \kappa_{\rm max}\,, \tag{6.27}$$

we get the maximum amount by which a speed meter can beat the SQL

$$\xi^2_{\rm min} = \frac{1}{2\kappa_{\rm max}} = \frac{\delta(\omega_{\rm opt}^2 + \delta^2/4)}{2\Omega_{\rm I}^3}\,. \tag{6.28}$$

As ω differs from $\omega_{\rm opt}$ in either direction, κ decreases from $\kappa_{\rm max}$. This causes the noise to increase since (i) the term $(\cot\Phi - \kappa)^2$ in the numerator of ξ^2 [Eq. (6.21)] increases and (ii) the denominator of ξ^2 decreases. In order to have broadband performance, we should make the peak of $\kappa(\omega)$ as flat as possible. As we can see from both Eq. (6.24) and Fig. 6.6, the shape of the peak can be adjusted by changing δ: for the same optical power, a larger δ means a wider peak but a smaller maximum. Therefore, changing δ is one method of balancing sensitivity against bandwidth. Some examples are shown in Figs. 6.6, 6.7, and 6.8, where $\kappa(\omega)$, $\xi^2(\omega)$, and $S_h(\omega)$, respectively, are plotted for

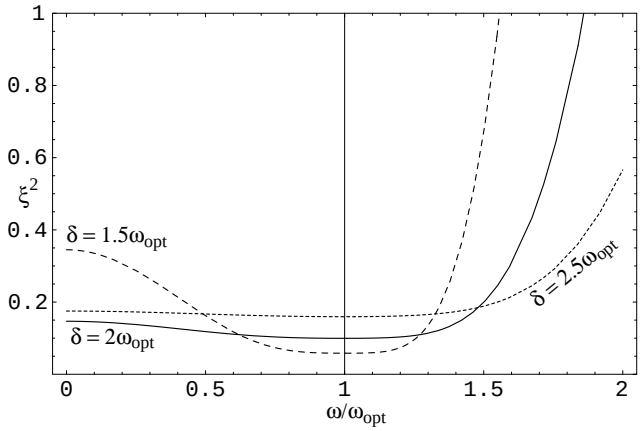

Figure 6.7: The squared amount by which the speed meter beats the SQL with a given circulating power, which is determined by setting (for the solid curve) $\xi^2_{\rm min} = 0.1$ and the condition (6.31). Note that the requirement on $\xi^2_{\rm min}$ sets the power relative to the SQL power $W^{SQL}_{\rm circ}$, the value of which is dependent on $\omega_{\rm opt}$. (For $\omega_{\rm opt} = 100$ Hz, we have $W_{\rm circ} = 8$ MW.) If we hold the power fixed and change δ to $1.5\omega_{\rm opt}$ and $2.5\omega_{\rm opt}$, we get the other two curves.

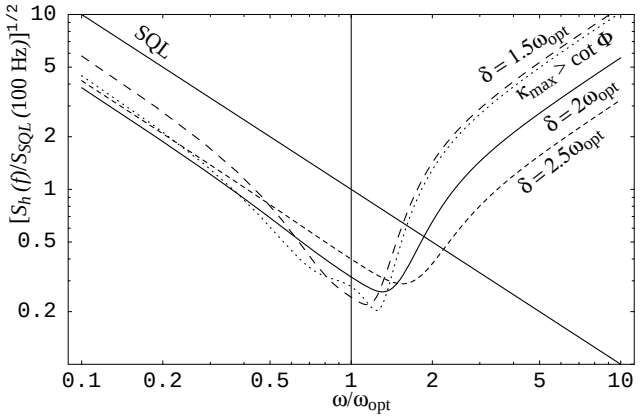

Figure 6.8: Noise curves corresponding to the ξ^2 curves in Fig. 6.7, the caption of which describes the parameters used here as well. The dotted line is an example of a noise curve for which κ is not quite flat and $\cot\Phi$ was chosen to be slightly smaller than $\kappa_{\rm max}$ (see the end of Sec. 6.3.2 for details.)

configurations with the same $\omega_{\rm opt}$ and optical power $W_{\rm circ}$, but with several values of δ.

To be more quantitative, a simple analytic form for $\xi^2(\omega)$ can be obtained by inserting Eqs. (6.24), (6.26), and (6.28) into Eq. (6.21) to get

$$\xi^2(\omega) = \left[1 + \Delta + \frac{1}{4\xi^4_{\rm min}}\frac{\Delta^2}{(1+\Delta)}\right]\xi^2_{\rm min}\,. \tag{6.29}$$

Here

$$\Delta \equiv \frac{\left(\omega^2 - \omega^2_{\rm opt}\right)^2}{\delta^2(\omega^2_{\rm opt} + \delta^2/4)} \tag{6.30}$$

is a dimensionless offset from the optimal frequency $\omega_{\rm opt}$. From Eq. (6.30), it is evident that Δ, and thus ξ^2, are the same for $\omega = 0$ and $\omega = \sqrt{2}\omega_{\rm opt}$ [see also Eq. (47) of BGKT or Eq. (49) of Paper I].

For definiteness, let us impose that

$$\xi^2(0) = \xi^2(\sqrt{2}\omega_{\rm opt}) = \frac{3}{2}\xi^2_{\rm min} \tag{6.31}$$

as is done by BGKT. For $\xi^2_{\rm min} = 0.1$, this gives $\delta = 1.977\omega_{\rm opt} \approx 2\omega_{\rm opt}$ (as assumed in BGKT and Paper I). Plugging these numbers into Eq. (6.28) and combining with Eq. (6.25) gives

$$\begin{aligned} W_{\rm circ} \qquad (\delta = 2\omega_{\rm opt}) &= \frac{mLc\,\omega_{\rm opt}^3}{8\omega_0\xi^2_{\rm min}} \\ &\simeq 8.4\,{\rm MW}\left(\frac{\omega_{\rm opt}}{2\,\pi\times 100\,{\rm Hz}}\right)^3\left(\frac{m}{40\,{\rm kg}}\right)\left(\frac{L}{4000\,{\rm km}}\right)\left(\frac{1.78\times 10^{15}\,{\rm Hz}}{\omega_0}\right)\left(\frac{0.1}{\xi^2_{\rm min}}\right). \end{aligned} \tag{6.32}$$

Therefore, when $\omega_{\rm opt}$ is chosen at $2\pi \times 100\,{\rm Hz}$, this speed meter (with $\delta = 2\omega_{\rm opt}$) requires $W_{\rm circ} \simeq 8.4\,{\rm MW}$ to beat the SQL by a factor of 10 in power ($\xi^2_{\rm min} = 0.1$). [Note that, keeping $\delta = 2\omega_{\rm opt}$, the speed meter reaches the SQL with $W^{\rm SQL}_{\rm circ} = 840\,{\rm kW}$, comparable to the value given by KLMTV Eq. (132) for conventional interferometers with 40-kilogram test masses.] The ξ^2 and S_h curves for this configuration are plotted as solid lines in Fig. 6.7 and 6.8, respectively.

Please note that Eq. (6.32) should be applied with caution because significantly changing $\xi^2_{\rm min}$ in the above equation (without changing the ratio between δ and $\omega_{\rm opt}$) will change the wide-band performance of the interferometer, since there is some "hidden" power dependence in Eq. (6.31). To determine the behavior of the speed meter with significantly higher power or lower $\xi^2_{\rm min}$ *while maintaining the same wideband performance*, we must re-apply the requirement (6.31) to determine the appropriate ratio between δ and $\omega_{\rm opt}$. For example, solving Eqs. (6.28) and (6.31) simultaneously for $\xi^2_{\rm min}$ and δ, with chosen values $W_{\rm circ} = 20$ MW and $\omega_{\rm opt} = 2\pi \times 100$ Hz, gives $\delta = 2.334\omega_{\rm opt}$ and $\xi^{-2}_{\rm min} \simeq 17$. Keeping this in mind, a general expression for the circulating power is

$$\begin{aligned} W_{\rm circ} &= \frac{mLc(\omega^2_{\rm opt} + \delta^2/4)\delta}{32\omega_0\,\xi^2_{\rm min}} \\ &= \frac{209\,{\rm kW}}{\xi^2_{\rm min}}\left[\frac{(\omega^2_{\rm opt} + \delta^2/4)\delta}{(2\pi\times 100\,{\rm Hz})^3}\right]\left(\frac{m}{40\,{\rm kg}}\right)\left(\frac{L}{4000\,{\rm km}}\right)\left(\frac{1.78\times 10^{15}\,{\rm Hz}}{\omega_0}\right), \end{aligned} \tag{6.33}$$

where the relationship between δ and $\omega_{\rm opt}$ determines whether the noise curve is deep but narrow or wide but shallow [with the requirement (6.31) giving the latter].

So far, we have only changed δ to modify the performance of the speed meter. Another method is to change $\omega_{\rm opt}$. In this case, the shape of the noise curve changes very little, but the minima occur at different frequencies, causing the interferometer to have either broader bandwidth or higher sensitivity (relative to the SQL). This is shown in Fig. 6.9. Maintaining condition (6.31) with $\omega_{\rm opt}$ chosen at $2\pi \times 150\,{\rm Hz}$, we get a broader but shallower curve (short dashes); this configuration beats the SQL by a factor of $\xi^{-2}_{\rm min} \sim 4.7$, up to $f \sim 240\,{\rm Hz}$. With $\omega_{\rm opt} = 2\pi \times 75\,{\rm Hz}$, we get a narrower

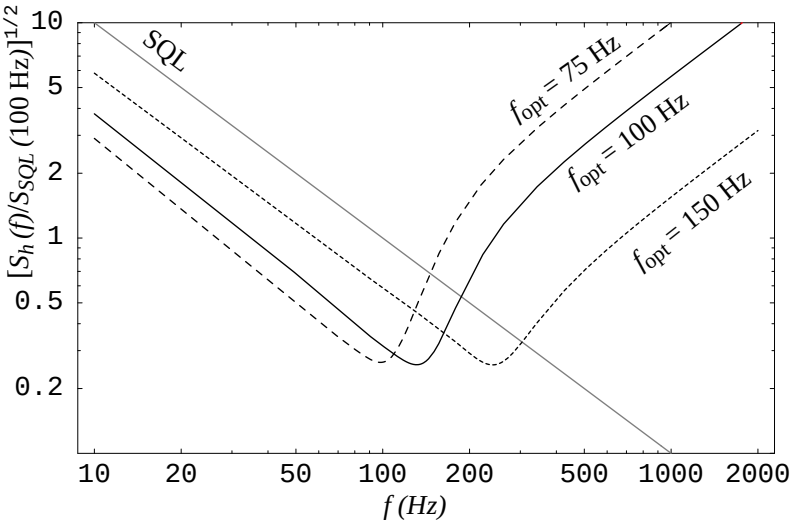

Figure 6.9: Noise curves for varying optimal frequencies. The solid curve has $f_{\rm opt} = 100$ Hz and is identical to the solid curve of Fig. 6.8. Maintaining the same power and the condition imposed by Eq. (6.31), we show two examples of noise curves with other optimal frequencies, specifically $f_{\rm opt} = 75$ Hz and $f_{\rm opt} = 150$ Hz.

Table 6.1: Three-arm speed-meter interferometer parameters and their fiducial values, as used throughout except where other parameters are specified.

Parameter	Symbol	Fiducial Value
carrier frequency	ω_0	$1.78 \times 10^{15}\mathrm{s}^{-1}$
mirror mass	m	40 kg
arm length	L	4 km
sloshing mirror transmissivity	$T_{\rm s}$	0.0008
output mirror transmissivity	$T_{\rm o}$	0.017
end mirror transmissivity	$T_{\rm e}$	2×10^{-5}
internal and RSE mirror trans.	$T_{\rm i}$	0.005
optimal frequency	$\omega_{\rm opt}$	$2\pi \times 100$ Hz
sloshing frequency	Ω	$2\pi \times 170$ Hz
extraction rate (half-bandwidth)	δ	$2\pi \times 200$ Hz
SQL circulating power	$W_{\rm circ}^{SQL}$	820 kW

but deeper curve (long dashes), which beats the SQL by a factor of $\xi_{\rm min}^{-2} \sim 17$, up to $f \sim 100\,\mathrm{Hz}$. The power was kept fixed at $W_{\rm circ} = 8.2\,\mathrm{MW}$.

One more potential optimization method is to choose a κ with a peak that is not quite flat and then choose a $\cot\Phi$ that is slightly smaller than $\kappa_{\rm max}$. This will give a wider bandwidth on either side of $\omega_{\rm opt}$, at the price of decreased sensitivity at the region near $\omega_{\rm opt}$ (see dotted line in Fig. 6.8).

For simplicity, we will choose a typical (but somewhat arbitrary) set of parameters for the lossless interferometer of Fig. 6.2. These values, given in Table 6.1, will be used (except as otherwise noted) for subsequent plots and calculations comparing this speed-meter design to other configurations.

6.3.3 Discussion of three-cavity speed-meter design

In this section, we discuss how the three-cavity speed-meter design compares to the two-cavity design presented in Paper I, focusing on the three major problems of that design: it required (i) a high circulating power, (ii) a large amount of power coming out of the interferometer with the signal, and (iii) an exorbitantly high input laser power.

With the three-cavity speed meter, we are able to replicate the performance of the two-cavity design in Paper I, but without the exorbitantly high input power. The reason why our three-cavity speed meter does not need a high input power is the same as for conventional interferometers: in both cases, the excited cavities are fed directly by the laser. According to Bose statistics, carrier photons will be "sucked" into the cavities, producing a strong amplification. This was not the case in the two-cavity speed meter of Paper I. There, an essentially empty cavity stood between the input and the excited cavity, thereby thwarting Bose statistics and resulting in a required input laser power much greater than the power that was circulating in the excited cavity (see Paper I for more details). In this chapter, we have returned to a case where the laser is driving an excited cavity directly, thereby allowing the input laser power to be small relative to the circulating power.

Because the cavity from which we are reading out the signal does not contain large amounts of carrier light (by contrast with the two-cavity design), this three-cavity speed meter does not have large amounts of power exiting the interferometer with the velocity signal, unlike the two-cavity design. By making use of the different modes of the Michelson interferometer, we have solved the problem of the exorbitantly high input power and the problem of the amount of light that comes out of the interferometer.

The problem of the high circulating power $W_{\rm circ}$, unfortunately, is not solved by the three-cavity design. This is actually a common characteristic of "external-readout" interferometer designs capable of beating the SQL. The reason for this high power is the energetic quantum limit (EQL), which was first derived for gravitational-wave interferometers by Braginsky, Gorodetsky, Khalili and Thorne [20]. The EQL arises from the phase-energy uncertainty principle

$$\Delta E \Delta\phi \geq \frac{\hbar\omega_0}{2}\,, \tag{6.34}$$

where E is the stored energy in the interferometer and ϕ is the phase of the light. The uncertainty ΔE of the stored light energy during the measurement process must be large enough to allow a small uncertainty $\Delta\phi$ in the stored light's optical phase, in which the GW signal is contained. For an interferometer with coherent light (so $\Delta E = \hbar\omega_0\sqrt{E/\hbar\omega_0}$), the EQL dictates that the energy stored in the arms must be larger than

$$E_\xi \sim \frac{mL^2\omega^2\Delta\omega}{4\omega_0\xi^2} \tag{6.35}$$

in order to beat the SQL by a factor of ξ near frequency ω with a bandwidth $\Delta\omega$ (Eq. (1) of Ref. [11] and Eq. (29) of Ref. [20]). In a broadband configuration with $\Delta\omega \sim \omega$, we have

$$E_\xi \sim \frac{mL^2\omega^3}{4\omega_0\xi^2}\,. \tag{6.36}$$

For comparison, in the broadband regime of the speed meter, we have, from Eq. (6.28),

$$\xi^2_{\rm min} = \frac{mL^2\delta(\omega^2_{\rm opt}+\delta^2/4)}{4\,E\omega_0} \sim \frac{mL^2\omega^3_{\rm opt}}{4\,E\omega_0}\,, \tag{6.37}$$

where the stored energy is $E = 2W_{\rm circ}L/c$. Comparison between Eqs. (6.36) and (6.37) confirms that our speed meter is EQL limited.

As a consequence of the EQL, designs with coherent light will all require a similarly high circulating power in order to achieve a similar sensitivity. Moreover, given the sharp dependence $E \propto \omega^3$, this circulating power problem will become much more severe when one wants to improve sensitivities at high frequencies.

Nevertheless, the EQL in the form (6.35) above only applies to coherent light. Using nonclassical light will enable the interferometer to circumvent it substantially. One possible method was invented by Braginsky, Gorodetsky, and Khalili [10] using a special optical topology and intracavity signal extraction. A more conventional solution for our external-readout interferometer is to inject squeezed light into the dark port, as we shall discuss in Sec. 6.4.1 (and as was also discussed in the original paper [20] on the EQL).

6.4 Squeezed vacuum and FD homodyne dectection

In this section, we discuss two modifications to the three-cavity speed-meter design analyzed in Sec. 6.3.1. This discussion applies to both the simple and practical versions, shown in Figs. 6.2 and 6.3; the modifications are shown in Fig. 6.4. The first modification is to inject squeezed vacuum (with fixed squeeze angle) into the output port of the speed meter, as shown in Fig. 6.4. This will reduce the amount of power circulating in the interferometer. The second modification, also shown in Fig. 6.4, is the introduction of two filter cavities on the output, which allow us to perform *frequency-dependent* homodyne detection (described in KLMTV) that will dramatically improve the performance of the speed meter at frequencies $f \gtrsim f_{\rm opt}$.

6.4.1 Injection of squeezed vacuum into dark port

Because the amount of circulating power required by our speed meter remains uncomfortably large, it is desirable to reduce it by injecting squeezed vacuum into the dark port. The idea of using squeezed

light in gravitational-wave interferometers was first conceived by Caves [14] and further developed by Unruh [4] and KLMTV. We shall start in this section with a straightforward scheme that will decrease the effective circulating power without otherwise changing the speed meter performance.

As discussed in Sec. IV B and Appendix A of KLMTV, a squeezed input state is related to the vacuum input state (assumed in Sec. 6.3.1) by a unitary squeeze operator $S(R,\lambda)$ [see Eqs. (41) and (A5) of KLMTV]

$$|\mathrm{in}\rangle = S(R,\lambda)|0\rangle\,. \tag{6.38}$$

Here R is the squeeze amplitude and λ is the squeeze angle, both of which in principle can depend on sideband frequency. However, the squeezed light generated using nonlinear crystals [21, 22] has frequency-independent R and λ in our frequency band of interest, i.e., $f < 10\,\mathrm{kHz}$ [23]; and in this section, we shall assume frequency independence.

The effect of input squeezing is most easily understood in terms of the following unitary transformation,

$$|\mathrm{in}\rangle \;\rightarrow\; S^\dagger(R,\lambda)|\mathrm{in}\rangle = |0\rangle \tag{6.39}$$

$$\tilde{p}_j \;\rightarrow\; S^\dagger(R,\lambda)\tilde{p}_j S(R,\lambda)\,, \tag{6.40}$$

$$\tilde{q}_j \;\rightarrow\; S^\dagger(R,\lambda)\tilde{q}_j S(R,\lambda)\,, \tag{6.41}$$

where $j = 1, 2$. This brings the input state back to vacuum and transforms the input quadratures into linear combinations of themselves, in a rotate-squeeze-rotate way [Eq. (A8) of KLMTV, in matrix form]:

$$\begin{aligned}
\begin{pmatrix} \tilde{p}_1 \\ \tilde{p}_2 \end{pmatrix} \;&\rightarrow\; \begin{pmatrix} \tilde{p}_{1s} \\ \tilde{p}_{2s} \end{pmatrix} \\
&= S^\dagger(R,\lambda) \begin{pmatrix} \tilde{p}_1 \\ \tilde{p}_2 \end{pmatrix} S(R,\lambda) \\
&= \begin{pmatrix} \cos\lambda & -\sin\lambda \\ \sin\lambda & \cos\lambda \end{pmatrix} \begin{pmatrix} e^{-R} & 0 \\ 0 & e^{R} \end{pmatrix} \begin{pmatrix} \cos\lambda & \sin\lambda \\ -\sin\lambda & \cos\lambda \end{pmatrix} \begin{pmatrix} \tilde{p}_1 \\ \tilde{p}_2 \end{pmatrix}.
\end{aligned} \tag{6.42}$$

In particular, the GW noise can be calculated by using the squeezed noise operator [Eq. (29) of KLMTV]

$$h_{ns} = S^\dagger(R,\lambda) h_n S(R,\lambda)\,, \tag{6.43}$$

and the vacuum state.

A special case—the case that we want—occurs when $R =$ constant and $\lambda = \pi/2$. Then there is

no rotation between the quadratures but only a frequency-independent squeezing or stretching,

$$\tilde{p}_1 \rightarrow \tilde{p}_{1s} = e^R \tilde{p}_1 \,, \tag{6.44}$$

$$\tilde{p}_2 \rightarrow \tilde{p}_{2s} = e^{-R} \tilde{p}_2 \,. \tag{6.45}$$

Consequently, Eqs. (6.3.1) for the output quadratures $\tilde{q}_{1,2s} = S^\dagger(R, \pi/2)\tilde{q}_{1,2}S(R, \pi/2)$ are transformed into

$$\tilde{q}_{1s} = e^R \tilde{p}_1 e^{2i\psi} \tag{6.46}$$

$$\tilde{q}_{2s} = e^{-R}\left[\left(\tilde{p}_2 - \kappa e^{2R}\tilde{p}_1\right) e^{2i\psi} + \sqrt{\kappa e^{2R}}\frac{\tilde{h}}{h_{SQL}} e^{i\psi}\right] . \tag{6.47}$$

The corresponding noise can be put into the same form as Eq. (6.19),

$$h_{ns} = \frac{h_{SQL}}{\sqrt{\kappa_{\rm eff}}} e^{i\psi} \left[\tilde{p}_1(\cot\Phi_{\rm eff} - \kappa_{\rm eff}) + \tilde{p}_2\right] , \tag{6.48}$$

with

$$\cot\Phi_{\rm eff} \equiv e^{2R}\cot\Phi \,, \quad \kappa_{\rm eff} \equiv e^{2R}\kappa \,. \tag{6.49}$$

Since κ is proportional to the circulating power [see Eqs. (6.16)], gaining a factor e^{2R} in κ is equivalent to gaining this factor in $W_{\rm circ}$.

In other words, by injecting squeezed vacuum with squeeze factor e^{2R} and squeeze angle $\lambda = \pi/2$ into the interferometer's dark port, we can achieve precisely the same interferometer performance as in Sec. 6.3.1, but with a circulating light power that is lower by $W_{\rm circ,SISM} = e^{-2R} W_{\rm circ,OSM}$. (Here "SISM" means "squeezed-input speed meter" and "OSM" means "ordinary speed meter." Since squeeze factors $e^{-2R} \sim 0.1$ are likely to be available in the time frame of LIGO-III [7], this squeezed-input speed meter can function with $W_{\rm circ,SISM} \simeq 0.1 W_{\rm circ,OSM}$.

6.4.2 Frequency-dependent homodyne detection

One can take further advantage of squeezed light by using frequency-dependent (FD) homodyne detection at the interferometer output [24, 25, 26, 27, 28]. As KLMTV have shown, FD homodyne detection can be achieved by sending the output light through one or more optical filters (as in Fig. 6.4) and then performing ordinary homodyne detection. If its implemention is feasible, FD homodyne detection will dramatically improve the speed meter's sensitivity at high frequencies (above $f_{\rm opt} = 100$ Hz). Note that the KLMTV design that used FD homodyne detection was called a "variational-output" interferometer; consequently, we shall use the term "variational-output speed meter" to refer to our speed meter with FD homodyne detection. Continuing the analogy, when we have both squeezed-input and FD homodyne detection, we will use the term "squeezed-variational

speed meter." The following discussion is analogous to Secs. IV and V of KLMTV.

For a generic frequency-dependent[6] squeeze angle $\lambda(\omega)$ and homodyne detection phase $\Phi(\omega)$, we have, for the squeezed noise operator [Eqs. (6.43) and (6.42)],

$$h_{ns} = -\frac{h_{SQL}}{\sqrt{\kappa}} e^{i\psi}\sqrt{1+\tilde{\kappa}^2} \qquad \Big(\tilde{p}_1\big\{\cosh R\cos\tilde{\Psi} - \sinh R\cos\big[\tilde{\Psi} - 2(\tilde{\Psi}+\lambda)\big]\big\} \\ -\tilde{p}_2\big\{\cosh R\sin\tilde{\Psi} - \sinh R\sin\big[\tilde{\Psi} - 2(\tilde{\Psi}+\lambda)\big]\big\}\Big)\,, \tag{6.50}$$

where

$$\cot\tilde{\Psi} \equiv \tilde{\kappa} \equiv \kappa - \cot\Phi\,. \tag{6.51}$$

The corresponding noise spectral density [computed by using the ordinary vacuum spectral densities, $S_{\tilde{p}_1} = S_{\tilde{p}_2} = 1$ and $S_{\tilde{p}_1\tilde{p}_2} = 0$, in Eq. (6.50)] is

$$S_h = \frac{(h_{SQL})^2}{\kappa}(1+\tilde{\kappa}^2)\Big\{e^{-2R} + \sinh 2R[1-\cos 2(\tilde{\Psi}+\lambda)]\Big\}\,. \tag{6.52}$$

Note that these expressions are analogous to KLMTV Eqs. (69)–(71) for a squeezed-variational interferometer (but the frequency dependence of their $\mathcal{K}$ is different from that for our κ). From Eq. (6.52), S_h can be no smaller than the case when

$$\tilde{\kappa} = 0\,, \quad \cos 2(\tilde{\Psi}+\lambda) = 1\,. \tag{6.53}$$

The optimization conditions (6.53) are satisfied when

$$\cot\Phi = \kappa\,, \quad \lambda = \pi/2\,, \tag{6.54}$$

which corresponds to frequency-dependent homodyne detection on the (frequency-independent) squeezed-input speed meter discussed in the previous section.

As it turns out, the condition $\cot\Phi = \kappa$ can readily be achieved by the family of two-cavity optical filters invented by KLMTV and discussed in their Sec. V and Appendix C. We summarize and generalize their main results in our Appendix 6.7. The two filter cavities are both Fabry-Perot cavities with (ideally) only one transmitting mirror. They are characterized by their bandwidths, δ_J, (where $J = \mathrm{I}$, II denote the two cavities) and by their resonant frequencies, $\omega_0 + \xi_J\delta_J$ (the ones nearest ω_0). The output light from the squeezed-input speed meter is sent through the two filters, and then a homodyne detection with frequency-independent phase θ is performed on it.

For the squeezed-variational speed meter (shown in Fig. 6.4) with the parameters in Table 6.1,

[6]For generality of the equations, we allow the squeeze angle and the the homodyne phase both to be frequency dependent, but the squeeze angle will be fixed (frequency independent) later in the argument [specifically, in Eq. (6.54)].

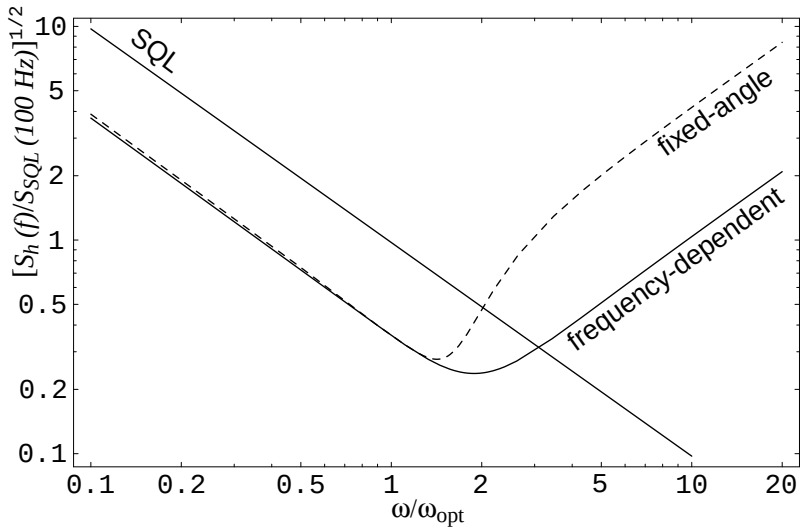

Figure 6.10: Comparison of typical noise curves for frequency-dependent and fixed-angle homodyne detection. The FD homodyne angle $\Phi(\omega)$ is that of Eqs. (6.54) and (6.55); the fixed homodyne angle Φ is that of Eq. (6.49); the circulating power is e^{-2R} times that of Table 6.1; and all other parameters are identical for the two interferometers and are given in Table 6.1.

plus $\xi^2_{\rm min} = 0.1$, $\delta = 2\omega_{\rm opt}$, $\Lambda^4 = 4\,\omega^4_{\rm opt}$, and $e^{-2R} = 0.1$, we have

$$\kappa = \frac{4\,\omega^4_{\rm opt}}{(\omega^2 - \omega^2_{\rm opt})^2 + 8\,\omega^4_{\rm opt}} \tag{6.55}$$

and the required filter and detection configuration is $\xi_{\rm I} = 1.7355$, $\delta_{\rm I} = 2\pi \times 91.57\,{\rm Hz}$, $\xi_{\rm II} = -1.1133$, $\delta_{\rm II} = 2\pi \times 114.3\,{\rm Hz}$, and $\theta = \pi/2$. [These values are reached by solving Eqs. (C4) of KLMTV, or by using the simpler method described in Appendix 6.7 of this Chapter.] The resulting performance is plotted in Fig. 6.10. Note the substantial improvement at $\omega \gtrsim \omega_{\rm opt}$.

In the case of position-meter interferometers with optical filters (the interferometers analyzed by KLMTV), the optical losses due to the filter cavities contribute significantly to the noise spectral density and drastically reduce the ability to beat the SQL. It turns out that the squeezed-variational speed meter is less sensitive to such losses, as we shall see in Sec. 6.5.

6.5 Optical losses

In order to understand the issue of optical losses in this speed meter, we shall start by addressing its *internal* losses. These include scattering and absorption at each optical element, finite transmissivities of the end mirrors, and imperfections of the mode-matching between cavities. The effect of *external* losses (i.e., losses in the detection system and any filter cavities) will be discussed separately. Note that the analysis in this section includes the internal and RSE mirrors, so it applies primarily to the speed meter designs in Figs. 6.3 and 6.4.

6.5.1 Internal losses

In this subsection, we will consider only noise resulting from losses associated with optical elements inside the interferometer. These occur

- in the optical elements: arm cavities, sloshing cavity, extraction mirror, port-closing mirror, beam splitter, RSE mirror;

- due to mode-mismatching[7]; and

- due to the imperfect matching of the transmissivities of the RSE and internal mirrors[8].

Since the optical losses will dominate, we focus only on that type of loss here. The loss at each optical element will decrease the amplitude of the sideband light (which carries the gravitational-wave information) and will simultaneously introduce additional vacuum fluctuations into the optical train. Schematically, for some sideband $\tilde{a}(\omega)$, the loss is described by

$$\tilde{a}(\omega) \to \sqrt{1-\mathcal{E}(\omega)}\,\tilde{a}(\omega) + \sqrt{\mathcal{E}(\omega)}\,\tilde{n}(\omega)\,, \tag{6.56}$$

where $\mathcal{E}$ is the (power) loss coefficient, and $\tilde{n}(\omega)$ is the vacuum field entering the optical train at the loss point.

It should be noted that there are various methods of grouping these losses together in order to simplify calculations. For example, we combine all of the losses occurring in the arm (or sloshing) cavities, into one loss coefficient of $\mathcal{L} \sim 20 \times 10^{-6}$ [according to KLMTV Eq. (93)]. Then we assume that the end mirrors have transmissivity $T_{\rm e} = 2 \times 10^{-5}$, thereby absorbing all of the arm losses into one term [see KLMTV Eq. (B5) and preceding discussion].

Assuming that the noise entering at the end mirrors of the arm cavities is denoted $\tilde{n}_{e1,2}$ and $\tilde{n}_{n1,2}$ for the east and north arms respectively, at the end mirror of the sloshing cavity $\tilde{s}_{1,2}$, at the port-closing mirror $\widetilde{w}_{1,2}$, and at the RSE mirror $\widetilde{m}_{n1,2}$ and $\widetilde{m}_{s1,2}$ [representing the losses described in the previous paragraph; see Appendix 6.8.3 for details], the output of the lossy three-cavity speed-meter system (Fig. 6.3; the simplified and practical versions are no longer equivalent, since there will be

[7] According to our simple analysis in Appendix 6.9, this effect will be insignificant in comparison with the losses in the optical elements, so we shall ignore it.

[8] This effect is negligibly small so we shall ignore it; see Appendix 6.10 for details.

additional losses due to the presence of the internal and RSE mirrors) is

$$\begin{aligned}
\tilde{q}_1 &= -\frac{\mathcal{L}^*(\omega)}{\mathcal{L}(\omega)}\tilde{p}_1 + \frac{i\omega\sqrt{\delta\delta_{\rm e}}}{\mathcal{L}(\omega)}(\tilde{n}_{e1} - \tilde{n}_{n1}) + \frac{\Omega\sqrt{2\delta\delta_{\rm e}}}{\mathcal{L}(\omega)}\tilde{s}_1 \\
&\quad - \frac{\sqrt{T_{\rm e}}(\Omega^2 - \omega^2 + i\omega\delta_{\rm s})}{\mathcal{L}(\omega)}\widetilde{w}_1 - \frac{i\omega\sqrt{2\delta\delta_\epsilon}}{\mathcal{L}(\omega)}\widetilde{m}_{s1} \\
&\quad + \frac{\omega\sqrt{2L\delta\delta_\epsilon}(\omega - i\delta_{\rm i})}{\sqrt{c\delta_{\rm i}}\mathcal{L}(\omega)}\widetilde{m}_{n1}\,, \qquad (6.57) \\
\tilde{q}_2 &= \frac{2i\omega\sqrt{\omega_0 T_{\rm o} W^*_{\rm circ}}}{L\sqrt{\hbar}\mathcal{L}(\omega)}\tilde{x} - \frac{\mathcal{L}^*(\omega)}{\mathcal{L}(\omega)}\tilde{p}_2 + \frac{\Omega\sqrt{2\delta\delta_{\rm e}}}{\mathcal{L}(\omega)}\tilde{s}_2 \\
&\quad + \frac{i\omega\sqrt{\delta\delta_{\rm e}}}{\mathcal{L}(\omega)}(\tilde{n}_{e2} - \tilde{n}_{n2}) - \frac{\sqrt{T_{\rm e}}(\Omega^2 - \omega^2 + i\omega\delta_{\rm s})}{\mathcal{L}(\omega)}\widetilde{w}_2 \\
&\quad - \frac{i\omega\sqrt{2\delta\delta_\epsilon}}{\mathcal{L}(\omega)}\widetilde{m}_{s2} + \frac{\omega\sqrt{2L\delta\delta_\epsilon}(\omega - i\delta_{\rm i})}{\sqrt{c\delta_{\rm i}}\mathcal{L}(\omega)}\widetilde{m}_{n2}\,, \qquad (6.58)
\end{aligned}$$

where

$$\begin{aligned}
\tilde{x} &= L\tilde{h} - \frac{4\sqrt{2\hbar\omega_0 W^*_{\rm circ}}}{mc\omega^2\mathcal{L}(\omega)}\left[\frac{i\omega\sqrt{2c\delta}}{\sqrt{L}}\tilde{p}_1 + \frac{i\omega\sqrt{c\delta_\epsilon}}{\sqrt{L}}\widetilde{m}_{s1}\right. \\
&\quad - \frac{\sqrt{\delta_\epsilon}[\Omega^2 - i\omega(\delta + \delta_{\rm i})]}{\sqrt{\delta_{\rm i}}}\widetilde{m}_{n1} - \frac{\Omega\sqrt{c\delta_{\rm e}}}{\sqrt{L}}\tilde{s}_1 \\
&\quad \left. + i\omega\sqrt{\delta\delta_{\rm e}}\widetilde{w}_1 - \frac{i\omega\sqrt{c\delta_{\rm e}}}{\sqrt{2L}}(\tilde{n}_{e1} - \tilde{n}_{n1})\right] \qquad (6.59)
\end{aligned}$$

with

$$\begin{aligned}
\delta_{\rm e} &= cT_{\rm e}/2L\,, \quad \delta_{\rm s} = cT_{\rm s}/2L\,, \\
\delta_{\rm i} &= cT_{\rm i}/4L\,, \quad \delta_\epsilon = c\mathcal{E}/2L\,. \qquad (6.60)
\end{aligned}$$

Note that the expression for the circulating power now has the form

$$W^*_{\rm circ} = \frac{1}{2}\hbar\omega_0 B_1^2 = \frac{4\hbar\omega_0 T_{\rm i} T_{\rm p} I_1^2}{(T_{\rm i}T_{\rm p} + 4T_{\rm e})^2} \qquad (6.61)$$

[cf. Eq. (6.11)].

Equations (6.5.1) are approximate expressions [accurate to about 6%, as were Eqs. (6.3.1); see Footnote 5], where the assumptions (6.7) regarding the relative sizes of the transmissivities were used to simplify from the exact expressions. Alternatively, they can be derived analytically by keeping the leading order of the small quantities $\omega L/c \sim \sqrt{T_{\rm s}} \sim T_{\rm o} \sim T_{\rm i}$, plus the various loss factors; see Sec. VI of KLMTV and Sec. IV of Paper I for details of the derivations for other inteferometer designs. In addition to confirming the approximate formulas, such a derivation can also clarify the origins of various noise terms and their connections to one another.

6.5.2 Internal and external losses in compact form

In order to simplify the above Eqs. (6.5.1) and (6.59), we define κ^* in identically the same way as we defined κ [Eq. (6.16) or (6.24)] but with $W_{\rm circ} \to W^*_{\rm circ}$. Let $\mathcal{E}^{\rm S}_{\mathcal{N}}$ and $\mathcal{E}^{\rm R}_{\mathcal{N}}$ represent the shot and radiation-pressure noises for the various parts of the interferometer, specified by $\mathcal{N}$. In Table 6.2, expressions for $\mathcal{E}^{\rm S}_{\mathcal{N}}$ and $\mathcal{E}^{\rm R}_{\mathcal{N}}$ are given for $\mathcal{N}$ = AES (arm cavities, extraction mirror, and sloshing cavity combined), close (port-closing mirror), $\rm RSE_{in}$ (RSE cavity in the north direction, or going "in" to the arms), and $\rm RSE_{out}$ (RSE cavity in the south direction, or going "out" of the arms). The various $\varepsilon_{\mathcal{N}}$ represent the characteristic (and frequency-independent) fractional losses for each of these terms; values are given in Table 6.3. Note that, by definition, $\mathcal{E}^{\rm S}_{\mathcal{N}}$ are required to be real, while $\mathcal{E}^{\rm R}_{\mathcal{N}}$ may have imaginary parts. For more information, including physical explanations of each of these terms, see Appendix 6.8.

It is simple at this point to include the losses associated with optical elements external to the interferometer. These include losses are associated with

- the local oscillator used for homodyne detection,
- the inefficiency of the photodiode,
- the circulator by which the squeezed vacuum is injected, and
- the external filter cavities used for the variational-output scheme.

These can be addressed in the same manner as the losses inside the speed meter. We need only include two more terms in the summation, $\mathcal{N}$ = OPC for the local oscillator, photodiode, and circulator and $\mathcal{N}$ = F for the filters. Again, these terms are shown in Tables 6.2 and 6.3 and described in more detail in Appendix 6.8.

Using these $\mathcal{E}^{\rm S}_{\mathcal{N}}$ and $\mathcal{E}^{\rm R}_{\mathcal{N}}$, we can rewrite the input-output relation (6.5.1) in the same form as Eq. (6.3.1) as follows:

$$\begin{aligned}\begin{pmatrix} \tilde{q}_1 \\ \tilde{q}_2 \end{pmatrix} &= e^{2i\psi} \begin{pmatrix} 1 & 0 \\ -\kappa^* & 1 \end{pmatrix} \begin{pmatrix} \tilde{p}_1 \\ \tilde{p}_2 \end{pmatrix} + \sum_{\mathcal{N}} e^{2i\alpha_{\mathcal{N}}} \begin{pmatrix} \mathcal{E}^S_{\mathcal{N}} & 0 \\ -\kappa^* \mathcal{E}^{\rm R}_{\mathcal{N}} & \mathcal{E}^S_{\mathcal{N}} \end{pmatrix} \begin{pmatrix} n_{\mathcal{N}1} \\ n_{\mathcal{N}2} \end{pmatrix} \\ &\quad + \sqrt{2\kappa^*} \frac{h}{h_{SQL}} e^{i\psi} \begin{pmatrix} 0 \\ 1 \end{pmatrix}, \end{aligned} \tag{6.62}$$

where the $\alpha_{\mathcal{N}}$ are uninteresting phases that do not affect the noise.

The relative magnitudes of the loss terms are shown in Fig. 6.11. From the plot, we can see that there are several loss terms—specifically, the shot noise from the AES, OPC, and filter cavities (if any)—that are of comparable magnitude at high frequencies and dominate there. The AES radiation-pressure term dominates at low frequencies, and the RSE radiation-pressure terms are

Table 6.2: Loss factors $\mathcal{E}^{\rm S}_{\mathcal{N}}$ due to shot noise and $\mathcal{E}^{\rm R}_{\mathcal{N}}$ due to radiation pressure for each type of loss source in the interferometer.

Source	$\mathcal{N}$	$\mathcal{E}^{\rm S}_{\mathcal{N}}$ (shot noise)	$\mathcal{E}^{\rm R}_{\mathcal{N}}$ (radiation pressure noise)
arm cavities, extract. mirror, sloshing cavity	AES	$\sqrt{\frac{\varepsilon_{\rm AES}}{T_{\rm o}}}\frac{\omega\delta}{\lvert\mathcal{L}(\omega)\rvert}$	$-\frac{e^{i\psi}}{2}\sqrt{\frac{\varepsilon_{\rm AES}}{T_{\rm o}}}$
port-closing mirror	close	$\sqrt{\varepsilon_{\rm close}}\,\frac{\Omega^2-\omega^2}{\lvert\mathcal{L}(\omega)\rvert}$	$-\frac{ie^{i\psi}}{2}\sqrt{\varepsilon_{\rm close}}$
RSE cavity "in" to arms	$\rm RSE_{in}$	$\sqrt{\frac{\varepsilon_{\rm RSE}T_{\rm i}}{4T_{\rm o}}\left(1+\frac{\omega^2}{\delta_{\rm i}^2}\right)}\frac{\omega\delta}{\lvert\mathcal{L}(\omega)\rvert}$	$e^{i\psi-i\beta_{\rm i}}\sqrt{\frac{\varepsilon_{\rm RSE}T_{\rm o}}{T_{\rm i}}}\frac{\omega(\delta_{\rm i}+\delta)+i\Omega^2}{\omega\delta}$
RSE cavity "out" to slosh	$\rm RSE_{out}$	$\sqrt{\frac{\varepsilon_{\rm RSE}T_{\rm i}}{4T_{\rm o}}\left(1+\frac{\omega^2}{\delta_{\rm i}^2}\right)}\frac{\omega\delta}{\lvert\mathcal{L}(\omega)\rvert}$	$e^{i\psi+i\beta_{\rm i}}\sqrt{\frac{\varepsilon_{\rm RSE}T_{\rm o}}{T_{\rm i}}}\frac{\omega(\delta_{\rm i}-\delta)-i\Omega^2}{\omega\delta}$
local oscillator, photodiode, and circulator	OPC	$\sqrt{\varepsilon_{\rm OPC}}$	0
filter cavities	F	$\sqrt{\varepsilon_{\rm F}}$	0

also significant. Since the largest noise sources at low frequencies are radiation-pressure terms, they will be dependent on the circulating power. Consequently, those terms will become smaller when the circulating power is reduced, as when squeezed vacuum is injected into the dark port. This will be demonstrated in Fig. 6.12 below.

To compute the spectral noise density, we suppose the output at homodyne angle Φ is measured, giving

$$S_{h_n}(\omega) = \frac{(h_{SQL})^2}{2\kappa^*}\left\{\left[(\cot\Phi-\kappa^*)^2+1\right]+\sum_{\mathcal{N}}\left[\lvert\mathcal{E}^{\rm S}_{\mathcal{N}}\cot\Phi-\mathcal{E}^{\rm R}_{\mathcal{N}}\kappa^*\rvert^2+(\mathcal{E}^{\rm S}_{\mathcal{N}})^2\right]\right\}, \quad (6.63)$$

where we have assumed all of the vacuum fluctuation spectral densities are unity and the cross-correlations are zero; this is the same technique that we used to derive Eqs. (6.20) and (6.52) and that was used in Paper I and KLMTV. Given the complicated behaviors of $\mathcal{E}^{\rm S}_{\mathcal{N}}$ and $\mathcal{E}^{\rm R}_{\mathcal{N}}$, including these loss terms in the optimization of the homodyne phase $\Phi(\omega)$ is unlikely to be helpful. Therefore, we will use $\cot\Phi=\kappa^*_{\rm max}$, as in the lossless case. This gives us a total noise with losses:

$$S_{h_n}(\omega) = \frac{(h_{SQL})^2}{2\kappa^*}\left\{\left[(\kappa^*_{\rm max}-\kappa^*)^2+1\right]+\sum_{\mathcal{N}}\left[\lvert\mathcal{E}^{\rm S}_{\mathcal{N}}\kappa^*_{\rm max}-\mathcal{E}^{\rm R}_{\mathcal{N}}\kappa^*\rvert^2+(\mathcal{E}^{\rm S}_{\mathcal{N}})^2\right]\right\}. \quad (6.64)$$

Table 6.3: Fiducial values for the fractional losses occuring in various parts of the interferometer. These losses and their values are discussed in more detail in Appendix 6.8.

Loss source	Symbol	Value
arm cavity	$\varepsilon_{\rm arm}$	2×10^{-5}
sloshing cavity	$\varepsilon_{\rm slosh}$	2×10^{-5}
extraction mirror	$\varepsilon_{\rm ext}$	2×10^{-5}
RSE cavity	$\varepsilon_{\rm RSE}$	2×10^{-5}
port-closing mirror	$\varepsilon_{\rm close}$	2×10^{-5}
local oscillator	$\varepsilon_{\rm lo}$	0.001
photodiode	$\varepsilon_{\rm pd}$	0.001
circulator	$\varepsilon_{\rm circ}$	0.001
mode-mismatch into filters	$\varepsilon_{\rm mm}$	0.001
Combined loss source terms		
arms, extraction mirror, & sloshing cavity [a]	$\varepsilon_{\rm AES}$	6×10^{-5}
local oscillator, photodiode, & circulator	$\varepsilon_{\rm OPC}$	0.003
filter cavities (with mode mismatch)	$\varepsilon_{\rm F}$	0.005

[a] This loss does have some weak frequency dependence, shown in Eq. (6.91), which will cause it to increase slightly at very low frequencies.

When we inject squeezed vacuum into the dark port, we get output operators

$$\begin{aligned}\begin{pmatrix}\tilde{q}_{1s}\\ \tilde{q}_{2s}\end{pmatrix} &= e^{2i\psi}\begin{pmatrix}1 & 0\\ -\kappa^* & 1\end{pmatrix}\begin{pmatrix}e^{R}\tilde{p}_1\\ e^{-R}\tilde{p}_2\end{pmatrix}+\sum_{\mathcal{N}}e^{2i\alpha_{\mathcal{N}}}\begin{pmatrix}\mathcal{E}^{S}_{\mathcal{N}} & 0\\ -\kappa^*\mathcal{E}^{\rm R}_{\mathcal{N}} & \mathcal{E}^{S}_{\mathcal{N}}\end{pmatrix}\begin{pmatrix}n_{\mathcal{N}1}\\ n_{\mathcal{N}2}\end{pmatrix}\\ &+ \sqrt{2\kappa^*}\frac{h}{h_{SQL}}e^{i\psi}\begin{pmatrix}0\\ 1\end{pmatrix}\end{aligned} \tag{6.65}$$

that can be regarded as acting on the ordinary vacuum states of the input. Once again assuming that the vacuum fluctuation spectral densities are unity and the cross-correlations are zero, the squeezed-input noise spectral density with homodyne detection at phase Φ is

$$S_{h_{ns}}(\omega)=\frac{(h_{SQL})^2}{2\kappa^*}\left\{\left[(\cot\Phi-\kappa^*)^2e^{2R}+e^{-2R}\right]+\sum_{\mathcal{N}}\left[|\mathcal{E}^{\rm S}_{\mathcal{N}}\cot\Phi-\mathcal{E}^{\rm R}_{\mathcal{N}}\kappa^*|^2+(\mathcal{E}^{\rm S}_{\mathcal{N}})^2\right]\right\}. \tag{6.66}$$

6.5.3 Performance of lossy speed meters and comparisons with other configurations

Examples of lossy speed meter noise curves with and without squeezed vacuum [Eqs. (6.64) and (6.66)] are shown in Fig. 6.12. Note that, as mentioned before, the losses are less significant when squeezed vacuum is used to reduce the circulating power, since the radiation-pressure noise coming from the losses is reduced. In the ordinary speed meter (no squeezed vacuum), the losses increase $\sqrt{S_{h_n}}$ by $5-9\%$ in the band $50-105$ Hz. The losses have little effect above this range, but below it, noise increases significantly, mostly due to the radiation-pressure noises shown in Fig. 6.11. For the

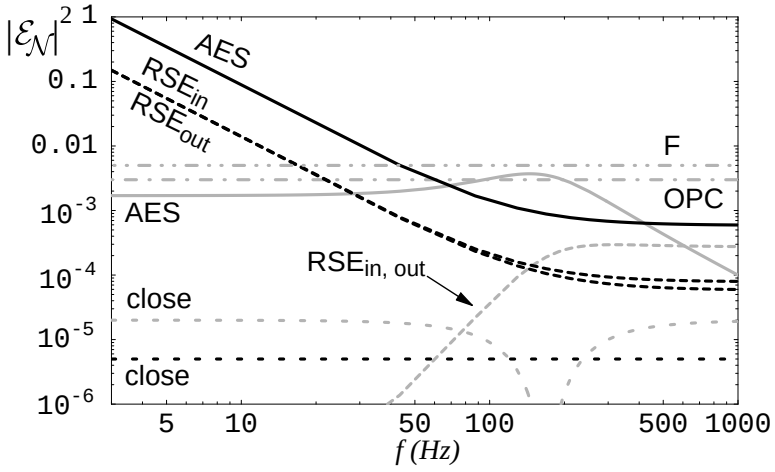

Figure 6.11: Moduli-squared of the loss factors shown in Table 6.2. In general, the black curves are the radiation-pressure noise and the gray curves are the shot noise. The parameters used for this plot are given in Tables 6.1 and 6.3.

squeezed-input speed meter (power squeeze-factor $e^{-2R} = 0.1$), the losses increase $\sqrt{S_{h_n}}$ by $3-4\%$ in the band $25-150$ Hz. Again, the losses have little effect above this range. At low frequencies, however, the losses get quite large: 11% at 10 Hz, 32% at 5 Hz, and 73% at 3 Hz. Losses in the squeezed-variational speed meter are much the same as in the squeezed-input speed meter. The slight difference at low frequencies is due to the fact that the lossless squeezed-variational speed meter is slightly better in that regime than the ordinary or squeezed-input speed meter.

The noise curves of squeezed-input speed meters (with ordinary homodyne detection) compared with the SQL are shown in Fig. 6.13, along with the noise of a conventional position meter with the same optical power. These speed meters beat the SQL in a broad frequency band, despite the losses. In particular, the noise curve for the speed meter with $W_{\rm circ} = 800\,{\rm kW}$ (and $f_{\rm opt} = 107\,{\rm Hz}$) matches the curve of the conventional position meter at high frequencies, while it beats the SQL by a factor of ~ 8 (in power) below $\sim 150\,{\rm Hz}$. In terms of the signal-to-noise ratio for neutron star binaries, for example, this configuration improves upon the conventional design by a factor of 3.6 in signal-to-noise ratio, which corresponds to a factor of 43 increase in event rate. If it is possible to have a higher circulating power, say $W_{\rm circ} = 2\,{\rm MW}$, the squeezed-input speed meter would be able to beat the SQL by a factor of ~ 14, corresponding to a factor of 4.6 in signal-to-noise and 97 in event rate. (Such a noise curve is shown in Fig. 6.13).

The broadband behaviors of the speed meters with losses are particularly interesting. We start by looking at the expression for the noise spectral density, Eq. (6.66). An ideal (lossless) speed meter in the broadband configuration beats the SQL from 0 Hz up to $\omega \sim \omega_{\rm opt}$, by roughly a constant factor, because κ is roughly constant in this band. *This is the essential feature of the speed meter*; see Sec. 6.3. Focusing on this region, we have, approximately (for squeezed-input speed meters that

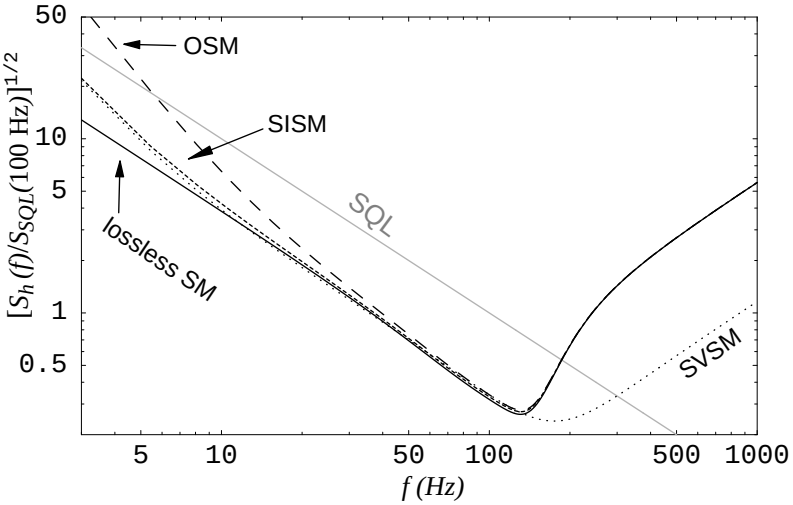

Figure 6.12: Noise curves showing the effects of losses. Noise curves for lossy versions of the ordinary (OSM), squeezed-input (SISM), and squeezed-variational (SVSM) speed meters are shown, along with a curve of the lossless ordinary speed meter for comparison. All speed meter curves here have the same parameters: $\delta = 2\omega_{\rm opt}$, $\Omega = \sqrt{3}\omega_{\rm opt}$, $\omega_{\rm opt} = 2\pi \times 100$ Hz, and $T_{\rm i} = 0.005$. The rest of the parameters are given in Tables 6.1 and 6.3.

are lossy):

$$S_{h_{ns}}(\omega) \;\approx\; \frac{h_{SQL}^2}{2\kappa_{\rm max}^*}\left[e^{-2R} + \sum_{\mathcal{N}} |\mathcal{E}_{\mathcal{N}}^{S}|^2 + \kappa^{*2}{}_{\rm max} \sum_{\mathcal{N}} |\mathcal{E}_{\mathcal{N}}^{\rm S} - \mathcal{E}_{\mathcal{N}}^{\rm R}|^2\right]. \tag{6.67}$$

Qualitatively, we can see that if the losses are not severe or if $\kappa_{\rm max}^*$ is relatively small (such that the later two terms in the above equation are small compared to the power squeeze factor e^{-2R}), the losses do not contribute significantly to the total noise. If, in addition, the dominant loss factors are (almost) frequency independent, then the noise due to losses gives a rather constant contribution, as shown by curves in Fig. 6.12. In particular, the large bandwidth is preserved. (There is a slight exception to this statement in the absence of squeezed input. Without squeezed input, the circulating power is higher, causing $\kappa_{\rm max}^*$ to be 10 times larger than the other cases. Consequently, the frequency dependence of $\mathcal{E}_{\rm AES}^{\rm R}$ to appear in the output.)

As $\kappa_{\rm max}$ increases, the noise from the losses may become dominant. In fact, when one minimizes the noise spectral density with respect to $\kappa_{\rm max}^*$, one obtains the following loss-dominated result:

$$S_h^{\rm L}(\omega) \approx h_{SQL}^2 \sqrt{\left(\sum_{\mathcal{N}} |\mathcal{E}_{\mathcal{N}}^{\rm S} - \mathcal{E}_{\mathcal{N}}^{\rm R}|^2\right)\left(e^{-2R} + \sum_{\mathcal{N}} |\mathcal{E}_{\mathcal{N}}^{\rm S}|^2\right)}, \tag{6.68}$$

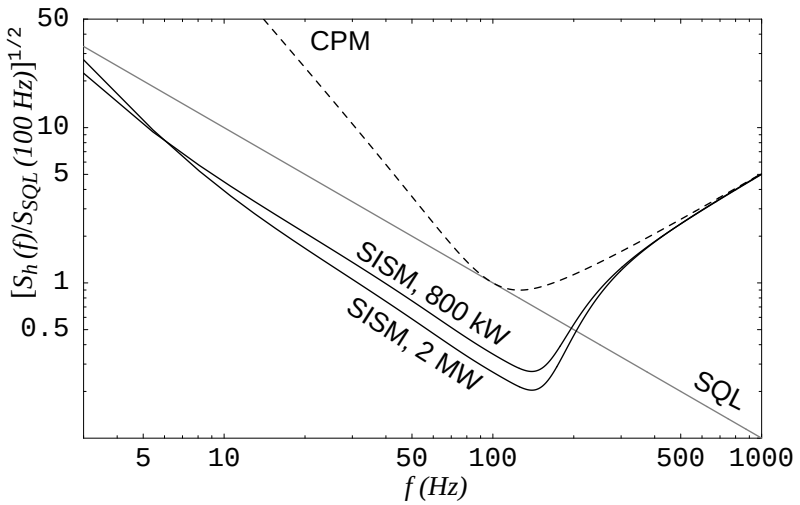

Figure 6.13: Comparison of noise curves of a conventional position meter (CPM) and squeezed-input speed meters (SISM) with circulating powers $W_{\rm circ} = 820$ kW and $W_{\rm circ} = 2$ MW. The speed meters have $f_{\rm opt} = 107$ Hz, with Ω and δ determined by Eq. (6.31). Other parameters used are those in Tables 6.1 and 6.3 with $T_{\rm i} = 0.005$ and $e^{-2R} = 0.1$.

which is achieved if and only if

$$\kappa^*_{\rm max} = \kappa^{\rm L} \equiv \sqrt{\frac{e^{-2R} + \sum_{\mathcal{N}} |\mathcal{E}^{\rm S}_{\mathcal{N}}|^2}{\sum_{\mathcal{N}} |\mathcal{E}^{\rm S}_{\mathcal{N}} - \mathcal{E}^{\rm R}_{\mathcal{N}}|^2}}\,. \tag{6.69}$$

This $\kappa^{\rm L}$ is rather constant and is comparable in magnitude to the values of $\kappa^*(\omega)$ of our speed meters, suggesting that the speed meters can become loss-limited over a broad band of frequencies. Contrast this with the KLMTV position meters, where $\mathcal{K}_*(\omega)$ grows as ω^{-2} at low frequencies; see Fig. 6.14. *This is a fundmental property of displacement meters.* As a result, a position meter optimized at some frequency $f_{\rm opt}$ may be able to reach its "loss limit" (the equivalent of $S^{\rm L}_h$) at that frequency $f_{\rm opt}$, but doing so will result in a sharp growth of noise at freqencies below $f_{\rm opt}$. In contrast, a speed meter similarly optimized is able to stay at the noise level of its loss limit $S^{\rm L}_h$ over a wide band of frequencies below $f_{\rm opt}$; see Fig. 6.15. While it is unfortunate that losses limit the performance of interferometers, the speed meter is at least able to retain a wide-band sensitivity even in the presence of a loss-limit.

To give a specific example of this loss-limit phenomenon, we first notice that, with the same circulating power, the conventional position-meter $\mathcal{K}_*$ and our (squeezed-variational) speed-meter κ agree[9] if $\delta = \gamma$ (where γ is the bandwidth of the arm cavities, as defined in KLMTV) and if we consider high frequencies ($\omega \gtrsim \{\gamma, \Omega\}$). Figure 6.14 shows an example of this [with $W_{\rm circ} = 820\,{\rm kW}$, $\gamma = \delta = 2\pi \times 100\,{\rm Hz}$, $\Omega = 2\pi \times 173\,{\rm Hz}$]. The noise curves of the two interferometers are shown in Fig. 6.15.

[9]In fact, $\mathcal{K}_*$ can be obtained from the speed meter κ^* by putting $\Omega \to 0$ and $\delta \to \gamma$.

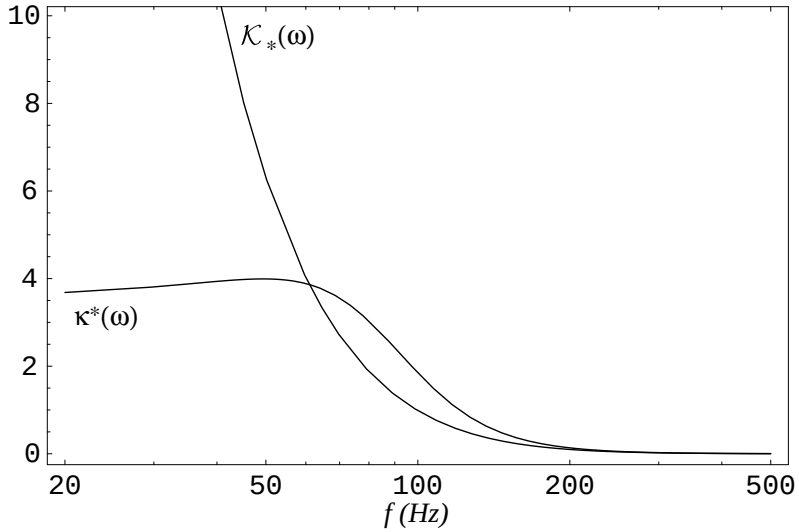

Figure 6.14: Comparison of the squeezed-variational speed meter's κ^* with the equivalent coupling constant $\mathcal{K}_*$ (as defined by KLMTV) for the squeezed-variational position meter. Parameters are $W_{\rm circ} = 820\,{\rm kW}$, $\gamma = \delta = 2\pi \times 100\,{\rm Hz}$, $\Omega = 2\pi \times 173\,{\rm Hz}$.

As expected, the two noise curves in Fig. 6.15 agree at very high frequencies. At intermediate frequencies, the speed meter's κ^* is larger than the position meter's $\mathcal{K}_*$, and thus the speed meter has better sensitivity than the position meter. As the frequency decreases, the speed meter reaches its loss limit first and stays at that limit for a wide range of frequencies. The position meter, however, only touches its loss limit and then increases rapidly.

6.6 Conclusions

We have described and analyzed a speed-meter interferometer that has the same performance as the two-cavity design analyzed in Paper I, but it does so without the substantial amount of power flowing through the system or the exorbitantly high input laser power required by the two-cavity speed meter. It was also shown that the injection of squeezed vacuum with $e^{-2R} = 0.1$ into the dark port of the interferometer will reduce the needed circulating power by an order of magnitude, bringing it into a range that is comparable to the expected circulating power of LIGO-II, if one wishes to beat the SQL by a factor of $\sqrt{10}$ in amplitude. Additional improvements to the sensitivity, particularly at high frequencies, can be achieved through the use of frequency-dependent homodyne detection.

In addition, it was shown that this type of speed-meter interferometer is not nearly as susceptible to losses as those presented in KLMTV. Its robust performance is due, in part, to the functional form the coupling factor κ, which is roughly constant at low frequencies. This helps to maintain the speed meters' wideband performance, even in the presence of losses. Losses for the various

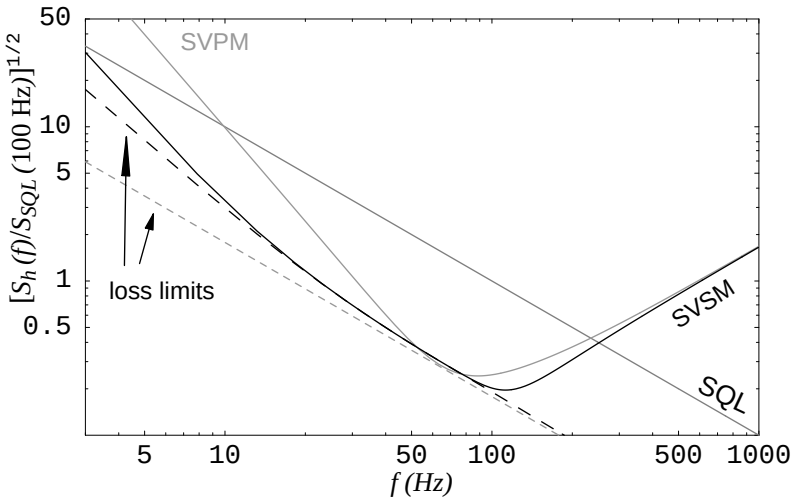

Figure 6.15: Comparison of noise curves for a squeezed-variational position meter (SVPM; analyzed in KLMTV) and for a squeezed-variational speed meter (SVSM; analyzed in this Chapter). Parameters used are those in Tables 6.1 and 6.3 with $T_{\rm i} = 0.005$ and $e^{-2R} = 0.1$. Also shown are the loss limits described in Sec. 6.5.3.

speed meters we discuss here are generally quite low. The dominant sources of loss-induced noise at low frequencies ($f \lesssim f_{\rm opt}$) are the radiation-pressure noise from losses in the arm, extraction, and sloshing cavities. Because this type of noise is dependent on the circulating power, it can be reduced by reducing the power by means of squeezed input.

6.7 Appendix. FP cavities as optical filters

As proposed by KLMTV [Sec. V B and Appendix C], Fabry-Perot cavities can be used as optical filters to achieve frequency-dependent homodyne detection. Here we shall briefly summarize and generalize their results.

Suppose we have one FP cavity of length $L_{\rm FP}$ and resonant frequency $\omega_0 - \xi_{\rm FP}\delta_{\rm FP}$. Also suppose this cavity has an input mirror with finite transmissivity $T_{\rm FP}$ and a perfect end mirror. When sideband fields at frequency $\omega_0 \pm \omega$ emerge from the cavity, they have a phase shift

$$\alpha_\pm \equiv 2\arctan(\xi_{\rm FP} \pm \omega/\delta_{\rm FP})\,, \tag{6.70}$$

where

$$\delta_{\rm FP} = \frac{cT_{\rm FP}}{4L_{\rm FP}} \tag{6.71}$$

is the half bandwidth of the cavity. [Note that Eq. (6.70) is KLMTV Eqs. (88) and (C2), but a factor of 2 was missing from their equations. Fortunately, this appears to be a typographical error only in that particular equation; the factor of 2 is included in their subsequent calculations.] As a result of this phase shift, the input ($\tilde{b}_{1,2}$)–output ($b_{1,2}$) relation for sideband quadratures at frequency ω will be [KLMTV Eqs. (78)]

$$\begin{pmatrix} \tilde{b}_1 \\ \tilde{b}_2 \end{pmatrix} = e^{i\,\alpha_{\rm m}}\,\mathbf{R}_{\alpha_{\rm p}} \begin{pmatrix} b_1 \\ b_2 \end{pmatrix}\,, \tag{6.72}$$

where

$$\alpha_{\rm m} \equiv \frac{1}{2}(\alpha_+ - \alpha_-)\,, \quad \alpha_{\rm p} \equiv \frac{1}{2}(\alpha_+ + \alpha_-)\,, \tag{6.73}$$

and

$$\mathbf{R}_\phi \equiv \begin{pmatrix} \cos\phi & -\sin\phi \\ \sin\phi & \cos\phi \end{pmatrix}\,. \tag{6.74}$$

If a frequency-independent homodyne detection at phase shift θ follows the optical filter, the measured quantity will be [KLMTV Eqs. (81) and (82)]

$$\tilde{b}_\theta = e^{i\alpha_{\rm m}} b_\zeta\,, \tag{6.75}$$

where

$$\zeta(\omega) = \theta - \alpha_{\rm p} \equiv \theta - \frac{1}{2}(\alpha_+ + \alpha_-)\,. \tag{6.76}$$

If more than one filter is applied in sequence (I, II, ...,) and followed by homodyne detection at

angle θ, the measured quadrature will be [Eq. (83)]

$$\zeta(\omega) = \theta - \frac{1}{2}(\alpha_{\mathrm{I}+} + \alpha_{\mathrm{I}-} + \alpha_{\mathrm{II}+} + \alpha_{\mathrm{II}-} + \ldots)\,. \tag{6.77}$$

[Note that this $\zeta(\omega)$ (KLMTV's notation) is the same homodyne angle $\Phi(\omega)$ that we want to produce.] By adjusting the parameters ξ_J and δ_J, one might be able to achieve the FD homodyne phases needed. KLMTV worked out a particular case for their design [their Sec. V B, V C, and Appendix C].

Here we shall seek a more complete solution that works in a large class of situations. With the help of Eq. (6.70), Eq. (6.77) can be written in an equivalent form

$$\frac{1 + i\tan\zeta}{1 - i\tan\zeta} = e^{2i\theta} \prod_{J=\mathrm{I,II},\ldots,s=\pm} \frac{1 - i\tan(\alpha_{Js}/2)}{1 + i\tan(\alpha_{Js}/2)} = e^{2i\theta} \prod_{J=\mathrm{I,II},\ldots,s=\pm} \frac{\omega - s(-\xi_J\delta_J - i\delta_J)}{\omega - s(-\xi_J\delta_J + i\delta_J)}\,. \tag{6.78}$$

Suppose the required $\tan\zeta(\omega)$ is a rational function in ω^2,

$$\tan\zeta(\omega) = \frac{\sum_{k=0}^{n} B_k\omega^{2k}}{\sum_{k=0}^{n} A_k\omega^{2k}}\,, \tag{6.79}$$

where A_k and B_k are real constants with $A_n^2 + B_n^2 > 0$. Then Eq. (6.78) requires that, for all ω,

$$\sum_{k=0}^{n}(A_k + iB_k)\omega^{2k} = D\,e^{i\theta} \prod_{J=\mathrm{I,II},\ldots,s=\pm} \Big[\omega - s(-\xi_J\delta_J - i\delta_J)\Big]\,, \tag{6.80}$$

where D can be any real constant. Equation (6.80) can be solved as follows. First, match the roots of the polynomials of ω on the two sides of the equation; denote these roots by $\pm\omega_{\mathrm{J}}$ with $J = 1, 2, \ldots, n$. Then we can deduce that n filters are needed, and their complex resonant frequencies must be offset from ω_0 by

$$\omega_J = -\delta_J\xi_J - i\delta_J\,, \quad J = \mathrm{I, II}, \ldots\,, \tag{6.81}$$

where $\pm\omega_{\mathrm{I,II},\ldots}$ [with $\Im(\omega_J) > 0$] are the $2n$ roots of

$$\sum_{k=0}^{n}(A_k + iB_k)\,\omega^{2k}\,. \tag{6.82}$$

After this, the polynomials on the two sides of Eq. (6.80) can only differ by a complex coefficient whose argument determines θ. In fact, by comparing the coefficients of ω^{2n} on both sides, we have

$$\theta = \arg(A_{2n} + iB_{2n})\,. \tag{6.83}$$

6.8 Appendix. Semi-analytical treatment of the loss terms

In this appendix, we present a semi-analytic treatment of each source of noise included in Sec. 6.5.1. We will use a notation similar to Eq. (6.3.1), but in matrix form:

$$\begin{pmatrix} \tilde{q}_1 \\ \tilde{q}_2 \end{pmatrix} = \begin{pmatrix} \tilde{q}_1 \\ \tilde{q}_2 \end{pmatrix}_{\text{lossless}} + \mathbf{N}_{\text{loss source}} \,, \tag{6.84}$$

where $\mathbf{N}_{\text{loss source}}$ is a vectorial representation of whichever source of loss we are considering at the moment. Each of these terms is associated with a vacuum field of the form $\sqrt{\mathcal{E}(\omega)}\tilde{n}(\omega)$ [cf. Eq. (6.56)], which enters the interferometer and increases the level of noise present. For generality, we let $\mathcal{E}(\omega)$ be frequency dependent. The (constant) characteristic fractional losses for each type of loss will be denoted by ε with an appropriate subscript. Each loss term appearing in Table 6.2 is presented in a subsection below.

6.8.1 Arms, Extraction mirror, and Sloshing cavity (AES)

The losses in the arms allow an unsqueezed vacuum field $\sqrt{\varepsilon_{\text{arm}}}\tilde{n}_{\text{arm}}$ to enter the optical train. By idealizing this field as arising entirely at the arm's end mirror, propagating the field through the interferometer to the output port, we obtain the following contribution to the output [cf. Eq. (6.56)]. The associated noise can be put into the following form

$$\mathbf{N}_{\text{arm}} = -\sqrt{\frac{\varepsilon_{\text{arm}}}{T_{\text{o}}}}\left[e^{i\psi}\frac{\omega\delta}{|\mathcal{L}(\omega)|}\begin{pmatrix} 1 & 0 \\ 0 & 1 \end{pmatrix} + e^{2i\psi}\begin{pmatrix} 0 & 0 \\ \kappa^*/2 & 0 \end{pmatrix}\right]\begin{pmatrix} \tilde{n}_{\text{arm1}} \\ \tilde{n}_{\text{arm2}} \end{pmatrix}, \tag{6.85}$$

where the vacuum operators from the two arms are combined as

$$\tilde{n}_{\text{arm}}j = \frac{\tilde{n}_{ej} - \tilde{n}_{nj}}{\sqrt{2}} \,. \tag{6.86}$$

The first term (independent of κ^*) is the shot-noise contribution, while the second term (proportional to κ^*) is the radiation-pressure noise. It turns out that several of the other loss sources $\mathcal{N}$ have a similar mathematical form.

We consider, specifically, the loss from the extraction mirror, which effectively allows $\sqrt{\varepsilon_{\text{ext}}}\,\tilde{n}_{\text{ext}}$ into the optical train. By propagating this field through the interferometer to the output port, we obtain the following contribution to the noise:

$$\mathbf{N}_{\text{ext}} = \sqrt{\frac{\varepsilon_{\text{ext}}}{T_{\text{o}}}}\left[e^{i\psi}\frac{\omega\delta}{|\mathcal{L}(\omega)|}\begin{pmatrix} 1 & 0 \\ 0 & 1 \end{pmatrix} + e^{2i\psi}\begin{pmatrix} 0 & 0 \\ \kappa^*/2 & 0 \end{pmatrix}\right]\begin{pmatrix} \tilde{n}_{\text{ext1}} \\ \tilde{n}_{\text{ext2}} \end{pmatrix}. \tag{6.87}$$

The loss from the sloshing cavity is a bit different: the imperfect end mirror of the sloshing cavity

produces a vacuum noise field $\sqrt{\varepsilon_{\rm slosh}}\,\tilde{n}_{\rm slosh}$ which exits the cavity with the form

$$\sqrt{\frac{4\varepsilon_{\rm slosh}/T_{\rm s}}{1+\omega^2/(\delta_{\rm s}/2)^2}}e^{i\beta_{\rm s}}\tilde{n}_{\rm slosh\,1,2}\approx\sqrt{\varepsilon_{\rm slosh}}\frac{i\Omega}{\omega}\tilde{n}_{\rm slosh\,1,2}\,, \tag{6.88}$$

where $\beta_{\rm s}\equiv\arctan(2\omega/\delta_s)\approx\pi/2$ for most of the frequency band of interest. The associated noise is

$$\mathbf{N}_{\rm slosh}=-\sqrt{\frac{\varepsilon_{\rm slosh}}{T_{\rm o}}}\frac{i\Omega}{\omega}\left[e^{i\psi}\frac{\omega\delta}{|\mathcal{L}(\omega)|}\begin{pmatrix}1&0\\0&1\end{pmatrix}+e^{2i\psi}\begin{pmatrix}0&0\\\kappa^*/2&0\end{pmatrix}\right]\begin{pmatrix}\tilde{n}_{\rm slosh1}\\\tilde{n}_{\rm slosh2}\end{pmatrix}. \tag{6.89}$$

Since the vacuum fields $\tilde{n}_{\rm arm}$, $\tilde{n}_{\rm ext}$, and $\tilde{n}_{\rm slosh}$ are independent and uncorrelated, we can effectively combine these four noises into a single expression

$$\mathbf{N}_{\rm AES}=\sqrt{\frac{\varepsilon_{\rm AES}}{T_{\rm o}}}\left[e^{i\psi}\frac{\omega\delta}{|\mathcal{L}(\omega)|}\begin{pmatrix}1&0\\0&1\end{pmatrix}+e^{2i\psi}\begin{pmatrix}0&0\\\kappa^*/2&0\end{pmatrix}\right]\begin{pmatrix}\tilde{n}_{\rm AES1}\\\tilde{n}_{\rm AES2}\end{pmatrix}, \tag{6.90}$$

with

$$\varepsilon_{\rm AES}\sim\mathcal{E}_{\rm AES}(\omega)\equiv\varepsilon_{\rm arm}+\varepsilon_{\rm ext}+\varepsilon_{\rm slosh}\Omega^2/\omega^2\,. \tag{6.91}$$

We expect that $\varepsilon_{\rm arm}\sim\varepsilon_{\rm slosh}\sim\varepsilon_{\rm ext}\sim2\times10^{-5}$, as discussed in the paragraph following Eq. (6.56) and as shown in Table 6.3.

6.8.2 Port-closing mirror

The imperfection of the closing mirror has two effects: (i) it introduces directly a fluctuation $-\sqrt{\varepsilon_{\rm close}R_{\rm o}}\,\tilde{n}_{\rm close}$ into the output, giving a shot noise

$$\mathbf{N}^{\rm shot\,direct}_{\rm close}=-\sqrt{\varepsilon_{\rm close}R_{\rm o}}\begin{pmatrix}\tilde{n}_{\rm close1}\\\tilde{n}_{\rm close2}\end{pmatrix}; \tag{6.92}$$

and (ii) it introduces a fluctuation $\sqrt{\varepsilon_{\rm close}T_{\rm o}}\,\tilde{n}_{\rm close}$ into the light that passes from the arms into the sloshing cavity, giving (after propagation through the sloshing cavity and interferometer and into the output):

$$\mathbf{N}^{\rm indirect}_{\rm close}=-\sqrt{\varepsilon_{\rm close}}\left[e^{i\psi}\frac{\omega\delta}{|\mathcal{L}(\omega)|}\begin{pmatrix}1&0\\0&1\end{pmatrix}+e^{2i\psi}\begin{pmatrix}0&0\\\kappa^*/2&0\end{pmatrix}\right]\begin{pmatrix}\tilde{n}_{\rm close1}\\\tilde{n}_{\rm close2}\end{pmatrix}. \tag{6.93}$$

Combining these two expressions gives, to leading order (in the various transmissivities and the small parameters $\omega L/c$ and $\varepsilon_{\rm close}$),

$$\mathbf{N}_{\rm close} = \sqrt{\varepsilon_{\rm close}} \left[i e^{i\psi} \frac{\Omega^2 - \omega^2}{|\mathcal{L}(\omega)|} \begin{pmatrix} 1 & 0 \\ 0 & 1 \end{pmatrix} - e^{2i\psi} \begin{pmatrix} 0 & 0 \\ \kappa^*/2 & 0 \end{pmatrix} \right] \begin{pmatrix} \tilde{n}_{\rm close1} \\ \tilde{n}_{\rm close2} \end{pmatrix} . \tag{6.94}$$

Since $\varepsilon_{\rm close}$ is simply the loss from the port-closing mirror itself, we can assume that $\varepsilon_{\rm close} \lesssim 2\times10^{-5}$. Then, this and the above expression (6.94) show that the output noise from the closing mirror is $T_{\rm o}$ times smaller than the AES loss [Eq. (6.91)].

6.8.3 The RSE cavity

The losses in the region between the internal mirrors and the RSE mirror, i.e., the RSE cavity, are more complicated than the previous cases. As before, we suppose that, during each propagation from one end to the other of the RSE cavity, a fraction $\varepsilon_{\rm RSE}$ of the light power is dissipated and replaced by a corresponding vacuum field, $\sqrt{\varepsilon_{\rm RSE}}\,\tilde{n}_{\rm in}$ or $\sqrt{\varepsilon_{\rm RSE}}\,\tilde{n}_{\rm out}$ (depending whether the light is propagating in towards the arms or out towards the extraction mirror and sloshing cavity). These two fields $\tilde{n}_{\rm in}$ and $\tilde{n}_{\rm out}$ are independent vacuum fields. At the leading order in $\varepsilon_{\rm RSE}$, we have a modified version of the "input–output" relation for the RSE cavity:

$$\begin{aligned} \begin{pmatrix} B \\ D \end{pmatrix} &= \begin{pmatrix} 1 - \frac{1+R_{\rm i}}{2T_{\rm i}}\varepsilon_{\rm RSE} & \frac{\sqrt{R_{\rm i}}}{\rm T_i}\varepsilon_{\rm RSE} \\ \frac{\sqrt{R_{\rm i}}}{\rm T_i}\varepsilon_{\rm RSE} & 1 - \frac{1+R_{\rm i}}{2T_{\rm i}}\varepsilon_{\rm RSE} \end{pmatrix} \begin{pmatrix} A \\ C \end{pmatrix} \\ &\quad + \sqrt{\frac{\varepsilon_{\rm RSE}}{T_{\rm i}}} \begin{pmatrix} 1 & -\sqrt{R_{\rm i}} \\ -\sqrt{R_{\rm i}} & 1 \end{pmatrix} \begin{pmatrix} \tilde{n}_{\rm in} \\ \tilde{n}_{\rm out} \end{pmatrix} , \end{aligned} \tag{6.95}$$

where A, B, C, D are the field amplitudes shown in Fig. 6.3. Note that, for simplicity, we are looking at only one arm; we could equally well use the other (substituting $B \to F$ and $C \to G$) or the proper combination of both. Also, notice that if $\varepsilon_{\rm RSE} = 0$, then we find $B = A$ and $D = C$, which illustrates the fact that the internal and RSE mirrors have no effect on the sidebands (described in Sec. 6.1 where we introduced the RSE mirror).

From Eq. (6.95), we find that the loss inside the RSE cavity has two effects. First, it makes the cancellation of the effect of the internal and the RSE mirrors imperfect. (Recall that an RSE mirror with the same transmissivity as the internal mirrors effectively cancels the effect of the internal mirrors on the sidebands; this was discussed in Sec. 6.1.) This imperfect cancellation will not be important in our situation. Indeed, there is no corresponding term appearing in the input–output relation given in Eq. (6.5.1).

Secondly, the loss inside the RSE cavity adds two vacuum fields to light that travels through the RSE cavity in opposite directions [i.e., from A to B (IN) and from C to D (OUT)]. We denote them

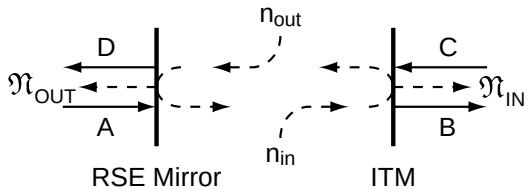

Figure 6.16: Schematic diagram of a simplified version of the RSE cavity. The quantities $\tilde{n}_{\rm in}$ and $\tilde{n}_{\rm out}$ enter inside the RSE cavity, whereas $\mathfrak{N}_{\rm in}$ and $\mathfrak{N}_{\rm out}$ are external to the cavity and exist in different locations.

by

$$\tilde{\mathfrak{N}}_{\rm IN} \equiv \sqrt{\frac{\varepsilon_{\rm RSE}}{T_{\rm i}}}(\tilde{n}_{\rm in} - \sqrt{R_{\rm i}}\tilde{n}_{\rm out})\,, \tag{6.96}$$

$$\tilde{\mathfrak{N}}_{\rm OUT} \equiv \sqrt{\frac{\varepsilon_{\rm RSE}}{T_{\rm i}}}(-\sqrt{R_{\rm i}}\tilde{n}_{\rm in} + \tilde{n}_{\rm out})\,. \tag{6.97}$$

Note that $\tilde{n}_{\rm in}$ and $\tilde{n}_{\rm out}$ arise *inside* the RSE cavity as a result of the loss that occurred there and that $\tilde{\mathfrak{N}}_{\rm IN}$ and $\tilde{\mathfrak{N}}_{\rm OUT}$ are the vacuum fluctuations *emerging* from the RSE cavity. As a result, $\tilde{\mathfrak{N}}_{\rm IN}$ and $\tilde{\mathfrak{N}}_{\rm OUT}$ *exist in different locations:* $\tilde{\mathfrak{N}}_{\rm IN}$ denotes the vacuum field inside the arm cavity with B, and $\tilde{\mathfrak{N}}_{\rm OUT}$ denotes the vacuum field at the RSE mirror, heading towards the extraction mirror and sloshing cavity with D. This is depicted in Fig. 6.16.

The fields $\tilde{\mathfrak{N}}_{\rm IN}$ and $\tilde{\mathfrak{N}}_{\rm OUT}$ both have a power spectral density a factor $\sim 1/T_{\rm i}$ larger than the one-time loss coefficient. This can be explained by the fact that the sideband light bounces back and forth inside the RSE cavity roughly $\sim 1/T_{\rm i}$ times before exiting. As a result, the (power) loss coefficient is amplified by the same factor. However, since these fields are quite correlated (both contain similar amounts of $\tilde{n}_{\rm in}$ and $\tilde{n}_{\rm out}$), we need to analyze them carefully.

For the shot noise, we need to find the amplitude of the vacuum fluctuations that the loss introduces into the output. To understand the effect of this type of loss, we ask how much vacuum fluctuation is added to the field D by $\tilde{\mathfrak{N}}_{\rm IN}$ and $\tilde{\mathfrak{N}}_{\rm OUT}$. The answer is obtained by propagating $\tilde{\mathfrak{N}}_{\rm IN}$ one round trip inside the interferometer's arm(s) and then combining it with $\tilde{\mathfrak{N}}_{\rm OUT}$. This gives

$$\begin{aligned} D &\rightarrow D + \left[\tilde{\mathfrak{N}}_{\rm OUT} + e^{2i\omega L/c}\tilde{\mathfrak{N}}_{\rm IN}\right] \\ &\approx D + \sqrt{\frac{\varepsilon_{\rm RSE}T_{\rm i}}{4}\left(1+\frac{\omega^2}{\delta_{\rm i}^2}\right)}\left(e^{i\beta_{\rm i}}\tilde{n}_{\rm in} + e^{-i\beta_{\rm i}}\tilde{n}_{\rm out}\right)\,, \end{aligned} \tag{6.98}$$

where $\delta_{\rm i} \equiv T_{\rm i}c/4L$ and $\beta_{\rm i} \equiv \arctan(\omega/\delta_{\rm i})$. Propagating this to the output, we get the shot noise contribution to be

$$\mathbf{N}^{\rm shot}_{\rm RSE} = \sqrt{\frac{\varepsilon_{\rm RSE}T_{\rm i}}{4T_{\rm o}}\left(1+\frac{\omega^2}{\delta_{\rm i}^2}\right)}e^{i\psi}\frac{\omega\delta}{|\mathcal{L}(\omega)|}\left[e^{+i\beta_{\rm i}}\begin{pmatrix}\tilde{n}_{\rm in1}\\ \tilde{n}_{\rm in2}\end{pmatrix} + e^{-i\beta_{\rm i}}\begin{pmatrix}\tilde{n}_{\rm out1}\\ \tilde{n}_{\rm out2}\end{pmatrix}\right]\,. \tag{6.99}$$

This noise is not of the magnitude that Eqs. (6.8.3) would appear to indicate. Instead of having a coefficient of $\sim \sqrt{\varepsilon_{\rm RSE}/T_{\rm i}}$, it has a much smaller value when $\omega \lesssim \delta_{\rm i}$. The reason is that the two vacuum fluctuations traveling in opposite directions are anticorrelated and largely cancel each other, since they are summed in the outgoing field D. This cancellation becomes less perfect as ω grows and becomes much larger than $\delta_{\rm i}$. This effect is shown in Fig. 6.11.

For the RSE contribution to the radiation-pressure noise, we are interested in how much the two noise fields $\tilde{\mathfrak{N}}_{\rm IN}$ and $\tilde{\mathfrak{N}}_{\rm OUT}$ contribute to the carrier amplitude fluctuation *at the position of the test masses*. Therefore, we ask what the sum of $\tilde{\mathfrak{N}}_{\rm IN}$ and $\tilde{\mathfrak{N}}_{\rm OUT}$ is when they combine at the end mirrors of the arm cavities. Since $\tilde{\mathfrak{N}}_{\rm OUT}$ is superposed on D, $\tilde{\mathfrak{N}}_{\rm OUT}$ must be propagated through the sloshing cavity and back to the arm cavity, where it is combined with $\tilde{\mathfrak{N}}_{\rm IN}$. There is a phase factor of $e^{i\omega L/c}$ due to the propagation from the internal mirror to the end mirror (in addition to the phases acquired on the way to and inside the sloshing cavity; these are explained below), producing

$$\begin{aligned} B &\rightarrow B + e^{i\omega L/c}\left[\tilde{\mathfrak{N}}_{\rm IN} - \tilde{\mathfrak{N}}_{\rm OUT}(1-T_{\rm o})\frac{e^{2i\beta_{\rm s}}}{1-T_{\rm o}e^{2i\beta_{\rm s}}}\right] \\ &\approx B + 2T_{\rm o}\sqrt{\frac{\varepsilon_{\rm RSE}}{\rm T_i}}\left[\frac{\omega(\delta_{\rm i}+\delta)+i\Omega^2}{\omega\delta}\tilde{n}_{\rm in} + \frac{\omega(\delta_{\rm i}-\delta)-i\Omega^2}{\omega\delta}\tilde{n}_{\rm out}\right]. \end{aligned} \tag{6.100}$$

where $\beta_{\rm s} = \arctan(2\omega/\delta_{\rm s})$ is the phase associated with the sloshing cavity. Propagating the new B to the output produces a radiation-pressure contribution

$$\begin{aligned} \mathbf{N}_{\rm RSE}^{\rm rad\,pres} &= \sqrt{\frac{\varepsilon_{\rm RSE}T_{\rm o}}{\rm T_i}}e^{2i\psi}\begin{pmatrix} 0 & 0 \\ -\kappa^* & 0 \end{pmatrix} \\ &\quad\times\left[\frac{\omega(\delta_{\rm i}+\delta)+i\Omega^2}{\omega\delta}\begin{pmatrix}\tilde{n}_{\rm in1}\\ \tilde{n}_{\rm in2}\end{pmatrix} + \frac{\omega(\delta_{\rm i}-\delta)-i\Omega^2}{\omega\delta}\begin{pmatrix}\tilde{n}_{\rm out1}\\ \tilde{n}_{\rm out2}\end{pmatrix}\right]. \end{aligned} \tag{6.101}$$

As before, this noise does not have a magnitude $\sim \sqrt{\varepsilon_{\rm RSE}/T_{\rm i}}$; it is much smaller. The reason is that when $\tilde{\mathfrak{N}}_{\rm OUT}$ travels to the sloshing cavity and back to the arms, it gains two phase shifts. First is a constant phase shift of π, due to the distance it traveled (twice) between the RSE and sloshing mirror. The other is from the sloshing cavity, where for frequencies much larger than the bandwidth $\delta_{\rm s}$ of the sloshing cavity, this phase shift is roughly π. Adding these two phase shifts, $\tilde{\mathfrak{N}}_{\rm OUT}$ will appear roughly unchanged when it combines with $\tilde{\mathfrak{N}}_{\rm IN}$ in the arm cavity. Since these two vacuum fields are anticorrelated, there is again an effective cancellation between the two noises at frequencies above $\delta_{\rm s}$. This cancellation becomes less complete at low frequencies; see Fig. 6.11.

We assume the fractional loss $\varepsilon_{\rm RSE} \sim 2\times10^{-5}$, since it arises primarily from losses in the RSE cavity's optical elements (mirrors and beam splitter). (See Appendix 6.9 for a discussion of the noise due to mode mismatching, which we do not consider here.)

6.8.4 Detection and filter cavities

First, we consider the losses involved in the detection of the signal (without filter cavities). Two important sources of photon loss are mode mismatching associated with the local oscillator used for frequency-independent homodyne detection ($\varepsilon_{\rm lo}$) and the inefficiency of the photodiode ($\varepsilon_{\rm pd}$). In a squeezed-input speed meter, there will also be a circulator (with fractional loss $\varepsilon_{\rm circ}$) through which the squeezed vacuum is fed into the system and through which the output light will have to pass. These losses have no frequency dependence, so they are modeled by an equation of the form of [Eq. (6.56)] with

$$\mathcal{E}_{\rm OPC}(\omega) = \varepsilon_{\rm OPC} = \varepsilon_{\rm lo} + \varepsilon_{\rm pd} + \varepsilon_{\rm circ} \tag{6.102}$$

[cf. KLMTV Eq. (104)]. The contribution to the noise is then

$$\mathbf{N}_{\rm OPC} = \sqrt{\varepsilon_{\rm OPC}} \begin{pmatrix} \tilde{n}_{\rm OPC1} \\ \tilde{n}_{\rm OPC2} \end{pmatrix} , \tag{6.103}$$

where the $\tilde{n}_{{\rm OPC}j}$ are linear combinations of the individual (independent) vacuum fields entering at each location (so the spectral densities of these fields are unity and there are no cross-correlations) and propagated to the output port. KLMTV assumed that each of these losses is about 0.001, giving $\varepsilon_{\rm OPC} \sim 0.003$.

We next turn our attention to optical filters on the output (as in the case of frequency-dependent homodyne detection for a squeezed-variational speed meter, discussed in Sec. 6.4.2). Such cavities will have losses that may contribute significantly to the noises of QND interferometers, as has been seen in KLMTV. In their Sec. VI, KLMTV carried out a detailed analyses of such losses; our investigation is essentially the same as theirs.

The loss in the optical filters can come from scattering or absorption in the cavity mirrors, which can be modeled by attributing a finite transmissivity $T_{\rm e}$ to the end mirrors, as we did for the arm cavities. The effect of lossy filters is again analogous to [Eq. (6.56)]. This time the loss coefficient $\mathcal{E}_{\rm F}(\omega)$ does have some frequency dependence:

$$\mathcal{E}_{\rm F} = 2\varepsilon_{\rm mm} + \sum_{J={\rm I,II}} \bar{\mathcal{E}}_J = 2\varepsilon_{\rm mm} + \frac{1}{2} \sum_{J={\rm I,II}} (\mathcal{E}_{J+} + \mathcal{E}_{J-}) , \tag{6.104}$$

where $\varepsilon_{\rm mm} \sim 0.001$ is the mode-mismatching into each filter cavity and where

$$\mathcal{E}_{J\pm} = \frac{4T_e}{T_J\,[1 + (\pm\omega/\delta_J - \xi_J)^2]} \tag{6.105}$$

are the loss coefficents of the two different filter cavities ($J = {\rm I, II}$) [cf. Eqs. (103) and (106) of

KLMTV]. The noise contribution is

$$\mathbf{N}_{\mathrm{F}} = \sqrt{\mathcal{E}_{\mathrm{F}}} \begin{pmatrix} \tilde{n}_{\mathrm{F}1} \\ \tilde{n}_{\mathrm{F}2} \end{pmatrix} . \tag{6.106}$$

The weak frequency-dependence of $\mathcal{E}_{\mathrm{F}}$ will be neglected (as KLMTV did), giving

$$\varepsilon_{\mathrm{F}} \simeq \mathcal{E}_{\mathrm{F}} \sim 0.005 \tag{6.107}$$

[cf. Eqs. (107) and (104) of KLMTV]. The value of ε_{F} may vary slightly for the different optimizations we have used, but it remains less than 0.006.

6.9 Appendix. Effects due to mode-mismatching: a simple analysis

In the practical implementation of GW interferometers, the mismatching of spatial modes between different optical cavities will degrade the sensitivity because signal power will be lost into higher-order modes and, correspondingly, vacuum noises from those modes will be introduced to the signal. In a way, this is similar to other sources of optical loss discussed in the previous appendix. However, the higher-order modes do not simply get dissipated — they too will propagate inside the interferometer (although with a different propagation law). As a consequence, the exchange of energy between fundamental and higher modes due to mode-mismatching is *coherent*, and the formalism we have been using for the loss does not apply. In this section, we shall extend our formalism to include one higher-order mode and give an extremely simplified model of the mode-mismatching effects[10].

In a conventional interferometer (LIGO-I), the mode-mismatching comes predominantly from the mismatch of the mirror shapes between the two arms, which makes the wavefronts from the two arms different at the beam splitter. In particular, the cancellation of the carrier light at the dark port is no longer perfect, and additional (bright-port) noises are introduced into the dark-port output. For our speed meter, a third cavity—the sloshing cavity—has to be matched to the two arm cavities, further complicating the problem.

In order to simplify the situation, we approximate all the waves propagating in the corner station (the region near the beam splitter, where the distances are short enough that) as following the same phase-propagation law as a plane wave. The only possible source of mismatch is assumed to come from the difference of wavefront shapes (to first order in the fractional difference of the radii of curvature) and waist sizes for the light beams emerging from the two arm cavities and the sloshing cavity. Suppose, in the region of the corner station, we have a fiducial fundamental Gaussian mode $\Psi^{(0)}$ (which is being pumped by the carrier) with waist size w_0 and wavefront curvature $\alpha_0 \equiv 1/R_0$ that is roughly the same as those of the three cavities[11]:

$$\Psi^{(0)}(x,y) \propto \frac{1}{w_0} \exp\left(-\frac{\rho^2}{w_0^2} + ik\frac{\alpha_0\rho^2}{2}\right)\ ,\ \rho = \sqrt{x^2+y^2}\,. \tag{6.108}$$

At leading order in the mismatches, the fundamental modes of the three cavities (in the region of the corner station), which have waist sizes $w_{\rm J}$ and curvatures $\alpha_{\rm J} \equiv 1/R_{\rm J}$ [J =n, e, or slosh (for the

[10] This way of modeling the mode-mismatching effects was suggested to us by Stan Whitcomb.

[11] We have chosen to use the curvature instead of the radius of curvature because in this region the wavefronts are very flat.

north arm, east arm, and sloshing cavity, respectively)], can be written in the form:

$$\Psi^{\rm J}_{\rm fnd}(x,y) \;\propto\; \frac{1}{w_0}\,\exp\left(ikw_0^2\,\frac{\alpha_{\rm J}-\alpha_0}{4}\right)\exp\left(-\frac{\rho^2}{w_0^2}+ik\frac{\alpha_0\rho^2}{2}\right) \times\left\{1+\left(\frac{w_{\rm J}-w_0}{4w_0}+ikw_0^2\frac{\alpha_{\rm J}-\alpha_0}{16}\right)\left[H_2\left(\frac{\sqrt{2}x}{w_0}\right)+H_2\left(\frac{\sqrt{2}y}{w_0}\right)\right]\right\}, \quad (6.109)$$

where $H_2(u)$ is the second-order Hermite polynomial of u. This $\Psi^{\rm J}_{\rm fnd}(\pi,y)$ can be expressed as $\Psi^{(0)}$ plus a small admixture of a higher-order mode $\Psi^{(1)}$, which consists of equal amounts of TEM_{02} and TEM_{20} modes [and thus is orthogonal to $\Psi^{(0)}$]. This admixture changes the waist size from ω_0 to $\omega_{\rm J}$ and the curvature from α_0 to $\alpha_{\rm J}$. We can choose our fiducial fundamental mode $\Psi^{(0)}$ in such a way that the two arm cavities have an opposite mismatch with it, i.e., $\alpha_{\rm n}+\alpha_{\rm e}=2\alpha_0$, $w_{\rm n}+w_{\rm e}=2w_0$, and at leading order,

$$\begin{pmatrix}\Psi^{\rm n,\,e}_{\rm fnd}\\ \Psi^{\rm n,\,e}_{\rm exc}\end{pmatrix}=\begin{pmatrix}1 & \pm\mu_{\rm arm}\\ \mp\mu^*_{\rm arm} & 1\end{pmatrix}\begin{pmatrix}\Psi^{(0)}\\ \Psi^{(1)}\end{pmatrix}, \quad (6.110)$$

where "exc" denotes the excited mode and the admixing amplitude $\mu_{\rm arm}$ is, in general, complex. We also denote the fundamental and excited modes of the sloshing cavity as

$$\begin{pmatrix}\Psi^{\rm slosh}_{\rm fnd}\\ \Psi^{\rm slosh}_{\rm exc}\end{pmatrix}=\begin{pmatrix}1 & \mu_{\rm slosh}\\ -\mu^*_{\rm slosh} & 1\end{pmatrix}\begin{pmatrix}\Psi^{(0)}\\ \Psi^{(1)}\end{pmatrix}; \quad (6.111)$$

again, $\mu_{\rm slosh}$ can be complex. We shall also assume that the higher-order modes involved here are far from resonance inside the cavities and will be rejected by them, gaining a phase of π upon reflection from each cavity's input mirror. In the output, we assume the mode $\Psi^{(0)}$ is selected for detection. (The local oscillator associated with the homodyne detection is chosen to have the same spatial mode as $\Psi^{(0)}$, thereby "selecting" $\Psi^{(0)}$. Note that the potential mode-mismatch effect here is already taken into account in the fractional loss $\varepsilon_{\rm lo}$ of the local oscillator, as described in Sec. 6.8.4.)

Quite naturally, we have to introduce two sets of quadrature operators to describe the two modes. For example, for the field $P(\zeta)$ entering through the extraction mirror, we have

$$\tilde{\mathbf{p}}^{(0)}\equiv\begin{pmatrix}\tilde{p}^{(0)}_1\\ \tilde{p}^{(0)}_2\end{pmatrix}, \quad \tilde{\mathbf{p}}^{(1)}\equiv\begin{pmatrix}\tilde{p}^{(1)}_1\\ \tilde{p}^{(1)}_2\end{pmatrix}. \quad (6.112)$$

For each of the three cavities, we have to decompose the optical field into its own fundamental and excited modes, propagate them separately and then combine them. The input–output (a–b) relation of one of the cavities with mirrors held fixed can be written as

$$\begin{pmatrix}\tilde{\mathbf{b}}^{(\mathbf{0})}\\ \tilde{\mathbf{b}}^{(\mathbf{1})}\end{pmatrix}=\left[e^{i\Phi_{\rm fnd}}\mathbf{P}_{\rm fnd}+e^{i\Phi_{\rm exc}}\mathbf{P}_{\rm exc}\right]\begin{pmatrix}\tilde{\mathbf{a}}^{(\mathbf{0})}\\ \tilde{\mathbf{a}}^{(\mathbf{1})}\end{pmatrix}, \quad (6.113)$$

where

$$\mathbf{P}_{\rm fnd} = \begin{pmatrix} 1 \\ \mu \end{pmatrix} \begin{pmatrix} 1 & \mu^* \end{pmatrix}, \tag{6.114}$$

$$\mathbf{P}_{\rm exc} = \begin{pmatrix} -\mu^* \\ 1 \end{pmatrix} \begin{pmatrix} -\mu & 1 \end{pmatrix}, \tag{6.115}$$

are the projection operators, and $\Phi_{\rm fnd}$ and $\Phi_{\rm exc} = \pi$ are the phases gained by the fundamental mode and excited mode after being reflected back by the cavity.

The mode-mismatching can cause both shot and radiation pressure noises at the output, giving:

$$\tilde{\mathbf{q}}^{(\mathbf{0})} \to \tilde{\mathbf{q}}^{(\mathbf{0})} + \mathbf{N}_{\rm MM}^{\rm shot} + \mathbf{N}_{\rm MM}^{\rm rad\,pres}. \tag{6.116}$$

Assuming the mirrors are held fixed and applying the new input–output relations (6.113) of the non-perfect cavities, we get the following shot noise in the output (to leading order in $\mu_{\rm arm}$ and $\mu_{\rm slosh}$):

$$\begin{aligned} \mathbf{N}_{\rm MM}^{\rm shot} &= -e^{i\psi}\mu_{\rm arm}^* \sqrt{\frac{4}{T_{\rm o}}} \frac{\sqrt{T_{\rm p}}}{1+\sqrt{1-T_{\rm p}}} \frac{1-\sqrt{1-T_{\rm i}}}{\sqrt{T_{\rm i}}} \frac{\omega\delta}{|\mathcal{L}(\omega)|} \tilde{\mathbf{i}}^{(\mathbf{1})} \\ &\approx e^{-i\psi}\mu_{\rm arm}^* \sqrt{\frac{T_{\rm i}T_{\rm p}}{4T_{\rm o}}} \frac{\omega\delta}{|\mathcal{L}(\omega)|} \tilde{\mathbf{i}}^{(\mathbf{1})}; \end{aligned} \tag{6.117}$$

see Eq. (6.84). The quantity $\tilde{\mathbf{i}}^{(\mathbf{1})}$ refers to the excited mode of the noise coming in the bright port [$I(\zeta)$ in Fig. 6.3].

The main results embedded in Eq. (6.117) are

(i) the mode-mismatching with the sloshing cavity does not give any contribution at leading order in μ, and

(ii) the mode-mismatching shot noise comes from the higher-order mode entering from the *bright port*, strongly suppressed by the presence of the internal and power-recycling mirrors.

These two effects are both due to the coherent interaction between the fundamental ($\Psi^{(0)}$) and excited ($\Psi^{(1)}$) modes (of our idealized cavity), in which energy is not simply dissipated from $\Psi^{(0)}$ but exchanged coherently between the two modes as the light flows back and forth between the sloshing cavity and the arm cavities. Detecting an appropriate linear combination of the two modes can then be expected to reverse the effect of mode mismatching. In our case, the properties of the cavities are carefully chosen such that $\Psi^{(0)}$ itself is the desired detection mode (for the sloshing mismatch). Consequently, the mode mismatching with the sloshing cavity does not contribute at leading order [item (i) above]. Regarding item (ii), the mismatch of the two arm cavities does give

rise to an additional noise, but it can only come from the higher mode in the bright port, because at leading order in mismatches, (a) the propagation of $\Psi^{(0)}$ from the bright port to the dark port is suppressed and (b) there is no propagation of dark-port $\Psi^{(1)}$ into dark-port $\Psi^{(0)}$ since we have chosen $\Psi^{(0)}$ in such a way that the two arm cavities have exactly opposite mismatches with it.

The reason why this noise is suppressed by the factor $1/T_{\rm p}$ is simple: because $\Psi^{(1)}$ is not on resonance with the composite cavity formed by the power-recycling mirror and the arm cavities, its fluctuations inside the system (like its classical component) are naturally suppressed by a factor $1/\sqrt{T_{\rm p}}$ compared to the level outside the cavity. The reason for the factor of $1/T_{\rm i}$ is similar: the $\Psi^{(1)}$ mode does not resonate within the system formed by the arm cavities and the RSE mirror and will consequently be suppressed.

By computing at the fields at the end mirrors and from them the fluctating radiation pressure, we obtain the radiation-pressure noise due to mode-mismatching:

$$\mathbf{N}^{\rm rad\,pres}_{\rm MM} = -\frac{e^{2i\psi}}{2}\mu^*_{\rm arm}\sqrt{\frac{T_{\rm i}T_{\rm p}}{4T_{\rm o}}}\begin{pmatrix} 0 & 0 \\ -\kappa^* & 0 \end{pmatrix}\tilde{\mathbf{i}}^{(\mathbf{1})}\,. \tag{6.118}$$

This radiation-pressure noise is suppressed by a factor similar to the shot noise.

By comparing Eqs. (6.117) and (6.118) with, e.g., Eqs. (6.90), we see that mode mismatching produces noise with essentially the same form as optical-element losses from the arms, extraction mirror and sloshing cavity (AES), with (assuming the input laser is shot-noise limited in the higher modes)

$$\varepsilon_{\rm MM} = \frac{T_{\rm i}T_{\rm p}}{4}|\mu^*_{\rm arm}|^2\,. \tag{6.119}$$

The factor $T_{\rm i}T_{\rm P}/4$ happens to be the ratio between the input power (at the power-recycling mirror) and the circulating power, which will be $\sim 10^{-4}$. Suppose $\Re(\mu_{\rm arm}) \sim \Im(\mu_{\rm arm}) \sim 0.03$. The effect of mode-mismatching will then be much less significant (*in our simple model*) than the losses from the optical elements.

It should be evident that other imperfections in the cavity mirrors, which cause admixtures of other higher-order ("excited") modes, will lead to similar "dissipation factors," $\mathcal{E}_{\rm MM} \sim \frac{T_{\rm i}T_{\rm p}}{4}|\mu^*_{\rm arm}|^2$. For this reason, we expect mode mismatching to contribute negligibly to the noise, and we ignore it in the body of the Chapter.

6.10 Appendix. Transmissivity mismatch between the internal mirror and the RSE mirror

Recall from Sec. 6.1 that when the internal and RSE mirrors have the same transmissivity, their effects on the gravity-wave sideband cancel. If, however, the transmissivity of the internal mirror, $T_{\rm i}$, is not perfectly matched by that of the RSE mirror, $T_{\rm RSE}$, then this cancellation will no longer be perfect. As a result, the RSE cavity (i.e., the cavity between the internal and RSE mirrors) will have the same effect as an additional mirror (with a small reflectivity). Suppose the transmissivity of this effective mirror is $T_{\rm RSE} = (1 + \varepsilon_{\rm RSE})T_{\rm i}$. Then a simple calculation yields its (amplitude) reflectivity:

$$\mu = \frac{\sqrt{1-T_{\rm i}} - \sqrt{1-T_{\rm RSE}}}{1 - \sqrt{1-T_{\rm i}}\sqrt{1-T_{\rm RSE}}} \approx \frac{\varepsilon_{\rm RSE}}{2\sqrt{1-T_{\rm i}}} \approx \frac{\varepsilon_{\rm RSE}}{2}\,. \tag{6.120}$$

Adding this effective mirror with reflectivity μ to our interferometer yields a new set of input–output relations similar to Eq. (6.3.1), but with modified κ and ψ. The functional form of κ can be maintained by appropriately redefining the quantities Ω and δ. To leading order in μ, we obtain

$$\kappa \to \kappa_{\rm TM} = \frac{\Omega_{\rm I}^3 \delta_{\rm TM}}{(\omega^2 - \Omega_{\rm TM}^2)^2 + \omega^2 \delta_{\rm TM}^2}\,, \tag{6.121}$$

with

$$\Omega \to \Omega_{\rm TM} = (1-\mu)\Omega\,, \quad \delta \to \delta_{\rm TM} = (1-2\mu)\delta\,. \tag{6.122}$$

Consequently, we can re-optimize the system to compensate for this transmissivity-mismatch effect.

6.11 Bibliography

[1] C. M. Caves, Phys. Rev. Lett. **45**, 75 (1980).

[2] A. Abramovici et al., Science **256**, 325 (1992).

[3] B. C. Barish and R. Weiss, Physics Today **52**, 44 (1999).

[4] W. G. Unruh, in *Quantum Optics, Experimental Gravitation, and Measurement Theory*, eds. P. Meystre and M. O. Scully (Plenum, 1982), p. 647.

[5] M. T. Jaekel and S. Reynaud, Europhys. Lett. **13**, 301 (1990).

[6] E. Gustafson, D. Shoemaker, K. Strain, and R. Weiss, *LSC White Paper on Detector Research and Development*, LIGO document T990080-00-D (1999); available along with other relevant information at http://www.ligo.caltech.edu/∼ligo2/ .

[7] H. J. Kimble, Yu. Levin, A. B. Matsko, K. S. Thorne, and S. P. Vyatchanin, Phys. Rev. D **65**, 022002 (2001); cited in text as KLMTV.

[8] P. Purdue, Phys. Rev. D **66**, 022001 (2002); cited in text as Paper I.

[9] V. B. Braginsky and F. Ya. Khalily, Phys. Lett. A **218**, 167 (1996); V. B. Braginsky, M. L. Gorodetsky, and F. Ya. Khalili, Phys. Lett. A **232**, 340 (1997).

[10] V. B. Braginsky, M. L. Gorodetsky, and F. Ya. Khalili, Phys. Lett. A **246**, 485 (1998); quant-ph/9806081.

[11] F. Ya. Khalili, qr-qc/0203002.

[12] V. B. Braginsky and F. Ya. Khalili, Phys. Lett. A **147**, 251 (1990).

[13] V. B. Braginsky, M. L. Gorodetsky, F. Ya. Khalili, and K. S. Thorne, Phys. Rev. D **61**, 044002 (2000); cited in text as BGKT.

[14] C. M. Caves, Phys. Rev. D **23**, 1693 (1981).

[15] J. Mizuno, Ph.D. thesis, Max Planck Institute für Quantenoptik, Garching, Germany, 1995.

[16] A. Freise, G. Heinzel, K. A. Strain, J. Mizuno, K. D. Skeldon, H. Lück, B. Wilke, R. Schilling, A. Rüdiger, W. Wingler and K. Danzmann, Phys. Lett. A **277**, 135 (2000)

[17] J. Mason, Ph.D. thesis, California Institute of Technology, Pasadena, CA, 2001; also available as LIGO document P010010-00-R at www.ligo.caltech.edu/docs/P/P010010-00.pdf .

[18] C. M. Caves and B. L. Schumaker, Phys. Rev. A **31**, 3068 (1985).

[19] B. L. Schumaker and C. M. Caves, Phys. Rev. A **31**, 3093 (1985).

[20] V. B. Braginsky, M. L. Gorodetsky, F. Ya. Khalili and K. S. Thorne, "Energetic Quantum Limit in Large-Scale Interferometers," in *Gravitational Waves*, Proceedings of the Third Edoardo Amaldi Conference, AIP Conference Proceedings Vol. 523, ed. Sydney Meshkov (American Institute of Physics, 2000) pp. 180–192; gr-qc/9907057.

[21] M. Xiao, L.-A. Wu and H. J. Kimble, Phys. Rev. Lett. **59** 278 (1987).

[22] P. Grangier, R. E. Slusher, B. Yurke and A. La Porta, Phys. Rev. Lett. **59**, 2153 (1987).

[23] K. S. Thorne (private communication).

[24] S. P. Vyatchanin and A. B. Matsko, JETP **77**, 218 (1993).

[25] S. P. Vyatchanin and E. A. Zubova, Phys. Lett. A **203**, 269 (1995).

[26] S. P. Vyatchanin and A. B. Matsko, JETP **82**, 1007 (1996).

[27] S. P. Vyatchanin and A. B. Matsko, JETP **83**, 690 (1996).

[28] S. P. Vyatchanin, Phys. Lett. A **239**, 201 (1998).

Chapter 7

Sagnac interferometer as a speed-meter-type, quantum-nondemolition gravitational-wave detector

According to quantum measurement theory, "*speed meters*" — devices that measure the momentum, or speed, of free test masses — are immune to the standard quantum limit (SQL). It is shown that a Sagnac-interferometer gravitational-wave detector is a speed meter and therefore in principle it can beat the SQL by large amounts over a wide band of frequencies. It is shown, further, that, when one ignores optical losses, a signal-recycled Sagnac interferometer with Fabry-Perot arm cavities has precisely the same performance, for the same circulating light power, as the Michelson speed-meter interferometer recently invented and studied by P. Purdue and the author. The influence of optical losses is not studied, but it is plausible that they be fairly unimportant for the Sagnac, as for other speed meters. With squeezed vacuum (squeeze factor $e^{-2R} = 0.1$) injected into its dark port, the recycled Sagnac can beat the SQL by a factor $\sqrt{10} \simeq 3$ over the frequency band $10\,\mathrm{Hz} < f < 150\,\mathrm{Hz}$ using the same circulating power $I_c \sim 820$ kW as is to be used by the (quantum limited) second-generation Advanced LIGO interferometers — if other noise sources are made sufficiently small. It is concluded that the Sagnac optical configuration, with signal recycling and squeezed-vacuum injection, is an attractive candidate for third-generation interferometric gravitational-wave detectors (LIGO-III and EURO).

Y. Chen, gr-qc/0208051, accepted for publication in Phys. Rev. D

7.1 Introduction

After decades of planning and development, an array of large-scale laser interferometric gravitational-wave detectors (interferometers for short), consisting of the Laser Interferometer Gravitational-wave

Observatory (LIGO), VIRGO, GEO and TAMA [1], is gradually becoming operative, targeted at gravitational waves in the high-frequency band (10–10^3 Hz). Michelson-type laser interferometry is used in these detectors to monitor gravitational-wave-induced changes in the separations of mirror-endowed test masses. More specifically, a laser beam is split in two by a 50/50 beamsplitter, and the two beams are sent into the two arms (which may contain Fabry-Perot cavities) and then brought back together and interfered, yielding a signal that senses the difference of the two arm lengths. Although it is plausible that gravitational waves will be detected, for the first time in history, by these initial interferometers, a significant upgrade of them must probably be made before a rich program of observational gravitational-wave astrophysics can be carried out [2]. In the planned upgrade of the LIGO interferometers (*Advanced LIGO*, tentatively scheduled to begin operations in 2008 [3]), the Michelson topology will still be used, as also is probably the case for Advanced LIGO's international counterparts, for example the Japanese LCGT [4].

An alternative to the Michelson topology, the Sagnac topology, originally invented in 1913 for rotation sensing [5], can also be used for gravitational-wave detection, if the light circumscribes zero area [6, 7]. In a Sagnac interferometer, as in a Michelson, a laser beam is split in two, but each of the two beams travels successively through both arms, though in the opposite order (in opposite directions). When the two beams are finally recombined, a signal sensitive to the *time-dependent part* of the arm-length difference is obtained.

Until now, there has been little motivation to switch from the more mature Michelson topology to the Sagnac topology, because: (i) the technical advantages provided by the Sagnac topology (e.g., simpler control system required, high tolerance to reflectivity imbalance between the arms) have not been able to overcome its disadvantages (e.g., low tolerance to beamsplitter reflectivity error and beamsplitter tilt) [7, 8, 9], and (ii) the *shot-noise limited* sensitivities of ideal Sagnac interferometers have not exhibited any interesting features with astrophysical distinction that cannot be equally realized by signal-recycled Michelson interferometers [10]. Nevertheless, a sustained research effort is still being made on the Sagnac topology, aimed at third generation gravitational-wave detectors (beyond Advanced LIGO). In particular, an all-reflective optical system suitable for the Sagnac is being developed [11], with the promise of being able to cope with the very high laser powers that may be needed in the third generation, by avoiding high-intensity light from passing through the substrate. At the same time, all-reflective optics also provides the flexibility of using non-transparent substrate materials that have superior thermal properties, e.g., silicon.

In this chapter, a theoretical study of the idealized noise performance of Sagnac-based interferometers at high laser powers is carried out. It is shown that, by contrast with the previously studied low-power regime, the (ideal) Sagnac interferometer might be significantly better at high powers than its ideal Michelson counterparts, and thus is an attractive candidate for third-generation interferometric gravitational-wave detectors, e.g., LIGO-III and EURO [12].

In advanced gravitational-wave interferometers, the laser power is increased to lower the shot noise. However, at these higher light powers, the photons in the arms exert stronger random forces on the test masses, thereby inducing stronger *radiation-pressure noise*. At high enough laser powers (above about 850 kW in Advanced LIGO), the radiation-pressure noise can become larger than the shot noise and dominate a significant part of the noise spectrum (usually at all frequencies below the noise-curve minimum). As was first pointed out by Braginsky in the 1960s [13, 14], a balance between the two noises gives rise to a Standard Quantum Limit (SQL). As was later realized, again by Braginsky [13, 14], the SQL can be circumvented by clever designs, which he named Quantum Non-Demolition (QND) schemes.

The advanced LIGO interferometers were originally planned to operate near or at the SQL [3], but it was later shown by Buonanno and Chen that they can actually beat the SQL by a moderate amount over a modest frequency band, due to a change in interferometer dynamics (Chapters 2 and 3) induced by detuned signal-recycling [15, 16].

Generations beyond Advanced LIGO, however, will have to beat the SQL by significant amounts over a broad frequency band; i.e., they must be *strongly QND*. Currently existing schemes for strongly QND interferometers with Michelson topology include: (i) The use of two additional kilometer-scale optical filters to perform frequency-dependent homodyne detection [17] at the output of a conventional Michelson interferometer, as invented and analyzed by Kimble, Levin, Matsko, Thorne and Vyatchanin (KLMTV) [18]. (Reference [18] can be used as a general starting point for the quantum-mechanical analysis of QND gravitational-wave interferometers.) (ii) The speed-meter interferometer, originally invented by Braginsky and Khalili [19], developed by Braginsky, Khalili, Gorodetsky and Thorne [20], and later incorporated into the Michelson topology by Purdue and Chen [21, 22]. In its Michelson form, the speed meter uses at least one additional kilometer-scale optical cavity to measure the relative momentum of the free test masses over a broad frequency band.

The speed meter is motivated, theoretically, by the fact that the momentum of a free test mass is a *QND observable* [24, 25], i.e., it can be measured continuously to arbitrary accuracy without being limited by the SQL. This fact can be understood by noticing that the momentum of a free mass is a conserved quantity. In a continuous measurement on free-mass momentum, the measurement-induced kicks on displacement, its canonical conjugate, will not affect its future values. In this way, there can in principle be vanishing back-action noise in such a measurement. Practically, QND schemes based on a Michelson speed meter can exhibit broadband QND performances using only one additional kilometer-scale cavity, by contrast with the two additional cavities needed for QND schemes based on a conventional Michelson interferometer (a *position meter*). Michelson–speed-meter-based QND schemes are also less susceptible to optical losses than those based on Michelson position meters (Sec. V of [22]).

Surprisingly, so far as we are aware nobody has previously noticed that, because the Sagnac interferometer is sensitive only to the *time-dependent part* of the arm-length difference, it is automatically a speed meter. Moreover, as we shall see in this chapter, with the help of *signal-recycling* [15, 16], i.e., by putting one additional mirror at its dark output port, a Sagnac interferometer can be optimized to have a comparable performance to a Michelson speed meter, *without the need for any additional kilometer-scale cavities*. In particular, a signal-recycled Sagnac interferometer with ring cavities in its arms has exactly the same performance as the Michelson speed meters of Ref. [22], aside from (presumably minor) differences due to optical losses.

This Chapter is organized as follows: in Sec. 7.2 we derive the input-output relation of signal-recycled Sagnac interferometers, with either optical delay lines or ring-shaped Fabry-Perot cavities in the arms, showing that they are indeed measuring the relative speed of test masses. In Sec. 7.3, we evaluate the noise spectral density of ideal Sagnac interferometers, obtaining comparable performances to the Michelson speed meters. In Sec. 7.4, we discuss some technical issues that deserve further investigation. Finally, Sec. 7.5 summarizes our conclusions. The Appendix (Sec. 7.6) contains details in the calculations of the input-output relation of a single interferometer arm, which might contain an optical delay line or a ring cavity.

7.2 The Sagnac as a speed meter, and its input-output relations

7.2.1 The Sagnac optical configuration

Two well-known variants of Sagnac interferometers are shown in Figs. 7.1 and 7.2, which use optical delay lines (henceforth abbreviated as DL) or ring-shaped Fabry-Perot cavities (henceforth abbrevaited as FP), formed by Input Test-mass Mirrors (ITMs) and End Test-mass Mirrors (ETMs), (the ring cavity has an additional perfect mirror), in the arms to enhance signal strength. A Power-Recycling Mirror (PRM) and a Signal-Recycling Mirror (SRM) are also used [6, 15], in order to enhance further the circulating power inside the arms, and to modify and improve the frequency response of the interferometer.

As a brief historical note, the ideas of using optical delay lines and Fabry-Perot cavities in arms were due to Weiss [23] and Drever [6], respectively. These two signal-recycled Sagnac configurations can be traced back equivalently to the two original designs of Drever, as shown in Figs. 9 and 10 of Ref. [6]. These original Sagnac designs by Drever were intended to explain the idea of what is currently known as signal recycling, instead of the zero-area Sagnac topology itself. However, the currently widely-used signal-recycling schemes were invented by Meers [15] based on the idea of Drever, but much simplified. In this chapter we have adopted the the signal-recycling scheme of

Meers.

In both variants shown in Figs. 7.1 and 7.2, the carrier light enters the interferometer from the left port (also called the "bright port") of the beamsplitter (BS). The light gets split in two and travels into the two arms in opposite orders; we denote by R the beam that enters the North (N) arm first and the East (E) arm second, and by L that which enters E first and N second. As the mirrors are all held fixed at their equilibrium positions, the carrier R and L beams, upon arriving again at the beamsplitter, will combine in such a way that no lights exits to the port below the beamsplitter (the "dark port"). Similarly, any vacuum fluctuations that enter the interferometer at the bright port along with the carrier light will also be suppressed in the dark-port output. Only vacuum fluctuations that entered the interferometer from the dark port can leave the interferometer through the dark port. As a result, the dark port is decoupled from the bright port, as in a Michelson interferometer. This fact is crucial to the suppression of laser noise in the dark-port output.

7.2.2 The Sagnac's speed-meter behavior

When the end mirrors of the two arms are allowed to move, they phase modulate the carrier light, generating sideband fields. Only antisymmetric, non-static changes in the arm lengths can contribute to the dark-port output; this is a result of the cancellation at the beamsplitter, and the fact that the two beams pass through the two arms in opposite order. A more detailed but still rough exploration of this point reveals the Sagnac's role as a speed-meter interferometer:

Denoting by $\tau_{\rm arm}$ the (average) storage time of light in the arms and by $x_{\rm N,\,E}$ the time-dependent displacements of the end mirrors, we have for the phase gained by the R and L beams after traveling from the bright entry port through the two arms to the dark exit port:

$$\begin{aligned} \delta\phi_{\rm R} &\sim {\rm x}_{\rm N}(t) + x_{\rm E}(t+\tau_{\rm arm})\,, \\ \delta\phi_{\rm L} &\sim {\rm x}_{\rm E}(t) + x_{\rm N}(t+\tau_{\rm arm})\,. \end{aligned}$$

The amplitude of the dark-port output is proportional to the phase difference of the two beams at the beamsplitter:

$$\delta\phi_{\rm R} - \delta\phi_{\rm L} \sim [x_{\rm N}(t) - x_{\rm N}(t+\tau_{\rm arm})] - [x_{\rm E}(t) - x_{\rm E}(t+\tau_{\rm arm})]\,.$$

As a consequence, the Sagnac interferometer is *not* sensitive to any time-independent displacement of the test masses. By expanding Eq. (7.1) in powers of $\tau_{\rm arm}$, we see that, at frequencies much smaller than $1/\tau_{\rm arm}$, the *speed* of the test-mass motion is measured, and at higher frequencies, a mixture of the speed and its time derivatives is measured — as also is the case in other speed meters [19, 21, 22].

Quantity	Value for optical delay line (DL)	Value for ring-shaped Fabry Perot cavity (FP)
$\Psi_{\rm arm}$	$\mathcal{B}\Omega L/c$	$\arctan\left(\dfrac{1+\sqrt{R}}{1-\sqrt{R}}\tan\dfrac{\Omega L}{c}\right)$
$\mathcal{K}_{\rm arm}$	$\dfrac{8I_{\rm c}\omega_0}{m\mathcal{B}\Omega^2c^2}\left(\dfrac{\sin\mathcal{B}\Omega L/c}{\sin\Omega L/c}\right)^2$	$\dfrac{8I_{\rm c}\omega_0}{m\Omega^2c^2}\left(\dfrac{T}{1-2\sqrt{R}\cos(2\Omega L/c)+R}\right)$
$\Psi_{\rm sagnac}$	$2\mathcal{B}\Omega L/c+\pi/2$	$2\arctan\left(\dfrac{1+\sqrt{R}}{1-\sqrt{R}}\tan\dfrac{\Omega L}{c}\right)+\pi/2$
$\mathcal{K}_{\rm sagnac}$	$\dfrac{32I_{\rm c}\omega_0}{mLc\left(\frac{c}{L\mathcal{B}}\right)^3}\left[\dfrac{\sin^2(\mathcal{B}\Omega L/c)}{(\mathcal{B}\Omega L/c)(\mathcal{B}\sin\Omega L/c)}\right]^2$	$\dfrac{32I_{\rm c}\omega_0}{m\Omega^2c^2}\left[\dfrac{(1+\sqrt{R})\sqrt{T}\sin(\Omega L/c)}{1-2\sqrt{R}\cos(2\Omega L/c)+R}\right]^2$

Table 7.1: Expressions for $\Psi_{\rm arm}$, $\mathcal{K}_{\rm arm}$, $\Psi_{\rm sagnac}$ and $\mathcal{K}_{\rm sagnac}$ in the DL (optical delay line) and FP (ring-shaped Fabry-Perot cavity) cases. Here where ω_0 is the carrier frequency, c the speed of light, L the arm length, m the mirror mass, I_c the circulating power in the arms, $\mathcal{B}$ the number of bounces inside the optical delay line, and T, R the power transmissivity and reflectivity of the ring-cavity ITM, with $T+R=1$.

In reality, the storage time $\tau_{\rm arm}$ is determined by the round-trip time of light inside the arm, $2L/c$, times the number of round trips the light makes before leaving the arm, which can either be fixed by the geometry of the optical delay lines, or be determined (in an average sense) by the input power transmissivity T the arm cavity (average number of bounces $\approx 2/T$). Although a smaller storage time can give a broader bandwidth, the sensitivity achieved with a fixed amount of optical power will also be lower. It is therefore advisable to put $1/\tau_{\rm arm}$ in the middle of interested frequency spectrum, which is around $2\pi\times 100\,{\rm Hz}$ for earth-based gravitational-wave interferometers. For the LIGO facility with $L=4\,{\rm km}$, this corresponds to the requirement of a 60-bounce optical delay line, or an input power transmissivity of around 3%.

7.2.3 Input-output relations without a signal-recycling mirror

As a foundation for evaluating the performances of Sagnac interferometers in the high-power regime, we shall now derive their quantum mechanical *input-output relations* — i.e., we shall derive equations for the quantum mechanical dark-port output field q in terms of the input (vacuum) fields p at the dark port and z at the bright port (see Figs. 7.1 and 7.2), which in the end does not appear in q, and the gravitational-wave strain h. Here we have denoted by $a^{\rm RN,\,RE,\,LN,\,LE}$ the input sideband fields of the R and L beams at the N and E arms, and by $b^{\rm RN,\,RE,\,LN,\,LE}$ the output sideband fields. For the moment, we shall ignore the existence of the signal-recycling mirror (SRM); and throughout we

shall ignore the power-recycling mirror (PRM) since (as for Michelson topologies) it merely serves to provide a larger input power at the beamsplitter and has no other significance for the interferometer's quantum noise.

In this chapter, we shall use the Caves-Schumaker two-photon formalism [26] (briefly introduced in Sec. IIA of KLMTV), which breaks the time-domain sideband fields, at any given spatial location, into the following form,

$$E(t) = \sqrt{\frac{4\pi\hbar\omega_0}{\mathcal{A}c}}\,[E_1(t)\cos(\omega_0 t) + E_2(t)\sin(\omega_0 t)]\ , \tag{7.1}$$

where ω_0 is the carrier frequency, $\mathcal{A}$ is the cross sectional area of the beam. Here $E_{1,2}(t)$ are slowly varying fields called the cosine (or amplitude) and sine (or phase) quadratures. These quadratures fields can be thought of as amplitude or phase modulations on a carrier field of the form $D\cos(\omega_0 t)$. The quadrature fields can be expanded as

$$E_{1,2}(t) = \int_0^{+\infty} \frac{d\Omega}{2\pi}\left(a_{1,2}e^{-i\,\Omega\,t} + a_{1,2}^\dagger e^{+i\,\Omega\,t}\right)\ , \tag{7.2}$$

in terms of the quadrature operators $a_{1,2}(\Omega)$. A more general quadrature operator can be constructed from $a_{1,2}$:

$$a_\Phi = a_1\cos\Phi + a_2\sin\Phi\,. \tag{7.3}$$

The set of propagation equations common to both of our Sagnac configurations [with either delay lines (DL) or ring-shaped Fabry-Perot cavities (FP) inside the arms] are (i) at the beamsplitter,

$$a^{\rm RN} = \frac{z+p}{\sqrt{2}}\,,\quad a^{\rm LE} = \frac{z-p}{\sqrt{2}}\,,\quad q = \frac{b^{\rm LN} - b^{\rm RE}}{\sqrt{2}}\,; \tag{7.4}$$

and (ii) when the beams leave one arm and enter the other,

$$a^{\rm RE} = b^{\rm RN}\,,\quad a^{\rm LN} = b^{\rm LE}\,. \tag{7.5}$$

The above equations, (7.4) and (7.5), are for both quadratures. By writing down these equations, we assume the distances between the BS and ITMs to be small, and also integer multiples of the laser wavelength.

The input-output relations for the arms, i.e., the b-a relations, are evaluated in the Appendix (in an manner analogous to that of KLMTV for Michelson configurations), for the distinct cases of DL and FP. The results can be put into the following simple form:

$$b_1^{IJ} = e^{2i\Psi_{\rm arm}}a_1^{IJ}\,, \tag{7.6}$$

$$b_2^{IJ} = e^{2i\Psi_{\rm arm}}\left[a_2^{IJ} - \mathcal{K}_{\rm arm}(a_1^{\rm L\,J} + a_1^{\rm R\,J})\right] + e^{i\Psi_{\rm arm}}\frac{\sqrt{2\mathcal{K}_{\rm arm}}}{h_{\rm SQL}}\sqrt{2}\,\tilde{x}_J^{\rm GW}/L\,. \tag{7.7}$$

Here I = L, R stands for either one of the two beams, and J = E, N stands for either one of the two arms. The quantity $\tilde{x}_J^{\rm GW}$ is the gravitational-wave induced displacement of the Jth ETM (in frequency domain), L is the arm length. The Standard Quantum Limit is given by

$$h_{\rm SQL} = \sqrt{\frac{8\hbar}{m\Omega^2 L^2}}\,, \tag{7.8}$$

where m is the mass of the ITM and the ETM. Expressions for $\Psi_{\rm arm}$ and $\mathcal{K}_{\rm arm}$, in the cases of DL and FP, are given in the Appendix [Eqs. (7.40), (7.41), (7.51) and (7.52)] and summarized in Table 7.1. Combining Eqs. (7.4)–(7.7), we obtain $q_{1,2}$ in terms of the input fields and the dimensionless gravitational-wave strain (in frequency domain), $\tilde{h}$ [also using $\tilde{h} = (\tilde{x}_{\rm E}^{\rm GW} - \tilde{x}_{\rm N}^{\rm GW})/L$]:

$$q_1 = e^{2i\Psi_{\rm sagnac}} p_1\,, \tag{7.9}$$

$$q_2 = e^{2i\Psi_{\rm sagnac}}(p_2 - \mathcal{K}_{\rm sagnac} p_1) + e^{i\Psi_{\rm sagnac}} \frac{\sqrt{2\mathcal{K}_{\rm sagnac}}}{h_{\rm SQL}} \tilde{h}\,; \tag{7.10}$$

with

$$\Psi_{\rm sagnac} = 2\Psi_{\rm arm} + \frac{\pi}{2}\,, \tag{7.11}$$

$$\mathcal{K}_{\rm sagnac} = 4\mathcal{K}_{\rm arm} \sin^2 \Psi_{\rm arm}\,. \tag{7.12}$$

Expressions for $\Psi_{\rm sagnac}$ and $\mathcal{K}_{\rm sagnac}$ in the DL and FP cases can be obtained by inserting Eqs. (7.40), (7.41), (7.51) and (7.52) into Eqs. (7.11) and (7.12), with results summarized again in Table 7.1. Indeed, as mentioned at the beginning of this section, the bright-port input field z does not appear in the dark-port output quadratures, $q_{1,2}$.

The input-output relations (7.9) and (7.10) have the same general form as those of a conventional Michelson interferometer, Eq. (16) of [18], and those of a Michelson speed meter, Eqs. (27) of [21] or Eqs. (12) of [22]. In particular, as discussed in the Appendix, the output phase quadrature q_2 [Eq. (7.9)] is a sum of three terms: the shot noise (first term), the radiation-pressure noise (second term) and the gravitational-wave signal (third term), while the output amplitude quadrature q_1 [Eq. (7.10)] contains only shot noise.

7.2.4 Influence of signal recycling on the input-output relations

Since the input-output relations of Sagnac interferometers have the same form as those of a conventional Michelson interferometer, the quantum noise of signal-recycled Sagnac interferometers can be obtained easily using the prescriptions of Chapter 2. For simplicity, we shall restrict the signal-recycling cavity to be either resonant with the carrier frequency ("tuned SR") or anti-resonant ("tuned RSE"), leaving the detuned case for future investigations. In these cases, the dynamics of

the interferometer are not modified by the signal recycling, and the input-output relation has the same form as Eqs. (7.9) and (7.10), with $\mathcal{K}_{\rm sagnac}$ replaced by (see Sec.2.3.3 of this thesis)

$$\mathcal{K}_{\rm sagnac\,SR} = \frac{\tau^2}{1 - 2\rho\cos 2\Psi_{\rm sagnac} + \rho^2}\mathcal{K}_{\rm sagnac}\,, \tag{7.13}$$

and $\Psi_{\rm sagnac}$ replaced by a quantity $\Psi_{\rm sagnac\,SR}$ whose value is not of interest to us. Here ρ and τ are the (amplitude) reflectivity and transmissivity of the signal-recycling mirror, with $\rho \in \Re$, $\tau > 0$ and $\rho^2 + \tau^2 = 1$. Expressions for $\mathcal{K}_{\rm sagnac\,SR}$ can be obtained by using results in Table 7.1.

Using the fact that $\Omega L/c \ll 1$ (for earth-based interferometers in the high-frequency band), $\mathcal{B} \gg 1$ (for the DL case) and $T \ll 1$ (for the FP case), we can obtain some approximate formulas for $\mathcal{K}_{\rm sagnac\,SR}$ (which also apply to the non-SR case, with $\rho \to 0$ and $\tau \to 1$): in the DL case

$$\mathcal{K}^{\rm DL}_{\rm sagnac\,SR} = \quad \frac{32 I_{\rm c}\omega_0}{mLc\gamma_{\rm DL}^3}\left[\frac{\tau^2}{1 + 2\rho\cos(4\Omega/\gamma_{\rm DL}) + \rho^2}\right]\left[\frac{\sin(\Omega/\gamma_{\rm DL})}{\Omega/\gamma_{\rm DL}}\right]^4\,, \tag{7.14}$$

with

$$\gamma_{\rm DL} = \frac{c}{\mathcal{B}L}\,; \tag{7.15}$$

and in the FP case

$$\mathcal{K}^{\rm FP}_{\rm sagnac\,SR} = \frac{16 I_{\rm c}\omega_0}{mLc}\frac{\delta}{(\Omega^2 - \Omega_{\rm s}^2)^2 + \delta^2\Omega^2}\,; \tag{7.16}$$

with

$$\delta = 2\left(1 + \frac{T}{2}\right)\frac{1-\rho}{1+\rho}\gamma_{\rm FP} \quad \Omega_{\rm s} = \left(1 + \frac{T}{2}\right)\gamma_{\rm FP}\,, \tag{7.17}$$

where

$$\gamma_{\rm FP} = \frac{Tc}{4L}\,. \tag{7.18}$$

Interestingly, Eq. (7.16) is identical to Eqs. (22) and (23) of Ref. [22], with substitutions (this chapter $\to$ Purdue and Chen) $I_c \to W_{\rm circ}$ (circulating power), $\Omega_{\rm s} \to \Omega$ (sloshing frequency), $\delta \to \delta$ (extraction rate), $\Omega \to \omega$ (sideband frequency), and $\mathcal{K}^{\rm FP}_{\rm sagnac\,SR} \to \kappa$. As we shall explain further in the following sections, the coupling constant $\mathcal{K}_{\rm sagnac\,SR}$ alone (besides $h_{\rm SQL}$, which depends on m and L) will determine the quantum noise of the interferometer. This means that a signal-recycled Sagnac interferometer with ring cavities in its arms is equivalent in performance to the Michelson speed meters proposed in Refs. [21, 22] (if we ignore the influence of optical losses and other noise sources).

7.2.5 Frequency dependence of coupling constants $\mathcal{K}$, and Sagnac interferometers as speed meters

As can be seen both analytically in Eqs. (7.16) and (7.17) and graphically in Fig. 7.3, the coupling constant $\mathcal{K}_{\rm sagnac}$ of a Sagnac interferometer without signal recycling (i.e., $\tau = 1$, $\rho = 0$) approaches a constant as $\Omega \to 0$, which also turns out to be its maximum. This fact, combined with the input-output relation (7.10), suggests that the second output quadrature q_2 is indeed sensitive to the speed of the interferometer induced by the gravitational wave, since at low frequencies

$$q_2(\text{signal part}) \propto \Omega\sqrt{\mathcal{K}(\Omega=0)}\tilde{x}^{\rm GW} \propto \text{momentum}\,. \tag{7.19}$$

(A more detailed discussion of the link between $\mathcal{K}$ and a speed meter's performance is given in Sec. IIIA of Ref. [22]; that discussion, in the framework of a Michelson speed meter, is equally valid for a Sagnac speed meter.) When signal recycling is added, the shape of $\mathcal{K}(\Omega)$ can be adjusted for optimization purposes; examples are shown in Fig. 7.4.

7.3 Noise spectral density

In this section, we shall assume that homodyne detection can be carried out on any (frequency-independent) quadrature,

$$q_\Phi = q_1 \cos\Phi + q_2 \sin\Phi\,. \tag{7.20}$$

Homodyne detection is essential for QND interferometers, if they are to beat the SQL by substantial amounts; the additional noise associated with heterodyne detection schemes can seriously limit an interferometer's ability to beat the SQL, see Ref. [27] and Chapter 5.

The noise spectral density associated with the input-output relations (7.9) and (7.10) can be obtained in a manner analogous to that of Sec. IV of KLMTV or Sec. III of Ref. [22]. The result is

$$S_h = \left[\frac{(\cot\Phi - \mathcal{K}_{\rm sagnac\,SR})^2 + 1}{2\mathcal{K}_{\rm sagnac\,SR}}\right] h^2_{\rm SQL}\,. \tag{7.21}$$

As is also discussed in Refs. [20, 21, 22], the optimal quadrature to observe is the one with

$$\cot\Phi = \mathcal{K}_{\rm max} \equiv \max_\Omega \mathcal{K}_{\rm sagnac\,SR}(\Omega)\,; \tag{7.22}$$

for this quadrature the noise spectral density is

$$S_h = \left[\frac{(\mathcal{K}_{\rm max} - \mathcal{K}_{\rm sagnac\,SR})^2 + 1}{2\mathcal{K}_{\rm sagnac\,SR}}\right] h^2_{\rm SQL}\,. \tag{7.23}$$

In the left panel of Fig. 7.5, we plot the noise spectral density of a delay-line Sagnac interferometer *without* signal recycling, with $m = 40\,\mathrm{kg}$ and $I_\mathrm{c} = 8.2\,\mathrm{MW}$ (the characteristic circulating power used for the Michelson speed meter in Refs. [21, 22]), and with $\mathcal{B} = 40$, 60, 80 [corresponding to powers in a single beam equal to 102.5 kW, 68.3 kW and 51.3 kW, respectively; see Eq. (7.32); these powers can be lowered by injecting squeezed vacuum into the dark port, as we shall discuss below]. The noise spectral density of the fiducial Michelson speed meter of Refs. [21, 22], with the same I_c and m, and (in their notation) $\Omega = 2\pi \times 173\,\mathrm{Hz}$, $\delta = 2\pi \times 200\,\mathrm{Hz}$, is also plotted for comparison. In the right panel, we plot the noise spectral density of a ring-cavity Sagnac interferometer *without* signal recycling, with the same m and I_c, and with $\gamma_\mathrm{FP} = 2\pi \times 200\,\mathrm{Hz}$, $2\pi \times 220\,\mathrm{Hz}$ and $2\pi \times 240\,\mathrm{Hz}$. As one can see in the two panels, both configurations of non-recycled Sagnac interferometers exhibit broadband QND performance, with the beating of the SQL concentrated at low frequencies.

Signal recycling allows us to improve and optimize the Sagnac interferometers so they have similar performance to a Michelson speed meter; i.e., so they beat the SQL by a roughly constant factor over a substantially broader frequency band than without signal recycling. In particular, since the spectral density (7.21) only depends on $\mathcal{K}$, and $\mathcal{K}^\mathrm{FP}_{\mathrm{sagnac\,SR}}$ is the same as that of a Michelson speed meter, the signal-recycled Sagnac interferometers with ring cavities will have the same performance as the Michelson speed meters. In Fig. 7.6, we give one example for each of the DL and FP configurations. In the left panel we plot the noise spectral density for a signal-recycled DL Sagnac with $m = 40\,\mathrm{kg}$, $I_\mathrm{c} = 8.2\,\mathrm{MW}$, $\mathcal{B} = 60$ (and therefore $I_\mathrm{b} = 68\,\mathrm{kW}$) and $\rho = 0.12$ (dark solid curve), compared with that of the corresponding non-recycled ($\rho = 0$) interferometer (dashed curve), and that of the fiducial Michelson speed meter (gray solid curve). In the right panel we plot the the noise spectral density of a signal-recycled FP Sagnac interferometer with $T = 0.0564$, $\rho = 0.268$, corresponding to $\Omega_\mathrm{s} = 2\pi \times 173\,\mathrm{Hz}$, and $\delta = 2\pi \times 200\,\mathrm{Hz}$ [from Eq. (7.17)]. This interferometer has the same noise spectral density as the fiducial Michelson speed meter. [The two noise curves agree perfectly, appearing as the solid curve in the panel.] The corresponding non-recycled noise curve (with $\rho = 0$) is also plotted (the dashed curve) for comparison.

As conceived by Caves [25] and discussed in Refs. [18, 22], injecting squeezed vacuum into the dark-port can lower the required circulating power. For example, as discussed in Sec. IVA of Ref. [22], for speed meters with input-output relations with the form of Eqs. (7.9) and (7.10), the circulating power can be lowered by the squeeze factor e^{-2R}, while maintaining the same performance. In the LIGO-III era, it is reasonable to expect $e^{-2R} \sim 0.1$ [18], so the circulating powers cited above can be lowered by a factor ~ 10. The resulting fiducial circulating power, $I_c = 8.2\,\mathrm{MW}/10 = 820\,\mathrm{kW}$ is about the same as planned for the second-generation Advanced LIGO interferometers.

Finally, for signal-recycled FP Sagnac interferometers, since they are equivalent to the Michelson speed meters of Ref. [22], one can further improve the high-frequency performance by performing frequency-dependent homodyne detection with the aid of two kilometer-scale optical filters at the

dark-port output; see Sec. IVB of [22].

7.4 Discussion of technical issues

We shall now comment on three technical issues that might affect significantly the performances of Sagnac speed-meter interferometers:

Optical Losses. So far in this chapter, we have regarded all interferometers as ideal; most importantly, we have ignored optical losses. As has been shown by several studies of the Michelson case [18, 22], optical losses can sometimes be the limiting factor on the sensitivity of a QND interferometer. However, as shown in Ref. [22], Michelson speed meters are *less susceptible to* optical losses than Michelson position meters (even though the losses may be enhanced by the larger number of optical surfaces on which to scatter or absorb, and by the fact that the coupling constant $\mathcal{K}(\Omega)$ remains finite as $\Omega \to 0$ rather than growing to infinity). It is plausible that this feature will be retained, at least for optical losses associated with the individual optical elements, and with the readout scheme, but rigorous calculations are yet to be carried out. Moreover, the losses due to the use of diffractive optics and polarization techniques in some Sagnac configurations [11] deserve serious study.

High Power Through the Beam Splitter. As we saw at the end of Sec. 7.3, for FP Sagnac interferometers, in order to optimize the shape of the noise curve, the required values of the power transmissivity of the ITM can become as large as 0.05, which may require optical powers at the level of tens of kilowatts through the beamsplitter (even when squeezed vacuum is injected into the dark port); this may pose a problem for implementation. In Michelson speed meters, a resonant-side-band-extraction technique can be used to greatly reduce the power through the beamsplitter without affecting the interferometer's performance, but it is not clear whether an analogous trick exists for Sagnac interferometers.

Susceptibility to Mirror Tilt and Imperfections. In the low-laser-power limit, the Sagnac interferometer is known to be more susceptible to mirror tilting than are Michelson interferometers, but less susceptible to geometric imperfections of mirrors [9]. A study of these susceptibilities needs to be carried out in the context of high laser power, in order to see whether they pose any serious difficulty in the implementation of Sagnac speed meters.

7.5 Conclusions

In this chapter, a quantum-mechanical study of idealized Sagnac interferometers, including radiation-pressure effects, has been carried out. As was already known, Sagnac interferometers are sensitive only to the time varying part of the antisymmetric mode of mirror displacement. It was a short and trivial step, in this chapter, to demonstrate that this means a Sagnac interferometer measures

the test masses' relative speed or momentum and therefore is a speed meter with QND capabilities. Detailed computations revealed that, as for other speed meters, a broadband QND performance can be obtained, when frequency-independent homodyne detection is performed at the dark port. Signal recycling can be employed to further optimize the noise spectrum so it is comparable to that of a Michelson speed meter (or exactly the same, for Sagnac configurations with ring cavities in the arms); and, by contrast with the Michelson, this can be achieved without the need for any additional kilometer-scale FP cavity. [In the case of frequency-dependent homodyne detection with the aid of two kilometer-scale filter cavities, the Sagnac speed meter still needs one less optical cavity than its Michelson counterpart.] If further technical issues, including those related to optical losses (Sec. 7.4), can be resolved, the Sagnac optical topology will be a strong candidate for third-generation gravitational-wave interferometers, such as LIGO-III and EURO.

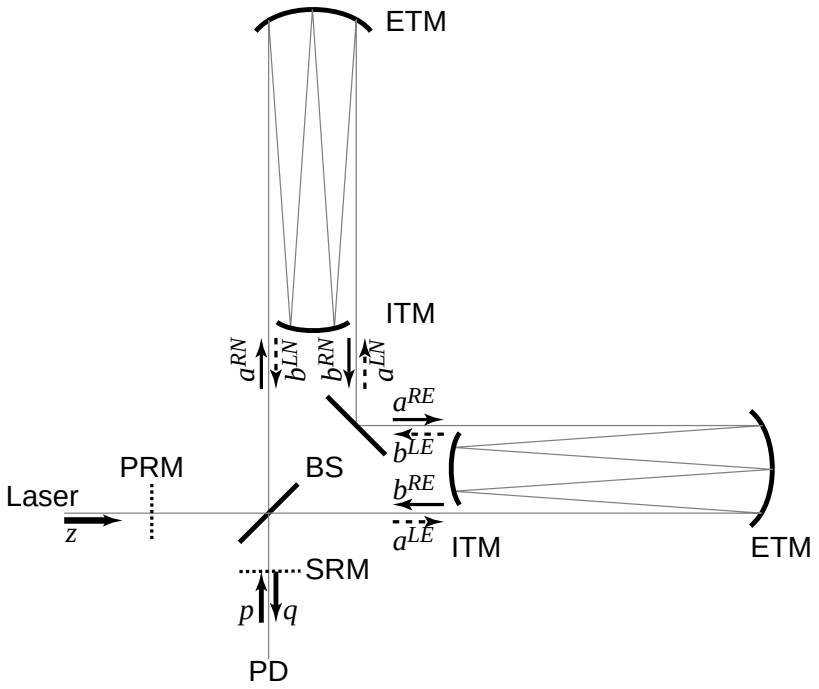

Figure 7.1: Schematic plot of a Sagnac interferometer with optical delay lines in the arms.

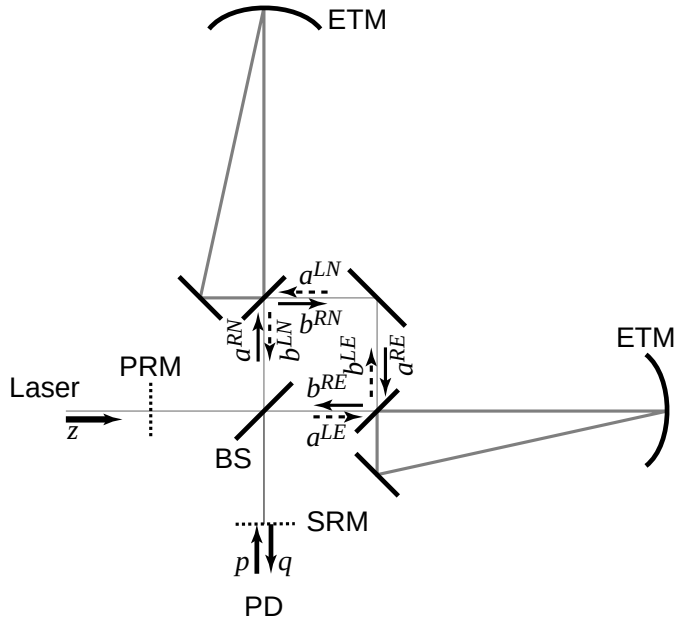

Figure 7.2: Schematic plot of a Sagnac interferometer with ring cavities in the arms.

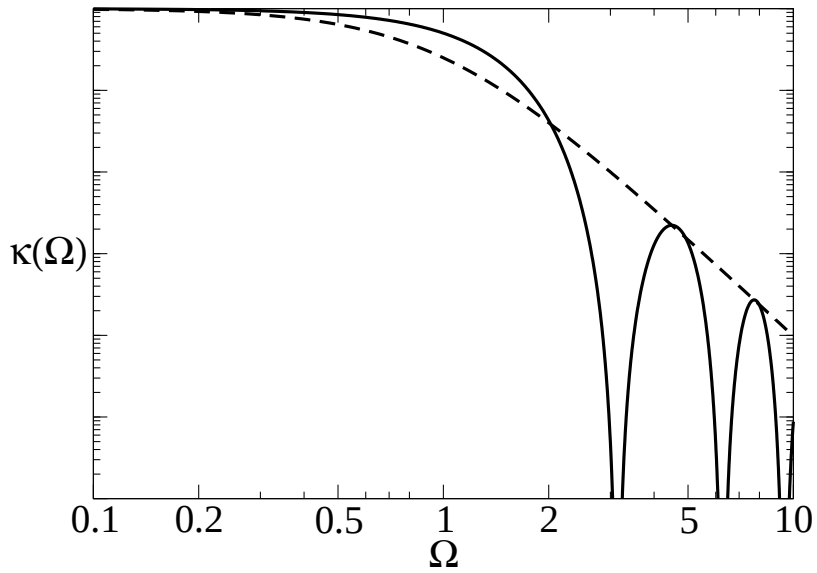

Figure 7.3: The coupling constant $\mathcal{K}_{\rm sagnac}(\Omega)$ for non-signal-recycled DL [in solid line, Eq. (7.14) with $\rho = 0$, $\tau = 1$] and FP [in dashed line, Eq. (7.16) with $\delta = 2\Omega_{\rm s}$] Sagnac interferometers, in arbitrary (logarithmic) units, with Ω measured in units of $\gamma_{\rm DL}$ (DL case) and $\Omega_{\rm s}$ (FP case), respectively.

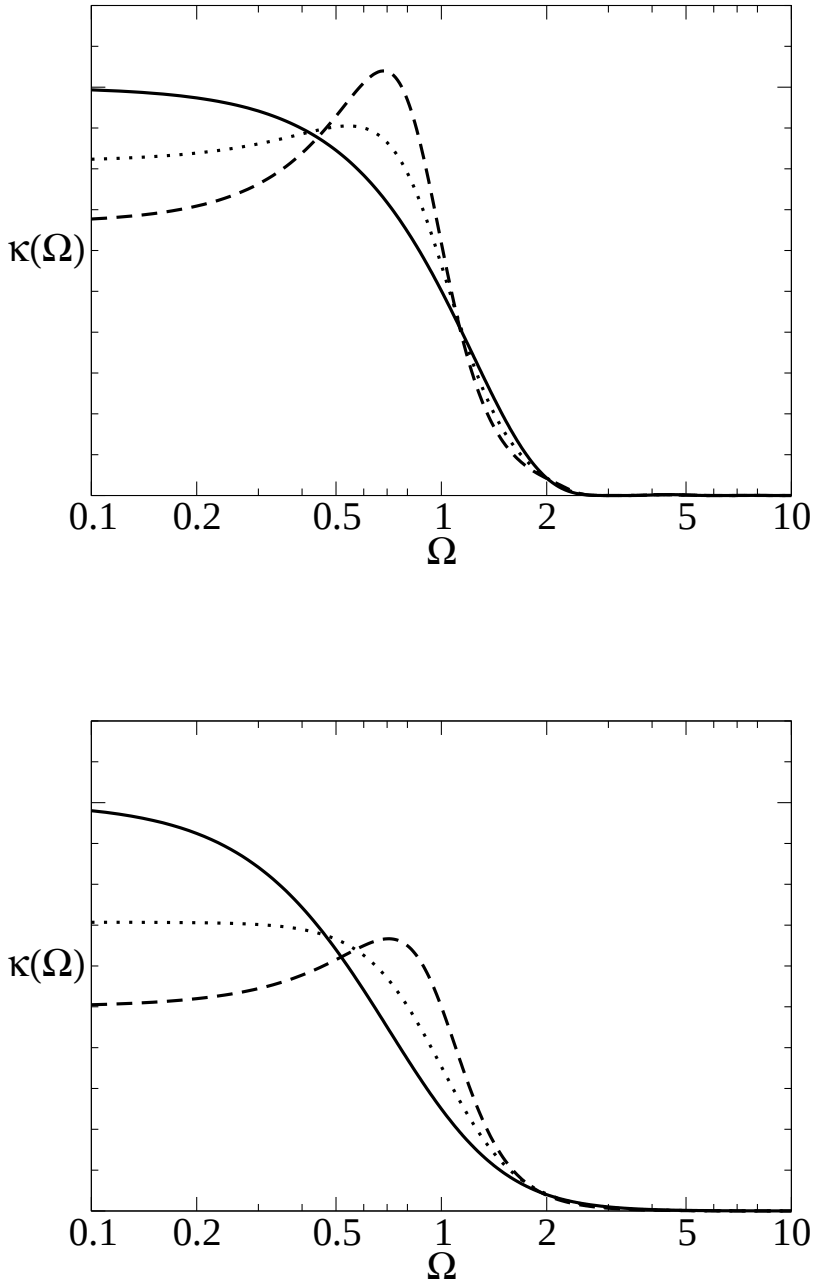

Figure 7.4: The coupling constant $\mathcal{K}_{\mathrm{sagnac\,SR}}(\Omega)$ for signal-recycled DL [upper panel, Eq. (7.14)] and FP [lower panel, Eq. (7.16)] Sagnac interferometers, in arbitrary (linear) units, with Ω measured in units of γ_{DL} (DL case) and Ω_{s} (FP case), respectively. For DL: cases with $\rho = 0$ (solid curve), 0.1 (dotted curve) and 0.2 (dashed curve) are plotted. For FP cases with $\delta = 2\Omega_{\mathrm{s}}$ (solid curve), $\sqrt{2}\Omega_{\mathrm{s}}$ (dotted curve), and Ω_{s} (dashed curve) are plotted, corresponding to $\rho = 0$, 0.172, and 0.333.

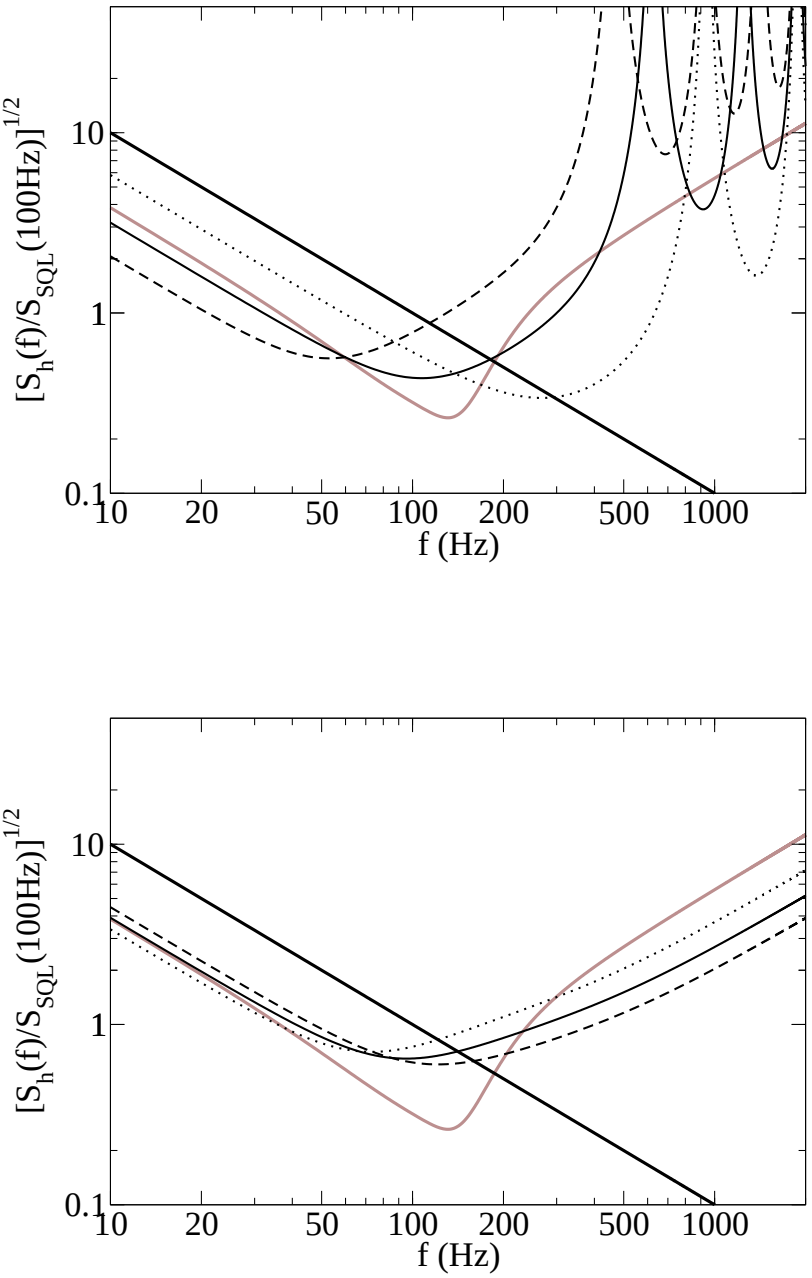

Figure 7.5: The noise spectral density [for the optimized quadrature, see Eq. (7.22)] of non-signal-recycled DL (upper panel) and FP (lower panel) Sagnac interferometers [Eq. (7.23), setting $\rho = 0$ and $\tau = 1$], assuming $I_c = 8.2\,\mathrm{MW}$ and $m = 40\,\mathrm{kg}$. [By injecting squeezed vacuum (with squeeze factor e^{-2R}) into the dark port, one can reduce I_c by a factor $e^{2R} \sim 10$.] For DL: cases with $\mathcal{B} = 40$ (dotted curve), 60 (solid curve) and 80 (dashed curve) are plotted. For FP: cases with $\Omega_s = 2\pi \times 200\,\mathrm{Hz}$ (dotted curve), $2\pi \times 220\,\mathrm{Hz}$ (solid curve) and $2\pi \times 240\,\mathrm{Hz}$ (dashed curve) are plotted. The noise curves for the fiducial speed meter (in gray) and the SQL (dark straight lines) are also plotted in both panels for comparison.

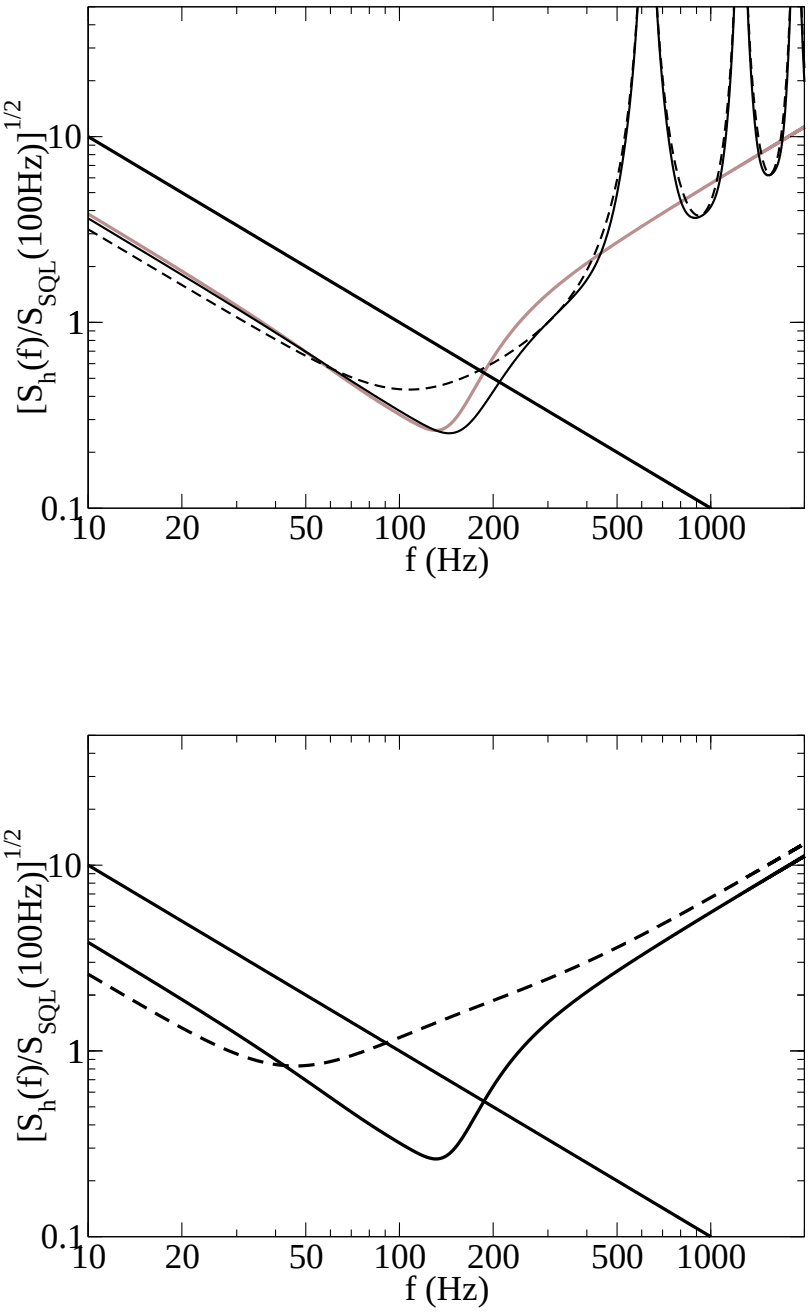

Figure 7.6: The solid curves are the noise spectral densities of signal-recycled DL (upper panel) and FP (lower panel) Sagnac interferometers [Eq. (7.23)], assuming $I_c = 8.2\,\mathrm{MW}$ and $m = 40\,\mathrm{kg}$. [By injecting squeezed vacuum into the dark port, one can reduce I_c by a factor $e^{2R} \sim 10$.] For DL, we take $\mathcal{B} = 60$, $\rho = 0.12$; for FP, we take $\Omega_s = 2\pi \times 173\,\mathrm{Hz}$ and $\delta = 2\pi \times 200\,\mathrm{Hz}$, which correspond to $T = 0.0564$ and $\rho = 0.268$. The corresponding non-recycled noise curves are also shown, as dashed curves. The noise curve of the fiducial Michelson speed meter is plotted in gray in the left panel and is identical to the solid, signal-recycled FP Sagnac noise curve in the right panel; the standard quantum limit is shown as dark straight lines.

7.6 Appendix. Input-output relations for the arms

Since the north and east arms are identical, we need only analyze one of them. For concreteness, we study the East arm. In Appendix B of Ref. [18], KLMTV derived the input-output relation for a simple FP cavity, using the same Caves-Schumaker quadrature formalism [26] as we use here. The input-output relations for optical delay-line arms and ring cavities can be derived analogously:

7.6.1 Optical delay line (DL)

Following the procedure of KLMTV, we initially suppose that the ITM is not moving (its motion will be accounted for later), and we denote the displacement of the ETM by $x_{\rm E}(t)$. Suppose the R beam has an electric field amplitude

$$E^{\rm RE\,in}(t) = [D + E_1^{\rm RE\,in}(t)]\cos\omega_0 t + E_2^{\rm RE\,in}(t)\sin\omega_0 t \tag{7.24}$$

at the location where it enters the E arm; here D is the (classical) carrier amplitude and $E_{1,2}^{\rm RE\,in}(t)$ are the sideband quadrature fields

$$E_{1,2}^{\rm RE\,in}(t) = \sqrt{\frac{4\pi\hbar\omega_0}{\mathcal{A}c}}\int_0^{+\infty}\frac{d\Omega}{2\pi}\left[a_{1,2}^{\rm RE}e^{-i\,\Omega\,t} + h.c.\right]\,, \tag{7.25}$$

with "h.c." meaning "Hermitian conjugate." The output beam after $\mathcal{B}$ bounces is delayed by

$$\Delta t = 2\mathcal{B}L/c + 2\big[x_{\rm E}(t-L/c) + x_{\rm E}(t-3L/c) + \cdots + x_{\rm E}(t-(2\mathcal{B}-1)L/c)\big]\,, \tag{7.26}$$

so

$$\begin{aligned} E^{\rm RE\,out}(t) = E^{\rm RE\,in}(t-\Delta t) &\approx [D + E_1^{\rm RE\,in}(t-2\mathcal{B}L/c)]\cos\omega_0 t + E_2^{\rm RE\,in}(t-2\mathcal{B}L/c)\sin\omega_0 t \\ &+ \frac{2\omega_0 D}{c}\sum_{k=1}^{\mathcal{B}} x_{\rm E}\left(t-(2k-1)L/c\right)\,. \end{aligned} \tag{7.27}$$

Comparing with

$$E_{1,2}^{\rm RE\,out}(t) = \sqrt{\frac{4\pi\hbar\omega_0}{\mathcal{A}c}}\int_0^{+\infty}\frac{d\Omega}{2\pi}\left[b_{1,2}^{\rm RE}e^{-i\,\Omega\,t} + h.c.\right]\,, \tag{7.28}$$

we obtain

$$b_1^{\rm RE} = e^{2i\mathcal{B}\Omega L/c}a_1^{\rm RE}\,, \tag{7.29}$$

$$b_2^{\rm RE} = e^{2i\mathcal{B}\Omega L/c}a_2^{\rm RE} + \frac{2\omega_0}{c}\sqrt{\frac{2I_{\rm b}}{\hbar\omega_0}}\left(\frac{\sin\mathcal{B}\Omega L/c}{\sin\Omega L/c}\right)e^{i\mathcal{B}\Omega L/c}\tilde{x}_{\rm E}\,. \tag{7.30}$$

where $\tilde{x}_{\rm E}$ is the Fourier transform of $x_{\rm E}(t)$. Here $I_{\rm b}$ is the power of the beam,

$$I_{\rm b} = \frac{D^2 \mathcal{A} c}{8\pi}\,, \tag{7.31}$$

which is related to the total circulating power by

$$I_{\rm b} = \frac{I_{\rm c}}{2\mathcal{B}}\,. \tag{7.32}$$

The physical meanings of Eqs. (7.29) and (7.30) can be roughly explained as follows: (i) the gravitational-wave signal embodied in $\tilde{x}_{\rm E}$ is only present in the second (phase) quadrature, $b_2^{\rm RE}$, of the output sideband field, i.e., in the second term of the right-hand side of Eq. (7.30); (ii) the first term on the right-hand sides of Eqs. (7.29) and (7.30) represents the shot noise, which originates from the quantum fluctuations of the input field. Obviously, the relations (7.29) and (7.30) also apply to the L beam, with the change of superscript R to L.

Next we must study the motion of the end mirror, which is influenced by both the passing gravitational wave and the radiation-pressure force:

$$x_{\rm E} = x_{\rm E}^{\rm GW} + x_{\rm E}^{\rm BA}\,, \quad \ddot{x}_{\rm BA} = \frac{1}{m} F_{\rm RP}. \tag{7.33}$$

Here $x_{\rm BA}$ is the displacement induced by the radiation-pressure force, or the *back action* of the measurement process, which eventually gives rise to the *radiation-pressure noise.* The radiation-pressure force $F_{\rm RP}$ comes from both the L and R beams:

$$F_{\rm RP}(t) = \frac{\mathcal{A}}{2\pi} \sum_{k=1}^{\mathcal{B}} \left\{ \left[E^{\rm RE\,in}(t-(2k-1)L/c) \right]^2 + \left[E^{\rm LE\,in}(t-(2k-1)L/c) \right]^2 \right\}. \tag{7.34}$$

However, we are only interested in the *fluctuating* and *low-frequency* part (in the gravitational-wave band) of the force, which comes from the beating of the sideband fields against the carrier:

$$F_{\rm RP}^{\rm fluc}(t) = \frac{D\mathcal{A}}{2\pi} \sum_{k=1}^{\mathcal{B}} \left[E_1^{\rm RE\,in}(t-(2k-1)L/c) + E_1^{\rm LE\,in}(t-(2k-1)L/c) \right]. \tag{7.35}$$

Combining Eqs. (7.33) and (7.35) and transforming into the frequency domain, we obtain the Fourier transform of the mirror displacement in the GW frequency band [note that Eq. (7.31) is used again]:

$$\tilde{x}_{\rm E} = \tilde{x}_{\rm E}^{\rm GW} - \frac{4}{m\Omega^2 c} \sqrt{2\hbar\omega_0 I_{\rm b}} \left(\frac{\sin \mathcal{B}\Omega L/c}{\sin \Omega L/c} \right) e^{i\mathcal{B}\Omega L/c} \left(\frac{a_1^{\rm RE} + a_1^{\rm LE}}{2} \right). \tag{7.36}$$

This, when combined with Eq. (7.30), yields:

$$b_2^{\rm RE} = e^{2i\mathcal{B}\Omega L/c} a_2^{\rm RE} - \frac{16 I_{\rm b}\omega_0}{m\Omega^2 c^2}\left(\frac{\sin\mathcal{B}\Omega L/c}{\sin\Omega L/c}\right)^2 e^{2i\mathcal{B}\Omega L/c}\left(\frac{a_1^{\rm RE}+a_1^{\rm LE}}{2}\right) + \frac{2\omega_0}{c}\sqrt{\frac{2I_{\rm b}}{\hbar\omega_0}}\left(\frac{\sin\mathcal{B}\Omega L/c}{\sin\Omega L/c}\right)\tilde{x}_{\rm E}^{\rm GW}\,. \tag{7.37}$$

The second term on the right-hand side is the radiation-pressure noise.

In reality, the ITM's, the beamsplitter, and the connection mirror will also move under the radiation-pressure force (but they are *not* influenced by gravitational waves). When $\mathcal{B} \gg 1$ and $\Omega L/c \ll 1$, only the ITM need be taken into account, in addition to the ETM, and the effect is just a doubling of the radiation pressure noise in Eq. (7.37). Hence we arrive at the complete input-output relation for the East arm, put into a more compact form (similar to those in KLMTV [18]):

$$b_1^{\rm RE} = e^{2i\Psi_{\rm DL}} a_1^{\rm RE}\,, \tag{7.38}$$

$$b_2^{\rm RE} = e^{2i\Psi_{\rm DL}}\left[a_2^{\rm RE} - \mathcal{K}_{\rm DL}(a_1^{\rm RE}+a_1^{\rm LE})\right] + e^{i\Psi_{\rm DL}}\frac{\sqrt{2\mathcal{K}_{\rm DL}}}{h_{\rm SQL}}\sqrt{2}\,\tilde{x}_E^{\rm GW}/L\,; \tag{7.39}$$

where

$$\Psi_{\rm DL} = \mathcal{B}\Omega L/c\,, \tag{7.40}$$

$$\mathcal{K}_{\rm DL} = \frac{16 I_{\rm b}\omega_0}{m\Omega^2 c^2}\left(\frac{\sin\mathcal{B}\Omega L/c}{\sin\Omega L/c}\right)^2 = \frac{8 I_{\rm c}\omega_0}{m\mathcal{B}\Omega^2 c^2}\left(\frac{\sin\mathcal{B}\Omega L/c}{\sin\Omega L/c}\right)^2\,. \tag{7.41}$$

The input-output relation for the L beam can be obtained by exchanging RE and LE in Eqs. (7.38) and (7.39).

7.6.2 Ring-shaped Fabry-Perot cavity (FP)

Again, let us consider the East arm. Suppose again initially that only the ETM is allowed to move (motions of the other two ring-cavity–mirrors will be accounted for later). Then the input-output relations for the fields immediately inside the ITM can be obtained easily from the results for optical delay lines [Eqs. (7.38)–(7.41), with a factor 1/2 multiplying the radiation-pressure noise term, since again as a first step we are only allowing the ETM to move]:

$$B_1^{\rm RE} = e^{2i\Omega L/c} A_1^{\rm RE}\,, \tag{7.42}$$

$$B_2^{\rm RE} = e^{2i\Omega L/c}\left[A_2^{\rm RE} - \mathcal{K}_{\rm DL}^{\mathcal{B}=1}\left(\frac{A_1^{\rm RE}+A_1^{\rm LE}}{2}\right)\right] + e^{i\Omega L/c}\frac{\sqrt{2\mathcal{K}_{\rm DL}^{\mathcal{B}=1}}}{h_{\rm SQL}}\sqrt{2}\,\tilde{x}_{\rm E}/L\,; \tag{7.43}$$

where

$$\mathcal{K}_{\rm DL}^{B=1} = \frac{8 I_{\rm c}\omega_0}{m\Omega^2 c^2}\,. \tag{7.44}$$

As before, the input-output relation for the L beam is obtained by exchanging RE and LE. The fields outside the ITM are related to these fields by

$$b_{1,2}^{\rm RE} = -\sqrt{R}a_{1,2}^{\rm RE} + \sqrt{T}B_{1,2}^{\rm RE}\,, \qquad A_{1,2}^{\rm RE} = \sqrt{T}a_{1,2}^{\rm RE} + \sqrt{R}B_{1,2}^{\rm RE}\,; \tag{7.45}$$

$$b_{1,2}^{\rm LE} = -\sqrt{R}a_{1,2}^{\rm LE} + \sqrt{T}B_{1,2}^{\rm LE}\,, \qquad A_{1,2}^{\rm LE} = \sqrt{T}a_{1,2}^{\rm LE} + \sqrt{R}B_{1,2}^{\rm LE}\,. \tag{7.46}$$

Here T and R are the power transmissivity and reflectivity of the ITM, $T + R = 1$. Combining Eqs. (7.42)–(7.46), we obtain

$$b_1^{\rm RE} = \frac{e^{2i\Omega L/c} - \sqrt{R}}{1 - e^{2i\Omega L/c}\sqrt{R}} a_1^{\rm RE}\,, \tag{7.47}$$

$$\begin{aligned} b_2^{\rm RE} &= \frac{e^{2i\Omega L/c} - \sqrt{R}}{1 - e^{2i\Omega L/c}\sqrt{R}} \left[a_2^{\rm RE} - \frac{T\mathcal{K}_{\rm DL}^{\mathcal{B}=1}}{1 - 2\sqrt{R}\cos(2\Omega L/c) + R}\left(\frac{a_1^{\rm RE} + a_1^{\rm LE}}{2}\right)\right] \\ &\quad + \frac{e^{i\Omega L/c}\sqrt{T}}{1 - e^{2i\Omega L/c}\sqrt{R}} \frac{\sqrt{2\mathcal{K}_{\rm DL}^{\mathcal{B}=1}}}{h_{\rm SQL}} \sqrt{2}\,\tilde{x}_{\rm E}/L\,. \end{aligned} \tag{7.48}$$

As before, the first terms on the right-hand sides of Eqs. (7.47) and (7.48) represent the shot noise, the second term on the right-hand side of Eq. (7.48) represents the radiation-pressure noise, and the third term on the right-hand side of Eq. (7.48) is the gravitational-wave signal. Again, other optical elements besides the ETM can also be influenced by the radiation-pressure force; but when $T \ll 1$, we need only consider the radiation-pressure force on the ITM and the other cavity mirror near the ITM, in addition to the ETM. Suppose all three sides of the ring cavity are on resonance with the carrier frequency. Then it is obvious that, at leading order in $\Omega L/c$ and T, the momentum fluxes carried by the beams at the locations of the three mirrors (to and from within the cavity) are the same. However, since the in-cavity light is incident on the two near mirrors at 45°, the motions of each of them induced by the radiation pressure is $1/\sqrt{2}$ that of the ITM, and are in the directions normal to their surfaces. Also because their motion directions are again 45° to the propagation direction of the beams, the resulting radiation-pressure noise is reduced by an additional $1/\sqrt{2}$. In the end, the net radiation-pressure noise due to the two near mirrors is equal to that due to the end mirror. Doubling the radiation-pressure noise in Eq. (7.48), we obtain the input-output relation of the ring cavity, which we put into a form similar to that of the optical delay line:

$$b_1^{\rm RE} = e^{2i\Psi_{\rm FP}} a_1^{\rm RE}\,, \tag{7.49}$$

$$b_2^{\rm RE} = e^{2i\Psi_{\rm FP}}\left[a_2^{\rm RE} - \mathcal{K}_{\rm FP}(a_1^{\rm RE} + a_1^{\rm LE})\right] + e^{i\Psi_{\rm FP}} \frac{\sqrt{2\mathcal{K}_{\rm FP}}}{h_{\rm SQL}} \sqrt{2}\,\tilde{x}_E^{\rm GW}/L\,; \tag{7.50}$$

with

$$\Psi_{\rm FP} = \arg \frac{e^{i\Omega L/c}}{1 - e^{2i\Omega L/c}\sqrt{R}} = \arctan\left(\frac{1+\sqrt{R}}{1-\sqrt{R}} \tan\frac{\Omega L}{c}\right), \tag{7.51}$$

$$\mathcal{K}_{\rm FP} = \left(\frac{T}{1 - 2\sqrt{R}\cos 2\Omega L/c + R}\right) \frac{8 I_{\rm c} \omega_0}{m\Omega^2 c^2}. \tag{7.52}$$

7.7 Bibliography

[1] A. Abramovici et al., Science **256**, 325 (1992); B. Caron et al., Class. Quantum Grav. **14**, 1461 (1997); B. Willke et al., Class. Quantum Grav. **19** (2002) M. Ando et al., Phys. Rev. Lett. **86**, 3950 (2001).

[2] K. S. Thorne, *"The scientific case for mature LIGO interferometers,"* LIGO Document Number P000024-00-R, `www.ligo.caltech.edu/docs/P/P000024-00.pdf`; C. Cutler and K. S. Thorne, *"An overview of gravitational-wave sources,"* `gr-qc/0204090`.

[3] E. Gustafson, D. Shoemaker, K.A. Strain and R. Weiss, *"LSC White paper on detector research and development,"* LIGO Document Number T990080-00-D, `www.ligo.caltech.edu/docs/T/T990080-00.pdf`.

[4] LCGT Collaboration, Int. J. of Mod. Phys. D, Vol. **8**, 557 (1999).

[5] G. Sagnac, C. R. Acad. Sci. **95**, 1410 (1913).

[6] R. W. P. Drever, *"Interferometric detectors for gravitational ratiaion,"* in *Gravitational Radiation,* edited by N. Deruelle and T. Piran (North-Holland, Amsterdam, 1983), p 321-338.

[7] K.-X. Sun, M. M. Fejer, E. Gustafson and R. L. Byer, Phys. Rev. Lett, **76**, 3053 (1996); The TAMA team, *Gravitational-wave Astronomy,* Report for the Japanese government, Kyoto University, pp 286–287 (1992); R. Weiss, in NSF proposal, 1987.

[8] D. A. Shaddock, M. B. Gray and D. E. McClelland, Appl. Opt. **37**, 7995 (1998).

[9] B. Petrovichev, M. Gray and D. McClelland, Gen. Rel. and Grav., **30**, 1055 (1998).

[10] J. Mizuno, A. Rüdiger, R. Schilling, W. Winkler and K. Danzmann, Opt. Comm. **138**, 383 (1997)

[11] K.-X. Sun and R. L. Byer, Gen. Rel. and Grav., **23**, 567 (1998); S. Traeger, P. Beyersdorf, L. Goddard, E.K. Gustafson, M. M. Fejer and R. L. Byer, Opt. Lett. **25**, 722 (2000); P. Beyersdorf, *The Polarization Sagnac interferometer for gravitational-wave detection,* Ph.D. Thesis, Stanford University, Feb. 2001.

[12] Although there are not yet detailed papers on EURO or LIGO-III, they have been discussed within the gravitational-wave community as long-range plans.

[13] V.B. Braginsky, Sov. Phys. JETP **26**, 831 (1968); V.B. Braginsky and Yu.I. Vorontsov, Sov. Phys. Usp. **17**, 644 (1975); V.B. Braginsky, Yu.I. Vorontsov, and F.Ya. Khalili, Sov. Phys. JETP, **46**, 705 (1977).

[14] V. B. Braginsky and F. Ya. Khalili, *Quantum Measurement,* edited by K. S. Thorne (Cambridge University Press, Cambridge, England, 1992).

Class. Quantum Grav. **19** 1569 (2002).

[15] B. J. Meers, Phys. Rev. **D 38**, 2317 (1988); J. Y. Vinet, B. Meers, C. N. Man and Brillet, Phys. Rev. **D 38**, 433 (1988).

[16] J. Mizuno, *"Comparison of optical configurations for laser-interferometric gravitational-wave detectors,"* PhD thesis, Max-Planck Institut f́ur Quantenoptik, Garching, Germany, 1995; J. Mizuno, K. A. Strain, P. G. Nelson, J. M. Chen, R. Schilling, A. Rüdiger, W. Winkler and K. Danzmann, Phys. Lett. **A 175**, 273 (1993) .

[17] S. P. Vyatchanin and A. B. Matsko, JETP **77**, 218 (1993) ; S.P. Vyatchanin and E. A. Zubova, Phys. Lett. **A 203**, 269 (1995); S. P. Vyatchanin and A. B. Matsko, JETP **82**, 1007 (1996); ibid. JETP **83**, 690 (1996); S. P. Vyatchanin, Phys. Lett. **A 239**, 201 (1998).

[18] H. J. Kimble, Yu. Levin, A. B. Matsko, K. S. Thorne and S. P. Vyatchanin, Phys. Rev. D **65**, 022002 (2002).

[19] V. B. Braginsky and F. Ya. Khalili, Phys. Lett. **A 147**, 251 (1990).

[20] V. B. Braginsky, M. L. Gorodetsky, F. Ya. Khalili, and K. S. Thorne, Phys. Rev. **D 61**, 044002 (2000).

[21] P. M. Purdue, Phys. Rev. **D 66**, 022001 (2002).

[22] P. Purdue and Y. Chen, submitted to Phys. Rev. **D**.

[23] R. Weise, MIT Quarterly Progress Report (Research Laboratory of Electronics) **105**, 54 (1972)

[24] W. Unruh, Phys. Rev. **D 19**, 2888 (1979); C. M. Caves, K. S. Thorne, R. W. P. Drever, V. D. Sandberg, and M. Zimmerman, Rev. Mod. Phys., **52**, 341 (1980).

[25] C. M. Caves, in *Quantum Optics, Experimental Gravitation, and Measurement Theory,* edited by P. Meystre and M. O. Scully (Plenum, New York, 1982), p. 567.

[26] C. M. Caves and B. L. Schumaker, Phys. Rev. **A 31** 3068 (1985); B. L. Schumaker and C. M. Caves, Phys. Rev. **A 31** 3093 (1985).

[27] T. Niebauer, Phys. Rev. **A 43**, 5022 (1991); B. J. Meers and K. Strain, Phys. Rev. **A 44**, 4693 (1991).

Chapter 8

Detection template families for gravitational waves from the final stages of binary–black-hole inspirals: Nonspinning case

We investigate the problem of detecting gravitational waves from binaries of nonspinning black holes with masses $m = 5$–$20M_\odot$, moving on quasicircular orbits, which are arguably the most promising sources for first-generation ground-based detectors. We analyze and compare all the currently available post–Newtonian approximations for the relativistic two-body dynamics; for these binaries, different approximations predict different waveforms. We then construct examples of detection template families that embed all the approximate models, and that could be used to detect the true gravitational-wave signal (but not to characterize accurately its physical parameters). We estimate that the fitting factor for our detection families is $\gtrsim 0.95$ (corresponding to an event-rate loss $\lesssim 15\%$) and we estimate that the discretization of the template family, for $\sim 10^4$ templates, increases the loss to $\lesssim 20\%$.

Originally published as A. Buonanno, Y. Chen and M. Vallisneri, Phys. Rev. D **67**, 024016 (2003).

8.1 Introduction

A network of broadband ground-based laser interferometers, aimed at detecting gravitational waves (GWs) in the frequency band 10–10^3 Hz, is currently beginning operation and, hopefully, will start the first science runs within this year (2002). This network consists of the British–German GEO, the American Laser Interferometer Gravitational-wave Observatory (LIGO), the Japanese TAMA and the Italian–French VIRGO (which will begin operating in 2004) [1].

The first detection of gravitational waves with LIGO and VIRGO interferometers is likely to

come from binary black-hole systems where each black hole has a mass [1] of a few $M_\odot$, and the total mass is roughly in the range 10–40$M_\odot$ [2], and where the orbit is quasicircular (it is generally assumed that gravitational radiation reaction will circularize the orbit by the time the binary is close to the final coalescence [3]). It is easy to see why. Assuming for simplicity that the GW signal comes from a quadrupole-governed, Newtonian inspiral that ends at a frequency outside the range of good interferometer sensitivity, the signal-to-noise ratio S/N is $\propto \mathcal{M}^{5/6}/d$ (See, e.g., Ref. [4]), where $\mathcal{M} = M\eta^{3/5}$ is the *chirp mass* (with $M = m_1 + m_2$ the total mass and $\eta = m_1 m_2/M^2$), and d is the distance between the binary and the Earth. Therefore, for a given signal-to-noise detection threshold (see Sec. 8.2) and for equal-mass binaries ($\eta = 1/4$), the larger is the total mass, the larger is the distance d that we are able to probe. [In Sec. 8.5 we shall see how this result is modified when we relax the assumption that the signal ends outside the range of good interferometer sensitivity.]

For example, a black-hole–black hole binary (BBH) of total mass $M = 20M_\odot$ at 100 Mpc gives (roughly) the same S/N as a neutron-star–neutron-star binary (BNS) of total mass $M = 2.8M_\odot$ at 20 Mpc. The expected measured-event rate scales as the third power of the probed distance, although of course it depends also on the system's coalescence rate per unit volume in the universe. To give some figures, computed using LIGO-I's sensitivity specifications, if we assume that BBHs originate from main-sequence binaries [5], the estimated detection rate per year is $\lesssim 4 \times 10^{-3}$–0.6 at 100 Mpc [6, 7], while if globular clusters are considered as incubators of BBHs [8] the estimated detection rate per year is ~ 0.04–0.6 at 100 Mpc [6, 7]; by contrast, the BNS detection rate per year is in the range 3×10^{-4}–0.3 at 20 Mpc [6, 7]. The very large cited ranges for the measured-event rates reflect the uncertainty implicit in using population-synthesis techniques and extrapolations from the few known galactic BNSs to evaluate the coalescence rates of binary systems. [In a recent article [9], Miller and Hamilton suggest that four-body effects in globular clusters might enhance considerably the BBH coalescence rate, brightening the prospects for detection with first-generation interferometers; the BBHs involved might have relatively high BH masses ($\sim 100M_\odot$) and eccentric orbits, and they will not be considered in this chapter.]

The GW signals from standard comparable-mass BBHs with $M = 10$–$40M_\odot$ contain only few (50–800) cycles in the LIGO–VIRGO frequency band, so we might expect that the task of modeling the signals for the purpose of data analysis could be accomplished easily. However, the frequencies of best interferometer sensitivity correspond to GWs emitted during the final stages of the inspiral, where the post–Newtonian (PN) expansion [10], which for compact bodies is essentially an expansion in the characteristic orbital velocity v/c, begins to fail. It follows that these sources require a very careful analysis. As the two bodies draw closer, and enter the nonlinear, strong-curvature phase, the motion becomes relativistic, and it becomes harder and harder to extract reliable information

[1] These are binaries formed either from massive main-sequence progenitor binary stellar systems (field binaries), or from capture processes in globular clusters or galactic centers (capture binaries).

from the PN series. For example, using the Keplerian formula $v = (\pi M f_{\rm GW})^{1/3}$ [where $f_{\rm GW}$ is the GW frequency] and taking $f_{\rm GW} = 153$ Hz [the LIGO-I peak-sensitivity frequency] we get $v(M) = 0.14(M/M_\odot)^{1/3}$; hence, for BNSs $v(2.8M_\odot) = 0.2$, but for BBHs $v(20M_\odot) = 0.38$ and $v(40M_\odot) = 0.48$.

The final phase of the inspiral (at least when BH spins are negligible) includes the transition from the adiabatic inspiral to the plunge, beyond which the motion of the bodies is driven (almost) only by the conservative part of the dynamics. Beyond the plunge, the two BHs merge, forming a single rotating BH in a very excited state; this BH then eases into its final stationary Kerr state, as the oscillations of its quasinormal modes die out. In this phase the gravitational signal will be a superposition of exponentially damped sinusoids (ringdown waveform). For nonspinning BBHs, the plunge starts roughly at the innermost stable circular orbit (ISCO) of the BBH. At the ISCO, the GW frequency [evaluated in the Schwarzschild test-mass limit as $f_{\rm GW}^{\rm ISCO}(M) \simeq 0.022/M$] is $f_{\rm GW}^{\rm ISCO}(20M_\odot) \simeq 220\,{\rm Hz}$ and $f_{\rm GW}^{\rm ISCO}(30M_\odot) \simeq 167\,{\rm Hz}$. These frequencies are well inside the LIGO and VIRGO bands.

The data analysis of inspiral, merger (or plunge), and ringdown of compact binaries was first investigated by Flanagan and Hughes [11], and more recently by Damour, Iyer and Sathyaprakash [12]. Flanagan and Hughes [11] model the inspiral using the standard quadrupole prediction (see, e.g., Ref. [4]), and assume an ending frequency of $0.02/M$ (the point where, they argue, PN and numerical-relativity predictions start to deviate by $\sim 5\%$ [13]). They then use a crude argument to estimate upper limits for the total energy radiated in the merger phase ($\sim 0.1M$) and in the ringdown phase ($\sim 0.03M$) of maximally spinning BBH coalescences. Damour, Iyer and Sathyaprakash [12] study the nonadiabatic PN-resummed model for non spinning BBHs of Refs. [14, 15, 16], where the plunge can be seen as a natural continuation of the inspiral [15] rather than a separate phase; the total radiated energy is $0.007M$ in the merger and $0.007M$ in the ringdown [17]. (All these values for the energy should be also compared with the value, 0.025–$0.03M$, estimated recently in Ref. [18] for the plunge and ringdown for non spinning BBHs.) When we deal with nonadiabatic models, we too shall choose not to separate the various phases. Moreover, because the ringdown phase does not give a significant contribution to the signal-to-noise ratio for $M \leq 200M_\odot$ [11, 12], we shall not include it in our investigations.

BHs could have large spins: various studies [19, 20] have shown that when this is the case, the time evolution of the GW phase and amplitude during the inspiral will be significantly affected by spin-induced modulations and irregularities. These effects can become dramatic, if the two BH spins are large and are not aligned or antialigned with the orbital angular momentum. There is a considerable chance that the analysis of interferometer data, carried out without taking into account spin effects, could miss the signals from spinning BBHs altogether. We shall tackle the crucial issue of spin in Chapter 9.

The purpose of this chapter is to discuss the problem of the failure of the PN expansion during the last stages of inspiral for nonspinning BHs, and the possible ways to deal with this failure. This problem is known in the literature as the intermediate binary black hole (IBBH) problem [21]. Despite the considerable progress made by the numerical-relativity community in recent years [13, 22, 23, 24], a reliable estimate of the waveforms emitted by BBHs is still some time ahead (some results for the plunge and ringdown waveforms were obtained very recently [18], but they are not very useful for our purposes, because they do not include the last stages of the inspiral before the plunge, and their initial data are endowed with large amounts of spurious GWs). To tackle the delicate issue of the late orbital evolution of BBHs, various nonperturbative analytical approaches to that evolution (also known as PN resummation methods) have been proposed [25, 14, 15, 16].

The main features of PN resummation methods can be summarized as follows: (i) they provide an analytic (gauge-invariant) resummation of the orbital energy function and gravitational flux function (which, as we shall see in Sec. 8.3, are the two crucial ingredients to compute the gravitational waveforms in the adiabatic limit); (ii) they can describe the motion of the bodies (and provide the gravitational waveform) beyond the adiabatic approximation; and (iii) in principle they can be extended to higher PN orders. More importantly, they can provide initial dynamical data for the two BHs at the beginning of the plunge (such as their positions and momenta), which can be used (in principle) in numerical relativity to help build the initial gravitational data (the metric and its time derivative) and then to evolve the full Einstein equations through the merger phase. However, these resummation methods are based on some assumptions that, although plausible, have not been proved: for example, when the orbital energy and the gravitational flux functions are derived in the comparable-mass case, it is assumed that they are smooth deformations of the analogous quantities in the test-mass limit. Moreover, in the absence of both exact solutions and experimental data, we can test the robustness and reliability of the resummation methods only by internal convergence tests.

In this chapter we follow a more conservative point of view. We shall maintain skepticism about waveforms emitted by BBH with $M = 10$–$40 M_\odot$ and evaluated from PN calculations, as well as all other waveforms ever computed for the late BBH inspiral and plunge, and we shall develop families of search templates that incorporate this skepticism. More specifically, we shall be concerned only with detecting BBH GWs, and not with extracting physical parameters, such as masses and spins, from the measured GWs. The rationale for this choice is twofold. First, detection is the more urgent problem at a time when GW interferometers are about to start their science runs; second, a viable detection strategy must be constrained by the computing power available to process a very long stream of data, while the study of detected signals to evaluate physical parameters can concentrate many resources on a small stretch of detector output. In addition, as we shall see in Sec. 8.6, and briefly discuss in Sec. 8.6.4, the different PN methods will give different parameter estimations for

the same waveform, making a full parameter extraction fundamentally difficult.

This is the strategy that we propose: we guess (and hope) that the conjunction of the waveforms from all the post–Newtonian models computed to date spans a region in signal space that includes (or almost includes) the true signal. We then choose a *detection* (or *effective*) template family that approximates very well all the PN expanded and resummed models (henceforth denoted as *target models*). If our guess is correct, the *effectualness* [25] of the effective model in approximating the targets (i.e., its capability of reproducing their signal shapes) should be indicative of its effectualness in approximating the true signals. Because our goal is the *detection* of BBH GWs, we shall not require the detection template family to be *faithful* [25] (i.e., to have a small bias in the estimation of the masses).

As a backup strategy, we require the detection template family to embed the targets in a signal space of higher dimension (i.e., with more parameters), trying to guess the functional directions in which the true signals might lie with respect to the targets (of course, this guess is rather delicate!). So, the detection template families constructed in this chapter cannot be guaranteed to capture the true signal, but they should be considered as indications.

This Chapter is organized as follows. In Sec. 8.2, we briefly review the theory of matched-filtering GW detections, which underlies the searches for GWs from inspiraling binaries. Then in Secs. 8.3, 8.4, and 8.5 we present the target models and give a detailed analysis of the differences between them, both from the point of view of the orbital dynamics and of the gravitational waveforms. More specifically, in Sec. 8.3 we introduce the two-body adiabatic models, both PN expanded and resummed; in Sec. 8.4 we introduce nonadiabatic approximations to the two-body dynamics; and in Sec. 8.5 we discuss the signal-to-noise ratios obtained for the various two-body models. Our proposals for the detection template families are discussed in the Fourier domain in Sec. 8.6, and in the time domain in Sec. 8.7, where we also build the mismatch metric [26, 27] for the template banks and use it to evaluate the number of templates needed for detection. Section 8.8 summarizes our conclusions.

Throughout this chapter we adopt the LIGO noise curve given in Fig. 8.1 and Eq. (8.28), and used also in Ref. [12]. Because the noise curve anticipated for VIRGO [see Fig. 8.1] is quite different (both at low frequencies, and in the location of its peak-sensitivity frequency) our results cannot be applied naively to VIRGO. We plan to repeat our study for VIRGO in the near future.

8.2 The theory of matched-filtering signal detection

The technique of matched-filtering detection for GW signals is based on the systematic comparison of the measured detector output s with a bank of theoretical *signal templates* $\{u_i\}$ that represent a good approximation to the class of physical signals that we seek to measure. This theory was developed by many authors over the years, who have published excellent expositions [28, 30, 31, 25, 27, 11, 29, 32, 33, 34, 39, 40, 41, 55]. In the following, we summarize the main results and equations that are relevant to our purposes, and we establish our notation.

8.2.1 The statistical theory of signal detection

The detector output s consists of noise n and possibly of a true gravitational signal h_i (part of a family $\{h_i\}$ of signals generated by different sources for different source parameters, detector orientations, and so on). Although we may be able to characterize the properties of the noise in several ways, each separate *realization* of the noise is unpredictable, and it might in principle fool us by hiding a physical signal (hence the risk of a *false dismissal*) or by simulating one (*false alarm*). Thus, the problem of signal detection is essentially probabilistic. In principle, we could try to evaluate the conditional probability $P(h|s)$ that the measured signal s actually contains one of the h_i. In practice, this is inconvenient, because the evaluation of $P(h|s)$ requires the knowledge of the *a priori* probability that a signal belonging to the family $\{h_i\}$ is present in s.

What we can do, instead, is to work with a *statistic* (a functional of s and of the h_i) that (for different realizations of the noise) will be distributed around low values if the physical signal h_i is absent, and around high value if the signal is present. Thus, we shall establish a *decision rule* as follows [31]: we will claim a detection if the value of a statistic (for a given instance of s and for a specific h_i) is higher than a predefined threshold. We can then study the probability distribution of the statistic to estimate the probability of false alarm and of false dismissal. The steps involved in this statistical study are easily laid down for a generic model of noise, but it is only in the much simplified case of *normal noise* that it is possible to obtain manageable formulas; and while noise will definitely *not* be normal in a real detector, the Gaussian formulas can still provide useful guidelines for the detection problems. Eventually, the statistical analysis of detector search runs will be carried out with numerical Montecarlo techniques that make use of the measured characteristics of the noise. So throughout this chapter we shall always assume Gaussian noise.

The statistic that is generally used is based on the symmetric inner product $\langle g, h\rangle$ between two real signals g and h, which represents essentially the cross-correlation between g and h, weighted to emphasize the correlation at the frequencies where the detector sensitivity is better. We follow

Cutler and Flanagan's conventions [34] and define

$$\langle g, h\rangle = 2\int_{-\infty}^{+\infty} \frac{\tilde{g}^*(f)\tilde{h}(f)}{S_n(|f|)}df = 4\,\mathrm{Re}\int_0^{+\infty} \frac{\tilde{g}^*(f)\tilde{h}(f)}{S_n(f)}df, \tag{8.1}$$

where $S_n(f)$, the one-sided *noise power spectral density*, is given by

$$\overline{\tilde{n}^*(f_1)\tilde{n}(f_2)} = \frac{1}{2}\delta(f_1 - f_2)S_n(f_1) \quad \text{for } f_1 > 0, \tag{8.2}$$

and $S_n(f_1) = 0$ for $f_1 < 0$. We then define the *signal-to-noise ratio* ρ (for the measured signal s after filtering by h_i), as

$$\rho(h_i) = \frac{\langle s, h_i\rangle}{\mathrm{rms}\,\langle n, h_i\rangle} = \frac{\langle s, h_i\rangle}{\sqrt{\langle h_i, h_i\rangle}}, \tag{8.3}$$

where the equality follows because $\overline{\langle h_i, n\rangle\langle n, h_i\rangle} = \langle h_i, h_i\rangle$ (see, e.g., [31]). In the case of Gaussian noise, it can be proved that this filtering technique is *optimal*, in the sense that it maximizes the probability of correct detection for a given probability of false detection.

In the case when $s = n$, and when noise is Gaussian, it is easy to prove that ρ is a normal variable with a mean of zero and a variance of one. If instead $s = h_i + n$, then ρ is a normal variable with mean $\sqrt{\langle h_i, h_i\rangle}$ and unit variance. The *threshold* ρ_* for detection is set as a tradeoff between the resulting false-alarm probability,

$$\mathcal{F} = \sqrt{\frac{1}{2\pi}}\int_{\rho_*}^{+\infty} e^{-\rho^2/2}d\rho = \frac{1}{2}\mathrm{erfc}\,(\rho_*/\sqrt{2}) \tag{8.4}$$

(where erfc is the *complementary error function* [35]), and the probability of correct detection

$$\mathcal{D} = \frac{1}{2}\mathrm{erfc}\,[(\rho_* - \sqrt{\langle h_i, h_i\rangle})/\sqrt{2}] \tag{8.5}$$

(the probability of false dismissal is just $1 - \mathcal{D}$).

8.2.2 Template families and extrinsic parameters

We can now go back to the initial strategy of comparing the measured signal against a bank of $\mathcal{N}_i$ templates $\{u_i\}$ that represent a plurality of sources of different types and physical parameters. For each stretch s of detector output, we shall compute the signal-to-noise ratio $\langle s, u_i\rangle/\sqrt{\langle u_i, u_i\rangle}$ for all the u_i, and then apply our rule to decide whether the physical signal corresponding to any one of the u_i is actually present within s [4]. Of course, the threshold ρ_* needs to be adjusted so that the probability $\mathcal{F}_{\mathrm{tot}}$ of false alarm *over all the templates* is still acceptable. Under the assumption that all the inner products $\langle n, u_i\rangle$ of the templates with noise alone are statistically independent variables [this hypothesis entails $\langle u_i, u_j\rangle \simeq 0$], $\mathcal{F}_{\mathrm{tot}}$ is just $1 - (1 - \mathcal{F})^{\mathcal{N}_i} \sim \mathcal{N}_i\mathcal{F}$. If the templates are not

statistically independent, this number is an upper limit on the false alarm rate. However, we first need to note that, for any template u_i, there are a few obvious ways (parametrized by the so-called *extrinsic parameters*) of changing the signal shape that do not warrant the inclusion of the modified signals as separate templates [2]

The extrinsic parameters are the signal *amplitude*, *phase* and *time of arrival*. Any true signal h can be written in all generality as

$$h(t) = \mathcal{A}_h a_h[t - t_h] \cos[\Phi_h(t - t_h) + \phi_h], \tag{8.6}$$

where $a_h(t) = 0$ for $t < 0$, where $\Phi_h(0) = 0$, and where $a_h(t)$ is normalized so that $\langle h, h\rangle = \mathcal{A}_h^2$. While the template bank $\{u_i\}$ must contain signal shapes that represent all the physically possible functional forms $a(t)$ and $\Phi(t)$, it is possible to modify our search strategy so that the variability in $\mathcal{A}_h$, ϕ_h and t_h is automatically taken into account without creating additional templates.

The signal amplitude is the simplest extrinsic parameter. It is expedient to *normalize* the templates u_i so that $\langle u_i, u_i\rangle = 1$, and $\rho(u_i) = \langle s, u_i\rangle$. Indeed, throughout the rest of this chapter we shall always assume normalized templates. If s contains a scaled version $h_i = \mathcal{A}u_i$ of a template u_i (here $\mathcal{A}$ is known as the signal *strength*), then $\overline{\rho(u_i)} = \mathcal{A}$. However, the statistical distribution of ρ is the same *in the absence of the signal*. Then the problem of detection signals of known shape and unknown amplitude is easily solved by using a single normalized template and the same threshold ρ_* as used for the detection of completely known signals [31]. Quite simply, the stronger an actual signal, the easier it will be to reach the threshold.

We now look at phase, and we try to match h with a continuous one-parameter subfamily of templates $u(\phi_t; t) = a_h(t) \cos[\Phi_h(t) + \phi_t]$. It turns out that for each time signal shape $\{a(t), \Phi(t)\}$, we need to keep in our template bank only two copies of the corresponding u_i, for $\phi_t = 0$ and $\phi_t = \pi/2$, and that the signal to noise of the detector output s against u_i, for the best possible value of ϕ_t, is automatically found as [31]

$$\rho_\phi = \max_{\phi_t} \langle s, u_i(\phi_t)\rangle = \sqrt{|\langle s, u_i(0)\rangle|^2 + |\langle s, u_i(\pi/2)\rangle|^2}\,, \tag{8.7}$$

where $u_i(0)$ and $u_i(\pi/2)$ have been orthonormalized. The statistical distribution of the phase-maximized statistic ρ_ϕ, for the case of (normal) noise alone, is the *Raleigh distribution* [31]

$$p_0(\rho_\phi) = \rho_\phi e^{-\rho_\phi^2/2}, \tag{8.8}$$

[2] Parameters that are not extrinsic are known as *intrinsic*. This nomenclature was introduced by Owen [27], but the underlying concept had been present in the data-analysis literature for a long time (see, e.g., [31]). Sathyaprakash [41] draws the same distinction between *kinematical* and *dynamical* parameters.

and the false-alarm probability for a threshold $\rho_{\phi *}$ is just

$$\mathcal{F} = e^{-\rho_{\phi *}^2/2}. \tag{8.9}$$

Throughout this chapter, we will find it useful to consider inner products that are maximized (or minimized) with respect to the phases of *both* templates and reference signals. In particular, we shall follow Damour, Iyer and Sathyaprakash in making a distinction between the *best match* or *maxmax match*

$$\mathrm{maxmax}\langle h, u_i\rangle = \max_{\phi_h}\max_{\phi_t}\langle h(\phi_h), u_i(\phi_t)\rangle, \tag{8.10}$$

which represents the most favorable combination of phases between the signals h and u_i, and the *minmax match*

$$\mathrm{minmax}\langle h, u_i\rangle = \min_{\phi_h}\max_{\phi_t}\langle h(\phi_h), u_i(\phi_t)\rangle, \tag{8.11}$$

which represents the safest estimate in the realistic situation, where we cannot choose the phase of the physical measured signal, but only of the template used to match the signal. Damour, Iyer and Sathyaprakash [see Appendix B of Ref. [25]] show that both quantities are easily computed as

$$\left(\begin{array}{c}\mathrm{maxmax}\\ \mathrm{minmax}\end{array}\right) = \left\{\frac{A+B}{2} \pm \left[\left(\frac{A-B}{2}\right)^2 + C^2\right]^{1/2}\right\}^{1/2}, \tag{8.12}$$

where

$$\begin{aligned} A &= \langle h(0), u_i(0)\rangle^2 + \langle h(0), u_i(\pi/2)\rangle^2, && (8.13)\\ B &= \langle h(\pi/2), u_i(0)\rangle^2 + \langle h(\pi/2), u_i(\pi/2)\rangle^2, && (8.14)\\ C &= \langle h(0), u_i(0)\rangle\langle h(\pi/2), u_i(0)\rangle + && (8.15)\\ &\quad \langle h(0), u_i(\pi/2)\rangle\langle h(\pi/2), u_i(\pi/2)\rangle. \end{aligned}$$

In these formulas we have assumed that the two bases $\{h(0), h(\pi/2)\}$ and $\{u_i(0), u_i(\pi/2)\}$ have been orthonormalized.

The *time of arrival* t_h is an extrinsic parameter because the signal to noise for the normalized, time-shifted template $u(t - t_0)$ against the signal s is just

$$\langle s, u(t_0)\rangle = 4\,\mathrm{Re}\int_0^{+\infty}\frac{\tilde{s}^*(f)\tilde{u}(f)}{S_n(f)}e^{i2\pi f t_0}df, \tag{8.16}$$

where we have used a well-known property of the Fourier transform of time-shifted signals. These integrals can be computed at the same time for all the time of arrivals $\{t_0\}$, using a *fast Fourier transform* technique that requires $\sim N_s \log N_s$ operations (where N_s is the number of the samples

that describe the signals) as opposed to $\sim N_s^2$ required to compute all the integrals separately [36]. Then we can look for the optimal t_0 that yields the maximum signal to noise.

We now go back to adjusting the threshold ρ_* for a search over a vast template bank, using the estimate (8.9) for the false-alarm probability. Assuming that the statistics ρ_ϕ for each signal shape *and* starting time are independent, we require that

$$e^{-\rho_{\phi*}^2/2} \simeq \frac{\mathcal{F}_{\rm tot}}{N_{\rm times}N_{\rm shapes}}, \tag{8.17}$$

or

$$\rho_* \simeq \sqrt{2(\log N_{\rm times} + \log N_{\rm shapes} - \log \mathcal{F}_{\rm tot})}. \tag{8.18}$$

It is generally assumed that $N_{\rm times} \sim 3 \times 10^{10}$ (equivalent to templates displaced by 0.01 s over one year [37, 11]) and that the false-alarm probability $\mathcal{F}_{\rm tot} \sim 10^{-3}$. Using these values, we find that an increase of ρ_* by about $\sim 3\%$ is needed each time we increase $N_{\rm shapes}$ by one order of magnitude. So there is a tradeoff between the improvement in signal-to-noise ratio obtained by using more signal shapes and the corresponding increase in the detection threshold for a fixed false-alarm probability.

8.2.3 Imperfect detection and discrete families of templates

There are two distinct reasons why the detection of a physical signal h by matched filtering with a template bank $\{u_i\}$ might result in signal-to-noise ratios lower than the optimal signal-to-noise ratio,

$$\rho_{\rm opt} = \sqrt{\langle h, h\rangle}. \tag{8.19}$$

First, the templates, understood as a *continuous* family $\{u(\lambda^A)\}$ of functional shapes indexed by one or more *intrinsic parameters* λ^A (such as the masses, spins, etc.), might give an unfaithful representation of h, introducing errors in the representation of the phasing or the amplitude. The loss of signal to noise due to unfaithful templates is quantified by the *fitting factor* FF, introduced by Apostolatos [38], and defined by

$$\mathrm{FF}(h, u(\lambda^A)) = \frac{\max_{\lambda^A} \langle h, u(\lambda^A)\rangle}{\sqrt{\langle h, h\rangle}}. \tag{8.20}$$

In general, we will be interested in the FF of the continuous template bank in representing a *family* of physical signals $\{h(\theta^A)\}$, dependent upon one or more physical parameters θ^A: so we shall write $\mathrm{FF}(\theta^A) = \mathrm{FF}(h(\theta^A), u(\lambda^A))$. Although it is convenient to index the template family by the same physical parameters θ^A that characterize $h(\theta^A)$, this is by no means necessary; the template parameters λ^A might be a different number than the physical parameters (indeed, this is desirable when the θ^A get to be very many), and they might not carry any direct physical meaning. Notice

also that the value of the FF will depend on the parameter range chosen to maximize the λ^A.

The second reason why the signal-to-noise will be degraded with respect to its optimal value is that, even if our templates are perfect representations of the physical signals, in practice we will not adopt a continuous family of templates, but we will be limited to using a discrete bank $\{u_i \equiv u(\lambda_i^A)\}$. This loss of signal to noise depends on how finely templates are laid down over parameter space [39, 40, 41]; a notion of metric in template space (the *mismatch metric* [27, 26, 42]) can be used to guide the disposition of templates so that the loss (in the perfect-template abstraction) is limited to a fixed, predetermined value, the *minimum match* MM, introduced in Refs. [39, 27], and defined by

$$\mathrm{MM} = \min_{\hat{\lambda}^A} \max_{\lambda_i^A} \langle u(\hat{\lambda}^A), u(\lambda_i^A)\rangle = \min_{\hat{\lambda}^A} \max_{\Delta\lambda_i^A} \langle u(\hat{\lambda}^A), u(\hat{\lambda}^A + \Delta\lambda_i^A)\rangle, \tag{8.21}$$

where $\Delta\lambda_i^A \equiv \lambda_i^A - \hat{\lambda}^A$. The *mismatch metric* $g_{BC}(\hat{\lambda}^A)$ for the template space $\{u(\lambda^A)\}$ is obtained by expanding the inner product (or *match*) $\langle u(\hat{\lambda}^A), u(\hat{\lambda}^A + \Delta\lambda^A)\rangle$ about its maximum of 1 at $\Delta\lambda^A = 0$:

$$\langle u(\hat{\lambda}^A), u(\hat{\lambda}^A + \Delta\lambda^A)\rangle = M(\hat{\lambda}^A, \hat{\lambda}^A + \Delta\lambda^A) = 1 + \frac{1}{2}\left.\frac{\partial^2 M}{\partial\Delta\lambda^B \partial\Delta\lambda^C}\right|_{\hat{\lambda}^A} \Delta\lambda^B \Delta\lambda^C + \cdots, \tag{8.22}$$

so the *mismatch* $1 - \mathrm{M}$ between $u(\hat{\lambda}^A)$ and the nearby template $u(\hat{\lambda}^A + \Delta\lambda^A)$ can be seen as the square of the proper distance in a differential manifold indexed by the coordinates λ^A [27],

$$1 - M(\hat{\lambda}^A, \hat{\lambda}^A + \Delta\lambda^A) = g_{BC}\Delta\lambda^B\Delta\lambda^C, \tag{8.23}$$

where

$$g_{BC} = -\frac{1}{2}\left.\frac{\partial^2 M}{\partial\Delta\lambda^B \partial\Delta\lambda^C}\right|_{\hat{\lambda}^A}. \tag{8.24}$$

If, for simplicity, we lay down the n-dimensional discrete template bank $\{u(\lambda_i^A)\}$ along a hypercubical grid of cellsize dl in the metric g_{AB} (a grid in which all the templates on nearby corners have a mismatch of dl with each other), the minimum match occurs when $\hat{\lambda}^A$ lies exactly at the center of one of the hypercubes: then $1 - \mathrm{MM} = n(dl/2)^2$. Conversely, given MM, the volume of the corresponding hypercubes is given by $V_{\mathrm{MM}} = (2\sqrt{(1-\mathrm{MM})/n})^n$. The number of templates required to achieve a certain MM is obtained by integrating the proper volume of parameter space within the region of physical interest, and then dividing by V_{MM}:

$$\mathcal{N}[g, \mathrm{MM}] = \frac{\int \sqrt{|g|} d\lambda^A}{\left(2\sqrt{[1-\mathrm{MM}]/n}\right)^n}. \tag{8.25}$$

In practice, if the metric is not constant over parameter space it will not be possible to lay down the templates on an exact hypercubical grid of cellsize dl, so $\mathcal{N}$ will be somewhat higher than predicted by Eq. (8.25). However, we estimate that this number should be correct within a factor of two,

which is adequate for our purposes.

In the worst possible case, the combined effect of unfaithful modeling (FF < 1) and discrete template family (MM < 1) will degrade the optimal signal to noise by a factor of about FF$+$MM-1. This estimate for the total signal-to-noise loss is exact when, in the space of signals, the two segments that join $h(\hat{\theta}^A)$ to its projection $u(\hat{\lambda}^A)$ and $u(\hat{\lambda}^A)$ to the nearest discrete template $u(\hat{\lambda}_i^A)$ can be considered orthogonal:

$$\langle h(\theta^A) - u(\hat{\lambda}^A), u(\hat{\lambda}^A) - u(\hat{\lambda}_i^A)\rangle \simeq 0. \tag{8.26}$$

This assumption is generally very accurate if FF and MM are small enough, as in this chapter; so we will adopt this estimate. However, it is possible to be more precise, by defining an *external metric* $g^{\rm E}_{AB}$ [26, 43] that characterizes directly the mismatch between $h(\hat{\theta}^A)$ and a template $u(\hat{\lambda}^A + \Delta\lambda^A)$ that is displaced with respect to the template $u(\hat{\lambda}^A)$ that is yields the maximum match with $h(\hat{\theta}^A)$.

Since the strength of gravity-wave signals scales as the inverse of the distance [3], the matched-filtering scheme, with a chosen signal-to-noise threshold ρ_*, will allow the reliable detection of a signal h, characterized by the signal strength $\mathcal{A}_{d_0} = \sqrt{\langle h, h\rangle}$ at the distance d_0, out to a maximum distance

$$\frac{d_{\rm max}}{d_0} = \frac{\mathcal{A}_{d_0}}{\rho_*}. \tag{8.27}$$

If we assume that the measured GW events happen with a homogeneous event rate throughout the accessible portion of the universe, then the detection rate will scale as $d^3_{\rm max}$. It follows that the use of unfaithful, discrete templates $\{u_i\}$ to detect the signal h will effectively reduce the signal strength, and therefore $d_{\rm max}$, by a factor FF$+$MM-1. This loss in the signal-to-noise ratio can also be seen as an increase in the detection threshold ρ_* necessary to achieve the required false-alarm rate, because the imperfect templates introduce an element of uncertainty. In either case, the detection rate will be reduced by a factor $({\rm FF} + {\rm MM} - 1)^3$.

8.2.4 Approximations for detector noise spectrum and gravitational-wave signal

For LIGO-I we use the analytic fit to the noise power spectral density given in Ref. [12], and plotted in Fig. 8.1:

$$\frac{S_n(f)}{{\rm Hz}^{-1}} = 9.00 \times 10^{-46} \left[\left(4.49\frac{f}{f_0}\right)^{-56} + 0.16\left(\frac{f}{f_0}\right)^{-4.52} + 0.52 + 0.32\left(\frac{f}{f_0}\right)^{2}\right], \tag{8.28}$$

[3] The amplitude of the measured gravity-wave signals depends not only on the actual distance to the source, but also on the reciprocal orientation between the detector and the direction of propagation of the waves. A combination of several detectors will be needed, in general, to evaluate the distance to a gravity-wave source starting from the signal-to-noise ratio alone.

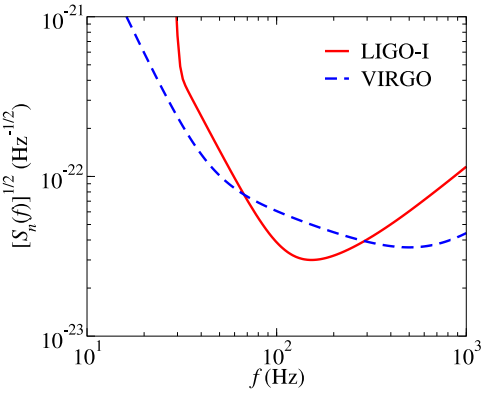

Figure 8.1: Square root of the noise spectral density $\sqrt{S_n(f)}$ versus frequency f, for LIGO-I [Eq. (8.28)], and VIRGO (from Tab. IV of Ref. [12]).

where $f_0 = 150$ Hz. The first term in the square brackets represents seismic noise, the second and third, thermal noise, and the fourth, photon shot noise.

Throughout this chapter, we shall compute BBH waveforms in the quadrupole approximation (we shall compute the phase evolution of the GWs with the highest possible accuracy, but we shall omit all harmonics higher than the quadrupole, and we shall omit post–Newtonian corrections to the amplitude; this is a standard approach in the field, see, e.g., [10]). The signal received at the interferometer can then be written as [4, 30]

$$h(t) = \frac{\Theta}{d_{\rm L}} M\eta(\pi M f_{\rm GW})^{2/3} \cos\varphi_{\rm GW}, \tag{8.29}$$

where f and $\varphi_{\rm GW}$ are the instantaneous GW frequency and phase at the time t, $d_{\rm L}$ is the *luminosity distance*, M and η are respectively the BBH total mass $m_1 + m_2$ and the dimensionless mass ratio $m_1 m_2/M^2$, and where we have taken $G = c = 1$. The coefficient Θ depends on the inclination of the BBH orbit with respect to the plane of the sky, and on the polarization and direction of propagation of the GWs with respect to the orientation of the interferometer. Finn and Chernoff [30] examine the distribution of Θ, and show that $\Theta_{\rm max} = 4$, while $\mathrm{rms}\,\Theta = 8/5$. We shall use this last value when we compute optimal signal-to-noise ratios. The waveform given by Eq. (8.29), after dropping the factor $\Theta M\eta/d_{\rm L}$, is known as *restricted waveform*.

model	shorthand	evolution equation	section
adiabatic model with Taylor-expanded energy $\mathcal{E}(v)$ and flux $\mathcal{F}(v)$	T(nPN, mPN; $\hat{\theta}$)	energy-balance equation	Sec. 8.3.1
adiabatic model with Padé-expanded energy $\mathcal{E}(v)$ and flux $\mathcal{F}(v)$	P(nPN, mPN; $\hat{\theta}$)	energy-balance equation	Sec. 8.3.2
adiabatic model with Taylor-expanded energy $\mathcal{E}(v)$ and flux $\mathcal{F}(v)$ in the stationary-phase approximation	SPA(nPN $\equiv$ mPN)	energy-balance equation in the freq. domain	Sec. 8.6.6
nonadiabatic Hamiltonian model with Taylor-expanded GW flux	HT(nPN, mPN; $\hat{\theta}$)	Hamilton equations	Sec. 8.4.1
nonadiabatic Hamiltonian model with Padé-expanded GW flux	HP(nPN, mPN; $\hat{\theta}$)	Hamilton equations	Sec. 8.4.1
nonadiabatic Lagrangian model	L(nPN, mPN)	$\mathbf{F} = m\mathbf{a}$	Sec. 8.4.2
nonadiabatic effective-one-body model with Taylor-expanded GW flux	ET(nPN, mPN; $\hat{\theta}$; $\tilde{z}_1$, $\tilde{z}_2$)	eff. Hamilton equations	Sec. 8.4.3
nonadiabatic effective-one-body model with Padé-expanded GW flux	EP(nPN, mPN; $\hat{\theta}$; $\tilde{z}_1$, $\tilde{z}_2$)	eff. Hamilton equations	Sec. 8.4.3

Table 8.1: Post–Newtonian models of two-body dynamics defined in this chapter. The notation X(nPN, mPN; $\hat{\theta}$) denotes the model X, with terms up to order nPN for the conservative dynamics, and with terms up to order mPN for radiation-reaction effects; for $m \geq 3$ we also need to specify the arbitrary flux parameter $\hat{\theta}$ (see Sec. 8.3.1); for $n \geq 3$, the effective-one-body models need also two additional parameters $\tilde{z}_1$ and $\tilde{z}_2$ (see Sec. 8.4.3).

8.3 Adiabatic models

We turn, now, to a discussion of the currently available mathematical models for the inspiral of BBHs. Table 8.1 shows a list of the models that we shall consider in this chapter, together with the shorthands that we shall use to denote them. We begin in this section with adiabatic models. BBH adiabatic models treat the orbital inspiral as a quasistationary sequence of circular orbits, indexed by the invariantly defined velocity

$$v = (M\dot{\varphi})^{1/3} = (\pi M f_{\rm GW})^{1/3}. \tag{8.30}$$

The evolution of the inspiral (and in particular of the orbital phase φ) is completely determined by the *energy-balance equation*

$$\frac{d\mathcal{E}(v)}{dt} = -\mathcal{F}(v), \tag{8.31}$$

This equation relates the time derivative of the energy function $\mathcal{E}(v)$ (which is given in terms of the total relativistic energy $\mathcal{E}_{\rm tot}$ by $\mathcal{E} = \mathcal{E}_{\rm tot} - m_1 - m_2$, and which is conserved in absence of radiation reaction) to the gravitational flux (or luminosity) function $\mathcal{F}(v)$. Both functions are known for quasicircular orbits as a PN expansion in v. It is easily shown that Eq. (8.31) is equivalent to the system (see, e.g., Ref. [25])

$$\frac{d\varphi_{\rm GW}}{dt} = \frac{2v^3}{M}\,, \qquad \frac{dv}{dt} = -\frac{\mathcal{F}(v)}{M\,d\mathcal{E}(v)/dv}. \tag{8.32}$$

In accord with the discussion around Eq. (8.29), we shall only consider the *restricted waveform* $h(t) = v^2 \cos\varphi_{\rm GW}(t)$, where the GW phase $\varphi_{\rm GW}$ is twice the orbital phase φ.

8.3.1 Adiabatic PN expanded models

The equations of motion for two compact bodies at 2.5PN order were first derived in Refs. [44]. The 3PN equations of motion have been obtained by two separate groups of researchers: Damour, Jaranowski and Schäfer [45] used the Arnowitt–Deser–Misner (ADM) canonical approach, while Blanchet, Faye and de Andrade [46] worked with the PN iteration of the Einstein equations in the harmonic gauge. Recently Damour and colleagues [47], working in the ADM formalism and applying dimensional regularization, determined uniquely the *static parameter* that enters the 3PN equations of motion [45, 46] and that was until then unknown. In this chapter we shall adopt their value for the static parameter. Thus at present the energy function $\mathcal{E}$ is known up to 3PN order.

The gravitational flux emitted by compact binaries was first computed at 1PN order in Ref. [48]. It was subsequently determined at 2PN order with a formalism based on multipolar and post–Minkowskian approximations, and, independently, with the direct integration of the relaxed Einstein

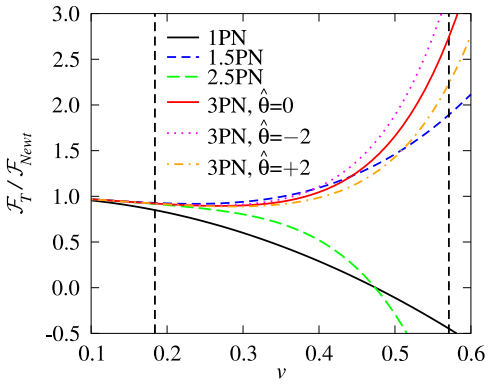

Figure 8.2: Normalized flux function $\mathcal{F}_{T_N}/\mathcal{F}_{\rm Newt}$ versus v, at different PN orders for equal-mass binaries, $\eta = 0.25$. Note that the 1.5PN and 2PN flux, and the 3PN and 3.5PN flux, are so close that they cannot be distinguished in these plots. The two long-dashed vertical lines correspond to $v \simeq 0.18$ and $v \simeq 0.53$; they show the velocity range that corresponds to the LIGO frequency band $40 \leq f_{\rm GW} \leq 240$ Hz for BBHs with total mass in the range 10–$40 M_\odot$.

equations [49]. Nonlinear effects of tails at 2.5PN and 3.5PN orders were computed in Refs. [50]. More recently, Blanchet and colleagues derived the gravitational-flux function for quasicircular orbits up to 3.5PN order [52, 51]. However, at 3PN order [52, 51] the gravitational-flux function depends on an arbitrary parameter $\hat{\theta}$ that could not be fixed in the regularization scheme used by these authors.

PN energy and flux

Denoting by $\mathcal{E}_{T_N}$ and $\mathcal{F}_{T_N}$ the $N^{\rm th}$-order Taylor approximants (T-approximants) to the energy and the flux functions, we have

$$\mathcal{E}_{T_{2N}}(v) \equiv \mathcal{E}_{\rm Newt}(v) \sum_{k=0}^{N} \mathcal{E}_k(\eta)\, v^{2k}\,, \tag{8.33}$$

$$\mathcal{F}_{T_N}(v) \equiv \mathcal{F}_{\rm Newt}(v) \sum_{k=0}^{N} \mathcal{F}_k(\eta)\, v^{k}\,, \tag{8.34}$$

where "Newt" stands for Newtonian order, and the subscripts $2N$ and N stand for post^{2N}–Newtonian and post^{N}–Newtonian order. The quantities in these equations are

$$\mathcal{E}_{\rm Newt}(v) = -\frac{1}{2}\eta\, v^2\,, \qquad \mathcal{F}_{\rm Newt}(v) = \frac{32}{5}\eta^2\, v^{10}\,, \tag{8.35}$$

$$\mathcal{E}_0(\eta) = 1\,, \qquad \mathcal{E}_1(\eta) = -\frac{3}{4} - \frac{\eta}{12}\,, \qquad \mathcal{E}_2(\eta) = -\frac{27}{8} + \frac{19}{8}\eta - \frac{\eta^2}{24}\,, \tag{8.36}$$

$$\mathcal{E}_3(\eta) = -\frac{675}{64} + \left(\frac{34445}{576} - \frac{205}{96}\pi^2\right)\eta - \frac{155}{96}\eta^2 - \frac{35}{5184}\eta^3\,, \tag{8.37}$$

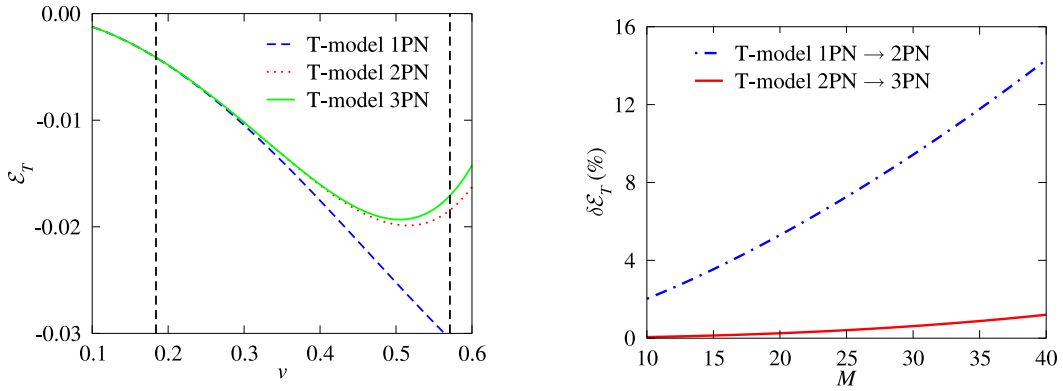

Figure 8.3: In the left panel, we plot the energy function $\mathcal{E}_{T_N}$ versus v, at different PN orders, for $\eta = 0.25$. The two long-dashed vertical lines in the left figure correspond to $v \simeq 0.18$ and $v \simeq 0.53$; they show the velocity range that corresponds to the LIGO frequency band $40 \leq f_{\rm GW} \leq 240$ Hz, for BBHs with total mass in the range 10–$40M_\odot$. In the right panel, we plot the percentage difference $\delta\mathcal{E}_{T_N} = 100\,|(\mathcal{E}_{T_{N+1}} - \mathcal{E}_{T_N})/\mathcal{E}_{T_N}|$ versus the total mass M, for $N = 1, 2$, at the LIGO-I peak-sensitivity GW frequency, $f_{\rm peak} = 153$ Hz [note: $v_{\rm peak} = (\pi M f_{\rm peak})^{1/3}$].

$$\mathcal{F}_0(\eta) = 1\,, \qquad \mathcal{F}_1(\eta) = 0\,, \qquad \mathcal{F}_2(\eta) = -\frac{1247}{336} - \frac{35}{12}\eta\,, \qquad \mathcal{F}_3(\eta) = 4\pi\,, \tag{8.38}$$

$$\mathcal{F}_4(\eta) = -\frac{44711}{9072} + \frac{9271}{504}\eta + \frac{65}{18}\eta^2\,, \qquad \mathcal{F}_5(\eta) = -\left(\frac{8191}{672} + \frac{535}{24}\eta\right)\pi\,, \tag{8.39}$$

$$\begin{aligned}\mathcal{F}_6(\eta) \;=\; & \frac{6643739519}{69854400} + \frac{16}{3}\,\pi^2 - \frac{1712}{105}\,\gamma_E - \frac{856}{105}\,\log(16v^2) + \\ & \left(-\frac{2913613}{272160} + \frac{41}{48}\,\pi^2 - \frac{88}{3}\,\hat{\theta}\right)\eta - \frac{94403}{3024}\,\eta^2 - \frac{775}{324}\,\eta^3\,,\end{aligned} \tag{8.40}$$

$$\mathcal{F}_7(\eta) = \left(-\frac{16285}{504} + \frac{176419}{1512}\eta + \frac{19897}{378}\eta^2\right)\pi\,. \tag{8.41}$$

Here $\eta = m_1 m_2/(m_1+m_2)^2$, γ_E is Euler's gamma, and $\hat{\theta}$ is the arbitrary 3PN flux parameter [52, 51]. From Tab. I of Ref. [51] we read that the extra number of GW cycles accumulated by the PN terms of a given order decreases (roughly) by an order of magnitude when we increase the PN order by one. Hence, we find it reasonable to expect that at 3PN order the parameter $\hat{\theta}$ should be of order unity, and we choose as typical values $\hat{\theta} = 0, \pm 2$.

In Fig. 8.2 we plot the normalized flux $\mathcal{F}_{T_N}/\mathcal{F}_{\rm Newt}$ as a function of v at various PN orders for the equal mass case $\eta = 0.25$. To convert v to a GW frequency we can use

$$f_{\rm GW} \simeq 3.2 \times 10^4 \left(\frac{20M_\odot}{M}\right) v^3. \tag{8.42}$$

The two long-dashed vertical lines in Fig. 8.2 correspond to $v \simeq 0.18$ and $v \simeq 0.53$; they show the velocity range that corresponds to the LIGO frequency band $40 \leq f_{\rm GW} \leq 240$ Hz for BBHs with total

M	$f_{\rm GW}$(Hz) at MECO					$f_{\rm GW}$(Hz) at ISCO			
	T (1PN)	T (2PN)	T (3PN)	P (2PN)	P (3PN)	H (1PN)	E (1PN)	E (2PN)	E (3PN)
$(5+5)M_\odot$	3376	886	832	572	866	183	446	473	570
$(10+10)M_\odot$	1688	442	416	286	433	92	223	236	285
$(15+15)M_\odot$	1125	295	277	191	289	61	149	158	190
$(20+20)M_\odot$	844	221	208	143	216	46	112	118	143

Table 8.2: Location of the MECO/ISCO. The first six columns show the GW frequency at the Maximum binding Energy for Circular Orbits (MECO), computed using the T- and P-approximants to the energy function; the remaining columns show the GW frequency at the Innermost Stable Circular Orbit (ISCO), computed using the H-approximant to the energy, and using the EOB improved Hamiltonian (8.90) with $\tilde{z}_1 = \tilde{z}_2 = 0$. For the H-approximant the ISCO exists only at 1PN order.

mass in the range 10–40$M_\odot$. At the LIGO-I peak-sensitivity frequency, which is 153 Hz according to our noise curve, and for a (10+10)$M_\odot$ BBH, we have $v \simeq 0.362$; and the percentage difference between subsequent PN orders is Newt $\to$ 1PN : -58%; 1PN $\to$ 1.5PN : $+142\%$; 1.5PN $\to$ 2PN : -0.2%; 2PN $\to$ 2.5PN : -34%; 2.5PN $\to$ 3PN($\hat{\theta} = 0$) : $+43\%$; 3PN $\to$ 3.5PN($\hat{\theta} = 0$) : $+0.04\%$. The percentage difference between the 3PN fluxes with $\hat{\theta} = \pm 2$ is $\sim 7\%$. It is interesting to notice that while there is a big difference between the 1PN and 1.5PN orders, and between the 2PN and 2.5PN orders, the 3PN and 3.5PN fluxes are rather close. Of course this observation is insufficient to conclude that the PN sequence is converging at 3.5PN order.

In the left panel of Fig. 8.3, we plot the T-approximants for the energy function versus v, at different PN orders, while in the right panel we plot (as a function of the total mass M, and at the LIGO-I peak-sensitivity GW frequency $f_{\rm peak} = 153$ Hz) the percentage difference of the energy function between T-approximants to the energy function of successive PN orders. We note that the 1PN and 2PN energies are distant, but the 2PN and 3PN energies are quite close.

Definition of the models

The evolution equations (8.32) for the adiabatic inspiral lose validity (the inspiral ceases to be adiabatic) a little before v reaches $v_{\rm MECO}^{T_N}$, where MECO stands for Maximum–binding-Energy Circular Orbit [53, 64]. This $v_{\rm MECO}^{T_N}$ is computed as the value of v at which $d\mathcal{E}_{T_N}(v)/dv = 0$. In building our adiabatic models we evolve Eqs. (8.32) right up to $v_{\rm MECO}$ and stop there. We shall refer to the frequency computed by setting $v = v_{\rm MECO}$ in Eq. (8.42) as the *ending frequency* for these waveforms, and in Tab. 8.2 we show this frequency for some BH masses. However, for certain binaries, the 1PN and 2.5PN flux functions can go to zero before $v = v_{\rm MECO}^{T_N}$ [see Fig. 8.2]. In those cases we choose as the ending frequency the value of $f = v^3/(\pi M)$ where $\mathcal{F}(v)$ becomes 10% of $\mathcal{F}_{\rm Newt}(v)$. [When using the 2.5PN flux, our choice of the ending frequency differs from the one used in Ref. [12], where the authors stopped the evolution at the GW frequency corresponding to the Schwarzschild innermost stable circular orbit. For this reason there are some differences between our overlaps and theirs.]

We shall refer to the models discussed in this section as T(nPN, mPN), where nPN (mPN)

N	$\langle \mathrm{T}_N, \mathrm{T}_{N+1} \rangle$							
	$(5+20)M_\odot$		$(10+10)M_\odot$				$(15+15)M_\odot$	
0	0.432		0.553	(0.861,	19.1,	0.241)	0.617	
1	0.528	[0.638]	0.550	(0.884,	22.0,	0.237)	0.645	[0.712]
2 ($\hat{\theta} = +2$)	0.482	[0.952]	0.547	(0.841,	18.5,	0.25)	0.563	[0.917]
2 ($\hat{\theta} = -2$)	0.457	[0.975]	0.509	(0.821,	18.7,	0.241)	0.524	[0.986]

Table 8.3: Test for the Cauchy convergence of the T-approximants. The values quoted are maxmax matches obtained by maximizing with respect to the extrinsic parameters, but not to the intrinsic parameters (i.e., the matches are computed for T waveforms with the same masses, but different PN orders). Here we define $\mathrm{T}_0 = \mathrm{T}(0,0)$, $\mathrm{T}_1 = \mathrm{T}(1,1.5)$, $\mathrm{T}_2 = \mathrm{T}(2,2.5)$, $\mathrm{T}_3 = \mathrm{T}(3,3.5,\hat{\theta})$. In the Newtonian case, $\mathrm{T}_0 = (0,0)$, the MECO does not exist and we stop the integration of the balance equation at $v = 1$. The values in brackets, "[...]," are obtained by setting $\mathrm{T}_2 = \mathrm{T}(2,2)$ instead of $\mathrm{T}(2,2.5)$; the values in parentheses, "(...)," are obtained by maximizing with respect to the extrinsic *and* intrinsic parameters, and they are shown together with the T_{N+1} parameters M and η where the maxima are achieved. In all cases the integration of the equations is started at a GW frequency of 20 Hz.

denotes the maximum PN order of the terms included for the energy (the flux). We shall consider $(n\mathrm{PN}, m\mathrm{PN}) = (1,1.5), (2,2), (2,2.5)$ and $(3,3.5,\hat{\theta})$ [at 3PN order we need to indicate also a choice of the arbitrary flux parameter $\hat{\theta}$].

Waveforms and matches

In Tab. 8.3, for three typical choices of BBH masses, we perform a convergence test using Cauchy's criterion [25], namely, the sequence T_N converges if and only if for each k, $\langle \mathrm{T}_N, \mathrm{T}_{N+k} \rangle \to 1$ as $N \to \infty$. One requirement of this criterion is that $\langle \mathrm{T}_N, \mathrm{T}_{N+1} \rangle \to 1$ as $N \to \infty$, and this is what we test in Tab. 8.3, setting $\mathrm{T}_N \equiv \mathrm{T}(N, N+0.5)$. The values quoted assume maximization on the extrinsic parameters but not on the intrinsic parameters. [For the case $(10+10)M_\odot$, we show in parentheses the maxmax matches obtained by maximizing with respect to the intrinsic and extrinsic parameters, together with the intrinsic parameters M and η of T_{N+1} where the maxima are attained.] These results suggest that the PN expansion is far from converging. However, the very low matches between $N = 1$ and $N = 2$, and between $N = 2$ and $N = 3$, are due to the fact that the 2.5PN flux goes to zero before the MECO can be reached. If we redefine T_2 as $\mathrm{T}(2,2)$ instead of $\mathrm{T}(2,2.5)$, we obtain the higher values shown in brackets is Tab. 8.3.

In Fig. 8.4, we plot the frequency-domain amplitude of the T-approximated waveforms, at different PN orders, for a $(15+15)M_\odot$ BBH. The Newtonian amplitude, $\mathcal{A}_{\mathrm{Newt}}(f) = f^{-7/6}$, is also shown for comparison. In the $\mathrm{T}(1,1)$ and $\mathrm{T}(2,2.5)$ cases, the flux function goes to zero before $v = v^{T_N}_{\mathrm{MECO}}$; this means that the radiation-reaction effects become negligible during the last phase of evolution, so the binary is able to spend many cycles at those final frequencies, skewing the amplitude with respect to the Newtonian result. For $\mathrm{T}(2,2)$, $\mathrm{T}(3,3)$ and $\mathrm{T}(3,3.5)$, the evolution is stopped at $v = v^{T_N}_{\mathrm{MECO}}$, and, although $f^{\mathrm{GW}}_{\mathrm{MECO}} \simeq 270$–$300$ Hz (see Tab. 8.2) the amplitude starts to deviate from

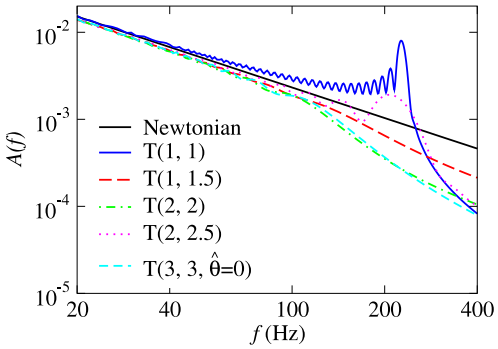

Figure 8.4: Frequency-domain amplitude versus frequency for the T-approximated (restricted) waveforms, at different PN orders, for a $(15 + 15)M_\odot$ BBH. The $\mathrm{T}(3, 3.5, \hat{\theta} = 0)$ curve, not plotted, is almost identical to the $\mathrm{T}(3, 3, \hat{\theta} = 0)$ curve.

$f^{-7/6}$ around 100 Hz. This is a consequence of the abrupt termination of the signal in the time domain.

The effect of the arbitrary parameter $\hat{\theta}$ on the T waveforms can be seen in Tab. 8.11 in the intersection between the rows and columns labeled $\mathrm{T}(3, 3.5, +2)$ and $\mathrm{T}(3, 3.5, -2)$. For three choices of BBH masses, this table shows the maxmax matches between the *search* models at the top of the columns and the *target* models at the left end of the rows, *maximized over the mass parameters of the search models in the columns*. These matches are rather high, suggesting that for the range of BBH masses we are concerned, the effect of changing $\hat{\theta}$ is just a remapping of the BBH mass parameters. Therefore, in the following we shall consider only the case of $\hat{\theta} = 0$.

A quantitative measure of the difference between the $\mathrm{T}(2, 2)$, $\mathrm{T}(2, 2.5)$ and $\mathrm{T}(3, 3.5)$ waveforms can be seen in Tab. 8.9 in the intersection between the rows and columns labeled $\mathrm{T}(\ldots)$. For four choices of BBH masses, this table shows the maxmax matches between the search models in the columns and the target models in the rows, maximized over the search-model parameters M and η; in the search, η is restricted to its physical range $0 < \eta \leq 1/4$, where 0 corresponds to the test-mass limit, while $1/4$ is obtained in the equal-mass case. These matches can be interpreted as the fitting factors [see Eq. (8.20)] for the projection of the target models onto the search models. For the case $\mathrm{T}(2, 2.5)$ the values are quite low: if the $\mathrm{T}(3, 3.5)$ waveforms turned out to give the true physical signals and if we used the $\mathrm{T}(2, 2.5)$ waveforms to detect them, we would lose $\sim$ 32–49% of the events. The model $\mathrm{T}(2, 2)$ would do match better, although it would still not be very faithful. Once more, the difference between $\mathrm{T}(2, 2)$ and $\mathrm{T}(2, 2.5)$ is due to the fact that the 2.5PN flux goes to zero before the BHs reach the MECO.

8.3.2 Adiabatic PN resummed methods: Padé approximants

The PN approximation outlined above can be used quite generally to compute the shape of the GWs emitted by BNSs or BBHs, but it *cannot be trusted* in the case of binaries with comparable masses in the range $M \simeq 10$–$40 M_\odot$, because for these sources LIGO and VIRGO will detect the GWs emitted when the motion is strongly relativistic, and the convergence of the PN series is very slow. To cope with this problem, Damour, Iyer and Sathyaprakash [25] proposed a new class of models based on the systematic application of Padé resummation to the PN expansions of $\mathcal{E}(v)$ and $\mathcal{F}(v)$. This is a standard mathematical technique used to accelerate the convergence of poorly converging or even divergent power series.

If we know the function $g(v)$ only through its Taylor approximant $G_N(v) = g_0 + g_1\, v + \cdots + g_N\, v^N \equiv T_N[g(v)]$, the central idea of Padé resummation [54] is the replacement of the power series $G_N(v)$ by the sequence of rational functions

$$P_K^M[g(v)] = \frac{A_M(v)}{B_K(v)} \equiv \frac{\sum_{j=0}^M a_j\, v^j}{\sum_{j=0}^K b_j\, v^j}\,, \tag{8.43}$$

with $M + K = N$ and $T_{M+K}[P_K^M(v)] = G_N(v)$ (without loss of generality, we can set $b_0 = 1$). We expect that for $M, K \to +\infty$, $P_K^M[g(v)]$ will converge to $g(v)$ more rapidly than $T_N[g(v)]$ converges to $g(v)$ for $N \to +\infty$.

PN energy and flux

Damour, Iyer and Sathyaprakash [25], and then Damour, Schäfer and Jaranowski [16], proposed the following Padé-approximated (P-approximated) $\mathcal{E}_{P_N}(v)$ and $\mathcal{F}_{P_N}(v)$ (for $N = 2, 3$):

$$\mathcal{E}_{P_N} = \sqrt{1 + 2\eta\left(\sqrt{1 + e_{P_N}(v)} - 1\right)} - 1\,, \tag{8.44}$$

$$\mathcal{F}_{P_N} = \frac{32}{5}\eta^2\, v^{10}\, \frac{1}{1 - v/v_{\rm pole}^{P_N}}\, f_{P_N}(v,\eta)\,, \tag{8.45}$$

where

$$e_{P_2}(v) = -v^2\, \frac{1 + \frac{1}{3}\eta - \left(4 - \frac{9}{4}\eta + \frac{1}{9}\eta^2\right)\, v^2}{1 + \frac{1}{3}\eta - \left(3 - \frac{35}{12}\eta\right)\, v^2}\,, \tag{8.46}$$

$$e_{P_3}(v) = -v^2\, \frac{1 - \left(1 + \frac{1}{3}\eta + w_3(\eta)\right)\, v^2 - \left(3 - \frac{35}{12}\eta - \left(1 + \frac{1}{3}\eta\right)\, w_3(\eta)\right)\, v^4}{1 - w_3(\eta)\, v^2}\,, \tag{8.47}$$

$$w_3 = \frac{40}{36 - 35\eta}\left[\frac{27}{10} + \frac{1}{16}\left(\frac{41}{4}\pi^2 - \frac{4309}{15}\right)\eta + \frac{103}{120}\eta^2 - \frac{1}{270}\eta^3\right]\,, \tag{8.48}$$

$$f_{P_2}(v) = \left(1 + \frac{c_1\, v}{1 + \frac{c_2\, v}{1 + \ldots}}\right)^{-1} \quad \text{(up to } c_5\text{)}, \tag{8.49}$$

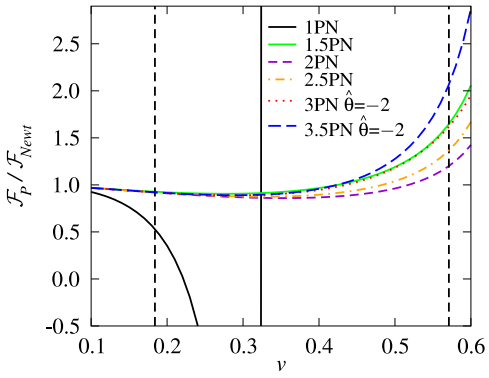

Figure 8.5: Normalized flux function $\mathcal{F}_{P_N}/\mathcal{F}_{\rm Newt}$ versus v, at different PN orders. The two long-dashed vertical lines give $v \simeq 0.18$ and $v \simeq 0.53$; they show the velocity range that corresponds to the LIGO frequency band $40 \leq f_{\rm GW} \leq 240$ Hz for BBHs with total mass in the range 10–$40 M_\odot$. Compare with Fig. 8.2.

$$f_{P_3}(v) = \left(1 - \frac{1712}{105}\, v^6 \, \log \frac{v}{v^{P_2}_{\rm MECO}}\right) \left(1 + \frac{c_1\, v}{1 + \frac{c_2\, v}{1+\ldots}}\right)^{-1} \text{(up to } c_7\text{)}. \tag{8.50}$$

Here the dimensionless coefficients c_i depend only on η. The c_k's are explicit functions of the coefficients f_k $(k = 1, \ldots 5)$,

$$c_1 = -f_1\,, \qquad c_2 = f_1 - \frac{f_2}{f_1}\,, \qquad c_3 = \frac{f_1\, f_3 - f_2^2}{f_1\,(f_1^2 - f_2)}\,, \tag{8.51}$$

$$c_4 = -\frac{f_1\,(f_2^3 + f_3^2 + f_1^2\, f_4 - f_2\,(2\, f_1\, f_3 + f_4))}{(f_1^2 - f_2)\,(f_1\, f_3 - f_2^2)}\,, \tag{8.52}$$

$$c_5 = -\frac{(f_1^2 - f_2)\,(-f_3^3 + 2 f_2\, f_3\, f_4 - f_1\, f_4^2 - f_2^2\, f_5 + f_1\, f_3\, f_5)}{(f_1\, f_3 - f_2^2)\,(f_2^3 + f_3^2 + f_1^2\, f_4 - f_2\,(2\, f_1\, f_3 + f_4))}\,, \tag{8.53}$$

where

$$f_k = \mathcal{F}_k - \frac{\mathcal{F}_{k-1}}{v^{P_2}_{\rm pole}}\,. \tag{8.54}$$

Here $\mathcal{F}_k$ is given by Eqs. (8.38)–(8.41) [for $k = 6$ and $k = 7$, the term $-856/105 \log 16 v^2$ should be replaced by $-856/105 \log 16 (v^{P_2}_{\rm MECO})^2$]. The coefficients c_7 and c_8 are straightforward to compute, but we do not show them because they involve rather long expressions. The quantity $v^{P_2}_{\rm MECO}$ is the MECO of the energy function e_{P_2} [defined by $de_{P_2}(v)/dv = 0$]. The quantity $v^{P_2}_{\rm pole}$, given by

$$v^{P_2}_{\rm pole} = \frac{1}{\sqrt{3}} \sqrt{\frac{1 + \frac{1}{3}\eta}{1 - \frac{35}{36}\eta}}\,, \tag{8.55}$$

is the pole of e_{P_2}, which plays an important role in the scheme proposed by Damour, Iyer and Sathyaprakash [25]. It is used to augment the Padé resummation of the PN expanded energy and flux with information taken from the test-mass case, where the flux (known analytically up to 5.5PN

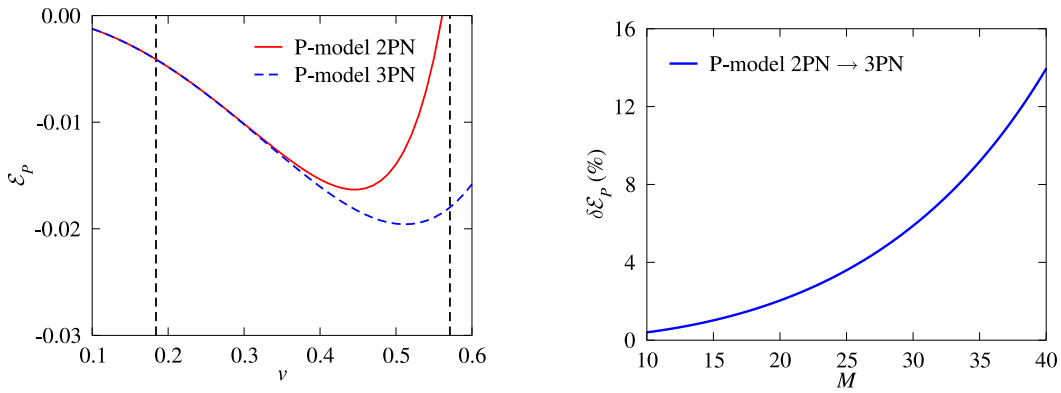

Figure 8.6: In the left panel, we plot the energy function $\mathcal{E}_{P_N}$ versus v, at different PN orders. In the right panel, we plot the percentage difference between 2PN and 3PN P-approximants, $\delta\mathcal{E}_P(v_{\rm peak}) = 100\,|[\mathcal{E}_{P_3}(v_{\rm peak}) - \mathcal{E}_{P_2}(v_{\rm peak})]/\mathcal{E}_{P_2}(v_{\rm peak})|$ versus the total mass M, again evaluated at the LIGO-I peak-sensitivity GW frequency $f_{\rm peak} = 153$ Hz [note: $v_{\rm peak} = (\pi M f_{\rm peak})^{1/3}$].

order) has a pole at the light ring. Under the hypothesis of *structural stability* [25], the flux should have a pole at the light ring also in the comparable-mass case. In the test-mass limit, the light ring corresponds to the pole of the energy, so the analytic structure of the flux is modified in the comparable-mass case to include $v^{P_2}_{\rm pole}(\eta)$. At 3PN order, where the energy has no pole, we choose (somewhat arbitrarily) to keep using the value $v^{P_2}_{\rm pole}(\eta)$; the resulting 3PN approximation to the test-mass flux is still very good.

In Fig. 8.5, we plot the P-approximants for the flux function $\mathcal{F}_{P_N}(\mathrm{v})$, at different PN orders. Note that at 1PN order the P-approximant has a pole. At the LIGO-I peak-sensitivity frequency, 153 Hz, for a $(10{+}10)M_\odot$ BBH, the value of v is $\simeq 0.362$, and the percentage difference in $\mathcal{F}_{P_N}(0.362)$, between successive PN orders is 1.5PN $\to$ 2PN : -8%; 2PN $\to$ 2.5PN : $+2.2\%$; 2.5PN $\to$ 3PN $(\hat{\theta} = -2)$: $+3.6\%$; 3PN $\to$ 3.5PN $(\hat{\theta} = -2)$: $+0.58\%$. So the percentage difference decreases as we increase the PN order. While in the test-mass limit it is known that the P-approximants converge quite well to the known exact flux function (see Fig. 3 of Ref. [25]), in the equal-mass case we cannot be sure that the same is happening, because the exact flux function is unknown. (If we assume that the equal-mass flux function is a smooth deformation of the test-mass flux function, with η the deformation parameter, then we could expect that the P-approximants are converging.) In the left panel of Fig. 8.6, we plot the P-approximants to the energy function as a function of v, at 2PN and 3PN orders; in the right panel, we plot the percentage difference between 2PN and 3PN P-approximants to the energy function, as a function of the total mass M, evaluated at the LIGO-I peak-sensitivity GW frequency $f_{\rm peak} = 153$ Hz.

N	$\langle P_N, P_{N+1}\rangle$					
	$(20+5)M_\odot$	$(10+10)M_\odot$				$(15+15)M_\odot$
2 ($\hat{\theta}=+2$)	0.902	0.915	(0.973,	20.5,	0.242)	0.868
2 ($\hat{\theta}=-2$)	0.931	0.955	(0.982,	20.7,	0.236)	0.923

Table 8.4: Test for the Cauchy convergence of the P-approximants. The values quoted are maxmax matches obtained by maximizing with respect to the extrinsic parameters, but not to the intrinsic parameters (i.e., the matches are computed for P waveforms with the same masses, but different PN orders). Here we define $\mathrm{P}_2 = \mathrm{P}(2, 2.5)$, $\mathrm{P}_3 = \mathrm{P}(3, 3.5)$. The values in parentheses are the maxmax matches obtained by maximizing with respect to the extrinsic *and* intrinsic parameters, shown together with the P_{N+1} parameters M and η where the maxima are attained. In all cases the integration of the equations is started at a GW frequency of 20 Hz.

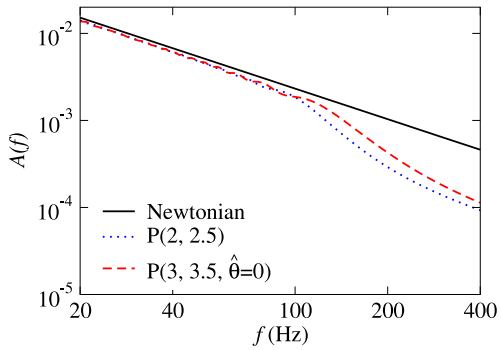

Figure 8.7: Frequency-domain amplitude versus frequency for the P-approximated (restricted) waveform, at different PN orders, for a $(15+15)M_\odot$ BBH.

Definition of the models

When computing the waveforms for P-approximant adiabatic models, the integration of the Eqs. (8.32) is stopped at $v = v^{P_N}_{\mathrm{MECO}}$, which is the solution of the equation $d\mathcal{E}_{P_N}(v)/dv = 0$. The corresponding GW frequency will be the *ending frequency* for these waveforms, and in Tab. 8.2 we show this frequency for typical BBH masses. Henceforth, we shall refer to the P-approximant models as $\mathrm{P}(n\mathrm{PN}, m\mathrm{PN})$, and we shall consider $(n\mathrm{PN}, m\mathrm{PN}) = (2, 2.5), (3, 3.5, \hat{\theta})$. [Recall that nPN and mPN are the maximum post–Newtonian order of the terms included, respectively, in the energy and flux functions $\mathcal{E}(v)$ and $\mathcal{F}(v)$; at 3PN order we need to indicate also a choice of the arbitrary flux parameter $\hat{\theta}$.]

Waveforms and matches

In Tab. 8.4, for three typical choices of BBH masses, we perform a convergence test using Cauchy's criterion [25]. The values are quite high, especially if compared to the same test for the T-approximants when the 2.5PN flux is used, see Tab. 8.3. However, as we already remarked, we

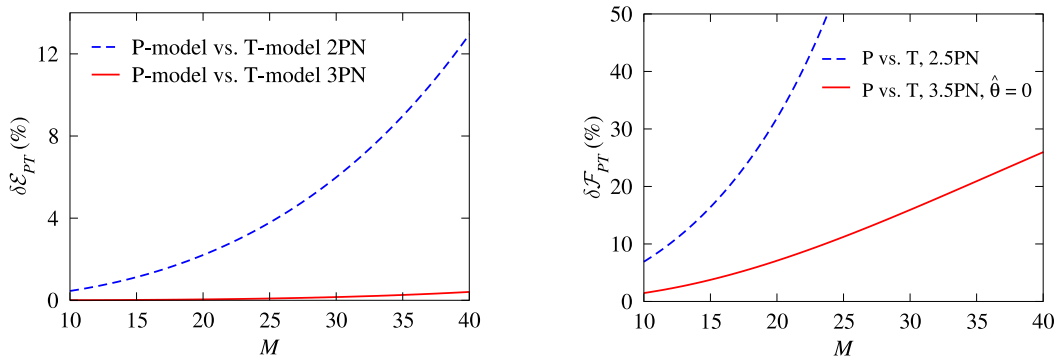

Figure 8.8: In the left panel, we plot the percentage difference $\delta\mathcal{E}_{PT}(v_{\rm peak}) = 100\,|[\mathcal{E}_{P_N}(v_{\rm peak}) - \mathcal{E}_{T_N}(v_{\rm peak})]/\mathcal{E}_{P_N}(v_{\rm peak})|$ versus the total mass M, for $N = 2, 3$, at the LIGO-I peak-sensitivity GW frequency $f_{\rm peak} = 153$ Hz [note: $v_{\rm peak} = (\pi M f_{\rm peak})^{1/3}$]. In the right panel, we plot the percentage difference between 2PN and 3PN P-approximants, $\delta\mathcal{F}_P(v_{\rm peak}) = 100\,|[\mathcal{F}_{P_3}(v_{\rm peak}) - \mathcal{F}_{P_2}(v_{\rm peak})]/\mathcal{F}_{P_2}(v_{\rm peak})|$ versus the total mass M, again evaluated at the LIGO-I peak-sensitivity GW frequency $f_{\rm peak} = 153$ Hz.

do not have a way of testing whether they are converging to the true limit. In Fig. 8.7, we plot the frequency-domain amplitude of the P-approximated (restricted) waveform, at different PN orders, for a $(15+15)M_\odot$ BBH. The Newtonian amplitude, $\mathcal{A}_{\rm Newt}(f) = f^{-7/6}$, is also shown for comparison. At 2.5PN and 3.5PN orders, the evolution is stopped at $v = v^{P_N}_{\rm MECO}$; although $f^{\rm GW}_{\rm MECO} \simeq 190 - 290$ Hz (see Tab. 8.2), the amplitude starts to deviate from $f^{-7/6}$ around 100 Hz, well inside the LIGO frequency band. Again, this is a consequence of the abrupt termination of the signal in the time domain.

A quantitative measure of the difference between the P(2, 2.5) and P(3, 3.5) waveforms can be seen in Tab. 8.9 in the intersection between the rows and columns labeled P(...). For three choices of BBH masses, this table shows the maxmax matches between the search models in the columns and the target models in the rows, maximized over the search-model parameters M and η, with the restriction $0 < \eta \leq 1/4$. These matches are quite high, but the models are not very faithful to each other. The same table shows also the maximized matches (i.e., fitting factors) *between T and P models*. These matches are low between T(2, 2.5) and P(2, 2.5) (and vice versa), between T(2, 2.5) and P(3, 3.5) (and vice versa), but they are high between T(2, 2), T(3, 3.5) and 3PN P-approximants (although the estimation of mass parameters is imprecise). Why this happens can be understood from Fig. 8.8 by noticing that at 3PN order the percentage difference between the T-approximated and P-approximated binding energies is rather small ($\leq 0.5\%$), and that the percentage difference between the T-approximated and P-approximated fluxes at 3PN order (although still $\sim 10\%$) is much smaller than at 2PN order.

8.4 Nonadiabatic models

By contrast with the models discussed in Sec. 8.3, in nonadiabatic models we solve equations of motions that involve (almost) all the degrees of freedom of the BBH systems. Once again, all waveforms are computed in the restricted approximation of Eq. (8.29), taking the GW phase $\varphi_{\rm GW}$ as twice the orbital phase φ.

8.4.1 Nonadiabatic PN expanded methods: Hamiltonian formalism

Working in the ADM gauge, Damour, Jaranowski and G. Schäfer have derived a PN expanded Hamiltonian for the general-relativistic two-body dynamics [45, 47, 16]:

$$\widehat{H}(\mathbf{q},\mathbf{p}) = \widehat{H}_{\rm Newt}(\mathbf{q},\mathbf{p}) + \widehat{H}_{\rm 1PN}(\mathbf{q},\mathbf{p}) + \widehat{H}_{\rm 2PN}(\mathbf{q},\mathbf{p}) + \widehat{H}_{\rm 3PN}(\mathbf{q},\mathbf{p})\,, \tag{8.56}$$

where

$$\widehat{H}_{\rm Newt}\left(\mathbf{q},\mathbf{p}\right) = \frac{\mathbf{p}^2}{2} - \frac{1}{q}\,, \tag{8.57}$$

$$\widehat{H}_{\rm 1PN}\left(\mathbf{q},\mathbf{p}\right) = \frac{1}{8}(3\eta-1)(\mathbf{p}^2)^2 - \frac{1}{2}\left[(3+\eta)\mathbf{p}^2 + \eta(\mathbf{n}\cdot\mathbf{p})^2\right]\frac{1}{q} + \frac{1}{2q^2}\,, \tag{8.58}$$

$$\begin{aligned}\widehat{H}_{\rm 2PN}\left(\mathbf{q},\mathbf{p}\right) &= \frac{1}{16}\left(1-5\eta+5\eta^2\right)(\mathbf{p}^2)^3 \\ &+ \frac{1}{8}\left[\left(5-20\eta-3\eta^2\right)(\mathbf{p}^2)^2 - 2\eta^2(\mathbf{n}\cdot\mathbf{p})^2\mathbf{p}^2 - 3\eta^2(\mathbf{n}\cdot\mathbf{p})^4\right]\frac{1}{q} \\ &+ \frac{1}{2}\left[(5+8\eta)\mathbf{p}^2 + 3\eta(\mathbf{n}\cdot\mathbf{p})^2\right]\frac{1}{q^2} - \frac{1}{4}(1+3\eta)\frac{1}{q^3}\,,\end{aligned} \tag{8.59}$$

$$\begin{aligned}\widehat{H}_{\rm 3PN}\left(\mathbf{q},\mathbf{p}\right) &= \frac{1}{128}\left(-5+35\eta-70\eta^2+35\eta^3\right)(\mathbf{p}^2)^4 \\ &+ \frac{1}{16}\Big[\left(-7+42\eta-53\eta^2-5\eta^3\right)(\mathbf{p}^2)^3 + (2-3\eta)\eta^2(\mathbf{n}\cdot\mathbf{p})^2(\mathbf{p}^2)^2 \\ &\qquad +3(1-\eta)\eta^2(\mathbf{n}\cdot\mathbf{p})^4\mathbf{p}^2 - 5\eta^3(\mathbf{n}\cdot\mathbf{p})^6\Big]\frac{1}{q} \\ &+ \left[\frac{1}{16}\left(-27+136\eta+109\eta^2\right)(\mathbf{p}^2)^2 + \frac{1}{16}(17+30\eta)\eta(\mathbf{n}\cdot\mathbf{p})^2\mathbf{p}^2\right. \\ &\qquad \left. +\frac{1}{12}(5+43\eta)\eta(\mathbf{n}\cdot\mathbf{p})^4\right]\frac{1}{q^2} \\ &+ \left\{\left[-\frac{25}{8} + \left(\frac{1}{64}\pi^2 - \frac{335}{48}\right)\eta - \frac{23}{8}\eta^2\right]\mathbf{p}^2 + \left(-\frac{85}{16} - \frac{3}{64}\pi^2 - \frac{7}{4}\eta\right)\eta(\mathbf{n}\cdot\mathbf{p})^2\right\}\frac{1}{q^3} \\ &+ \left[\frac{1}{8} + \left(\frac{109}{12} - \frac{21}{32}\pi^2\right)\eta\right]\frac{1}{q^4}.\end{aligned} \tag{8.60}$$

Here the reduced Non–Relativistic Hamiltonian in the center-of-mass frame, $\widehat{H} \equiv H^{\rm NR}/\mu$, is written as a function of the reduced canonical variables $\mathbf{p} \equiv \mathbf{p_1}/\mu = -\mathbf{p_2}/\mu$, and $\mathbf{q} \equiv (\mathbf{x}_1 - \mathbf{x}_2)/M$, where $\mathbf{x_1}$ and $\mathbf{x_2}$ are the positions of the BH centers of mass in quasi–Cartesian ADM coordinates (see

Refs. [45, 47, 16]); the scalars q and p are the (coordinate) lengths of the two vectors; and the vector $\mathbf{n}$ is just $\mathbf{q}/q$.

Equations of motion

We now restrict the motion to a plane, and we introduce radiation-reaction (RR) effects as in Ref. [15]. The equations of motion then read (using polar coordinates r and φ obtained from the $\mathbf{q}$ with the usual Cartesian-to-polar transformation)

$$\frac{dr}{d\widehat{t}} = \frac{\partial \widehat{H}}{\partial p_r}(r, p_r, p_\varphi)\,, \quad \frac{d\varphi}{d\widehat{t}} \equiv \widehat{\omega} = \frac{\partial \widehat{H}}{\partial p_\varphi}(r, p_r, p_\varphi)\,, \tag{8.61}$$

$$\frac{dp_r}{d\widehat{t}} = -\frac{\partial \widehat{H}}{\partial r}(r, p_r, p_\varphi) + \widehat{F}^r(r, p_r, p_\varphi)\,, \quad \frac{dp_\varphi}{d\widehat{t}} = \widehat{F}^\varphi[\widehat{\omega}(r, p_r, p_\varphi)]\,, \tag{8.62}$$

where $\widehat{t} = t/M$, $\widehat{\omega} = \omega M$; and where $\widehat{F}^\varphi \equiv F^\varphi/\mu$ and $\widehat{F}^r \equiv F^r/\mu$ are the reduced angular and radial components of the RR force. Assuming $F^r \ll F^\varphi$ [15], averaging over an orbit, and using the balance equation (8.31), we can express the angular component of the radiation-reaction force in terms of the GW flux at infinity [15]. More explicitly, if we use the P-approximated flux, we have

$$\widehat{F}^\varphi \equiv F_{P_N}[v_\omega] = -\frac{1}{\eta\, v_\omega^3}\,\mathcal{F}_{P_N}[v_\omega] = -\frac{32}{5}\,\eta\, v_\omega^7\,\frac{f_{P_N}(v_\omega;\eta)}{1 - v_\omega/v_{\rm pole}^{P_2}(\eta)}\,, \tag{8.63}$$

while if we use the T-approximated flux we have

$$\widehat{F}^\varphi \equiv F_{T_N}[v_\omega] = -\frac{1}{\eta\, v_\omega^3}\,\mathcal{F}_{T_N}[v_\omega], \tag{8.64}$$

where $v_\omega \equiv \widehat{\omega}^{1/3} \equiv (d\varphi/d\widehat{t})^{1/3}$. This v_ω is used in Eq. (8.29) to compute the restricted waveform. Note that at each PN order, say nPN, we define our Hamiltonian model by evolving the Eqs. (8.61) and (8.62) without truncating the partial derivatives at the nPN order (differentiation with respect to the canonical variables can introduce terms of order higher than nPN). Because of this choice, and because of the approximation used to incorporate radiation-reaction effects, these nonadiabatic models are not, strictly speaking, purely post–Newtonian.

Innermost stable circular orbit

Circular orbits are defined by setting $r =$ constant while neglecting radiation-reaction effects. In our PN Hamiltonian models, this implies $\partial\widehat{H}/\partial p_r = 0$ through Eq. (8.61); because at all PN orders the Hamiltonian $\widehat{H}$ [Eqs. (8.56)–(8.60)] is quadratic in p_r, this condition is satisfied for $p_r = 0$; in turn, this implies also $\partial\widehat{H}/\partial r = 0$ [through Eq. (8.62)], which can be solved for p_φ. The orbital frequency is then given by $\hat{\omega} = \partial\widehat{H}/\partial p_\varphi$.

The stability of circular orbits under radial perturbations depends on the second derivative of the Hamiltonian:

$$\frac{\partial^2 \widehat{H}}{\partial r^2} > 0 \Leftrightarrow \text{stable orbit}\,; \qquad \frac{\partial^2 \widehat{H}}{\partial r^2} < 0 \Leftrightarrow \text{unstable orbit}\,. \tag{8.65}$$

For a test particle in Schwarzschild geometry (the $\eta \to 0$ of a BBH), an Innermost Stable Circular Orbit (ISCO) always exists, and it is defined by

$$\text{ISCO (Schwarzschild)}: \quad \frac{\partial \widehat{H}^{\rm Schw}}{\partial r}_{|_{p_r=0}} = \frac{\partial^2 \widehat{H}^{\rm Schw}}{\partial r^2}_{|_{p_r=0}} = 0, \tag{8.66}$$

where $\widehat{H}^{\rm Schw}(r, p_r, p_\varphi)$ is the (reduced) nonrelativistic test-particle Hamiltonian in the Schwarzschild geometry. Similarly, if such an ISCO exists for the (reduced) nonrelativistic PN Hamiltonian $\widehat{H}$ [Eq. (8.56)], it is defined by

$$\text{ISCO (Hamiltonian)}: \quad \frac{\partial \widehat{H}}{\partial r}_{|_{p_r=0}} = \frac{\partial^2 \widehat{H}}{\partial r^2}_{|_{p_r=0}} = 0. \tag{8.67}$$

Any inspiral built as an adiabatic sequence of quasicircular orbits cannot be extended to orbital separations smaller than the ISCO. In our model, we integrate the Hamiltonian equations (8.61) and (8.62) including terms up to a given PN order, without re-truncating the equations to exclude terms of higher order that have been generated by differentiation with respect to the canonical variables. Consistently, the value of the ISCO that is relevant to our model should be derived by solving Eq. (8.67) without any further PN truncation.

How is the ISCO related to the Maximum binding Energy for Circular Orbit (MECO), used above for nonadiabatic models such as T? The PN expanded energy for circular orbits $\mathcal{E}_{T_n}(\widehat{\omega})$ at order nPN can be recovered by solving the equations

$$\frac{\partial \widehat{H}(r, p_r = 0, p_\varphi)}{\partial r} = 0, \qquad \frac{\partial \widehat{H}(r, p_r = 0, p_\varphi)}{\partial p_\varphi} = \hat{\omega}, \tag{8.68}$$

for r and p_φ as functions of $\hat{\omega}$, and by using the solutions to define

$$\widehat{H}(\hat{\omega}) \equiv \widehat{H}[r(\hat{\omega}), p_r = 0, p_\varphi(\hat{\omega})]. \tag{8.69}$$

Then $\widehat{H}(\hat{\omega} \equiv v^3) = \mathcal{E}_{T_n}(v)$ as given by Eq. (8.33), *if and only if* in this procedure we are careful to eliminate all terms of order higher than nPN (see, e.g., Ref. [53]).

In the context of nonadiabatic models, the MECO is then defined by

$$\text{MECO}: \qquad \frac{d\widehat{H}}{d\widehat{\omega}} = 0; \tag{8.70}$$

and it also characterizes the end of adiabatic sequences of circular orbits. Computing the variation of Eq. (8.69) between nearby circular orbits, and setting $p_r = 0$, $dp_r = 0$, we get

$$d\widehat{\omega} = \frac{\partial^2 \widehat{H}}{\partial r \partial p_\varphi}\, dr + \frac{\partial^2 \widehat{H}}{\partial p_\varphi^2}\, dp_\varphi \,, \qquad \frac{\partial^2 \widehat{H}}{\partial r^2}\, dr + \frac{\partial^2 \widehat{H}}{\partial r \partial p_\varphi}\, dp_\varphi = 0 \,; \tag{8.71}$$

and combining these two equations we get

$$\frac{dp_\varphi}{d\widehat{\omega}} = -\frac{\partial^2 \widehat{H}}{\partial r^2} \left[\left(\frac{\partial^2 \widehat{H}}{\partial r \partial p_\varphi} \right)^2 - \frac{\partial^2 \widehat{H}}{\partial p_\varphi^2} \frac{\partial^2 \widehat{H}}{\partial r^2} \right]^{-1} . \tag{8.72}$$

So finally we can write

$$\frac{d\widehat{H}}{d\widehat{\omega}} = \frac{\partial \widehat{H}}{\partial p_\varphi} \frac{dp_\varphi}{d\widehat{\omega}} = -\frac{\partial^2 \widehat{H}}{\partial r^2} \frac{\partial \widehat{H}}{\partial p_\varphi} \left[\left(\frac{\partial^2 \widehat{H}}{\partial r \partial p_\varphi} \right)^2 - \frac{\partial^2 \widehat{H}}{\partial p_\varphi^2} \frac{\partial^2 \widehat{H}}{\partial r^2} \right]^{-1} . \tag{8.73}$$

Not surprisingly, Eqs. (8.73) and (8.69) together are formally equivalent to the definition of the ISCO, Eq. (8.67) [note that the second and third terms on the right-hand side of Eq. (8.73) are never zero.] Therefore, if we knew the Hamiltonian $\widehat{H}$ *exactly*, we would find that the MECO defined by Eq. (8.70), is numerically the same as the ISCO defined by Eq. (8.67). Unfortunately, we are working only up to a finite PN order (say nPN); thus, to recover the MECO as given by Eq. (8.33), all three terms on the right-hand side of Eq. (8.73) must be written in terms of $\widehat{\omega}$, truncated at nPN order, then combined and truncated again at nPN order. This value of the MECO, however, will *no longer* be the same as the ISCO obtained by solving Eq. (8.67) *exactly without truncation*.

If the PN expansion was converging rapidly, then the difference between the ISCO and the MECO would be mild; but for the range of BH masses that we consider the PN convergence is bad, and the discrepancy is rather important. The ISCO is present only at 1PN order, with $r_{\rm ISCO} = 9.907$ and $\widehat{\omega}_{\rm ISCO} = 0.02833$. The corresponding GW frequencies are given in Tab. 8.2 for a few BBHs with equal masses. At 3PN order we find the formal solution $r^{\rm ISCO} = 1.033$ and $p_\varphi^{\rm ISCO} = 0.355$, but since we do not trust the PN expanded Hamiltonian when the radial coordinate gets so small, we conclude that there is no ISCO at 3PN order.

Definition of the models

In order to build a quasicircular orbit with initial GW frequency f_0, our initial conditions $(r_{\rm init}, p_{r\,\rm init}, p_{\varphi\,\rm init})$ are set by imposing $\dot{\varphi}_{\rm init} = \pi f_0$, $\dot{p}_{r\,\rm init} = 0$ and $dr_{\rm init}/d\hat{t} = -\mathcal{F}/(\eta d\hat{H}/dr)_{\rm circ}$, as in Ref. [55]. The initial orbital phase $\varphi_{\rm init}$ remains a free parameter. For these models, the criterion used to stop the integration of Eqs. (8.61), (8.62) is rather arbitrary. We decided to push the integration of the dynamical equations up to the time when we begin to observe unphysical effects due to the failure of

N	$\langle \mathrm{HT}_N, \mathrm{HT}_{N+1}\rangle$			$\langle \mathrm{HP}_N, \mathrm{HP}_{N+1}\rangle$		
	$(5+20)M_\odot$	$(10+10)M_\odot$	$(15+15)M_\odot$	$(5+20)M_\odot$	$(10+10)M_\odot$	$(15+15)M_\odot$
0	0.118	0.191 (0.553, 13.7, 0.243)	0.206	0.253	0.431 (0.586, 16.7, 0.242)	0.316
1	0.102	0.174 (0.643, 61.0, 0.240)	0.170	0.096	0.161 (0.623, 17.4, 0.239)	0.151
2 ($\hat{\theta}=+2$)	0.292	0.476 (0.656, 18.6, 0.241)	0.377	0.266	0.369 (0.618, 17.6, 0.240)	0.325
2 ($\hat{\theta}=-2$)	0.287	0.431 (0.671, 19.0, 0.241)	0.377	0.252	0.354 (0.622, 17.4, 0.239)	0.312

Table 8.5: Test for the Cauchy convergence of the HT- and HP-approximants. The values quoted are maxmax matches obtained by maximizing with respect to the extrinsic parameters, but not to the intrinsic parameters (i.e., the matches are computed for H waveforms with the same masses, but different PN orders). Here we define $\mathrm{HT}_0 = \mathrm{HT}(0,0)$, $\mathrm{HT}_1 = \mathrm{HT}(1,1.5)$, $\mathrm{HT}_2 = \mathrm{HT}(2,2)$ [because the 2.5PN flux goes to zero before the MECO is reached, so we use the 2PN flux], $\mathrm{HT}_3 = \mathrm{HT}(3,3.5,\hat{\theta})$; we also define $\mathrm{HP}_0 = \mathrm{HP}(0,0)$, $\mathrm{HP}_1 = \mathrm{HP}(1,1.5)$, $\mathrm{HP}_2 = \mathrm{HP}(2,2.5)$, and $\mathrm{HP}_3 = \mathrm{HP}(3,3.5,\hat{\theta})$. The values in parentheses are the maxmax matches obtained by maximizing with respect to the extrinsic *and* intrinsic parameters, shown together with the H_{N+1} parameters M and η where the maxima are attained. In all cases the integration of the equations is started at a GW frequency of 20 Hz.

the PN expansion, or when the assumptions that underlie Eqs. (8.62) [such as $\widehat{F}^r \ll \widehat{F}^\varphi$], cease to be valid. When the 2.5PN flux is used, we stop the integration when $\mathcal{F}_{T_N}$ equals 10% of $\mathcal{F}_{\mathrm{Newt}}$, and we define the *ending frequency* for these waveforms as the instantaneous GW frequency at that time. To be consistent with the assumption of quasicircular motion, we require also that the radial velocity be always much smaller than the orbital velocity, and we stop the integration when $|\dot{r}| > 0.3(r\dot{\varphi})$, if this occurs before $\mathcal{F}_{T_N}$ equals 10% of $\mathcal{F}_{\mathrm{Newt}}$. In some cases, during the last stages of inspiral $\widehat{\omega}$ reaches a maximum and then drops quickly to zero [see discussion in Sec. 8.5]. When this happens, we stop the evolution at $\dot{\widehat{\omega}} = 0$.

We shall refer to these models as $\mathrm{HT}(n\mathrm{PN}, m\mathrm{PN})$ (when the T-approximant is used for the flux) or $\mathrm{HP}(n\mathrm{PN}, m\mathrm{PN})$ (when the P-approximant is used for the flux), where nPN (mPN) denotes the maximum PN order of the terms included in the Hamiltonian (the flux). We shall consider $(n\mathrm{PN}, m\mathrm{PN}) = (1,1.5), (2,2), (2,2.5)$, and $(3,3.5,\hat{\theta})$ [at 3PN order we need to indicate also a choice of the arbitrary flux parameter $\hat{\theta}$].

Waveforms and matches

In Tab. 8.5, for three typical choices of BBH masses, we perform a convergence test using Cauchy's criterion [25]. The values are very low. For $N = 0$ and $N = 1$, the low values are explained by the fact that at 1PN order there is an ISCO [see the discussion below Eq. (8.73)], while at Newtonian and 2PN, 3PN order there is not. Because of the ISCO, the stopping criterion [$|\dot{r}| > 0.3(r\dot{\varphi})$ or $\dot{\widehat{\omega}} = 0$] is satisfied at a much lower frequency, hence at 1PN order the evolution ends much earlier than in the Newtonian and 2PN order cases. In Fig. 8.9, we show the inspiraling orbits in the (x, y) plane for equal-mass BBHs, computed using the $\mathrm{HT}(1,1.5)$ model (in the left panel) and the $\mathrm{HT}(3,3.5,0)$ model (in the right panel). For $N = 2$, the low values are due mainly to differences in

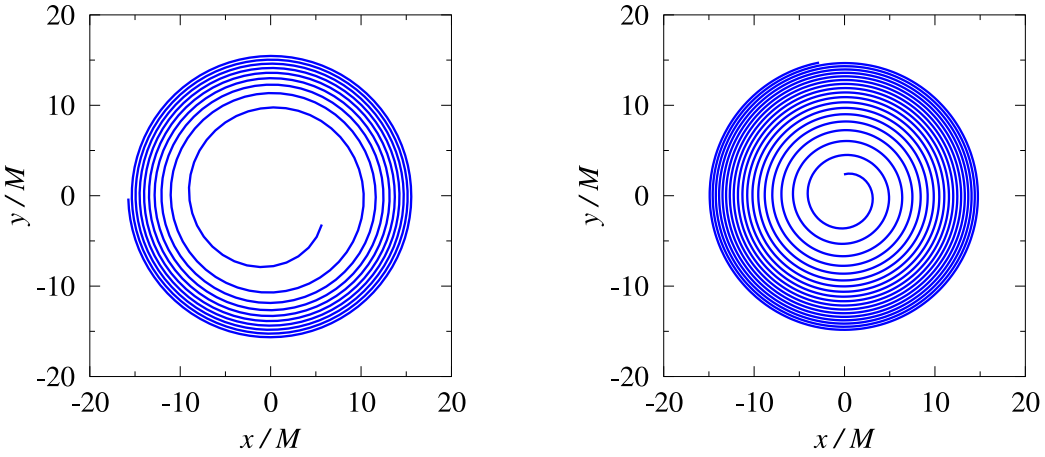

Figure 8.9: Inspiraling orbits in (x, y)-plane when $\eta = 0.25$ for HT$(1, 1.5)$ (in the left panel) and HT$(3, 3.5, 0)$ (in the right panel). For a $(15 + 15)M_\odot$ BBH the evolution starts at $f_{\rm GW} = 34$ Hz and ends at $f_{\rm GW} = 97$ Hz for HT$(1, 1.5)$ panel and at $f_{\rm GW} = 447$ Hz for HT$(3, 3.5, 0)$. The dynamical evolution is rather different because at 1PN order there is an ISCO ($r_{\rm ISCO} \simeq 9.9M$), while at 3PN order it does not exist.

the conservative dynamics, that is, to differences between the 2PN and 3PN Hamiltonians. Indeed, for a $(10+10)M_\odot$ BBH we find $\langle \mathrm{HT}(2,2), \mathrm{HT}(3,2)\rangle = 0.396$, still low, while $\langle \mathrm{HT}(2,2), \mathrm{HT}(2,3.5)\rangle = 0.662$, considerably higher than the values in Tab. 8.5.

In Fig. 8.10, we plot the frequency-domain amplitude of the HT-approximated (restricted) waveforms, at different PN orders, for a $(15+15)M_\odot$ BBH. The Newtonian amplitude, $\mathcal{A}_{\rm Newt}(f) = f^{-7/6}$, is also shown for comparison. For HT$(1, 1.5)$, because the ISCO is at $r \simeq 9.9M$, the stopping criterion $|\dot r| > 0.3\,\dot\varphi\, r$ is reached at a very low frequency and the amplitude deviates from the Newtonian prediction already at $f \sim 50$Hz. For HT$(2, 2.5)$, the integration of the dynamical equation is stopped as the flux function goes to zero; just before this happens, the RR effects become weaker and weaker, and in the absence of an ISCO the two BHs do not plunge, but continue on a quasicircular orbit until $\mathcal{F}_T(v)$ equals 10% of $\mathcal{F}_{\rm Newt}$. So the binary spends many cycles at high frequencies, skewing the amplitude with respect to the Newtonian result, and producing the oscillations seen in Fig. 8.10. We consider this behavior rather unphysical, and in the following we shall no longer take into account the HT$(2, 2.5)$ model, but at 2PN order we shall use HT$(2, 2)$.

The situation is similar for the HP models. Except at 1PN order, the HT and HP models do not end their evolution with a plunge. As a result, the frequency-domain amplitude of the HT and HP waveforms does not decrease markedly at high frequencies, as seen in Fig. 8.10, and in fact it does not deviate much from the Newtonian result (especially at 3PN order).

Quantitative measures of the difference between HT and HP models at 2PN and 3PN orders,

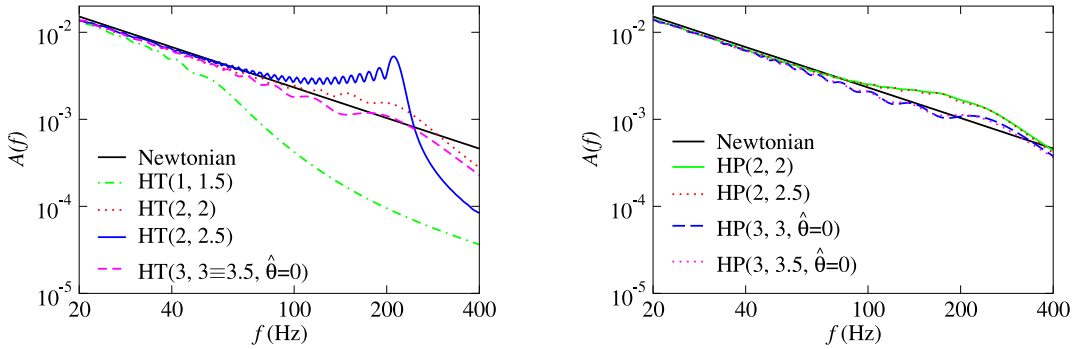

Figure 8.10: Frequency-domain amplitude versus frequency for the HT and HP (restricted) waveforms, at different PN orders, for a $(15+15)M_\odot$ BBH. The HT$(3, 3.5, \hat{\theta}=0)$ curve, not plotted, is almost identical to the HT$(3, 3, \hat{\theta}=0)$ curve.

and of the difference between the Hamiltonian models and the adiabatic models, can be seen in Tables 8.9, 8.10. For some choices of BBH masses, these tables show the maxmax matches between the search models in the columns and the target models in the rows, maximized over the search-model parameters M and η, with the restriction $0 < \eta \leq 1/4$. The matches between the H$(2,2)$ and the H$(3,3.5)$ waveforms are surprisingly low. More generally, the H$(2,2)$ models have low matches with all the other PN models. We consider these facts as an indication of the unreliability of the H models. In the following we shall not give much credit to the H$(2,2)$ models, and when we discuss the construction of detection template families we shall consider only the H$(3,3.5)$ models. [We will however comment on the projection of the H$(2,2)$ models onto the detection template space.]

As for the H$(3,3.5)$ models, their matches with the 2PN adiabatic models are low; but their matches with the 3PN adiabatic models are high, at least for $M \leq 30M_\odot$. For $M = 40M_\odot$ (as shown in Tables 8.9 and 8.10), the matches can be quite low, as the differences in the late dynamical evolution become significant.

8.4.2 Nonadiabatic PN expanded methods: Lagrangian formalism

Equations of motion

In the harmonic gauge, the equations of motion for the general-relativistic two-body dynamics in the Lagrangian formalism read [44, 56, 57]:

$$\ddot{\mathbf{x}} = \mathbf{a}_{\rm N} + \mathbf{a}_{\rm PN} + \mathbf{a}_{\rm 2PN} + \mathbf{a}_{\rm 2.5RR} + \mathbf{a}_{\rm 3.5RR}\,, \tag{8.74}$$

where

$$\mathbf{a}_{\rm N} = -\frac{M}{r^2}\hat{\mathbf{n}}\,, \tag{8.75}$$

$$\mathbf{a}_{\rm PN} = -\frac{M}{r^2}\left\{\hat{\mathbf{n}}\left[(1+3\eta)v^2 - 2(2+\eta)\frac{M}{r} - \frac{3}{2}\eta\dot{r}^2\right] - 2(2-\eta)\dot{r}\mathbf{v}\right\}\,, \tag{8.76}$$

$$\begin{aligned}\mathbf{a}_{\rm 2PN} \;=\; & -\frac{M}{r^2}\left\{\hat{\mathbf{n}}\left[\frac{3}{4}(12+29\eta)\left(\frac{M}{r}\right)^2 + \eta(3-4\eta)v^4 + \frac{15}{8}\eta(1-3\eta)\dot{r}^4\right.\right.\\ & \left. -\frac{3}{2}\eta(3-4\eta)v^2\dot{r}^2 - \frac{1}{2}\eta(13-4\eta)\frac{M}{r}v^2 - (2+25\eta+2\eta^2)\frac{M}{r}\dot{r}^2\right]\\ & \left. -\frac{1}{2}\dot{r}\mathbf{v}\left[\eta(15+4\eta)v^2 - (4+41\eta+8\eta^2)\frac{M}{r} - 3\eta(3+2\eta)\dot{r}^2\right]\right\},\end{aligned} \tag{8.77}$$

$$\mathbf{a}_{\rm 2.5RR} = \frac{8}{5}\eta\frac{M^2}{r^3}\left\{\dot{r}\hat{\mathbf{n}}\left[18v^2 + \frac{2}{3}\frac{M}{r} - 25\dot{r}^2\right] - \mathbf{v}\left[6v^2 - 2\frac{M}{r} - 15\dot{r}^2\right]\right\}, \tag{8.78}$$

$$\begin{aligned}\mathbf{a}_{\rm 3.5RR} \;=\; & \frac{8}{5}\eta\frac{M^2}{r^3}\left\{\dot{r}\hat{\mathbf{n}}\left[\left(\frac{87}{14} - 48\eta\right)v^4 - \left(\frac{5379}{28} + \frac{136}{3}\eta\right)v^2\,\frac{M}{r} + \frac{25}{2}(1+5\eta)v^2\dot{r}^2\right.\right.\\ & \left. + \left(\frac{1353}{4} + 133\eta\right)\dot{r}^2\frac{M}{r} - \frac{35}{2}(1-\eta)\dot{r}^4 + \left(\frac{160}{7} + \frac{55}{3}\eta\right)\left(\frac{M}{r}\right)^2\right]\\ & -\mathbf{v}\left[-\frac{27}{14}v^4 - \left(\frac{4861}{84} + \frac{58}{3}\eta\right)v^2\frac{M}{r} + \frac{3}{2}(13-37\eta)v^2\,\dot{r}^2\right.\\ & \left.\left. + \left(\frac{2591}{12} + 97\eta\right)\dot{r}^2\,\frac{M}{r} - \frac{25}{2}(1-7\eta)\dot{r}^4 + \frac{1}{3}\left(\frac{776}{7} + 55\eta\right)\,\left(\frac{M}{r}\right)^2\right]\right\}.\end{aligned} \tag{8.79}$$

For the sake of convenience, in this section we are using same symbols of Sec. 8.4.1 to denote different physical quantities (such as coordinates in different gauges). Here the vector $\mathbf{x} \equiv \mathbf{x_1} - \mathbf{x_2}$ is the difference, in pseudo–Cartesian harmonic coordinates [44], between the positions of the BH centers of mass; the vector $\mathbf{v} = d\mathbf{x}/dt$ is the corresponding velocity; the scalar r is the (coordinate) length of $\mathbf{x}$; the vector $\hat{\mathbf{n}} \equiv \mathbf{x}/r$; and overdots denote time derivatives with respect to the post–Newtonian time. We have included neither the 3PN order corrections $a_{\rm 3PN}$ derived in Ref. [46], nor the 4.5PN order term $a_{\rm 4.5PN}$ for the radiation-reaction force computed in Ref. [58]. Unlike the Hamiltonian models, where the radiation-reaction effects were averaged over circular orbits but were present up

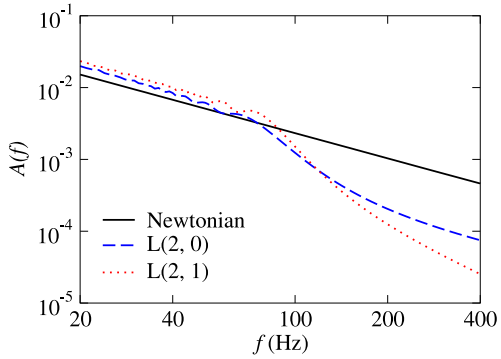

Figure 8.11: Frequency-domain amplitude versus frequency for the L-approximated (restricted) waveforms, at different PN orders, for a $(15+15)M_\odot$ BBH.

to 3PN order, here radiation-reaction effects are instantaneous, and can be used to compute generic orbits, but are given only up to 1PN order beyond the leading quadrupole term.

We compute waveforms in the quadrupole approximation of Eq. (8.29), defining the orbital phase φ as the angle between $\mathbf{x}$ and a fixed direction in the orbital plane, and the invariantly defined velocity v as $(M\dot{\varphi})^{1/3}$.

Definition of the models

For these models, just as for the HT and HP models, the choice of the endpoint of evolution is rather arbitrary. We decided to stop the integration of the dynamical equations when we begin to observe unphysical effects due to the failure of the PN expansion. For many (if not all) configurations, the PN-expanded center-of-mass binding energy (given by Eqs. (2.7a)–(2.7e) of Ref. [19]) begins to increase during the late inspiral, instead of continuing to decrease. When this happens, we stop the integration. The instantaneous GW frequency at that time will then be the *ending frequency* for these waveforms. We shall refer to these models as L(nPN, mPN), where nPN (nPN) denotes the maximum PN order of the terms included in the Hamiltonian (the radiation-reaction force). We shall consider $(n\text{PN}, m\text{PN}) = (2,0), (2,1)$.

Waveforms and matches

In Fig. 8.11, we plot the frequency-domain amplitude versus frequency for the L-approximated (restricted) waveforms, at different PN orders, for a $(15+15)M_\odot$ BBH. The amplitude deviates from the Newtonian prediction slightly before 100 Hz. Indeed, the GW ending frequencies are 116 Hz and 107 Hz for the L$(2,0)$ and L$(2,1)$ models, respectively. These frequencies are quite low, because the unphysical behavior of the PN-expanded center-of-mass binding energy appears quite early [at $r_{\rm end} = 6.6$ and $r_{\rm end} = 7.0$ for the L$(2,0)$ and L$(2,1)$ models, respectively]. So the L models

	T(2, 2)			T(3, 3.5, 0)			P(2, 2.5)			P(3, 3.5, 0)			EP(2, 2.5)			EP(3, 3.5, 0)			HT(3, 3.5, 0)		
	mm	M	η	mm	M	η	mm	M	η	mm	M	η	mm	M	η	mm	M	η	mm	M	η
L(2, 1) (20+20)$M_\odot$	0.994	78.83	0.05	0.998	61.24	0.09	0.999	52.76	0.13	0.998	57.96	0.11	0.935	70.76	0.05	0.9446	72.04	0.06	0.994	49.53	0.14
(15+15)$M_\odot$	0.991	55.16	0.06	0.995	44.50	0.10	0.999	39.96	0.13	0.998	43.57	0.11	0.912	46.67	0.09	0.916	50.90	0.07	0.994	37.08	0.15
(15+5)$M_\odot$	0.981	35.51	0.05	0.991	29.03	0.08	0.995	26.02	0.10	0.994	27.99	0.09	0.942	27.46	0.09	0.941	28.85	0.08	0.994	22.89	0.13
(5+5)$M_\odot$	0.956	10.68	0.20	0.965	11.49	0.18	0.971	11.33	0.19	0.964	11.89	0.17	0.964	11.03	0.19	0.960	11.69	0.17	0.966	11.32	0.18

Table 8.6: Fitting factors [see Eq. (8.20)] for the projection of the L(2, 1) (target) waveforms onto the T, P, EP and HP (search) models at 2PN and 3PN order. The values quoted are obtained by maximizing the maxmax (mm) match over the search-model parameters M and η.

		L(2, 0)			T(2, 0)			L(2, 1)			T(2, 1)		
		mm	M	η	mm	M	η	mm	M	η	mm	M	η
	(15+15)$M_\odot$				0.884	42.02	0.237						
L(2, 0)	(15+5)$M_\odot$				0.769	24.71	0.201						
	(5+5)$M_\odot$				0.996	21.70	0.068						
	(15+15)$M_\odot$	0.834	23.44	0.247									
T(2, 0)	(15+5)$M_\odot$	0.823	14.90	0.250									
	(5+5)$M_\odot$	0.745	9.11	0.250									
	(15+15)$M_\odot$										0.837	60.52	0.236
L(2, 1)	(15+5)$M_\odot$										0.844	55.70	0.052
	(5+5)$M_\odot$										0.626	11.47	0.238
	(15+15)$M_\odot$							0.663	19.38	0.250			
T(2, 1)	(15+5)$M_\odot$							0.672	13.56	0.250			
	(5+5)$M_\odot$							0.631	9.22	0.243			

Table 8.7: Fitting factors [see Eq. (8.20)] for the projection of the L(2, 1) and L(2, 0) (target) waveforms onto the T(2, 0) and T(2, 1) (search) models. The values quoted are obtained by maximizing the maxmax (mm) match over the search-model parameters M and η.

do not provide waveforms for the last stage of inspirals and plunge.

Table 8.6 shows the maxmax matches between the L-approximants and a few other selected PN models. The overlaps are quite high, except with the EP(2, 2.5) and EP(3, 3.5, 0) at high masses, but extremely unfaithful. Moreover, we could expect the L(2, 0) and L(2, 1) models to have high fitting factors with the adiabatic models T(2, 0) and T(2, 1). However, this is not the case. As Table 8.7 shows, the T models are neither effectual nor faithful in matching the L models, and vice versa. This might be due to one of the following factors: (i) the PN-expanded conservative dynamics in the adiabatic limit (T models) and in the nonadiabatic case (L models) are rather different; (ii) there is an important effect due to the different criteria used to end the evolution in the two models, which make the ending frequencies rather different. All in all, the L models do not seem very reliable, so we shall not give them much credit when we discuss detection template families. However, we shall investigate where they lie in the detection template space.

8.4.3 Nonadiabatic PN resummed methods: the Effective-One-Body (EOB) approach

The basic idea of the effective-one-body (EOB) approach [14] is to map the *real* two-body conservative dynamics, generated by the Hamiltonian (8.56) and specified up to 3PN order, onto an *effective* one-

body problem where a test particle of mass $\mu = m_1 m_2/M$ (with m_1 and m_2 the BH masses, and $M = m_1 + m_2$) moves in an effective background metric $g^{\rm eff}_{\mu\nu}$ given by

$$ds^2_{\rm eff} \equiv g^{\rm eff}_{\mu\nu}\, dx^\mu\, dx^\nu = -A(R)\, c^2 dt^2 + \frac{D(R)}{A(R)}\, dR^2 + R^2\left(d\theta^2 + \sin^2\theta\, d\varphi^2\right), \tag{8.80}$$

where

$$A(R) = 1 + a_1 \frac{GM}{c^2 R} + a_2 \left(\frac{GM}{c^2 R}\right)^2 + a_3 \left(\frac{GM}{c^2 R}\right)^3 + a_4 \left(\frac{GM}{c^2 R}\right)^4 + \cdots, \tag{8.81}$$

$$D(R) = 1 + d_1 \frac{GM}{c^2 R} + d_2 \left(\frac{GM}{c^2 R}\right)^2 + d_3 \left(\frac{GM}{c^2 R}\right)^3 + \cdots. \tag{8.82}$$

The motion of the particle is described by the action

$$S_{\rm eff} = -\mu c \int ds_{\rm eff}\,. \tag{8.83}$$

For the sake of convenience, in this section we shall use the same symbols of Secs. 8.4.1 and 8.4.2 to denote different physical quantities (such as coordinates in different gauges). The mapping between the real and the effective dynamics is worked out within the Hamilton–Jacobi formalism, by imposing that the action variables of the real and effective description coincide (i.e., $J_{\rm real} = J_{\rm eff}$, $\mathcal{I}_{\rm real} = \mathcal{I}_{\rm eff}$, where J denotes the total angular momentum, and $\mathcal{I}$ the radial action variable [14]), while allowing the energy to change,

$$\frac{\mathcal{E}^{\rm NR}_{\rm eff}}{\mu c^2} = \frac{\mathcal{E}^{\rm NR}_{\rm real}}{\mu c^2}\left[1 + \alpha_1 \frac{\mathcal{E}^{\rm NR}_{\rm real}}{\mu c^2} + \alpha_2 \left(\frac{\mathcal{E}^{\rm NR}_{\rm real}}{\mu c^2}\right)^2 + \alpha_3 \left(\frac{\mathcal{E}^{\rm NR}_{\rm real}}{\mu c^2}\right)^3 + \cdots\right], \tag{8.84}$$

here $\mathcal{E}^{\rm NR}_{\rm eff}$ is the Non–Relativistic *effective* energy, while is related to the relativistic effective energy $\mathcal{E}_{\rm eff}$ by the equation $\mathcal{E}^{\rm NR}_{\rm eff} = \mathcal{E}_{\rm eff} - \mu\, c^2$; $\mathcal{E}_{\rm eff}$ is itself defined uniquely by the action (8.83). The Non–Relativistic *real* energy $\mathcal{E}^{\rm NR}_{\rm real} \equiv H(\mathbf{q}, \mathbf{p})$, where $H(\mathbf{q}, \mathbf{p})$ is given by Eq. (8.56) with $H(\mathbf{q}, \mathbf{p}) = \mu \widehat{H}(\mathbf{q}, \mathbf{p})$. From now on, we shall relax our notation and set $G = c = 1$.

Equations of motion

Damour, Jaranowski and Schäfer [16] found that, at 3PN order, this matching procedure contains more equations to satisfy than free parameters to solve for ($a_1, a_2, a_3, d_1, d_2, d_3$, and $\alpha_1, \alpha_2, \alpha_3$). These authors suggested the following two solutions to this conundrum. At the price of modifying the energy map and the coefficients of the effective metric at the 1PN and 2PN levels, it is still possible at 3PN order to map uniquely the real two-body dynamics onto the dynamics of a test mass moving on a geodesic (for details, see App. A of Ref. [16]). However, this solution appears very complicated; more importantly, it seems awkward to have to compute the 3PN Hamiltonian

as a foundation for deriving the matching at the 1PN and 2PN levels. The second solution is to abandon the hypothesis that the effective test mass moves along a geodesic, and to augment the Hamilton–Jacobi equation with (arbitrary) higher-derivative terms that provide enough coefficients to complete the matching. With this procedure, the Hamilton-Jacobi equation reads

$$0 = \mu^2 + g_{\rm eff}^{\mu\eta}(x)\, p_\mu\, p_\eta + A^{\mu\eta\rho\sigma}(x)\, p_\mu\, p_\eta\, p_\rho\, p_\sigma + \cdots \,. \tag{8.85}$$

Because of the quartic terms $A^{\alpha\beta\gamma\delta}$, the effective 3PN relativistic Hamiltonian is not uniquely fixed by the matching rules defined above; the general expression is [16]:

$$\mathcal{E}_{\rm eff}^{\rm NR} \equiv \widehat{H}_{\rm eff}(\mathbf{q},\mathbf{p}) = \sqrt{A(q)\left[1 + \mathbf{p}^2 + \left(\frac{A(q)}{D(q)} - 1\right)(\mathbf{n}\cdot\mathbf{p})^2 + \frac{1}{q^2}\left(z_1(\mathbf{p}^2)^2 + z_2\,\mathbf{p}^2(\mathbf{n}\cdot\mathbf{p})^2 + z_3(\mathbf{n}\cdot\mathbf{p})^4\right)\right]}\,, \tag{8.86}$$

here we use the reduced relativistic effective Hamiltonian $\widehat{H}_{\rm eff} = H_{\rm eff}/\mu$, and $\mathbf{q}$ and $\mathbf{p}$ are the reduced canonical variables, obtained by rescaling the canonical variables by M and μ, respectively. The coefficients z_1, z_2 and z_3 are arbitrary, subject to the constraint

$$8z_1 + 4z_2 + 3z_3 = 6(4 - 3\eta)\,\eta\,. \tag{8.87}$$

Moreover, we slightly modify the EOB model at 3PN order of Ref. [16] by requiring that in the test mass limit the 3PN EOB Hamiltonian equal the Schwarzschild Hamiltonian. Indeed, one of the original rationales of the PN resummation methods was to recover known exact results in the test-mass limit. To achieve this, z_1, z_2 and z_3 must go to zero as $\eta \to 0$. A simple way to enforce this limit is to set $z_1 = \eta\tilde{z}_1, z_2 = \eta\tilde{z}_2$ and $z_3 = \eta\tilde{z}_3$. With this choice the coefficients $A(r)$ and $D(r)$ in Eq. (8.86) read:

$$A(r) = 1 - \frac{2}{r} + \frac{2\eta}{r^3} + \left[\left(\frac{94}{3} - \frac{41}{32}\pi^2\right) - \tilde{z}_1\right]\frac{\eta}{r^4}\,, \tag{8.88}$$

$$D(r) = 1 - \frac{6\eta}{r^2} + \left[7\tilde{z}_1 + \tilde{z}_2 + 2(3\eta - 26)\right]\frac{\eta}{r^3}\,, \tag{8.89}$$

where we set $r = |\mathbf{q}|$. The authors of Ref. [16] restricted themselves to the case $z_1 = z_2 = 0$ ($\tilde{z}_1 = \tilde{z}_2 = 0$). Indeed, they observed that for quasicircular orbits the terms proportional to z_2 and z_3 in Eq. (8.86) are very small, while for circular orbits the term proportional to z_1 contributes to the coefficient $A(r)$, as seen in Eq. (8.88). So, if the coefficient $z_1 = \eta\tilde{z}_1 \neq 0$, its value could be chosen such as to cancel the 3PN contribution in $A(r)$. To avoid this fact, which can be also thought as a gauge effect due to the choice of the coordinate system in the effective description, the authors of Ref. [16] decided to pose $z_1 = 0$ ($\tilde{z}_1 = 0$). By contrast, in this chapter we prefer to explore the effect of having $z_{1,2} \neq 0$. So we shall depart from the general philosophy followed by the authors in

Ref. [16], pushing (or expanding) the EOB approach to more extreme regimes.

Now, the reduction to the one-body dynamics fixes the arbitrary coefficients in Eq. (8.84) uniquely to $\alpha_1 = \eta/2$, $\alpha_2 = 0$, and $\alpha_3 = 0$, and provides the *resummed* (improved) Hamiltonian [obtained by solving for $\mathcal{E}^{\rm NR}_{\rm real}$ in Eq. (8.84) and imposing $H^{\rm improved} \equiv \mathcal{E}^{\rm NR}_{\rm real}$]:

$$H^{\rm improved} = M \sqrt{1 + 2\eta \left(\frac{H_{\rm eff} - \mu}{\mu} \right)} \,. \tag{8.90}$$

Including radiation-reaction effects, we can then write the Hamilton equations in terms of the reduced quantities $\widehat{H}^{\rm improved} = H^{\rm improved}/\mu$, $\widehat{t} = t/M$, $\widehat{\omega} = \omega\, M$ [15],

$$\frac{dr}{d\widehat{t}} = \frac{\partial \widehat{H}^{\rm improved}}{\partial p_r}(r, p_r, p_\varphi) \,, \tag{8.91}$$

$$\frac{d\varphi}{d\widehat{t}} \equiv \widehat{\omega} = \frac{\partial \widehat{H}^{\rm improved}}{\partial p_\varphi}(r, p_r, p_\varphi) \,, \tag{8.92}$$

$$\frac{dp_r}{dt} = -\frac{\partial \widehat{H}^{\rm improved}}{\partial r}(r, p_r, p_\varphi) \,, \tag{8.93}$$

$$\frac{dp_\varphi}{d\widehat{t}} = \widehat{F}^{\varphi}[\widehat{\omega}(r, p_r, p_\varphi)] \,, \tag{8.94}$$

where for the φ component of the radiation-reaction force we use the T- and P-approximants to the flux function [see Eqs. (8.63), (8.64)]. Note that at each PN order, say nPN, we integrate the Eqs. (8.91)–(8.94) without further truncating the partial derivatives of the Hamiltonian at nPN order (differentiation with respect to the canonical variables can introduce terms of order higher than nPN).

Following the discussion around Eq. (8.67), the ISCO of these models is determined by setting $\partial H_0^{\rm improved}/\partial r = \partial^2 H_0^{\rm improved}/\partial r^2 = 0$, where $H_0^{\rm improved}(r, p_r, p_\varphi) = H^{\rm improved}(r, 0, p_\varphi)$. If we define

$$\widehat{H}^2_{\rm eff}(r, 0, p_\varphi) \equiv W_{p_\varphi} = A(r) \left(1 + \frac{p_\varphi^2}{r^2} + \eta\, \tilde{z}_1\, \frac{p_\varphi^4}{r^6} \right) , \tag{8.95}$$

we extract the ISCO by imposing $\partial W_{p_\varphi}(r)/\partial r = 0 = \partial^2 W_{p_\varphi}(r)/\partial^2 r$. Damour, Jaranowski and Schäfer [16] noticed that at 3PN order, for $\tilde{z}_1 = \tilde{z}_2 = 0$, and using the PN expanded form for $A(r)$ given by Eq. (8.88), there is no ISCO. To improve the behavior of the PN expansion of $A(r)$ and introduce an ISCO, they proposed replacing $A(r)$ with the Padé approximants

$$A_{P_2}(r) = \frac{r(-4 + 2r + \eta)}{2r^2 + 2\eta + r\eta} \,, \tag{8.96}$$

and

$$A_{P_3}(r) = \frac{r^2[(a_4(\eta, 0) + 8\eta - 16) + r(8 - 2\eta)]}{r^3\,(8 - 2\eta) + r^2\,(a_4(\eta, 0) + 4\eta) + r\,(2a_4(\eta, 0) + 8\eta) + 4(\eta^2 + a_4(\eta, 0))} \,, \tag{8.97}$$

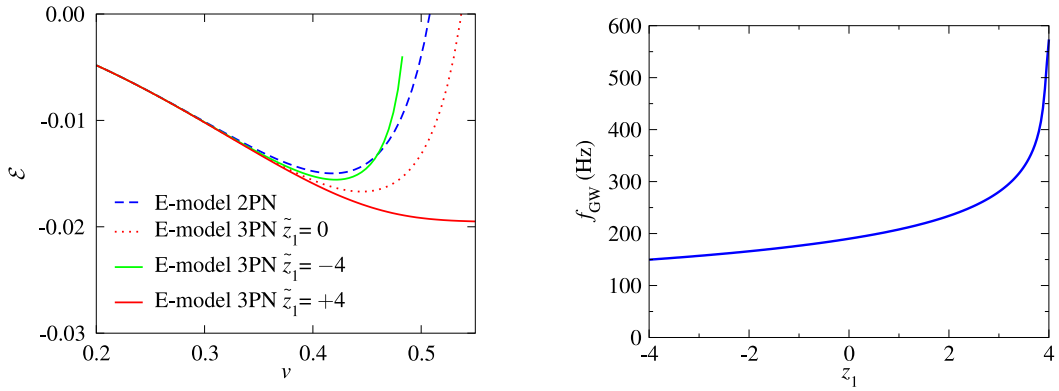

Figure 8.12: In the left panel, we plot the binding energy evaluated using the improved Hamiltonian (8.90), as a function of the velocity parameter v, for equal-mass BBHs, $\eta = 0.25$. We plot different PN orders for the E-model varying also the parameter $\tilde{z}_1$. In the right panel, we plot the GW frequency at the ISCO at 3PN order as a function of the parameter $\tilde{z}_1$ for (15+15)$M_\odot$ BBH.

where

$$a_4(\eta, \tilde{z}_1) = \left[\frac{94}{3} - \frac{41}{32}\pi^2 - \tilde{z}_1\right] \eta \,. \tag{8.98}$$

In Table 8.2, we show the GW frequency at the ISCO for some typical choices of BBH masses, computed using the above expressions for $A(r)$ in the improved Hamiltonian (8.90) with $\tilde{z}_1 = \tilde{z}_2 = 0$.

We use the Padé resummation for $A(r)$ of Ref. [16] also for the general case $\tilde{z}_1 \neq 0$, because for the PN expanded form of $A(r)$ the ISCO does not exist for a wide range of values of $\tilde{z}_1$. [However, when we discuss Fourier-domain detection template families in Sec. 8.6, we shall investigate also EOB models with PN-expanded $A(r)$.]

In Fig. 8.12, we plot the binding energy as evaluated using the improved Hamiltonian (8.90), at different PN orders, for equal-mass BBHs. At 3PN order, we use as typical values $\tilde{z}_1 = 0, \pm 4$. [For $\tilde{z}_1 > 4$ the location of the ISCO is no longer a monotonic function of $\tilde{z}_1$. So we set $\tilde{z}_1 \leq 4$.] In the right panel of Fig. 8.12, we show the variation in the GW frequency at the ISCO as a function of $\tilde{z}_1$ for a (15+15)$M_\odot$ BBH. Finally, in Fig. 8.13, we compare the binding energy for a few selected PN models, where for the E models we fix $\tilde{z}_1 = \tilde{z}_2 = 0$ [see the left panel of Fig. 8.12 for the dependence of the binding energy on the coefficient $\tilde{z}_1$]. Notice, in the left panel, that the 2PN and 3PN T energies are much closer to each other than the 2PN and 3PN P energies are, and than the 2PN and 3PN E energies are; notice also that the 3PN T and P energies are very close. The closeness of the binding energies (and of the MECOs and ISCOs) predicted by PN expanded and resummed models at 3PN order (with $\tilde{z}_1 = 0$), and of the binding energy predicted by the numerical quasiequilibrium BBH models of Ref. [24] was recently pointed out in Refs. [53, 64]. However, the EOB results are very close to the numerical results of Ref. [24] only if the range of variation of $\tilde{z}_1$ is restricted.

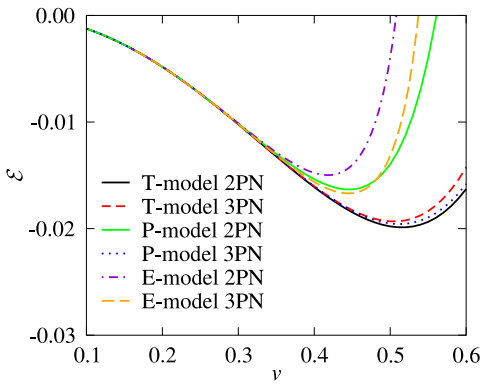

Figure 8.13: Binding energy as a function of the velocity parameter v, for equal-mass BBHs. We plot different PN orders for selected PN models. For the E model at 3PN order we fix $\tilde{z}_1 = 0 = \tilde{z}_2$.

Definition of the models

For these models, we use the initial conditions laid down in Ref. [55], and also adopted in this chapter for the HT and HP models (see Sec. 8.4.1). At 2PN order, we stop the integration of the Hamilton equations at the light ring given by the solution of the equation $r^3 - 3r^2 + 5\eta = 0$ [15]. At 3PN order, the light ring is defined by the solution of

$$\frac{d}{du}\left[u^2\, A_{P_3}(u)\right] = 0, \tag{8.99}$$

with $u = 1/r$ and A_{P_3} is given by Eq. (8.97). For some configurations, the orbital frequency and the binding energy start to decrease before the binary can reach the 3PN light ring, so we stop the evolution when $\dot{\hat{\omega}} = 0$ [see discussion in Sec. 8.4.4 below]. For other configurations, it happens that the radial velocity becomes comparable to the angular velocity before the binary reaches the light ring; in this case, the approximation used to introduce the RR effects into the conservative dynamics is no longer valid, and we stop the integration of the Hamilton equations when $|\dot{r}/(r\dot{\varphi})|$ reaches 0.3. For some models, usually those with $\tilde{z}_{1,2} \neq 0$, the quantity $|\dot{r}/(r\dot{\varphi})|$ reaches a maximum during the last stages of evolution, then it starts decreasing, and $\dot{r}$ becomes positive. In such cases, we choose to stop at the maximum of $|\dot{r}/(r\dot{\varphi})|$.

In any of these cases, the instantaneous GW frequency at the time when the integration is stopped defines the *ending frequency* for these waveforms.

We shall refer to the EOB models (E-approximants) as ET(nPN, mPN) (when the T-approximant is used for the flux) or EP(nPN, mPN) (when the P-approximant is used for the flux), where nPN (mPN) denotes the maximum PN order of the terms included in the Hamiltonian (flux). We shall consider (nPN, mPN) = $(1, 1.5)$, $(2, 2.5)$, and $(3, 3.5, \hat{\theta})$ [at 3PN order we need to indicate also a choice of the arbitrary flux parameter $\hat{\theta}$].

Waveforms and matches

In Table 8.12, we investigate the dependence of the E waveforms on the values of the unknown parameters $\tilde{z}_1$ and $\tilde{z}_2$ that appear in the EOB Hamiltonian at 3PN order. The coefficients $\tilde{z}_1$ and $\tilde{z}_2$ are in principle completely arbitrary. When $\tilde{z}_1 \neq 0$, the location of the ISCO changes, as shown in Fig. 8.12. Moreover, because in Eq. (8.86) $\tilde{z}_1$ multiplies a term that is not zero on circular orbits, the motion tends to become noncircular much earlier, and the criteria for ending the integration of the Hamilton equations are satisfied earlier. [See the discussion of the ending frequency in the previous section.] This effect is much stronger in equal-mass BBHs with high M. For example, for $(15{+}15)M_\odot$ BBHs and for $\tilde{z}_2 = 0$, the fitting factor (the maxmax match, maximized over M and η) between an EP target waveform with $\tilde{z}_1 = 0$ and EP search waveforms with $-40 \lesssim \tilde{z}_1 < -4$ can well be ≤ 0.9. However, if we restrict $\tilde{z}_1$ to the range $[-4, 4]$, we get very high fitting factors, as shown in Table 8.12.

In Eq. (8.86), the coefficients $\tilde{z}_2$ and $\tilde{z}_3$ multiply terms that are zero on circular orbits. [The coefficient $\tilde{z}_2$ appears also in $D(r)$, given by Eq. (8.89).] So their effect on the dynamics is not very important, as confirmed by the very high matches obtained in Table 8.12 between EP waveforms with $\tilde{z}_2 = 0$ and EP waveforms with $\tilde{z}_2 = \pm 4$. It seems that the effect of changing $\tilde{z}_2$ is nearly the same as a remapping of the BBH mass parameters.

We investigated also the case in which we use the PN expanded form for $A(r)$ given by Eq. (8.88). For example, for $(15{+}15)M_\odot$ BBHs and $\tilde{z}_2 = 0$, the fitting factors between EP target waveforms with $\tilde{z}_1 = -40, -4, 4, 40$ and EP search waveforms with $\tilde{z}_1 = 0$ are $(\mathrm{maxmax}, M, \eta) = (0.767, 39.55, 0.240)$, $(0.993, 30.83, 0.241)$, $(0.970, 30.03, 0.241)$, and $(0.915, 28.23, 0.242)$, respectively. So the overlaps can be quite low.

In Table 8.8, for three typical choices of BBH masses, we perform a convergence test using Cauchy's criterion. The values are quite high. However, as for the P-approximants, we have no way to test whether the E-approximants are converging to the true limit. In Fig. 8.14, we plot the frequency-domain amplitude of the EP-approximated (restricted) waveforms, at different PN orders, for a $(15\ {+}15)M_\odot$ BBH. The evolution of the EOB models contains a plunge characterized by quasicircular motion [15]. This plunge causes the amplitude to deviate from the Newtonian amplitude, $\mathcal{A}_{\mathrm{Newt}} = f^{-7/6}$ around 200 Hz, which is a higher frequency than we found for the adiabatic models [see Figs. 8.4, 8.7].

In Table 8.11, for some typical choices of the masses, we evaluate the fitting factors between the $\mathrm{ET}(2, 2.5)$ and $\mathrm{ET}(3, 3.5)$ waveforms (with $\tilde{z}_1 = \tilde{z}_2 = 0$) and the $\mathrm{T}(2, 2.5)$ and $\mathrm{T}(3, 3.5)$ waveforms. This comparison should emphasize the effect of moving from the adiabatic orbital evolution, ruled by the energy-balance equation, to the (almost) full Hamiltonian dynamics, ruled by the Hamilton equations. More specifically, we see the effect of the differences *in the conservative dynamics* between the PN expanded T-model and the PN resummed E-model (the radiation-reaction effects are

N	$\langle \mathrm{EP}_N, \mathrm{EP}_{N+1} \rangle$					
	$(5+20)M_\odot$	$(10+10)M_\odot$				$(15+15)M_\odot$
0	0.677	0.584	(0.769,	17.4,	0.246)	0.811
1	0.766	0.771	(0.999,	21.8,	0.218)	0.871
2 ($\hat{\theta}=+2$)	0.862	0.858	(0.999,	21.3,	0.222)	0.898
2 ($\hat{\theta}=-2$)	0.912	0.928	(0.999,	21.9,	0.211)	0.949

Table 8.8: Test for the Cauchy convergence of the EP-approximants. The values quoted assume optimization on the extrinsic parameters but the same intrinsic parameters (i.e., they assume the same masses). Here we define $\mathrm{EP}_0 = \mathrm{EP}(0,0)$, $\mathrm{EP}_1 = \mathrm{EP}(1,1.5)$, $\mathrm{EP}_2 = \mathrm{EP}(2,2.5)$, and $\mathrm{EP}_3 = \mathrm{EP}(3,3.5,\hat{\theta},\tilde{z}_1=\tilde{z}_2=0)$. The values in parentheses are the maxmax matches obtained by maximizing with respect to the extrinsic *and* intrinsic parameters, shown together with the EP_{N+1} parameters M and η where the maxima are attained. In all cases the integration of the equations is started at a GW frequency of 20 Hz.

introduced in the same way in both models). While the matches are quite low at 2PN order, they are high (≥ 0.95) at 3PN order, at least for $M \leq 30M_\odot$, but the estimation of m_1 and m_2 is poor. This result suggests that, for the purpose of signal detection as opposed to parameter estimation, the conservative dynamics predicted by the EOB resummation and by the PN expansion are very close at 3PN order, at least for $M \leq 30M_\odot$. Moreover, the results of Table 8.11 suggest also that the effect of the unknown parameter $\hat{\theta}$ is rather small, at least if $\hat{\theta}$ is of order unity, so in the following we shall always set $\hat{\theta}=0$.

In Tables 8.9 and 8.10 we study the difference between the $\mathrm{EP}(2,2.5)$ and $\mathrm{EP}(3,3.5)$ models (with $\tilde{z}_1=\tilde{z}_2$=0), and all the other adiabatic and nonadiabatic models. For some choices of BBH masses, these tables show the maxmax matches between the search models in the columns and the target models in the rows, maximized over the search-model parameters M and η, with the restriction $0<\eta\leq 1/4$. At 2PN order, the matches with the $\mathrm{T}(2,2.5)$, $\mathrm{HT}(2,2)$ and $\mathrm{HP}(2,2.5)$ models are low, while with the matches with the $\mathrm{T}(2,2)$ and $\mathrm{P}(2,2.5)$ models are high, at least for $M \leq 30M_\odot$ (but the estimation of the BH masses is poor). At 3PN order, the matches with $\mathrm{T}(3,3.5,\hat{\theta})$, $\mathrm{P}(3,3.5,\hat{\theta})$, $\mathrm{HP}(3,3.5,\hat{\theta})$ and $\mathrm{HT}(3,3.5,\hat{\theta})$ are quite high if $M \leq 30M_\odot$. However, for $M=40M_\odot$, the matches can be quite low. We expect that this happens because in this latter case the differences in the late dynamical evolution become crucial.

8.4.4 Features of the late dynamical evolution in nonadiabatic models

While studying the numerical evolution of nonadiabatic models, we encounter two kinds of dynamical behavior that are inconsistent with the assumption of quasicircular motion used to include the radiation-reaction effects, so when one of these two behaviors occurs, we immediately stop the integration of the equations of motion. First, in the late stage of evolution $\widehat{\omega}$ can reach a maximum, and then drop quickly to zero; so we stop the integration if $\dot{\widehat{\omega}}=0$. Second, the radial velocity $\dot{r}$ can become a significant portion of the total speed, so we stop the integration if $\dot{r}=0.3(r\widehat{\omega})$.

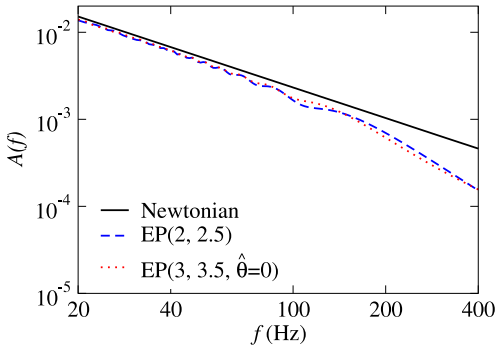

Figure 8.14: Frequency-domain amplitude versus frequency for the EP-approximated (restricted) waveform, at different PN orders, for a $(15+15)M_\odot$ BBH.

The first behavior is found mainly in the H models at 3PN order, when η is relatively small ($\lesssim 0.21$). As we shall see below, it is *not* characteristic of either the Schwarzschild Hamiltonian or the EOB Hamiltonian. In the left panel of Fig. 8.15, we plot the binding energy evaluated from $\widehat{H}(r, p_r = 0, p_\varphi)$ [given by Eq. (8.56)] as a function of r at $\eta = 0.16$, for various values of the (reduced) angular momentum p_φ. As this plot shows, there exists a *critical radius*, $r_{\rm crit}$, below which no circular orbits exist. This $r_{\rm crit}$ can be derived as follows. From Fig. 8.15 (left), we deduce that

$$\left.\frac{d\widehat{H}}{dr}\right|_{\rm circ} \to \infty\,, \qquad r \to r_{\rm crit}\,. \tag{8.100}$$

Because circular orbits satisfy the conditions

$$p_r = 0\,, \qquad \frac{\partial \widehat{H}}{\partial r} = 0\,, \tag{8.101}$$

and

$$\left.\frac{dp_\varphi}{dr}\right|_{\rm circ} = -\frac{\partial^2 \widehat{H}}{\partial r^2}\left(\frac{\partial^2 \widehat{H}}{\partial r \partial p_\varphi}\right)^{-1}\,, \tag{8.102}$$

we get

$$\left.\frac{d\widehat{H}}{dr}\right|_{\rm circ} = \frac{\partial \widehat{H}}{\partial r} + \frac{\partial \widehat{H}}{\partial p_\varphi}\left.\frac{dp_\varphi}{dr}\right|_{\rm circ} = -\frac{\partial \widehat{H}}{\partial p_\varphi}\frac{\partial^2 \widehat{H}}{\partial r^2}\left(\frac{\partial^2 \widehat{H}}{\partial r \partial p_\varphi}\right)^{-1}\,. \tag{8.103}$$

Combining these equations we obtain two conditions that define $r_{\rm crit}$:

$$\left.\frac{\partial \widehat{H}}{\partial r}\right|_{r_{\rm crit}} = 0\,, \qquad \left.\frac{\partial^2 \widehat{H}}{\partial r \partial p_\varphi}\right|_{r_{\rm crit}} = 0\,. \tag{8.104}$$

In the right panel of Fig. 8.15, we plot the critical orbital frequency $\widehat{\omega}_{\rm crit}$ as a function of η in the range [0.1, 0.21]. In the same figure, we show also the ending frequencies for the HT$(3, 3.5, \pm 2)$ and

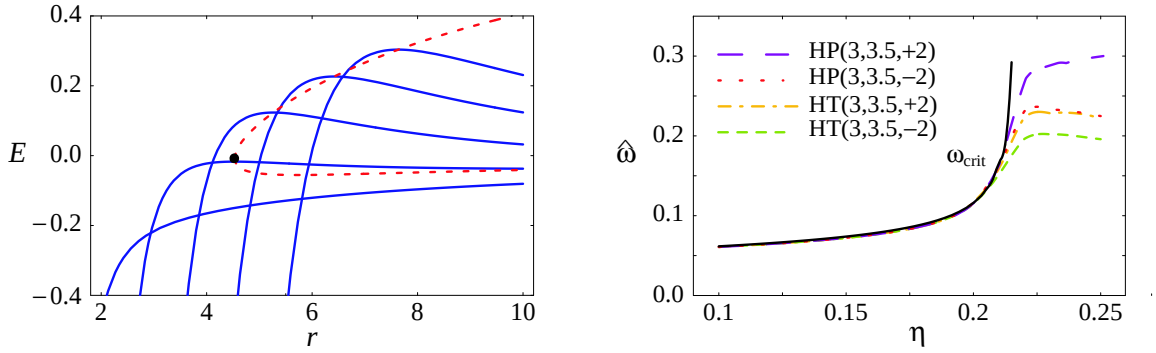

Figure 8.15: Ending points of the H models at 3PN order for low values of η. In the left panel, we plot as a function of r the Hamiltonian $\widehat{H}(r, p_r = 0, p_\varphi)$ [given by Eq. (8.56)], evaluated at $\eta = 0.16$ for a $(5{+}20)M_\odot$ BBH, for various values of the (reduced) angular momentum p_φ. The circular-orbit solutions are found at the values of r and $\hat{H}$ joined by the dashed line. At $r_{\rm crit} = 4.524$ there is a critical radius, below which there is no circular orbit. In the right panel, we plot as a function of η the orbital angular frequency $\widehat{\omega}_{\rm crit}(\eta)$ corresponding to the critical radius, for $0.1 < \eta < 0.21$ (solid line). This curve agrees well with the ending frequencies of the HT and HP models at 3PN order, which are shown as dotted and dashed lines in the figure.

HP$(3, 3.5, \pm 2)$ models. For $0.1 < \eta < 0.21$, these ending frequencies are in good agreement with the critical frequencies $\hat{\omega}_{\rm crit}$; for $\eta > 0.21$, the ending condition $\dot{r} = 0.3(r\widehat{\omega})$ is satisfied before $\dot{\widehat{\omega}} = 0$. For $0.1 < \eta < 0.21$, this good agreement can be explained as follows: for the H models at 3PN order with $\eta \lesssim 0.21$, the orbital evolution is almost quasicircular (i.e., $\dot{r}$ remains small and $\widehat{\omega}$ keeps increasing) until the critical point is reached; beyond this point, there is no way to keep the orbit quasicircular, as the angular motion is converted significantly into radial motion, and $\widehat{\omega}$ begins to decrease. This behavior ($\dot{\widehat{\omega}} \to 0$) is also present in the E model in the vicinity of the light ring, because the light ring is also a minimal radius for circular orbits [the conditions (8.100) are satisfied also in this case]. However, the behavior of the energy is qualitatively different for the H and E models: in the E models (just as for a test particle in Schwarzchild spacetime) the circular-orbit energy goes to infinity, while this is not the case for the H models.

The second behavior is usually caused by radiation-reaction effects, and accelerated by the presence of an ISCO (and therefore of a *plunge*). However, it is worth to mention another interesting way in which the criterion $\dot{r} = 0.3(r\widehat{\omega})$ can be satisfied for some E evolutions at 3PN order. During the late stages of evolution, $\dot{r}$ sometimes increases suddenly and drastically, and the equations of motion become singular. This behavior is quite different from a plunge due to the presence of an ISCO (in that case the equations of motion do *not* become singular). The cause of this behavior is that at 3PN order the coefficient $D(r)$ [see Eq. (8.89)] can go to zero and become negative for a sufficiently small r. For $\tilde{z}_1 = \tilde{z}_2 = 0$, this occurs at the radius r_D given by

$$r_{\rm D}^3 - 6\eta r_{\rm D} + 2(3\eta - 26)\eta = 0; \tag{8.105}$$

r_D can fall outside the light ring. For example, for $\eta = 0.25$ we have $r_{\rm D} = 2.54$, while the light rings sits at $r = 2.31$. On the transition from $D(r) > 0$ to $D(r) < 0$, the effective EOB metric unphysical, and the E model then becomes invalid. Using the Hamiltonian equation of motion (8.91), it is straightforward to prove that a negative $D(r)$ causes the radial velocity to blow up:

$$\dot{r} = \frac{\partial \widehat{H}}{\partial p_r} \propto \frac{p_r}{D(r)} \to \infty \qquad \text{as} \quad r \to r_{\rm D}\,. \tag{8.106}$$

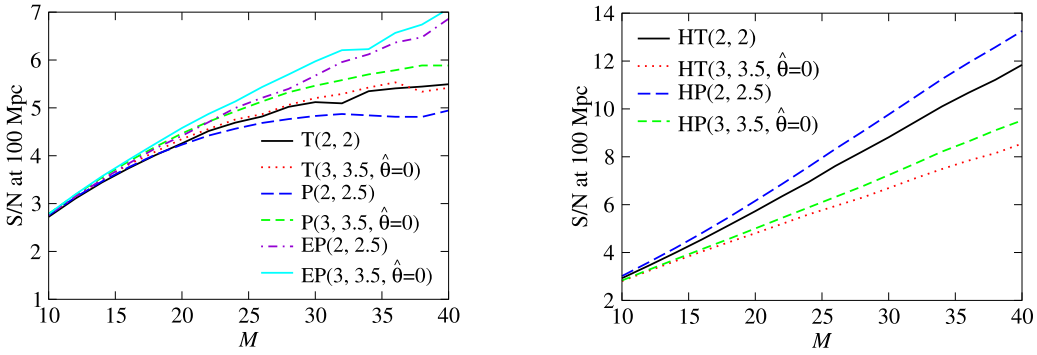

Figure 8.16: Signal-to-noise ratio at 100 Mpc versus total mass M, for selected PN models. The S/N is computed for equal-mass BBHs using the LIGO-I noise curve (8.28) and the waveform expression (8.29) with the rms $\Theta = 8/5$; for the E model at 3PN we set $\tilde{z}_1 = \tilde{z}_2 = 0$.

8.5 Signal-to-noise ratio for the two-body models

In Fig. 8.16, we plot the optimal signal-to-noise ratio $\rho_{\rm opt}$ for a few selected PN models. The value of $\rho_{\rm opt}$ is computed using Eqs. (8.1) and (8.19) with the waveform given by Eq. (8.29), for a luminosity distance of 100 Mpc and the rms $\Theta = 8/5$ [see discussion around Eq. (8.29)]; for the EP model we set $\tilde{z}_1 = \tilde{z}_2 = 0$. Notice that, because the E models have a plunge, their signal-to-noise ratios are much higher (at least for $M \geq 30 M_\odot$) than those for the adiabatic models, which we cut off at the MECO. See also Fig. 8.17, which compares the S/N for EP$(2, 2.5)$ waveforms with and without the plunge; for $M = 20 M_\odot$, excluding the plunge decreases the S/N by $\sim 4\%$ (which corresponds to a decrease in detection rate of 12% for a fixed detection threshold); while for $M = 30 M_\odot$, excluding the plunge decreases the S/N by $\sim 22\%$ (which corresponds to a decrease in detection rate of 54%). This result confirms the similar conclusion drawn in Ref. [12].

Because at 2PN and 3PN order the H models do not have a plunge, but the two BHs continue to move on quasicircular orbits even at close separations, the number of total GW cycles is increased, and so is the signal-to-noise ratio, as shown in the right panel of Fig. 8.16. However, we do not trust the H models much, because they show a very different behavior at different PN orders, as already emphasized in Sec. 8.4.1.

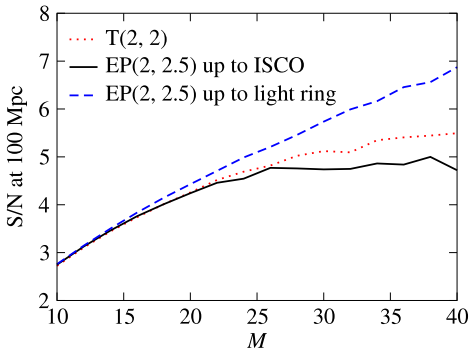

Figure 8.17: Effect of the plunge on the signal-to-noise ratio. The S/N is computed at 100 Mpc for equal-mass BBHs, as a function of the total mass, for the $\mathrm{T}(2,2)$ adiabatic model (for comparison), and for the $\mathrm{EP}(2,2.5)$ model with ending frequency at the ISCO, and at the light ring (in this latter case the signal includes a plunge). Here we use the LIGO-I noise curve (8.28) and the waveform expression (8.29) with the rms $\Theta = 8/5$.

		T(2, 2)			T(2, 2.5)			T(3, 3.5, 0)			P(2, 2.5)			P(3, 3.5, 0)		
		mm	M	η	mm	M	η	mm	M	η	mm	M	η	mm	M	η
T(2, 2)	$(20{+}20)M_\odot$				0.924	54.47	0.23	0.999	40.47	0.24	0.977	39.13	0.25	0.999	41.93	0.24
	$(15{+}15)M_\odot$				0.873	39.46	0.24	0.999	30.35	0.24	0.980	29.69	0.25	0.998	31.54	0.23
	$(15{+}5)M_\odot$				0.885	29.45	0.10	0.998	19.64	0.19	0.992	18.07	0.22	0.998	20.23	0.18
	$(5{+}5)M_\odot$				0.988	21.28	0.06	0.998	10.61	0.22	0.994	10.54	0.22	0.999	11.16	0.20
T(2, 2.5)	$(20{+}20)M_\odot$	0.882	31.44	0.25				0.870	31.54	0.25	0.824	30.25	0.25	0.893	33.09	0.25
	$(15{+}15)M_\odot$	0.845	24.85	0.25				0.835	25.21	0.25	0.796	25.35	0.25	0.863	26.20	0.25
	$(15{+}5)M_\odot$	0.848	15.34	0.25				0.865	15.74	0.25	0.870	15.85	0.25	0.894	15.90	0.25
	$(5{+}5)M_\odot$	0.801	9.41	0.25				0.823	9.51	0.25	0.826	9.51	0.25	0.849	9.61	0.25
T(3, 3.5, 0)	$(20{+}20)M_\odot$	0.999	39.57	0.24	0.916	54.63	0.23				0.989	39.03	0.24	0.997	41.56	0.23
	$(15{+}15)M_\odot$	0.999	29.71	0.24	0.855	39.46	0.24				0.992	29.25	0.25	1.000	31.97	0.21
	$(15{+}5)M_\odot$	0.999	20.98	0.16	0.877	29.20	0.10				0.997	18.82	0.20	1.000	20.81	0.17
	$(5{+}5)M_\odot$	0.991	9.67	0.25	0.986	19.49	0.07				0.998	9.90	0.24	1.000	10.57	0.22
P(2, 2.5)	$(20{+}20)M_\odot$	0.970	40.47	0.24	0.879	56.77	0.23	0.991	41.80	0.22				0.999	46.01	0.18
	$(15{+}15)M_\odot$	0.967	30.15	0.24	0.816	39.66	0.24	0.998	32.66	0.20				0.999	34.02	0.19
	$(15{+}5)M_\odot$	0.989	23.77	0.12	0.792	20.56	0.20	0.996	21.55	0.15				0.998	21.83	0.15
	$(5{+}5)M_\odot$	0.989	9.67	0.25	0.882	13.04	0.15	0.998	10.08	0.24				0.997	10.75	0.21
P(3, 3.5, 0)	$(20{+}20)M_\odot$	0.999	38.33	0.24	0.923	51.51	0.24	0.997	38.97	0.24	0.971	37.70	0.25			
	$(15{+}15)M_\odot$	0.997	28.47	0.25	0.979	51.01	0.10	0.997	28.96	0.25	0.961	28.88	0.25			
	$(15{+}5)M_\odot$	0.997	19.53	0.18	0.825	20.89	0.19	1.000	19.12	0.19	0.998	18.32	0.21			
	$(5{+}5)M_\odot$	0.949	9.80	0.24	0.988	17.70	0.09	0.993	9.75	0.25	0.991	9.75	0.25			
EP(2, 2.5)	$(20{+}20)M_\odot$	0.954	38.10	0.25	0.936	51.14	0.24	0.933	39.10	0.25	0.878	38.22	0.25	0.962	39.94	0.25
	$(15{+}15)M_\odot$	0.965	29.34	0.25	0.895	37.45	0.25	0.960	29.60	0.25	0.903	29.56	0.25	0.975	30.15	0.25
	$(15{+}5)M_\odot$	0.988	20.79	0.16	0.769	21.97	0.19	0.983	20.22	0.18	0.969	19.54	0.19	0.980	20.85	0.17
	$(5{+}5)M_\odot$	0.996	9.70	0.25	0.980	20.46	0.07	0.997	10.29	0.23	0.995	10.22	0.23	0.997	10.83	0.21
EP(3, 3.5, 0)	$(20{+}20)M_\odot$	0.946	37.11	0.25	0.949	48.90	0.24	0.930	37.84	0.25	0.867	36.72	0.25	0.954	38.80	0.24
	$(15{+}15)M_\odot$	0.955	28.78	0.24	0.913	35.38	0.24	0.948	28.89	0.25	0.893	28.82	0.25	0.968	29.50	0.25
	$(15{+}5)M_\odot$	0.992	18.51	0.20	0.808	22.15	0.18	0.985	18.92	0.20	0.970	18.34	0.21	0.983	19.63	0.19
	$(5{+}5)M_\odot$	0.968	9.65	0.25	0.985	18.41	0.08	0.994	9.76	0.25	0.992	9.77	0.25	0.998	10.16	0.23
HT(2, 2)	$(20{+}20)M_\odot$	0.777	21.39	0.25	0.890	27.58	0.25	0.768	21.61	0.25	0.732	21.63	0.25	0.789	22.57	0.25
	$(15{+}15)M_\odot$	0.674	20.20	0.24	0.780	21.83	0.25	0.673	21.02	0.25	0.657	21.03	0.25	0.687	21.07	0.25
	$(15{+}5)M_\odot$	0.616	15.88	0.20	0.666	18.84	0.18	0.625	17.37	0.18	0.645	16.10	0.22	0.631	17.14	0.18
	$(5{+}5)M_\odot$	0.796	9.62	0.25	0.935	10.00	0.25	0.833	9.73	0.25	0.834	9.74	0.25	0.856	9.75	0.25
HT(3, 3.5, 0)	$(20{+}20)M_\odot$	0.812	32.35	0.25	0.925	44.91	0.24	0.795	34.76	0.25	0.737	32.98	0.25	0.812	37.10	0.24
	$(15{+}15)M_\odot$	0.848	27.97	0.25	0.919	33.30	0.25	0.835	28.70	0.25	0.788	28.78	0.25	0.875	29.07	0.25
	$(15{+}5)M_\odot$	0.998	23.08	0.13	0.788	21.15	0.20	0.999	21.25	0.16	0.994	19.77	0.18	0.999	21.81	0.15
	$(5{+}5)M_\odot$	0.952	9.65	0.25	0.828	10.36	0.24	0.984	9.76	0.25	0.984	9.77	0.25	0.992	9.99	0.24
HP(2, 2.5)	$(20{+}20)M_\odot$	0.756	18.71	0.25	0.853	23.74	0.24	0.752	18.96	0.25	0.725	19.09	0.25	0.769	19.70	0.25
	$(15{+}15)M_\odot$	0.631	17.87	0.24	0.714	18.06	0.25	0.634	17.86	0.25	0.630	18.46	0.25	0.642	18.53	0.25
	$(15{+}5)M_\odot$	0.582	14.33	0.25	0.631	16.88	0.20	0.587	14.54	0.25	0.600	16.40	0.18	0.589	17.88	0.15
	$(5{+}5)M_\odot$	0.731	9.41	0.25	0.869	9.75	0.25	0.755	9.51	0.25	0.755	9.54	0.25	0.765	9.54	0.25
HP(3, 3.5, 0)	$(20{+}20)M_\odot$	0.748	32.36	0.25	0.879	42.53	0.25	0.733	32.51	0.25	0.679	30.72	0.25	0.756	34.48	0.25
	$(15{+}15)M_\odot$	0.789	27.41	0.24	0.915	31.80	0.25	0.782	27.43	0.25	0.741	27.43	0.25	0.817	28.60	0.25
	$(15{+}5)M_\odot$	0.998	21.75	0.15	0.792	20.41	0.21	1.000	20.57	0.17	0.995	19.29	0.19	0.999	21.17	0.16
	$(5{+}5)M_\odot$	0.912	9.62	0.25	0.990	16.20	0.10	0.959	9.73	0.25	0.961	9.76	0.25	0.982	9.76	0.25

Table 8.9: (Continued into Table 8.10.) Fitting factors between several PN models, at 2PN and 3PN orders. For three choices of BBH masses, this table shows the maxmax matches [see Eq. (8.10)] between the *search* models at the top of the columns and the *target* models at the left end of the rows, *maximized over the intrinsic parameters of the search models in the columns*. For each intersection, the three numbers mm, $M = m_1 + m_2$ and $\eta = m_1 m_2/M^2$ denote the maximized match and the search-model mass parameters at which the maximum is attained. In computing these matches, the parameter η of the search models was restricted to its physical range $0 < \eta \leq 1/4$. The arbitrary flux parameter $\hat{\theta}$ was always set equal to zero. These matches represent the fitting factors [see Eq. (8.20)] for the projection of the target models onto the search models. The reader will notice that the values shown are not symmetric across the diagonal: for instance, the match for the search model $\mathrm{T}(2, 2.5)$ against the target model $\mathrm{P}(2, 2.5)$ is higher than the converse. This is because the matches represent the inner product (8.1) between two different pairs of model parameters: in the first case, the target parameters $(m_1 = 15M_\odot, m_2 = 15M_\odot)_P \equiv (M = 30M_\odot, \eta = 0.25)_P$ are mapped to the maximum-match search parameters $(M = 39.7M_\odot, \eta = 0.24)_T$; in the second case, the target parameters $(m_1 = 15M_\odot, m_2 = 15M_\odot)_T \equiv (M = 30M_\odot, \eta = 0.25)_T$ are mapped to the maximum-match parameters $(M = 25.37M_\odot, \eta = 0.24)_P$ [so the symmetry of the inner product (8.1) is reflected by the fact that the search parameters $(M = 25.3M_\odot, \eta = 0.24)_P$ are mapped into the target parameters $(M = 30M_\odot, \eta = 0.25)_T$].

		EP(2, 2.5)			EP(3, 3.5, 0)			HT(2, 2)			HT(3, 3.5, 0)			HP(2, 2.5)			HP(3, 3.5, 0)		
		mm	M	η	mm	M	η	mm	M	η	mm	M	η	mm	M	η	mm	M	η
T(2, 2)	(20+20)$M_\odot$	0.953	41.67	0.24	0.952	43.00	0.24	0.951	80.34	0.24	0.855	56.69	0.24	0.965	90.12	0.24	0.859	74.80	0.25
	(15+15)$M_\odot$	0.962	30.41	0.24	0.991	35.32	0.17	0.899	58.93	0.24	0.997	33.03	0.20	0.922	67.38	0.24	0.998	33.67	0.20
	(15+5)$M_\odot$	0.988	19.11	0.20	0.992	20.93	0.17	0.924	69.96	0.05	0.998	19.38	0.19	0.876	57.94	0.07	0.999	19.81	0.18
	(5+5)$M_\odot$	0.997	10.33	0.23	0.998	11.09	0.20	0.788	9.93	0.25	0.998	10.92	0.21	0.727	10.19	0.25	0.999	11.19	0.20
T(2, 2.5)	(20+20)$M_\odot$	0.908	31.37	0.25	0.929	32.98	0.25	0.959	58.39	0.24	0.928	35.74	0.24	0.955	67.85	0.24	0.892	36.87	0.23
	(15+15)$M_\odot$	0.861	24.52	0.25	0.893	25.58	0.25	0.932	53.46	0.17	0.926	26.82	0.25	0.920	51.38	0.24	0.921	27.99	0.24
	(15+5)$M_\odot$	0.822	15.40	0.25	0.867	15.81	0.25	0.790	16.59	0.25	0.903	15.81	0.25	0.839	51.91	0.07	0.955	16.03	0.25
	(5+5)$M_\odot$	0.814	9.52	0.25	0.839	9.59	0.25	0.941	9.63	0.25	0.838	9.52	0.25	0.872	9.80	0.25	0.866	9.61	0.25
T(3, 3.5, 0)	(20+20)$M_\odot$	0.925	40.09	0.24	0.918	42.90	0.24	0.940	80.76	0.24	0.833	57.71	0.24	0.958	89.85	0.24	0.840	73.84	0.25
	(15+15)$M_\odot$	0.955	29.98	0.24	0.937	30.78	0.24	0.887	58.83	0.24	0.996	32.67	0.20	0.914	66.56	0.24	0.758	31.32	0.24
	(15+5)$M_\odot$	0.983	19.68	0.18	0.985	20.97	0.16	0.926	69.81	0.05	0.999	19.47	0.19	0.887	60.02	0.07	1.000	19.79	0.18
	(5+5)$M_\odot$	0.992	9.99	0.24	0.997	10.40	0.22	0.826	9.83	0.25	0.993	10.48	0.22	0.749	10.07	0.25	0.995	10.81	0.21
P(2, 2.5)	(20+20)$M_\odot$	0.866	41.72	0.24	0.859	43.14	0.24	0.912	83.09	0.24	0.795	65.45	0.24	0.934	92.91	0.24	0.805	82.71	0.25
	(15+15)$M_\odot$	0.898	30.06	0.24	0.963	38.21	0.14	0.857	62.07	0.24	0.992	33.28	0.19	0.890	69.31	0.24	0.709	59.88	0.25
	(15+5)$M_\odot$	0.966	20.48	0.17	0.966	21.86	0.15	0.907	70.42	0.05	0.993	20.08	0.17	0.904	64.71	0.06	0.997	20.29	0.17
	(5+5)$M_\odot$	0.995	9.79	0.25	0.994	10.43	0.22	0.825	9.81	0.25	0.990	10.51	0.22	0.748	10.05	0.25	0.992	10.83	0.21
P(3, 3.5, 0)	(20+20)$M_\odot$	0.960	40.10	0.23	0.953	41.06	0.24	0.943	76.61	0.24	0.835	53.85	0.24	0.961	86.56	0.24	0.842	70.76	0.25
	(15+15)$M_\odot$	0.965	29.33	0.24	0.966	30.14	0.24	0.893	56.29	0.24	0.993	31.83	0.20	0.920	63.91	0.24	0.996	32.41	0.20
	(15+5)$M_\odot$	0.982	18.87	0.20	0.983	20.29	0.17	0.926	68.98	0.05	0.996	19.15	0.19	0.886	58.97	0.07	0.999	19.45	0.19
	(5+5)$M_\odot$	0.973	9.74	0.25	0.998	9.85	0.25	0.849	9.81	0.25	0.992	10.02	0.24	0.761	10.04	0.25	0.993	10.46	0.22
EP(2, 2.5)	(20+20)$M_\odot$				0.996	41.72	0.24	0.953	75.09	0.24	0.929	47.51	0.24	0.948	84.61	0.24	0.907	59.72	0.24
	(15+15)$M_\odot$				0.999	32.66	0.21	0.908	56.68	0.24	0.889	32.89	0.24	0.915	64.87	0.24	0.997	33.00	0.20
	(15+5)$M_\odot$				0.999	21.35	0.16	0.909	70.41	0.05	0.992	19.52	0.19	0.858	64.23	0.06	0.986	20.00	0.18
	(5+5)$M_\odot$				0.999	10.75	0.21	0.807	9.84	0.25	0.997	10.69	0.21	0.733	10.08	0.25	0.998	10.99	0.20
EP(3, 3.5, 0)	(20+20)$M_\odot$	0.995	38.25	0.25				0.958	72.99	0.24	0.918	45.74	0.24	0.956	81.66	0.24	0.896	59.30	0.25
	(15+15)$M_\odot$	0.992	28.77	0.25				0.938	70.37	0.14	0.999	31.41	0.21	0.922	61.77	0.24	1.000	32.11	0.21
	(15+5)$M_\odot$	0.999	18.53	0.20				0.905	69.04	0.05	0.998	18.97	0.20	0.858	61.43	0.06	0.994	19.26	0.19
	(5+5)$M_\odot$	0.982	9.74	0.25				0.832	10.00	0.24	0.996	10.24	0.23	0.748	10.06	0.25	0.997	10.61	0.22
HT(2, 2)	(20+20)$M_\odot$	0.794	21.34	0.25	0.815	22.35	0.25				0.840	24.31	0.25	0.968	46.75	0.25	0.835	25.77	0.25
	(15+15)$M_\odot$	0.651	18.40	0.24	0.674	19.03	0.24				0.377	37.58	0.25	0.936	36.99	0.24	0.392	47.22	0.25
	(15+5)$M_\odot$	0.624	14.96	0.25	0.632	15.15	0.25				0.608	17.70	0.17	0.965	17.85	0.22	0.612	17.35	0.18
	(5+5)$M_\odot$	0.817	9.72	0.25	0.845	9.74	0.25				0.845	9.74	0.25	0.841	9.97	0.25	0.865	9.76	0.25
HT(3, 3.5, 0)	(20+20)$M_\odot$	0.904	34.61	0.24	0.920	37.64	0.24	0.903	65.68	0.24				0.873	74.44	0.25	0.999	41.41	0.23
	(15+15)$M_\odot$	0.891	27.49	0.25	0.926	28.59	0.25	0.883	49.56	0.24				0.867	59.23	0.24	1.000	31.02	0.23
	(15+5)$M_\odot$	0.986	20.73	0.16	0.986	21.99	0.15	0.919	71.02	0.05				0.886	61.90	0.07	1.000	20.34	0.17
	(5+5)$M_\odot$	0.964	9.75	0.25	0.993	9.79	0.25	0.834	9.83	0.25				0.749	10.07	0.25	1.000	10.35	0.23
HP(2, 2.5)	(20+20)$M_\odot$	0.762	18.74	0.25	0.784	19.44	0.25	0.973	36.64	0.21	0.794	20.75	0.24				0.801	21.53	0.25
	(15+15)$M_\odot$	0.595	16.37	0.24	0.617	16.40	0.24	0.931	27.84	0.21	0.329	40.09	0.25				0.343	48.60	0.25
	(15+5)$M_\odot$	0.577	16.04	0.20	0.599	14.32	0.25	0.957	22.10	0.14	0.589	15.53	0.21				0.593	15.59	0.21
	(5+5)$M_\odot$	0.741	9.50	0.25	0.754	9.53	0.25	0.975	11.46	0.18	0.755	9.52	0.25				0.770	9.61	0.25
HP(3, 3.5, 0)	(20+20)$M_\odot$	0.832	31.43	0.25	0.840	35.15	0.25	0.850	60.63	0.25	0.974	37.71	0.25	0.806	72.61	0.25			
	(15+15)$M_\odot$	0.831	26.96	0.25	0.860	28.03	0.25	0.852	46.65	0.24	0.975	28.95	0.25	0.842	55.71	0.24			
	(15+5)$M_\odot$	0.986	20.13	0.17	0.986	21.50	0.15	0.922	70.24	0.05	1.000	19.64	0.18	0.884	60.67	0.07			
	(5+5)$M_\odot$	0.933	9.72	0.25	0.971	9.75	0.25	0.857	9.80	0.25	0.991	9.75	0.25	0.758	10.03	0.25			

Table 8.10: (Continued from Table 8.9.) Fitting factors between several PN models, at 2PN and 3PN orders. Please see the caption to Table 8.9.

		T(2, 2.5)			ET(2, 2.5)			T(3, 3.5, +2)			T(3, 3.5, −2)			ET(3, 3.5, +2)			ET(3, 3.5, −2)		
		mm	M	η	mm	M	η	mm	M	η	mm	M	η	mm	M	η	mm	M	η
	$(15{+}15)M_\odot$				0.914	27.58	0.248												
T(2, 2.5)	$(15{+}5)M_\odot$				0.916	16.81	0.249												
	$(5{+}5)M_\odot$				0.900	10.13	0.241												
	$(15{+}15)M_\odot$	0.922	33.93	0.241															
ET(2, 2.5)	$(15{+}5)M_\odot$	0.971	33.17	0.076															
	$(5{+}5)M_\odot$	0.984	13.57	0.147															
	$(15{+}15)M_\odot$										0.995	29.83	0.243	0.963	30.52	0.240	0.974	30.32	0.240
T(3, 3.5, +2)	$(15{+}5)M_\odot$										1.000	19.06	0.204	0.984	20.03	0.186	0.974	20.09	0.182
	$(5{+}5)M_\odot$										0.981	9.96	0.250	0.991	10.16	0.242	0.972	9.94	0.250
	$(15{+}15)M_\odot$							0.998	30.94	0.242				0.951	31.27	0.239	0.960	30.59	0.241
T(3, 3.5, −2)	$(15{+}5)M_\odot$							1.000	20.93	0.173				0.985	20.89	0.173	0.983	20.27	0.181
	$(5{+}5)M_\odot$							0.999	10.61	0.226				0.994	10.26	0.240	0.993	10.19	0.241
	$(15{+}15)M_\odot$							0.951	30.39	0.240	0.931	29.76	0.241				0.994	30.06	0.241
ET(3, 3.5, +2)	$(15{+}5)M_\odot$							0.981	20.16	0.186	0.985	18.97	0.207				1.000	19.23	0.201
	$(5{+}5)M_\odot$							0.996	10.22	0.240	0.985	9.96	0.250				0.979	9.95	0.250
	$(15{+}15)M_\odot$							0.963	30.94	0.240	0.953	30.30	0.241	0.999	31.07	0.238			
ET(3, 3.5, −2)	$(15{+}5)M_\odot$							0.983	20.65	0.179	0.980	20.32	0.182	1.000	20.83	0.175			
	$(5{+}5)M_\odot$							0.987	10.27	0.240	0.996	10.21	0.241	1.000	10.51	0.230			

Table 8.11: Fitting factors between T and ET models, at 2PN and 3PN orders, and for different choices of the arbitrary flux parameter $\hat{\theta}$. For three choices of BBH masses, this table shows the maxmax matches [see Eq. (8.10)] between the *search* models at the top of the columns and the *target* models at the left end of the rows, *maximized over the mass parameters of the models in the columns*. For each intersection, the three numbers mm, M and η denote the maximized match and the search-model mass parameters at which the maximum is attained. The matches can be interpreted as the fitting factors for the projection of the target models onto the search models. See the caption to Table 8.10 for further details.

		EP(3, 3.5, 2, −4, 0)			EP(3, 3.5, 2, 0, −4)			EP(3, 3.5, 2, 0, 0)			EP(3, 3.5, 2, 0, 4)			EP(3, 3.5, 2, 4, 0)		
		mm	M	η	mm	M	η	mm	M	η	mm	M	η	mm	M	η
EP(3, 3.5, 2, −4, 0)	(15+15)$M_\odot$				0.995	30.93	0.238	0.994	30.85	0.240	0.995	30.87	0.239	0.952	31.17	0.242
	(15+5)$M_\odot$				0.998	20.61	0.177	0.999	20.71	0.176	0.999	20.60	0.177	0.993	21.59	0.162
	(5+5)$M_\odot$				0.999	10.22	0.240	0.999	10.22	0.240	0.999	10.22	0.240	0.996	10.46	0.231
EP(3, 3.5, 2, 0, −4)	(15+15)$M_\odot$	0.983	30.12	0.241				0.999	30.47	0.240	0.999	30.43	0.241	0.987	30.88	0.240
	(15+5)$M_\odot$	0.999	19.28	0.201				1.000	20.06	0.186	1.000	20.03	0.187	0.999	20.70	0.175
	(5+5)$M_\odot$	0.993	10.01	0.249				0.996	10.19	0.241	0.996	10.19	0.241	0.998	10.22	0.240
EP(3, 3.5, 2, 0, 0)	(15+15)$M_\odot$	0.983	30.12	0.241	0.999	30.47	0.241				0.999	30.42	0.241	0.987	30.88	0.240
	(15+5)$M_\odot$	0.999	19.26	0.202	1.000	20.06	0.186				1.000	20.03	0.187	0.999	20.70	0.175
	(5+5)$M_\odot$	0.993	9.99	0.250	1.000	10.00	0.250				0.996	10.19	0.241	0.998	10.22	0.240
EP(3, 3.5, 2, 0, 4)	(15+15)$M_\odot$	0.982	30.12	0.241	0.999	30.54	0.240	0.999	30.54	0.240				0.987	30.88	0.240
	(15+5)$M_\odot$	0.999	19.35	0.200	1.000	20.05	0.187	1.000	19.98	0.188				0.998	20.73	0.175
	(5+5)$M_\odot$	0.993	10.01	0.249	1.000	10.00	0.250	0.996	10.19	0.241				0.998	10.22	0.240
EP(3, 3.5, 2, 4, 0)	(15+15)$M_\odot$	0.929	29.60	0.240	0.968	30.11	0.242	0.968	30.16	0.240	0.967	30.15	0.240			
	(15+5)$M_\odot$	0.992	18.42	0.219	0.998	19.29	0.201	0.998	19.36	0.199	0.998	19.29	0.201			
	(5+5)$M_\odot$	0.970	10.17	0.241	0.993	9.99	0.250	0.993	9.99	0.250	0.993	9.99	0.250			

Table 8.12: Fitting factors for the projection of EP$(3, 3.5, 0)$ templates onto themselves, for various choices of the parameters z_1 and z_2. The values quoted are obtained by maximizing the maxmax (mm) match over the mass parameters of the (search) models in the columns, while keeping the mass parameters of the (target) models in the rows fixed to their quoted values, $(15 + 15)M_\odot$, $(15 + 5)M_\odot$ $(5 + 5)M_\odot$. The three numbers shown at each intersection are the maximized match and the search parameters at which the maximum was attained. In labeling rows and columns we use the notation EP$(3, 3.5, \hat{\theta}, z_1, z_2)$. See the caption to Table 8.10 for further details.

8.6 Performance of Fourier-domain detection templates, and construction of a Fourier-domain detection-template bank

In the previous sections we have seen [for instance, in Table 8.9] that the overlaps between the various PN waveforms are not very high, and that there could be an important loss in event rate if, for the purpose of detection, we restricted ourselves to *only one* of the two-body models [see Figs. 8.16, 8.17]. To cope with this problem we propose the following strategy. We *guess* that the conjunction of the waveforms from all the PN models spans a region in signal space that includes (or almost includes) the true signals, and we build a *detection* template family that embeds all the PN models in a higher-dimensional space. The PN models that we have considered (expanded and resummed, adiabatic and nonadiabatic) rely on a wide variety of very different dynamical equations, so the task of consolidating them under a single set of generic equations seems arduous. On the other hand, we have reason to suspect, from the values of the matches, and from direct investigations, that the frequency-domain amplitude and phasing (the very ingredients that enter the determination of the matches) are, qualitatively, rather similar functions for all the PN models. We shall therefore create a family of templates that model *directly* the Fourier transform of the GW signals, by writing the amplitude and phasing as simple polynomials in the GW frequency $f_{\rm GW}$. We shall build these polynomials with the specific powers of $f_{\rm GW}$ that appear in the Fourier transform of PN expanded adiabatic waveforms, as computed in the stationary-phase approximation. However, we shall not constrain the coefficients of these powers to have the same functional dependence on the physical parameters that they have in that scheme. More specifically, we define our generic family of Fourier-domain effective templates as

$$h_{\rm eff}(f) = \mathcal{A}_{\rm eff}(f)\, e^{i\psi_{\rm eff}(f)}\,, \tag{8.107}$$

where

$$\mathcal{A}_{\rm eff}(f) = f^{-7/6}\left(1-\alpha\, f^{2/3}\right)\theta(f_{\rm cut}-f)\,, \tag{8.108}$$

$$\psi_{\rm eff}(f) = 2\pi f t_0 + \phi_0 + f^{-5/3}\left(\psi_0 + \psi_{1/2}\, f^{1/3} + \psi_1\, f^{2/3} + \psi_{3/2}\, f + \psi_2\, f^{4/3} + \cdots\right)\,, \tag{8.109}$$

where t_0 and ϕ_0 are the time of arrival and the frequency-domain phase offset, and where $\theta(\ldots)$ is the Heaviside step function. This detection template family is similar in some respects to the template banks implicitly used in Fast Chirp Transform techniques [62]. However, because we consider BBHs with masses 10–$40M_\odot$, the physical GW signal can end within the LIGO frequency band; and the predictions for the ending frequency given by different PN models can be quite different. Thus, we modify also the Newtonian formula for the amplitude, by introducing the cutoff frequency $f_{\rm cut}$ and the shape parameter α.

The significance of $f_{\rm cut}$ with respect to true physical signals deserves some discussion. If the best match for the physical signal g is the template $h_{f_{\rm cut}}$, which ends at the instantaneous GW frequency $f_{\rm cut}$ (so that $h_{f_{\rm cut}}(f) \simeq g(f)$ for $f < f_{\rm cut}$ and $h_{f_{\rm cut}}(f) = 0$ for $f > f_{\rm cut}$), then we can be certain to lose a fraction of the optimal ρ that is given approximately by

$$\frac{\rho_{\rm cut}}{\rho_{\rm opt}} \leq \frac{\sqrt{\int_0^{f_{\rm cut}} \frac{|\tilde{g}(f)|^2}{S_n(f)} df}}{\sqrt{\int_0^{\infty} \frac{|\tilde{g}(f)|^2}{S_n(f)} df}} \simeq 1 - \frac{1}{2} \frac{\int_{f_{\rm cut}}^{\infty} \frac{|\tilde{g}(f)|^2}{S_n(f)} df}{\int_0^{\infty} \frac{|\tilde{g}(f)|^2}{S_n(f)} df}. \tag{8.110}$$

On the other hand, if we try to match g with the same template family *without cuts* (and if indeed the h's are completely inadequate at modeling the amplitude and phasing of g above $f_{\rm cut}$), then even the best-match template $h_{\rm no\,cut}$ (defined by $h_{\rm no\,cut}(f) \simeq g(f)$ for $f < f_{\rm cut}$, and by zero correlation, $\overline{h_{\rm no\,cut}(f) g^*(f)} \simeq 0$ for $f > f_{\rm cut}$) will yield an additional loss in ρ caused by the fact that we are spreading the power of the template beyond the range where it can successfully match g. Mathematically, this loss comes from the different normalization factor for the templates $h_{f_{\rm cut}}$ and $h_{\rm no\,cut}$, and it is given by

$$\frac{\rho_{\rm no\,cut}}{\rho_{\rm cut}} \leq \frac{\sqrt{\int_0^{f_{\rm cut}} \frac{|\tilde{h}(f)|^2}{S_n(f)} df}}{\sqrt{\int_0^{\infty} \frac{|\tilde{h}(f)|^2}{S_n(f)} df}} \simeq 1 - \frac{1}{2} \frac{\int_{f_{\rm cut}}^{\infty} \frac{|\tilde{h}(f)|^2}{S_n(f)} df}{\int_0^{\infty} \frac{|\tilde{h}(f)|^2}{S_n(f)} df}. \tag{8.111}$$

If we assume that g and $h_{\rm no\,cut}$ have roughly the same amplitude distribution, the two losses are similar.

In the end, we might be better off cutting templates if we cannot be sure that their amplitude and phasing, beyond a certain frequency, are faithful representations of the true signal. Doing so, we approximately halve the *worst-case* loss of ρ, because instead of losing a factor

$$\frac{\rho_{\rm no\,cut}}{\rho_{\rm cut}} \frac{\rho_{\rm cut}}{\rho_{\rm opt}} \simeq 1 - \frac{1}{2} \frac{\int_{f_{\rm cut}}^{\infty} \frac{|\tilde{h}(f)|^2}{S_n(f)} df}{\int_0^{\infty} \frac{|\tilde{h}(f)|^2}{S_n(f)} df} - \frac{1}{2} \frac{\int_{f_{\rm cut}}^{\infty} \frac{|\tilde{g}(f)|^2}{S_n(f)} df}{\int_0^{\infty} \frac{|\tilde{g}(f)|^2}{S_n(f)} df} \simeq 1 - \frac{\int_{f_{\rm cut}}^{\infty} \frac{|\tilde{g}(f)|^2}{S_n(f)} df}{\int_0^{\infty} \frac{|\tilde{g}(f)|^2}{S_n(f)} df}, \tag{8.112}$$

we lose only the factor $\rho_{\rm cut}/\rho_{\rm opt}$. On the other hand, we do not want to lose the signal-to-noise ratio that is accumulated at high frequencies if our templates have a fighting chance of matching the true signal there; so it makes sense to include in the detection bank the *same* template with several different values of $f_{\rm cut}$.

It turns out that using only the two parameters ψ_0 and $\psi_{3/2}$ in the phasing (and setting all other ψ coefficients to zero) and the two amplitude parameters, $f_{\rm cut}$ and α, we obtain a family that can already match all the PN models of Secs. 8.3, 8.4 with high fitting factors FF. This is possible largely because we restrict our focus to BBHs with relatively high masses, where the number of GW cycles in the LIGO range (and thus the total range of the phasing $\psi(f)$ that we need to consider) is small.

In Tab. 8.15 we list the minmax (see Sec. 8.2) fitting factor for the projection of the PN models onto our frequency-domain effective templates, for a set of BBH masses ranging from $(5+5)M_\odot$ to

$(20 + 20)M_\odot$. In computing the fitting factors, we used the simplicial search algorithm `amoeba` [60] to search for the optimal set of parameters (ψ_0, $\psi_{3/2}$, $f_{\rm cut}$, α) (as always, the time of arrival and initial phase of the templates were automatically optimized as described in Sec. 8.2). From Tab. 8.15 we draw the following conclusions:

1. All the adiabatic models (T and P) are matched with fitting factors FF > 0.97. Lower-mass BBHs are matched better than higher-mass BBHs, presumably because for the latter the inspiral ends at lower frequencies within the LIGO band, producing stronger edge effects, which the effective templates cannot capture fully. 3PN models are matched better than 2PN models.

2. The Effective-One-Body models (ET and EP) are matched even better than the adiabatic models, presumably because they have longer inspirals and less severe edge effects at the end of inspiral. Unlike the adiabatic models, however, ET and EP are matched better for higher-mass BBHs. In fact, all the FFs are > 0.99 except for $(5 + 5)M_\odot$ BBHs, where FF $\gtrsim 0.979$. The reason for this is probably that this low-mass BBH has more GW cycles in the LIGO frequency band than any other one, and the two phasing parameters of our effective templates cannot quite model the evolution of the phasing. [In the adiabatic models, these effects may be overshadowed by the loss in signal to noise ratio due to the edge effects at high frequencies.] When the parameters $\tilde{z}_{1,2}$ are allowed to be nonzero, the matches get worse, but not by much. For all the plausible values of $\tilde{z}_1$, the worst situation seems to happen at $\tilde{z}_1 = -40$, where the overlaps are still higher than ~ 0.95 [with minimum 0.947.]

3. The Hamiltonian models (HT and HP) at 3PN order are not matched as precisely, but the detection template family still works reasonably well. We usually have FF > 0.96, but there are several exceptions, with FF as low as 0.948. For these models, the overlaps are lower in the equal-mass cases, where the ending frequencies of the waveforms are much higher than for the other models; it seems that the effective templates are not able to reproduce this late portion of the waveforms (this might not be so bad, because it does not seem likely that this part of the signal reflects the true behavior of BBH waveforms).

4. The Lagrangian models (L) are matched a bit worse than the Hamiltonian models (HT and HP) at 3PN, but they still have FF higher than 0.95 in most cases, with several exceptions [at either $(20 + 20)M_\odot$ or $(5 + 5)M_\odot$], which can be as low as 0.93.

5. HT and HP models at 2PN are matched the worst, with typical values lower than 0.95 and higher than 0.85.

Finally, we note that our amplitude function $\mathcal{A}_{\rm eff}(f)$ is a linear combination of two terms, so we can search automatically over the correction coefficient α, in essentially the same way as discussed

in Sec. 8.2 for the orbital phase. In other words, α is an *extrinsic parameter*. [Although we do search over α, it is only to show the required range, which will be a useful piece of information when one is deciding how to lay down a mesh of discrete templates on the continuous detection-template space.]

8.6.1 Internal match and metric

To understand the matches between the Fourier-domain templates and the PN models, and to prepare to compute the number of templates needed to achieve a given (internal) MM, we need to derive an expression for the match between two Fourier-domain effective templates.

We shall first restrict our consideration to effective templates with the same amplitude function (i.e., the same α and $f_{\rm cutoff}$). The overlap $\langle h(\psi_0,\psi_{3/2}), h(\psi_0+\Delta\psi_0,\psi_{3/2}+\Delta\psi_{3/2})\rangle$ between templates with close values of ψ_0 and $\psi_{3/2}$ can be described (to second order in $\Delta\psi_0$ and $\Delta\psi_{3/2}$) by the mismatch metric g_{ij} [27]:

$$\langle h(\psi_0,\psi_{3/2}), h(\psi_0+\Delta\psi_0,\psi_{3/2}+\Delta\psi_{3/2})\rangle = 1 - \sum_{i,j=0,3/2} g_{\rm ij}\,\Delta\psi_i\Delta\psi_j. \tag{8.113}$$

The metric coefficients g_{ij} can be evaluated analytically from the overlap

$$\begin{aligned}
&\langle h(\psi_0,\psi_{3/2}), h(\psi_0+\Delta\psi_0,\psi_{3/2}+\Delta\psi_{3/2})\rangle \\
&\simeq \left[\max_{\Delta\phi_0,\Delta t_0}\int df\,\frac{|\mathcal{A}(f)|^2}{S_h(f)}\cos\left(\sum_i \frac{\Delta\psi_i}{f^{n_i}} + \Delta\phi_0 + 2\pi f\Delta t_0\right)\right] \Bigg/ \left[\int df\,\frac{|\mathcal{A}(f)|^2}{S_h(f)}\right] \\
&\simeq 1 - \frac{1}{2}\left[\max_{\Delta\phi_0,\Delta t_0}\int df\,\frac{|\mathcal{A}(f)|^2}{S_h(f)}\left(\sum_i \frac{\Delta\psi_i}{f^{n_i}} + \Delta\phi_0 + 2\pi f\Delta t_0\right)^2\right] \Bigg/ \left[\int df\,\frac{|\mathcal{A}(f)|^2}{S_h(f)}\right].
\end{aligned} \tag{8.114}$$

where $n_0 \equiv 5/3$ and $n_{3/2} \equiv 2/3$. Comparison with Eq. (8.113) then gives

$$\begin{aligned}
&\sum_{i,j} g_{\rm ij}\,\Delta\psi_i\Delta\psi_j \\
&= \frac{1}{2}\min_{\Delta\phi_0,\Delta t_0}\left\{ \begin{pmatrix} \Delta\psi_0 & \Delta\psi_{3/2} \end{pmatrix} \mathbf{M}_{(1)} \begin{pmatrix} \Delta\psi_0 \\ \Delta\psi_{3/2} \end{pmatrix} + 2\begin{pmatrix} \Delta\phi_0 & 2\pi\Delta t_0 \end{pmatrix} \mathbf{M}_{(2)} \begin{pmatrix} \Delta\psi_0 \\ \Delta\psi_{3/2} \end{pmatrix} \right. \\
&\qquad \left. + \begin{pmatrix} \Delta\phi_0 & 2\pi\Delta t_0 \end{pmatrix} \mathbf{M}_{(3)} \begin{pmatrix} \Delta\phi_0 \\ 2\pi\Delta t_0 \end{pmatrix} \right\},
\end{aligned} \tag{8.115}$$

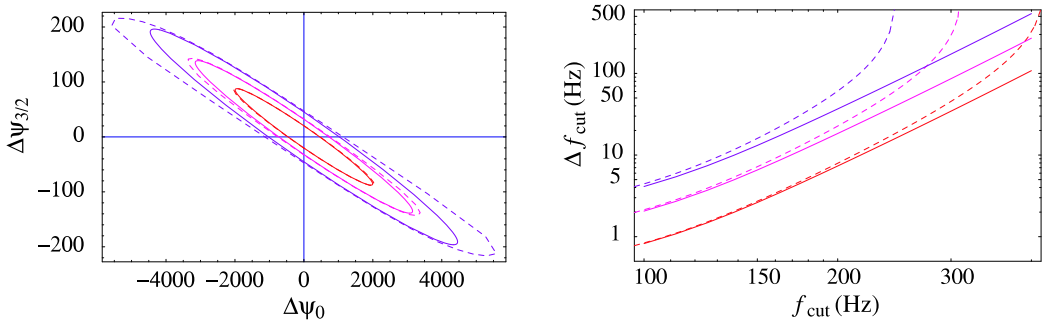

Figure 8.18: In the left panel, we plot the iso-match contours for the function $\langle h(\psi_0, \psi_{3/2}), h(\psi_0 + \Delta\psi_0, \psi_{3/2} + \Delta\psi_{3/2})\rangle$; contours are given at matches of 0.99, 0.975 and 0.95. Solid lines give the indications of the mismatch metric; dashed lines give actual values. Here we use a Newtonian amplitude function $\mathcal{A}(f) = f^{-7/6}$ [we set $\alpha = 0$ and we do not cut the template in the frequency domain. In fact $f_{\rm cut} = 400\,{\rm Hz}$]. In the right panel we plot the values of $\Delta f_{\rm cut}$ (versus $f_{\rm cut}$) required to obtain matches $\langle h(f_{\rm cut}), h(f_{\rm cut} + \Delta f_{\rm cut})\rangle$ of 0.95 (uppermost curve), 0.975 and 0.99 (lowermost). In the region below each contour the match is larger than the value quoted for the contour. Again, here we use a Newtonian amplitude function $\mathcal{A}(f) = f^{-7/6}$ [we set $\alpha = 0$].

where the $\mathbf{M}_{(1)\ldots(3)}$ are the matrices

$$\mathbf{M}_{(1)} = \begin{bmatrix} J(2n_0) & J(n_0 + n_{3/2}) \\ J(n_0 + n_{3/2}) & J(2n_{3/2}) \end{bmatrix}, \tag{8.116}$$

$$\mathbf{M}_{(2)} = \begin{bmatrix} J(n_0) & J(n_{3/2}) \\ J(n_0 - 1) & J(n_{3/2} - 1) \end{bmatrix}, \tag{8.117}$$

$$\mathbf{M}_{(3)} = \begin{bmatrix} J(0) & J(-1) \\ J(-1) & J(-2) \end{bmatrix}, \tag{8.118}$$

and where

$$J(n) \equiv \left[\int df \frac{|\mathcal{A}(f)|^2}{S_h(f)} \frac{1}{f^n}\right] \Big/ \left[\int df \frac{|\mathcal{A}(f)|^2}{S_h(f)}\right]. \tag{8.119}$$

Since $\mathbf{M}_{(3)}$ describes the mismatch caused by $(\Delta\phi_0, \Delta t_0)$, it must be positive definite; because the right-hand side of (8.115) reaches its minimum with respect to variations of $\Delta\phi_0$ and Δt_0 when

$$2\mathbf{M}_{(2)} \begin{pmatrix} \Delta\psi_0 \\ \Delta\psi_{3/2} \end{pmatrix} + 2\mathbf{M}_{(3)} \begin{pmatrix} \Delta\phi_0 \\ 2\pi\Delta t_0 \end{pmatrix} = 0\,, \tag{8.120}$$

we obtain

$$g_{\rm ij} = \frac{1}{2}\left[\mathbf{M}_{(1)} - \mathbf{M}_{(2)}^{\rm T}\mathbf{M}_{(3)}^{-1}\mathbf{M}_{(2)}\right]_{ij}. \tag{8.121}$$

We note also that the mismatch $\langle h(\psi_0, \psi_{3/2}), h(\psi_0 + \Delta\psi_0, \psi_{3/2} + \Delta\psi_{3/2})\rangle$ is translationally invariant in the $(\psi_0, \psi_{3/2})$ plane, so the metric g_{ij} is constant everywhere. In the left panel of Fig. 8.18, we

plot the iso-match contours (at matches of 0.99, 0.975 and 0.95) in the $(\Delta\psi_0, \Delta\psi_{3/2})$ plane, as given by the metric (8.121) [solid ellipses], compared with the actual values obtained from the numerical computation of the matches [dashed lines]. For our purposes, the second-order approximation given by the metric is quite acceptable. In this computation we use a Newtonian amplitude function $\mathcal{A}(f) = f^{-7/6}$ [i.e., we set $\alpha = 0$ and we set our cutoff frequency at 400 Hz].

We move now to the mismatch induced by different cutoff frequencies $f_{\rm cut}$. Unlike the case of the ψ_0, $\psi_{3/2}$ parameters, this mismatch is first order in $\Delta f_{\rm cut}$, so it cannot be described by a metric. Suppose that we have two effective templates $h(f_{\rm cut})$ and $h(f_{\rm cut} + \Delta f_{\rm cut})$ with the same phasing and amplitude $\Delta f > 0$, but different cutoff frequencies. The match is then given by

$$\begin{aligned} & \langle h(f_{\rm cut}), h(f_{\rm cut} + \Delta f_{\rm cut})\rangle \\ = & \frac{\left[\int_0^{f_{\rm cut}} df \frac{|\mathcal{A}(f)|^2}{S_h(f)}\right]}{\left[\int_0^{f_{\rm cut}} df \frac{|\mathcal{A}(f)|^2}{S_h(f)}\right]^{1/2} \left[\int_0^{f_{\rm cut}+\Delta f_{\rm cut}} df \frac{|\mathcal{A}(f)|^2}{S_h(f)}\right]^{1/2}} \qquad (8.122) \\ = & \left[\frac{\int_0^{f_{\rm cut}} df \frac{|\mathcal{A}(f)|^2}{S_h(f)}}{\int_0^{f_{\rm cut}+\Delta f_{\rm cut}} df \frac{|\mathcal{A}(f)|^2}{S_h(f)}}\right]^{1/2} \\ \simeq & 1 - \left[\frac{\Delta f_{\rm cut}}{2} \frac{|\mathcal{A}(f_{\rm cut})|^2}{S_h(f_{\rm cut})}\right] \Bigg/ \left[\int_0^{f_{\rm cut}} df \frac{|\mathcal{A}(f)|^2}{S_h(f)}\right]^{1/2} . \qquad (8.123) \end{aligned}$$

This result depends strongly on $f_{\rm cut}$. In the right panel of Fig. 8.18 we plot the values of $\Delta f_{\rm cut}$ that correspond to matches of 0.95, 0.975 and 0.99, according to the first order approximation [solid lines], and to the exact numerical calculations [dashed lines], both of which are given in the second line of Eq. (8.123). In the region below each contour the match is larger than the value that characterizes the contour. As we can see from the graph, the linear approximation is not very accurate, thus in the following we shall use the exact formula.

8.6.2 Construction of the effective template bank: parameter range

All the PN target models are parametrized by two independent numbers (e.g., the two masses or the total mass and the mass ratio); if we select a range of interest for these parameters, the resulting set of PN signals can be seen as a two-dimensional region in the (m_1, m_2) or (M, η) plane. Under the mapping that takes each PN signal into the Fourier-domain effective template that matches it best, this two-dimensional region is *projected* into a two-dimensional surface in the $(\psi_0, \psi_{3/2}, f_{\rm cut})$ parameter space (with the fourth parameter $\alpha = 0$). As an example, we show in Fig. 8.19 the projection of the ET(2, 2.5) waveforms with (single-BH) masses 5–20 $M_\odot$. The 26 models tested in Secs. 8.3, 8.4 would be projected into 26 similar surfaces. In constructing the detection template families, we shall first focus on 17 of the 26 models, namely, the adiabatic T and P models at 2PN

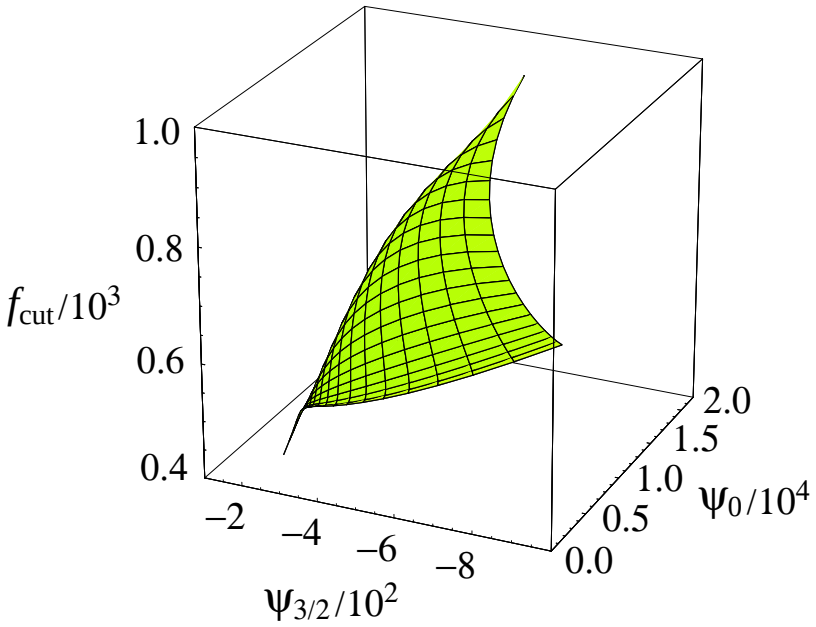

Figure 8.19: Projection of the ET$(2, 2.5)$ waveforms onto the frequency-domain effective template space. For α we choose the optimal value found by the search. The $(\psi_0, \psi_{3/2}, f_{\rm cut})$ surface is interpolated from the then mass pairs shown in Tab. 8.15.

and 3PN, the E models at 2PN and at 3PN but with $\tilde{z}_{1,2} = 0$, and the H models at 3PN. We will comment on the E models with $\tilde{z}_{1,2} \neq 0$, on the L models, and on the HT and HP models at 2PN order at the end of this section.

It is hard to visualize all three parameters at once, so we shall start with the phasing parameters ψ_0 and $\psi_{3/2}$. In Fig. 8.20, we plot the $(\psi_0, \psi_{3/2})$ section of the PN-model projections into the $(\psi_0, \psi_{3/2}, f_{\rm cutoff})$ space, with solid diamonds showing the projected points corresponding to BBHs with the same set of ten mass pairs as in Tab. 8.15. Each PN model is projected to a curved-triangular region, with boundaries given by the sequences of BBHs with masses $(m + m)$ (equal mass), $(20 + m)$ and $(m + 5)$. In Fig. 8.20, these boundaries are plotted using thin dashed lines, for the models T$(2, 2.5)$ (the uppermost in the plot), HT$(3, 3.5, \hat{\theta} = 2)$ (in the middle), and P$(2, 2.5)$ (lowest).

As we can see, different PN models can occupy regions with very different areas, and thus require a very different number of effective templates to match them with a given $\mathrm{MM_T}$. Among these three models, T$(2, 2.5)$ requires the least number of templates, P$(2, 2.5)$ requires a few times more, and HT$(3, 3.5, \hat{\theta} = 2)$ requires many more. This is consistent with the result by Porter [59] who found that, for the same range of physical parameters, T waveforms are more closely spaced than P waveforms, so fewer are needed to achieve a certain MM. In this plot we have also linked the points that correspond to the same BBH parameters in different PN models. In Fig. 8.20, these

M	end-to-end match	$\mathcal{N}_{\text{end to end}}$	$f_{\text{cut min}}$	$\langle h(f_{\text{cut min}}), h(+\infty)\rangle$	$\mathcal{N}^{\text{cut}}_{\text{mass line}}$
$(5+5)M_\odot$	0.478	37	572	1.00	0.2
$(10+5)M_\odot$	0.434	41	346	0.98	0.9
$(15+5)M_\odot$	0.398	46	232	0.94	3.1
$(10+10)M_\odot$	0.449	40	246	0.95	2.6
$(20+5)M_\odot$	0.347	52	192	0.90	5.3
$(15+10)M_\odot$	0.443	40	226	0.94	3.3
$(20+10)M_\odot$	0.428	42	185	0.89	5.9
$(15+15)M_\odot$	0.482	36	191	0.90	5.4
$(20+15)M_\odot$	0.464	38	162	0.84	8.5
$(20+20)M_\odot$	0.438	41	143	0.79	11.9

Table 8.13: End-to-end matches and ending frequencies along the BH mass lines of Fig. 8.20. The first three columns show the end-to-end matches and the corresponding number of templates (for MM $\simeq 0.98$) along the BH mass lines; the remaining columns show the minimum ending frequencies of PN waveforms along the BH mass lines, the match between the two effective templates at the ends of the range, and the number of templates needed to step along the range while always maintaining a match $\simeq 0.98$ between neighboring templates. When computing these matches, we use a Newtonian amplitude function $\mathcal{A}(f) = f^{-7/6}$ [we set $\alpha = 0$], and we maximize over the parameters ψ_0 and $\psi_{3/2}$ (which is equivalent to assuming perfect phasing synchronization).

lines (we shall call them *BH mass lines*) lie all roughly along one direction.

A simple way to characterize the difference between the PN target models is to evaluate the maxmax *end-to-end match* between effective templates at the two ends of the BH mass lines (i.e., the match between the effective templates with the largest and smallest $\psi_{3/2}$ among the projections of PN waveforms with the same mass parameters m_1, m_2); we wish to focus first on the effects of the phasing parameters, so we do not cut the templates in the frequency domain and we set $\alpha = 0$. We compute also a naive end-to-end number of templates, $\mathcal{N}_{\text{end to end}}$, by counting the templates required to step all along the BH mass line while maintaining at each step a match $\simeq 0.98$ between neighboring templates. A simple computation yields $\mathcal{N}_{\text{end to end}} = \log(\text{end-to-end match})/\log(0.98)$. The results of this procedure are listed in Table 8.13. Notice that, as opposed to the fitting factors between template families computed elsewhere in this Chapter (which are maximized over the BBH mass parameters of one of the families), these matches give a measure of the dissimilarity between different PN models *for the same values of the BBH parameters*; thus, they provide a crude estimate of how much the effective template bank must be enlarged to embed all the various PN models.

We expect that the projection of a true BBH waveform onto the $(\psi_0, \psi_{3/2})$ plane will lie near the BH mass line with the true BBH parameters, or perhaps near the extension of the BH mass line in either direction. For this reason we shall lay down our effective templates in the region traced out by the thick dashed lines in Fig. 8.20, which was determined by extending the BH mass lines in both directions by half of their length.

We move on to specifying the required range of f_{cut} for each $(\psi_0, \psi_{3/2})$. For a given PN model and BBH mass parameters, we have defined the *ending frequency* f_{end} as the instantaneous GW

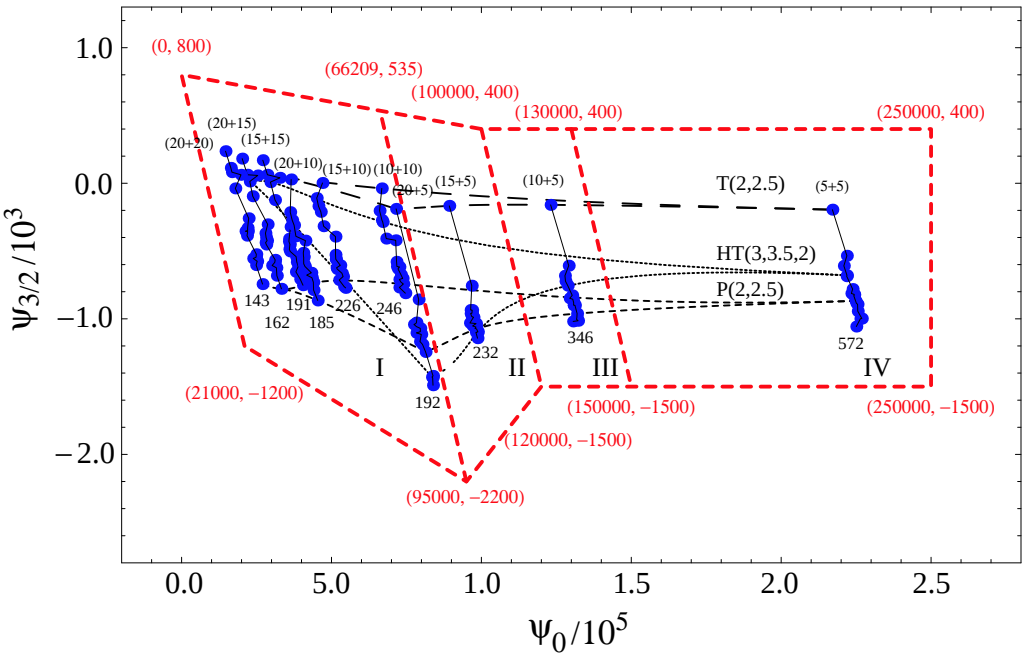

Figure 8.20: Projection of the PN waveforms onto the $(\psi_0,\psi_{3/2})$ plane, for BBHs with masses $(5+5)M_\odot$, $(10+5)M_\odot$, …, $(20+20)M_\odot$ (see Tab. 8.15). The projection was computed by maximizing the maxmax match over the parameters ψ_0, $\psi_{3/2}$ and $f_{\rm cut}$; the correction coefficient α was set to zero. The thin dotted and dashed lines show the boundaries of the projected images for the models (from the top) $\mathrm{T}(2,2.5)$, $\mathrm{HT}(3,3.5,\hat\theta=2)$ and $\mathrm{P}(2,2.5)$. Solid lines (the *BH mass lines*) link the images of the same BBH for different PN models. The ends of the BH mass lines are marked with the BBH masses and with the minimum value $\min\{f_{\rm end}, f_{\rm cut}\}$ across all the PN models. The thick dashed lines delimit the region that will be covered by the effective template bank; the $(\psi_0,\psi_{3/2})$ coordinates are marked on the vertices. The region is further subdivided into four subregions I–IV that group the BH mass lines with very similar ending frequencies $f_{\rm end\,min}$.

frequency at which we stop the integration of the PN orbital equations. We find that usually the $f_{\rm cut}$ of the optimally-matched projection of a PN template is larger than the $f_{\rm end}$ of the PN template. This is because the abrupt termination of the PN waveforms in the time domain creates a tail in the spectrum for frequencies higher than $f_{\rm end}$. With $f_{\rm cut} > f_{\rm end}$ and $\alpha > 0$, the effective templates can mimic this tail and gain a higher match with the PN models. In some cases, however, the optimal $f_{\rm cut}$ can be smaller than $f_{\rm end}$ [for example, $\mathrm{P}(2,2.5)$ with $(10+5)M_\odot$, $(15+5)M_\odot$ and $(10+10)M_\odot$] suggesting that the match of the phasing in the entire frequency band up to $f_{\rm end}$ is not very good and we have to shorten the Fourier-domain template. Now, since we do not know the details of the plunge for true BBH inspiral, it is hard to estimate where the optimal $f_{\rm cut}$ might lie, except perhaps imposing that it should be larger than $\min(f_{\rm end}, f_{\rm cut})$. A possibility is to set the range of $f_{\rm cut}$ to be above $f_{\rm cut\,min} \equiv \min\{f_{\rm cut}, f_{\rm end}\}$, with the minimum evaluated among all the PN models.

In Table 8.13 we show the $f_{\rm cut\,min}$ found across the PN models for given BBH mass parameters.

We have also marked this minimum frequency in Fig. 8.20 under the corresponding BH mass lines. In the table we also show the match of the two detection templates $h(f_{\rm cut} = f_{\rm cut\,min})$ and $h(f_{\rm cut} = +\infty)$, and the number $\mathcal{N}^{\rm cut}_{\rm mass\,line}$ of intermediate templates with different $f_{\rm cut}$ needed to move from $h(f_{\rm cut\,min})$ to $h(+\infty)$ while maintaining at each step a match $\simeq 0.98$ between neighboring templates. It is easy to see that this number is $\mathcal{N}^{\rm cut}_{\rm mass\,line} = \log\langle h(f_{\rm cut\,min}), h(+\infty)\rangle / \log(0.98)$. The match was computing using a Newtonian amplitude function $\mathcal{A}(f) = f^{-7/6}$ [we set $\alpha = 0$], and maximizing over the parameters ψ_0 and $\psi_{3/2}$. Under our previous hypothesis that the projection of a true BBH waveform would lie near the corresponding BH mass line, we can use the numbers in Table 8.13 to provide a rough estimate of the range of $f_{\rm cut}$ that should be taken at each point $(\psi_0, \psi_{3/2})$ within the dashed contour of Fig. 8.20. We trace out four subregions I, II, III, IV, such that the BH mass lines of each subregion have approximately the same values of $f_{\rm cut\,min}$; we then use these minimum ending frequencies to set a lower limit for the values of $f_{\rm cut}$ required in each subregion: $f_{\rm cut\,min}({\rm I}) = 143$, $f_{\rm cut\,min}({\rm II}) = 192$, $f_{\rm cut\,min}({\rm III}) = 232$, $f_{\rm cut\,min}({\rm IV}) = 346$. The maximum $f_{\rm cut}$ is effectively set by the detector noise curve, which limits the highest frequency at which signal-to-noise can be still accumulated.

Moving on to the last parameter, α, we note that it is probably only meaningful to have $\alpha f_{\rm cut}^{2/3} \leq 1$, so that $\mathcal{A}_{\rm eff}(f)$ cannot become negative for $f < f_{\rm cut}$. [A negative amplitude in the detection template will usually give a negative contribution to the overlap, unless the phasing mismatch is larger than $\pi/2$, which does not seem plausible in our cases.] Indeed, the optimized values found for α in Tab. 8.15 seem to follow this rule, except for a few slight violations that are probably due to numerical error (since we had performed a search to find the optimal value of α). For the 17 models considered here, the optimal α is always positive [Tab. 8.15] which means that, due to cutoff effects, the amplitude at high frequencies becomes always lower than the $f^{-7/6}$ power law. So for the 17 models considered in this section $0 \leq \alpha f_{\rm cut}^{2/3} \leq 1$. [Note that this range will have to be extended to include negative α's if we want to incorporate the models discussed in Sec. 8.6.5.]

8.6.3 Construction of the effective templates bank: parameter density

At this stage, we have completed the specification of the region in the $(\psi_0, \psi_{3/2}, f_{\rm cut}, \alpha)$ parameter space where we shall lay down our bank of templates. We expect that the FF for the projection of the true physical signals (emitted by *nonspinning* BBHs with $M = 10$–$40 M_\odot$) onto this template bank should be very good. We now wish to evaluate the total number of templates $\mathcal{N}$ needed to achieve a certain MM.

We shall find it convenient to separate the mismatch due to the phasing from the mismatch due to the frequency cuts by introducing two minimum match parameters MM_ψ and $\mathrm{MM}_{\rm cut}$, with $\mathrm{MM} = \mathrm{MM}_\psi \cdot \mathrm{MM}_{\rm cut} \simeq \mathrm{MM}_\psi + \mathrm{MM}_{\rm cut} - 1$. As mentioned at the beginning of this section, the correction coefficient α is essentially an *extrinsic* parameter [see Sec. 8.2.2]: we do not need to

discretize the template bank with respect to α, and there is no corresponding MM parameter.

We evaluate $\mathcal{N}$ in three refinement steps:

1. We start by considering only the phasing parameters, and we compute the parameter area S_i [in the $(\psi_0, \psi_{3/2})$ plane] for each of the subregions i = I, II, III, IV of Fig. 8.20. We then multiply by the determinant $\sqrt{g}$ of the constant metric, and divide by $2(1–\mathrm{MM}_\psi)$, according to Eq. (8.25), to get
$$\mathcal{N} = \sum_i \frac{S_i \sqrt{g}}{2(1-\mathrm{MM}_\psi)}. \tag{8.124}$$
This expression is for the moment only formal, because we cannot compute $\sqrt{g}$ without considering the amplitude parameters α and f_{cut}.

2. Next, we include the effect of f_{cut}. In the previous section, we have set $f_{\mathrm{min\,cut}}$ for each of the subregions by considering the range swept by f_{end} along the mass lines. Recalling our discussion of $\mathcal{N}^{\mathrm{cut}}_{\mathrm{mass\,line}}$, we approximate the number of distinct values of f_{cut} that we need to include for each parameter pair $(\psi_0, \psi_{3/2})$ as
$$n_i^{\mathrm{cut}}(\psi_0, \psi_{3/2}, \alpha) \simeq 1 + \frac{\log \left\langle h(\psi_0, \psi_{3/2}, \alpha, f_{\mathrm{min\,cut}}), h(\psi_0, \psi_{3/2}, \alpha, \mathrm{no\,cut}) \right\rangle}{\log \mathrm{MM}_{\mathrm{cut}}}. \tag{8.125}$$
For α in the physical range $0 \le \alpha \le f_{\mathrm{cut}}^{-2/3}$ this match is minimized for $\alpha = 0$, so this is the value that we use to evaluate the n_i^{cut}'s. Note that the choice of cutoff frequencies does not depend on the values of the phasing parameters. This allows us to have a single set of cutoff frequencies for all points in one subregion. For subregion i, we denote this set by F_i.

3. The final step is to include the effect of α and f_{cut} on the computation of $\sqrt{g}$. For simplicity, we shoot for an upper limit by maximizing $\sqrt{g}$ with respect to α. [Because α is essentially an extrinsic parameter, we do not multiply $\mathcal{N}$ by the number of its discrete values: the matches are automatically maximized on the continuous range $0 \le \alpha \le f_{\mathrm{cut}}^{-2/3}$.] Our final estimate for the total number of templates is
$$\mathcal{N} = \frac{1}{2(1-\mathrm{MM}_\psi)} \sum_i S_i \sum_{f_{\mathrm{cut}} \in F_i} \max_\alpha [\sqrt{g}] \tag{8.126}$$

We have evaluated this $\mathcal{N}$ numerically. *We find that the contributions to the total number of templates from the four subregions, for* $\mathrm{MM} = 0.96$ *(taking* $\mathrm{MM}_\psi = \mathrm{MM}_{\mathrm{cut}} = 0.98$*), are* $\mathcal{N}(\mathrm{I}) \simeq 6,410$*,* $\mathcal{N}(\mathrm{II}) \simeq 2,170$*,* $\mathcal{N}(\mathrm{III}) \simeq 1,380$*,* $\mathcal{N}(\mathrm{IV}) \simeq 1,230$*, for a total of* $\mathcal{N} = 11,190$*. This number scales approximately as* $[0.04/(1-\mathrm{MM})]^2$. Notice that subregion I, which contains all the BBHs with total mass above $25M_\odot$, requires by far the largest number of templates. This is mostly because these waveforms end in the LIGO band, and many values of f_{cut} are needed to match different

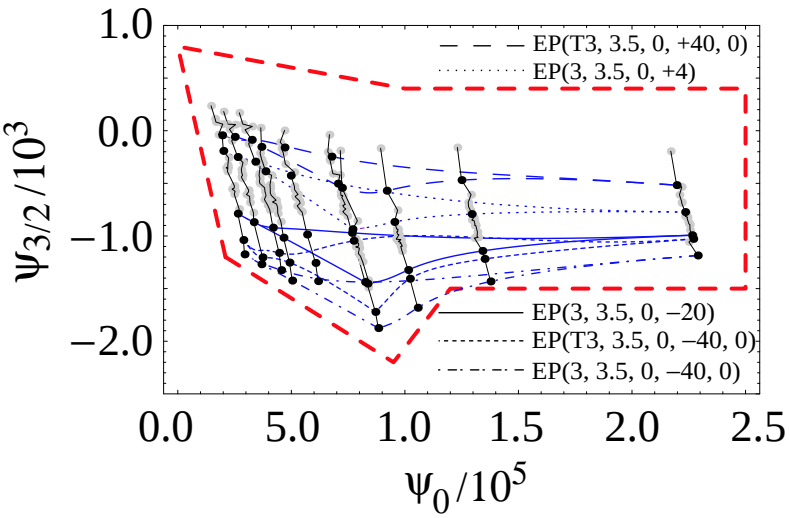

Figure 8.21: Projection of the E models with nonzero $\tilde{z}_1$ into the $(\psi_0, \psi_{3/2})$ plane (shown in black dots.) The new points sit quite well along the BH mass lines of the 17 models investigated in Secs. 8.6.2, 8.6.3 and 8.6.4. We use the notation EP$(3, 3.5, \hat{\theta}, \tilde{z}_1, \tilde{z}_2)$ and denote by EP(T3, ...) the two-body model in which the coefficient $A(r)$ is PN expanded [see Eq. (8.88)].

ending frequencies.

Remember that the optimal signal-to-noise ratio ρ for filtering the true GW signals by a template bank is approximately degraded (in the worst case) by the factor $\mathrm{MM_T} = \mathrm{FF} + \mathrm{MM} - 1$ [4].

While MM depends on the geometry of the template bank, we can only guess at the fitting factor FF for the projection of the true signal onto the template space. In this section we have seen that all PN models can be projected onto the effective frequency-domain templates with a good FF: for a vast majority of the waveforms FF $\gtrsim 0.96$ (and the few exceptions can be explained). *It is therefore reasonable to hope that the FF for the true GW signals is* ~ 0.96*, so the total degradation from the optimal* ρ *will be* $\mathrm{MM_T} \gtrsim 0.92$*, corresponding to a loss of* $\lesssim$ *22% in event rate.* This number can be improved by scaling up the number of templates, but of course the actual FF represents an upper limit for $\mathrm{MM_T}$. For instance, about 47,600 templates should get us $\mathrm{MM_T} \gtrsim 0.94$, corresponding to a loss of $\lesssim 17\%$ in event rate.

[4] This is true only when the waveform and the neighboring detection templates are all sufficiently close so that the metric formalism is still valid. As we have seen in Fig. 8.18, by imposing $\mathrm{MM}_\psi = 0.98$, the overlaps between the neighboring detection templates are well described by the metric. However, due to the fact we do not know the true waveforms, and thus the true FF, it is not quite certain how exact this formula will eventually be. In some sense, this formula could be regarded an additional assumption.

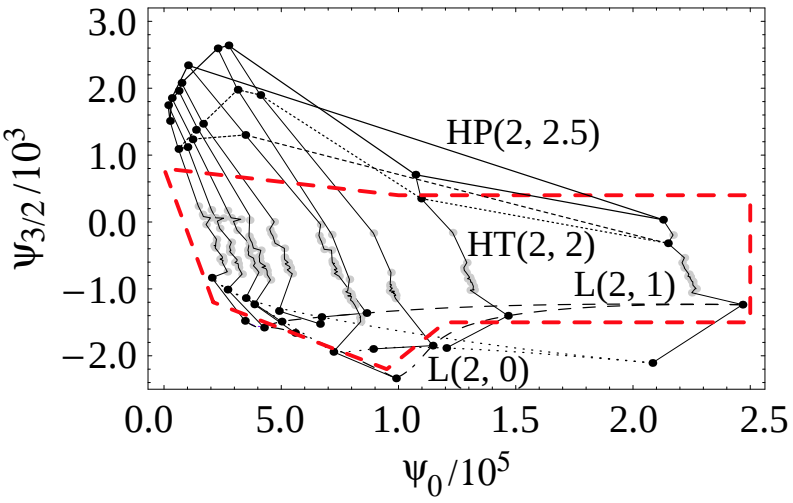

Figure 8.22: Projections of HT and HP models at 2PN and L models into the $(\psi_0, \psi_{3/2})$ plane (shown in black dots.) The projections of the previous 17 models are shown in gray dots.

M	$\mathcal{M}$	$\mathcal{M}^{\rm approx}_{\rm min}$	$\mathcal{M}^{\rm approx}_{\rm max}$	$\epsilon\%$
$(5+5)M_\odot$	4.35	4.16	4.27	2.6
$(10+5)M_\odot$	6.08	5.75	6.00	4.2
$(15+5)M_\odot$	7.33	6.85	7.28	5.9
$(10+10)M_\odot$	8.71	8.10	8.72	7.1
$(20+5)M_\odot$	8.33	7.55	8.31	9.1
$(15+10)M_\odot$	10.62	9.76	10.96	11.3
$(20+10)M_\odot$	12.17	10.92	12.50	13.0
$(15+15)M_\odot$	13.06	11.69	14.88	24.4
$(20+15)M_\odot$	15.05	13.15	17.74	30.6
$(20+20)M_\odot$	17.41	14.91	21.52	38.0

Table 8.14: Estimation of the chirp masses $\mathcal{M}$ from the projections of the PN target models onto the Fourier-domain effective template space. The numbers in the second column (labeled "$\mathcal{M}$") give the values of the chirp mass corresponding to the BH masses to their left; the numbers in the third and fourth columns give the range of estimates obtained from Eq. (8.127) for the values of ψ_0 at the projections of the target models shown in Fig. 8.20. The last column shows the percentage error $\epsilon \equiv (\mathcal{M}^{\rm approx}_{\rm max} - \mathcal{M}^{\rm approx}_{\rm min})/\mathcal{M}$.

8.6.4 Parameter estimation with the detection template family

Although our family of effective templates was built for the main purpose of detecting BBHs, we can still use it (once a detection is made) to extract partial information about the BH masses. It is obvious from Fig. 8.20 that the masses cannot in general be determined unambiguously from the best-match parameters [i.e., the projection of the true waveform onto the $(\psi_0, \psi_{3/2})$ plane], because the images of different PN models in the plane have overlaps. Therefore different PN models will have different ideas, as it were, about the true masses. Another way of saying this is that the BH mass lines can cross.

However, it still seems possible to extract at least one mass parameter, the chirp mass $\mathcal{M} = M\eta^{3/5}$, with some accuracy. Since the phasing is dominated by the term $\psi_0 f^{-5/3}$ at low frequencies, we can use the leading Newtonian term $\psi_{\rm N}(f) = \frac{3}{128}(\pi\mathcal{M}f)^{-5/3}$ obtained for a PN expanded adiabatic model in the stationary-phase approximation to infer

$$\psi_0 \sim \frac{3}{128}\left(\frac{1}{\pi\mathcal{M}}\right)^{5/3} \quad \Longrightarrow \quad \mathcal{M}^{\rm approx} = \frac{1}{\pi}\left(\frac{3}{128\,\psi_0}\right)^{3/5}. \tag{8.127}$$

If this correspondence was exact, the BH mass lines in Fig. 8.20 would all be vertical. They are not, so this estimation has an error that gets larger for smaller ψ_0 (i.e., for binaries with higher masses). In Table 8.14 we show the range of chirp-mass estimates obtained from Eq. (8.127) for the values of ψ_0 at the projections of the PN models in Fig. 8.20, together with their percentage error $\epsilon \equiv (\mathcal{M}^{\rm approx}_{\rm max} - \mathcal{M}^{\rm approx}_{\rm min})/\mathcal{M}$. In this table, $\mathcal{M}_{\rm max}$ and $\mathcal{M}_{\rm min}$ correspond to the endpoints of the BH mass lines. If we take into account the extension of the BH mass lines by a factor of two in the effective template bank, we should double the ϵ of the table.

It seems quite possible that a more detailed investigations of the geometry of the projections into the effective template space (and especially of the BH mass lines) could produce better algorithms to estimate binary parameters. But again, probably only one parameter can be estimated with certain accuracy.

8.6.5 Extension of the two-dimensional Fourier-domain detection template

In our construction of the effective template bank, we have been focusing until now on a subset of 17 models. The models we left out are: E models at 3PN with $\tilde{z}_{1,2}$ nonzero, HT and HP models at 2PN, and L models.

As we can see from Fig. 8.21, E models with $\tilde{z}_{1,2}$ nonzero have a very similar behavior to the 17 models investigated above. Indeed: (i) the projection of the PN waveforms from the same model occupy regions that are triangular, and (ii) the projections of PN waveforms of a given mass lies on the BH mass line spanned by the previous 17 models. In addition, their projections lie roughly in the region we have already defined in Secs. 8.6.2, 8.6.3 and 8.6.4. However, the ending frequencies of these models can be much lower than the values we have set for the detection templates: the detection templates (in all four subregions) should be extended to lower cutoff frequencies if we decide to match these models, up to FF ~ 0.95. A rough estimate shows that this increases the number of templates to about twice the original value.

In Fig. 8.22, we plot the projections of the L$(2,0)$, L$(2,1)$, HT$(2,2)$ and HP$(2,2.5)$ waveforms into the $(\psi_0, \psi_{3/2})$ plane. As we already know, these models are not matched by the detection templates as well as the other 17 models. Here we can see that their projections onto the $(\psi_0, \psi_{3/2})$ plane are also quite dissimilar from those models. For L models, although different masses project into a triangular region, the projection of each mass configuration does not align along the corresponding BH mass line generated by the 17 models. In order to cover the L models up to FF~ 0.93, we need to expand the $(\psi_0, \psi_{3/2})$ region only slightly. However, as we read from Tab. 8.15, the cutoff frequencies need to be extended to even lower values than for the E models with nonzero $\tilde{z}_{1,2}$. Luckily, this expansion will not cost much. In the end the total number of templates needed should be about three times the original value.

For HT and HP models at 2PN, the projections almost lie along the BH mass lines, but the regions occupied by these projections have weird shapes. We have to extend the $(\psi_0, \psi_{3/2})$ region by a factor ~ 2 in order to cover the phasings. [The ending/cutoff frequencies for these models are higher than for the previous two types of models.] An additional subtlety in this case is that, as we can read from Tab. 8.15, the optimal values of α are often negative, since the amplitude becomes higher than the $f^{-7/6}$ power law at higher frequencies. This expansion of the range of α affects both

the choice of the discrete cutoff frequencies and the placement of $(\psi_0, \psi_{3/2})$ lattices. This effect is yet to be estimated.

Finally, we notice that if these extensions are made, then the estimation of the chirp mass from the coefficient ψ_0 becomes less accurate than the one given in Table 8.14.

8.6.6 Extension of the Fourier-domain detection template family to more than two phasing parameters

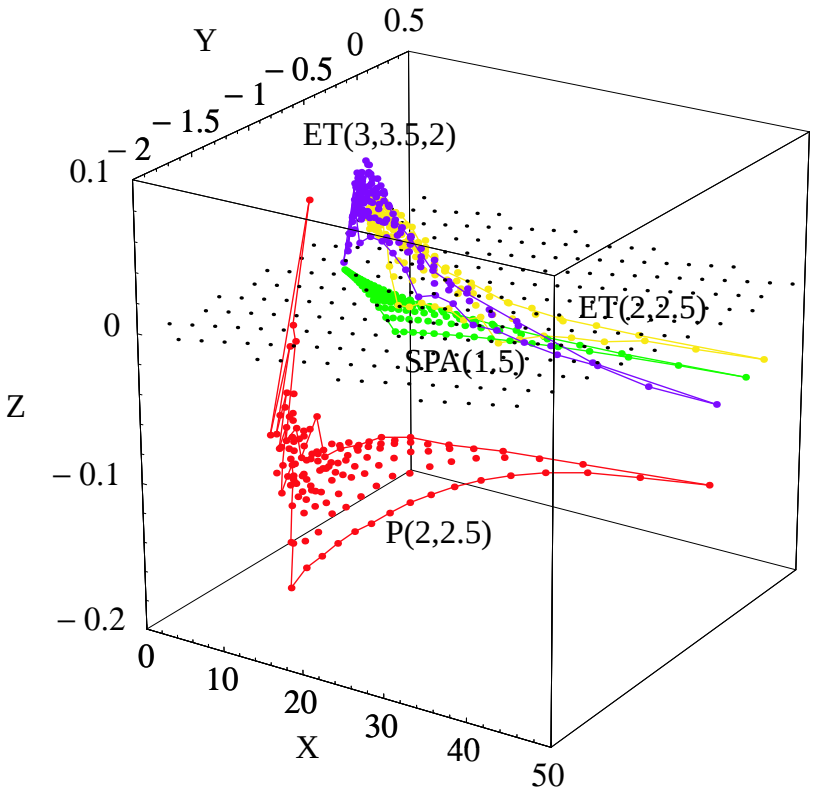

Figure 8.23: Projection of the models P$(2, 2.5)$, ET$(2, 2.5)$, ET$(3, 3.5, 0)$, and SPA(1.5) onto the three-parameter Fourier-domain detection template, for many BBH masses that lie within the same ranges taken in Fig. 8.20. The variables (X, Y, Z) are related to $(\psi_0, \psi_1, \psi_{3/2})$ by a linear transformation, constructed so that the mismatch metric is just δ_{ij} and that the $(\psi_0, 0, \psi_{3/2})$ plane is mapped to the $(X, Y, 0)$ plane. The dots show the value of the parameters (X, Y, Z) where the match with one of the PN waveforms is maximum.

It might seem an accident that by using only two phasing parameters, ψ_0 and $\psi_{3/2}$, we are able to match very precisely the wide variety of PN waveforms that we have considered. Indeed, since the waveforms predicted by each PN model span a two-dimensional manifold (generated by varying the two BH masses m_1 and m_2 or equivalently the mass parameters M and η), we could naturally expect that a *third parameter* is required to incorporate all the PN models in a more general family, and to add even more signal shapes that extrapolate beyond the phasings and amplitudes seen in the PN models.

In particular, because the accumulation of signal-to-noise ratio is more sensitive to how well we can match *the phasing* (rather than the amplitude) of PN templates, such a third parameter should probably interpolate between phasings predicted by different PN models. As a consequence,

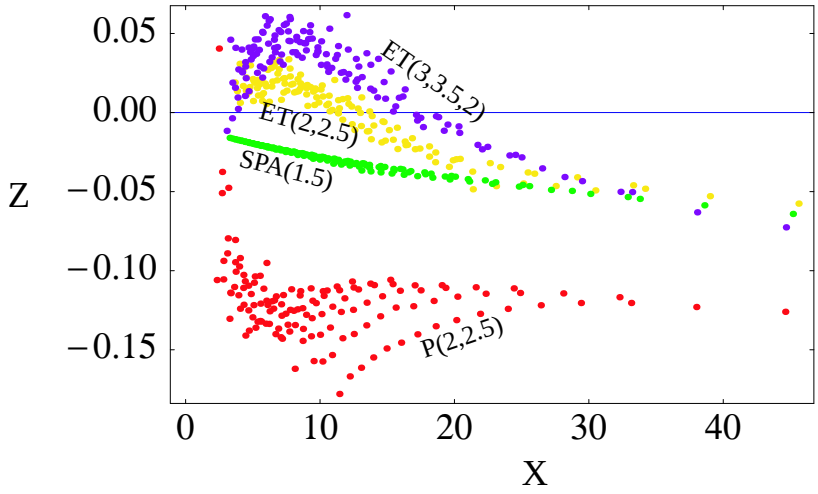

Figure 8.24: (X, Z) section of Fig. 8.23. Comparison with Fig. 8.23 shows that all the projections lie near the $(X, 0, Z)$ plane.

the amplitude parameters $f_{\rm cut}$ and $\mathcal{A}$ do not generate a real dimensional extension of our detection template family. In this section, we present a qualitative study of the extension of our detection template family obtained by adding one phasing parameter, the parameter ψ_1 of Eq. (8.109).

We use the $(\psi_0, \psi_1, \psi_{3/2})$ Fourier-domain detection templates to match the PN waveforms from the models P$(2, 2.5)$, ET$(2, 2.5)$, and ET$(3, 3.5, 0)$; these models were chosen because their projections onto the $(\psi_0, \psi_{3/2})$ detection templates were rather distant in the $(\psi_0, \psi_{3/2})$ parameter space. Throughout this section (and unlike the rest of this chapter), we use an approximated search procedure whereby we essentially replace the amplitude of the target models with the Newtonian amplitude $\mathcal{A}(f) = f^{-7/6}$ with a cutoff frequency $f_{\rm cut}$ [we always assumed $\mathcal{A} = 0$ and $f_{\rm cut} = 400$ Hz]. As expected, the matches increase, and indeed they are almost perfect: always higher than 0.994 (it should be remembered however that these should be considered as matches *of the* PN *phasings* rather than as matches of the PN waveforms; especially for high masses, the frequency dependence of the amplitude is likely to change these values).

If we plot the projections of the PN waveforms in the $(\psi_0, \psi_1, \psi_{3/2})$ space, we find that the clusters of points corresponding to each PN target model look quite different from the projections [onto the $(\psi_0, \psi_{3/2})$ template space] shown in Fig. 8.20; but this is just an artifact of the parametrization. We can perform a linear transformation $(\psi_0, \psi_1, \psi_{3/2}) \to (X, Y, Z)$, defined in such a way that (i) in the (X, Y, Z) parameters, the mismatch metric is just δ_{ij}, and that (ii) the $(\psi_0, 0, \psi_{3/2})$ plane is mapped to the $(X, Y, 0)$ plane. These conditions define the linear transformation up to a translation and a rotation along the Z axis; to specify the transformation completely we require also that all the projections of the PN models lie near the origin, and be concentrated around the X axis. Figure 8.23 shows the projection of the PN models P$(2, 2.5)$, ET$(2, 2.5)$, and ET$(3, 3.5, 0)$ onto the

$(\psi_0, \psi_1, \psi_{3/2})$ detection template family, as parametrized by the (X, Y, Z) coordinate system, for many BBH masses that lie within the same ranges of Fig. 8.20. Each dot marks the parameters (X, Y, Z) that best match the phasing of one of the PN waveforms. We include also the projection of a further PN model, SPA(1.5), obtained by solving the frequency-domain version of the balance equation, obtained in the stationary-phase approximation from our T model. The expression of the SPA(1.5) phasing as a function of f coincides with our Eq. (8.109), but the coefficients that correspond to $(\psi_0, \psi_1, \psi_{3/2})$ *are functions of the two mass parameters* M and η.

By construction, the match between nearby detection templates is related to their Euclidian distance in the (X, Y, Z) by

$$1 - \text{overlap} = \Delta X^2 + \Delta Y^2 + \Delta Z^2 \,. \tag{8.128}$$

We see immediately that all the PN models are not very distant from the $(X, Y, 0)$ plane [also shown in the figure], which coincides with the $(\psi_0, \psi_{3/2})$ plane. The farthest model is P$(2, 2.5)$, with a maximum distance ~ 0.18. It is important to notice that, since this number is obtained by assuming $f_{\rm cut} = 400$ Hz and $\mathcal{A} = 0$, it tends to underestimate the true overlaps for models that end below 400 Hz, such as the P models at higher masses. See also Fig. 8.24 for an (X, Z) section of Fig. 8.23.

We can study the relation between this three-dimensional family of templates and the two-dimensional family considered earlier by projecting the points of Fig. 8.23 onto the $(X, Y, 0)$ plane [which corresponds to the $(\psi_0, 0, \psi_{3/2})$ plane]. The resulting images resemble closely the projections of the PN models onto the $(\psi_0, \psi_{3/2})$ parameter space of the two-dimensional family, as seen in the left panel of Fig. 8.25. However, the agreement is poor for P$(2, 2.5)$ because of the relatively high cut frequency $f_{\rm cut} = 400$ Hz. The right panel of Fig. 8.25 was obtained by taking $f_{\rm cut} = 200$ Hz. The agreement is much better. This result goes some way toward explaining why using only two phasing parameters was enough to match most PN models in a satisfactory way.

As stated at the beginning of this section, the parameter Z can indeed be used to expand the dimensionality of our detection template family, because it appears to interpolate between different PN models. It is possible that the number of Z values needed when laying down a discrete template family might not be too large, because the PN models do not seem to lie very far from the $Z = 0$ plane [remember that distances in the (X, Y, Z) parameter space are approximately mismatch distances].

The good performance that we find for the two- and three-dimensional Fourier-domain families confirms the results obtained in Refs. [12], [43] and [63]. In Ref. [12], the authors point out that the waveforms obtained from the stationary phase approximation at 2PN and 2.5PN order are able to approximate the E models, throughout most of the LIGO band, by maximizing over the mass parameters [see Ref. [12], in particular the discussion of their model "Tf2," and the discussion around their Fig. 2].

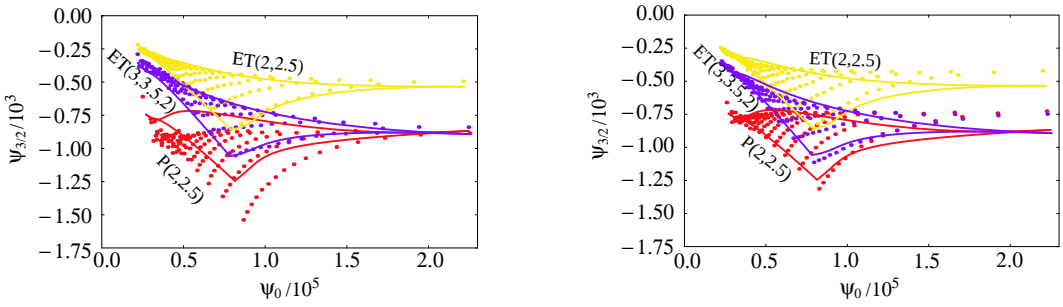

Figure 8.25: In this figure, we compare the projection of the PN models onto the three-dimensional $(\psi_0, \psi_1, \psi_{3/2})$ Fourier-domain detection template family [shown by the dots as a two-dimensional section in the $(\psi_0, \psi_{3/2})$ submanifold] with the projection of the PN models in the two-dimensional $(\psi_0, \psi_{3/2})$ template family [shown by the lines]. In the left panel, we use $\mathcal{A} = 0$ and $f_{\rm cut} = 400$ Hz to maximize the matches; in the right panel we use $\mathcal{A} = 0$ and $f_{\rm cut} = 200$ Hz.

In Ref. [43], Chronopolous and Apostolatos show that what would be in our notation the SPA(2) model (where the phasing is described by a fourth-order polynomial in the variable $f^{1/3}$) can be approximated very well, at least for the purpose of signal detection, by the SPA(1.5) model, with the advantage of having a much lower number of templates. In Ref. [63], the authors go even further, investigating the possibility of approximating the SPA(2) phasing with a polynomial of third, second and even first degree obtained using Chebyshev approximants.

It is important to underline that in all of these analyses the coefficients that appear in the expression of the phasing [corresponding to our $\psi_0, \psi_1, \ldots$ in Eq. (8.109)] depend on only two BBH mass parameters, either directly [12, 43], or indirectly [63] through specific PN relations at each PN order. As a consequence, the phasings assumed in these references are confined to a two-dimensional submanifold analog to the surface labeled "SPA(1.5)" in Fig. 8.23.

In this chapter we follow a more general approach, because the phasing coefficients ψ_i are initially left completely arbitrary. Only after studying systematically the projection of the PN models onto the template bank we have determined the region where a possible detection template bank would be laid down. The high matches that we find between detection templates and the various PN models depend crucially on this assumption. As a consequence, our parameters ψ_i do not have a direct physical meaning, and they cannot easily be traced back to specific functions of the BBH masses, except for the chirp mass, as seen in Sec. 8.6.4. This is natural, because our detection templates are built to interpolate between different PN models, each of which has, as it were, a different idea of what the waveform for a BBH of given masses should be.

PN model		FF for projection onto the Fourier-domain detection template families												
		$f_{\rm end}$	mn	ψ_0	$\psi_{3/2}$	$\alpha f_{\rm cut}^{2/3}$	$f_{\rm cut}$		$f_{\rm end}$	mn	ψ_0	$\psi_{3/2}$	$\alpha f_{\rm cut}^{2/3}$	$f_{\rm cut}$
T(2, 2)	$(20{+}20)M_\odot$	221.4	0.983	23891.	−554.63	0.949	240.7	$(20{+}5)M_\odot$	341.2	0.992	77508.	−1041.30	0.897	347.0
	$(20{+}15)M_\odot$	252.4	0.987	30200.	−606.41	0.975	272.5	$(10{+}10)M_\odot$	442.8	0.992	72639.	−768.78	0.632	331.4
	$(15{+}15)M_\odot$	295.2	0.989	38126.	−653.61	0.968	313.5	$(15{+}5)M_\odot$	431.3	0.993	96191.	−1030.20	0.831	440.8
	$(20{+}10)M_\odot$	291.7	0.989	41735.	−677.51	1.002	314.2	$(10{+}5)M_\odot$	583.4	0.993	130600.	−1019.10	1.001	805.3
	$(15{+}10)M_\odot$	352.7	0.991	52565.	−713.54	0.968	387.1	$(5{+}5)M_\odot$	885.6	0.989	225060.	−1056.80	0.531	894.4
T(2, 2.5)	$(20{+}20)M_\odot$	161.2	0.970	19807.	62.32	0.691	224.4	$(20{+}5)M_\odot$	281.6	0.987	71552.	−188.92	0.227	312.7
	$(20{+}15)M_\odot$	185.9	0.975	25398.	57.59	0.347	220.3	$(10{+}10)M_\odot$	322.4	0.983	66783.	−37.92	0.490	630.9
	$(15{+}15)M_\odot$	214.9	0.979	32787.	40.11	0.210	245.0	$(15{+}5)M_\odot$	345.6	0.988	89296.	−166.70	0.107	373.8
	$(20{+}10)M_\odot$	222.3	0.980	36540.	28.23	0.160	255.5	$(10{+}5)M_\odot$	443.3	0.989	123100.	−159.28	0.379	746.0
	$(15{+}10)M_\odot$	261.2	0.983	47008.	2.24	0.107	293.7	$(5{+}5)M_\odot$	643.9	0.994	217090.	−194.81	0.253	1033.1
T(3, 3.5, +2)	$(20{+}20)M_\odot$	207.9	0.983	25219.	−575.44	1.002	265.8	$(20{+}5)M_\odot$	276.1	0.986	79630.	−1095.00	0.743	238.3
	$(20{+}15)M_\odot$	234.5	0.984	31622.	−623.54	1.005	268.5	$(10{+}10)M_\odot$	415.9	0.988	73738.	−701.48	0.923	437.8
	$(15{+}15)M_\odot$	277.2	0.987	38891.	−612.96	0.990	306.3	$(15{+}5)M_\odot$	362.3	0.990	97371.	−988.17	0.617	277.0
	$(20{+}10)M_\odot$	259.3	0.986	43944.	−729.80	0.979	301.6	$(10{+}5)M_\odot$	518.5	0.990	131210.	−899.96	0.642	392.3
	$(15{+}10)M_\odot$	324.3	0.987	53869.	−688.38	0.865	315.6	$(5{+}5)M_\odot$	831.7	0.985	224370.	−826.19	0.563	886.2
T(3, 3.5, −2)	$(20{+}20)M_\odot$	207.9	0.981	24857.	−603.44	0.983	246.4	$(20{+}5)M_\odot$	276.1	0.987	80359.	−1188.90	0.825	257.0
	$(20{+}15)M_\odot$	234.5	0.985	31773.	−681.75	0.983	252.8	$(10{+}10)M_\odot$	415.8	0.988	74637.	−810.89	0.750	350.3
	$(15{+}15)M_\odot$	277.2	0.986	39565.	−707.26	0.933	277.9	$(15{+}5)M_\odot$	362.3	0.989	97861.	−1070.50	0.661	267.7
	$(20{+}10)M_\odot$	259.3	0.985	44027.	−787.96	0.900	251.9	$(10{+}5)M_\odot$	518.5	0.988	131840.	−992.35	0.901	553.3
	$(15{+}10)M_\odot$	324.3	0.988	54194.	−761.61	0.984	341.1	$(5{+}5)M_\odot$	831.7	0.982	225550.	−943.65	0.577	916.3
P(2, 2.5)	$(20{+}20)M_\odot$	142.9	0.972	27006.	−743.88	0.991	208.5	$(20{+}5)M_\odot$	207.8	0.978	81397.	−1244.40	0.698	192.4
	$(20{+}15)M_\odot$	162.5	0.977	33307.	−778.72	0.987	206.7	$(10{+}10)M_\odot$	285.9	0.985	73970.	−743.09	0.681	245.7
	$(15{+}15)M_\odot$	190.6	0.980	40486.	−752.07	0.991	237.0	$(15{+}5)M_\odot$	267.5	0.984	98390.	−1074.60	0.709	231.8
	$(20{+}10)M_\odot$	185.0	0.977	45403.	−864.50	1.116	288.3	$(10{+}5)M_\odot$	370.0	0.985	131920.	−961.15	0.758	346.4
	$(15{+}10)M_\odot$	226.3	0.981	54709.	−771.73	0.867	232.9	$(5{+}5)M_\odot$	571.8	0.983	224810.	−867.58	0.813	764.5
P(3, 3.5, +2)	$(20{+}20)M_\odot$	216.4	0.984	24922.	−523.74	0.995	265.2	$(20{+}5)M_\odot$	265.0	0.985	79624.	−1070.20	0.830	258.4
	$(20{+}15)M_\odot$	243.6	0.985	31204.	−564.86	1.007	299.3	$(10{+}10)M_\odot$	432.8	0.990	72663.	−617.31	0.896	488.2
	$(15{+}15)M_\odot$	288.5	0.987	38194.	−541.27	0.971	328.2	$(15{+}5)M_\odot$	359.2	0.990	96933.	−935.65	0.619	279.6
	$(20{+}10)M_\odot$	265.7	0.986	43280.	−660.41	1.001	328.8	$(10{+}5)M_\odot$	531.3	0.991	130310.	−827.00	0.843	588.6
	$(15{+}10)M_\odot$	336.2	0.987	52941.	−605.52	0.902	356.7	$(5{+}5)M_\odot$	865.6	0.988	223830.	−780.35	0.537	896.7
P(3, 3.5, −2)	$(20{+}20)M_\odot$	216.4	0.984	24830.	−545.66	1.062	291.4	$(20{+}5)M_\odot$	265.0	0.986	79956.	−1114.80	0.831	259.7
	$(20{+}15)M_\odot$	243.6	0.984	31086.	−583.34	0.988	269.5	$(10{+}10)M_\odot$	432.8	0.990	73167.	−674.59	0.760	390.9
	$(15{+}15)M_\odot$	288.5	0.988	38426.	−581.05	0.994	326.6	$(15{+}5)M_\odot$	359.2	0.990	96850.	−958.04	0.662	277.7
	$(20{+}10)M_\odot$	265.7	0.986	43464.	−696.77	1.006	311.2	$(10{+}5)M_\odot$	531.3	0.990	130780.	−881.70	0.810	539.0
	$(15{+}10)M_\odot$	336.2	0.987	53475.	−663.65	0.882	333.4	$(5{+}5)M_\odot$	865.6	0.987	224210.	−828.64	0.538	896.0
ET(2, 2.5)	$(20{+}20)M_\odot$	231.0	0.991	22372.	−258.47	0.935	477.8	$(20{+}5)M_\odot$	359.4	0.995	79070.	−857.02	0.748	519.2
	$(20{+}15)M_\odot$	263.5	0.992	28710.	−302.99	0.770	425.5	$(10{+}10)M_\odot$	462.0	0.995	71411.	−420.76	0.668	722.3
	$(15{+}15)M_\odot$	308.0	0.993	36351.	−321.50	0.717	512.3	$(15{+}5)M_\odot$	452.7	0.994	96788.	−755.70	0.718	706.8
	$(20{+}10)M_\odot$	305.1	0.993	41308.	−423.25	0.756	473.1	$(10{+}5)M_\odot$	610.1	0.993	129130.	−607.98	0.665	910.1
	$(15{+}10)M_\odot$	368.3	0.995	51338.	−393.70	0.769	764.8	$(5{+}5)M_\odot$	924.0	0.991	221910.	−534.76	0.424	920.4
ET(3, 3.5, +2)	$(20{+}20)M_\odot$	212.1	0.990	22048.	−356.02	0.997	367.7	$(20{+}5)M_\odot$	351.3	0.992	78355.	−1057.40	0.763	402.3
	$(20{+}15)M_\odot$	245.1	0.992	28516.	−423.30	0.971	415.7	$(10{+}10)M_\odot$	428.8	0.994	72187.	−631.44	0.707	616.2
	$(15{+}15)M_\odot$	285.8	0.992	36119.	−450.40	0.775	408.3	$(15{+}5)M_\odot$	433.7	0.994	96772.	−982.67	0.757	572.4
	$(20{+}10)M_\odot$	286.6	0.993	40717.	−545.11	0.790	376.5	$(10{+}5)M_\odot$	573.1	0.995	130830.	−899.77	0.686	856.6
	$(15{+}10)M_\odot$	344.5	0.993	51507.	−563.26	0.785	515.2	$(5{+}5)M_\odot$	847.9	0.986	225490.	−892.59	0.552	914.8
ET(3, 3.5, −2)	$(20{+}20)M_\odot$	207.1	0.990	21818.	−386.23	0.848	300.4	$(20{+}5)M_\odot$	345.9	0.991	78349.	−1103.70	0.692	379.0
	$(20{+}15)M_\odot$	238.2	0.992	28247.	−451.93	0.884	347.0	$(10{+}10)M_\odot$	411.0	0.994	72645.	−709.64	0.685	499.9
	$(15{+}15)M_\odot$	274.0	0.992	36218.	−502.72	0.903	452.4	$(15{+}5)M_\odot$	424.8	0.993	97086.	−1052.50	0.846	600.5
	$(20{+}10)M_\odot$	277.0	0.992	41148.	−613.88	0.786	364.2	$(10{+}5)M_\odot$	556.9	0.995	131730.	−1003.30	0.699	821.5
	$(15{+}10)M_\odot$	330.6	0.992	51702.	−623.17	0.822	501.2	$(5{+}5)M_\odot$	816.8	0.983	226430.	−999.02	0.539	900.4
EP(2, 2.5)	$(20{+}20)M_\odot$	218.1	0.991	21315.	−353.42	0.773	376.1	$(20{+}5)M_\odot$	345.8	0.990	79526.	−1167.70	0.709	366.2
	$(20{+}15)M_\odot$	249.1	0.991	28013.	−437.59	0.746	380.6	$(10{+}10)M_\odot$	436.2	0.994	73183.	−729.74	0.714	645.1
	$(15{+}15)M_\odot$	290.8	0.991	35947.	−486.80	0.672	432.2	$(15{+}5)M_\odot$	433.1	0.994	98170.	−1099.60	0.630	460.4
	$(20{+}10)M_\odot$	289.8	0.990	40730.	−593.65	0.656	391.0	$(10{+}5)M_\odot$	579.6	0.993	132250.	−1014.20	0.691	868.7
	$(15{+}10)M_\odot$	348.5	0.991	51920.	−632.99	0.637	451.6	$(5{+}5)M_\odot$	872.5	0.979	226910.	−997.82	0.571	833.0
EP(3, 3.5, +2)	$(20{+}20)M_\odot$	219.7	0.990	22025.	−329.13	0.967	398.3	$(20{+}5)M_\odot$	354.0	0.993	78344.	−1027.30	0.668	376.6
	$(20{+}15)M_\odot$	251.9	0.991	27970.	−368.53	0.888	386.4	$(10{+}10)M_\odot$	439.6	0.994	71704.	−579.45	0.719	658.8
	$(15{+}15)M_\odot$	293.1	0.991	35861.	−409.25	0.813	452.7	$(15{+}5)M_\odot$	444.9	0.995	96416.	−934.82	0.773	608.4
	$(20{+}10)M_\odot$	291.4	0.993	40598.	−512.88	0.820	429.6	$(10{+}5)M_\odot$	582.5	0.995	130480.	−855.36	0.685	879.7
	$(15{+}10)M_\odot$	353.7	0.993	51343.	−527.79	0.731	495.5	$(5{+}5)M_\odot$	874.7	0.989	224370.	−820.10	0.488	916.2

		FF for projection onto the Fourier-domain detection template families												
PN model		$f_{\rm end}$	mn	ψ_0	$\psi_{3/2}$	$\alpha f_{\rm cut}^{2/3}$	$f_{\rm cut}$		$f_{\rm end}$	mn	ψ_0	$\psi_{3/2}$	$\alpha f_{\rm cut}^{2/3}$	$f_{\rm cut}$
	$(20{+}20)M_\odot$	214.4	0.990	22029.	−349.92	0.986	384.7	$(20{+}5)M_\odot$	353.0	0.992	78099.	−1035.10	0.692	400.3
	$(20{+}15)M_\odot$	248.3	0.992	28185.	−400.30	0.849	361.2	$(10{+}10)M_\odot$	430.5	0.994	71820.	−613.97	0.718	642.1
EP$(3, 3.5, -2)$	$(15{+}15)M_\odot$	287.0	0.992	35793.	−429.31	0.880	510.6	$(15{+}5)M_\odot$	439.1	0.994	96411.	−960.71	0.770	591.0
	$(20{+}10)M_\odot$	289.1	0.993	40653.	−537.88	0.869	452.9	$(10{+}5)M_\odot$	575.7	0.995	130760.	−899.02	0.696	877.1
	$(15{+}10)M_\odot$	347.3	0.993	51423.	−558.41	0.779	494.7	$(5{+}5)M_\odot$	864.9	0.988	225110.	−886.01	0.501	909.7
	$(20{+}20)M_\odot$	318.1	0.989	20061.	−192.06	0.509	379.7	$(20{+}5)M_\odot$	457.4	0.987	76939.	−936.06	0.683	450.0
	$(20{+}15)M_\odot$	364.6	0.988	26379.	−249.89	0.437	385.7	$(10{+}10)M_\odot$	647.2	0.990	70495.	−502.74	0.585	666.7
EP$(3, 3.5, 0, 4, 0)$	$(15{+}15)M_\odot$	432.0	0.987	34134.	−293.98	0.321	422.8	$(15{+}5)M_\odot$	600.6	0.992	95378.	−866.93	0.651	601.3
	$(20{+}10)M_\odot$	420.4	0.987	38610.	−385.18	0.455	446.0	$(10{+}5)M_\odot$	831.6	0.995	129410.	−792.01	0.680	798.8
	$(15{+}10)M_\odot$	510.8	0.988	49757.	−426.26	0.515	493.4	$(5{+}5)M_\odot$	1292.2	0.992	223410.	−772.85	0.339	1003.8
	$(20{+}20)M_\odot$	118.9	0.970	26410.	−787.54	0.964	189.8	$(20{+}5)M_\odot$	215.1	0.989	83591.	−1452.50	1.087	364.1
	$(20{+}15)M_\odot$	136.9	0.983	33451.	−868.80	1.010	238.9	$(10{+}10)M_\odot$	237.8	0.983	76684.	−970.56	1.074	373.8
EP$(3, 3.5, 0, -20, 0)$	$(15{+}15)M_\odot$	158.5	0.983	41909.	−921.14	1.045	285.0	$(15{+}5)M_\odot$	258.0	0.984	101440.	−1323.20	1.158	486.7
	$(20{+}10)M_\odot$	164.2	0.985	46550.	−1016.40	1.138	321.2	$(10{+}5)M_\odot$	327.9	0.977	134130.	−1142.10	1.157	589.3
	$(15{+}10)M_\odot$	192.4	0.985	56925.	−986.07	1.096	339.8	$(5{+}5)M_\odot$	476.1	0.969	226450.	−992.89	1.167	844.2
	$(20{+}20)M_\odot$	94.0	0.947	29400.	−1174.60	1.097	184.5	$(20{+}5)M_\odot$	174.0	0.972	88302.	−1874.90	1.073	337.6
	$(20{+}15)M_\odot$	108.2	0.962	36837.	−1268.40	0.960	169.2	$(10{+}10)M_\odot$	188.0	0.959	82469.	−1437.30	1.059	411.8
EP$(3, 3.5, 0, -40, 0)$	$(15{+}15)M_\odot$	125.3	0.969	45552.	−1324.90	1.010	228.4	$(15{+}5)M_\odot$	206.7	0.967	105660.	−1681.70	1.357	468.5
	$(20{+}10)M_\odot$	130.4	0.970	50375.	−1423.70	1.048	252.8	$(10{+}5)M_\odot$	260.8	0.957	137720.	−1431.90	1.111	537.6
	$(15{+}10)M_\odot$	152.5	0.964	61789.	−1428.90	1.077	338.4	$(5{+}5)M_\odot$	376.1	0.955	228960.	−1185.20	1.122	874.4
	$(20{+}20)M_\odot$	349.5	0.986	19559.	−43.77	0.483	374.1	$(20{+}5)M_\odot$	561.5	0.981	72281.	−542.92	0.533	549.7
	$(20{+}15)M_\odot$	399.4	0.989	25098.	−58.70	0.387	384.9	$(10{+}10)M_\odot$	699.0	0.988	67699.	−246.28	0.166	463.5
EP$(T_3, 3.5, 0, +40, 0)$	$(15{+}15)M_\odot$	465.3	0.987	32573.	−86.76	0.155	341.5	$(15{+}5)M_\odot$	704.9	0.963	92003.	−570.09	1.128	522.3
	$(20{+}10)M_\odot$	468.3	0.989	36812.	−153.63	0.243	430.2	$(10{+}5)M_\odot$	935.2	0.989	124940.	−469.29	0.458	787.7
	$(15{+}10)M_\odot$	558.6	0.989	47015.	−159.41	0.316	652.3	$(5{+}5)M_\odot$	1398.0	0.989	219670.	−517.04	0.986	928.5
	$(20{+}20)M_\odot$	95.0	0.953	28875.	−1038.40	0.998	168.8	$(20{+}5)M_\odot$	175.2	0.973	87007.	−1721.30	1.072	348.7
	$(20{+}15)M_\odot$	109.5	0.968	37319.	−1203.50	1.186	244.7	$(10{+}10)M_\odot$	190.3	0.975	77432.	−1045.60	0.648	192.8
EP$(T_3, 3.5, 0, -40, 0)$	$(15{+}15)M_\odot$	126.9	0.949	44601.	−1160.40	1.069	322.3	$(15{+}5)M_\odot$	208.4	0.975	102210.	−1406.10	0.805	214.6
	$(20{+}10)M_\odot$	131.9	0.978	49188.	−1252.90	0.999	207.7	$(10{+}5)M_\odot$	263.3	0.969	135110.	−1218.00	1.231	548.3
	$(15{+}10)M_\odot$	154.1	0.952	60648.	−1255.90	1.017	404.3	$(5{+}5)M_\odot$	380.3	0.965	226990.	−1027.60	0.960	883.4
	$(20{+}20)M_\odot$	87.0	0.937	18859.	−726.78	0.997	175.1	$(20{+}5)M_\odot$	148.9	0.987	72221.	−1938.50	0.970	209.6
	$(20{+}15)M_\odot$	99.7	0.953	26088.	−939.25	1.005	175.0	$(10{+}10)M_\odot$	174.0	0.990	67126.	−1420.30	0.986	252.5
L$(2,\ 0)$	$(15{+}15)M_\odot$	116.0	0.972	34155.	−1087.60	0.999	189.8	$(15{+}5)M_\odot$	181.6	0.991	89333.	−1908.10	0.996	259.5
	$(20{+}10)M_\odot$	118.0	0.974	38075.	−1201.00	0.990	191.1	$(10{+}5)M_\odot$	235.9	0.991	120130.	−1869.90	0.830	274.6
	$(15{+}10)M_\odot$	140.0	0.985	48463.	−1295.00	0.996	219.6	$(5{+}5)M_\odot$	348.0	0.994	207730.	−2077.90	0.709	379.0
	$(20{+}20)M_\odot$	80.3	0.935	33179.	−1379.20	0.998	136.5	$(20{+}5)M_\odot$	140.1	0.968	99046.	−2345.10	0.996	191.6
	$(20{+}15)M_\odot$	92.1	0.960	41065.	−1465.70	0.997	152.3	$(10{+}10)M_\odot$	160.5	0.969	85317.	−1293.90	0.707	167.5
L$(2,\ 1)$	$(15{+}15)M_\odot$	107.0	0.969	50159.	−1486.50	1.003	164.3	$(15{+}5)M_\odot$	169.6	0.966	114410.	−1835.70	0.673	165.1
	$(20{+}10)M_\odot$	109.4	0.970	55990.	−1663.30	0.994	166.4	$(10{+}5)M_\odot$	218.8	0.964	146040.	−1373.00	0.402	194.6
	$(15{+}10)M_\odot$	129.4	0.969	66431.	−1519.40	0.998	187.9	$(5{+}5)M_\odot$	321.0	0.932	244970.	−1159.90	0.743	404.3
	$(20{+}20)M_\odot$	389.2	0.964	6138.	1091.40	−0.539	242.5	$(20{+}5)M_\odot$	733.9	0.928	31397.	1977.90	−0.634	981.8
	$(20{+}15)M_\odot$	451.2	0.937	10015.	1120.00	0.583	693.5	$(10{+}10)M_\odot$	758.8	0.868	34673.	1301.30	0.951	783.1
HT$(2, 2)$	$(15{+}15)M_\odot$	507.1	0.961	12166.	1236.10	−1.842	322.1	$(15{+}5)M_\odot$	849.2	0.905	41087.	1898.60	−2.966	1192.5
	$(20{+}10)M_\odot$	536.2	0.960	13624.	1378.00	−0.711	334.7	$(10{+}5)M_\odot$	1057.3	0.870	109640.	351.04	0.939	899.7
	$(15{+}10)M_\odot$	632.6	0.950	16662.	1468.50	−1.780	378.9	$(5{+}5)M_\odot$	1525.5	0.937	214890.	−317.77	0.967	969.4
	$(20{+}20)M_\odot$	403.9	0.923	2544.	1511.00	0.547	459.7	$(20{+}5)M_\odot$	611.2	0.918	22867.	2595.60	−1.053	1200.0
	$(20{+}15)M_\odot$	459.0	0.961	1774.	1747.20	−1.790	279.7	$(10{+}10)M_\odot$	816.6	0.901	10216.	2343.10	−1.861	509.6
HP$(2, 2.5)$	$(15{+}15)M_\odot$	536.6	0.921	3321.	1853.80	0.063	1155.9	$(15{+}5)M_\odot$	771.6	0.892	27498.	2640.30	−2.977	1200.0
	$(20{+}10)M_\odot$	530.3	0.958	6259.	1961.60	−1.844	331.6	$(10{+}5)M_\odot$	1050.2	0.850	107210.	707.41	0.893	918.8
	$(15{+}10)M_\odot$	638.8	0.914	7474.	2079.90	−1.449	1193.8	$(5{+}5)M_\odot$	1601.2	0.921	212810.	33.93	0.694	916.8
	$(20{+}20)M_\odot$	358.4	0.977	16787.	81.92	0.187	346.4	$(20{+}5)M_\odot$	196.3	0.983	83529.	−1429.20	0.856	232.3
	$(20{+}15)M_\odot$	420.3	0.975	22751.	13.30	0.414	728.7	$(10{+}10)M_\odot$	726.0	0.964	67085.	−285.69	0.594	922.2
HT$(3, 3.5, +2)$	$(15{+}15)M_\odot$	484.0	0.971	29634.	8.43	0.016	417.1	$(15{+}5)M_\odot$	303.3	0.992	98845.	−1096.60	0.782	395.9
	$(20{+}10)M_\odot$	495.8	0.983	37522.	−309.28	0.693	731.8	$(10{+}5)M_\odot$	970.3	0.992	128810.	−755.33	0.526	909.7
	$(15{+}10)M_\odot$	586.9	0.967	46435.	−210.60	0.586	916.7	$(5{+}5)M_\odot$	1433.6	0.992	221940.	−679.22	0.400	907.7
	$(20{+}20)M_\odot$	316.4	0.981	17922.	−37.78	0.640	498.6	$(20{+}5)M_\odot$	196.1	0.984	83861.	−1489.90	0.869	232.7
	$(20{+}15)M_\odot$	375.2	0.980	23737.	−95.75	0.603	618.2	$(10{+}10)M_\odot$	639.4	0.972	68270.	−408.04	0.640	917.6
HT$(3, 3.5, -2)$	$(15{+}15)M_\odot$	426.3	0.975	31166.	−123.77	0.506	587.6	$(15{+}5)M_\odot$	303.1	0.993	98715.	−1142.80	0.802	389.2
	$(20{+}10)M_\odot$	436.0	0.986	38125.	−390.93	0.538	434.1	$(10{+}5)M_\odot$	868.1	0.992	129460.	−848.59	0.675	852.1
	$(15{+}10)M_\odot$	514.5	0.974	47366.	−316.76	0.654	806.4	$(5{+}5)M_\odot$	1273.2	0.993	223420.	−812.58	0.425	883.0

PN model		FF for projection onto the Fourier-domain detection template families												
		$f_{\rm end}$	mn	ψ_0	$\psi_{3/2}$	$\alpha f_{\rm cut}^{2/3}$	$f_{\rm cut}$		$f_{\rm end}$	mn	ψ_0	$\psi_{3/2}$	$\alpha f_{\rm cut}^{2/3}$	$f_{\rm cut}$
HP$(3, 3.5, +2)$	$(20{+}20)M_\odot$	474.6	0.968	14652.	236.51	0.215	863.4	$(20{+}5)M_\odot$	196.4	0.982	83872.	−1421.20	0.928	261.4
	$(20{+}15)M_\odot$	539.6	0.966	20205.	181.76	0.071	1076.9	$(10{+}10)M_\odot$	952.2	0.948	66050.	−202.66	0.548	898.9
	$(15{+}15)M_\odot$	634.8	0.955	27087.	170.17	0.009	1200.0	$(15{+}5)M_\odot$	304.1	0.990	98220.	−1035.20	0.796	405.4
	$(20{+}10)M_\odot$	598.9	0.975	36238.	−213.15	0.438	900.5	$(10{+}5)M_\odot$	1212.8	0.991	127870.	−682.01	0.555	621.0
	$(15{+}10)M_\odot$	752.5	0.948	45078.	−109.24	0.539	911.2	$(5{+}5)M_\odot$	1921.0	0.989	220910.	−608.88	0.313	925.7
HP$(3, 3.5, -2)$	$(20{+}20)M_\odot$	363.2	0.973	16421.	113.38	0.384	525.9	$(20{+}5)M_\odot$	196.3	0.983	83747.	−1435.60	0.996	289.7
	$(20{+}15)M_\odot$	421.8	0.972	21952.	62.83	0.337	690.9	$(10{+}10)M_\odot$	734.7	0.958	66819.	−271.94	0.680	893.8
	$(15{+}15)M_\odot$	489.8	0.968	28632.	62.71	0.000	422.7	$(15{+}5)M_\odot$	303.7	0.992	98202.	−1060.60	0.749	368.8
	$(20{+}10)M_\odot$	510.0	0.982	36893.	−272.30	0.263	463.2	$(10{+}5)M_\odot$	998.3	0.991	128060.	−722.63	0.491	887.7
	$(15{+}10)M_\odot$	591.3	0.959	45653.	−168.47	0.469	924.6	$(5{+}5)M_\odot$	1445.9	0.991	221850.	−685.53	0.390	930.8

Table 8.15: Fitting factors for the projection of the target models (in the rows) onto the $(\psi_0, \psi_{3/2}, \alpha, f_{\rm cut})$ Fourier-domain detection template family. For ten choices of BBH masses, this table shows the minmax matches between the target (adiabatic) models and the Fourier-domain search model, *maximized over the intrinsic parameters* ψ_0, $\psi_{3/2}$, and $\alpha, f_{\rm cut}$, and over the extrinsic parameter α. For each intersection, the six numbers shown report the *ending frequency* $f_{\rm end}$ (defined in Sec. 8.6.2) of the PN model for the BBH masses quoted, the minmax FF mn, and the search parameters at which the maximum is attained.

8.7 Performance of the time-domain detection templates and construction of the detection bank in time domain

Another possibility of building a detection template family is to adopt one or more of the physical models discussed in Secs. 8.4 as the effective template bank used for detection. Under the general hypothesis that underlies this work (that is, that the *target* models span the region in signal space where the true physical signals reside), if we find that one of the target models matches all the others very well, we can use it as the effective model; and we can estimate its effectualness in matching the true physical signal from its effectualness in matching all the other models.

As shown in Tables 8.9, 8.10 and discussed in Sec. 8.5, the fitting factors FF for the projection of the PN models onto each other are low (at least for PN order $n \leq 2.5$ or for high masses); in other words, the models appear to be quite distant in signal space. This conclusion is overturned, however, if we let the dimensionless mass ratio η move beyond its physical range $0 \leq \eta \leq 1/4$. For instance, the P$(2, 2.5)$ and EP$(3, 3.5, 0)$ models can be extended formally to the range $0 \leq \eta \leq 1$. Beyond those ranges, either the equations (of energy-balance, or motion) become singular, or the determination of the MECO or light ring (the evolutionary endpoint of the inspiral for the P$(2, 2.5)$ model and the EP$(3, 3.5, 0)$ model, respectively) fails.

When the models are extended to $0 < \eta \leq 1$, they appear to lie much closer to each other in signal space. In particular, the P$(2, 2.5)$ and EP$(3, 3.5, 0)$ models are able to match all the other models, with minmax FF > 0.95, for almost all the masses in our range, and in any case with much improved FF for most masses; see Tables 8.16 and 8.17. Apparently, part of the effect of the different resummation and approximation schemes is just to modulate the strength of the PN effects in a way that can be simulated by changing η to nonphysical values in any one model. This fact can be appreciated by looking at Figs. 8.26, 8.27 and 8.28, 8.29, which show the projection of several models onto the P$(2, 2.5)$ and EP$(3, 3.5, 0)$ effective template spaces, respectively. For instance, in comparison with T$(2, 2.5)$, the model P$(2, 2.5)$ seems to underestimate systematically the effect of η, so a satisfactory FF for $\eta_T = 0.25$ can be obtained only if we let $\eta_P > 0.25$ (quite consistently, in the comparison of Tables 8.9, 8.10, where η was confined to its physical range, T$(2, 2.5)$ could match P$(2, 2.5)$ effectively, but the reverse was not true).

The other (and perhaps crucial) effect of raising η is to change the location of the MECO for the P-approximant model (or the light ring, for the EP model), where orbital evolution ends. (Remember that one of the differences between the Padé and the EOB models is that the latter includes a plunge part between the ISCO and the light ring.) More specifically, for P$(2, 2.5)$ [EP$(3, 3.5, 0)$] the position of the MECO [light ring] is pushed to smaller radii as η is increased. This effect can increase the FF for target models that have very different ending frequencies from those of P$(2, 2.5)$ and EP$(3, 3.5)$ at comparable η's.

Because for the EP model the frequency at the light ring is already quite high, we cannot simply operate on η to improve the match between the EP model and other models that end at much lower frequencies [see the values of minmax matches in Table 8.17]. Thus, we shall enhance the effectualness of EP by adding an arbitrary *cut* parameter that modifies the radius r (usually the light-ring radius) at which we stop the integration of the Hamilton equations (8.91)–(8.94); the effect is to modify the final instantaneous GW frequency of the waveform. This is therefore a *time-domain cut*, as opposed to the frequency-domain cuts of the frequency-domain effective templates examined in the previous section.

We can then compute the FF by searching over $f_{\rm cut}$ in addition to M and η, and we shall correspondingly account for the required number of distinct $f_{\rm cut}$ when we estimate the number of templates required to give a certain $\mathrm{MM}_{\rm tot}$. Even so, if we are unsure whether we can model successfully a given source over a certain range of frequencies that falls within LIGO range (as it is the case for the heavy BBHs with MECOs at frequencies < 200 Hz), the correct way to estimate the optimal ρ (and therefore the expected detection rate) is to include only the signal power in the frequency range that we know well.

The best matches shown in Tables 8.16 and 8.17, and in Figs. 8.26–8.29 were obtained by searching over the target model parameter space with the simplicial `amoeba` algorithm [60]. We found (empirically) that it was expedient to conduct the searches on the parameters $\beta \equiv M\eta^{2/5}$ and η rather than on M and η. This is because iso-match surfaces tend to look like thin ellipses clustered around the best match parameter pair, with principal axes along the β and η directions. As shown in Table 8.16, the values of the maxmax and minmax FFs are very close to each other for the $\mathrm{P}(2, 2.5)$ model; the same is true for the $\mathrm{EP}(3, 3.5)$ model (so in Table 8.17 we do not show both). For $\mathrm{EP}(3, 3.5)$, the search over the three parameters $(\beta, \eta, f_{\rm cut})$ was performed as a refinement step after a first search on (β, η).

We have evaluated the mismatch metric [27] g_{ij} (see Sec. 8.2) with respect to the parameters (β, η) for the models $\mathrm{P}(2, 2.5)$ and $\mathrm{EP}(3, 3.5, 0)$ (while evaluating g_{ij}, the EP waveforms were not cut). The metric components at the point (β_0, η_0) were obtained by first determining the ranges $(\beta_{\rm min}, \beta_{\rm max})$, $(\eta_{\rm min}, \eta_{\rm max})$ for which

$$\langle u(\beta_0, \eta_0), u(\beta_{\rm min}, \eta_0)\rangle = \langle u(\beta_0, \eta_0), u(\beta_{\rm max}, \eta_0)\rangle = 1 - 0.05 \tag{8.129}$$

$$\langle u(\beta_0, \eta_0), u(\beta_0, \eta_{\rm min})\rangle = \langle u(\beta_0, \eta_0), u(\beta_0, \eta_{\rm max})\rangle = 1 - 0.05; \tag{8.130}$$

then a quadratic form was least-squares–fit to 16 values of the match along the ellipse Γ_1 with axes given by $(\beta_{\rm min}, \beta_{\rm max})$ and $(\eta_{\rm min}, \eta_{\rm max})$. The first quadratic form was used only to determine the principal axes of two further ellipses Γ_2 and Γ_3, at projected matches of $1 - 0.025$ and $1 - 0.0125$. Another quadratic form (giving the final result for the metric) was then fit at the same time to 16

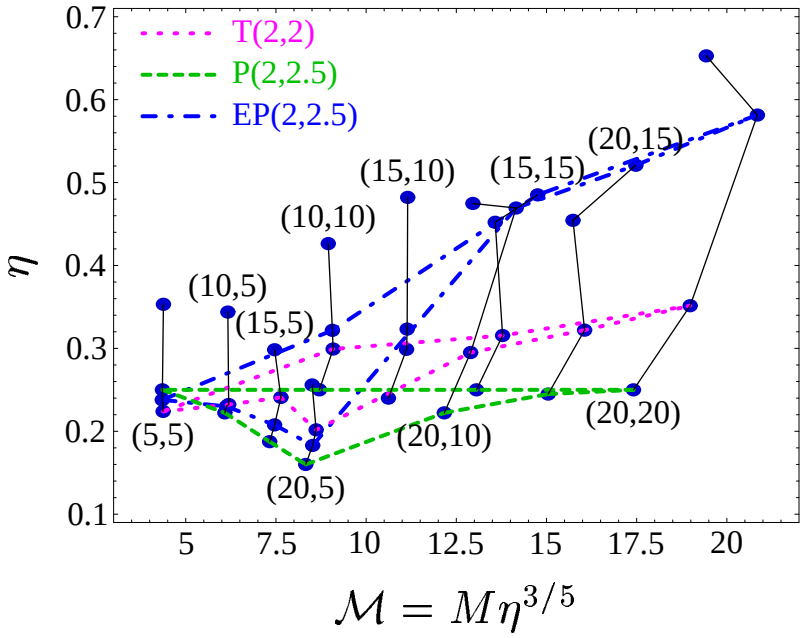

Figure 8.26: Projection of 2PN waveforms onto the P(2, 2.5) effective template space. Dots are shown for the same BBH masses of Tab. 8.15, and for PN models T(2, 2.5), P(2, 2.5), ET(2, 2.5), and EP(2, 2.5). The thin solid lines show the *BH mass lines* (introduced in Sec. 8.6.2), while the dashed and dotted lines show the contours of the projections of selected PN models.

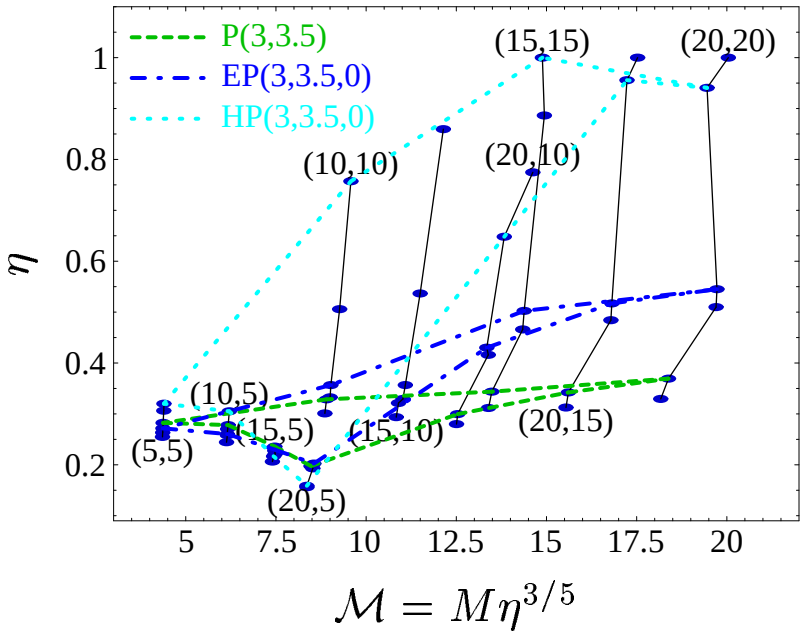

Figure 8.27: Projection of 3PN waveforms onto the P(2, 2.5) effective template space. Dots are shown for the same BBH masses of Tab. 8.15, and for PN models T(3, 3.5, +2), P(3, 3.5, +2), ET(3, 3.5, +2), EP(3, 3.5, +2), HT(3, 3.5, +2), and HP(3, 3.5, 0). The dots for $\hat{\theta} = -2$ are only slightly displaced, and they are not shown. The thin solid lines show the *BH mass lines* (introduced in Sec. 8.6.2), while the dashed and dotted lines show the contours of the projections of selected PN models.

points along Γ_2 and to 16 points along Γ_3, but the two ellipses were given different fitting weights to cancel the quartic correction terms in the Taylor expansion of the match around (β_0, η_0) [the cubic terms were canceled automatically by taking symmetric points along the ellipses]. The rms error of the fit was in all cases very good, establishing that the quadratic approximation held in the close vicinity (matches ~ 0.95) of each point.

We estimate that the numerical error $\sim 20\%$ is in any case less than the error associated with using Eq. (8.25) to evaluate the required number of templates, instead of laying down a lattice of templates more accurately.

The resulting $\sqrt{|g|}$ for P$(2, 2.5)$ and EP$(3, 3.5, 0)$ is shown in Fig. 8.30. It is evident that most of the mismatch volume is concentrated near the smallest β's and η's in parameter space. This is encouraging, because it means that the extension of the effective template family to high masses and high η's (necessary, as we have seen, to match several target models with very high FF) will be relatively cheap with respect to the size of the template bank (this picture, however, changes when we introduce frequency-domain cuts for the EP models). With the $\sqrt{|g|}$'s we then computed the number of P and EP templates necessary to cover the parameter ranges $\beta : (4, 24)$, $\eta : (0.15, 1.00)$, and $\beta : (4, 24)$, $\eta : (0.1, 1.00)$ which span comfortably all the projected images of the target spaces onto the P and EP template spaces, respectively. [Note the ranges include also BBHs where one of the BH has a mass less than $5M_\odot$.] We obtained

$$\mathcal{N}_P \simeq 3260 \left(\frac{0.02}{1 - \mathrm{MM}}\right), \qquad \mathcal{N}_E \simeq 6700 \left(\frac{0.02}{1 - \mathrm{MM}}\right), \tag{8.131}$$

where MM is the required minimum match (analog to the parameter MM_ψ of the preceding section). By comparison, these numbers are reduced to respectively 1230 and 3415 if we restrict η to the physical range.

The number $\mathcal{N}_E$ does not include the effect of multiple ending frequencies (cuts). We estimate the number of distinct f_{cut} needed for each β by an argument similar to the one used for the Fourier-domain effective templates (see Sec. 8.6); it turns out that more cuts are required for higher masses. The resulting number of templates is $\mathcal{N}_{Ec} \simeq 51,000$ for MM $= 0.98$, which is comparable to the result for the effective Fourier-domain templates.

If we assume that the distance between the time-domain templates and the target models is representative of the distance to the true physical signal, we can guess that FF $\gtrsim 0.95$ for P and FF $\gtrsim 0.97$ for EP with cuts. Under these hypotheses, 6,500 P templates can buy us a (worst-case) $\mathrm{MM_T} \simeq 0.94$, corresponding to a loss in event rate of $\sim 17\%$. For 51,000 EP templates, we get $\mathrm{MM_T} \simeq 0.95$, corresponding to a loss in event rate of $\sim 14\%$.

Before ending this section we would like to point out another time-domain detection-template family which can be consider kindred of the Fourier-domain detection-template family introduced

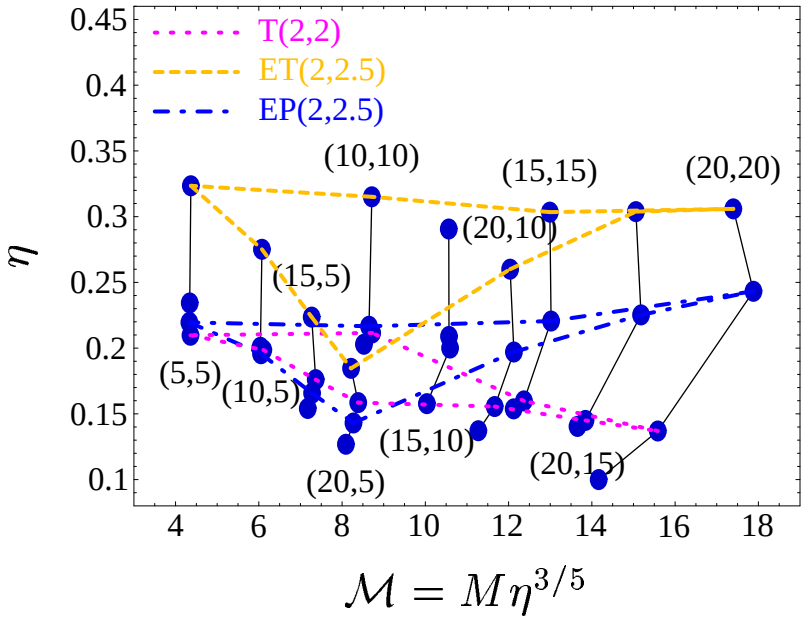

Figure 8.28: Projection of 2PN waveforms onto the EP$(3, 3.5)$ effective template space. This projection includes the effect of the frequency cut. Dots are shown for the same BBH masses of Tab. 8.15, and for PN models T$(2, 2.5)$, P$(2, 2.5)$, ET$(2, 2.5)$, and EP$(2, 2.5)$. The thin solid lines show the *BH mass lines* (introduced in Sec. 8.6.2), while the dashed and dotted lines show the contours of the projections of selected PN models.

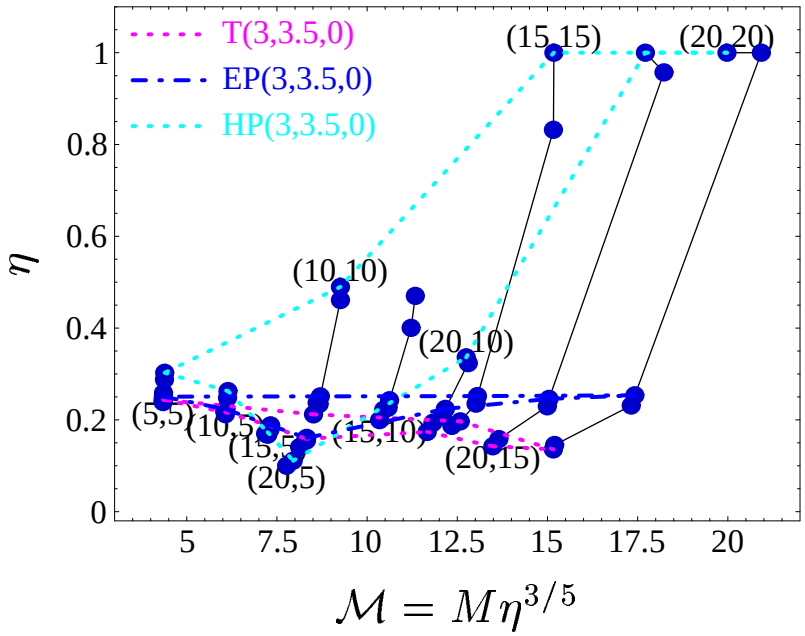

Figure 8.29: Projection of 3PN waveforms onto the EP$(3, 3.5)$ effective template space. This projection includes the effect of the frequency cut. Dots are shown for the same BBH masses of Tab. 8.15, and for PN models T$(3, 3.5, +2)$, P$(3, 3.5, +2)$, ET$(3, 3.5, +2)$, EP$(3, 3.5, +2)$, HT$(3, 3.5, +2)$, and HP$(3, 3.5, +2)$. The dots for $\hat{\theta} = -2$ are only slightly displaced, and they are not shown. The thin solid lines show the *BH mass lines* (introduced in Sec. 8.6.2), while the dashed and dotted lines show the contours of the projections of selected PN models.

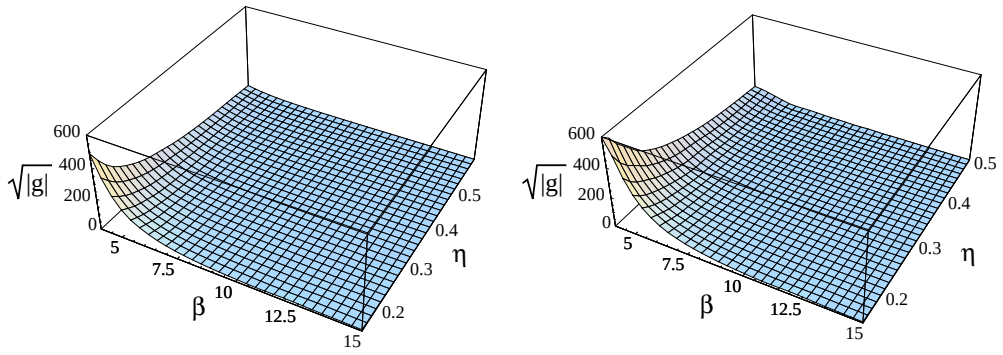

Figure 8.30: Determinant of the mismatch metric for the P(2, 2.5) models [left panel], and for the EP(3, 3.5, 0) models [right panel]. The determinant $\sqrt{|g|}$ is shown as a function of η and $\beta = M\eta^{2/5}$.

in Sec. 8.6, see Eq. (8.107). We can use, for example, the following expression suggested by PN calculations [see, e.g., Ref. [61]]

$$h_{\rm eff}(t) = \mathcal{A}^{\rm T}_{\rm eff}(t)\, e^{i\psi^{\rm T}_{\rm eff}(t)}\,, \tag{8.132}$$

where

$$\mathcal{A}^{\rm T}_{\rm eff}(t) = (t_c - t)^{7/16}\, \left[1 - \alpha^{\rm T}\,(t_c - t)^{-1/4}\right]\, \theta(t_{\rm cut} - t)\,, \tag{8.133}$$

$$\begin{aligned}\psi_{\rm eff}(t) \;\; = \;\; & \phi_c + (t_c - t)^{5/8}\, \Big[\psi^{\rm T}_0 + \psi^{\rm T}_{1/2}\,(t_c - t)^{-1/8} + \psi^{\rm T}_1\,(t_c - t)^{-1/4} \\ & + \psi^{\rm T}_{3/2}\,(t_c - t)^{-3/8} + \psi^{\rm T}_2\,(t_c - t)^{-1/2} + \cdots\Big]\,,\end{aligned} \tag{8.134}$$

where $\phi_c, t_c, \alpha^{\rm T}, \psi^{\rm T}_0, \psi^{\rm T}_1, \psi^{\rm T}_{3/2}$ and $\psi^{\rm T}_2$ are arbitrary parameters whose range of values are determined maximizing the matches with the target two-body models.

		FF for projection onto P(2, 2.5), for $0 < \eta < 1$												
		mm	M	η	mn	M	η		mm	M	η	mn	M	η
	(20+20)$M_\odot$	0.997	35.53	0.35	0.994	35.55	0.35	(20+5)$M_\odot$	0.988	22.04	0.21	0.979	22.51	0.20
	(20+15)$M_\odot$	0.997	32.43	0.31	0.994	31.69	0.32	(10+10)$M_\odot$	0.996	19.29	0.28	0.990	18.74	0.30
T(2, 2)	(15+15)$M_\odot$	0.997	28.45	0.29	0.993	27.54	0.32	(15+5)$M_\odot$	0.993	18.31	0.23	0.985	17.94	0.24
	(20+10)$M_\odot$	0.996	27.72	0.27	0.992	26.83	0.30	(10+5)$M_\odot$	0.992	14.55	0.24	0.989	14.86	0.23
	(15+10)$M_\odot$	0.995	23.68	0.28	0.988	22.95	0.30	(5+5)$M_\odot$	0.994	10.60	0.23	0.992	10.73	0.22
	(20+20)$M_\odot$	0.821	18.77	0.94	0.962	22.59	0.65	(20+5)$M_\odot$	0.958	11.66	0.63	0.987	12.81	0.53
	(20+15)$M_\odot$	0.862	16.60	0.94	0.966	19.40	0.68	(10+10)$M_\odot$	0.948	9.96	0.89	0.984	10.71	0.77
T(2, 2.5)	(15+15)$M_\odot$	0.891	14.26	0.97	0.969	16.61	0.71	(15+5)$M_\odot$	0.965	9.72	0.69	0.989	10.26	0.62
	(20+10)$M_\odot$	0.905	13.67	0.94	0.974	15.95	0.69	(10+5)$M_\odot$	0.971	8.58	0.60	0.987	8.67	0.59
	(15+10)$M_\odot$	0.929	11.89	0.93	0.978	13.43	0.73	(5+5)$M_\odot$	0.981	6.55	0.52	0.985	6.52	0.53
	(20+20)$M_\odot$	0.997	37.04	0.31	0.994	36.96	0.31	(20+5)$M_\odot$	0.996	23.66	0.18	0.990	23.28	0.19
	(20+15)$M_\odot$	0.997	32.62	0.29	0.995	32.69	0.29	(10+10)$M_\odot$	0.998	19.70	0.26	0.993	19.24	0.27
T(3, 3.5, 0)	(15+15)$M_\odot$	0.998	28.89	0.28	0.994	28.07	0.30	(15+5)$M_\odot$	0.997	19.18	0.21	0.993	18.82	0.21
	(20+10)$M_\odot$	0.997	28.69	0.25	0.995	28.00	0.26	(10+5)$M_\odot$	0.997	14.89	0.23	0.993	14.67	0.23
	(15+10)$M_\odot$	0.998	24.35	0.26	0.994	23.72	0.27	(5+5)$M_\odot$	0.999	10.16	0.24	0.997	10.27	0.24
	(20+20)$M_\odot$	0.999	36.20	0.31	0.995	35.37	0.33	(20+5)$M_\odot$	0.997	22.95	0.19	0.993	22.53	0.20
	(20+15)$M_\odot$	0.999	31.40	0.31	0.997	31.22	0.31	(10+10)$M_\odot$	0.999	18.67	0.29	0.995	18.20	0.30
T(3, 3.5, 0)	(15+15)$M_\odot$	0.999	27.63	0.29	0.997	26.96	0.31	(15+5)$M_\odot$	0.997	18.61	0.22	0.995	18.15	0.23
	(20+10)$M_\odot$	0.999	27.42	0.27	0.996	26.84	0.28	(10+5)$M_\odot$	0.998	14.13	0.25	0.994	13.87	0.26
	(15+10)$M_\odot$	0.998	23.20	0.28	0.996	22.60	0.29	(5+5)$M_\odot$	0.998	9.57	0.27	0.996	9.71	0.26
	(20+20)$M_\odot$	0.998	35.30	0.33	0.996	34.73	0.34	(20+5)$M_\odot$	0.998	23.03	0.19	0.995	22.62	0.20
	(20+15)$M_\odot$	0.999	30.84	0.32	0.996	30.65	0.32	(10+10)$M_\odot$	0.998	18.11	0.31	0.994	17.86	0.31
P(3, 3.5, −2)	(15+15)$M_\odot$	0.999	27.01	0.31	0.996	26.38	0.33	(15+5)$M_\odot$	0.997	18.43	0.22	0.994	17.96	0.23
	(20+10)$M_\odot$	0.999	26.90	0.28	0.996	26.48	0.29	(10+5)$M_\odot$	0.998	13.99	0.25	0.993	13.75	0.26
	(15+10)$M_\odot$	0.998	22.76	0.29	0.995	22.18	0.31	(5+5)$M_\odot$	0.997	9.50	0.27	0.996	9.63	0.27
	(20+20)$M_\odot$	0.999	33.58	0.36	0.996	33.42	0.37	(20+5)$M_\odot$	0.998	22.71	0.19	0.996	22.42	0.20
	(20+15)$M_\odot$	0.999	30.03	0.33	0.997	29.70	0.34	(10+10)$M_\odot$	0.999	17.87	0.31	0.995	17.36	0.33
P(3, 3.5, +2)	(15+15)$M_\odot$	0.998	26.12	0.33	0.997	25.59	0.34	(15+5)$M_\odot$	0.998	18.15	0.23	0.996	17.77	0.24
	(20+10)$M_\odot$	0.999	26.38	0.29	0.997	25.84	0.30	(10+5)$M_\odot$	0.998	13.59	0.27	0.994	13.31	0.28
	(15+10)$M_\odot$	0.997	21.62	0.32	0.995	21.53	0.32	(5+5)$M_\odot$	0.998	9.25	0.29	0.996	9.34	0.28
	(20+20)$M_\odot$	0.994	26.75	0.56	0.989	25.10	0.65	(20+5)$M_\odot$	0.979	19.87	0.24	0.970	19.27	0.26
	(20+15)$M_\odot$	0.993	23.77	0.52	0.962	25.26	0.45	(10+10)$M_\odot$	0.989	14.75	0.43	0.983	14.93	0.43
ET(2, 2.5)	(15+15)$M_\odot$	0.991	20.87	0.50	0.970	21.86	0.45	(15+5)$M_\odot$	0.987	15.81	0.28	0.982	15.42	0.30
	(20+10)$M_\odot$	0.988	21.35	0.42	0.973	20.26	0.47	(10+5)$M_\odot$	0.994	11.98	0.33	0.990	11.70	0.34
	(15+10)$M_\odot$	0.987	17.99	0.44	0.969	17.28	0.48	(5+5)$M_\odot$	0.997	8.04	0.36	0.995	8.18	0.35
	(20+20)$M_\odot$	0.991	31.38	0.46	0.986	29.96	0.53	(20+5)$M_\odot$	0.952	22.75	0.20	0.941	23.33	0.19
	(20+15)$M_\odot$	0.989	28.48	0.40	0.978	26.83	0.47	(10+10)$M_\odot$	0.977	18.69	0.29	0.971	18.03	0.32
ET(3, 3.5, −2)	(15+15)$M_\odot$	0.985	25.24	0.38	0.970	23.83	0.43	(15+5)$M_\odot$	0.972	18.53	0.22	0.964	19.03	0.21
	(20+10)$M_\odot$	0.977	25.09	0.34	0.955	23.62	0.39	(10+5)$M_\odot$	0.983	15.04	0.22	0.979	14.79	0.23
	(15+10)$M_\odot$	0.974	21.65	0.33	0.963	22.39	0.31	(5+5)$M_\odot$	0.994	10.38	0.23	0.992	10.39	0.23
	(20+20)$M_\odot$	0.993	30.84	0.46	0.989	29.51	0.51	(20+5)$M_\odot$	0.957	22.28	0.20	0.946	22.87	0.19
	(20+15)$M_\odot$	0.991	27.38	0.43	0.981	25.94	0.48	(10+10)$M_\odot$	0.983	16.95	0.35	0.976	17.42	0.33
ET(3, 3.5, +2)	(15+15)$M_\odot$	0.986	24.02	0.41	0.973	22.67	0.47	(15+5)$M_\odot$	0.974	17.92	0.24	0.967	18.49	0.22
	(20+10)$M_\odot$	0.981	24.19	0.36	0.963	22.66	0.42	(10+5)$M_\odot$	0.984	14.43	0.24	0.982	14.28	0.24
	(15+10)$M_\odot$	0.977	20.84	0.35	0.966	21.46	0.33	(5+5)$M_\odot$	0.995	9.80	0.26	0.993	9.89	0.25
	(20+20)$M_\odot$	0.988	30.91	0.48	0.977	28.86	0.58	(20+5)$M_\odot$	0.947	24.15	0.17	0.940	23.60	0.18
	(20+15)$M_\odot$	0.980	27.79	0.43	0.963	25.85	0.52	(10+10)$M_\odot$	0.975	18.50	0.30	0.964	17.90	0.32
EP(2, 2.5)	(15+15)$M_\odot$	0.972	24.47	0.40	0.947	22.77	0.49	(15+5)$M_\odot$	0.970	18.73	0.22	0.963	19.16	0.21
	(20+10)$M_\odot$	0.965	24.97	0.34	0.938	22.29	0.47	(10+5)$M_\odot$	0.984	15.15	0.22	0.980	14.80	0.23
	(15+10)$M_\odot$	0.963	23.00	0.29	0.951	21.93	0.32	(5+5)$M_\odot$	0.995	10.24	0.24	0.993	10.29	0.24
	(20+20)$M_\odot$	0.993	30.25	0.48	0.990	29.04	0.53	(20+5)$M_\odot$	0.958	21.90	0.21	0.947	22.61	0.20
	(20+15)$M_\odot$	0.990	26.86	0.45	0.981	25.54	0.50	(10+10)$M_\odot$	0.983	16.74	0.36	0.976	17.26	0.34
EP(3, 3.5, −2)	(15+15)$M_\odot$	0.986	23.98	0.41	0.974	22.36	0.48	(15+5)$M_\odot$	0.975	17.83	0.24	0.967	18.24	0.23
	(20+10)$M_\odot$	0.982	23.79	0.37	0.964	22.56	0.42	(10+5)$M_\odot$	0.984	14.34	0.24	0.982	14.12	0.25
	(15+10)$M_\odot$	0.977	20.49	0.36	0.966	21.21	0.34	(5+5)$M_\odot$	0.994	9.74	0.26	0.993	9.84	0.26
	(20+20)$M_\odot$	0.994	29.47	0.50	0.991	28.39	0.55	(20+5)$M_\odot$	0.960	21.84	0.21	0.948	22.30	0.20
	(20+15)$M_\odot$	0.991	26.46	0.45	0.983	24.97	0.52	(10+10)$M_\odot$	0.983	16.14	0.39	0.976	16.75	0.36
EP(3, 3.5, +2)	(15+15)$M_\odot$	0.986	22.97	0.44	0.975	21.73	0.50	(15+5)$M_\odot$	0.977	17.52	0.24	0.968	18.08	0.23
	(20+10)$M_\odot$	0.982	23.18	0.39	0.966	22.14	0.43	(10+5)$M_\odot$	0.985	13.53	0.27	0.983	13.79	0.26
	(15+10)$M_\odot$	0.978	19.94	0.38	0.968	20.58	0.36	(5+5)$M_\odot$	0.994	9.54	0.27	0.993	9.55	0.27

		FF for projection onto P(2, 2.5), for $0 < \eta < 1$												
		mm	M	η	mn	M	η		mm	M	η	mn	M	η
HT(3, 3.5, −2)	(20+20)$M_\odot$	0.993	21.45	0.98	0.991	21.03	1.00	(20+5)$M_\odot$	0.995	26.36	0.15	0.986	25.79	0.15
	(20+15)$M_\odot$	0.986	19.86	0.84	0.982	18.48	1.00	(10+10)$M_\odot$	0.964	15.24	0.43	0.958	14.57	0.48
	(15+15)$M_\odot$	0.978	17.27	0.81	0.972	16.19	0.94	(15+5)$M_\odot$	0.988	19.17	0.21	0.980	19.60	0.20
	(20+10)$M_\odot$	0.965	20.87	0.49	0.949	18.74	0.66	(10+5)$M_\odot$	0.978	14.07	0.25	0.975	13.93	0.26
	(15+10)$M_\odot$	0.952	17.74	0.49	0.944	16.36	0.59	(5+5)$M_\odot$	0.987	9.61	0.27	0.986	9.55	0.27
HT(3, 3.5, +2)	(20+20)$M_\odot$	0.982	20.21	1.00	0.960	20.04	1.00	(20+5)$M_\odot$	0.997	25.94	0.15	0.990	25.48	0.16
	(20+15)$M_\odot$	0.984	17.81	0.98	0.967	17.53	1.00	(10+10)$M_\odot$	0.965	13.39	0.55	0.959	13.95	0.51
	(15+15)$M_\odot$	0.977	15.20	1.00	0.962	16.06	0.89	(15+5)$M_\odot$	0.991	18.63	0.22	0.984	19.08	0.21
	(20+10)$M_\odot$	0.964	19.18	0.57	0.950	17.04	0.77	(10+5)$M_\odot$	0.980	13.23	0.28	0.975	13.51	0.27
	(15+10)$M_\odot$	0.954	15.66	0.61	0.943	16.70	0.54	(5+5)$M_\odot$	0.986	9.03	0.30	0.985	8.93	0.31
HP(3, 3.5, −2)	(20+20)$M_\odot$	0.962	19.87	1.00	0.946	20.16	1.00	(20+5)$M_\odot$	0.997	25.87	0.15	0.990	25.26	0.16
	(20+15)$M_\odot$	0.971	17.46	1.00	0.960	17.69	1.00	(10+10)$M_\odot$	0.962	12.92	0.59	0.957	13.34	0.55
	(15+15)$M_\odot$	0.963	15.66	0.93	0.960	15.14	1.00	(15+5)$M_\odot$	0.992	18.51	0.22	0.982	17.98	0.23
	(20+10)$M_\odot$	0.961	17.81	0.69	0.950	19.45	0.55	(10+5)$M_\odot$	0.978	13.04	0.29	0.975	13.27	0.28
	(15+10)$M_\odot$	0.947	16.31	0.56	0.941	15.77	0.60	(5+5)$M_\odot$	0.984	8.97	0.30	0.982	9.02	0.30
HP(3, 3.5, +2)	(20+20)$M_\odot$	0.915	19.33	1.00	0.887	20.18	0.94	(20+5)$M_\odot$	0.998	25.69	0.15	0.992	25.21	0.16
	(20+15)$M_\odot$	0.942	17.26	1.00	0.921	17.71	0.96	(10+10)$M_\odot$	0.957	12.04	0.67	0.953	11.32	0.76
	(15+15)$M_\odot$	0.938	15.03	0.99	0.933	14.89	1.00	(15+5)$M_\odot$	0.993	18.25	0.23	0.985	18.61	0.22
	(20+10)$M_\odot$	0.959	16.40	0.81	0.947	17.94	0.65	(10+5)$M_\odot$	0.978	12.90	0.29	0.976	12.65	0.31
	(15+10)$M_\odot$	0.949	12.43	0.99	0.937	13.30	0.86	(5+5)$M_\odot$	0.982	8.62	0.33	0.982	8.70	0.32

Table 8.16: Fitting factors for the projection of the target models (in the rows) onto the P(2, 2.5) detection template family. For ten choices of BBH masses, this table shows the maxmax (mm) and minmax (mn) matches between the target models and the P(2, 2.5) search model, *maximized over the intrinsic parameters of the search model*. For each intersection, the triples (mm,M,η) and (mn,M,η) denote the maximized matches and the mass parameters $M = m_1 + m_2$ and $\eta = m_1 m_2/M^2$ at which the maxima are attained (maxmax and minmax matches give rise to slightly different optimal values of M and η). In computing these matches, the search parameter η was *not* restricted to its physical range $0 < \eta \leq 1/4$, but it was allowed to move in the range $0 < \eta < 1$, for which the energy-balance equation (8.31) is still formally integrable. With few exceptions, this table shows that maxmax and minmax matches are very similar, so we generally use the more conservative minmax matches.

		FF for projection onto EP(3, 3.5, 0), for $0 < \eta < 1$														
		mm	M	η	mmc	M	η	$f_{\rm cut}$		mm	M	η	mmc	M	η	$f_{\rm cut}$
T(2, 2)	(20+20)$M_\odot$	0.984	51.05	0.14	0.984	51.38	0.14	171.7	(20+5)$M_\odot$	0.981	25.34	0.16	0.981	25.32	0.16	347.1
	(20+15)$M_\odot$	0.981	44.12	0.14	0.981	44.11	0.15	199.7	(10+10)$M_\odot$	0.984	22.16	0.21	0.985	22.15	0.21	395.5
	(15+15)$M_\odot$	0.977	37.15	0.16	0.978	37.16	0.16	236.7	(15+5)$M_\odot$	0.986	20.90	0.18	0.987	20.89	0.18	424.3
	(20+10)$M_\odot$	0.974	35.85	0.15	0.974	35.62	0.16	246.7	(10+5)$M_\odot$	0.992	16.17	0.20	0.999	16.20	0.20	368.4
	(15+10)$M_\odot$	0.976	27.95	0.20	0.976	27.82	0.20	316.6	(5+5)$M_\odot$	0.996	11.05	0.21	0.999	11.12	0.21	553.1
T(2, 2.5)	(20+20)$M_\odot$	0.948	24.94	0.57	0.985	24.09	0.60	202.5	(20+5)$M_\odot$	0.975	14.60	0.41	0.975	14.52	0.42	567.2
	(20+15)$M_\odot$	0.956	21.50	0.58	0.990	20.77	0.62	241.9	(10+10)$M_\odot$	0.983	11.72	0.65	0.995	11.48	0.69	415.0
	(15+15)$M_\odot$	0.965	18.08	0.62	0.986	18.76	0.57	279.0	(15+5)$M_\odot$	0.983	11.38	0.51	0.994	11.50	0.50	448.1
	(20+10)$M_\odot$	0.965	17.57	0.58	0.992	17.00	0.62	285.7	(10+5)$M_\odot$	0.986	9.44	0.50	0.993	9.23	0.53	629.2
	(15+10)$M_\odot$	0.974	14.85	0.61	0.994	14.28	0.66	329.9	(5+5)$M_\odot$	0.989	6.89	0.48	0.990	6.93	0.47	787.5
T(3, 3.5, 0)	(20+20)$M_\odot$	0.979	53.09	0.12	0.979	52.83	0.12	166.4	(20+5)$M_\odot$	0.965	27.22	0.13	0.966	27.27	0.13	322.7
	(20+15)$M_\odot$	0.971	45.36	0.13	0.972	45.28	0.13	194.2	(10+10)$M_\odot$	0.979	22.77	0.19	0.979	22.79	0.19	384.8
	(15+15)$M_\odot$	0.969	37.79	0.15	0.969	37.79	0.15	232.8	(15+5)$M_\odot$	0.976	21.94	0.16	0.978	22.09	0.15	398.7
	(20+10)$M_\odot$	0.961	34.57	0.17	0.963	34.57	0.16	254.3	(10+5)$M_\odot$	0.985	16.47	0.19	0.985	16.47	0.19	533.1
	(15+10)$M_\odot$	0.971	28.74	0.18	0.971	28.63	0.18	306.5	(5+5)$M_\odot$	0.994	10.69	0.22	0.999	10.66	0.22	474.6
T(3, 3.5, 0)	(20+20)$M_\odot$	0.948	52.47	0.11	0.979	50.43	0.13	174.3	(20+5)$M_\odot$	0.956	25.06	0.16	0.963	26.47	0.14	332.4
	(20+15)$M_\odot$	0.967	43.35	0.14	0.968	43.41	0.14	202.7	(10+10)$M_\odot$	0.977	21.88	0.21	0.980	21.59	0.21	408.5
	(15+15)$M_\odot$	0.963	33.41	0.20	0.966	36.09	0.16	243.5	(15+5)$M_\odot$	0.973	19.98	0.19	0.976	21.32	0.16	411.8
	(20+10)$M_\odot$	0.963	33.33	0.17	0.964	33.17	0.18	267.0	(10+5)$M_\odot$	0.985	15.21	0.22	0.998	15.38	0.21	346.9
	(15+10)$M_\odot$	0.971	27.25	0.20	0.972	27.25	0.20	321.4	(5+5)$M_\odot$	0.994	10.14	0.24	0.999	10.13	0.24	522.3
P(2, 2.5)	(20+20)$M_\odot$	0.941	55.20	0.11	0.956	56.36	0.10	152.1	(20+5)$M_\odot$	0.937	27.97	0.13	0.938	27.93	0.13	315.3
	(20+15)$M_\odot$	0.940	44.34	0.14	0.940	44.34	0.14	198.2	(10+10)$M_\odot$	0.958	22.26	0.20	0.958	22.20	0.20	395.3
	(15+15)$M_\odot$	0.946	37.08	0.16	0.948	37.27	0.15	236.2	(15+5)$M_\odot$	0.959	22.06	0.15	0.961	22.26	0.15	395.1
	(20+10)$M_\odot$	0.943	37.06	0.14	0.943	37.13	0.14	236.9	(10+5)$M_\odot$	0.977	15.53	0.21	0.998	15.83	0.20	284.1
	(15+10)$M_\odot$	0.945	30.16	0.16	0.948	30.40	0.16	289.2	(5+5)$M_\odot$	0.992	10.42	0.23	0.999	10.37	0.23	408.0
P(3, 3.5, −2)	(20+20)$M_\odot$	0.979	49.53	0.14	0.979	49.58	0.14	179.2	(20+5)$M_\odot$	0.955	25.30	0.16	0.959	26.63	0.14	330.9
	(20+15)$M_\odot$	0.972	42.49	0.15	0.972	42.49	0.15	206.8	(10+10)$M_\odot$	0.982	21.04	0.22	0.982	21.04	0.22	416.3
	(15+15)$M_\odot$	0.962	33.09	0.20	0.970	35.17	0.17	250.1	(15+5)$M_\odot$	0.977	21.04	0.17	0.978	21.07	0.17	416.6
	(20+10)$M_\odot$	0.965	32.49	0.18	0.964	32.67	0.18	273.4	(10+5)$M_\odot$	0.987	15.39	0.21	0.998	15.27	0.21	356.4
	(15+10)$M_\odot$	0.974	26.67	0.21	0.974	26.65	0.21	328.4	(5+5)$M_\odot$	0.996	10.10	0.25	0.996	10.11	0.25	795.8
P(3, 3.5, +2)	(20+20)$M_\odot$	0.976	49.06	0.14	0.980	48.36	0.15	181.7	(20+5)$M_\odot$	0.956	26.37	0.14	0.957	26.37	0.14	333.4
	(20+15)$M_\odot$	0.972	41.31	0.16	0.974	41.27	0.16	213.0	(10+10)$M_\odot$	0.983	20.41	0.24	0.983	20.41	0.24	429.2
	(15+15)$M_\odot$	0.971	33.77	0.19	0.971	33.77	0.19	259.5	(15+5)$M_\odot$	0.976	20.81	0.17	0.976	20.72	0.17	423.6
	(20+10)$M_\odot$	0.966	31.61	0.19	0.966	31.66	0.19	277.0	(10+5)$M_\odot$	0.988	15.07	0.22	0.988	15.07	0.22	580.0
	(15+10)$M_\odot$	0.975	25.80	0.22	0.975	25.81	0.22	338.4	(5+5)$M_\odot$	0.996	9.84	0.26	1.000	9.81	0.26	566.3
ET(2, 2.5)	(20+20)$M_\odot$	0.998	35.41	0.31	0.999	35.10	0.31	244.8	(20+5)$M_\odot$	0.995	22.57	0.19	0.995	22.62	0.18	392.5
	(20+15)$M_\odot$	0.999	30.78	0.30	0.999	30.78	0.30	280.3	(10+10)$M_\odot$	0.999	17.42	0.32	0.999	17.42	0.32	492.4
	(15+15)$M_\odot$	0.998	26.43	0.31	0.998	26.53	0.30	324.7	(15+5)$M_\odot$	0.996	17.89	0.22	0.996	17.93	0.22	488.0
	(20+10)$M_\odot$	0.998	27.01	0.26	0.998	27.04	0.26	324.1	(10+5)$M_\odot$	0.997	13.19	0.27	0.997	13.09	0.28	658.5
	(15+10)$M_\odot$	0.998	22.16	0.29	0.998	22.17	0.29	393.8	(5+5)$M_\odot$	0.999	8.61	0.32	0.999	8.60	0.32	996.6
ET(3, 3.5, −2)	(20+20)$M_\odot$	0.999	43.15	0.22	0.999	43.17	0.22	203.2	(20+5)$M_\odot$	0.999	26.22	0.15	1.000	26.22	0.15	341.0
	(20+15)$M_\odot$	0.999	38.02	0.21	1.000	38.04	0.21	230.5	(10+10)$M_\odot$	1.000	21.64	0.22	1.000	21.76	0.22	407.4
	(15+15)$M_\odot$	0.999	32.70	0.21	0.999	32.65	0.22	269.6	(15+5)$M_\odot$	1.000	21.23	0.17	1.000	21.22	0.17	419.1
	(20+10)$M_\odot$	1.000	32.17	0.20	1.000	32.17	0.20	276.3	(10+5)$M_\odot$	0.999	16.14	0.20	1.000	16.08	0.20	544.9
	(15+10)$M_\odot$	0.999	26.96	0.21	0.999	27.00	0.21	327.5	(5+5)$M_\odot$	0.999	10.81	0.22	0.999	10.72	0.22	819.3
ET(3, 3.5, +2)	(20+20)$M_\odot$	0.999	41.85	0.23	0.999	41.69	0.23	211.1	(20+5)$M_\odot$	0.999	25.48	0.15	1.000	25.45	0.16	345.7
	(20+15)$M_\odot$	0.999	36.32	0.23	1.000	36.11	0.23	244.2	(10+10)$M_\odot$	0.999	20.75	0.23	0.999	20.69	0.23	421.9
	(15+15)$M_\odot$	0.999	31.11	0.23	1.000	31.01	0.24	284.6	(15+5)$M_\odot$	1.000	20.51	0.18	1.000	20.50	0.18	435.4
	(20+10)$M_\odot$	0.998	31.06	0.21	0.999	30.98	0.21	286.8	(10+5)$M_\odot$	0.999	15.40	0.21	0.999	15.38	0.21	572.7
	(15+10)$M_\odot$	0.999	25.95	0.22	0.999	25.85	0.23	339.7	(5+5)$M_\odot$	0.999	10.25	0.24	0.999	10.25	0.24	853.6
EP(2, 2.5)	(20+20)$M_\odot$	0.993	41.79	0.24	0.993	41.77	0.24	211.0	(20+5)$M_\odot$	0.997	26.39	0.15	0.998	26.57	0.14	335.7
	(20+15)$M_\odot$	0.994	37.13	0.23	0.994	37.60	0.22	236.5	(10+10)$M_\odot$	0.997	21.68	0.22	0.998	21.65	0.22	409.6
	(15+15)$M_\odot$	0.992	31.60	0.23	0.994	32.01	0.23	276.9	(15+5)$M_\odot$	0.998	21.37	0.17	0.999	21.42	0.17	417.6
	(20+10)$M_\odot$	0.996	32.19	0.20	0.996	32.14	0.20	276.8	(10+5)$M_\odot$	0.998	16.06	0.20	0.998	16.10	0.20	545.1
	(15+10)$M_\odot$	0.996	27.04	0.21	0.996	27.04	0.21	327.8	(5+5)$M_\odot$	0.998	10.75	0.22	0.998	10.76	0.22	817.3
EP(3, 3.5, −2)	(20+20)$M_\odot$	0.997	41.49	0.23	1.000	40.88	0.24	215.5	(20+5)$M_\odot$	1.000	25.25	0.16	1.000	25.26	0.16	352.1
	(20+15)$M_\odot$	0.997	35.06	0.25	1.000	35.64	0.24	245.9	(10+10)$M_\odot$	1.000	20.56	0.24	1.000	20.51	0.24	424.9
	(15+15)$M_\odot$	1.000	30.73	0.24	1.000	30.70	0.24	286.9	(15+5)$M_\odot$	1.000	20.33	0.18	1.000	20.30	0.18	433.1
	(20+10)$M_\odot$	1.000	30.64	0.21	1.000	30.63	0.21	287.1	(10+5)$M_\odot$	1.000	15.28	0.22	1.000	15.32	0.21	572.9
	(15+10)$M_\odot$	1.000	25.58	0.23	1.000	25.58	0.23	344.9	(5+5)$M_\odot$	1.000	10.21	0.24	1.000	10.22	0.24	854.4

		FF for projection onto EP$(3, 3.5, 0)$, for $0 < \eta < 1$													
		mm	M	η	mmc	M	η	$f_{\rm cut}$		mm	M	η	mmc	M	η	$f_{\rm cut}$
	$(20{+}20)M_\odot$	0.998	40.05	0.25	1.000	39.87	0.25	219.8	$(20{+}5)M_\odot$	0.999	24.98	0.16	1.000	24.93	0.16	353.0
	$(20{+}15)M_\odot$	0.998	34.91	0.24	1.000	34.92	0.25	252.7	$(10{+}10)M_\odot$	1.000	19.92	0.25	1.000	19.85	0.25	441.6
EP(3, 3.5, +2)	$(15{+}15)M_\odot$	1.000	29.87	0.25	1.000	29.87	0.25	290.6	$(15{+}5)M_\odot$	1.000	19.98	0.19	1.000	19.91	0.19	444.4
	$(20{+}10)M_\odot$	0.999	29.99	0.22	1.000	29.86	0.22	292.5	$(10{+}5)M_\odot$	1.000	14.98	0.22	0.999	14.96	0.22	584.0
	$(15{+}10)M_\odot$	1.000	24.83	0.24	1.000	24.83	0.24	355.4	$(5{+}5)M_\odot$	0.999	9.99	0.25	1.000	9.98	0.25	877.7
	$(20{+}20)M_\odot$	0.988	26.79	0.62	0.990	24.74	0.76	290.7	$(20{+}5)M_\odot$	0.941	31.21	0.10	0.962	30.26	0.11	287.2
	$(20{+}15)M_\odot$	0.982	23.90	0.59	0.982	23.91	0.59	322.7	$(10{+}10)M_\odot$	0.980	17.14	0.35	0.982	17.25	0.34	493.8
HT(3, 3.5, −2)	$(15{+}15)M_\odot$	0.976	20.86	0.56	0.979	21.27	0.54	372.2	$(15{+}5)M_\odot$	0.988	21.56	0.16	0.988	21.56	0.16	407.3
	$(20{+}10)M_\odot$	0.985	27.05	0.29	0.986	27.08	0.28	321.0	$(10{+}5)M_\odot$	0.991	15.05	0.22	0.993	15.02	0.22	582.1
	$(15{+}10)M_\odot$	0.978	22.28	0.31	0.978	22.32	0.31	389.3	$(5{+}5)M_\odot$	0.991	9.81	0.26	0.992	9.83	0.26	798.6
	$(20{+}20)M_\odot$	0.987	20.90	1.00	0.988	20.93	1.00	319.4	$(20{+}5)M_\odot$	0.932	30.88	0.10	0.955	29.95	0.11	292.5
	$(20{+}15)M_\odot$	0.979	18.72	0.96	0.979	18.72	0.96	360.2	$(10{+}10)M_\odot$	0.973	14.84	0.45	0.974	14.74	0.46	553.2
HT(3, 3.5, +2)	$(15{+}15)M_\odot$	0.970	16.93	0.83	0.970	16.93	0.83	414.9	$(15{+}5)M_\odot$	0.987	21.20	0.17	0.987	21.15	0.17	416.8
	$(20{+}10)M_\odot$	0.977	25.19	0.32	0.977	24.51	0.35	349.6	$(10{+}5)M_\odot$	0.992	14.15	0.25	0.992	14.15	0.25	615.7
	$(15{+}10)M_\odot$	0.973	19.43	0.40	0.973	19.46	0.40	428.2	$(5{+}5)M_\odot$	0.989	9.23	0.29	0.989	9.28	0.29	754.7
	$(20{+}20)M_\odot$	0.973	20.64	1.00	0.973	20.64	1.00	323.2	$(20{+}5)M_\odot$	0.930	30.83	0.10	0.953	29.87	0.11	294.6
	$(20{+}15)M_\odot$	0.965	21.55	0.69	0.966	21.79	0.67	340.8	$(10{+}10)M_\odot$	0.970	15.51	0.41	0.970	15.54	0.41	531.0
HP(3, 3.5, −2)	$(15{+}15)M_\odot$	0.963	19.64	0.59	0.966	18.72	0.66	398.9	$(15{+}5)M_\odot$	0.986	21.04	0.17	0.987	20.98	0.17	420.3
	$(20{+}10)M_\odot$	0.974	26.00	0.30	0.975	26.27	0.29	331.0	$(10{+}5)M_\odot$	0.991	13.83	0.26	0.991	13.85	0.26	633.8
	$(15{+}10)M_\odot$	0.963	17.92	0.48	0.964	18.16	0.46	451.5	$(5{+}5)M_\odot$	0.987	9.20	0.29	0.987	9.23	0.29	640.9
	$(20{+}20)M_\odot$	0.938	19.98	1.00	0.938	19.98	1.00	335.0	$(20{+}5)M_\odot$	0.951	29.72	0.11	0.951	29.70	0.11	296.4
	$(20{+}15)M_\odot$	0.957	17.71	1.00	0.957	17.71	1.00	377.3	$(10{+}10)M_\odot$	0.964	14.15	0.49	0.964	14.28	0.48	559.8
HP(3, 3.5, +2)	$(15{+}15)M_\odot$	0.950	15.18	1.00	0.950	15.18	1.00	439.4	$(15{+}5)M_\odot$	0.986	20.84	0.17	0.987	20.76	0.17	423.1
	$(20{+}10)M_\odot$	0.972	24.34	0.34	0.973	24.52	0.34	348.3	$(10{+}5)M_\odot$	0.988	13.44	0.27	0.988	13.65	0.26	634.4
	$(15{+}10)M_\odot$	0.954	18.03	0.46	0.955	17.83	0.47	452.8	$(5{+}5)M_\odot$	0.985	8.86	0.31	0.986	8.99	0.30	724.4

Table 8.17: Fitting factors for the projection of the target models (in the rows) onto the EP$(3, 3.5, 0)$ detection template family. For ten choices of BBH masses, this table shows the maxmax matches between the target models and the EP$(3, 3.5, 0)$ search model, *with* (mmc) and *without* (mm) the time-domain cut discussed in Sec. 8.7. The matches are *maximized over the intrinsic parameters of the search model* (over M and η for the mm values; over M, η and $f_{\rm cut}$ for the mmc values). For each intersection, the triple (mm,M,η) and the quadruple (mm,M,η,$f_{\rm cut}$) denote the maximized matches and the mass (and cut) parameters at which the maxima are attained. In computing these matches, the search parameter η was *not* restricted to its physical range $0 < \eta \leq 1/4$, but it was allowed to move in the range $0 < \eta < 1$ for which the energy-balance equation (8.31) is still formally integrable. This table shows that the addition of the time-domain cut can improve the fitting factors considerably, especially for the higher M's in the in the left half of the table, and for the models whose orbital evolution is ended within the range of good interferometer sensitivity.

8.8 Summary

This Chapter deals with the problem of detecting GWs from the most promising sources for ground-based GW interferometers: comparable-mass BBHs with total mass $M = 10$–$40 M_\odot$ moving on quasicircular orbits. The detection of these sources poses a delicate problem, because their transition from the adiabatic phase to the plunge, at least in the nonspinning case, is expected to occur in the LIGO and VIRGO frequency bands. Of course, the true GW signals from these inspirals should be obtained from exact solutions of the Einstein equations for two bodies of comparable mass. However, the theoretical templates used to search for these signals will be, at best, finite-order approximations to the exact solutions, usually derived in the PN formalism. Because the perturbative PN approach begins to fail during the final stages of the inspiral, when strong curvature and nonlinear effects can no longer be neglected, various PN resummation methods have been introduced [14, 15, 16] to improve the convergence of the PN series.

In the first part of this chapter [see Sec. 8.3, 8.4 and 8.5] we studied and compared in detail all the PN models of the relativistic two-body dynamics currently available, including PN Taylor-expanded and resummed models both in the adiabatic approximation and in the nonadiabatic case. We noticed the following features [see Tables 8.9, 8.10]. At least for PN orders $n \leq 2.5$, the *target* models T, P, and E have low cross matches, if the 2.5PN Taylor flux is used. For example, for almost all the masses in our range, we found $\mathrm{maxmax}\,\mathrm{FF} \leq 0.9$; the matches were much better only for P against E (and vice versa). However, if the 2PN Taylor flux is used the overlaps are rather high. At 3PN order we found much higher matches between T, P, and E, and also with the nonadiabatic model H, at least for masses $M \leq 30 M_\odot$, and restricting to $\tilde{z}_1 = 0 = \tilde{z}_2$. These results make sense because at 3PN order the various approximations to the binding energy and the flux seem to be much closer to each other than at lower orders. This "closeness" of the different analytical approaches, which at 3PN order are also much closer to some examples of numerical quasiequilibrium BBH models [24], was recently pointed out in Refs. [53, 64]. On the other hand, the extraction of BBH parameters from a true measured signal, if done using the 3PN models, would still give a range of rather different estimates. However, we want to point out that for quite high masses, e.g., $M = 40 M_\odot$, the 3PN models can have again lower overlaps, also from the point of view of detection.

In addition, by studying the frequency-domain amplitude of the GW signals that end inside the LIGO frequency band [see Figs. 8.4, 8.7, 8.14, 8.10], we understood that if high matches are required it is crucial to reproduce their deviations from the Newtonian amplitude evolution, $f^{-7/6}$ (on the contrary, the Newtonian formula seems relatively adequate to model the PN amplitude for GW frequencies below the instantaneous GW frequency at the endpoint of orbital evolution).

Finally, the introduction of the HT, HP and L models in Secs. 8.4.1, 8.4.2 provided another example of two-body nonadiabatic dynamics, quite different from the E models. In the H models,

the conservative dynamics does not have an ISCO [see the discussion below Eq. (8.73)] at 2PN and 3PN orders. As a consequence, the transition to the plunge is due to secular radiation-reaction effects, and it is pushed to much higher frequencies. This means that, for the H models, the GW signals for BBHs of total mass $M = 10$–$40 M_\odot$ end outside the LIGO frequency band, and the frequency-domain amplitude does not deviate much from the Newtonian result, at least until very high frequencies [see Fig. 8.10]. The L models do not provide the waveforms during the late inspiral and plunge. This is due to the fact that because of the appearance of unphysical effects, e.g., the binding energy starts to increase with time instead of continuing decreasing, we are obliged to stop the evolution before the two BHs enter the last stages of inspiral. It is important to point out that differently from the nonadiabatic E models, the nonadiabatic H and L models give rather different predictions when used at various PN orders. So, from these point of view they are less reliable and robust than the E models.

In the second part of this chapter [Secs. 8.6, 8.7] we pursued the following strategy. We assumed that the target models spanned a region in signal space that (almost) included the true GW signal. We were then able to provide a few detection template families (either chosen among the time-domain target models, or built directly from polynomial amplitude and phasings in the frequency domain) that approximate quite well all the targets [FF ≥ 0.95 for almost all the masses in our range, with much better FFs for most masses]. We speculate that the effectualness of the detection model in approximating the targets is indicative of its effectualness in approximating the true signals.

The Fourier-domain detection template family, discussed in Sec. 8.6, is simple and versatile. It uses a PN polynomial structure for the frequency-domain amplitude and phasing, but it does not constrain the coefficients to the PN functional dependencies on the physical parameters. In this sense this bank follows the basic idea that underlies the Fast Chirp Transform [62]. However, because for the masses that we consider the GW signal can end within the LIGO frequency band, we were forced to modify the Newtonian-order formula for the amplitude, introducing a cutoff frequency and a parameter to modify the shape of the amplitude curve (the parameter α). As discussed at the end of Sec. 8.6.6 the good performance of the two and three-dimensional families confirms also results obtained in Refs. [12], [43] and [63].

We showed that our Fourier-domain detection template space has a FF higher than 0.97 for the T, P and E models, and $\gtrsim 0.96$ for most of the 3PN HT and HP models; we then speculate that it will match true BBH waveforms with FF ~ 0.96. We have computed the number of templates required to give MM $\simeq 0.96$ (about 10^4). The total $\mathrm{MM_T}$ should be larger than FF $\cdot$ MM ~ 0.92, which corresponds to a loss of event rate of $1 - \mathrm{MM_T^3} \approx 22\%$. This performance could be improved at the price of introducing a larger number of templates, with the rough scaling law of $\mathcal{N} = 10^4 [0.04/(0.96 - \mathrm{MM})]^2$.

In Sec. 8.6.5 we investigated where the less reliable 2PN H and L models, and the E models at

3PN order further expanded considering $\tilde{z}_1 \neq 0$, lie in the detection template space. The Fourier-domain template family has FF in the range [0.85,0.95] with the 2PN H models, and FF mostly higher than 0.95, but with several exceptions which can be as low as 0.93 with the L models. The E models with $\tilde{z}_1 \neq 0$ are matched by the detection template family with FF almost always higher than 0.95. The E models with $\tilde{z}_1 \neq 0$ and the L models are (almost) covered by the region delimiting the adiabatic models and the E models with $\tilde{z}_1 = 0$. However, these models require lower cutoff frequencies, which will increase the number of templates up to a factor of 3. The 2PN H models sit outside this region and if we want to include them the number of templates should be doubled.

The time-domain detection template families, discussed in Sec. 8.7, followed a slightly different philosophy. The idea in this case was to provide a template bank that, for some choices of the parameters, could coincide with one of the approximate two-body models. Quite interestingly, this can be achieved by relaxing the physical hypothesis that $0 \leq \eta \leq 0.25$. However, the good performances of these banks are less systematic, and harder to generalize than the performance of the Fourier-domain effective bank. As suggested at the end of Sec. 8.7 [see Eq. (8.132)], the time-domain bank could be improved by using a parametrization of the time-domain amplitude and phase similar to the one used for the Fourier-domain templates. The detection template families based on the extension of the $\mathrm{P}(2, 2.5)$ and $\mathrm{EP}(3, 3.5)$ to nonphysical values of η were shown to have FF respectively $\gtrsim 0.95$ and $\gtrsim 0.97$ for all the PN target models, and considerably higher for most models and masses. We have computed the number of P templates needed to obtain a MM = 0.99 (about 6,500) and of EP templates to obtain a MM = 0.98 (about 51,000). The expected total $\mathrm{MM_T}$ is then respectively $\gtrsim 0.94$ and $\gtrsim 0.95$, corresponding to losses in event rate of $\lesssim 17\%$ and $\lesssim 14\%$. The MMs scale roughly as $[0.01/(1 - \mathrm{MM})]$ for P and $[0.02/(1 - \mathrm{MM})]^2$ for EP (because of the additional frequency-cut parameter).

We notice that the number of templates that we estimate for the Fourier- and time-domain detection template families is higher than the number of templates we would obtain using only one PN model. However, the number of *independent shapes* that enters the expression for the ρ_* threshold [see Eq. 8.18] does not coincide with the number of templates that are laid down within a discrete template bank to achieve a given MM; indeed, if MM is close to one, these are almost guaranteed to be to yield S/N statistics that are strongly correlated. A rough estimate of the number of independent shapes can be obtained taking a coarse-grained grid in template space. For example by setting MM=0 in Eq. (8.25), the number of independent shapes would be given roughly by the volume of the template space. As explained at the end of Sec. 8.2.2, if we wish to keep the same false-alarm probability, we have to increase the threshold by $\sim 3\%$ if we increase the number of independent shapes by one order of magnitude. This effect will cause a further loss in event rates [65].

Finally, in Sec. 8.6.6 we extended the detection template family in the Fourier domain by requiring

that it embeds the targets in a signal space of higher dimension (with more parameters). We investigated the three dimensional case and we found, as expected, the maxmax matches increase. In particular, the match of the phasings are nearly perfect: always higher than 0.994 for the two-body models which are farthest apart in the detection template space. Moreover, by projecting the points in the three-dimensional space back to the two-dimensional space, we can get nearly the same projections we would have got from matching directly the PN waveforms with the two-parameter–phasing model. The analysis done in Sec. 8.6.6 could suggest ways of systematically expand the Fourier-domain templates. Trying to guess the functional directions in which the true signals might lie with respect to the targets was the most delicate challenge of our investigation. However, our suggestions are not guaranteed to produce templates that will capture the true signal, and they should be considered as indications. When numerical relativity provides the first good examples of waveforms emitted in the last stages of the binary inspiral and plunge, it will be very interesting to investigate whether the matches with our detection template families are high and in which region of the detection template space do they sit.

8.9 Bibliography

[1] A. Abramovici et al., *Science* **256**, 325 (1992); B. Caron et al., *Class. Quantum Grav.* **14**, 1461 (1997); H. Lück et al., *Class. Quantum Grav.* **14**, 1471 (1997); M. Ando et al., *Phys. Rev. Lett.* **86** 3950 (2001).

[2] C. L. Fryer and V. Kalogera, *Astrophys. J.* **554**, 548 (2001).

[3] C. W. Lincoln and C. M. Will, *Phys. Rev. D* **42**, 1123 (1990).

[4] K. S. Thorne, in *300 Years of Gravitation* S. W. Hawking and W. Israel, eds. (Cambridge University Press, Cambridge, England, 1987), pp. 330-458.

[5] V. M. Lipunov, K. A. Postnov and M. E. Prokhorov, *New Astron.* **2**, 43 (1997).

[6] K. Belczynski, V. Kalogera and T. Bulik, *Astrophys. J.* **572**, 407 (2002); V. Kalogera, R. Narayan, D. N. Spergel and J. H. Taylor, *Astrophys. J.* **556**, 340 (2001); V. Kalogera, in *Gravitational Waves, Third Edoardo Amaldi Conference*, S. Meshkov, ed. (AIP, New York, 2000); V. Kalogera, in *Astrophysical Sources for Ground-Based Gravitational Wave Detectors*, J. M. Centrella, ed. (AIP, New York, 2001).

[7] K. S. Thorne, "The scientific case for mature LIGO interferometers," LIGO Document Number P000024-00-R, `www.ligo.caltech.edu/docs/P/P000024-00.pdf`; C. Cutler and K. S. Thorne, "An overview of gravitational-wave sources," `gr-qc/0204090`.

[8] S. F. Portegies Zwart and S. L. McMillan, *Astrophys. J.* **528**, L17 (2000).

[9] M. C. Miller, D. P. Hamilton, *Astrophys. J.* **576**, 894 (2002).

[10] T. Damour, *300 Years of Gravitation*, S. W. Hawking and W. Israel, eds. (Cambridge University Press, Cambridge, England, 1987); L. Blanchet, *Living Reviews in Relativity*, 2002-3 (2002), `http://www.livingreviews.org/Articles/Volume5/2002-3blanchet`.

[11] É. É. Flanagan and S. A. Hughes, *Phys. Rev. D* **57**, 4535 (1998); *ibid.*, 4566 (1998).

[12] T. Damour, B. R. Iyer and B. S. Sathyaprakash, *Phys. Rev. D* **63**, 044023 (2001); **66**, 027502 (2002).

[13] G. B. Cook, *Phys. Rev. D* **50**, 5025 (1994).

[14] A. Buonanno and T. Damour, *Phys. Rev. D* **59**, 084006 (1999).

[15] A. Buonanno and T. Damour, *Phys. Rev. D* **62**, 064015 (2000).

[16] T. Damour, P. Jaranowski and G. Schäfer, *Phys. Rev. D* **62**, 084011 (2000).

[17] A. Buonanno and T. Damour, contributed paper to the IX$^{\rm th}$ Marcel Grossmann Meeting (Rome, July 2000), `gr-qc/0011052`.

[18] J. Baker, B. Brügmann, M. Campanelli, C. O. Lousto and R. Takahashi, *Phys. Rev. Lett.* **87**, 121103 (2001); J. Baker, M. Campanelli, C. O. Lousto and R. Takahashi, *Phys. Rev. D* **65**, 124012 (2002).

[19] L. E. Kidder, C. M. Will and A. G. Wiseman, *Phys. Rev. D* **47**, 4183(R) (1993); L. E. Kidder, *Phys. Rev. D* **52**, 821 (1995).

[20] T. A. Apostolatos, C. Cutler, G. J. Sussman and K. S. Thorne, *Phys. Rev. D* **15**, 6274 (1994); T. A. Apostolatos, *Phys. Rev. D* **54**, 2438 (1996).

[21] P. R. Brady, J. D. E. Creighton and K. S. Thorne, *Phys. Rev. D* **58**, 061501 (1998).

[22] T. W. Baumgarte, *Phys. Rev. D* **62**, 024018 (2000).

[23] H. P. Pfeiffer, S. A. Teukolsky and G. B. Cook *Phys. Rev. D* **62**, 104018 (2000).

[24] E. Gourgoulhon, P. Grandclément and S. Bonazzola, *Phys. Rev. D* **65**, 044020 (2002); P. Grandclément, E. Gourgoulhon and S. Bonazzola, *Phys. Rev. D* **65**, 044021 (2002).

[25] T. Damour, B. R. Iyer and B. S. Sathyaprakash, *Phys. Rev. D* **57**, 885 (1998).

[26] R. Balasubramanian, B. S. Sathyaprakash and S. V. Dhurandhar, *Phys. Rev. D* **53**, 3033 (1996).

[27] B. J. Owen, *Phys. Rev. D* **53**, 6749 (1996).

[28] L. S. Finn, *Phys. Rev. D* **46**, 5236 (1992).

[29] M. H. A. Davis, in *Gravitational Wave Data Analysis*, B. F. Schutz, ed. (Kluwer, Dordrecht, 1989).

[30] L. S. Finn and D. F. Chernoff, *Phys. Rev. D* **47**, 2198–2219 (1993).

[31] L. A. Wainstein and L. D. Zubakov, *Extraction of signals from noise* (Prentice-Hall, Englewood Cliffs NJ, 1962).

[32] A. V. Oppenheim, A. S. Willskly and I. T. Young, *Signals and systems* (Prentice-Hall, Englewood Cliffs, NJ, 1983).

[33] J. C. Hancock and P. A. Wintz, *Signal detection theory* (McGraw-Hill, New York, 1966).

[34] C. Cutler and É. É. Flanagan, *Phys. Rev. D* **49**, 2658 (1994).

[35] M. Abramowitz and I. A. Stegun, *Handbook of mathematical functions* (Dover, New York, 1972), pp. 299–300.

[36] B. F. Schutz, in *The Detection of Gravitational Radiation*, D. Blair, ed. (Cambridge University Press, Cambridge, England, 1989).

[37] C. Cutler et al., Phys. Rev. Letters**70**, 2984 (1993).

[38] T. A. Apostolatos, *Phys. Rev. D* **52**, 605 (1995).

[39] B. S. Sathyaprakash and S. V. Dhurandhar, *Phys. Rev. D* **44**, 3819 (1991).

[40] S. V. Dhurandhar and B. S. Sathyaprakash, *Phys. Rev. D* **49**, 1707 (1994).

[41] B. S. Sathyaprakash, *Phys. Rev. D* **50**, R7111 (1994).

[42] B. J. Owen and B. Sathyaprakash, *Phys. Rev. D* **60**, 022002 (1999).

[43] A. E. Chronopoulos and T. A. Apostolatos, *Phys. Rev. D* **64**, 042003 (2001).

[44] T. Damour and N. Deruelle, *Phys. Lett.* **87A**, 81 (1981); T. Damour, C. R. Séances Acad. Sci. Ser. 2 **294**, 1355 (1982).

[45] P. Jaranowski and G. Schäfer, *Phys. Rev. D* **57**, 7274 (1998); ibid. **60**, 124003 (1999); T. Damour, P. Jaranowski and G. Schäfer, *Phys. Rev. D* **62**, 044024 (2000); ibid., 021501(R) (2000); **63**, 044021 (2001).

[46] L. Blanchet and G. Faye, *Phys. Lett.* **A271**, 58 (2000); *J. Math. Phys* **42**, 4391 (2001); *Phys. Rev. D* **63**, 062005 (2000); V. C. de Andrade, L. Blanchet and G. Faye, *Class. Quant. Grav.* **18**, 753 (2001).

[47] T. Damour, P. Jaranowski and G. Schäfer, *Phys. Lett. B* **513**, 147 (2001).

[48] R. V. Wagoner and C. M. Will, *Astrophys. J.* **210**, 764 (1976).

[49] L. Blanchet, T. Damour, B. R. Iyer, C. M. Will and A. G. Wiseman, *Phys. Rev. Lett.* **74**, 3515 (1995); L. Blanchet, T. Damour and B. R. Iyer, *Phys. Rev. D* **51**, 536 (1995); C. M. Will and A. G. Wiseman, *Phys. Rev. D* **54**, 4813 (1996).

[50] L. Blanchet, *Phys. Rev. D* **54**, 1417 (1996); L. Blanchet, *Class. Quantum Grav.* **15**, 113 (1998).

[51] L. Blanchet, G. Faye, B. R. Iyer, B. Joguet, *Phys. Rev. D* **65**, 061501 (2002);

[52] L. Blanchet, B. R. Iyer and B. Joguet, *Phys. Rev. D* **65**, 064005 (2002).

[53] L. Blanchet, *Phys. Rev. D* **65**, 124009 (2002).

[54] C. M. Bender and S. A. Orszag, *Advanced Mathematical Methods for Scientists and Engineers* (McGraw Hill, Singapore, 1984).

[55] T. Damour, B. R. Iyer and B. S. Sathyaprakash, *Phys. Rev. D* **62**, 084036 (2000).

[56] L. E. Kidder, C. M. Will and A. G. Wiseman, *Class. Quantum Grav.* **9**, L127 (1992); *Phys. Rev. D* **47**, 3281 (1993).

[57] B. R. Iyer and C. Will, *Phys. Rev. Lett.* **70**, 113 (1993); *Phys. Rev. D* **52**, 6882 (1995)

[58] A. Gopakumar, B. R. Iyer and S. Iyer, *Phys. Rev. D* **55**, 6030 (1997).

[59] E. Porter, *Class. Quant. Grav.* **19**, 4343 (2002).

[60] W. H. Press, S. A. Teukolsky, W. T. Vetterling, B. P. Flannery, *Numerical recipes in C: the art of scientific computing* (Cambridge University Press, Cambridge, England, 1992).

[61] L. Blanchet, B. R. Iyer, C. M. Will and A. G. Wiseman, *Class. Quantum Grav.* **13**, 575 (1996).

[62] F. A. Jenet and T. Prince, *Phys. Rev. D* **62**, 122001 (2000).

[63] J. Edlund, T. Prince and M. Tinto, in preparation; "Chebyshev approximations to the 2PN waveform," talk given at LSC workshop, Livingston, March 20-24, 2002.

[64] T. Damour, P. Grandclément and E. Gourgoulhon, *Phys. Rev. D* **66**, 024007 (2002).

[65] B.S. Sathyaprakash, private communication.

Chapter 9

Detecting gravitational waves from precessing binaries of spinning compact objects: Adiabatic limit

Black-hole (BH) binaries with single-BH masses $m = 5$–$20M_\odot$, moving on quasi-circular orbits, are among the most promising sources for first-generation ground-based gravitational-wave (GW) detectors. Until now, the development of data-analysis techniques to detect GWs from these sources has been focused mostly on nonspinning BHs. The data-analysis problem for the spinning case is complicated by the necessity to model the precession-induced modulations of the GW signal, and by the large number of parameters needed to characterize the system, including the initial directions of the spins, and the position and orientation of the binary with respect to the GW detector. In this chapter we consider binaries of maximally spinning BHs, and we work in the adiabatic-inspiral regime to build families of modulated detection templates that (i) are functions of very few physical and phenomenological parameters, (ii) model remarkably well the dynamical and precessional effects on the GW signal, with fitting factors on average $\gtrsim 0.97$, but (iii) might require increasing the detection thresholds, offsetting at least partially the gains in the fitting factors. Our detection-template families are quite promising also for the case of neutron-star–black-hole binaries, with fitting factors on average ≈ 0.93. For these binaries we also suggest (but do not test) a further template family, which would produce essentially exact waveforms written directly in terms of the physical spin parameters.

A. Buonanno, Y. Chen and M. Vallisneri, gr-qc/0211087. Accepted for publication in Phys. Rev. D

9.1 Introduction

A worldwide network of laser-interferometer gravitational-wave (GW) detectors, recently built [1], has by now begun operation. Inspiraling binaries of compact objects, such as black holes (BHs) and

neutron stars (NSs) are among the most promising astrophysical sources for these detectors. The GWs from the inspirals are expected to enter the frequency band of good detector sensitivity during the last few seconds or minutes of evolution of the binaries; GW scientists plan to track the phase of the signals very accurately, and to enhance the signal-to-noise ratio by integrating the signals coherently over their duration in the detector band. This is achieved by filtering the detector output with a bank of *templates* that represent our best theoretical predictions for the signals.

Until now, the development of data-analysis techniques has been focused mostly on binaries containing NSs (whose spins are negligible for data-detection purposes) and nonspinning BHs [2]. Nonspinning, high-mass BHs pose a delicate problem: the breakdown of the post–Newtonian (PN) expansion in the last stages of the inspiral makes it hard to prepare reliable templates for the detection of binary BHs (BBHs) of relatively high total mass (say, 10–40$M_\odot$) with LIGO–VIRGO interferometers. Various resummation techniques, such as Padé approximants [3] and Effective One-Body (EOB) techniques [4, 5] have been developed to extend the validity of PN formalism [6]. Damour, Iyer, and Sathyaprakash [7] compared the templates generated by different PN treatments, and found that they can be very different. In Chapter 8, we investigated this issue for the GW signals emitted by comparable-mass BBHs with a total mass $M = 10$–$40M_\odot$. In Chapter 8 we proposed a few examples of detection template families (DTFs), built either as time series or directly in the frequency domain, which try to address the failure of the PN expansion. The philosophy behind DTFs is to replace a family of signals that correspond to a specific mathematical model of the binary with families that can cover a broader range of plausible signals. Because the direct correspondence with the mathematical model is lost, DTFs are appropriate for the purpose of first detecting GW signals, but do not give direct estimates of physical parameters, such as the masses of the binary constituents. [Within the EOB framework, see also the recent paper by Damour, Iyer, Jaranowski, and Sathyaprakash [8], where the authors extend 3PN EOB templates with seven *flexibility parameters* and then show that the unextended 3PN templates already *span* the ranges of the flexibility parameters consistent with plausible 4PN effects.]

Very little is known about the statistical distribution of spins for the BHs in binaries: the spins could very well be large. Apostolatos, Cutler, Sussman, and Thorne [9, 10, henceforth ACST] have shown that when this is the case, the evolution of the GW phase and amplitude during the inspiral will be significantly affected by spin-induced modulations and irregularities. In a BBH, these effects can become dramatic if the two spins are large and they are not exactly aligned or antialigned with the orbital angular momentum. If this happens, there is a considerable chance that the analysis of interferometer data, carried out without taking spin effects into accounts, could miss the signals from these spinning BBHs altogether. The gravitational waveforms from binaries of spinning compact objects depend on many parameters: the masses and spins of the objects, the angles that describe the relative orientations of detector and binary, and the direction of propagation of GWs to the detector.

In practice it is impossible, due to the extremely high computational cost, to filter the signals with a template bank parametrized by all of these parameters. One strategy is that of providing *effective* templates that depend on fewer parameters, but that have still reasonably high overlaps with the expected physical signals. An interesting suggestion, built on the results obtained in Ref. [9], came from Apostolatos [10], who introduced a modulational sinusoidal term in the frequency-domain phase of the templates to capture the effects of precession. However, while Apostolatos' family reduces the number of parameters considerably, its computational requirements are still very high. Moreover, using an approximated analytical model of NS–BH waveforms, Grandclément, Kalogera and Vecchio [11] showed that this family fails to capture those waveforms satisfactorily (see however Ref. [12] for a hierarchical scheme that can improve the fit by adding "spikes?? in the template phasing).

In this chapter, complementary to Chapter 8, we study the data analysis of GWs from binaries with spinning BHs; for simplicity, we restrict our analysis to the adiabatic limit, where the two compact objects in the binary (either two BHs, or a NS and a BH) follow an adiabatic sequence of *spherical orbits* driven by radiation reaction (RR). The denomination of spherical orbits comes from the fact that the orbital plane is not fixed in space, but precesses, so the orbits trace a complicated path on a (slowly shrinking) spherical surface. We neglect the problems caused by the failure of PN expansion in these binaries (note that the conservative part of the EOB framework [4] has already been extended to the spinning case by Damour [13], providing a tool to move beyond the adiabatic approximation; we plan to add radiation-reaction effects to this model, and to study the consequences on GW emission and detection elsewhere). Here, we carry out a detailed study of PN precessional dynamics and of GW generation in precessing binaries in the adiabatic limit, and we use the resulting insights to build a new class of modulated effective templates where modulational effects are introduced in both the frequency-domain amplitude and frequency-domain phase of the templates. The mathematical structure of our templates suggests a way to search automatically over several of the parameters (in strict analogy to the automatic search over initial template phase in the data analysis of nonspinning binaries), reducing computational costs significantly. We argue that our families should capture very well the expected physical signals.

We note here a shift in perspective from Chapter 8. In this chapter, we use the PN equations for the two-body dynamics of spinning compact objects to build a *fiducial* model (our *target* model) that represents our best knowledge of the expected physical signals. Because we cannot use the target model directly for data analysis (it has too many parameters), we build effective template families with fewer parameters. These families are then compared with the target model for a variety of binary parameters, to gauge their ability to match the physical signals (their *effectualness* [3]). On the other hand, in Chapter 8 we employed several variants of the PN equations (with diverging behaviors in the late phase of inspiral) to identify a range of *plausible* physical signals; we then built our DTFs so that they would match *all* of the PN target models satisfactorily. This said, we shall

still refer to the template families developed in the present Chapter as DTFs. We direct the reader to Chapter 8 for a simple introduction to matched-filtering techniques and their use in GW data analysis (developed in the literature by various authors [2, 3, 7]), and for an explanation of some of the notation used in this chapter.

This Chapter is organized as follows. In Sec. 9.2 we define the target model, and we explain the conventions used to represent the generation and propagation of GWs. In Sec. 9.3 we study the two-body dynamics of spinning compact objects, looking for the features that are especially relevant to the data-analysis problem. Using this insight, in Sec. 9.4 we formulate our DTFs, and we also describe two families of standard stationary-phase–approximation (SPA) templates, to be used as a comparison when evaluating the performance of the DTFs. In Sec. 9.5 we discuss the overlap and false-alarm statistics of our DTFs. In Sec. 9.6 we evaluate the performance of our DTFs for BBHs and NS–BH binaries, and we briefly discuss a more advanced (and very promising) template family for NS–BH systems. In Sec. 9.7 we summarize our conclusions.

Throughout this chapter we adopt the noise spectral density for LIGO-I given by Eq. (8.28) in Chapter 8. The projected VIRGO noise curve is quite different (deeper at low frequencies, with a displaced peak-sensitivity frequency). So our results for high-mass binaries cannot be applied naively to VIRGO. We plan to repeat this study for VIRGO in the near future.

9.2 Definition of the target model

In this section we define the *target model* used in this chapter as a fiducial representation of the GW signals expected from precessing binaries of spinning compact objects. We restrict our analysis to the adiabatic regime where the inspiral of the compact objects can be represented as a sequence of quasi-circular orbits. At any point along the inspiral, a binary of total mass $M = m_1 + m_2$ and symmetric mass ratio $\eta = m_1 m_2 / M^2$ is completely described by the orbital angular frequency ω, the orbital phase Ψ, the direction $\hat{\mathbf{L}}_N \propto \mathbf{r} \times \mathbf{v}$ of the orbital angular momentum, and the two spins $\mathbf{S}_1 = \chi_1 m_1^2 \hat{\mathbf{S}}_1$ and $\mathbf{S}_2 = \chi_2 m_2^2 \hat{\mathbf{S}}_2$, where $\hat{\mathbf{S}}_{1,2}$ are unit vectors and $0 < \chi_{1,2} < 1$. Throughout this chapter we shall use carets to denote unit vectors, and we shall adopt geometrical units.

In Sec. 9.2.1 we write the PN equations that govern the adiabatic evolution of the binary and the precession of $\hat{\mathbf{L}}_N$ and of $\mathbf{S}_{1,2}$. All the target waveforms used to test the effectualness [3] of our DTFs are obtained by integrating these equations numerically. The validity of the adiabatic approximation is discussed in App. 9.8. In Sec. 9.2.2 we discuss our criterion for stopping the numerical integration of the evolution equations at the point where the adiabatic approximation ceases to be valid. In Sec. 9.2.3, building on Refs. [14, 9, 15], we describe a formalism for computing the response of a ground-based detector to the GWs generated by a spinning binary; the response is not just a function of the trajectory of the binary, but also of the relative direction and orientation of binary

and detector. The formalism describes also how the precession of the binary modulates the detector response. Last, in Sec. 9.2.4 we give a classification of all the parameters that enter the expression for the detector response, distinguishing those that specify the evolution of the binary itself from those that describe the relative direction and orientation of binary and detector.

9.2.1 Equations for an adiabatic sequence of precessing spherical orbits

The path of the binary across the sequence of quasi-circular orbits is described by the adiabatic evolution of the orbital angular frequency ω up to 3.5PN order [16, 17, 18, 19, 7] with spin effects included up to 2PN order [20, 16, 15],

$$\begin{aligned}
\frac{\dot{\omega}}{\omega^2} &= \frac{96}{5}\,\eta\,(M\omega)^{5/3}\Bigg\{1 - \frac{743+924\,\eta}{336}\,(M\omega)^{2/3} - \left(\frac{1}{12}\sum_{i=1,2}\left[\chi_i\left(\hat{\mathbf{L}}_N\cdot\hat{\mathbf{S}}_i\right)\left(113\frac{m_i^2}{M^2}+75\eta\right)\right] - 4\pi\right)(M\omega) \\
&+ \left(\frac{34\,103}{18\,144} + \frac{13\,661}{2\,016}\,\eta + \frac{59}{18}\,\eta^2\right)(M\omega)^{4/3} - \frac{\eta\chi_1\chi_2}{48}\left[247(\hat{\mathbf{S}}_1\cdot\hat{\mathbf{S}}_2) - 721(\hat{\mathbf{L}}_N\cdot\hat{\mathbf{S}}_1)(\hat{\mathbf{L}}_N\cdot\hat{\mathbf{S}}_2)\right](M\omega)^{4/3} \\
&- \frac{1}{672}\,(4\,159+14\,532\,\eta)\,\pi\,(M\omega)^{5/3} + \Bigg[\left(\frac{16\,447\,322\,263}{139\,708\,800} - \frac{1\,712}{105}\gamma_E + \frac{16}{3}\pi^2\right) \\
&+ \left(-\frac{273\,811\,877}{1\,088\,640} + \frac{451}{48}\pi^2 - \frac{88}{3}\hat{\theta}\right)\eta + \frac{541}{896}\eta^2 - \frac{5\,605}{2\,592}\eta^3 - \frac{856}{105}\log\left[16(M\omega)^{2/3}\right]\Bigg](M\omega)^2 \\
&+ \left(-\frac{4\,415}{4\,032} + \frac{661\,775}{12\,096}\,\eta + \frac{149\,789}{3\,024}\,\eta^2\right)\pi\,(M\omega)^{7/3}\Bigg\}, \qquad (9.1)
\end{aligned}$$

where $\gamma_E = 0.577\ldots$ is Euler's constant, and where $\hat{\theta}$ is an arbitrary parameter that enters the GW flux at 3PN order [19] and that could not be fixed in the regularization scheme used by the authors of Ref. [19]. Note that in Eq. (9.1) we set the static parameter $\omega_s = 0$ [21]. The precession equations for the two spins are (see, for instance, Eqs. (4.17b,c) of Ref. [15] or Eqs. (11b,c) of Ref. [9])

$$\dot{\mathbf{S}}_1 = \frac{(M\omega)^2}{2M}\left\{\eta\,(M\omega)^{-1/3}\left(4+3\frac{m_2}{m_1}\right)\hat{\mathbf{L}}_N + \frac{1}{M^2}\left[\mathbf{S}_2 - 3(\mathbf{S}_2\cdot\hat{\mathbf{L}}_N)\hat{\mathbf{L}}_N\right]\right\}\times\mathbf{S}_1\,, \qquad (9.2)$$

$$\dot{\mathbf{S}}_2 = \frac{(M\omega)^2}{2M}\left\{\eta\,(M\omega)^{-1/3}\left(4+3\frac{m_1}{m_2}\right)\hat{\mathbf{L}}_N + \frac{1}{M^2}\left[\mathbf{S}_1 - 3(\mathbf{S}_1\cdot\hat{\mathbf{L}}_N)\hat{\mathbf{L}}_N\right]\right\}\times\mathbf{S}_2\,, \qquad (9.3)$$

where we have replaced r and $|\mathbf{L}_N|$ by their leading-order Newtonian expressions in ω,

$$r = \left(\frac{M}{\omega^2}\right)^{1/3}, \qquad |\mathbf{L}_N| = \mu\,r^2\omega = \eta\,M^{5/3}\omega^{-1/3}\,. \qquad (9.4)$$

This approximation is appropriate because the next spin-precession term is $\mathcal{O}(\omega^{1/3})$ higher than the leading order, while next terms in the expressions of r and $|\mathbf{L}_N|$ are $\mathcal{O}(\omega^{2/3})$ higher.

The precession of the orbital plane (defined by the normal vector $\hat{\mathbf{L}}_N$) can be computed as follows. From Eqs. (4.7) and (4.11) of Ref. [15] we see that the total angular momentum $\mathbf{J}$ and its rate of

change $\dot{\mathbf{J}}_{\rm RR}$ (due to RR) depend on ω, $\hat{\mathbf{L}}_{\rm N}$ and $\mathbf{S}_{1,2}$ (schematically) as ($\mathbf{S}=\mathbf{S}_1+\mathbf{S}_2$)

$$\mathbf{J}=\mathbf{L}+\mathbf{S}=\underbrace{\eta\,M^2\,(M\omega)^{-1/3}\,\hat{\mathbf{L}}_{\rm N}\,\left[1+\mathcal{O}(\omega^{2/3})\right]-2\eta\,(M\omega)^{2/3}\,\mathbf{S}_{\rm eff}}_{\mathbf{L}}+\mathbf{S}\,, \tag{9.5}$$

$$\dot{\mathbf{J}}_{\rm RR}=-\frac{32}{5}\eta^2 M(M\omega)^{7/3}\,\hat{\mathbf{L}}_N\left[1+\mathcal{O}(\omega^{2/3})\right]+\mathcal{O}(\omega^{10/3})\,\hat{\mathbf{S}}_1+\mathcal{O}(\omega^{10/3})\,\hat{\mathbf{S}}_2\,, \tag{9.6}$$

where the combination

$$\mathbf{S}_{\rm eff}\equiv\left(1+\frac{3}{4}\,\frac{m_2}{m_1}\right)\,\mathbf{S}_1+\left(1+\frac{3}{4}\,\frac{m_1}{m_2}\right)\,\mathbf{S}_2 \tag{9.7}$$

is known as *effective spin* [13]. Note that both terms in the $\mathbf{L}$ brace of Eq. (9.5) originate from orbital angular momentum (the second term comes from the spin-orbit coupling). Taking the time derivative of (9.5), we obtain

$$\dot{\mathbf{J}}=\eta\,M^2\,(M\omega)^{-1/3}\,\dot{\hat{\mathbf{L}}}_{\rm N}\left[1+\mathcal{O}(\omega^{2/3})\right]-\mathcal{O}(\omega^{2/3})\,\dot{\mathbf{S}}_{\rm eff}+\dot{\mathbf{S}}+\left[\mathcal{O}(\omega^{7/3})\,\hat{\mathbf{L}}_{\rm N}-\mathcal{O}(\omega^{10/3})\,\mathbf{S}_{\rm eff}\right]\,, \tag{9.8}$$

where to get the last term on the right-hand side we have used $\dot{\omega}=\mathcal{O}(\omega^{11/3})$. Comparing Eqs. (9.8) and (9.6), projecting out only the direction perpendicular to $\hat{\mathbf{L}}_{\rm N}$, and keeping only the terms up to the leading and next-to-leading orders, we get

$$\dot{\hat{\mathbf{L}}}_N=-\frac{(M\omega)^{1/3}}{\eta M^2}\,\dot{\mathbf{S}}=\frac{\omega^2}{2M}\Bigg\{\quad\left[\left(4+3\frac{m_2}{m_1}\right)\,\mathbf{S}_1+\left(4+3\frac{m_1}{m_2}\right)\,\mathbf{S}_2\right]\times\hat{\mathbf{L}}_N$$
$$-\frac{3\,\omega^{1/3}}{\eta\,M^{5/3}}\left[(\mathbf{S}_2\cdot\hat{\mathbf{L}}_N)\,\mathbf{S}_1+(\mathbf{S}_1\cdot\hat{\mathbf{L}}_N)\,\mathbf{S}_2\right]\times\hat{\mathbf{L}}_N\Bigg\}\,. \tag{9.9}$$

Thus, we now have the set of four equations (9.1)–(9.3) and (9.9) for the four variables ω, $\mathbf{S}_1$, $\mathbf{S}_2$, and $\hat{\mathbf{L}}_N$. We follow Ref. [15], Eq. (4.15), in defining the *accumulated orbital phase* Ψ as

$$\Psi\equiv\int_{t_i}^{t}\omega\,dt=\int_{\omega_i}^{\omega}\frac{\omega}{\dot{\omega}}\,d\omega\,. \tag{9.10}$$

This phase describes the position of the two compact objects along the instantaneous circular orbits of the adiabatic sequence; the phase of the GW waveforms, as detected by a ground-based detectors, differs from this by precessional effects, as explained below in Sec. 9.2.3.

9.2.2 Endpoint of evolution

The orbital energy of the two-body system at 2PN and 3PN orders, expressed as a function of ω, and assuming the static parameter $\omega_s = 0$ [22, 21], reads [16, 20, 19]

$$\begin{aligned} E_{\rm 2PN}(\omega) &= -\frac{\mu}{2}\,(M\omega)^{2/3}\left\{1 - \frac{(9+\eta)}{12}\,(M\omega)^{2/3} + \frac{8}{3}\hat{\mathbf{L}}_N\cdot\mathbf{S}_{\rm eff}\,(M\omega) + \frac{1}{24}(-81+57\eta-\eta^2)\,(M\omega)^{4/3}\right. \\ &\quad \left. +\frac{1}{\eta}\left[\mathbf{S}_1\cdot\mathbf{S}_2 - 3(\hat{\mathbf{L}}_N\cdot\mathbf{S}_1)(\hat{\mathbf{L}}_N\cdot\mathbf{S}_2)\right]\,(M\omega)^{4/3}\right\}\,, \qquad (9.11) \\ E_{\rm 3PN}(\omega) &= E_{\rm 2PN}(\omega) \\ &\quad - \frac{\mu}{2}\,(M\omega)^{2/3}\left\{\left[-\frac{675}{64} + \left(\frac{34445}{576} - \frac{205}{96}\pi^2\right)\eta - \frac{155}{96}\eta^2 - \frac{35}{5184}\eta^3\right]\,(M\omega)^2\right\}\,. \qquad (9.12) \end{aligned}$$

In the context of our adiabatic approximation, it is natural to stop the integration of Eqs. (9.1)–(9.3) and (9.9) at the point (the Minimum Energy Circular Orbit, or MECO) where the energy $E_{n\rm PN}$ reaches a minimum,

$$\text{MECO}: \quad \frac{dE_{n\rm PN}}{d\omega} = 0\,; \qquad (9.13)$$

after this point the adiabatic approximation breaks down. [1] (The MECO is discussed by Blanchet [23] for nonspinning binaries under the name ICO, for Innermost Circular Orbit.) However, if we find that $\dot{\omega} = 0$ (which implies certainly that the adiabatic approximation has become invalid) before the MECO is reached, we stop the evolution there. In Chapter 8 we noticed that for nonspinning binaries this behavior occurs for the 2.5PN evolutions, but not at 2PN, 3PN and 3.5PN orders.

Throughout this chapter, we shall call the instantaneous frequency of GWs at the endpoint of evolution the *ending frequency*, which, up to a correction that arises from precessional effects, is twice the instantaneous orbital frequency defined in this section. It so happens (see Chapter 8) that a knowledge of the ending frequency is important to cut off the candidate detection templates at the point where we know too little about the physical signals to model them further. In Sec. 9.3.2 we study the dependence of the ending frequency on the spins of the binary.

9.2.3 Gravitational waveforms

As we have seen, the trajectory of the inspiraling binary is obtained by integrating Eqs. (9.1)–(9.3) and (9.9) for the time evolution of $\omega(t)$, $\mathbf{S}_1(t)$, $\mathbf{S}_2(t)$ and $\hat{\mathbf{L}}_N(t)$. To determine the corresponding gravitational waveforms, we need to choose a specific coordinate system. We follow the convention proposed by Finn and Chernoff [14, henceforth FC], and also adopted by Kidder [15]. FC employ a fixed (*source*) coordinate system with unit vectors $\{\mathbf{e}_x^S, \mathbf{e}_y^S, \mathbf{e}_z^S\}$ (see Fig. 9.1). For a circular orbit,

[1] Note that the MECO, as defined by Eq. (9.13) via a total derivative, depends also on the evolution of $\mathbf{L}$, $\mathbf{S}_1$ and $\mathbf{S}_2$. However, later in this chapter (Sec. 9.3.2) we shall see that this dependence is rather weak.

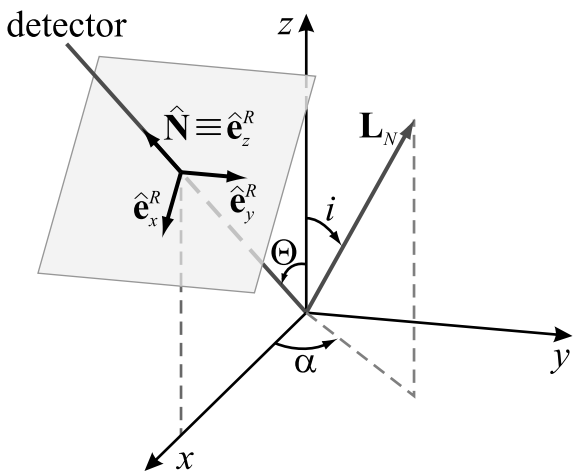

Figure 9.1: Source and radiation frames in the FC convention [14].

the leading-order mass-quadrupole waveform is (throughout this chapter, we use geometrical units)

$$h^{ij} = \frac{2\mu}{D}\left(\frac{M}{r}\right) Q_c^{ij}\,, \tag{9.14}$$

where D is the distance between the source and the Earth, and where Q_c^{ij} is proportional to the second time derivative of the mass-quadrupole moment of the binary,

$$Q_c^{ij} = 2\left[\lambda^i\,\lambda^j - n^i\,n^j\right]\,, \tag{9.15}$$

with n^i and λ^i the unit vectors along the separation vector of the binary $\mathbf{r}$ and along the corresponding relative velocity $\mathbf{v}$. These unit vectors are related to the adiabatic evolution of the dynamical variables by

$$\hat{\mathbf{n}} = \mathbf{e}_1^S\,\cos\Phi_S + \mathbf{e}_2^S\,\sin\Phi_S\,, \quad \hat{\lambda} = -\mathbf{e}_1^S\,\sin\Phi_S + \mathbf{e}_2^S\,\cos\Phi_S\,; \tag{9.16}$$

the vectors $\mathbf{e}_{1,2}^S$ form an orthonormal basis for the instantaneous orbital plane, and in the FC convention they are given by

$$\mathbf{e}_1^S = \frac{\mathbf{e}_z^S \times \hat{\mathbf{L}}_N}{\sin i}\,, \quad \mathbf{e}_2^S = \frac{\mathbf{e}_z^S - \hat{\mathbf{L}}_N\,\cos i}{\sin i}\,. \tag{9.17}$$

The vector $\mathbf{e}_1^S$ points in the direction of the ascending node of the orbit on the (x, y) plane. The quantity Φ_S is the orbital phase with respect to the ascending node; its evolution is given by

$$\dot{\Phi}_S = \omega - \dot{\alpha}\,\cos i\,, \tag{9.18}$$

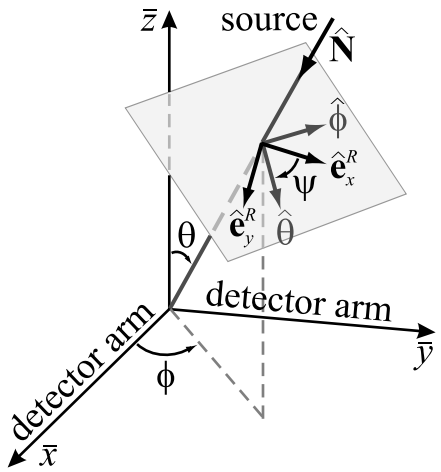

Figure 9.2: Detector and radiation frames in the FC convention [14].

where i and α are the spherical coordinates of $\hat{\mathbf{L}}_{\rm N}$ in the source frame, as shown in Fig. 9.1. Using Eqs. (9.14) and (9.16), we can write Eq. (9.15) as

$$Q_c^{ij} = -2([\mathbf{e}_+^S]^{ij}\,\cos 2\Phi_S - [\mathbf{e}_\times^S]^{ij}\,\sin 2\Phi_S)\,, \tag{9.19}$$

where the polarization tensors $\mathbf{e}_+^S$ and $\mathbf{e}_\times^S$ are given by

$$\mathbf{e}_+^S \equiv \mathbf{e}_1^S \otimes \mathbf{e}_1^S - \mathbf{e}_2^S \otimes \mathbf{e}_2^S\,, \quad \mathbf{e}_\times^S \equiv \mathbf{e}_1^S \otimes \mathbf{e}_2^S + \mathbf{e}_2^S \otimes \mathbf{e}_1^S\,. \tag{9.20}$$

For a detector lying in the direction $\hat{\mathbf{N}} = \mathbf{e}_z^S\cos\Theta + \mathbf{e}_x^S\sin\Theta$, it is expedient to express GW propagation in the *radiation* coordinate system with unit vectors $\{\mathbf{e}_x^R,\mathbf{e}_y^R,\mathbf{e}_z^R\}$ (see our Fig. 9.1 together with, for instance, Eq. (4.22) of Ref. [15]), given by

$$\mathbf{e}_x^R = \mathbf{e}_x^S\,\cos\Theta - \mathbf{e}_z^S\,\sin\Theta\,, \tag{9.21}$$

$$\mathbf{e}_y^R = \mathbf{e}_y^S\,, \tag{9.22}$$

$$\mathbf{e}_z^R = \mathbf{e}_x^S\,\sin\Theta + \mathbf{e}_z^S\,\cos\Theta = \hat{\mathbf{N}}\,. \tag{9.23}$$

In writing Eqs. (9.21)–(9.23) we used the fact that for a generic binary-detector configuration, the entire system consisting of the binary and the detector can be always rotated along the z axis, in such a way that the detector will lie in the (x,z) plane. Later in this chapter (in Sec. 9.4) we shall find it convenient to conserve the explicit dependence of our formulas on the azimuthal angle φ that specifies the direction of the detector.

In the transverse-traceless (TT) gauge, the metric perturbations are

$$\mathbf{h}^{TT} = h_+ \, \mathbf{T}_+ + h_\times \, \mathbf{T}_\times \, , \tag{9.24}$$

where

$$\mathbf{T}_+ \equiv \mathbf{e}_x^R \otimes \mathbf{e}_x^R - \mathbf{e}_y^R \otimes \mathbf{e}_y^R \, , \quad \mathbf{T}_\times \equiv \mathbf{e}_x^R \otimes \mathbf{e}_y^R + \mathbf{e}_y^R \otimes \mathbf{e}_x^R \, , \tag{9.25}$$

and

$$h_+ = \frac{1}{2} \, h^{ij} \, [\mathbf{T}_+]_{ij} \, , \quad h_\times = \frac{1}{2} \, h^{ij} \, [\mathbf{T}_\times]_{ij} \, . \tag{9.26}$$

The response of a ground-based, interferometric detector (such as LIGO or VIRGO) to the GWs is [14]

$$\begin{aligned} h_{\rm resp} &= F_+ \, h_+ + F_\times \, h_\times \\ &= -\frac{2\mu}{D} \frac{M}{r} \left[e_+^{S\,ij} \, \cos 2\Phi_S + e_\times^{S\,ij} \, \sin 2\Phi_S \right] \left([\mathbf{T}_+]_{ij} \, F_+ + [\mathbf{T}_\times]_{ij} \, F_\times \right) , \end{aligned} \tag{9.27}$$

where F_+ and $F_\times$ are the *antenna patterns*, given by

$$F_{+,\,\times} = \frac{1}{2} [\bar{\mathbf{e}}_x \otimes \bar{\mathbf{e}}_x - \bar{\mathbf{e}}_y \otimes \bar{\mathbf{e}}_y]^{ij} [\mathbf{T}_{+,\,\times}]_{ij} \, , \tag{9.28}$$

with $\bar{\mathbf{e}}_{x,\,y}$ the unit vectors along the orthogonal interferometer arms. For the geometric configuration shown in Fig. 9.2, with detector orientation parametrized by the angles θ, ϕ and ψ, we have

$$F_+ = \frac{1}{2} (1 + \cos^2 \theta) \, \cos 2\phi \, \cos 2\psi - \cos\theta \, \sin 2\phi \, \sin 2\psi \, , \tag{9.29}$$

$$F_\times = \frac{1}{2} (1 + \cos^2 \theta) \, \cos 2\phi \, \sin 2\psi + \cos\theta \, \sin 2\phi \, \cos 2\psi \, . \tag{9.30}$$

Inserting Eqs. (9.17), (9.20), (9.21)–(9.23), and (9.25) into Eq. (9.27), we get the final result [15],

$$h_{\rm resp} = C_Q \, \cos 2\Phi_S + S_Q \, \sin 2\Phi_S \, , \tag{9.31}$$

where

$$C_Q = -\frac{4\mu}{D} \, (M \, \omega)^{2/3} \, \left[C_+ \, F_+ + C_\times \, F_\times \right] \, , \tag{9.32}$$

$$S_Q = -\frac{4\mu}{D} \, (M \, \omega)^{2/3} \, \left[S_+ \, F_+ + S_\times \, F_\times \right] \, , \tag{9.33}$$

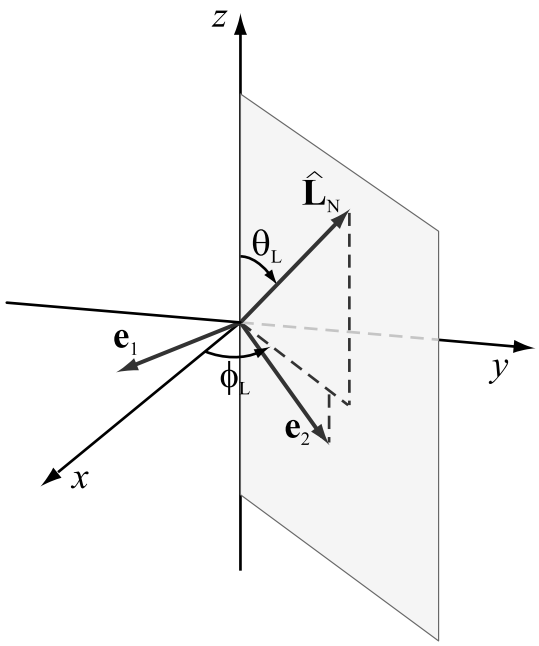

Figure 9.3: Specification of the initial Newtonian orbital angular momentum in the source frame $\{\mathbf{e}_x, \mathbf{e}_y, \mathbf{e}_z\}$.

and

$$
\begin{aligned}
C_+ &= \frac{1}{2}\cos^2\Theta(\sin^2\alpha - \cos^2 i\cos^2\alpha) + \frac{1}{2}(\cos^2 i\sin^2\alpha - \cos^2\alpha) \\
&\quad -\frac{1}{2}\sin^2\Theta\sin^2 i - \frac{1}{4}\sin 2\Theta\sin 2i\cos\alpha\,, \qquad (9.34)\\
S_+ &= \frac{1}{2}(1+\cos^2\Theta)\cos i\sin 2\alpha + \frac{1}{2}\sin 2\Theta\sin i\sin\alpha\,, \qquad (9.35)\\
C_\times &= -\frac{1}{2}\cos\Theta(1+\cos^2 i)\sin 2\alpha - \frac{1}{2}\sin\Theta\sin 2i\sin\alpha\,, \qquad (9.36)\\
S_\times &= -\cos\Theta\cos i\cos 2\alpha - \sin\Theta\sin i\cos\alpha\,. \qquad (9.37)
\end{aligned}
$$

9.2.4 Binary and detector parameters

We shall refer to the total mass M, to the mass ratio $\eta = m_1 m_2/M^2$, and to the magnitudes of the two BH (or NS) spins S_1 and S_2 as the *basic parameters* of the binary. Once these are set, we complete the specification of a binary configuration by giving the initial orbital phase and the components of the orbital and spin angular momenta *in the source frame*, for a given initial frequency. In our convention, the initial orbital angular momentum is determined by the angles $(\theta_{\rm L_N}, \phi_{\rm L_N})$, as shown in Fig. 9.3. The directions of the spins are specified by the angles $(\theta_{S_1}, \phi_{S_1})$ and $(\theta_{S_2}, \phi_{S_2})$,

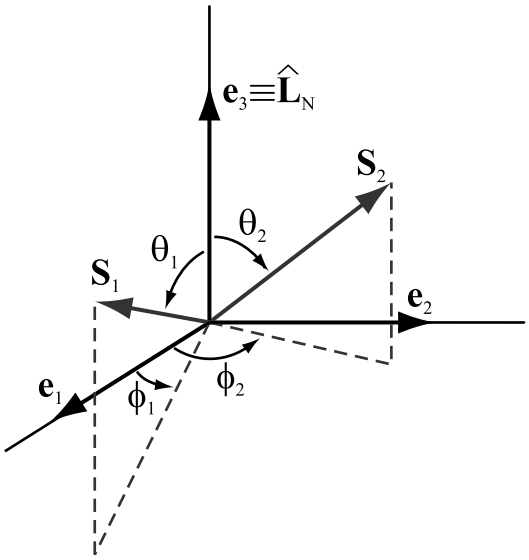

Figure 9.4: Specification of the initial directions of the spins with respect to the FC orthonormal basis $\{\mathbf{e}_1, \mathbf{e}_2, \mathbf{e}_3\}$ [Eq. (9.38)].

Binary			GW propagation	Detector orientation
M, η, S_1, S_2	θ_{S_1}, θ_{S_2}, $\phi_{S_1} - \phi_{S_2}$	$\theta_{\rm L_N}$, $\phi_{\rm L_N}$, $\phi_{S_1} + \phi_{S_2}$	Θ, φ	θ, ϕ, ψ
Basic	Local		Directional	

Table 9.1: Classification of binary, GW-propagation, and detector parameters.

defined with respect to an orthonormal basis aligned with $\hat{\mathbf{L}}_{\rm N}$,

$$\mathbf{e}_1 \equiv \frac{\hat{\mathbf{L}}_{\rm N} \times \mathbf{e}_z^S}{|\hat{\mathbf{L}}_{\rm N} \times \mathbf{e}_z^S|}\,, \quad \mathbf{e}_2 \equiv \hat{\mathbf{L}}_{\rm N} \times \mathbf{e}_1\,, \quad \mathbf{e}_3 \equiv \hat{\mathbf{L}}_{\rm N}\,, \tag{9.38}$$

shown in Fig. 9.4. We then have

$$\hat{\mathbf{S}}_1 = \mathbf{e}_1 \sin\theta_{S_1} \cos\phi_{S_1} + \mathbf{e}_2 \sin\theta_{S_1} \sin\phi_{S_1} + \mathbf{e}_3 \cos\theta_{S_1}\,, \tag{9.39}$$

$$\hat{\mathbf{S}}_2 = \mathbf{e}_1 \sin\theta_{S_2} \cos\phi_{S_2} + \mathbf{e}_2 \sin\theta_{S_2} \sin\phi_{S_2} + \mathbf{e}_3 \cos\theta_{S_2}\,. \tag{9.40}$$

Among the six angles $(\theta_{\rm L_N}, \phi_{\rm L_N})$, $(\theta_{S_1}, \phi_{S_1})$, and $(\theta_{S_2}, \phi_{S_2})$, only three are intrinsically relevant to the evolution of the binary: θ_{S_1}, θ_{S_2} and $\phi_{S_1} - \phi_{S_2}$. We shall refer to them as *local* parameters. The other three independent parameters, which are relevant to the computation of the waveform, describe the rigid rotation of the binary as a whole in space, and we shall refer to them as *directional* parameters. In fact, there are five more directional parameters: Θ and φ specify the direction to the detector in the source frame, and θ, ϕ, and ψ specify the orientation of the detector with respect to the radiation frame. All these parameters have already been introduced in the previous section. Our classification of the 15 binary and detector parameters is summarized in Tab. 9.1.

9.3 Analysis of precessional dynamics

In a seminal paper [9], ACST investigated in detail the evolution of binaries of spinning compact objects, focusing on orbital precession and on its influence on the gravitational waveforms. In this section, we build on their analysis to discuss several aspects of quasi-circular precessional dynamics that are especially important to the formulation of a reliable DTFs for these systems. Note also that Wex [24] has derived analytic solutions for quasielliptical solutions to the 2PN conservative dynamics, including spin-orbit effects.

We complement ACST's analytical arguments with the empirical evidence obtained by studying the orbits generated by the numerical integration of Eqs. (9.1)–(9.3) and (9.9). We select the following typical binaries: BBHs with masses $(m_1 + m_2)$ given by $(20 + 10)M_\odot$, $(15 + 15)M_\odot$, $(20 + 5)M_\odot$, $(10 + 10)M_\odot$, $(7 + 5)M_\odot$; and NS–BH binaries with masses $m_1 = 10M_\odot$ (BH) and $m_2 = 1.4M_\odot$ (NS). The BHs are always chosen to be maximally rotating ($S = m^2$), while the NSs are assumed to be nonspinning. There are neither astrophysical data nor theoretical results which suggest that maximal spins are preferred. However, in this chapter we decide to investigate the most pessimistic (in terms of precessional effects) scenario. The initial GW frequency is chosen at 30 Hz for binaries with total mass larger than $20\,M_\odot$, and 40 Hz for all the other cases. For each set of masses, we consider 1000 (or, when the numerical study is very computationally expensive, only 200) orbital evolutions obtained with random initial orientations of the orbital and spin angular momenta. (These initial configurations are taken from the pseudorandom sequence specified in Sec. 9.6.2 and used in Sec. 9.6.3 to evaluate the effectualness [3] of our DTF in matching the target signals.)

In Sec. 9.3.1 we introduce the ACST results, and in particular the distinction between simple and transitional precession. In Sec. 9.3.2 we study the dependence of the GW ending frequency (defined in Sec. 9.2.2) on the initial values of spins and on their evolution, and we link this dependence to the conservation of certain functions of the spins through evolution. As mentioned above, a knowledge of the ending frequencies of our target model is important to decide what extension each of the detection templates should have in the frequency domain. In Sec. 9.3.3 we examine the value of the binding energy and of the total angular momentum at the end of evolution, and we estimate the amount of GWs that must be emitted during plunge, merger and ringdown to reduce the spin of the final BH to the maximal value. In Sec. 9.3.4 we discuss, largely on the basis on numerical evidence, the effects of spin on the accumulated orbital phase Ψ [defined by Eq. (9.10)]; we argue that these effects are mainly *nonmodulational*, and that, for data-analysis purposes, they can be treated in the same way as the standard PN corrections to the orbits of nonspinning binaries. It follows that the precession of the orbital angular momentum is the primary source of modulations in the signal (as already emphasized by ACST for particular classes of binaries). In Sec. 9.3.5 we show, again on the basis of numerical evidence, that transitional precession has little relevance to the data-analysis

problem under consideration. In Sec. 9.3.6 we discuss the power-law approximations introduced by ACST to describe the precession of the orbital plane as a function of frequency in particular binaries, and we show that they are appropriate in general for the larger class of binaries under consideration in this chapter. These approximations are a basic building block of the effective template families developed by Apostolatos [10] and, indeed, of our generalized and improved families.

9.3.1 The ACST analysis

In their paper [9] on precessing binaries of compact objects as GW sources, ACST chose to work at the leading order in both the orbital phasing and the precessional effects to highlight the main features of dynamical evolution. For orbital evolution, they retained only the first term on the right-hand side of Eq. (9.1): as a consequence, the precession of the orbital plane is the only source of GW modulation considered in the analysis. [The resulting accumulated orbital phase Ψ, given by Eq. (9.10), is known as *Newtonian Chirp*.] For the precession of the orbital angular momentum and of the spins, ACST retained only the first terms (the *spin-orbit* terms) in Eqs. (9.2), (9.3) and (9.9). On the basis of these approximations, and in the context of binaries with either $m_1 \approx m_2$ (and spin-spin terms neglected) or $S_2 \approx 0$, ACST classified the possible evolutions of spinning binaries into two categories: *simple precession* and *transitional precession*.

The vast majority of evolutions is characterized by simple precession, where the direction of the total angular momentum remains roughly constant, and where both the orbital angular momentum and the total spin $\mathbf{S} = \mathbf{S}_1 + \mathbf{S}_2$ precess around that direction. ACST provided a simple analytic solution for the evolutions in this class. They also showed that the orbital precession angle, expressed as a function of the orbital frequency, follows approximately a power law (see Eq. (45) of Ref. [9]).

Transitional precession happens when, at some point during the evolution, the orbital angular momentum and the total spin become antialigned and have roughly the same magnitude, so the total angular momentum is almost zero,

$$\mathbf{J} = \mathbf{L} + \mathbf{S} \approx 0\,. \tag{9.41}$$

When this condition is satisfied, the total angular momentum is liable to sudden and repeated changes of direction. The evolutions in this class cannot be easily treated analytically, but they occur only for a small portion of the possible initial conditions.

In this chapter, we shall refer to the special cases investigated by ACST (with either $m_1 \approx m_2$, or $S_2 \approx 0$) as *ACST configurations*. NS–BH binaries and BBHs with $m_1 \gg m_2$ are astrophysically relevant cases among ACST configurations, because for both we can set $S_2 \approx 0$. The ACST formalism can also describe well BBHs with equal masses, but where spin-spin effects are negligible.

9.3.2 Conservation laws and GW ending frequencies

For the ACST configurations, both the total spin and its projection on the orbital angular momentum are constants of the motion:

$$\left[\hat{\mathbf{L}}_{\rm N}(t)\cdot\mathbf{S}(t)\right]_{\rm ACST} = {\rm const}\,; \tag{9.42}$$

$$\left[\mathbf{S}^2(t)\right]_{\rm ACST} = {\rm const}\,. \tag{9.43}$$

For generic non–ACST configurations (as discussed, for instance, by Damour [13]), the *effective spin* $\mathbf{S}_{\rm eff}$ [Eq. (9.7)] can, to some extent, replace the total spin in these conservation laws.

From Eqs. (9.2), (9.3), and (9.9), we see also that if we ignore the spin-spin effects in the precession equations, then the projection

$$\kappa_{\rm eff} \equiv \frac{\hat{\mathbf{L}}_{\rm N}\cdot\mathbf{S}_{\rm eff}}{M^2} \tag{9.44}$$

of the effective spin onto the Newtonian orbital angular momentum is a constant of motion,

$$\left[\kappa_{\rm eff}(t)\right]_{\rm SO} = {\rm const} \tag{9.45}$$

(where the subscript "SO" stands for the inclusion of spin-orbit effects only); on the other hand, neither $\mathbf{S}^2(t)$ nor $\mathbf{S}^2_{\rm eff}(t)$ are conserved.

The conservation of $\kappa_{\rm eff}$ has important consequences for the endpoints of evolution, defined in Sec. 9.2.2 by Eq. (9.13) for the MECO. In the nonspinning case, as discussed in Chapter 8, if the dynamics was known at all PN orders, then the MECO would agree with the Innermost Stable Spherical Orbit (ISCO), defined as the orbit beyond which circular orbits become dynamically unstable. When only spin-orbit (henceforth, SO) effects are included, the conservation of $\kappa_{\rm eff}$ preserves this correspondence between MECO and ISCO, because the leading-order SO term in the energy is proportional to $\kappa_{\rm eff}$: in fact, the frequency of the MECO has a precise functional dependence on $\kappa_{\rm eff}$ [see Eqs. (9.11)–(9.13)].

When spin-spin (henceforth, SS) couplings are also included, $\kappa_{\rm eff}$ is no longer conserved, and the MECOs (and therefore the ending frequencies) of binaries with the same initial $\kappa_{\rm eff}$ become smeared around their SO-only values, which are functions only of $\kappa_{\rm eff}$. In addition to this smearing, the SS contribution to the energy introduces also a bias. In the end, however, the SS correction is not very important for the ending frequencies, as we can see in the following examples. In the left panel of Fig. 9.5, we plot the ending frequency at 2PN and 3.5PN orders [2] versus the initial value of $\kappa_{\rm eff}$ for BBHs with $M = (15+15)M_\odot$ (in gray dots), as compared to the SO-only predictions (in solid lines).

[2] When referring to results at 3PN and 3.5PN orders we shall always set the arbitrary parameter $\widehat{\theta} = 0$ in Eq. (9.1). In the nonspinning case, the dependence of the GW signal on $\widehat{\theta}$ is rather mild, at least if $\widehat{\theta}$ is limited to values of order one [19], as investigated in Chapter 8.

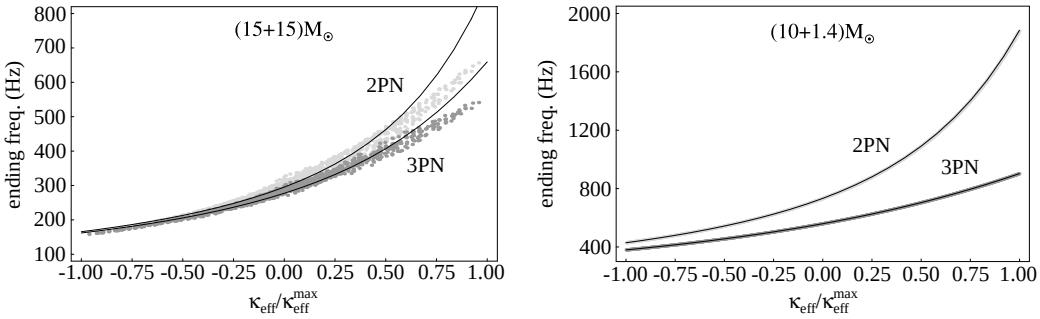

Figure 9.5: Binary ending frequencies (gray dots) as functions of the initial value of $\kappa_{\rm eff}/\kappa_{\rm eff}^{\rm max}$, for 1000 initial spin configurations of $M = (15{+}15)M_\odot$ BBHs (in the left panel), and $M = (10{+}1.4)M_\odot$ NS–BH binaries (in the right panel), at 2PN and 3.5PN orders. The solid lines plot the SO-only predictions for the ending frequencies.

The smearing of the ending frequencies is relatively mild, and so is the systematic deviation from the SO-only predictions. We have checked that this behavior characterizes all the mass configurations enumerated just before Sec. 9.3.2, at both 2PN and 3.5PN orders. In the right panel of Fig. 9.5, we plot the ending frequencies for NS–BH binaries [with $M = (10 + 1.4)M_\odot$]. The ending frequencies follow exactly the expected functional dependence on $\kappa_{\rm eff}$.

The mildness of these deviations can be understood (in part) by looking at the variation of $\kappa_{\rm eff}$ during the evolution. For example, for the $(15 + 15)M_\odot$ BBHs shown in Fig. 9.5, the maximum deviation of $\kappa_{\rm eff}$ from being a constant (measured as $\mathrm{maxdev}(\kappa_{\rm eff}) = [\max(\kappa_{\rm eff}) - \min(\kappa_{\rm eff})]/2$) is 0.036, to be compared with the maximum kinematically allowed deviation, 0.875; for $(20 + 5)M_\odot$ BBHs at 2PN order, $\mathrm{maxdev}(\kappa_{\rm eff}) = 0.033$, to be compared with the maximum kinematically allowed deviation 0.92.

As we can infer from Fig. 9.5, the ending frequencies depend also on the PN order, and the difference between 2PN and 3.5PN orders is more striking for NS–BH binaries than for BBHs. This trend is present also in the nonspinning case (see Chapter 8): for nonspinning ($\chi_1 = \chi_2 = 0$) equal-mass BBHs, we have $\omega^{\rm 2PN}_{\rm MECO} = 0.137M^{-1}$ and $\omega^{\rm 3PN}_{\rm MECO} = 0.129M^{-1}$. To give a few numbers, for a $(10 + 10)M_\odot$ BBH, we have $f^{\rm MECO}_{\rm GW,2PN} = 443\,{\rm Hz}$, and $f^{\rm MECO}_{\rm GW,3PN} = 416\,{\rm Hz}$; for a $(15 + 15)M_\odot$ BBH, $f^{\rm MECO}_{\rm GW,2PN} = 295\,{\rm Hz}$, and $f^{\rm MECO}_{\rm GW,3PN} = 277\,{\rm Hz}$; on the other hand, for a $(10 + 1.4)\,M_\odot$ NS–BH binary, we have $f^{\rm MECO}_{\rm GW,2PN} = 734\,{\rm Hz}$, and $f^{\rm MECO}_{\rm GW,3PN} = 559\,{\rm Hz}$. For the second and third binaries, these values can be read off from the solid lines of Fig. 9.5, by setting $\kappa_{\rm eff} = 0$ (no spins).

Finally, in Fig. 9.6 we show the ending frequencies for $(20{+}5)\,M_\odot$ BBHs, when Eq. (9.1) (which rules the evolution of the orbital phase) is evaluated at 2.5PN order. In this case, if $\kappa_{\rm eff} \geq 0.5$, then $\dot\omega$ goes to zero before the MECO can be reached. The resulting ending frequencies deviate considerably from SO-only predictions. As already discussed in Chapter 8, $\dot\omega$ goes to zero because at 2.5PN order the gravitational flux goes to zero for high orbital velocities; since this very nonphysical

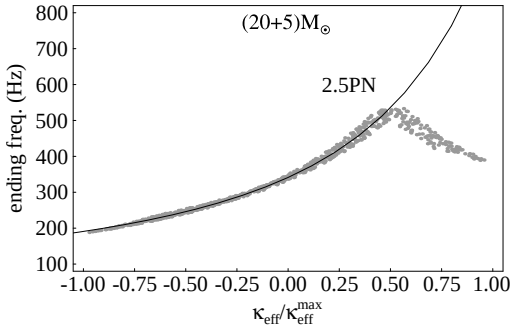

Figure 9.6: Binary ending frequencies (gray dots) as functions of the initial value of $\kappa_{\rm eff}/\kappa_{\rm eff}^{\rm max}$, for 1000 initial spin configurations of $M = (20+5)M_\odot$ BBHs, at 2.5PN order. The solid lines plot the SO-only predictions for the ending frequencies.

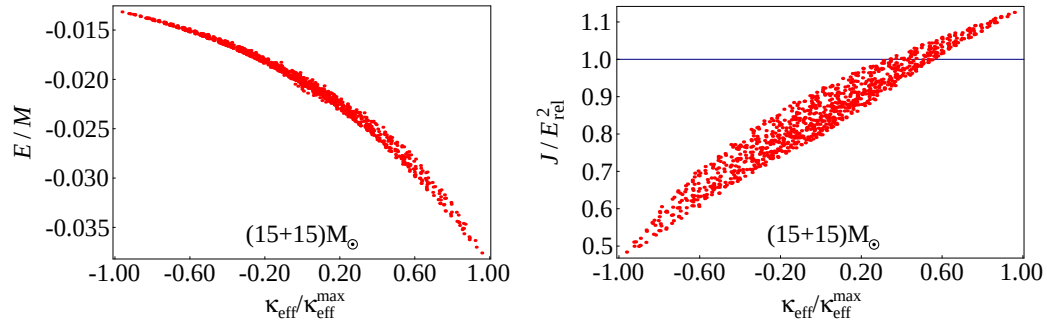

Figure 9.7: For 1000 $(15+15)M_\odot$ BBHs with different initial spin configurations, in the left panel we plot the ratio between the (nonrelativistic) 2PN energy [Eq. (9.11)] at the ending frequency and the mass-energy initially available M, versus the initial $\kappa_{\rm eff}/\kappa_{\rm eff}^{\rm max}$; in the right panel we plot the ratio between the total angular momentum J at 2PN order and the square of the (relativistic) 2PN energy [Eq. (9.11)] at the ending frequency, versus the initial $\kappa_{\rm eff}/\kappa_{\rm eff}^{\rm max}$.

behavior happens systematically, we then choose to exclude the 2.5PN order from our analysis.

9.3.3 Energy radiated during inspiral and (estimated) total angular-momentum emitted after inspiral

It is interesting to evaluate how much energy can be radiated in GWs before the final plunge, especially for binaries whose inspiral end in the LIGO–VIRGO frequency band. In the left panel of Fig. 9.7, for $M = (15+15)M_\odot$ BBHs, we plot the ratio between the 2PN (nonrelativistic) energy, given by Eq. (9.11) and evaluated at the endpoint of evolution (as defined in Sec. 9.2.2), and the total mass–energy initially available, M. Depending on the initial relative orientation between the spins and the orbital angular momentum (as expressed by the initial $\kappa_{\rm eff}/\kappa_{\rm eff}^{\rm max}$), the energy that can be released in GWs during the inspiral ranges between ~ 1.5 and 3.5% of M. More energy can

be emitted when the initial spins are aligned with the orbital angular momentum. We find similar results for all the other BBHs investigated, and similar results were also obtained by Damour in the EOB framework (see Fig. 1 of Ref. [13]).

It is also interesting to estimate how much total angular momentum can be radiated during the coalescence phases that follow the inspiral (plunge and merger), especially when those phases fall in the LIGO–VIRGO band. In general, we have

$$\mathbf{J}_{\rm rad} = \mathbf{J} - \mathbf{S}_{\rm BH}\,, \tag{9.46}$$

where $\mathbf{J}_{\rm rad}$ is the angular momentum radiated during plunge–merger, $\mathbf{J}$ is the total angular momentum of the binary at the end of the inspiral, and $\mathbf{S}_{\rm BH}$ is the spin of the final black hole. A lower limit on the angular momentum radiated in these phases can be obtained using the fact that the magnitude of the final spin can be at most $M_{\rm BH}^2$ (where $M_{\rm BH}$ is the mass of the final black hole). To derive this lower limit we follow Flanagan and Hughes [25], and we write, using Eq. (9.46),

$$|\mathbf{J}_{\rm rad}| \geq |\mathbf{J}| - |\mathbf{S}_{\rm BH}| \geq |\mathbf{J}| - M_{\rm BH}^2 \geq |\mathbf{J}| - E_{\rm rel}^2\,, \tag{9.47}$$

where $E_{\rm rel} = M + E$ is the relativistic energy of the binary at the end of inspiral; in deriving Eq. (9.47) we used the relation $|\mathbf{S}_{\rm BH}| \leq M_{\rm BH}^2 \leq E_{\rm rel}^2$. It is straightforward to see from Eq. (9.47) that this lower limit is nontrivial (that is, greater than zero) only when $|\mathbf{J}| > E_{\rm rel}^2$.

In the right panel of Fig. 9.7, for $M = (15+15)M_\odot$ BBHs, we plot $|\mathbf{J}|/E_{\rm rel}^2$, where the angular momentum is evaluated at 2PN order [20, 15],

$$\begin{aligned}
\mathbf{J}/M^2 &= \eta\,(M\omega)^{-1/3}\,\hat{\mathbf{L}}_N \left\{1 + \frac{(9+\eta)}{6}\,(M\omega)^{2/3} - \frac{7}{3}\,\hat{\mathbf{L}}_N\cdot\mathbf{S}_{\rm eff}\,(M\omega)\right. \\
&\qquad \left. + \left[\frac{1}{24}(81 - 57\eta + \eta^2) - \frac{1}{\eta}\,(\mathbf{S}_1\cdot\mathbf{S}_2 - 3(\hat{\mathbf{L}}_N\cdot\mathbf{S}_1)(\hat{\mathbf{L}}_N\cdot\mathbf{S}_2))\right]\,(M\omega)^{4/3}\right\} \\
&- \eta\,(M\omega)^{2/3}\,\mathbf{S}_{\rm eff} + \mathbf{S}\,.
\end{aligned} \tag{9.48}$$

We see that $J/E_{\rm rel}^2$ is generally less than one, except when $\kappa_{\rm eff} \geq 0.4$ (which happens for 13% of all the initial spin configurations); the maximum value of $|\mathbf{J}|/E_{\rm rel}^2$ is 1.13. (For a similar plot obtained in the EOB framework see Fig. 2 of Ref. [13].) Such large values of $\kappa_{\rm eff}$ imply large ending frequencies [for the $(15+15)M_\odot$ BBHs shown, larger than 400 Hz], which do not lie in the LIGO–VIRGO band of good interferometer sensitivity, unless the BBHs have higher masses; then all the frequencies are scaled down. In any case, for $\kappa_{\rm eff} = 1$ (spins and orbital momenta initially aligned), in the high-mass binaries investigated, Eq. (9.47) suggests the lower limit

$$|\mathbf{J}_{\rm rad}| \geq 0.13\,E_{\rm rel}^2 \sim 0.1\,M^2, \tag{9.49}$$

	Maximum modulational correction $\Delta\Psi^{\rm res}$					
	$(20+10)M_\odot$	$(15+15)M_\odot$	$(20+5)M_\odot$	$(10+10)M_\odot$	$(7+5)M_\odot$	$(10+1.4)M_\odot$ [NS–BH]
$\langle\Delta\Psi^{\rm res}\rangle_{200}$	0.0247	0.0214	0.0450	0.0402	0.0828	0.1228
$\Delta\Psi^{\rm res}_{90\%\,(200)}$	0.0460	0.0411	0.0676	0.0787	0.1504	0.1884
$\max_{200}\Delta\Psi^{\rm res}$	0.0680	0.0523	0.1227	0.1186	0.2196	0.1895

Table 9.2: Maximum modulational effects in the accumulated orbital phase Ψ. We give the average over the 200 samples, the 90% quantile of the distribution, and the maximum value for the diagnostic $\Delta\Psi^{\rm res}$, defined in Eq. (9.53).

to be compared with the value $0.4M^2$ obtained by Flanagan and Hughes [25] using BH spins aligned with the orbital angular momentum (estimated to be $\sim 0.9M^2$).

A (trivial) upper limit for $\mathbf{J}_{\rm rad}$ is obtained by setting $\mathbf{S}_{\rm BH}=0$:

$$|\mathbf{J}^{\rm rad}| \leq |\mathbf{J}|\,. \tag{9.50}$$

For different values of $\kappa_{\rm eff}$, the upper limit for our $(15+15)M_\odot$ binary is ~ 0.5 – $1.1M^2$. However, in order for the inspiral to end within the LIGO–VIRGO band of good interferometer sensitivity (which requires a MECO frequency lower than 400 Hz), we need $\kappa_{\rm eff}<0.4$, which corresponds to an upper limits ~ 0.5 – $0.7\,M^2$.

To put this section into context, we point out that most reliable PN estimates for the energy and the angular momentum radiated after the MECO can be achieved only with models that include information about the plunge phase, such as the model that can be built on Damour's spinning-EOB equations [13].

9.3.4 Spin-orbit and spin-spin effects on the accumulated orbital phase

While for nonspinning binaries the accumulated orbital phase [defined by Eq. (9.10)] coincides with (half) the GW phase at the detector, for spinning binaries the two phases differ by precessional effects; in the FC convention, these are found *in part* in the relation

$$\dot\Phi_S = \dot\Psi - \dot\alpha\cos i, \tag{9.51}$$

where Φ_S is the orbital phase with respect to the ascending node of the orbit, which appears in Eq. (9.31) for the detector response to GW; and in part in the explicit time dependence of the coefficients C_Q and S_Q on α and i [see Eqs. (9.32)–(9.37)]. In this section, we are going to argue that the evolution of the accumulated orbital phase is very similar in spinning and nonspinning binaries; and that, as a consequence, the effect of spins on detector response *through the accumulated orbital phase* can be reproduced using nonspinning-binary templates, such as those studied in Chapter 8

[see also Eqs. (9.92)–(9.94)]. Of course, precessional effects *do* enter the detector response through the other dependences mentioned above, and these cannot be neglected when building templates to detect physical signals.

Both the spin-orbit and spin-spin couplings can affect the accumulated orbital phase Ψ through the 1.5PN and 2PN terms in Eq. (9.1). However, as we shall discuss in this section, this effect is largely *nonmodulational*. For each binary configuration, we introduce three different functions of time: (a) the accumulated orbital phase $\Psi^{\rm full}$, obtained by solving the *full* set of Eqs. (9.1)–(9.3) and (9.9), including the SO and SS couplings; (b) the accumulated orbital phase $\Psi^{\rm fix}$, obtained by using the initial orbital angular momentum and spins *at all times* in the SO and SS couplings; and (c) the accumulated orbital phase $\Psi^{\rm nospin}$ for a nonspinning binary, obtained by dropping the SO and SS couplings altogether.

In general, $\Psi^{\rm fix}$ and $\Psi^{\rm nospin}$ are quite different for the same set of binary masses. However, the difference $\Psi^{\rm fix} - \Psi^{\rm nospin}$ is not a strongly oscillating function (that is, it does not show any modulation), and it can be reduced considerably by modifying the 1.5PN and 2PN coefficients in the phasing equation for the nonspinning binary. It is then reasonable to assume that such a nonmodulational effect could be captured by the nonspinning DTFs constructed in Chapter 8. Moreover, the difference between $\Psi^{\rm full}$ and $\Psi^{\rm fix}$ is due to the nonconservation of the SO and SS terms that appear in Eq. (9.1) for $\dot{\omega}$. These terms have relatively high PN orders, so we expect that they will be small.

Thus, we expect that $\Psi^{\rm full}$ can be well described by a nonmodulational phasing of the kind

$$\Psi^{\rm nonmod}(f) = \mathcal{C}_0 + \mathcal{C}_1\, f + \frac{\mathcal{C}_2}{f^{5/3}} + \frac{\mathcal{C}_3}{f^{2/3}}\,, \tag{9.52}$$

which looks rather like the frequency-domain phasings employed in the DTFs of Chapter 8. [Here $\mathcal{C}_2$ and $\mathcal{C}_3$ can be seen as actual (intrinsic) template parameters, whereas $\mathcal{C}_0$ and $\mathcal{C}_1$ represent, respectively, the initial phase and the time of arrival of the GW signal, both of which are extrinsic parameters in the sense discussed in Chapter 8.] To verify this hypothesis, we first evaluate $\Psi^{\rm full}$ in the frequency range 50 Hz–250 Hz (which is appropriate for first-generation ground-based GW detectors), using Eqs. (9.1)–(9.3) and (9.9) at 2PN order, for all the BBH and NS–BH configurations considered earlier [(5 + 1) masses × 200 angles]. We then (least-square) fit $\Psi^{\rm full}$ with functions of the form (9.52). A measure of the goodness of the fit, given by

$$\Delta\Psi^{\rm res} = \max_{50\,{\rm Hz}<f<250\,{\rm Hz}} \left|\Psi^{\rm full}(f) - \Psi^{\rm nonmod}(f)\right|\,, \tag{9.53}$$

is shown in Tab. 9.2. The maximum deviations are all smaller than ~ 0.1 rad, except for the lighter $(7+5)M_\odot$ BBH and $(10+1.4)M_\odot$ NS–BH systems (where however the *average* deviations are still ~ 0.1 rad). This suggests that templates with phasing expressions similar to (9.52) (such as those

	Percentage of binary configurations where $\exists t : \hat{\mathbf{J}}(t) \cdot \hat{\mathbf{J}}(0) < 1 - \epsilon_J$					
	$(20+10)M_\odot$	$(15+15)M_\odot$	$(20+5)M_\odot$	$(10+10)M_\odot$	$(7+5)M_\odot$	$(10+1.4)M_\odot$ [NS–BH]
$\epsilon_{\rm J} = 0.05$	17.5%	6.0%	33.5%	7.0%	3.5%	0.0%
$\epsilon_{\rm J} = 0.10$	2.5%	0.0%	11.0%	0.0%	0.0%	0.0%

Table 9.3: Deviation of the total angular momentum $\hat{\mathbf{J}}$ from its initial direction. This table shows the percentage of the binary configurations where $\hat{\mathbf{J}}(t) \cdot \hat{\mathbf{J}}(0)$ goes below $1 - \epsilon_{\rm J}$, for the $\epsilon_{\rm J}$ given in the first column.

proposed in Chapter 8) could already approximate rather well the full target model studied in this chapter.

9.3.5 Simple and transitional precession of total angular momentum

For most of the binary configurations investigated, we find, in analogy with the ACST analysis, that the direction of total angular momentum does not change much during evolution. In other words, transitional precession does not occur. Table 9.3 shows the fraction of configurations that yield

$$\min_t \hat{\mathbf{J}}(t) \cdot \hat{\mathbf{J}}_0 < 1 - \epsilon_{\rm J} \,, \tag{9.54}$$

when $\epsilon_{\rm J} = 0.05$ and 0.10. Let us now try to understand the numbers of Tab. 9.3 in more detail.

We first focus on the columns two to six, which deal with binaries of maximally spinning BHs. For BBHs with single masses $m = 5$–$20\,M_\odot$, the total spin is not usually large enough to satisfy the transitional-precession condition (9.41), as we can prove easily by using all the evolution equations at the leading PN order: during the evolution, the magnitude of the orbital angular momentum decreases with the GW frequency f, as in

$$|\mathbf{L}| \approx |\mathbf{L}_{\rm N}| = \eta\,(\pi M f)^{-1/3} M^2 \,, \tag{9.55}$$

while the total spin is bounded by

$$|\mathbf{S}| < |\mathbf{S}_1| + |\mathbf{S}_2| = m_1^2 + m_2^2 = (1 - 2\eta) M^2 \,. \tag{9.56}$$

In order for transitional precession to occur, we need at the very least $|\mathbf{L}_{\rm N}| = |\mathbf{S}|$ [see Eq. (9.41)], which requires

$$\eta (\pi M f)^{-1/3} < (1 - 2\eta) \,, \tag{9.57}$$

or

$$f > f_{\rm trans}^{\rm min} \equiv \frac{\eta^3}{\pi M (1 - 2\eta)^3} \,. \tag{9.58}$$

For transitional precession to occur before we reach the Schwarzschild ISCO frequency $f_{\rm Schw} =$

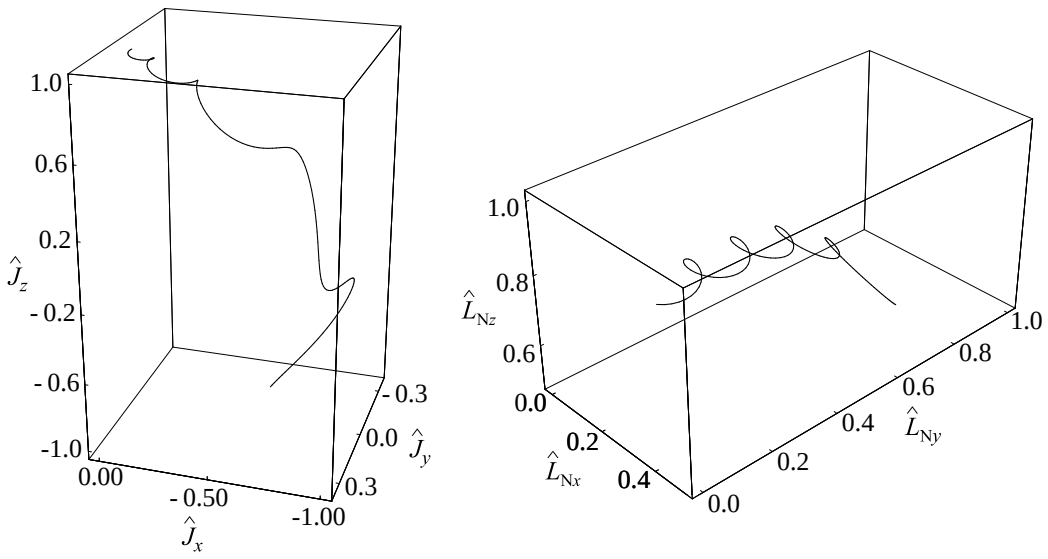

Figure 9.8: Transitional precession. Evolution of the direction of total angular momentum (left panel) and of Newtonian orbital angular momentum (right panel) in the transitionally precessing $(20 + 5)M_\odot$ BBH with initial angles $\theta_{S_1} = 175.4°$, $\theta_{S_2} = 105.4°$, and $\phi_{S_1} - \phi_{S_2} = 92.0°$ (at $f_{\rm GW} = 30\,{\rm Hz}$).

$1/\sqrt{6^3}\pi M$, we then need

$$\frac{f^{\rm min}_{\rm trans}}{f_{\rm Schw}} = \left(\frac{\sqrt{6}\eta}{1-2\eta}\right)^3 \gtrsim 1 \quad \Rightarrow \quad \eta \gtrsim 0.22\,. \tag{9.59}$$

Although the ending frequencies obtained within our target model are usually higher than $f_{\rm Schw}$, the very configurations that can have transitional precession (those with nearly antialigned total spin and orbital angular momenta) have always *lower* ending frequencies, making 0.22 too large an estimate for the critical value of η.

As a consequence, among all the configurations we have considered, only $(20 + 5)M_\odot$ and $(20 + 10)M_\odot$ BBHs can then have *observable* transitional-precession phases. These latter binaries are characterized by significantly larger changes in $\mathbf{J}$ [see Tab. 9.3]. However, $(20 + 10)M_\odot$ BBHs still require $f > f^{\rm min}_{\rm tran} = 138\,{\rm Hz}$, which is very close to the relevant ending frequency; so the change in $\mathbf{J}$ is smaller, and we never observed episodes of transitional precession in the 200 initial configurations analyzed. On the contrary, we observed a few for $(20 + 5)M_\odot$ BBHs; one example follows from the initial configuration given by $\theta_{S_1} = 175.4°$, $\theta_{S_2} = 105.4°$, and $\phi_{S_1} - \phi_{S_2} = 92.0°$ (at $f_{\rm GW} = 30\,{\rm Hz}$). In this configuration the initial spin of the more massive body is almost exactly antialigned with the orbital angular momentum. The trajectories of $\hat{\mathbf{J}}$ and $\hat{\mathbf{L}}_{\rm N}$ during this evolution are shown, respectively, in the left and right panels of Fig. 9.8.

By contrast, none of the NS–BH configurations examined exhibits transitional precessions. This

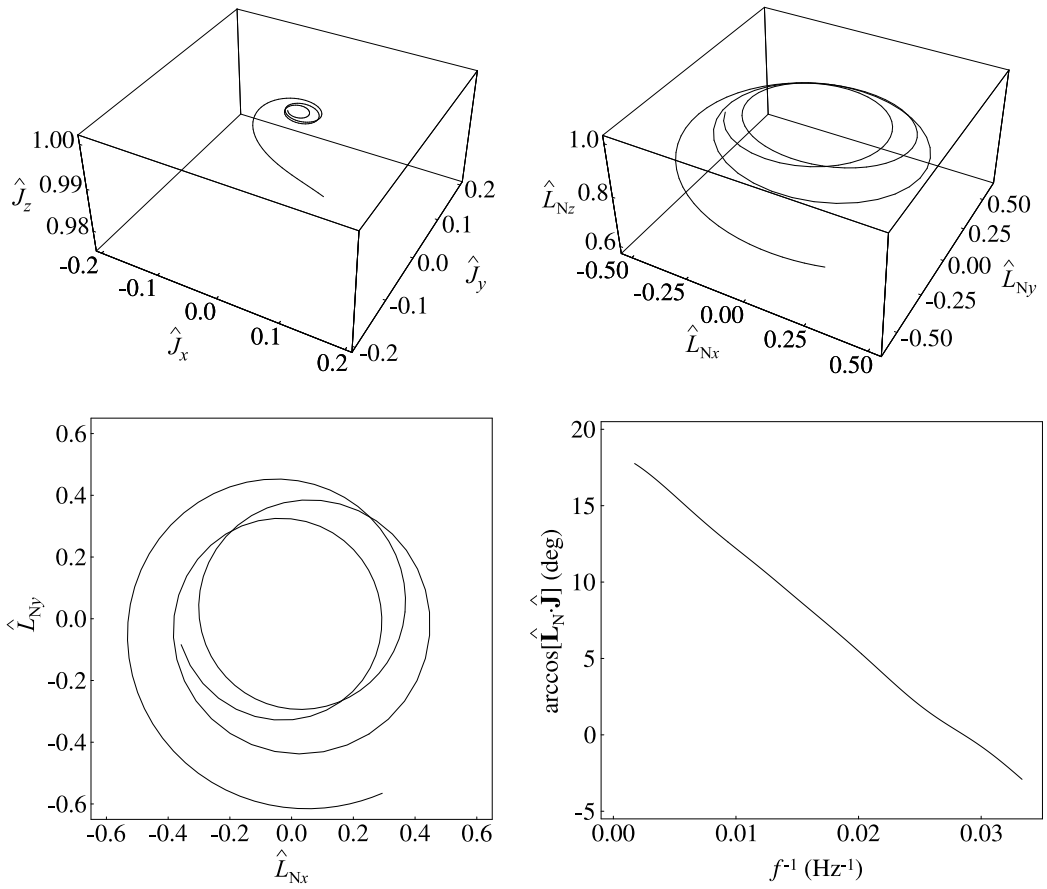

Figure 9.9: Simple precession. The upper graphs show the evolution of the direction of total angular momentum $\hat{\mathbf{J}}$ (left), and of Newtonian orbital angular momentum $\hat{\mathbf{L}}_{\rm N}$ (right), in the case of the simply precessing $(20+5)M_\odot$ BBH with initial angles $\theta_{S_1} = 44.6°$, $\theta_{S_2} = 101.0°$, and $\phi_{S_1} - \phi_{S_2} = -39.7°$ (at 30 Hz). The lower graphs show the projection of $\hat{\mathbf{L}}_{\rm N}$ onto the plane perpendicular to the initial $\hat{\mathbf{J}}$ (left), and the angle between $\hat{\mathbf{L}}_{\rm N}$ and $\hat{\mathbf{J}}$, plotted as a function of inverse GW frequency (right). The BBH was rotated in space so that the initial direction of $\hat{\mathbf{J}}$ would be parallel to the z axis.

is because the BH is taken as maximally spinning, so $\mathbf{S}$ is always much larger than $\mathbf{L}$ in the frequency band under consideration.

9.3.6 Apostolatos' power law for orbital precession

As discussed in the previous section, the vast majority of binary configurations undergoes simple precession, where $\hat{\mathbf{J}}$ remains constant, while $\hat{\mathbf{L}}_{\rm N}$ and $\mathbf{S}_{1,2}$ precess around it. For ACST configurations ($m_1 \approx m_2$ and negligible SS interactions, or $S_2 \approx 0$), both $\hat{\mathbf{L}}_N$ and $\hat{\mathbf{S}}$ precess around $\mathbf{J}$ with the precession frequency [9, Eq. (42)]

$$\Omega_{\rm p} \equiv \frac{d\alpha_{\rm p}}{dt} = \left(2 + \frac{3}{2}\frac{m_2}{m_1}\right) J\omega^2 \,. \tag{9.60}$$

ACST identified two regimes where the evolution of $\alpha_{\rm p}$ can be approximated very well by a power law in ω (or f). For $L_N \gg S$, the total angular-momentum $J \approx L_N \sim \omega^{-1/3}$; using $\dot\omega \sim \omega^{11/3}$, it is straightforward to derive from Eq. (9.60) that $\alpha_{\rm p}$ is approximated well by a linear function of f^{-1},

$$\alpha^{\rm fit}_{{\rm p}(-1)}(f) \approx \frac{\mathcal{B}_1}{f} + \mathcal{B}_2\,, \tag{9.61}$$

where $\mathcal{B}_1$ and $\mathcal{B}_2$ are constant coefficients. Since $L_N/S \sim \eta\,\omega^{-1/3}$, the condition $L_N \gg S$ corresponds to comparable-mass binaries ($\eta \sim 1/4$) or to large separations. For $L_N \ll S$, we have $J \approx S$; in this case we derive from Eq. (9.60) that $\alpha_{\rm p}$ is approximated well by a linear function of $f^{-2/3}$,

$$\alpha^{\rm fit}_{{\rm p}(-2/3)}(f) \approx \frac{\mathcal{B}'_1}{f^{2/3}} + \mathcal{B}'_2\,, \tag{9.62}$$

where $\mathcal{B}'_1$ and $\mathcal{B}'_2$ are constant coefficients. The condition $L_N \ll S$ corresponds to $m_1 \ll m_2$ or to small separations (late inspiral).

It turns out that Eqs. (9.61) and (9.62) apply also to a large fraction of the BBHs and NS–BH binaries studied in this chapter. This can be tested semiquantitatively by the following procedure. For each configuration, we take the precession angle $\alpha_{\rm p}(f)$ and we fit it with a function $\alpha^{\rm fit}_{{\rm p}(-1,-2/3)}(f)$ of the form (9.61) or (9.62), for frequencies in the range 50–250 Hz. We then evaluate the maximum difference

$$\Delta\alpha_{\rm max(-1,-2/3)} \equiv \max_{50\,{\rm Hz}<f<250\,{\rm Hz}} \left|\alpha_{\rm p}(f) - \alpha^{\rm fit}_{{\rm p}(-1,-2/3)}(f)\right|\,. \tag{9.63}$$

In Tab. 9.4, we show the values of $\Delta\alpha^{90\%}_{\rm max(-1)}$ (that is, the 90% percentile of $\Delta\alpha_{\rm max(-1)}$) and $\Delta\alpha^{90\%}_{\rm max(-2/3)}$, for $(15+15)M_\odot$, $(20+10)M_\odot$, $(10+10)M_\odot$, and $(7+5)M_\odot$ BBHs, and for $(10+1.4)M_\odot$ NS–BH binaries. The numbers show that Eqs. (9.61) and (9.62) yield (roughly) comparable approximation. This result is confirmed also by the more detailed analyses discussed later in this chapter.

Figure 9.9 plots the 2PN evolutions of $\hat{\mathbf{J}}$ (upper left panel) and $\hat{\mathbf{L}}_{\rm N}$ (upper right panel) for a $(20+5)M_\odot$ BBH with initial conditions $\theta_{S_1} = 44.6°$, $\theta_{S_2} = 101.0°$, and $\phi_{S_1} - \phi_{S_2} = -39.7°$ (at 30 Hz). The figure plots also the projection of $\hat{\mathbf{L}}_{\rm N}$ onto the plane perpendicular to the initial $\hat{\mathbf{J}}$ (lower left panel), and the precession angle $\alpha_{\rm p}$ between $\hat{\mathbf{L}}_{\rm N}$ and $\hat{\mathbf{J}}$, plotted as a function of inverse GW frequency f^{-1} (lower right panel), and showing a very nearly linear dependence.

Building on the results obtained by ACST, Apostolatos [10] conjectured (quite reasonably) that orbital precession will modulate the gravitational waveforms with functional dependencies given by Eqs. (9.61) and (9.62). On the basis of this conjecture and of the observation that, in matched-filtering techniques, matching the phase of signals is more important than matching their amplitudes, Apostolatos proposed a family of detection templates [10] obtained by modifying the phasing of

	90% percentiles of error in precession angle, $\Delta\alpha_{\max}$					
	$(15+15)M_\odot$	$(20+10)M_\odot$	$(20+5)M_\odot$	$(10+10)M_\odot$	$(7+5)M_\odot$	$(10+1.4)M_\odot$ [NS–BH]
$\Delta\alpha^{90\%}_{\max(-1)}$	0.30	0.24	0.23	0.34	0.64	0.61
$\Delta\alpha^{90\%}_{\max(-2/3)}$	0.52	0.48	0.50	0.68	1.14	0.72

Table 9.4: Approximation of binary precession histories using best-fit parameters $\mathcal{B}_1$ and $\mathcal{B}_2$ in Eqs. (9.61) and (9.62). This table shows the 90% percentiles of $\Delta\alpha_{\max(-1)}$ [Eq. (9.63)] and $\Delta\alpha_{\max(-2/3)}$ in the BBH and NS–BH populations studied throughout this section.

nonspinning PN templates as in

$$\text{Apostolatos' ansatz:} \quad \psi_{\text{spinning}} \to \psi_{\text{non spinning}} + \mathcal{C}\cos(\delta + \mathcal{B}f^{-2/3})\,, \tag{9.64}$$

while keeping a Newtonian amplitude $f^{-7/6}$. Recently, Grandclément, Kalogera and Vecchio [11] applied Apostolatos' suggestion to an approximated analytical model of NS–BH binaries and low-mass BBHs: whereas the addition of phase modulations according to Eq. (9.64) *did* increase the effectualness [3] of nonspinning PN templates, the resulting DTF family was still not good enough to recommend its application when trying to capture the real modulated waveforms. Moreover, this DTF requires three additional *intrinsic* parameters ($\mathcal{C}, \delta$, and $\mathcal{B}$) on top of the two BH (or NS) masses. The resulting GW searches would then be plagued by an extremely high computational cost.

In the rest of this chapter, we shall propose a better template family, inspired by old and new insight on the precessional effects that appear in the gravitational waveforms. As we shall see, Apostolatos' ansatz can be improved to build DTFs that have both high effectualness [3] and low computational requirements.

9.4 Definition of modulated DTFs for precessing binaries

We are now going to bring together all the observations reported in Sec. 9.3 to build DTFs that perform well in capturing the detector response to the GWs emitted by precessing binaries of NSs and spinning BHs (at least as long as the actual physical signals are modeled faithfully enough by the adiabatic target model described in Sec. 9.2).

In Sec. 9.4.1 we develop a new (as far as we know) convention for the generation and propagation of GW from spinning binaries; this convention has the desirable property of factorizing the waveform into a *carrier signal* whose phase is essentially the accumulated orbital phase of the binary, and a *modulated amplitude* term which is sensitive to the precession of the orbital plane. In Sec. 9.4.2 we then use the results of Sec. 9.3.4 to build an approximation of the carrier signal, and the results of Secs. 9.3.2, 9.3.5, and 9.3.6 to build an approximation to the modulated amplitude; using these terms together, we define three families of detection templates. In Sec. 9.4.3 we describe two standard families of nonspinning-binary templates; in Sec. 9.6 we shall compare their performance with the performance of our DTFs, to evaluate the performance improvements brought about by our treatment of precession.

9.4.1 A new convention for GW generation in spinning binaries

At least two conventions are used to express the gravitational waveforms generated by binaries of spinning compact objects, as computed in the quadrupolar approximation : [3] the ACST convention [9], which uses a rotating reference frame, and the FC convention [14], which uses a nonrotating reference frame. We discussed the FC convention in Sec. 9.2.3, and we used it throughout this chapter to generate gravitational waveforms from the numerical integration of the equations of motion of the target model. Before going to the specific conventions, we shall first sketch a generic procedure to write the gravitational waveform.

In general, the unit vector along the separation vector of the binary, $\hat{\mathbf{n}}(t)$, and the unit vector along the corresponding relative velocity, $\hat{\lambda}(t)$, can be written as

$$\hat{\mathbf{n}}(t) = \mathbf{e}_1(t)\,\cos\Phi(t) + \mathbf{e}_2(t)\,\sin\Phi(t)\,, \quad \hat{\lambda}(t) = -\mathbf{e}_1(t)\,\sin\Phi(t) + \mathbf{e}_2(t)\,\cos\Phi(t)\,, \tag{9.65}$$

where $\mathbf{e}_1(t)$, $\mathbf{e}_2(t)$, and $\mathbf{e}_3(t) \equiv \hat{\mathbf{L}}_N(t)$ are orthonormal vectors, and $\mathbf{e}_{1,2}(t)$ forms a basis for the instantaneous orbital plane [see Fig. 9.4]; the quantity $\Phi(t)$ is then the orbital phase with respect to $\mathbf{e}_{1,2}(t)$. The definition of $\mathbf{e}_{1,2}(t)$ and of $\Phi(t)$ is not unique: an arbitrary function of time can be added to $\Phi(t)$, and then compensated by a time-dependent rotation of $\mathbf{e}_{1,2}(t)$ around $\hat{\mathbf{L}}_N(t)$, leaving $\hat{\mathbf{n}}(t)$ and $\hat{\lambda}(t)$ unchanged. In nonspinning binaries the orbital plane (and therefore $\hat{\mathbf{L}}_N$) does not

[3] Here "quadrupole" refers to the multipolar expansion used to compute GWs, and not to the expansion used to introduce RR effects in the inspiral

precess, so the natural choice is to keep $\mathbf{e}_{1,2}$ constant. In spinning binaries $\hat{\mathbf{L}}_N(t)$ precesses, and different, but nonetheless meaningful, conventions can be given for $\mathbf{e}_{1,2}(t)$ and $\Phi(t)$. Note that $\Phi(t)$ is *not*, in general, the same as the accumulated orbital phase $\Psi(t) = \int \omega(t)\, dt$. Given a convention for $\mathbf{e}_{1,2}(t)$ and $\Phi(t)$, the tensor Q_c^{ij} that appears in Eq. (9.14) can be written as

$$Q_c^{ij} = -2\left([\mathbf{e}_+]^{ij}\cos 2\Phi - [\mathbf{e}_\times]^{ij}\sin 2\Phi\right) \tag{9.66}$$

where

$$\mathbf{e}_+ = \mathbf{e}_1\otimes\mathbf{e}_1 - \mathbf{e}_2\otimes\mathbf{e}_2\,, \quad \mathbf{e}_\times = \mathbf{e}_1\otimes\mathbf{e}_2 + \mathbf{e}_2\otimes\mathbf{e}_1\,. \tag{9.67}$$

With the detector lying along the direction $\hat{\mathbf{N}}$, one goes on to define a radiation frame, formed by orthonormal vectors $\mathbf{e}_x^R$, $\mathbf{e}_y^R$ and $\mathbf{e}_z^R = \hat{\mathbf{N}}$. The GW response is then given by

$$h_{\rm resp} = -\frac{2\mu}{D}\frac{M}{r}\underbrace{\left([\mathbf{e}_+]^{ij}\,\cos 2\Phi + [\mathbf{e}_\times]^{ij}\,\sin 2\Phi\right)}_{\text{factor Q: quadrupole moment}}\underbrace{\left([\mathbf{T}_+]_{ij}\,F_+ + [\mathbf{T}_\times]_{ij}\,F_\times\right)}_{\text{factor P: detector projection}}, \tag{9.68}$$

where the tensors $[\mathbf{T}_{+,\times}]_{ij}$ are given by (9.25), namely,

$$\mathbf{T}_+ \equiv \mathbf{e}_x^R\otimes\mathbf{e}_x^R - \mathbf{e}_y^R\otimes\mathbf{e}_y^R\,, \quad \mathbf{T}_\times \equiv \mathbf{e}_x^R\otimes\mathbf{e}_y^R + \mathbf{e}_y^R\otimes\mathbf{e}_x^R\,, \tag{9.69}$$

and where F_+ and $F_\times$ are given by Eq. (9.28), namely,

$$F_{+,\times} = \frac{1}{2}[\bar{\mathbf{e}}_x\otimes\bar{\mathbf{e}}_x - \bar{\mathbf{e}}_y\otimes\bar{\mathbf{e}}_y]^{ij}[\mathbf{T}_{+,\times}]_{ij}\,, \tag{9.70}$$

with $\bar{\mathbf{e}}_{x,y}$ the unit vectors along the orthogonal arms of the interferometer. Again, $\mathbf{e}_x^R$ and $\mathbf{e}_y^R$ are not uniquely defined, because they can be rotated at will around $\hat{\mathbf{N}}$, of course changing the values of F_+ and $F_\times$.

ACST refer $\Phi(t)$ to the direction $\hat{\mathbf{N}}$ of GW propagation, by imposing that $\mathbf{e}_1^{\rm ACST}(t) \propto \hat{\mathbf{N}}\times\hat{\mathbf{L}}_N(t)$; they also set $\mathbf{e}_x^R(t) \propto \pm\hat{\mathbf{N}}\times\hat{\mathbf{L}}_{\rm N}(t)$. Although the ACST convention has allowed some insight into the waveforms, it is rather inconvenient for the purpose of data analysis, because almost all the quantities that come into Eq. (9.68) [$\mathbf{e}_{1,2}$, $\mathbf{T}_{+,\times}$, and $F_{+,\times}$] depend both on the time evolution of the binary and on the direction to the detector. Using the terminology introduced in Sec. 9.2.3 and Tab. 9.1, under the ACST convention the local and directional parameters are entangled in a time-dependent manner.

FC introduce the fixed source axes $\{\mathbf{e}_x^S, \mathbf{e}_y^S, \mathbf{e}_z^S\}$ [see Sec. 9.2.3], and they impose that $\mathbf{e}_1^S(t) \propto \mathbf{e}_z^S\times\hat{\mathbf{L}}_N(t)$ [see Eq. (9.17)]. The radiation frame does not change with time [see Eqs. (9.21)–(9.23)]. As a consequence, the factors Q and P in Eq. (9.68) become disentangled: factor Q expresses the components of the quadrupole moment, which depend only on the evolution of the binary

inside the source frame; factor P expresses the projection of the quadrupole moment onto the radiation frame and onto the antisymmetric mode of the detector, which depend only on the relative orientation between the source frame and the detector. However, for our purposes there are still two shortcomings in the FC convention:

1. The FC convention defines $\mathbf{e}_{1,2}(t)$ and $\Phi(t)$ in terms of the fixed source frame $\mathbf{e}^S_{x,y,z}$, which is quite artificial, because only the relative orientation between binary and detector affects the detector response $h_{\rm resp}$.

2. In Sec. 9.3.4 we saw that the accumulated orbital phase $\Psi(t)$ is (almost) nonmodulated, so the modulations of the waveform come mainly from the precession of the orbital plane. Under the FC convention, the modulations appear only in factor Q of Eq. (9.68), but they appear both in the phase $\Phi(t)$ and in the precession of the tensors $\mathbf{e}_{+,\times}(t)$. It would be nice to isolate the precessional effects in either element.

Both issues would be solved if we could find a modification of the FC convention where Φ coincides with the accumulated orbital phase, Ψ. As it turns out, it is possible to do so: we need to redefine the vectors $\mathbf{e}_{1,2}(t)$ so that they precess alongside $\hat{\mathbf{L}}_N$,

$$\dot{\mathbf{e}}_i(t) = \mathbf{\Omega}_e(t) \times \mathbf{e}_i(t)\,, \quad i = 1, 2\,, \tag{9.71}$$

with

$$\mathbf{\Omega}_e(t) \equiv \mathbf{\Omega}_L(t) - [\mathbf{\Omega}_L(t) \cdot \hat{\mathbf{L}}_N(t)]\, \hat{\mathbf{L}}_N(t)\,, \tag{9.72}$$

where $\mathbf{\Omega}_L$ is obtained by collecting the terms that (cross-product) multiply $\hat{\mathbf{L}}_N$ in Eq. (9.9). In App. 9.9 we prove that this convention yields $\dot{\Phi} = \omega = \dot{\Psi}$, as desired. Qualitatively, one can reason as follows. The angular velocity of the binary lies along $\hat{\mathbf{L}}_N(t)$, and has magnitude $\dot{\Psi} = \omega$. The reason why Φ and Ψ differ is that the orbital basis $\mathbf{e}_{1,2}$, used to define Φ, must rotate to keep up with the precession of the orbital plane. However, the difference vanishes if we constrain the angular velocity of $\mathbf{e}_{1,2}$ to be orthogonal to $\hat{\mathbf{L}}_N$; Eq. (9.72) provides just the right constraint. In the following, we shall refer to our new convention as the *precessing* convention.

In Tab. 9.5 we summarize the parameter dependence of the terms that make up the detector response function [Eq. (9.68)], under the three conventions. It is important to remark that in the precessing convention the polarization tensors $\mathbf{e}_{+,\times}(t)$, as geometric objects, do *not* depend on the source frame, but only on the basic and local parameters. In practice, however, we need to introduce an arbitrary choice of the source frame to relate the orientation of the binary to the direction and orientation of the detector (that is, to write explicitly the products $[\mathbf{e}_{+,\times}]_{ij}[\mathbf{T}_{+,\times}]_{ij}$). We can avoid this arbitrariness by setting the source frame according to the initial configuration of the binary at

convention	factor P		factor Q	
	$\mathbf{T}_{+,\times}$	$F_{+,\times}$	$\Phi(t)$	$\mathbf{e}_{+,\times}(t)$
ACST	function of basic, local, and directional parameters; time dependent		function of basic, local, and directional parameters	function of basic, local, and directional parameters
FC	function of directional parameters; time independent		function of basic, local, and directional parameters	function of basic, local, and directional parameters
precessing	function of directional parameters; time independent		function of basic and local parameters only; coincides with $\Psi(t)$	function of basic and local parameters only

Table 9.5: Parametric dependence of the building elements of the detector response function $h_{\rm resp}$ [Eq. (9.68)] under the ACST, FC, and precessing conventions.

a fiducial orbital frequency; for example, we can impose (without loss of generality)

$$\mathbf{e}_x^S \propto \mathbf{S}_1(0) - [\mathbf{S}_1(0)\cdot\hat{\mathbf{L}}_{\rm N}(0)]\hat{\mathbf{L}}_{\rm N}(0)\,, \quad \mathbf{e}_y^S = \hat{\mathbf{L}}_{\rm N}(0)\times\mathbf{e}_x^S\,, \quad \mathbf{e}_z^S = \hat{\mathbf{L}}_{\rm N}(0)\,, \tag{9.73}$$

and

$$\mathbf{e}_1(0) = \mathbf{e}_x^S\,, \quad \mathbf{e}_2(0) = \mathbf{e}_y^S\,, \quad \mathbf{e}_3(0) = \mathbf{e}_z^S\,. \tag{9.74}$$

[If $\mathbf{S}_1(0)$ and $\hat{\mathbf{L}}_{\rm N}(0)$ are parallel, $\mathbf{e}_x^S$ can be chosen to lie in any direction within the plane orthogonal to $\hat{\mathbf{L}}_{\rm N}(0)$.] Then the initial conditions, as expressed by their components with respect to the source frame, are determined only by the local parameters,

$$\hat{\mathbf{L}}_{\rm N}(0) = (0,0,1)\,, \tag{9.75}$$

$$\mathbf{S}_1(0) = (\sin\theta_{S_1}, 0, \cos\theta_{S_1})\,, \tag{9.76}$$

$$\mathbf{S}_2(0) = (\sin\theta_{S_2}\cos(\phi_{S_2}-\phi_{S_1}), \sin\theta_{S_2}\sin(\phi_{S_2}-\phi_{S_1}), \cos\theta_{S_2})\,, \tag{9.77}$$

along with an initial orbital phase Ψ_0 given by

$$\mathbf{n}(0) = \mathbf{e}_1(0)\cos\Psi_0 + \mathbf{e}_2(0)\sin\Psi_0\,. \tag{9.78}$$

With this choice, all the directional parameters are isolated in factor P of Eq. (9.68), while the basic and local parameters (which affect the dynamics of the binary) are isolated in factor Q. We will call upon this property of the precessing convention in Sec. 9.6.4, where we propose a new family of templates for NS–BH binaries built by writing a set of orthonormal component templates that contain all the dynamical information expressed by factor Q, and then using their linear combinations to reproduce the projection operation expressed by factor P.

Going back to the main thrust of this section, we obtain the detector response $h_{\rm resp}$ by setting the direction to the detector $\hat{\mathbf{N}}$ (specified by the angles Θ and φ with respect to the source frame),

and by introducing the radiation frame, oriented along the axes

$$\mathbf{e}_x^R = -\mathbf{e}_x^S \sin\varphi + \mathbf{e}_y^S \cos\varphi\,, \tag{9.79}$$

$$\mathbf{e}_y^R = -\mathbf{e}_x^S \cos\Theta\cos\varphi - \mathbf{e}_y^S \cos\Theta \sin\varphi + \mathbf{e}_z^S \sin\Theta\,, \tag{9.80}$$

$$\mathbf{e}_z^R = +\mathbf{e}_x^S \sin\Theta \cos\varphi + \mathbf{e}_y^S \sin\Theta \sin\varphi + \mathbf{e}_z^S \cos\Theta = \hat{\mathbf{N}}\,; \tag{9.81}$$

we then get

$$h_{\rm resp} = -\frac{2\mu}{D}\frac{M}{r}\left([\mathbf{e}_+]^{ij}\cos 2\Psi + [\mathbf{e}_\times]^{ij}\sin 2\Psi\right)\left([\mathbf{T}_+]_{ij}\,F_+ + [\mathbf{T}_\times]_{ij}\,F_\times\right)\,. \tag{9.82}$$

Applying the stationary-phase approximation (SPA) at the leading order, we can write the Fourier transform of $h_{\rm resp}$ as

$$\tilde{h}_{\rm resp}(f) = -\tilde{h}_C(f)\,\left([\mathbf{e}_+(t_f)]^{jk} + i\,[\mathbf{e}_\times(t_f)]^{jk}\right)\,\left([\mathbf{T}_+]_{jk}\,F_+ + [\mathbf{T}_\times]_{jk}\,F_\times\right) \quad \text{for } f>0\,, \tag{9.83}$$

where $\tilde{h}_C(f)$ is the SPA Fourier transform of the *carrier signal*,

$$h_C = \frac{2\mu}{D}\frac{M}{r}\cos 2\Psi\,, \tag{9.84}$$

and where t_f is the time at which the carrier signal has instantaneous frequency f.

9.4.2 Definition of a new DTF for precessing binaries

By adopting the precessing convention, we isolate all the modulational effects due to precession in the evolving polarization tensors $[\mathbf{e}_{+,\times}]^{ij}$ (these effects will show up both in the amplitude *and* in the phase of $h_{\rm resp}$). The discussion of Sec. 9.3.4 shows that, to a very good approximation, the carrier signal is not modulated, so we expect that $\tilde{h}_C(f)$ should be approximated well by the nonspinning PN templates studied in Chapter 8, or variations thereof. As for the time dependence of the tensors $[\mathbf{e}_{+,\times}]^{ij}$, the discussion of Secs. 9.3.5 and 9.3.6 suggests that we adopt the Apostolatos' ansatz [26], and write expressions in the generic forms

$$[\mathrm{e}_{+,\times}]^{ij}[\mathbf{T}_{+,\times}]_{jk} \propto \mathcal{C}_{+,\times}\cos\left(\mathcal{B}\,f^{-2/3} + \delta_{+,\times}\right) \quad \text{or} \quad \propto \mathcal{C}_{+,\times}\cos\left(\mathcal{B}\,f^{-1} + \delta_{+,\times}\right)\,. \tag{9.85}$$

Indeed, our extended numerical investigations provide evidence that expressions of the form (9.85) should work quite well for the binaries under consideration.

All these elements suggest that we introduce a family of detection templates of the general

(Fourier-domain) form

$$h(\psi_{\rm NM}, \mathcal{A}_k, t_0, \alpha_k; f) = \left[\sum_{k=1}^{n} (\alpha_k + i\alpha_{k+n}) \mathcal{A}_k(f)\right] e^{2\pi i f t_0} e^{i\psi_{\rm NM}(f)} \quad (\text{for } f > 0) \tag{9.86}$$

[and $h(f) = h^*(-f)$ for $f < 0$], where the $\mathcal{A}_k(f)$ are real *amplitude functions*, the α_k are their (real) coefficients, and t_0 is the time of arrival of the GW signals. The function $\psi_{\rm NM}$ represents the phase of the unmodulated carrier signal; we write it as a series in the powers of $f^{1/3}$,

$$\psi_{\rm NM}(f) = f^{-5/3} \left(\psi_0 + \psi_{1/2} f^{1/3} + \psi_1 f^{2/3} + \psi_{3/2} f + \ldots\right). \tag{9.87}$$

As discussed in Chapter 8, this phasing works well for relatively high-mass, nonspinning BBHs, and for NS–BH binaries; in addition, as anticipated in Sec. 9.3.4, the PN coefficients ψ_i are able to capture the nonmodulational effects of spin-orbit and spin-spin couplings on the orbital phase. In this chapter we examine three specific families of detection templates of this form, listed in Tab. 9.6. The subscripts "2," "4," and "6" in our abbreviations for the template families denote the number of α_k coefficients that appear in Eq. (9.86).

The families $(\psi_0\psi_{3/2})_2$ and $(\psi_0\psi_{3/2}\alpha)_4$ were already studied in Chapter 8 for the case of nonspinning binaries. Both families contain the leading $f^{-7/6}$ Newtonian dependence of the amplitude; however, $(\psi_0\psi_{3/2}\alpha)_4$ contains a correction to the Newtonian amplitude (introduced in Chapter 8, where it was parametrized by α) which can account for the variation of the rate of inspiral in the late stages of orbital evolution. The first family is given by

$$(\psi_0\psi_{3/2})_2: \quad h(\ldots; f) = (\alpha_1 + i\alpha_2) f^{-7/6}\, \theta(f_{\rm cut} - f)\, e^{2\pi i f t_0} \exp i[\psi_0 f^{-5/3} + \psi_{3/2} f^{-2/3}]; \tag{9.88}$$

here $\alpha_1 + i\alpha_2$ can also be written as $\mathcal{A} \exp i\phi_0^{\rm GW}$, where $\phi_0^{\rm GW}$ is the initial GW phase, and $\mathcal{A}$ is an overall normalization factor for the template. So the two α_k coefficients encode the initial global phase of the waveform, plus a normalization factor. The second family is given by

$$(\psi_0\psi_{3/2}\alpha)_4: \quad h(\ldots; f) = [(\alpha_1 + i\alpha_2) f^{-7/6} + (\alpha_3 + i\alpha_4) f^{-1/2}]\, \theta(f_{\rm cut} - f)\, e^{2\pi i f t_0} \exp i[\psi_0 f^{-5/3} + \psi_{3/2} f^{-2/3}]; \tag{9.89}$$

another way to rewrite the coefficients $\alpha_{1\text{–}4}$ more physically is $\mathcal{A} \exp[i\phi_0^{\rm GW}] f^{-7/6} (1 + \alpha \exp[i\phi^\alpha] f^{2/3})$, where α is the additional amplitude parameter and ϕ^α is the relative phase of the amplitude correction (as in Chapter 8, in this chapter we always set $\phi^\alpha = 0$). So the four coefficients α_k encode the global phase, the strength of the correction to the Newtonian amplitude, and the relative phase of this correction with respect to the Newtonian amplitude, plus an overall normalization factor.

The third family, $(\psi_0\psi_{3/2}\mathcal{B})_6$, contains the leading Newtonian amplitude, modified by two modulation terms [a generalization of the Apostolatos' ansatz (9.85)] that account for the precession of

DTF	$\psi_{\rm NM}(f)$	$\mathcal{A}_1$(f)	$\mathcal{A}_2(f)$	$\mathcal{A}_3(f)$
$(\psi_0\psi_{3/2})_2$	$\psi_0 f^{-5/3}+\psi_{3/2}f^{-2/3}$	$f^{-7/6}\,\theta(f_{\rm cut}-f)$		
$(\psi_0\psi_{3/2}\alpha)_4$	$\psi_0 f^{-5/3}+\psi_{3/2}f^{-2/3}$	$f^{-7/6}\,\theta(f_{\rm cut}-f)$	$f^{-1/2}\,\theta(f_{\rm cut}-f)$	
$(\psi_0\psi_{3/2}\mathcal{B})_6$	$\psi_0 f^{-5/3}+\psi_{3/2}f^{-2/3}$	$f^{-7/6}\,\theta(f_{\rm cut}-f)$	$f^{-7/6}\cos(\mathcal{B}f^{-2/3})\,\theta(f_{\rm cut}-f)$	$f^{-7/6}\sin(\mathcal{B}f^{-2/3})\,\theta(f_{\rm cut}-f)$
$(\psi_0\psi_{3/2}\mathcal{B}')_6$	$\psi_0 f^{-5/3}+\psi_{3/2}f^{-2/3}$	$f^{-7/6}\,\theta(f_{\rm cut}-f)$	$f^{-7/6}\cos(\mathcal{B}f^{-1})\,\theta(f_{\rm cut}-f)$	$f^{-7/6}\sin(\mathcal{B}f^{-1})\,\theta(f_{\rm cut}-f)$

Table 9.6: Specification of the DTFs examined in this chapter.

the orbital angular momentum due to spin effects. It is given by

$$\begin{aligned}(\psi_0\psi_{3/2}\mathcal{B})_6: \quad h(\ldots;f) &= f^{-7/6}[(\alpha_1+i\alpha_2)+(\alpha_3+i\alpha_4)\cos(\mathcal{B}f^{-2/3})+(\alpha_5+i\alpha_6)\sin(\mathcal{B}f^{-2/3})]\\ &\quad\times\theta(f_{\rm cut}-f)\,e^{2\pi i f t_0}\exp i[\psi_0 f^{-5/3}+\psi_{3/2}f^{-2/3}];\end{aligned} \tag{9.90}$$

another way to rewrite the six coefficients α_{1-6} in close analogy to Apostolatos' ansatz is

$$\begin{aligned}&\mathcal{A}\,e^{i\phi_0^{\rm GW}}f^{-7/6}\left[1+\mathcal{C}\,e^{i\phi^{\rm mod}}\cos(\beta f^{-2/3}+\delta_1+i\delta_2)\right]\\ \equiv\;&\mathcal{A}\,e^{i\phi_0^{\rm GW}}f^{-7/6}\left[1+\mathcal{C}_{\cos}\,e^{i\phi^{\cos}}\cos(\beta f^{-2/3})+\mathcal{C}_{\sin}\,e^{i\phi^{\sin}}\sin(\beta f^{-2/3})\right]\end{aligned} \tag{9.91}$$

(where all the coefficients are still real). So the six coefficients α_k encode the global phase, the strength of the amplitude modulation, its relative phase with respect to the Newtonian amplitude, and the internal (complex) phase of the modulation. It is clear that our family implements a generalization of Apostolatos' ansatz, because we allow a *complex* phase offset between the Newtonian and the sinusoidal amplitude terms, and also between the cosine and sine modulational terms. We consider also a variant $(\psi_0\psi_{3/2}\mathcal{B}')_6$ of this family where the $f^{-2/3}$ frequency dependence in the sinusoidal amplitude functions is replaced by f^{-1}. For all three families, the templates are terminated at a *cut* frequency $f_{\rm cut}$, above which the amplitude drops to zero; this $f_{\rm cut}$ is in effect one of the (intrinsic) search parameters. For all three families, the frequency dependence of the phase includes the leading Newtonian term, $f^{-5/3}$, and a term $f^{-2/3}$ that corresponds to the 1.5PN correction in the phase evolution of nonspinning binaries (as obtained, in the SPA, by integrating the energy-balance equation through an adiabatic sequence of circular orbits, using PN expanded energy and flux). In Chapter 8 we found that including either the 1PN or 1.5PN term is in general sufficient to model the phase evolution of nonspinning binaries of high mass.

9.4.3 Definition of the standard SPA template families

In this section we define two families of standard nonspinning-binary templates, obtained by solving the Taylor-expanded energy-balance equation for an adiabatic sequence of quasi-circular orbits, and using the stationary-phase approximation (SPA) to express the result as a function of the GW frequency f (see Chapter 8). In Sec. 9.6 we compare the matching performance of these templates

to the performance of our new DTFs, to show that the various tricks used to build the new families do indeed improve their effectualness [3]. The standard SPA families are built from the analytic expressions of Refs. [16, 18]. The frequency-domain phasing (under the assumption of nonevolving orbital angular momentum and spins) is given by [10]

$$\begin{aligned}\psi_{\rm SPA}(f) &= 2\pi\, f\, t_c - \phi_c \\ &+ \frac{3}{128}\,(\pi\mathcal{M}\, f)^{-5/3}\Bigg[1+\frac{20}{9}\left(\frac{743}{336}+\frac{11}{4}\eta\right)(\pi M\, f)^{2/3} - 4(4\pi - {\rm SO})\,(\pi M\, f) \\ &\qquad +10\left(\frac{3058673}{1016064}+\frac{5429}{1008}\eta+\frac{617}{144}\eta^2-{\rm SS}\right)(\pi M\, f)^{4/3}\Bigg], \quad (9.92)\end{aligned}$$

where $\mathcal{M} = M\eta^{3/5}$ is the *chirp mass*, and where SO and SS are the spin-orbit and spin-spin terms, given explicitly by

$$\begin{aligned}{\rm SO} &= \frac{1}{M^2}\left[\left(\frac{113}{12}+\frac{25}{4}\,\frac{m_2}{m_1}\right)\mathbf{S}_1+\left(\frac{113}{12}+\frac{25}{4}\,\frac{m_1}{m_2}\right)\mathbf{S}_2\right]\cdot\hat{\mathbf{L}}_N\,, \quad (9.93)\\ {\rm SS} &= \frac{1}{48 m_1\, m_2\, M^2}\left[-247\,\mathbf{S}_1\cdot\mathbf{S}_2+721(\mathbf{S}_1\cdot\hat{\mathbf{L}}_N)\,(\mathbf{S}_2\cdot\hat{\mathbf{L}}_N)\right]. \quad (9.94)\end{aligned}$$

We neglect all PN corrections to the amplitude, by adopting its Newtonian functional form, $f^{-7/6}$; we also neglect all precessional effects, by setting ${\rm SO} = {\rm SS} = 0$. Templates of this form are routinely used in searches for GW signals from nonspinning binaries. In that case, the templates are generally ended at the GW frequency corresponding to the Schwarzschild ISCO $f_{\rm Schw} \simeq 0.022/M$. We denote such templates as SPAs. We introduce also a variant of this family, SPAc, characterized by the additional frequency-cut parameter $f_{\rm cut}$, used also in our DTFs. Altogether, we get

$${\rm SPAs}: h(\mathcal{M},\eta,t_0,\psi_0,\alpha_N;f) = \alpha_N f^{-7/6}\theta(f_{\rm Schw}-f)e^{2\pi i f t_0}\exp i[\psi_{\rm SPA}+\psi_0]; \quad (9.95)$$

$${\rm SPAc}: h(\mathcal{M},\eta,f_{\rm cut},t_0,\psi_0,\alpha_N;f) = \alpha_N f^{-7/6}\theta(f_{\rm cut}-f)e^{2\pi i f t_0}\exp i[\psi_{\rm SPA}+\psi_0]. \quad (9.96)$$

9.5 GW data analysis with the DTF

In searching for GW signals using matched-filtering techniques, we construct a discrete bank of templates that represent all the possible signals that we expect to receive from a given class of sources. We then proceed to compare each stretch of detector output with each of the templates, computing their *overlap* (essentially, a weighted correlation). A high value of the overlap statistic for a given stretch of detector output and for a particular template implies that there is a high probability that during that time the detector actually received a GW signal similar to the template. This technique is intrinsically probabilistic because, for any template, detector noise alone can (rarely) yield high values of the statistic. In general, the higher the value of the statistic, the harder it is to obtain it from noise alone. So it is important to set the *detection threshold* (above which we confidently claim a detection) by considering the resulting probability of the *false alarms* caused by noise.

To verify whether the DTFs developed in Sec. 9.5 can be used to search reliably and effectually for the GWs from spinning binaries, we need to evaluate the *fitting factor* FF of the DTFs in matching the target signals for a variety of binary and detector parameters. The FF is defined as the ratio between the overlap of the target signal with the best possible template in the family and the overlap of the target signal with itself. [4] So in Sec. 9.5.1 we discuss the maximization of the overlap over template parameters for a given target signal. The other important element to evaluate the reliability and effectualness [3] of the DTFs are the detection thresholds that the DTFs yield for a given false-alarm probability. In Sec. 9.5.2 we discuss these thresholds under the simplifying hypothesis of Gaussian detector noise. The material presented in this section builds on the treatment of matched-filtering data analysis for GW sources given in Sec. 8.2 of this thesis (which is built on Refs. [2, 3, 7]), and it uses the same notations.

9.5.1 Maximization of the overlap over template parameters

Among all the template parameters that appear in Eq. (9.86), we are going to treat the ψ_i, $f_{\rm cut}$ and $\mathcal{B}$ as *intrinsic* parameters; and the α_k and t_0 as *extrinsic* parameters: that is, when we look within one of our DTFs for the template that best matches a given target signal, we will need to consider *explicitly* many different values of the ψ_i, of $f_{\rm cut}$, and of $\mathcal{B}$; however, for any choice of these parameters, the best α_k and t_0 are determined automatically by simple algebraic expressions (see Sec. 8.2.2 of this thesis). For the next few paragraphs, where we discuss the optimization of the coefficients α_k, we shall not indicate the dependence of the templates on the intrinsic parameters.

For a given signal s, we seek the maximum of the overlap,

$$\max_{t_0,\alpha_k} \langle s, h(t_0,\alpha_k)\rangle\,, \tag{9.97}$$

[4] Because the amplitude of signals is generally unknown, the FF is generally defined in terms of *normalized* signals in the sense of Eq. (9.98).

under the normalization condition

$$\langle h(t_0,\alpha_k), h(t_0,\alpha_k)\rangle = 1 \tag{9.98}$$

[this condition is necessary to set a scale for the statistic distribution of the overlap between a given template and pure noise]. Here the inner product $\langle g,h\rangle$ of two real signals with Fourier transforms $\tilde{g}$, $\tilde{h}$ is defined by

$$\langle g,h\rangle = 2\int_{-\infty}^{+\infty} \frac{\tilde{g}^*(f)\tilde{h}(f)}{S_n(|f|)}df = 4\,\mathrm{Re}\int_0^{+\infty} \frac{\tilde{g}^*(f)\tilde{h}(f)}{S_n(f)}df \tag{9.99}$$

(see Chapter 8). We proceed constructively: first, we build a new set of amplitude functions $\hat{\mathcal{A}}_k(f)$ that are linear combinations of the $\mathcal{A}_k(f)$, and that satisfy the orthonormality condition $\langle\hat{\mathcal{A}}_i(f),\hat{\mathcal{A}}_j(f)\rangle = \delta_{ij}$ for $i,j = 1,2,\ldots n$; we then define an orthonormal set of single-$\hat{\mathcal{A}}_k$ templates,

$$\hat{h}_k(t_0;f) \equiv \hat{\mathcal{A}}_k(f)e^{2\pi i f t_0}e^{i\psi_{\rm NM}}\,, \qquad \hat{h}_{k+n}(t_0;f) \equiv i\hat{\mathcal{A}}_k(f)e^{2\pi i f t_0}e^{i\psi_{\rm NM}} \quad (\text{for } f>0) \tag{9.100}$$

[and $\hat{h}_k(f) = \hat{h}_k^*(-f)$ for $f<0$], which satisfy $\langle\hat{h}_i(t_0),\hat{h}_j(t_0)\rangle = \delta_{ij}$ (with $i,j = 1,2,\ldots,2n$) for any t_0. The maximized overlap [Eq. (9.97)] can now be rewritten as

$$\max_{t_0,\alpha_k}\langle s,h(t_0,\alpha_k)\rangle = \max_{t_0}\max_{\hat{\alpha}_k}\sum_{k=1}^{2n}\hat{\alpha}_k\langle s,\hat{h}_k(t_0)\rangle\,, \tag{9.101}$$

while the condition (9.98) is now simply $\sum_{k=1}^{2n}\hat{\alpha}_k^2 = 1$. The inner maximum of Eq. (9.101) (over the $\hat{\alpha}_k$) is achieved when

$$\hat{\alpha}_k = \frac{\langle s,\hat{h}_k(t_0)\rangle}{\sqrt{\sum_{j=1}^{2n}\langle s,\hat{h}_j(t_0)\rangle^2}}\,, \tag{9.102}$$

and the maximum overlap itself is

$$\max_{t_0,\alpha_k}\langle s,h(t_0,\alpha_k)\rangle = \max_{t_0}\max_{\hat{\alpha}_k}\sum_{k=1}^{2n}\hat{\alpha}_k\langle s,\hat{h}_k(t_0)\rangle = \sqrt{\max_{t_0}\sum_{j=1}^{2n}\langle s,\hat{h}_j(t_0)\rangle^2}\,. \tag{9.103}$$

This happens essentially because the sum in Eq. (9.101) can be seen as a scalar product in a $2n$-dimensional Euclidean space, which is maximized when the unit $2n$-vector $\hat{\alpha}_k$ lies along the direction of the $2n$-vector $\langle s,\hat{h}_k(t)\rangle$. The quantities $\langle s,\hat{h}_j(t_0)\rangle$ for $j = 1,2,3,\ldots,n$ are given by the two related Fourier integrals

$$\langle s,\hat{h}_j\rangle = 2\,\mathrm{Re}\int_0^{+\infty}\frac{\hat{\mathcal{A}}_j(f)e^{i\psi_{\rm NM}(f)}s^*(f)}{S_h(f)}\,e^{2\pi i f t_0}df\,, \tag{9.104}$$

$$\langle s,\hat{h}_{j+n}\rangle = -2\,\mathrm{Im}\int_0^{+\infty}\frac{\hat{\mathcal{A}}_j(f)e^{i\psi_{\rm NM}(f)}s^*(f)}{S_h(f)}\,e^{2\pi i f t_0}df\,. \tag{9.105}$$

We now go back to discussing the full set of template parameters. The relevant measure of the *effectualness* [3] of a template family at matching a physical signal s is the *fitting factor* FF,

$$\mathrm{FF} = \max_{t_0,\alpha_k,f_{\rm cut},\psi_i} \frac{\langle s, h(t_0,\alpha_k)\rangle}{\sqrt{\langle s,s\rangle}}\,, \tag{9.106}$$

(see, for instance, Sec. 8.2 of this thesis) which is maximized over the α_k, but also over the time of arrival t_0 (also an extrinsic parameter), and over all the intrinsic parameters, ψ_i, $f_{\rm cut}$, and $\mathcal{B}$. The fitting factor is a function of the physical parameters of the physical signal s, and of course of the template family used to match it. We define also the *signal amplitude* SA for a given signal,

$$\mathrm{SA} = \sqrt{\langle s,s\rangle}. \tag{9.107}$$

SA gives the *optimal* overlap obtained for a template that is exactly equal to the signal (except for its normalization), and it is inversely proportional to the luminosity distance to the source; where we do not indicate otherwise, we always assume the fiducial distance $d_0 = 100$ Mpc.

The maximization of the overlap over t_0 is easy to obtain, because the integrals (9.104) and (9.105) can be evaluated at the same time for all the t_0 using Fast Fourier Transform techniques [27]. On the other hand, the maximization over $f_{\rm cut}$ and over the other intrinsic parameters is obtained by an explicit search over a multidimensional parameter range, where we look for the maximum of the partially maximized (over extrinsic parameters) overlap, given by Eq. (9.97). For all the actual searches discussed in this chapter we employ with good results the simplicial algorithm `amoeba` [28].

9.5.2 False-alarm statistics of the DTFs

In the practice of GW data analysis, template *families* are used to build discrete template *banks* parametrized by a discrete set of ntuples of the intrinsic parameters. Then each of the templates is correlated with the detector output, to see if the detection statistic [in our case, the partially maximized correlation (9.97)] is greater than the detection threshold. It is important to notice that the statistic is already maximized with respect to the extrinsic parameters, while the intrinsic parameters serve as labels for each of the templates. Therefore, we are effectively setting up a separate detection test for each of the templates in the bank.

In this section we are going to evaluate the false-alarm probability for one such test, defined as the probability that detector noise alone will yield an overlap greater than the detection threshold. The total false-alarm probability is then obtained by multiplying the false-alarm probability for a single template by the number $\mathcal{N}_{\rm shapes}$ of independent signal shapes (generally of the same order of magnitude as the number of templates in the bank), and by the number $\mathcal{N}_{\rm times}$ of possible times

of arrival t_0, distanced in such a way that the displaced templates are essentially orthogonal. [5] At the end of this exercise, we are going to set the detection threshold so that the total false-alarm probability is acceptably low.

Under the assumption of Gaussian noise, the inner product $\langle n, \hat{h}_j \rangle$ of noise n alone with a normalized template component $\hat{h}_i$ is (by construction) a Gaussian random variable with zero mean and unit variance (see, for instance, Sec. 8.2 of this thesis). Because (for the same t_0 and for the same intrinsic parameters) all the $\hat{h}_j$ are orthogonal, the inner products $\langle n, \hat{h}_j \rangle$ (for $j = 1, \ldots, 2n$) are all independent normal variables. It follows that the statistic $X = \max_{t_0,\alpha_k} \langle n, h(t_0, \alpha_k) \rangle$ [see Eq. (9.103)], given by the square root of the sum of their squares, follows the χ distribution with $2n$ degrees of freedom, characterized by the probability density function and cumulative distribution function

$$\mathrm{PDF}_{\chi(2n)}(X = x) = \frac{x^{2n-1} e^{-x^2/2}}{2^{n-1}\Gamma(n)}, \quad \mathrm{CDF}_{\chi(2n)}(X < x) = \frac{\Gamma(n, 0, x^2/2)}{\Gamma(n)}, \tag{9.108}$$

where we have used the *generalized incomplete gamma function* $\Gamma(n, z_0, z_1) = \int_{z_0}^{z_1} t^{n-1} e^{-t} dt$. For $n = 1$ we obtain the *Rayleigh distribution*, typical of the maximization of the amplitude of signals with two quadratures.

In Tab. 9.7 we show the thresholds needed to obtain a total false alarm probability of 10^{-3}, with $\mathcal{N}_{\mathrm{times}} = 3\,10^{10}$ (typical of about three years of observation with LIGO), and with the $\mathcal{N}_{\mathrm{shapes}}$ given in the first column. We observe that each time we increase $\mathcal{N}_{\mathrm{shapes}}$ by one order of magnitude, the threshold increases by about 2% (this happens uniformly for all n's). On the other hand, each step in n increases the threshold by about 4%. Thus, when we design DTFs we should keep in mind that the best possible overlap increases with the number of templates employed, and with the complexity of the templates (clearly, the complexity of our DTFs increases with the number of amplitude functions); but the detection threshold increases as well, reducing the number of signals that pass the detection test. So in principle we are justified in using more numerous and more complex templates only if the gain in the overlap is larger than the increase in the detection threshold.

The prospects shown in Tab. 9.7 for the models with $n = 2$ and $n = 3$ improve somewhat if we constrain the values that the α_k can attain when they are (algebraically) maximized. We can do this, for instance, if we judge that certain combinations of the α_k correspond to unphysical waveforms, but then we must be consistent and exclude any detections that cross the threshold within the excluded parameter region. In any case, we should remember that our study of false-alarm statistics is based on the idealization of Gaussian noise, which will not be realized in practice: real-world data-analysis schemes relie on matched-filtering techniques complemented by *vetoing schemes* [29], which remove

[5] The time of arrival of the GW signal is an extrinsic parameter (it is searched automatically for the best possible value using FFT integrals); however, when we evaluate the total false-alarm probability it is easier to consider a single detection test for each possible time of arrival. So the probability distributions discussed in Sec. 9.5.2 are for an overlap statistic that is *not* automatically maximized over the time of arrival.

$\mathcal{N}_{\text{shapes}}$	Threshold for false-alarm probability $= 10^{-3}$		
	$(\psi_0\,\psi_{3/2})_2$ $n=1$	$(\psi_0\,\psi_{3/2}\,\alpha)_4$ $n=2$	$(\psi_0\,\psi_{3/2}\,\mathcal{B})_6$ $n=3$
10^2	8.44	8.87	9.22
10^3	8.71	9.13	9.48
10^4	8.97	9.39	9.73
10^5	9.22	9.63	9.97
10^6	9.47	9.87	10.21

Table 9.7: Detection thresholds for a false-alarm probability $= 10^{-3}$ for a χ-distributed detection statistic with $2n$ degrees of freedom, for $\mathcal{N}_{\text{times}} = 3\,10^{10}$, and for the $\mathcal{N}_{\text{shapes}}$ given in the first column. The values given for $(\psi_0, \psi_{3/2}\,\alpha)_4$ do not take into account the $\phi^\alpha = 0$ constraint.

detection candidates using nonlinear tests on the signal. Therefore, any DTF should be evaluated in that context before it is excluded for producing excessive detection thresholds within the Gaussian analysis.

9.6 Evaluation of DTF performance

We wish to investigate the effectualness [3] of our DTFs in matching the GW signals generated by precessing binaries of spinning compact objects, at least as approximated by the target model described in Sec. 9.2. To do so, we shall evaluate the fitting factor FF [Eq. (9.106)] of the DTFs over a population of binaries with a variety of basic, local and directional parameters, and compare the results with the FF obtained for the standard SPA families [Sec. 9.4.3]. In Sec. 9.6.1 we study the effect of the directional parameters on FF (and SA), with the aim of reducing the dimensionality of the test populations. In Sec. 9.6.2 we describe the Monte Carlo scheme used to generate the populations, and we identify two performance indices for the template families (namely, the simple and SA-weighted averages of FF). In Sec. 9.6.3 we give our results for these indices, focusing first on the BBHs considered in this chapter. Finally, in Sec. 9.6.4 we give our results for NS–BH binaries, and we briefly describe a new, very promising family of templates for these systems, suggested by the insights accreted during the development of this chapter.

9.6.1 Effect of directional parameters on FF and SA

As we have seen in Secs. 9.2.3 and 9.2.4, the detector response $h_{\rm resp}$ is a function not only of the basic and local parameters of the binary (which describe respectively the masses and spin magnitudes, and the initial relative directions of the spins and the orbital angular momentum, and therefore change the dynamical evolution of the binary), but also of the directional parameters (which describe the relative direction and orientation of binary and detector, and alter the *presentation* of the precessing orbital plane of the binary with respect to the direction and orientation of the detector). Thus, *all* the parameters will affect *both* the amplitude $\mathrm{SA} = \langle h_{\rm resp}, h_{\rm resp}\rangle^{1/2}$ of the signals received at the detector *and* the ability of our DTFs to match them, as codified in the fitting factor FF; it is therefore clear that, in evaluating the effectualness of our DTFs at matching the target signals, we will need to compute FF not only for a range of binary masses and spins, but also for a suitable sampling of the local and directional parameters.

In the case of nonspinning binaries (see Chapter 8), there are no local parameters as we defined them in this chapter; the directional parameters *do* change the GW signal, but only by multiplying its amplitude by a constant factor, and by adding a constant offset to its phase (as opposed to modulating amplitude and phase as in the case of spinning binaries). In Chapter 8 (following a common practice in the GW data-analysis literature), we included the variation of the amplitude *in the definition* of the target signals, by averaging the amplitude factor over uniform solid-angle distributions of the directional parameters [see Eq. (29) of Sec. II D]. As for the initial phase of the signal, we defined the FF on the basis of *minmax* overlaps [3], which are maximized over the initial *template* phase (and over all the other extrinsic and intrinsic template parameters) but *minimized*

over the initial signal phase; this minimization is obtained algebraically, just as for extrinsic template parameters. In fact, it turns out that minimizing or maximizing the overlap over the initial signal phase changes the resulting FF by a very small quantity.

In the case of the spinning binaries examined in this chapter, this picture changes radically, because minimizing the overlap over the directional parameters yields very low FFs that are not representative of the typical results that we would get in actual observations. So we take a different approach: we study the distribution of FF for a population of binaries characterized by different basic, local, and directional parameters. In particular, we select several astrophysically relevant combinations of basic parameters, and we sample randomly (but as uniformly as possible) the space spanned by the local and directional parameters. In practice, we can exploit certain symmetries of this space (that is, the fact that different combinations of the local and directional parameters yield the same signal) to reduce its effective dimensionality. Let us see how.

Under the FC convention, the complete specification of a target signal requires (at least formally) 15 parameters: according to our classification (Sec. 9.2.4), four of these are the basic parameters (M, η, S_1, and S_2); three are the local binary angles (θ_{S_1}, θ_{S_2}, and $\phi_{S_1} - \phi_{S_2}$); three are the directional binary angles ($\theta_{\mathrm{L_N}}$, $\phi_{\mathrm{L_N}}$, and $\phi_{S_1} + \phi_{S_2}$); and five are the directional GW and detector angles (Θ, φ, θ, ϕ, and ψ). Of the latter, θ, ϕ, and ψ come into the waveform only through the antenna patterns F_+ and $F_\times$ [see Eqs. (9.29) and (9.30)]. It is redundant to specify *both* the directional binary angles (which determine the orientation of the binary as a whole in space) *and* the directional GW angles (which determine the direction $\hat{\mathbf{N}}$ of GW propagation to the detector), because if we apply the same rotation to $\hat{\mathbf{N}}$ and to the binary vectors $\hat{\mathbf{L}}_N$, $\hat{\mathbf{S}}_1$, and $\hat{\mathbf{S}}_2$, we do not change the response of the detector h_{resp}. So we can use this freedom to set $\Theta = \pi/2$ and $\varphi = 0$. Once this is done, we still have the freedom to rotate the detector–binary system around the axis $\hat{\mathbf{N}}$. Such a rotation (by an angle ν) will transform the F_+ and $F_\times$ antenna patterns according to

$$F_+ \quad \rightarrow \quad F_+ \cos 2\nu - F_\times \sin 2\nu, \tag{9.109}$$

$$F_\times \quad \rightarrow \quad F_+ \sin 2\nu + F_\times \cos 2\nu. \tag{9.110}$$

Looking at Eqs. (9.29) and (9.30), we see that, for any original θ, ϕ, and ψ, we can always find an angle ν for which $F_+ = 0$. The corresponding new $F_\times$ becomes

$$F_\times = \pm \frac{1}{2} \sqrt{(1 + \cos^2\theta)^2 \cos^2 2\phi + 4 \cos^2\theta \sin^2 2\phi}\,; \tag{9.111}$$

once again, the detector response does not change. For future use, let us define as $p[F_\times]$ (with $\int_0^1 p[F_\times] dF_\times = 1$) the probability density for $|F_\times|$ induced by uniform solid-angle distributions for θ and ϕ [notice that ψ does not appear in (9.111)].

Now, for a given DTF and for given basic parameters, consider the distribution of FF and SA obtained for an 11-parameter population of target signals specified by uniform solid-angle distributions of $\theta_{\mathrm{L_N},S_1,S_2}$, $\phi_{\mathrm{L_N},S_1,S_2}$, Θ, φ, θ, ϕ, and ψ. By the above arguments, we obtain the same distribution of FF and SA from a 6-parameter population of target signals specified by uniform solid-angle distributions of $\theta_{\mathrm{L_N},S_1,S_2}$, $\phi_{\mathrm{L_N},S_1,S_2}$, by $\Theta = \pi/2$, $\varphi = 0$, $F_+ = 0$, and by $F_\times$ distributed according to $p[F_\times]$. Moreover, because $F_\times$ appears only as a normalization factor in front of the expression (9.27) for the signal (once $F_+ = 0$), we can simply set $F_\times = 1$: this operation does not change FF [because $F_\times$ appears homogeneously in the numerator and denominator of Eq. (9.106)], while the distribution of SA for the original 11-parameter population can be recovered from its moments on the 6-parameter population:

$$\langle \mathrm{SA}^m \rangle_{\text{11-par}} = \left\langle \int_0^1 (F_\times)^m \mathrm{SA}^m p[F_\times] dF_\times \right\rangle_{\text{6-par}} = \langle \mathrm{SA}^m \rangle_{\text{6-par}} \int_0^1 (F_\times)^m p[F_\times] dF_\times . \tag{9.112}$$

9.6.2 A Monte Carlo procedure to evaluate DTF performance

We are going to evaluate the effectualness [3] of our DTFs within a Monte Carlo framework, by studying the distribution of FF (and $\mathrm{FF}^3\mathrm{SA}^3$, see below) over six sampled populations of 1000 binaries each, specified as follows. We study the binary systems already examined in Sec. 9.3: BBHs with masses $(20 + 10)M_\odot$, $(15 + 15)M_\odot$, $(20 + 5)M_\odot$, $(10 + 10)M_\odot$, and $(7 + 5)M_\odot$, and NS–BH binaries with masses $(10 + 1.4)M_\odot$. All the BHs have maximal spin, while the NSs have no spin. We integrate numerically the target-model equations starting from initial configurations that correspond to instantaneous GW frequencies of 30 Hz when $M > 20M_\odot$, and 40 Hz otherwise. For each set of masses, we use the Halton sequence with bases 2, 3, 5, 7, 11, and 13 to generate 1000 *quasirandom* sets of the six angles $\theta_{\mathrm{L_N},S_1,S_2}$ and $\phi_{\mathrm{L_N},S_1,S_2}$; the directions of the resulting orbital angular momentum and spins are uniformly distributed over the solid angle. We denote each sestuple by the sequential index l, for $l = 1, \ldots, \mathcal{N} = 1000$. We always set $\Theta = \pi/2$, $\varphi = 0$, $F_+ = 0$, $F_\times = 1$, and we take $d_0 = 100$ Mpc.

For each set of masses, and for each DTF, we compute the Monte Carlo average of the FF,

$$\overline{\mathrm{FF}} = \langle \mathrm{FF} \rangle = \frac{1}{\mathcal{N}} \sum_{l=1}^{\mathcal{N}} \mathrm{FF}[l], \tag{9.113}$$

and its variance

$$\sigma^2_{\mathrm{FF}} = \langle \Delta\mathrm{FF}^2 \rangle = \frac{1}{\mathcal{N}-1} \sum_{l=1}^{\mathcal{N}} \left(\mathrm{FF}[l] - \overline{\mathrm{FF}} \right)^2 , \tag{9.114}$$

which can be used to estimate the sampling error of the Monte Carlo average as $\Delta\mathrm{FF} \simeq \sigma_{\mathrm{FF}}/\sqrt{\mathcal{N}}$.

There is another function of FF and SA that has a particular interest for our purposes. Consider each configuration l as a representative of a subclass of physical signals that have the same binary,

GW, and detector parameters (except for the degenerate parameters discussed above), but that are generated uniformly throughout the universe. The rate of successful signal detections using a given DTF is then

$$\mathcal{R}_{\rm detect}[l, F_\times = 1] = \mathcal{R}_{d_0} \left(\frac{\mathrm{FF}[l]\,\mathrm{SA}[l]}{\mathrm{threshold[DTF]}} \right)^3 , \tag{9.115}$$

where $\mathcal{R}_{d_0}$ is the rate of events out to the distance d_0 from Earth. Here we assume that $\mathcal{R}_{d_0}$ is a function of the basic parameters of the binary, but not of l. This equation holds because FF[l] SA[l] is the signal-to-noise ratio (that is, the overlap maximized over the DTF) for the signal l at the distance d_0; the ratio of FF[l] SA[l] to the DTF threshold gives the fraction or multiple of the distance d_0 out to which signals of the class l will pass the detection test. Folding in $p[F_\times]$ we get

$$\mathcal{R}_{\rm detect}[l] = \mathcal{R}_{\rm detect}[l, F_\times = 1] \cdot \int_0^1 (F_\times)^3 p[F_\times] dF_\times = 0.293 \cdot \mathcal{R}_{\rm detect}[l, F_\times = 1]. \tag{9.116}$$

Summing over the l, we get an estimate of the total detection rate, $\mathcal{R}_{\rm detect} = (1/\mathcal{N}) \sum_{l=1}^{\mathcal{N}} \mathcal{R}_{\rm detect}[l]$. On the other hand, the *optimal* detection rate that we would obtain with a perfectly faithful DTF is

$$\mathcal{R}_{\rm optimal} = \mathcal{R}_{d_0} \frac{1}{\mathcal{N}} \sum_{l=1}^{\mathcal{N}} \left(\frac{\mathrm{SA}[l]}{\mathrm{threshold[DTF]}} \right)^3 \cdot \int_0^1 (F_\times)^3 p[F_\times] dF_\times . \tag{9.117}$$

We can therefore define the *effective average fitting factor* $\overline{\mathrm{FF}}_{\rm eff}$ (which is a function of the basic parameters of the binary, but which is already integrated over l) from the equation

$$\mathcal{R}_{\rm detect} = \overline{\mathrm{FF}}^3_{\rm eff} \mathcal{R}_{\rm optimal}. \tag{9.118}$$

We then get

$$\overline{\mathrm{FF}}_{\rm eff} = \left\{ \frac{\langle \mathrm{FF}^3 \mathrm{SA}^3 \rangle}{\langle \mathrm{SA}^3 \rangle} \right\}^{1/3} . \tag{9.119}$$

To compute the Monte Carlo results presented below we use the *jackknifed* [30] version of this statistic to remove bias, and we estimate the error $\Delta\overline{\mathrm{FF}}_{\rm eff}$ as the jackknifed sampling variance. For each class of binaries and for a specific DTF, the effective fitting factor $\overline{\mathrm{FF}}_{\rm eff}$ represents the reduction in the detection range due to the imperfection of the DTF. The corresponding reduction in the detection rate is $\overline{\mathrm{FF}}^3_{\rm eff}$.

In Fig. 9.10 we show two examples of the distribution of signal amplitudes for the $(15 + 15)M_\odot$ BBHs and for the $(10{+}1.4)M_\odot$ NS–BH binaries in our Monte Carlo population (as computed with the 2PN target model). The plots show SA as a function of the initial $\hat{\mathbf{J}}_N \cdot \hat{\mathbf{N}}$, normalized at distances that yield SAs comparable to typical detection thresholds, and averaged over the probability distribution $p[F_\times]$. For heavy, comparable-mass BBHs (except perhaps for the last stages of the inspiral), the orbital angular momentum $\mathbf{L}_N$ is much larger than $\mathbf{S}_{1,2}$, so the initial total angular momentum $\mathbf{J}_N$

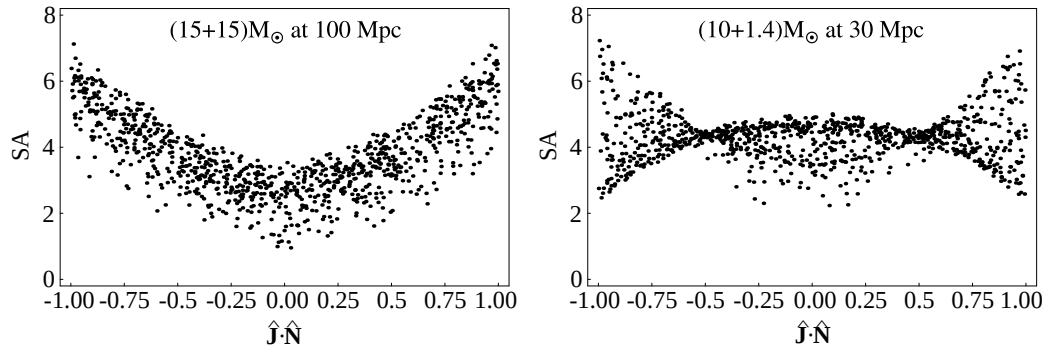

Figure 9.10: GW signal amplitude SA as a function of the initial $\hat{\mathbf{J}}_N \cdot \hat{\mathbf{N}}$ (that is, the cosine of the angle between the direction of GW propagation and the initial total angular momentum at the Newtonian order), for our Monte Carlo populations of $(15+15)M_\odot$ BBHs (in the left panel) and $(10+1.4)M_\odot$ NS–BH binaries (in the right panel). The signal amplitude is computed for a LIGO-I noise curve [Eq. (8.28) of this thesis, in Chapter 8]; it is normalized at fiducial distances of 100 and 30 Mpc, and averaged over the probability distribution $p[F_\times]$.

is almost perpendicular to the orbital plane; furthermore, as seen in Sec. 9.3.5, the direction of $\mathbf{J}_N$ does not change much during evolution. Because in the quadrupole approximation the emission of GWs is stronger along the direction perpendicular to the orbital plane, values of $|\hat{\mathbf{J}}_N \cdot \hat{\mathbf{N}}|$ close to one give stronger signals, as seen in the left panel of Fig. 9.10. For NS–BH binaries, where η is small, the BH spin $\mathbf{S}_1$ is much larger than $\mathbf{L}_N$, and $\mathbf{J}_N$ lies roughly along $\mathbf{S}_1$. So the upward curve of the left panel appears when $\mathbf{L}_N$ is roughly parallel or antiparallel to $\mathbf{S}_1$ and $\hat{\mathbf{J}}_N$ (that is, when the conserved quantity $\kappa_{\rm eff} \propto \hat{\mathbf{L}}_N \cdot \hat{\mathbf{S}}_1$ has a large absolute value), while a downward curve appears when $\mathbf{L}_N$ is orthogonal to $\mathbf{S}_1$ and $\hat{\mathbf{J}}_N$ (that is, when $\kappa_{\rm eff}$ has a value close to zero [6]). The mixture of these two tendencies creates the shape seen in the right panel of Fig. 9.10.

9.6.3 Performance indices for the standard SPA templates and for the modulated DTFs

Figure 9.11 shows the distribution of FFs, evaluated for our DTFs and for the SPA standard templates against the 2PN target model, within the Monte Carlo populations of BBHs and NS–BH binaries described in the previous section. The vertical lines show the Monte Carlo estimates of $\overline{\rm FF}$ and $\overline{\rm FF}_{\rm eff}$ (the latter is always larger), with their estimated errors; these numbers are given also in Tabs. 9.8 and 9.9. We wish to discuss several features of the FFs.

1. The SPA template families (solid and long-dashed black lines) always give the worst performance. Except for the lighter systems, $(7+5)M_\odot$ BBHs and $(10+1.4)M_\odot$ NS–BH binaries, [7]

[6] The downward-arcing envelope of Fig. 9.10b actually corresponds to $\kappa_{\rm eff} \simeq -0.3$, possibly because the ending frequency (a function of $\kappa_{\rm eff}$) plays into SA.

[7] Because the template family SPAs is a subset of SPAc, SPAs should always be more effectual. In fact, for $(7+5)M_\odot$

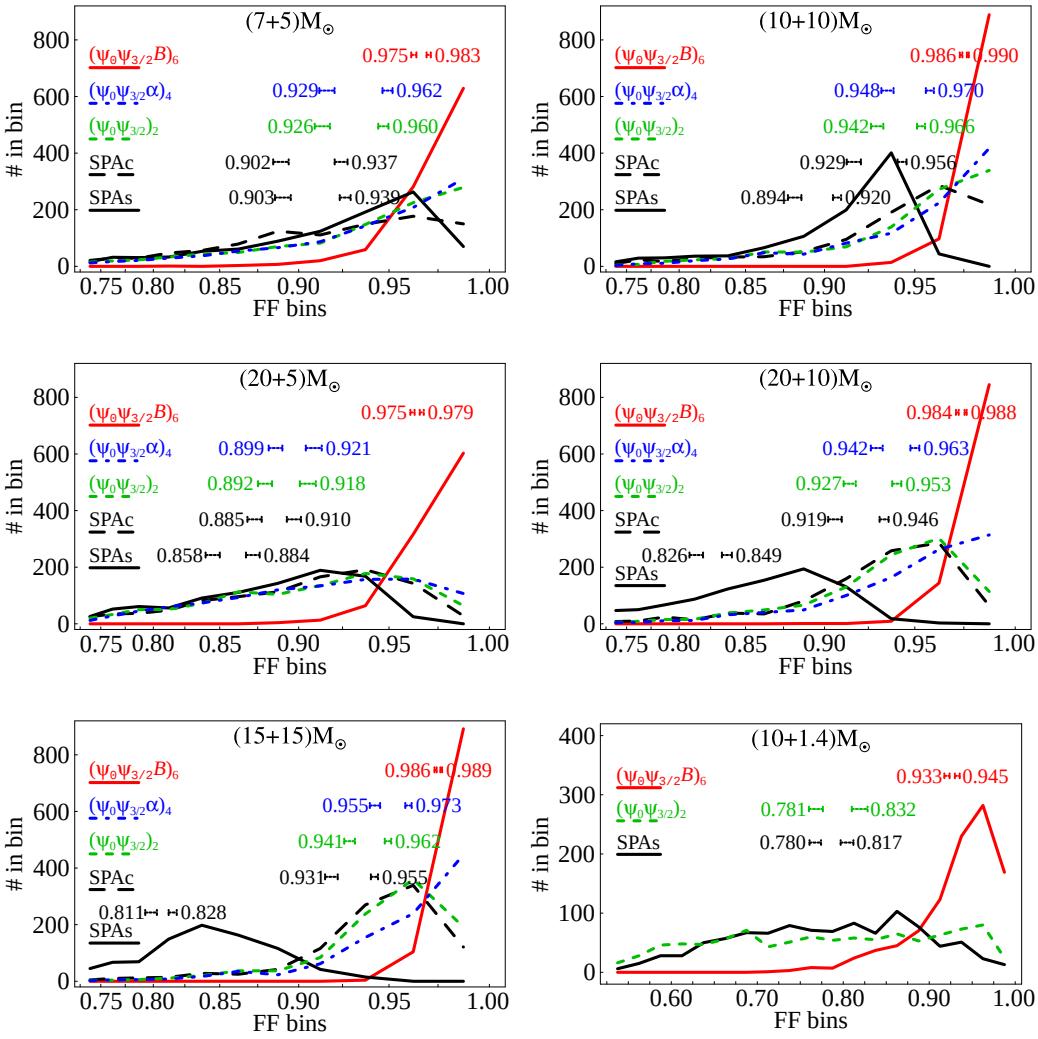

Figure 9.11: Distribution of fitting factor FF against the 2PN target model for the DTFs and for the standard SPA template families, for our BBH and NS–BH Monte Carlo populations. The vertices of the segmented curves show the number of samples (out of 1000) for which the FF falls within the equispaced bins $[0.725, 0.75)$, $[0.75, 0.775)$, ... (the bins are plotted logarithmically to emphasize the region of FF close to one; notice that the NS–BH figure in the bottom right corner shows a different bin range). The vertical lines show the averages $\overline{\mathrm{FF}}$ and $\overline{\mathrm{FF}}_{\mathrm{eff}}$ with their 1σ error bars ($\overline{\mathrm{FF}}_{\mathrm{eff}}$ is always the larger number).

	Fitting factors against 2PN target model									
	$(7+5)M_\odot$		$(10+10)M_\odot$		$(15+15)M_\odot$		$(20+5)M_\odot$		$(20+10)M_\odot$	
	$\overline{\mathrm{FF}}$	$\overline{\mathrm{FF}}_{\mathrm{eff}}$	$\overline{\mathrm{FF}}$	$\overline{\mathrm{FF}}_{\mathrm{eff}}$	$\overline{\mathrm{FF}}$	$\overline{\mathrm{FF}}_{\mathrm{eff}}$	$\overline{\mathrm{FF}}$	$\overline{\mathrm{FF}}_{\mathrm{eff}}$	$\overline{\mathrm{FF}}$	$\overline{\mathrm{FF}}_{\mathrm{eff}}$
SPAs	0.9030(24)	0.9390(15)	0.8944(21)	0.9198(12)	0.8105(25)	0.8282(16)	0.8576(25)	0.8844(22)	0.8264(27)	0.8494(18)
SPAc	0.9018(23)	0.9367(18)	0.9294(20)	0.9558(12)	0.9313(18)	0.9548(10)	0.8854(23)	0.9096(21)	0.9186(20)	0.9461(12)
$(\psi_0\psi_{3/2})_2$	0.9262(22)	0.9595(13)	0.9423(17)	0.9657(10)	0.9414(15)	0.9620(08)	0.8921(22)	0.9178(23)	0.9270(17)	0.9529(12)
$(\psi_0\psi_{3/2}\alpha)_4$	0.9288(22)	0.9617(13)	0.9480(16)	0.9703(10)	0.9551(14)	0.9726(08)	0.8986(21)	0.9212(23)	0.9421(16)	0.9625(12)
$(\psi_0\psi_{3/2}\mathcal{B})_6$	0.9753(07)	0.9828(05)	0.9861(03)	0.9895(02)	0.9863(03)	0.9891(02)	0.9746(05)	0.9794(05)	0.9843(03)	0.9884(03)
	Fitting factors against 3.5PN target model									
	$(7+5)M_\odot$		$(10+10)M_\odot$		$(15+15)M_\odot$		$(20+5)M_\odot$		$(20+10)M_\odot$	
	$\overline{\mathrm{FF}}$	$\overline{\mathrm{FF}}_{\mathrm{eff}}$	$\overline{\mathrm{FF}}$	$\overline{\mathrm{FF}}_{\mathrm{eff}}$	$\overline{\mathrm{FF}}$	$\overline{\mathrm{FF}}_{\mathrm{eff}}$	$\overline{\mathrm{FF}}$	$\overline{\mathrm{FF}}_{\mathrm{eff}}$	$\overline{\mathrm{FF}}$	$\overline{\mathrm{FF}}_{\mathrm{eff}}$
$(\psi_0\psi_{3/2}\mathcal{B})_6$	0.9708(08)	0.9802(06)	0.9854(03)	0.9887(02)	0.9854(03)	0.9883(03)	0.9738(06)	0.9775(05)	0.9844(03)	0.9882(02)

Table 9.8: Averages $\overline{\mathrm{FF}}$ and $\overline{\mathrm{FF}}_{\mathrm{eff}}$ of the fitting factor FF against the 2PN and 3.5PN target models, for the DTFs and for the standard SPA template families, as computed on our BBH Monte Carlo populations. The numbers in parentheses give the estimated Monte Carlo errors on the last two digits of $\overline{\mathrm{FF}}$ and $\overline{\mathrm{FF}}_{\mathrm{eff}}$.

	2PN target model	
	$(10+1.4)M_\odot$	
	$\overline{\mathrm{FF}}$	$\overline{\mathrm{FF}}_{\mathrm{eff}}$
SPAs	0.7800(34)	0.8169(37)
SPAc	0.7747(49)	0.8129(54)
$(\psi_0\psi_{3/2})_2$	0.7807(41)	0.8316(46)
$(\psi_0\psi_{3/2}\mathcal{B})_6$	0.9331(15)	0.9452(14)
	3.5PN target model	
$(\psi_0\psi_{3/2}\mathcal{B})_6$	0.9263(15)	0.9378(14)

Table 9.9: Averages $\overline{\mathrm{FF}}$ and $\overline{\mathrm{FF}}_{\mathrm{eff}}$ of the fitting factor FF against the 2PN and 3.5PN target models, for the DTFs and for the standard SPA template families, as computed on the $(10+1.4)M_\odot$ NS–BH Monte Carlo populations. The numbers in parentheses give the estimated Monte Carlo errors on the last two digits of $\overline{\mathrm{FF}}$ and $\overline{\mathrm{FF}}_{\mathrm{eff}}$.

the SPAs family (solid black line) is consistently less effectual than SPAc, because the target-model ending frequencies are usually different from the Schwarzchild-ISCO frequencies used to terminate the SPAs templates (in the majority of cases, they are higher). The improvement [SPAs to SPAc] in $\overline{\mathrm{FF}}$ is $\simeq 3\%$ for $M \simeq 20$–$25M_\odot$, and $\gtrsim 10\%$ for $M = 30M_\odot$. As pointed out in Chapter 8, it is important to add the frequency-cut parameter $f_{\rm cut}$ whenever the ending frequency is not known very well, but it is expected to fall within the band of good interferometer sensitivity.

2. Although the $(\psi_0\,\psi_{3/2})_2$ DTF (short-dashed green lines) is essentially a reparametrization of SPAc (both families have the $f_{\rm cut}$ parameter), it is slightly more effectual. The reason for this is that the *physical* ranges of M and η used to optimize FF (and in particular the constraint $\eta < 0.25$) limit the ability of the expression $\psi_{\rm SPA}(f)$ to reproduce the phasing of the target. On the contrary, in the $(\psi_0\,\psi_{3/2})_2$ DTF the coefficients of $f^{-5/3}$ and $f^{-2/3}$ are not functions of M and η, but free phenomenological parameters that can achieve the best possible values to match the target phasing. This added freedom does not buy a dramatic improvement for the spinning binaries studied in this chapter, because the SPAc templates are already rather close to the adiabatic target model (except of course for precessional modulations). On the contrary, in Chapter 8 we saw that using unconstrained phenomenological parameters with extended ranges is very important to follow the nonadiabatic dynamics of late inspiral, as predicted by some PN models for nonspinning binaries.

3. The $(\psi_0\,\psi_{3/2}\,\alpha)_4$ DTF (dot-dashed blue lines) introduces the amplitude-remodeling coefficient α. In Chapter 8 we found that α (together with the extension of parameter ranges) helped follow the nonadiabatic dynamics of some target PN models [see Tab. 9.10]. In this chapter, however, the only target model is obtained in the adiabatic limit, so the frequency-domain amplitude (except of course for the modulations due to precession) is always very close to the Newtonian expression $f^{-7/6}$. As a result, the improvement [$(\psi_0\,\psi_{3/2})_2$ to $(\psi_0\,\psi_{3/2}\,\alpha)_4$] in $\overline{\mathrm{FF}}$ is only $\simeq 0.3$–1.6%, while (at least according to the simple Gaussian analysis of Sec. 9.5.2) the detection threshold increases by $\simeq 4\%$ (although this number does not take into account the $\phi^\alpha = 0$ constraint). It seems therefore that the $(\psi_0\,\psi_{3/2}\,\alpha)_4$ DTF is not a useful upgrade of $(\psi_0\,\psi_{3/2})_2$ for the purpose of detecting the signals emitted by precessing binaries.

4. The $(\psi_0\,\psi_{3/2}\,\mathcal{B})_6$ DTF [lighter–red solid lines] includes modulational corrections for both amplitude and phase. The resulting improvement in $\overline{\mathrm{FF}}$ over the SPA families is remarkable (for BBHs, 8–22% over SPAs, and 6–10% over SPAc; for NS–BH binaries, 20% over both). How-

BBHs and $(10 + 1.4)M_\odot$ NS–BH binaries, we find slightly higher numbers for SPAs. In these lighter systems, SPAc has no advantage over SPAs because the ending frequency is above the range of good detector sensitivity, so the FFs should be the same. However, evaluating the effectualness of SPAc requires a three-parameter numerical maximization of the overlap, which is inevitably less precise than the two-parameter maximization needed for SPAs. So numerical error explains the discrepancy.

	FF against selected PN models in Chapter 8, for the SPAc and $(\psi_0\psi_{3/2}\alpha)$ template families											
	T(2,2)		T(3,3.5,$\hat{\theta}=2$)		P(2,2.5)		P(3,3.5,$\hat{\theta}=2$)		EP(2,2.5)		EP(3,3.5,$\hat{\theta}=2$)	
	SPAc	$(\psi_0\psi_{3/2}\alpha)_4$	SPAc	$(\psi_0\psi_{3/2}\alpha)_4$	SPAc	$(\psi_0\psi_{3/2}\alpha)_4$	SPAc	$(\psi_0\psi_{3/2}\alpha)_4$	SPAc	$(\psi_0\psi_{3/2}\alpha)_4$	SPAc	$(\psi_0\psi_{3/2}\alpha)_4$
$(10+10)M_\odot$	0.984	0.992	0.984	0.988	0.979	0.985	0.959	0.990	0.988	0.994	0.949	0.994
$(20+5)M_\odot$	0.970	0.992	0.960	0.986	0.950	0.978	0.968	0.985	0.930	0.993	0.967	0.993
$(20+10)M_\odot$	0.964	0.989	0.959	0.986	0.925	0.977	0.964	0.986	0.978	0.993	0.982	0.993
$(15+15)M_\odot$	0.939	0.989	0.941	0.987	0.931	0.980	0.967	0.987	0.971	0.991	0.983	0.991

Table 9.10: Fitting factors against selected PN models of *nonspinning* binaries (see Chapter 8), for the SPAc and $(\psi_0\,\psi_{3/2}\,\alpha)_4$ template families. Notice that the $(\psi_0\,\psi_{3/2}\,\alpha)_4$ DTF yields consistently higher FFs.

ever, the effect of the modulational terms is seen best by comparing $(\psi_0\,\psi_{3/2}\,\mathcal{B})_6$ to $(\psi_0\,\psi_{3/2})_2$: we get an improvement of 5–9% for BBHs, and 20% for NS–BH binaries. This numbers should be compared with the projected increase $\simeq 8\%$ in the detection threshold (Sec. 9.5.2).

5. For the $(\psi_0\,\psi_{3/2}\,\mathcal{B}')_6$ DTF, where the frequency dependence of the modulating terms is $f^{-2/3}$ rather than f^{-1}, fitting factors are not significantly different from $(\psi_0\,\psi_{3/2}\,\mathcal{B})_6$. Therefore we do not show these numbers. Tables 9.8 and 9.9 also contain a few FFs computed against the 3.5PN order target model (with $\widehat{\theta}=0$). The FFs, shown for the $(\psi_0\psi_{3/2}\mathcal{B})_6$ DTF, are essentially in line with their 2PN counterparts.

Our results suggest two strategies to search for the signals from the precessing BBHs examined in this chapter. We can try to follow the modulations induced by precession, using a DTF similar to $(\psi_0\,\psi_{3/2}\,\mathcal{B})_6$; or we can just use $(\psi_0\,\psi_{3/2})_2$, which is considerably better than SPAs (mostly because of $f_{\rm cut}$), and slightly better than SPAc (because of the extended parameter range). The gain in FF when we upgrade $(\psi_0\,\psi_{3/2})_2$ to $(\psi_0\,\psi_{3/2}\,\mathcal{B})_6$ is offset by a similar increase in the detection threshold, but the latter increase might be contained by reducing the range of the allowed α_k, or by other data-analysis considerations that do come into the simple Gaussian analysis of Sec. 9.5.2.

Figure 9.12 shows the projection of the 2PN target waveforms onto the $(\psi_0,\psi_{3/2})$ section of the $(\psi_0\psi_{3/2})_2$ parameter space; Fig. 9.13 shows the projections of the waveforms onto the $(\psi_0,\psi_{3/2})$ and $(\psi_0,\mathcal{B})$ sections of the $(\psi_0\,\psi_{3/2}\,\mathcal{B})_6$ parameter space. It is interesting to notice that, with either strategy, the ranges of ψ_0 and $\psi_{3/2}$ needed to match effectually the signals in our populations are essentially the same found in Chapter 8 to match the signals predicted by a variety of PN models for BBHs without spins. In Figs. 9.12 and 9.13 these ranges are delimited by the thick dashed lines; the thin *mass lines* represent the range of detection templates needed to match effectually the signals predicted by different PN models for the same binary masses. As we can see, the projections of the spinning-binary signals are smeared around the nonspinning-binary mass lines with the same masses.

Thus, a signal search based on the $(\psi_0\,\psi_{3/2})_2$ DTF is a good starting point for both nonspinning and spinning binaries. It might also pay off, depending on the results of a more realistic evaluation of false-alarm probabilities, to upgrade this DTF to $(\psi_0\,\psi_{3/2}\,\alpha)_4$, with improved performance for

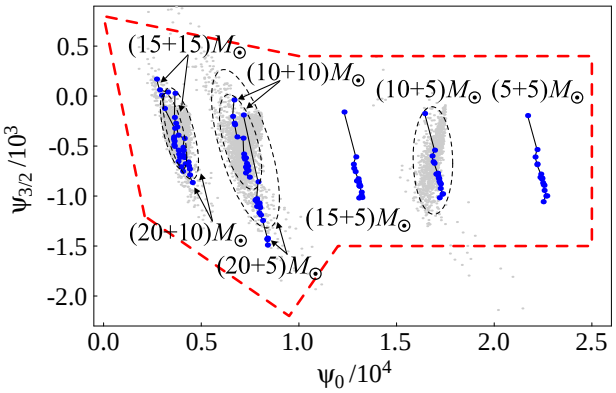

Figure 9.12: Projection of the 2PN target signals onto the $(\psi_0\,\psi_{3/2})_2$ DTF. For the $(10+10)M_\odot$, $(15+15)M_\odot$, $(20+5)M_\odot$, $(7+5)M_\odot$, and $(20+10)M_\odot$ BBHs in our Monte Carlo populations, the clusters of gray dots show the projection of the 2PN target waveforms onto the $(\psi_0, \psi_{3/2})$ parameter plane of the $(\psi_0\,\psi_{3/2})_2$ DTF (the projection of a given target signal is given by the values of ψ_0 and $\psi_{3/2}$ that maximize the FF; here $f_{\rm cut}$ is not shown). For each set of masses, we draw a dashed ellipse centered on the parameter-space baricenter of the dots, and sized to include 90% of the dots (the proportions of the axes follow the two-dimensional quadratic moments of the dots). The larger blue dots, joined by the thin lines (*mass lines*), show the projections of the nonspinning PN models studied in Chapter 8, for the same sets of masses plus $(5+5)M_\odot$ and $(10+5)M_\odot$; each line joins signals with the same binary masses, but obtained from different PN target models. As we can see, for each set of masses, the projections of the spinning-binary signals are clustered around the corresponding mass line; moreover, all the projections fall within the region (delimited by the thick dashed lines) suggested in Chapter 8 to match all the nonspinning PN models.

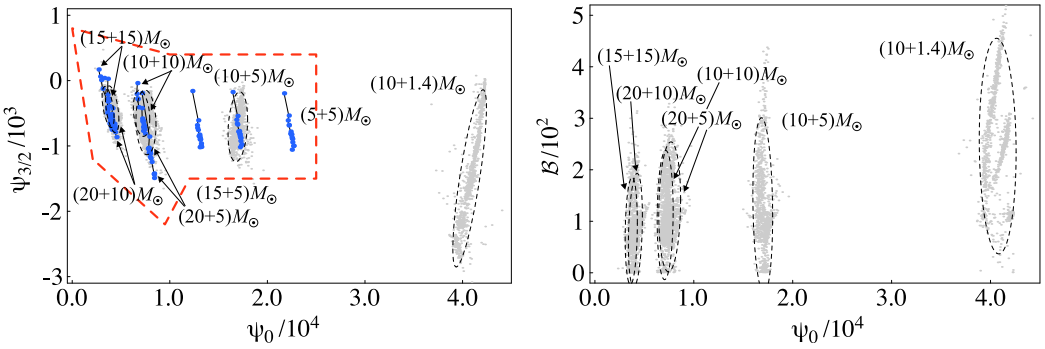

Figure 9.13: Projection of the 2PN target signals onto the $(\psi_0\,\psi_{3/2}\,\mathcal{B})_6$ DTF. For the $(10+10)M_\odot$, $(15+15)M_\odot$, $(20+5)M_\odot$, $(7+5)M_\odot$, and $(20+10)M_\odot$ BBHs, and for the $(10+1.4)M_\odot$ NS–BH binaries in our Monte Carlo populations, the clusters of gray dots show the projection of the 2PN target waveforms onto the $(\psi_0, \psi_{3/2})$ [on the left] and $(\psi_0, \mathcal{B})$ [on the right] parameter plane of the $(\psi_0\,\psi_{3/2}\,\mathcal{B})_6$ DTF. For each set of masses, we draw a dashed ellipse centered on the parameter-space baricenter of the dots, and sized to include 90% of the dots (the proportions of the axes follow the two-dimensional quadratic moments of the dots). The nonspinning-model mass lines and the boundary of the suggested parameter ranges are shown as in Fig. 9.12.

nonspinning but nonadiabatic BBHs, as shown in Chapter 8; or even to $(\psi_0\,\psi_{3/2}\,\mathcal{B})_6$, with the best FFs for spinning binaries and without any deterioration for nonspinning ones.

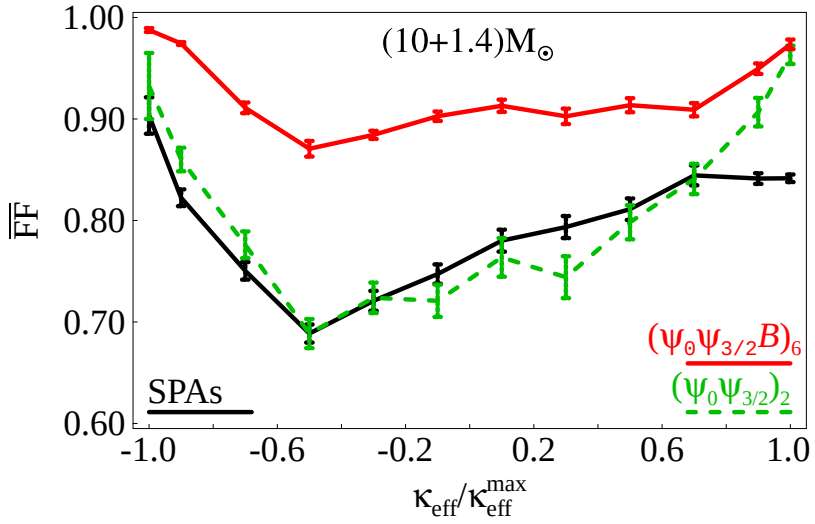

Figure 9.14: Average fitting factor for the DTFs and for the SPAs template families for $(10+1.4)M_\odot$ NS–BH binaries, plotted against the initial $\kappa_{\rm eff} = \hat{\mathbf{L}}_N \cdot \mathbf{S}_{\rm eff}$. The vertices of the segmented curves show the FF averaged on the sets of samples that fall within the equispaced $\kappa_{\rm eff}$ bins $[-1,-0.8)$, $[-0.8,-0.6)$, …, $[0.8,1]$. The error bars show the sampling error on the bin averages. We plot also two additional vertices, aligned with the abscissae -1 and 1, which show the FF averaged over the $\kappa_{\rm eff}$ bins $[-1,-0.98)$ and $[0.98,1]$.

9.6.4 Modulated DTFs for NS–BH binaries

Let us now look in detail at the FFs achieved by the DTFs and standard template families against the signals generated by $(10+1.4)M_\odot$ NS–BH binaries where the BH is spinning rapidly (see Tab. 9.9 and Figs. 9.11 and 9.14). First of all, we notice that there is little difference between the performance of the SPAs and SPAc templates, because the ending frequency lies outside of the band of good interferometer sensitivity. Furthermore, the number of GW cycles within this band is very high, so it is crucial that a DTF reproduce very accurately the evolution of the GW phase; so using the $(\psi_0\,\psi_{3/2})_2$ DTF improves only slightly on the performance of the SPA templates. Introducing precessional corrections brings about a dramatic change: for the $(\psi_0\,\psi_{3/2}\,\mathcal{B})_6$ DTF, the increase in $\overline{\rm FF}$ and $\overline{\rm FF}_{\rm eff}$ with respect to SPA is respectively 20% and 16%, which is enough to justify the introduction of six α_k coefficients, according the Gaussian analysis of Sec. 9.5.2.

The dependence of the FF on the spin configuration is shown in Fig. 9.14. For the NS–BH signals in our Monte Carlo population, Figs. 9.15 and 9.16 show the template parameters ψ_0, $\psi_{3/2}$, and $\mathcal{B}$ that maximize the overlap plotted against the initial κ (conserved in NS–BH binaries). In the left panel, we see that the parameter ψ_0, which is related to the Newtonian chirp mass, has only a weak dependence on κ (it varies by $\sim 8\%$); on the other hand, the parameter $\psi_{3/2}$ has a strong dependence. A plausible explanation is that the SO term in the SPA phasing is formally 1.5PN [see Eqs. (9.92) and (9.93)], and so is the term $\psi_{3/2} f$ in $\psi_{\rm NM}(f)$, which takes on the job, as it were, of

reproducing the nonmodulational effects of the SO coupling. In the right panel, we see that for most of the binary configurations the values of $\mathcal{B}$ cluster around three lines [$\mathcal{B} = 100$, $\mathcal{B} = (1+\kappa)\,110+110$, and $\mathcal{B} = (1+\kappa)\,240+160$]. Further analysis are needed to provide an explanation for this interesting behavior.

Thus, the $(\psi_0\,\psi_{3/2}\,\mathcal{B})_6$ DTF is a good candidate for the data-analysis problem of detecting GW signals from NS–BH binaries with rapidly spinning BHs. However, the analysis of precessional dynamics and GW emission carried out in this chapter suggests an even more specialized DTF, which could be built with the following guidelines.

1. The waveform can be computed directly from Eq. (9.82) (obtained in the precessing convention): the necessary ingredients are the time evolution of the orbital phase Ψ and of the binary polarization tensors $[\mathbf{e}_{+,\times}]_{ij}$, plus the fixed detector polarization tensors $[\mathbf{T}_{+,\times}]_{ij}$.

2. The evolution of Ψ is obtained by solving Eq. (9.1), where $\mathbf{S}_2$ can be set to zero, and $\mathbf{S}_1$ enters only in the *conserved* term $\hat{\mathbf{L}}_N \cdot \mathbf{S}_1$. As a consequence, Eq. (9.1) is effectively uncoupled from the evolution of $\hat{\mathbf{L}}_N$, Eq. (9.9).

3. The evolution of the tensors $[\mathbf{e}_{+,\times}(t)]_{ij}$ is obtained from Eq. (9.71), after integrating Eqs. (9.2) and (9.9) for the coupled evolution of $\hat{\mathbf{L}}_N$ and $\mathbf{S}$, which depends only on $\hat{\mathbf{L}}_N \cdot \mathbf{S}_1$, on S_1 (conserved), and on $\omega(t)$.

4. A source frame attached to the initial configuration of the binary, similar to the frame constructed in Sec. 9.4.1 [see Eqs. (9.73)], can be used to carry out the explicit construction. By way of the initial conditions (9.74)–(9.77), the tensors $\mathbf{e}_{+,\times}$ and the orbital phase Ψ (up to an additive constant Ψ_0) are then well defined as functions of the basic and local binary parameters only. We have therefore completed the specification of the first part of Eq. (9.82), which expresses the components of the mass quadrupole moment.

5. The remaining part of Eq. (9.82), which expresses the projection on the polarization tensor of the detector,

$$P^{ij} \equiv [\mathbf{T}_+]^{ij} F_+ + [\mathbf{T}_\times]^{ij} F_\times, \tag{9.120}$$

   is determined by the directional parameters Θ, φ, ϕ, θ, and ψ, which are now referred to the source frame attached to the binary. When we look for GWs using matched filtering, we can search rapidly over such a parametrization by treating the P^{ij} as extrinsic parameters, along with the time of arrival and the initial orbital phase Ψ_0. The only intrinsic parameters would then be m_1, m_2, S_1, and $\mathbf{S} \cdot \hat{\mathbf{L}}_N$, all of which are conserved.

This family of templates adds a further intrinsic parameter with respect to $(\psi_0\,\psi_{3/2}\,\mathcal{B})_6$, but it has the advantage of producing essentially exact waveforms (valid in the adiabatic regime, and up to

the highest PN order included), and of expressing these waveforms directly in terms of the physical spin parameters S_1 and $\mathbf{S} \cdot \hat{\mathbf{L}}_N$. We believe that the implementation and the false-alarm statistics of this family are worthy of further investigation [31].

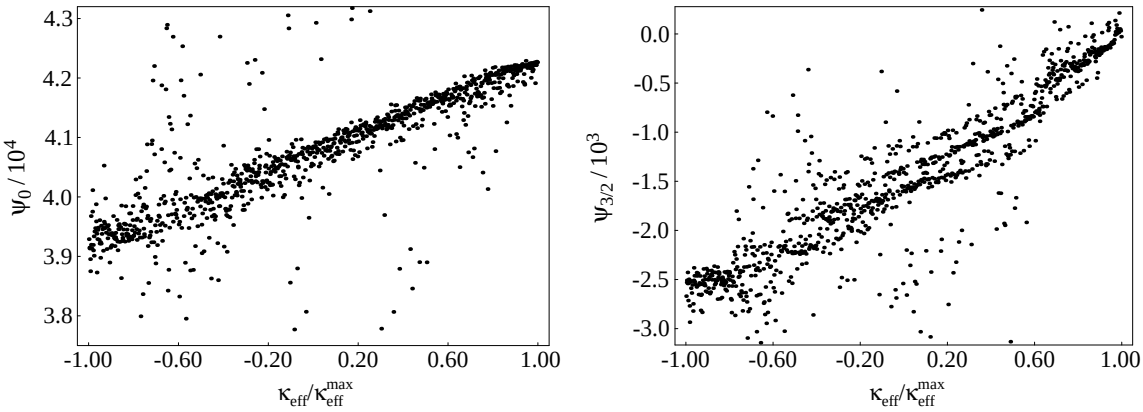

Figure 9.15: Projection of the $(10 + 1.4)M_\odot$ NS–BH target signals (computed at 2PN order) onto the $(\psi_0\,\psi_{3/2}\,\mathcal{B})_6$ DTF. The dots show the values of the ψ_0 (left panel) and $\psi_{3/2}$ (right panel) target parameters that yield maximum overlaps with the signals in the target populations.

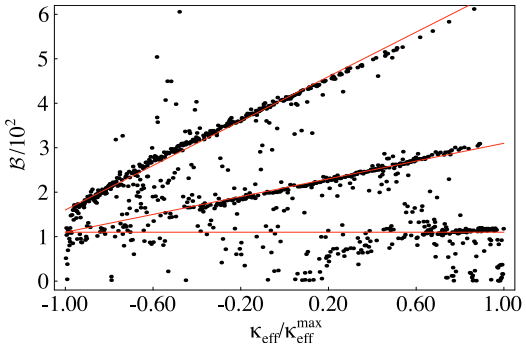

Figure 9.16: Projection of the $(10 + 1.4)M_\odot$ NS–BH target signals (computed at 2PN order) onto the $(\psi_0\,\psi_{3/2}\,\mathcal{B})_6$ DTF. The dots show the values of the $\mathcal{B}$ target parameter that yield maximum overlaps with the signals in the target populations.

9.7 Summary

In Chapter 8, the nonmodulated DTFs $(\psi_0\psi_{3/2})_2$ and $(\psi_0\psi_{3/2}\alpha)_4$ were shown to have FF $\gtrsim$ 0.95 against several nonspinning-BBH target models, obtained under different PN approximation schemes. In this chapter, we have shown that these two families are also rather effectual at matching the signals from BH–BH and NS–BH precessing binaries with single-BH masses between 5 and 20 $M_\odot$ and with maximal BH spins, at least if these signals can be described by an adiabatic sequence of quasi-circular orbits up to 2PN order.

More specifically, for $(7+5)M_\odot$, $(10+10)M_\odot$, $(20+10)M_\odot$, and $(15+15)M_\odot$ BBHs, we obtain $\overline{\mathrm{FF}} \gtrsim 0.93$ and $\overline{\mathrm{FF}}_{\mathrm{eff}} \gtrsim 0.95$. The improvement is 2–16% over Schwarzschild-terminated SPAs templates, thanks largely to the ending-frequency parameter f_{cut}; and 1–2% over SPAc templates, thanks to the effective extension in the range of parameters, released from their functional dependence on the masses of the binary. Although the latter improvement seems negligible, we should keep in mind that $(\psi_0\,\psi_{3/2})_2$ DTFs are also more suitable to match the nonspinning BH binaries studied in Chapter 8 with PN expanded and resummed models. Results are worse for binaries that have smaller mass ratios η, and therefore more GW cycles in the band of good interferometer sensitivity. In this case the modulational effects due to precession become important, and must be included in the detection templates. Indeed, for $(20+5)M_\odot$ BBHs, the $(\psi_0\psi_{3/2})_2$ and $(\psi_0\psi_{3/2}\alpha)_4$ DTFs have $\overline{\mathrm{FF}} \simeq 0.89$ and $\overline{\mathrm{FF}}_{\mathrm{eff}} \simeq 0.92$; for a $(10+1.4)M_\odot$ NS–BH binary, we find $\overline{\mathrm{FF}} \simeq 0.78$, and $\overline{\mathrm{FF}}_{\mathrm{eff}} \simeq 0.83$.

Motivated by these shortcomings, we have investigated in detail the dynamics of precession in these binaries, and we have introduced a new convention to write the GW signal (as computed in the quadrupole approximation) as a function of binary and detector parameters, isolating the oscillatory effects of precession in the evolution of the polarization tensors $[\mathbf{e}_{+,\times}]_{ij}$. As a result, the detector response to GWs can be written as the product of a carrier signal, which very closely resembles the nonspinning signals studied in Chapter 8, and a modulational correction, which can be handled using an extension of Apostolatos' ansatz (9.64). On the basis of these observations, we build the modulated DTF $(\psi_0, \psi_{3/2}\mathcal{B})_6$, which yields $\overline{\mathrm{FF}}$ and $\overline{\mathrm{FF}}_{\mathrm{eff}} \simeq 0.98$–$0.99$ for the BBHs investigated, and $\overline{\mathrm{FF}} \simeq 0.93$, $\overline{\mathrm{FF}}_{\mathrm{eff}} \simeq 0.95$ for $(10+1.4)M_\odot$ NS–BH binaries. This DTF has the advantage that all the modulational parameters (except for $\mathcal{B}$) can be treated as extrinsic parameters, reducing considerably the computational cost of signal searches. According to the simple analysis of Sec. 9.5.2, the detection thresholds for this DTF should be set higher than those for simpler families; still, the gain in FF is still somewhat larger than the increase in the threshold, and more realistic analyses of false-alarm statistics might provide a way to sidestep this difficulty. The same arguments that lead to the $(\psi_0, \psi_{3/2}\mathcal{B})_6$ DTF suggest a new, very promising class of templates for NS–BH binaries, which we discuss briefly in Sec. 9.6.4, and which we plan to investigate more thoroughly elsewhere [31].

We wish to make a few final remarks. First, in this chapter we limited our analysis to compact

objects moving on quasi-circular orbits; from the results on the ending frequencies (see Fig. 9.5) we see that there exist spin initial conditions for which the ending frequencies (end of inspiral) are in the LIGO–VIRGO band. So, in these cases we should use spinning dynamics that goes beyond the adiabatic approximation. This dynamics (without radiation-reaction effects) is already available in the EOB framework [4, 5] thanks to the work of Damour [13]. We plan to investigate the effects of nonadiabatic PN dynamics in the near future.

Second, a few years ago Levin pointed out [32] that spin-spin effects can introduce chaos into the trajectories; as a consequence, the gravitational waveforms would come to depend sensitively on the initial conditions. More studies followed [33, 34]. Considering only conservative dynamics (no RR), Cornish and Levin [34] found some examples of rather eccentric ($e \sim 0.6$ or 0.9) chaotic orbits, and a few quasi-circular chaotic orbits. However, these authors observed that chaos would be damped by RR effects, and that it would not affect the inspiral waveforms, except (perhaps) at the very end (the plunge). Still, at this time the dynamical structure of phase space has not been explored systematically, and a more conclusive study tuned to the LIGO–VIRGO detection problem remains desirable. The analysis of this chapter assumes that, by the time the GW signal enters the band of good detector sensitivity, RR effects have circularized the orbit, and have brought the binary into the adiabatic regime, which is valid until the MECO. We did not try to perturb the initial conditions slightly and to investigate the resulting changes in the orbital evolution and in the waveforms.

Third, we have evaluated the performance of our DTFs by averaging over *uniform* distributions of the initial spin angles. Of course it would be preferable to assume more realistic, nonuniform distributions derived from astrophysical considerations. Some results for spin distributions in BBHs (with only one spinning BH), and in NS–BH binaries were obtained by Kalogera using population-synthesis techniques [35]. In particular, Kalogera found that 30–80% of the NS–BH binaries that will coalesce within a Hubble time can have a tilt angle (the angle between the spin and the orbital angular momentum) larger than 30 degrees. These results assume that the spinning BH in the binary forms first, and that its spin is aligned with the orbital angular momentum; the tilt angle originates from the supernova explosion that forms the NS. For the case of the binaries formed in globular clusters, there is no theoretical argument to suggest any particular spin distribution.

Finally, recent analyses of spin-spin effects in the PN inspiral equations [36] suggest that, for comparable-mass BBHs, by the time the GW signal enters the band of good interferometer sensitivity the two BH spins may have become roughly *locked* into a fixed relative configuration. If these results are confirmed, they could provide preferred initial spin conditions, and simplify the data-analysis problem for comparable mass binaries, by reducing the variability of expected GW signals.

9.8 Appendix. Validity of the adiabatic sequence of spherical orbits

In the target model defined in Sec. 9.2.1, the inspiral of the two compact bodies is described as an adiabatic sequence of spherical orbits. In this Appendix we wish to discuss the validity of this assumption. Introducing the orthonormal basis $(\hat{\lambda}, \hat{\mathbf{n}}, \hat{\mathbf{L}}_N)$, where $\hat{\mathbf{n}} = \mathbf{x}/r$, $\hat{\mathbf{L}}_N = \mathbf{L}_N/L_N$, $\hat{\lambda} = \hat{\mathbf{L}}_N \times \hat{\mathbf{n}}$ and $\mathbf{L}_N = \mu\, \mathbf{x} \times \mathbf{v}$ (with μ the reduced mass), it is straightforward to write the equations of motion as [see Eqs. (4.1) of Ref. [15]; we use the relations $\mathbf{v} = \dot{r}\, \hat{\mathbf{n}} + r\, \omega\, \hat{\lambda}, v^2 = \dot{r}^2 + r^2\, \omega^2$]:

$$\hat{\mathbf{n}} \cdot \mathbf{a} = \ddot{r} - r\, \omega^2 \,, \tag{9.121}$$

$$\hat{\lambda} \cdot \mathbf{a} = r\, \dot{\omega} + 2\dot{r}\, \omega \,, \tag{9.122}$$

$$\hat{\mathbf{L}}_N \cdot \mathbf{a} = -r\, \omega\, \frac{d\hat{\mathbf{L}}_N}{dt} \cdot \hat{\lambda} \,, \tag{9.123}$$

where $\mathbf{a}$ is the acceleration in harmonic gauge given by Eqs. (2.2a), (2.2c) of Ref. [15]. If we impose $\dot{r} = 0 = \ddot{r}$, Eq. (9.122) then implies $\dot{\omega} = 0$; and from Eq. (9.121) we get

$$r^2\, \omega^2 = \frac{1}{r} \left(1 - \frac{2}{r^2}\, \mathbf{L}_N \cdot \mathbf{S}_\omega \right) , \qquad \mathbf{S}_\omega \equiv \left(1 + \frac{3}{2}\, \frac{m_2}{m_1} \right) \mathbf{S}_1 + \left(1 + \frac{3}{2}\, \frac{m_1}{m_2} \right) \mathbf{S}_2 \,, \tag{9.124}$$

where for simplicity we have set $M = 1$. Although spherical orbits (orbits where both r and ω remain constant) exist at any given instant, they are not preserved along dynamical evolution because the quantity $\mathbf{L}_N \cdot \mathbf{S}_\omega$ that appears in Eq. (9.124) is not conserved. Indeed, averaging over an orbit [8] (and, for simplicity, neglecting spin-spin effects), we get

$$\left\langle \frac{d\mathbf{L}_N}{dt} \right\rangle = \frac{2\mu}{r^3} \mathbf{S}_{\rm eff} \times \mathbf{L}_N \,, \qquad \mathbf{S}_{\rm eff} \equiv \left(1 + \frac{3}{4}\, \frac{m_2}{m_1} \right) \mathbf{S}_1 + \left(1 + \frac{3}{4}\, \frac{m_1}{m_2} \right) \mathbf{S}_2 \,, \tag{9.125}$$

where $\langle A \rangle$ denotes the quantity A when the spin-orbit (and spin-spin) terms have been averaged over an orbit. Using the precession equations for the spins we derive

$$\left\langle \frac{d(\mathbf{L}_N \cdot \mathbf{S}_\omega)}{dt} \right\rangle = -3 \frac{(m_1^2 - m_2^2)}{m_1\, m_2}\, \mathbf{L}_N \cdot (\mathbf{S}_1 \times \mathbf{S}_2)\, \frac{1}{r^3} \,. \tag{9.126}$$

Hence, because the circular-orbit condition is not preserved during the evolution, either $\langle \dot{\omega} \rangle \neq 0$ or $\langle \dot{r} \rangle \neq 0$ (or both).

Let us now see how Eq. (9.1) for $\dot{\omega}$ changes if effects of this kind are included. The usual argument

[8] We are implicitly assuming that the precession frequency ω_p is much smaller than both the orbital frequency and the effective radiation-reaction frequency $1/T_{\rm RR}$, where $T_{\rm RR}$ is the radiation-reaction folding time.

[15, 20] used to obtain the adiabatic evolution of ω rests on the energy-balance equation,

$$\dot{E}_{\rm RR} = \frac{d}{dt} E(\omega, \hat{\mathbf{L}}_N, \mathbf{S}_1, \mathbf{S}_2) = \frac{\partial E}{\partial \omega}\dot{\omega} + \left(\frac{\partial E}{\partial \hat{\mathbf{L}}_N} \cdot \dot{\hat{\mathbf{L}}}_N + \frac{\partial E}{\partial \mathbf{S}_1} \cdot \dot{\mathbf{S}}_1 + \frac{\partial E}{\partial \mathbf{S}_2} \cdot \dot{\mathbf{S}}_2 \right) , \tag{9.127}$$

where

$$\begin{aligned} & E(\omega, \hat{\mathbf{L}}_N, \mathbf{S}_1, \mathbf{S}_2) \\ = \; & -\frac{\mu}{2} (M\omega)^{2/3} \\ & \left\{ 1 - \frac{(9+\eta)}{12} (M\omega)^{2/3} + \frac{8}{3M^2} \hat{\mathbf{L}}_N \cdot \mathbf{S}_{\rm eff} (M\omega) \right. \\ & \left. + \left[\frac{1}{24}(-81 + 57\eta - \eta^2) + \frac{1}{\eta M^4} \left[(\mathbf{S}_1 \cdot \mathbf{S}_2) - 3(\hat{\mathbf{L}}_N \cdot \mathbf{S}_1)(\hat{\mathbf{L}}_N \cdot \mathbf{S}_2) \right] \right] (M\omega)^{4/3} \right\} \end{aligned} \tag{9.128}$$

is the orbital energy evaluated at Newtonian order, but including spin-orbit and spin-spin effects, and where $\dot{E}_{\rm RR}$ is the RR energy loss [20, 15]. From Eqs. (9.128), (9.9), (9.2) and (9.3), we notice that the sum of the last three terms in parentheses in Eq. (9.127) does not vanish: at leading order, its value is

$$\dot{E}_{\rm extra} = \frac{1}{4} \frac{(m_1 - m_2)}{M} \eta^2 \, \chi_1 \, \chi_2 \, (M\omega)^{11/3} \left[\left(\hat{\mathbf{S}}_1 \times \hat{\mathbf{S}}_2 \right) \cdot \hat{\mathbf{L}}_N \right] . \tag{9.129}$$

This expression is zero if masses are equal, or if spins are either aligned or antialigned. Retaining the term (9.129) in the calculation yields an additional contribution in the evolution of ω, with a leading order correction

$$\frac{\dot{\omega}_{\rm extra}}{\omega^2} = \frac{3}{4} \frac{(m_1 - m_2)}{M} \eta \, \chi_1 \, \chi_2 \, (M\omega)^2 \left[\left(\hat{\mathbf{S}}_1 \times \hat{\mathbf{S}}_2 \right) \cdot \hat{\mathbf{L}}_N \right] . \tag{9.130}$$

Thus, compared with the other terms in Eq. (9.1), $\dot{\omega}_{\rm extra}$ appears formally at 0.5 PN order (very low!) in the expansion of $\dot{\omega}$. Note that the spin-orbit term in the energy (9.128), combined with the leading-order precessions, does not produce such a term; this makes the adiabatic approach fully consistent up to 1.5PN order. In fact, $\dot{E}_{\rm extra}$ originates from taking the derivative of $\dot{E}_{\rm SO}$ and using next-to-leading order terms in the precession equations, and the derivative $\dot{E}_{\rm SS}$ while using the leading-order terms in the precession equations.

However, the effect of this term in the regime that we consider is not as large as suggested by its formal PN order. For example, under the worst possible assumption (that the geometric factor $[(\hat{\mathbf{S}}_1 \times \hat{\mathbf{S}}_2) \cdot \hat{\mathbf{L}}_N]$ has always the maximum value of one, and that spins are maximal), we get the correction

$$\frac{\Delta\Psi_{\rm extra}}{2\pi} = \frac{1}{2\pi} \frac{25}{16384} \frac{\sqrt{1-4\eta}}{\eta} \left[(M\omega_f)^{-4/3} - (M\omega_i)^{-4/3} \right] \tag{9.131}$$

to the number of orbital cycles, where ω_i and ω_f are the initial and final orbital frequencies under

consideration. This is formally a 0.5PN correction, as can be seen by comparing it with Eq. (4.16) of Ref. [15]. Nevertheless, for (say) a $(20+5)M_\odot$ BBH, this correction will be at most 0.34 orbital cycles from $\omega_i = \pi \times 30\,\mathrm{Hz}$ to $\omega_i = \pi \times 400\,\mathrm{Hz}$, to be compared with a baseline of 52 orbital cycles from the Newtonian term and 8 from the 1PN term. For a $(10+1.4)M_\odot$ binary, the correction will be 1.6 orbital cycles, to be compared with 175 orbital cycles from the Newtonian term and 30 from the 1PN term. The correction is small because, although the PN order is formally low, the numerical coefficient of the geometric factor $[(\hat{\mathbf{S}}_1 \times \hat{\mathbf{S}}_2) \cdot \hat{\mathbf{L}}_N]$ is very small.

So far, we have assumed $[(\hat{\mathbf{S}}_1 \times \hat{\mathbf{S}}_2) \cdot \hat{\mathbf{L}}_N] \sim 1$ along the evolution. Let us now estimate the more important effect that comes from the precession of $\hat{\mathbf{L}}_N$, $\mathbf{S}_1$ and $\mathbf{S}_2$, which is especially important for binaries with small mass ratios, which have longer RR time scales and more precessional cycles. At the leading order (with $M=1$)

$$\frac{d}{dt}\left[\left(\hat{\mathbf{S}}_1 \times \hat{\mathbf{S}}_2\right) \cdot \hat{\mathbf{L}}_N\right] = \frac{3}{2}(m_1 - m_2)\,\omega^{5/3}\,\left[\hat{\mathbf{S}}_1 \cdot \hat{\mathbf{S}}_2 - (\hat{\mathbf{S}}_1 \cdot \hat{\mathbf{L}}_N)\,(\hat{\mathbf{S}}_2 \cdot \hat{\mathbf{L}}_N)\right] + \mathcal{O}(\omega^2)\,, \tag{9.132}$$

and

$$\frac{d}{dt}\left[\hat{\mathbf{S}}_1 \cdot \hat{\mathbf{S}}_2 - (\hat{\mathbf{S}}_1 \cdot \hat{\mathbf{L}}_N)(\hat{\mathbf{S}}_2 \cdot \hat{\mathbf{L}}_N)\right] = -\frac{3}{2}(m_1 - m_2)\,\omega^{5/3}\left[\left(\hat{\mathbf{S}}_1 \times \hat{\mathbf{S}}_2\right) \cdot \hat{\mathbf{L}}_N\right] + \mathcal{O}(\omega^2)\,. \tag{9.133}$$

Combining the above equations, we get (at leading order)

$$\frac{d^2}{dt^2}\left[\left(\hat{\mathbf{S}}_1 \times \hat{\mathbf{S}}_2\right) \cdot \hat{\mathbf{L}}_N\right] \simeq -\frac{9}{4}(m_1 - m_2)^2\,\omega^{10/3}\,\left[\left(\hat{\mathbf{S}}_1 \times \hat{\mathbf{S}}_2\right) \cdot \hat{\mathbf{L}}_N\right]\,. \tag{9.134}$$

This means that the geometric factor $[(\hat{\mathbf{S}}_1 \times \hat{\mathbf{S}}_2) \cdot \hat{\mathbf{L}}_N]$ oscillates around zero with a time scale $\sim \omega^{-5/3}$. Thus the effect of $\dot{\omega}_{\rm extra}$ accumulates only within this timescale, which is 1.5 PN orders shorter than the RR timescale. Therefore, we expect that the real $\Delta\Psi_{\rm extra}$ will be even smaller than the formal prediction given by Eq. (9.131), and that it will contribute effectively at 2PN order. As a check, we evaluated the FF between the gravitational waveforms obtained, for a $(10+1.4)M_\odot$ binary, by first including and then dropping the extra term in $\dot{\omega}$. We found that the FF is $\simeq 0.99$. On the basis of this last check and of the analysis outlined above, we conclude that the adiabatic assumption is quite adequate for the purposes of this chapter.

9.9 Appendix. Proof that the precessing convention yields $\omega = \dot{\Phi}_S$

First of all, it is easy to confirm that, as long as $\mathbf{e}_{1,2}(0)$ and $\hat{\mathbf{L}}_N(0)$ form an orthonormal basis at some initial time, the evolution equation $\dot{\mathbf{e}}_{1,2} = \boldsymbol{\Omega}_e \times \mathbf{e}_{1,2}$ will always keep the triplet an orthonormal basis. It is then always possible to have a $\Phi(t)$, such that

$$\hat{\mathbf{n}}(t) = \mathbf{e}_1 \cos\Phi(t) + \mathbf{e}_2 \sin\Phi(t)\,, \quad \hat{\lambda}(t) = -\mathbf{e}_1 \sin\Phi(t) + \mathbf{e}_2 \cos\Phi(t)\,. \tag{9.135}$$

Taking the time derivative of $\hat{\mathbf{n}}(t)$, we have

$$\dot{\hat{\mathbf{n}}} = \dot{\Phi}\hat{\lambda} + \boldsymbol{\Omega}_e \times \hat{\mathbf{n}}, \tag{9.136}$$

Now, the adiabatic condition for a sequence of circular orbits states that $\dot{\hat{\mathbf{n}}} = \omega\hat{\lambda}$, so we have

$$\dot{\hat{\mathbf{n}}} = \omega\hat{\lambda} = \dot{\Phi}\hat{\lambda} + \boldsymbol{\Omega}_e \times \hat{\mathbf{n}}. \tag{9.137}$$

By definition [Eq. (9.72)], $\boldsymbol{\Omega}_e$ has no components along $\mathbf{e}_3 \equiv \hat{\mathbf{L}}_N$. It also has no components along $\hat{\lambda}$, because

$$\boldsymbol{\Omega}_e \times \dot{\hat{\mathbf{L}}}_N = \dot{\hat{\mathbf{L}}}_N = \dot{\hat{\mathbf{n}}} \times \hat{\lambda} + \hat{\mathbf{n}} \times \dot{\hat{\lambda}} = \omega\hat{\lambda} \times \hat{\lambda} + \hat{\mathbf{n}} \times (-\dot{\Phi}\hat{\mathbf{n}} + \boldsymbol{\Omega}_e \times \hat{\lambda}) \tag{9.138}$$

$$= \boldsymbol{\Omega}_e(\hat{\mathbf{n}} \cdot \hat{\lambda}) - \hat{\lambda}(\hat{\mathbf{n}} \cdot \boldsymbol{\Omega}_e) \propto \hat{\lambda}, \tag{9.139}$$

where in the last step we used $\hat{\mathbf{n}} \cdot \hat{\lambda} = 0$ and the vector–triple-product rule. It follows that $\boldsymbol{\Omega}_e$ lies along $\hat{\mathbf{n}}$, and therefore $\boldsymbol{\Omega}_e \times \hat{\mathbf{n}} = 0$. Equation (9.137) then gives the desired result, $\dot{\Phi} = \omega$, i.e., $\Phi(t) = \Psi(t) + \text{const}$.

9.10 Bibliography

[1] A. Abramovici et al., *Science* **256**, 325 (1992); B. Caron et al., *Class. Quantum Grav.* **14**, 1461 (1997); H. Lück et al., *Class. Quantum Grav.* **14**, 1471 (1997); M. Ando et al., *Phys. Rev. Lett.* **86**, 3950 (2001).

[2] B. S. Sathyaprakash and S. V. Dhurandhar, *Phys. Rev. D* **44**, 3819 (1991); L. S. Finn, *Phys. Rev. D* **46**, 5236 (1992); S. V. Dhurandhar and B. S. Sathyaprakash, *Phys. Rev. D* **49**, 1707 (1994); B. S. Sathyaprakash, *Phys. Rev. D* **50**, R7111 (1994); C. Cutler and É. É. Flanagan, *Phys. Rev. D* **49**, 2658 (1994); B. J. Owen, *Phys. Rev. D* **53**, 6749 (1996); B. J. Owen and B. Sathyaprakash, *Phys. Rev. D* **60**, 022002 (1999); É. É. Flanagan and S. A. Hughes, *Phys. Rev. D* **57**, 4535 (1998); *ibid.*, 4566 (1998); T. Damour, B. R. Iyer and B. S. Sathyaprakash, *Phys. Rev. D* **62**, 084036 (2000); F. A. Jenet and T. Prince, *Phys. Rev. D* **62**, 122001 (2000); A. E. Chronopoulos and T. A. Apostolatos, *Phys. Rev. D* **64**, 042003 (2001); E. Porter, *Class. Quant. Grav.* **19**, 4343 (2002).

[3] T. Damour, B. R. Iyer and B. S. Sathyaprakash, *Phys. Rev. D* **57**, 885 (1998).

[4] A. Buonanno and T. Damour, *Phys. Rev. D* **59**, 084006 (1999); **62**, 064015 (2000).

[5] T. Damour, P. Jaranowski and G. Schäfer, *Phys. Rev. D* **62**, 084011 (2000).

[6] T. Damour, *300 Years of Gravitation*, S. W. Hawking and W. Israel, eds. (Cambridge University Press, Cambridge, England, 1987); L. Blanchet, *Living Reviews in Relativity*, 2002-3 (2002), `http://www.livingreviews.org/Articles/Volume5/2002-3blanchet`.

[7] T. Damour, B. R. Iyer and B. S. Sathyaprakash, *Phys. Rev. D* **63**, 044023 (2001); **66**, 027502 (2002).

[8] T. Damour, B. R. Iyer, P. Jaranowski and B. S. Sathyaprakash, *Phys.Rev. D* **67**, 064028 (2003).

[9] T. A. Apostolatos, C. Cutler, G. J. Sussman and K. Thorne, *Phys. Rev. D* **49**, 49 (1994).

[10] T. A. Apostolatos, *Phys. Rev. D* **54**, 2438 (1996).

[11] P. Grandclément, V. Kalogera and A. Vecchio, *Phys. Rev. D* **67**, 042003 (2003).

[12] P. Grandclément and V. Kalogera, *Phys. Rev. D*, in print (2003).

[13] T. Damour, *Phys. Rev. D* **64**, 124013 (2001).

[14] L. S. Finn and D. F. Chernoff, *Phys. Rev. D* **47**, 2198 (1993).

[15] L. E. Kidder, *Phys. Rev. D* **52**, 821 (1995).

[16] L. Blanchet, T. Damour, B. R. Iyer, C. M. Will and A. G. Wiseman, *Phys. Rev. Lett.* **74**, 3515 (1995); L. Blanchet, T. Damour and B. R. Iyer, *Phys. Rev. D* **51**, 536 (1995); C. M. Will and A. G. Wiseman, *Phys. Rev. D* **54**, 4813 (1996).

[17] L. Blanchet, B. R. Iyer, C. M. Will and A. G. Wiseman, *Class. Quantum Grav.* **13**, 575 (1996).

[18] L. Blanchet, *Phys. Rev. D* **54**, 1417 (1996); L. Blanchet, *Class. Quantum Grav.* **15**, 113 (1998).

[19] L. Blanchet, G. Faye, B. R. Iyer, B. Joguet, *Phys. Rev. D* **65**, 061501 (2002); L. Blanchet, B. R. Iyer and B. Joguet, *Phys. Rev. D* **65**, 064005 (2002).

[20] L. E. Kidder, C. M. Will and A. G. Wiseman, *Phys. Rev. D* **47**, 4183 (R) (1993).

[21] T. Damour, P. Jaranowski and G. Schäfer, *Phys. Lett. B* **513**, 147 (2001).

[22] P. Jaranowski and G. Schäfer, *Phys. Rev. D* **57**, 7274 (1998); *ibid.* **60**, 124003 (1999); T. Damour, P. Jaranowski and G. Schäfer, *Phys. Rev. D* **62**, 044024 (2000); *ibid.*, 021501(R) (2000); **63**, 044021 (2001).

[23] L. Blanchet, *Phys. Rev. D* **65**, 124009 (2002).

[24] N. Wex, *Class. Quantum Grav.* **12**, 983 (1995).

[25] É. É. Flanagan and S. A. Hughes, *Phys. Rev. D* **57**, 4535 (1998).

[26] T. A. Apostolatos, *Phys. Rev. D* **52**, 605 (1995).

[27] B. F. Schutz, in *The Detection of Gravitational Radiation*, D. Blair, ed. (Cambridge University Press, Cambridge, England, 1989).

[28] W. H. Press, S. A. Teukolsky, W. T. Vetterling and B. P. Flannery, *Numerical recipes in C: the art of scientific computing* (Cambridge University Press, Cambridge, England, 1992).

[29] B. Allen et al., *Phys. Rev. Lett.* **83**, 1498 (1999).

[30] R. G. Miller, *Biometrika* **61**, 1 (1974).

[31] Y. Pan, A. Buonanno, Y. Chen, and M. Vallisneri, in preparation.

[32] J. Levin, *Phys. Rev. Lett.* **84**, 3515 (2000); J. Levin, *Phys. Rev. D* **67**, 044013 (2003).

[33] J. D. Schnittman and F. Rasio, *Phys. Rev. Lett.* **87**, 121101 (2001).

[34] N. J. Cornish and J. Levin, `gr-qc/0207016`; N. J. Cornish and J. Levin, *Phys. Rev. Lett.* **89**, 179001 (2002).

[35] V. Kalogera, *Astrophysical Journal* **541**, 319 (2000).

[36] J. D. Schnittman, private communication; *"Spin-Orbit Resonance in Compact Binary LIGO Sources,"* talk given at LSC workshop, Hanford, August 2002.